Related titles

Handbook of Laser Welding Technology
(ISBN 978-0-85709-264-9)

Handbook of Solid State Lasers
(ISBN 978-0-85709-272-4)

Semiconductor Lasers
(ISBN 978-0-85709-121-5)

Woodhead Publishing Series in Electronic and Optical Materials: Number 88

Laser Additive Manufacturing

Materials, Design, Technologies, and Applications

Edited by

Milan Brandt

AMSTERDAM • BOSTON • CAMBRIDGE • HEIDELBERG
LONDON • NEW YORK • OXFORD • PARIS • SAN DIEGO
SAN FRANCISCO • SINGAPORE • SYDNEY • TOKYO
Woodhead Publishing is an imprint of Elsevier

Woodhead Publishing is an imprint of Elsevier
The Officers' Mess Business Centre, Royston Road, Duxford, CB22 4QH, United Kingdom
50 Hampshire Street, 5th Floor, Cambridge, MA 02139, United States
The Boulevard, Langford Lane, Kidlington, OX5 1GB, United Kingdom

Copyright © 2017 Elsevier Ltd. All rights reserved.

No part of this publication may be reproduced or transmitted in any form or by any means, electronic or mechanical, including photocopying, recording, or any information storage and retrieval system, without permission in writing from the publisher. Details on how to seek permission, further information about the Publisher's permissions policies and our arrangements with organizations such as the Copyright Clearance Center and the Copyright Licensing Agency, can be found at our website: www.elsevier.com/permissions.

This book and the individual contributions contained in it are protected under copyright by the Publisher (other than as may be noted herein).

Notices
Knowledge and best practice in this field are constantly changing. As new research and experience broaden our understanding, changes in research methods, professional practices, or medical treatment may become necessary.

Practitioners and researchers must always rely on their own experience and knowledge in evaluating and using any information, methods, compounds, or experiments described herein. In using such information or methods they should be mindful of their own safety and the safety of others, including parties for whom they have a professional responsibility.

To the fullest extent of the law, neither the Publisher nor the authors, contributors, or editors, assume any liability for any injury and/or damage to persons or property as a matter of products liability, negligence or otherwise, or from any use or operation of any methods, products, instructions, or ideas contained in the material herein.

Library of Congress Cataloging-in-Publication Data
A catalog record for this book is available from the Library of Congress

British Library Cataloguing-in-Publication Data
A catalogue record for this book is available from the British Library

ISBN: 978-0-08-100433-3 (print)
ISBN: 978-0-08-100434-0 (online)

For information on all Woodhead Publishing publications visit our website at https://www.elsevier.com/

Publisher: Matthew Deans
Acquisition Editor: Kayla Dos Santos
Editorial Project Manager: Heather Cain
Production Project Manager: Poulouse Joseph
Designer: Victoria Pearson

Typeset by TNQ Books and Journals

List of contributors

R.C.Y. Auyeung Naval Research Laboratory, Washington, DC, United States

T. Baldacchini Newport Corporation, Irvine, CA, United States

M. Brandt RMIT University, Centre for Additive Manufacturing, Melbourne, VIC, Australia

F. Brückner Fraunhofer IWS, Dresden, Germany

N. Charipar Naval Research Laboratory, Washington, DC, United States

B. Chichkov Laser Zentrum Hannover e.V., Hannover, Germany

A. Deiwick Laser Zentrum Hannover e.V., Hannover, Germany

M. Easton RMIT University, Centre for Additive Manufacturing, Melbourne, VIC, Australia

C. Emmelmann Hamburg University of Technology (TUHH), Hamburg, Germany; LZN Laser Zentrum Nord GmbH, Hamburg, Germany

R.J. Friel Loughborough University, Loughborough, United Kingdom

R. Goodridge University of Nottingham, Nottingham, United Kingdom

A. Goulas Loughborough University, Loughborough, United Kingdom

Y. Hagedorn Aconity3D, Aachen, North Rhine-Westphaila, Germany

D. Herzog Hamburg University of Technology (TUHH), Hamburg, Germany

R. Hölker-Jäger Technische Universität Dortmund, Dortmund, Germany

U. Jahnke Paderborn University, Paderborn, Germany

L.J. Jiang University of Nebraska-Lincoln, Lincoln, NE, United States

H. Kim Naval Research Laboratory, Washington, DC, United States

L. Koch Laser Zentrum Hannover e.V., Hannover, Germany

J.H. Koo The University of Texas at Austin, Austin, TX, United States; KAI, LLC, Austin, TX, United States

J. Kranz Hamburg University of Technology (TUHH), Hamburg, Germany

M. Leary RMIT University, Centre for Additive Manufacturing, Melbourne, VIC, Australia

C. Leyens Fraunhofer IWS, Dresden, Germany, and Technische Universität Dresden, Dresden, Germany

C.F.W. Lindemann Paderborn University, Paderborn, Germany

F. Liou Missouri University of Science and Technology, Rolla, Missouri, United States

R. Liu Missouri University of Science and Technology, Rolla, Missouri, United States

Y.F. Lu University of Nebraska-Lincoln, Lincoln, NE, United States

S. Mathews Naval Research Laboratory, Washington, DC, United States

J. Mazumder The University of Michigan, Ann Arbor, MI, United States

M. Mazur RMIT University, Centre for Additive Manufacturing, Melbourne, VIC, Australia

M. McMillan RMIT University, Centre for Additive Manufacturing, Melbourne, VIC, Australia

M. Munsch Implantcast GmbH, Buxtehude, Germany

J. Newkirk Missouri University of Science and Technology, Rolla, Missouri, United States

B. Ong The University of Texas at Austin, Austin, TX, United States

R. Ortiz The University of Texas at Austin, Austin, TX, United States

A. Piqué Naval Research Laboratory, Washington, DC, United States

D. Shidid RMIT University, Centre for Additive Manufacturing, Melbourne, VIC, Australia

T. Sparks Missouri University of Science and Technology, Rolla, Missouri, United States

S. Sun RMIT University, Centre for Additive Manufacturing, Melbourne, VIC, Australia

A.E. Tekkaya Technische Universität Dortmund, Dortmund, Germany

Z. Wang Missouri University of Science and Technology, Rolla, Missouri, United States

H. Wu The University of Texas at Austin, Austin, TX, United States

W. Xiong University of Nebraska-Lincoln, Lincoln, NE, United States; Huazhong University of Science and Technology, Wuhan, Hubei, China

S. Ziegelmeier BMW Group, Munich, Germany

Woodhead Publishing Series in Electronic and Optical Materials

1 **Circuit analysis**
J. E. Whitehouse
2 **Signal processing in electronic communications: For engineers and mathematicians**
M. J. Chapman, D. P. Goodall and N. C. Steele
3 **Pattern recognition and image processing**
D. Luo
4 **Digital filters and signal processing in electronic engineering: Theory, applications, architecture, code**
S. M. Bozic and R. J. Chance
5 **Cable engineering for local area networks**
B. J. Elliott
6 **Designing a structured cabling system to ISO 11801: Cross-referenced to European CENELEC and American Standards**
Second edition
B. J. Elliott
7 **Microscopy techniques for materials science**
A. Clarke and C. Eberhardt
8 **Materials for energy conversion devices**
Edited by C. C. Sorrell, J. Nowotny and S. Sugihara
9 **Digital image processing: Mathematical and computational methods**
Second edition
J. M. Blackledge
10 **Nanolithography and patterning techniques in microelectronics**
Edited by D. Bucknall
11 **Digital signal processing: Mathematical and computational methods, software development and applications**
Second edition
J. M. Blackledge
12 **Handbook of advanced dielectric, piezoelectric and ferroelectric materials: Synthesis, properties and applications**
Edited by Z.-G. Ye
13 **Materials for fuel cells**
Edited by M. Gasik
14 **Solid-state hydrogen storage: Materials and chemistry**
Edited by G. Walker
15 **Laser cooling of solids**
S. V. Petrushkin and V. V. Samartsev

16 **Polymer electrolytes: Fundamentals and applications**
Edited by C. A. C. Sequeira and D. A. F. Santos
17 **Advanced piezoelectric materials: Science and technology**
Edited by K. Uchino
18 **Optical switches: Materials and design**
Edited by S. J. Chua and B. Li
19 **Advanced adhesives in electronics: Materials, properties and applications**
Edited by M. O. Alam and C. Bailey
20 **Thin film growth: Physics, materials science and applications**
Edited by Z. Cao
21 **Electromigration in thin films and electronic devices: Materials and reliability**
Edited by C.-U. Kim
22 ***In situ* characterization of thin film growth**
Edited by G. Koster and G. Rijnders
23 **Silicon-germanium (SiGe) nanostructures: Production, properties and applications in electronics**
Edited by Y. Shiraki and N. Usami
24 **High-temperature superconductors**
Edited by X. G. Qiu
25 **Introduction to the physics of nanoelectronics**
S. G. Tan and M. B. A. Jalil
26 **Printed films: Materials science and applications in sensors, electronics and photonics**
Edited by M. Prudenziati and J. Hormadaly
27 **Laser growth and processing of photonic devices**
Edited by N. A. Vainos
28 **Quantum optics with semiconductor nanostructures**
Edited by F. Jahnke
29 **Ultrasonic transducers: Materials and design for sensors, actuators and medical applications**
Edited by K. Nakamura
30 **Waste electrical and electronic equipment (WEEE) handbook**
Edited by V. Goodship and A. Stevels
31 **Applications of ATILA FEM software to smart materials: Case studies in designing devices**
Edited by K. Uchino and J.-C. Debus
32 **MEMS for automotive and aerospace applications**
Edited by M. Kraft and N. M. White
33 **Semiconductor lasers: Fundamentals and applications**
Edited by A. Baranov and E. Tournie
34 **Handbook of terahertz technology for imaging, sensing and communications**
Edited by D. Saeedkia
35 **Handbook of solid-state lasers: Materials, systems and applications**
Edited by B. Denker and E. Shklovsky
36 **Organic light-emitting diodes (OLEDs): Materials, devices and applications**
Edited by A. Buckley
37 **Lasers for medical applications: Diagnostics, therapy and surgery**
Edited by H. Jelínková
38 **Semiconductor gas sensors**
Edited by R. Jaaniso and O. K. Tan

39 **Handbook of organic materials for optical and (opto)electronic devices: Properties and applications**
Edited by O. Ostroverkhova
40 **Metallic films for electronic, optical and magnetic applications: Structure, processing and properties**
Edited by K. Barmak and K. Coffey
41 **Handbook of laser welding technologies**
Edited by S. Katayama
42 **Nanolithography: The art of fabricating nanoelectronic and nanophotonic devices and systems**
Edited by M. Feldman
43 **Laser spectroscopy for sensing: Fundamentals, techniques and applications**
Edited by M. Baudelet
44 **Chalcogenide glasses: Preparation, properties and applications**
Edited by J.-L. Adam and X. Zhang
45 **Handbook of MEMS for wireless and mobile applications**
Edited by D. Uttamchandani
46 **Subsea optics and imaging**
Edited by J. Watson and O. Zielinski
47 **Carbon nanotubes and graphene for photonic applications**
Edited by S. Yamashita, Y. Saito and J. H. Choi
48 **Optical biomimetics: Materials and applications**
Edited by M. Large
49 **Optical thin films and coatings**
Edited by A. Piegari and F. Flory
50 **Computer design of diffractive optics**
Edited by V. A. Soifer
51 **Smart sensors and MEMS: Intelligent devices and microsystems for industrial applications**
Edited by S. Nihtianov and A. Luque
52 **Fundamentals of femtosecond optics**
S. A. Kozlov and V. V. Samartsev
53 **Nanostructured semiconductor oxides for the next generation of electronics and functional devices: Properties and applications**
S. Zhuiykov
54 **Nitride semiconductor light-emitting diodes (LEDs): Materials, technologies and applications**
Edited by J. J. Huang, H. C. Kuo and S. C. Shen
55 **Sensor technologies for civil infrastructures**
Volume 1: Sensing hardware and data collection methods for performance assessment
Edited by M. Wang, J. Lynch and H. Sohn
56 **Sensor technologies for civil infrastructures**
Volume 2: Applications in structural health monitoring
Edited by M. Wang, J. Lynch and H. Sohn
57 **Graphene: Properties, preparation, characterisation and devices**
Edited by V. Skákalová and A. B. Kaiser
58 **Silicon-on-insulator (SOI) technology**
Edited by O. Kononchuk and B.-Y. Nguyen

59 **Biological identification: DNA amplification and sequencing, optical sensing, lab-on-chip and portable systems**
Edited by R. P. Schaudies

60 **High performance silicon imaging: Fundamentals and applications of CMOS and CCD sensors**
Edited by D. Durini

61 **Nanosensors for chemical and biological applications: Sensing with nanotubes, nanowires and nanoparticles**
Edited by K. C. Honeychurch

62 **Composite magnetoelectrics: Materials, structures, and applications**
G. Srinivasan, S. Priya and N. Sun

63 **Quantum information processing with diamond: Principles and applications**
Edited by S. Prawer and I. Aharonovich

64 **Advances in non-volatile memory and storage technology**
Edited by Y. Nishi

65 **Laser surface engineering: Processes and applications**
Edited by J. Lawrence, C. Dowding, D. Waugh and J. Griffiths

66 **Power ultrasonics: Applications of high-intensity ultrasound**
Edited by J. A. Gallego-Juárez and K. F. Graff

67 **Advances in delay-tolerant networks (DTNs): Architectures, routing and challenges**
Edited by J. J. P. C. Rodrigues

68 **Handbook of flexible organic electronics: Materials, manufacturing and applications**
Edited by S. Logothetidis

69 **Machine-to-machine (M2M) communications: Architecture, performance and applications**
Edited by C. Anton-Haro and M. Dohler

70 **Ecological design of smart home networks: Technologies, social impact and sustainability**
Edited by N. Saito and D. Menga

71 **Industrial tomography: Systems and applications**
Edited by M. Wang

72 **Vehicular communications and networks: Architectures, protocols, operation and deployment**
Edited by W. Chen

73 **Modeling, characterization and production of nanomaterials: Electronics, photonics and energy applications**
Edited by V. Tewary and Y. Zhang

74 **Reliability characterisation of electrical and electronic systems**
Edited by J. Swingler

75 **Industrial wireless sensor networks: Monitoring, control and automation**
Edited by R. Budampati and S. Kolavennu

76 **Epitaxial growth of complex metal oxides**
Edited by G. Koster, M. Huijben and G. Rijnders

77 **Semiconductor nanowires: Materials, synthesis, characterization and applications**
Edited by J. Arbiol and Q. Xiong

78 **Superconductors in the Power Grid**
Edited by C. Rey

79 **Optofluidics, sensors and actuators in microstructured optical fibres**
Edited by S. Pissadakis

80 **Magnetic nano- and microwires: Design, synthesis, properties and applications**
Edited by M. Vázquez
81 **Robust design of microelectronic assemblies against mechanical shock, temperature and moisture**
E.-H. Wong and Y.-W. Mai
82 **Biomimetic technologies: Principles and applications**
Edited by T. D. Ngo
83 **Directed self-assembly of block co-polymers for nano-manufacturing**
Edited by R. Gronheid and P. Nealey
84 **Photodetectors**
Edited by B. Nabet
85 **Fundamentals and applications of nanophotonics**
Edited by J. Haus
86 **Advances in chemical mechanical planarization (CMP)**
Edited by S. Babu
87 **Wireless MEMs networks and applications**
Edited by D. Uttamchandani
88 **Laser additive manufacturing: Materials, design, technologies, and applications**
Edited by M. Brandt

The role of lasers in additive manufacturing

M. Brandt
RMIT University, Centre for Additive Manufacturing, Melbourne, VIC, Australia

Introduction

The discovery of the laser 56 years ago [1] aroused the imagination of many in the scientific and engineering communities, the general public, and the media. It was hailed as one of the major scientific discoveries of the 20th century, and for many of its early years was indiscriminately applied to a whole range of applications earning the tag of a "solution looking for a problem." The laser has come a long way since those early days. In the manufacturing arena, the laser is now mature technology that has been instrumental in the development of many products and has helped create many new market opportunities. Compared with the early days of laser development, during which the laser was the domain of physicists and hence considered very much a research device to be investigated and optimized, today a number of these lasers are sufficiently mature technologies, allowing them to be designed and constructed using the principles of machine tool design and manufacture. This transition from a more or less scientific device to a machine tool has had an enormous impact on the laser's use in a diverse range of applications in manufacturing: to replace conventional manufacturing methods, to increase productivity, to improve the quality of products, and to reduce manufacturing costs.

The applications of lasers have been steadily increasing over the years, and their impact has been felt in many industrial sectors such as instrumentation, mining, defense, aerospace, automotive, energy, entertainment, and biomedical. In the manufacturing sense the major applications of lasers are in cutting, welding, drilling, marking, treating material surfaces, and, in the past 5 years, additive manufacturing (AM) [2–5].

AM, more commonly referred to three-dimensional (3D) printing, is differentiated from conventional manufacturing processes in that the material is added to form a desired solid geometry instead of subtracted, as in conventional machining processes. AM processes are not subject to the constraints associated with traditional manufacturing methods, and they provide significant opportunities for the design of novel geometries and complex internal structures to enhance component properties, such as the strength-to-weight ratio and cooling, in comparison to traditional manufacturing methods. AM is now the fastest-growing sector of manufacturing globally. Wohlers Associates' 2016 annual Wohlers Report [6], the most recognized and comprehensive account of the state of the global additive manufacturing industry, indicates that the 3D printing industry grew by US$1 billion to a total of $5165 billion in

2015. This represents a total compound annual growth rate of 25.9% in 2015, which is slightly lower than the 33.8% compound annual growth rate of the past 3 years. This trend is continuing. Global companies such as Stryker, Audi, BMW, Boeing, Ford, General Electric, Hewlett-Packard, and Nike—to name a few—as well as many small and medium-sized organizations globally, use the technology extensively. Airbus and Alcoa signed a US$1 billion contract in 2015 in which Alcoa agreed to manufacture bolts and fasteners that now fly on every Airbus platform [7]. Popular press, trade, and technical journals are reporting almost daily on new and innovative printers, parts additively manufactured in both metal alloys and polymers, and component designs for AM that challenge the imagination. Many countries have also recently established large national programs in AM to further accelerate the development of both new AM technology and its applications.

This move to direct digital manufacturing is being greatly driven by globalization. Globalization is changing the nature and economics of manufacturing in "high-wage" or "first-world" countries. On one hand, globalization has led to new markets but, on the other, to new competitors, in particular those from "low-wage" countries. In addition, globalization has also led to increased product individualization and product segmentation, with the associated cost pressures and production scaling effects. Therefore, handling the challenge of product cost pressures, diversity, and dynamics becomes the central focus for manufacturing companies in "high-wage" countries such as the United States, Germany, United Kingdom, France, Japan, and Australia. Advanced technology and research are seen as critical elements in addressing some of these challenges to deliver cost-competitive approaches to manufacturing for the companies in high-wage countries to remain profitable and in business. AM is seen as a solution to boost in-country manufacturing because of the many benefits it offers compared with traditional subtractive manufacturing. With current additive technologies, functional polymer and metal parts can be built directly from computer models or from measurements of existing components to be reengineered, as opposed to the early days of rapid prototyping, and therefore bypass traditional manufacturing processes such as cutting, milling, and grinding. Benefits of AM, shown in Fig. 1, include (1) new designs not possible using conventional subtractive technology; (2) dramatic savings in time, materials, waste, energy, and other costs in producing new components; (3) significant reductions in environmental impact; and (4) faster time to market for products.

Part One of this book discusses technology, processes, and materials used in laser AM. Discussed in Part Two are the new design principles behind laser AM, and Part Three describes some applications that are so advanced in terms of productivity, product quality, and ease of operation that they have replaced or almost eliminated equivalent traditional processes. The size of the global industrial laser market for all laser sources in 2016 is estimated to be some US$3.3 billion and for additive laser sources approximately US$100 million [9]. This diversity of applications stems from the following main benefits of lasers, including as AM tools:

- The ability to produce a wide range of wavelengths
- The ability to produce a wide range of irradiance (power per unit area) levels at the surface of a workpiece, thereby changing the physical state of that surface from solid to melting through a noncontact interaction

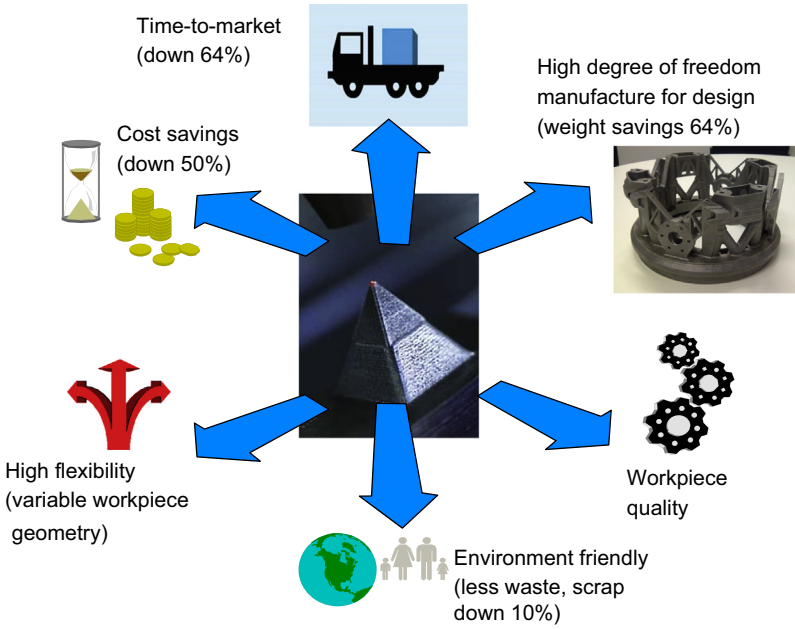

Figure 1 Benefits of additive manufacturing. Percentages in parentheses refer to savings in the aerospace and defense sectors [8].

- The ability to easily manipulate the beam through computer numerical control techniques because it has no weight or mechanical contact with the workpiece
- The ability to shape the laser beam on the workpiece both spatially and temporally, thus enabling the processing of a wide range of materials and component shapes

The most serious drawback of laser technology for AM and in general is still its cost. Although the unit cost of laser power from different industrial lasers has been steadily declining because of technological improvements and increases in volume sales, for many applications the laser is still too costly compared with alternative manufacturing technologies, even though it can perform the application well. In general, lasers offer the most promise and economic benefits for processes that are difficult or impossible to perform using conventional technologies, or in situations that can lead to the elimination of one or more manufacturing steps in the production of a component (or part) or for production of a limited number of parts.

Laser as tool in AM

The laser is seen as playing a pivotal role in the growth of AM systems and metal AM, in particular recently. It is at the "heart" of metal AM technology, and its developments in terms of power, efficiency, beam quality, and reliability parallel the growth and application of metal AM systems globally. The laser metal AM approaches involve "powder or

wire-fed" or laser metal deposition and "powder bed" or selective laser melting. These two technologies are discussed in detail in Chapters 1 and 2, and only highlights and trends are included here. In general it can be said that both technologies have significantly affected the manufacture of new components and maintenance, repair, and overhaul of small and large components in the aerospace, defense, power generation, mining, and general manufacturing industries globally and will continue to do so in the future. The two laser metal AM technologies are compared in Table 1.

Of the many laser sources that have been discovered over the years, the carbon dioxide (CO_2) and the flashlamp and diode-pumped neodymium-doped yttrium-aluminum-garnet (Nd:YAG) lasers have dominated metal AM from about the late 1980s to early 2000s. Since then fiber, disk, and diode lasers have become the lasers of choice for these applications, primarily because of their overall efficiency (around 30–40%), fiber beam delivery, and general robustness, which have considerably simplified and improved processing [2]. In the case of polymer powder processing, the CO_2 laser is the laser of choice because of the high polymer absorptivity at the CO_2 laser wavelength. Similarly, for the processing of photo polymers, blue diode lasers have replaced traditional ultraviolet lamps.

Although the laser is at the "heart" of an AM system from a manufacturing point of view, the laser by itself is seemingly ineffectual. The laser must be used in conjunction with several different pieces of optical and mechanical equipment, which need to be integrated into a functional unit to be able to process materials and manufacture parts. The key elements of an AM system comprise:

- Laser source
- Beam delivery and processing optics for focusing the beam and delivering powder and wire

Table 1 Comparison of the general characteristics of the two laser metal additive manufacturing technologies

Selective laser melting (SLM)

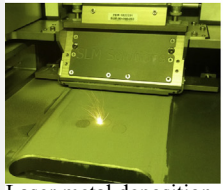

Laser metal deposition (LMD)

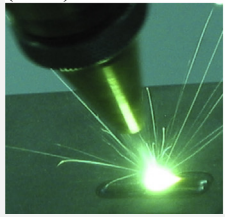

Characteristics	LMD (powder-fed)	SLM (powder-bed)
Materials	Large materials diversity	• Limited and lower experience in comparison to LMD
Part dimensions	Limited by the handling system	Limited by the process chamber
Part complexity	Limited	Nearly unlimited
Dimensional accuracy	≥ 0.1 mm	≥ 0.1 mm
Build-up rate	10–80 cm^3/h	2–40 cm^3/h
Build-up on	• 3D-surface • On existing parts	• Flat surface • Flat preforms
Roughness R_z	60–500 µm	10–50 µm
Layer thickness	≥ 0.03–1 mm	≥ 0.03–1 mm

- Multiaxis, numerically controlled motion system covering both Cartesian and robot-based systems for controlling part movement
- Operating software

The research and advances in these key system elements over many years are now contributing to the growth of AM technology globally.

Laser–matter interaction in AM

The physics of laser–matter interaction in AM processes are now reasonably well understood, and many references describe this [3,10]. In general, laser processing of materials (metals in particular) is a controlled heating process whereby the laser acts as a source of controllable heat because light carries energy. In the case of photopolymers, the absorbed laser light polymerizes or hardens the area of the polymer that it irradiates, producing a solid part. When a laser beam impinges on the surface of a material—either a solid, powder, or liquid—some light is reflected, some is absorbed, and some may be transmitted, depending on the optical properties of the workpiece. The fraction of the laser beam that is absorbed by the surface of a material in the case of metals is transformed into heat through electron–phonon interaction, and this heat raises the temperature of the surface to achieve the required melting state of the material for AM.

Laser output power, spatial distribution, time dependence (pulsed or continuous), beam diameter, and beam divergence affect how well the beam can be controlled in terms of the rate at which energy can be delivered to the material and how this energy is distributed spatially. Wavelength is a key factor in determining the laser most suitable for a particular process. The coupling of energy into the material will be zero, and consequently no heating or change of state will occur unless a wavelength at which there is some absorption is selected. The angle of incidence of the beam to the material and its polarization characteristics determine how much of the incident laser light is reflected from its surface. Spatial distribution [2,3] of the laser beam on the surface of a material affects the maximum irradiance obtained and the resultant temperature distribution. For example, for a Gaussian laser beam intensity distribution with the maximum intensity at the center, the temperature of the melt pool surface is higher at the center in comparison to its boundary, producing a radial temperature gradient across it. This temperature gradient implies a surface tension gradient because the surface tension is dependent on temperature. Surface tension drives the surface profile and mass flow in a melt pool through the Marangoni (convection) currents. The physics of melt pool interactions with injected particles in the case of "powder- and wire-fed" systems and subsequent mass flow has been investigated and modeled by a number of groups, and it is reasonably well understood [3]. The physics of melt pool generation and mass transfer in a "powder bed" system is not as well understood and is attracting more attention as the maximum output power of the lasers used increases [11].

From a systems engineering perspective, spatial distribution of laser beams in AM systems is governed by the system manufacturers, who tend to optimize it for the

application. For powder bed systems, the beam is usually Gaussian in nature; for powder- and wire-fed systems it is "top-hat."

Properties of the laser beam are only one part of the process governing laser AM. The other aspect is material properties because they influence how easily and quickly the material can be processed. These include the reflectivity of the surface at the laser wavelength, its thermal conductivity and diffusivity, material density, latent heat of melting, and heat capacity. Of these, surface reflectivity is perhaps the dominant material property because it influences the absorption of laser radiation. In general, the reflectivity of metals decreases with decreasing wavelength so that the efficiency of the process is improved by using a shorter-wavelength laser. Laser AM of metals with a fiber, diode, or disk laser with a wavelength around 1 μm is more efficient compared with processing with a CO_2 laser operating at 10 μm because of greater metal absorptivity at the shorter wavelength. In the case of AM of nonmetals, such as ceramics and polymer powders, the reflectivity is lower at longer wavelengths so that the CO_2 laser is the laser of choice for processing them. In the case of metals, the exact value of the reflectivity is a function of a number of variables, including surface finish and the state of oxidation. Rough and/or oxidized surfaces, for example, during a build, have lower reflectivity and hence assist in coupling more energy into the surface [2,3]. The roughness of the surface can decrease reflectivity by 50% [2]. It should be noted, however, that oxidation of the metal is not always beneficial because the oxide might have a much higher melting temperature than the pure metal, as in the case of aluminum, so that process efficiency is reduced. The reflectivity of metal surfaces also decreases with increasing surface temperature and so changes dynamically during processing [2,3], thus increasing considerably the coupling of radiation into the material and the generated melt pool.

In the case of metal powder, the beam−matter interaction is more complicated because of multiple laser beam reflections from the alloy particles that can take place either in powder-fed or powder bed systems, which increases absorption. King et al. [11] calculated and measured powder absorptivity at 1 μm as a function of powder temperature for SS316, Ti64, and pure Al powder for a powder bed system, and the results indicate absorptivity values in the range of 0.65 to 0.55. These values are higher compared with those for powder-fed systems, which are on the order of 10−20% for typical powder mass flow rates of 0.1−0.4 g/s as a result of the predominantly surface absorptivity of the layer being deposited on. The light−particle interaction during flight contributes to the overall absorptivity, but to a lesser degree compared with the powder bed scenario. Depending on the laser parameters used, and therefore the resultant melt pool temperature, sintering of the powder or vaporization of alloys with a low melting temperature can occur during processing in both cases, which can affect the mechanical properties of the manufactured components.

The flow of heat in a material is determined by its thermal diffusivity and conductivity. The significance of these terms is that they determine how rapidly a material accepts and conducts thermal energy and consequently influence the temperature distribution in the part as it is being built. A low thermal diffusivity limits the

penetration of heat into the part, necessitating a different build strategy compared with materials with a high thermal diffusivity. The specific heat, density, and latent heat of the material determine how much of the absorbed energy is consumed in phase changes. From a laser AM point of view, metals such as aluminum and copper alloys possess a combination of thermal and optical properties that make them more difficult to process compared with steels, titanium, and nickel-based alloys. To process these materials, higher laser intensities and shorter dwell times are generally adopted to minimize conduction losses and obtain requisite temperature increases for melt pool creation.

Trends in powder- or wire-fed technology

In the powder- or wire-fed approach, spherical metal alloy powder, with particles typically 50−100 μm in diameter, and solid wire around 1−2 mm in diameter is injected into a melt pool created by a laser on the surface of a workpiece. The laser radiation melts the powder or wire and fuses it to the layer below, producing a clad bead as a result of the relative motion of the processing head and the workpiece. The two materials are metallurgically bonded, with a relatively small heat-affected zone present in the substrate material. By overlapping single beads, typically 50−60% of the track width, 2-dimensional and 2.5-dimensional layers are produced, and by depositing layers in the *z* direction, 3D parts can be manufactured. The 2-dimensional and 2.5-dimensional technology has been around since the 1980s, is well researched and understood, and has been adopted by many industries for repairing and rebuilding parts and improving the wear and corrosion properties of engineering surfaces [2,3,12]. The manufacture of 3D structures is more recent and focuses on materials and process monitoring and control since the process is still run open-loop in commercial systems and subject to poor control of part dimensions as it is being built as a result of metal slumping caused by local overheating. A schematic of the process is illustrated in Fig. 2.

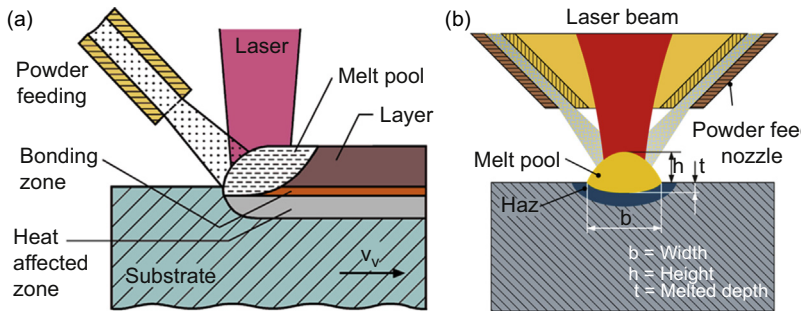

Figure 2 Schematic of the "powder-fed" process with (a) off-axis powder feeding and (b) continuous coaxial powder feeding [13]. *HAZ*, Heat-affected zone.

The laser is the source of heat for the process and its power, beam diameter, and intensity profile on the surface of the workpiece affect build rates, microstructure, and, through the microstructure, component properties. The diode, fiber, and disk lasers commonly used for AM of components have powers at the workpiece typically in the range 3−5 kW and laser spot sizes up to 7 mm, although lasers with powers up to 10 and 20 kW have been reported. The key feature of the process is technology for delivering powder or wire consistently and efficiently into the melt pool. The powder nozzle technology is now also well designed and engineered. Illustrated in Table 2 are the three common types of powder delivery nozzles and their characteristics.

All powder nozzles feature specific advantages and disadvantages dependent on the powder delivery concept. The choice of a suitable powder nozzle is application specific and, consequently, part and material dependent as well as process specific. The characteristics of the three common powder delivery nozzles used for AM are listed in Table 2 [14].

Under normal AM operation, the laser spot size is preset to maximize the build rate, for example, or minimize the heat buildup in more delicate components. In some cases of part repair—for example the repair of blisks (Fig. 3), the cross-sectional area of the part varies in the XY plane.

To achieve a near-net-shape deposit and avoid bead overlap within a layer with potential defects, a variable beam focus optic has been developed (Fig. 4) that is numerically controlled. This allows a variable beam diameter and, consequently, melt pool with an adjusted powder mass flow rate to be achieved in a single pass.

In component repair, in particular where part accessibility is restricted, internal powder deposition nozzles have been developed. Illustrated in Fig. 5 is the internal deposition configuration at RMIT University. These nozzles are based on powder delivery principles similar to those for powder nozzles used for external surfaces, can access minimal internal bore diameters of typically 30 mm and a depth up to 700 mm. The applied laser power is up to 3 kW.

Laser-based AM processes concentrate the heat to a relatively small localized area of the part based on the laser spot size. Hence high precision is achieved, with good metallurgical bonding between layers and relatively low distortion because of the low heat input. In some cases, however, materials are difficult to deposit and can suffer cold or hot cracking, completely negating the benefits of AM. One major reason for this is the thermal contraction of molten material during cooling to an ambient temperature. Residual stresses yield plastic deformation, distortion, and even cracking and delamination in the case of brittle materials. Unfavorable phase transformations, for example, martensite formation, can also increase such adverse effects. A solution for this is the addition of another heat source to pre and post heat the deposited material and the substrate and thus reduce the heating and cooling rates experienced by the material. The additional heat is supplied by an induction coil mounted in close proximity to the powder deposition head. By means of this additional heat source, the propensity for cracking can be reduced, extending the applicability of the technology to a greater variety of materials and applications. This hybrid laser AM technology is discussed in more detail in Chapter 3 by Bruckner and Leyens.

Table 2 Specific advantages and disadvantages of powder nozzles used in "powder-fed" additive manufacturing [14]

Powder feeding arrangement	Advantages	Disadvantages	Suitable for
Lateral or off-axis 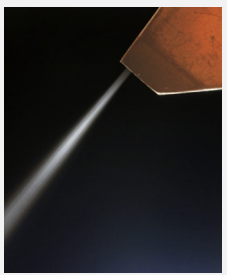	• Part accessibility • Width of deposited track: 0.5−25 mm • Laser power up to 20 kW maximum	• Directional deposition • Less powder efficiency • Alignment between powder and laser beam • No integrated protective gas feeding	• Directional deposition • Specific requirements in terms of part accessibility
Continuous coaxial 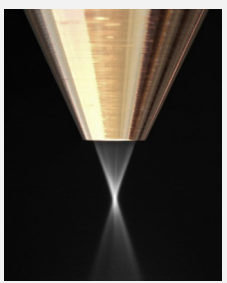	• Unidirectional deposition • Width of deposited track: 0.3−5 mm • Applied laser power: up to 3 kW maximum • Powder efficiency: maximum 90% (diameter of powder-gas jet in the focus: minimum 400 µm) • Integrated protective gas feeding	• Restricted part accessibility • Gravity influence, no deposition for tilting angles >20 degrees because of inhomogeneous powder density distribution	• 3D deposition up to tilting angles of approximately 20 degrees • Largest effect from integrated protective gas feeding

Continued

Table 2 Continued

Powder feeding arrangement	Advantages	Disadvantages	Suitable for
Discontinuous coaxial 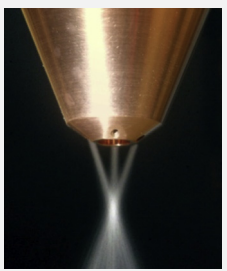	• Unidirectional deposition • Width of deposited track: 2−7 mm • Applied laser power up to 5 kW maximum • Unrestricted 3D functionality • Integrated protective gas feeding	• Restricted part accessibility • Low powder efficiency (diameter of powder-gas jet in the focus: minimum 2.5 mm)	• 3D deposition up to tilting angles of 180 degrees (overhead processing is feasible)

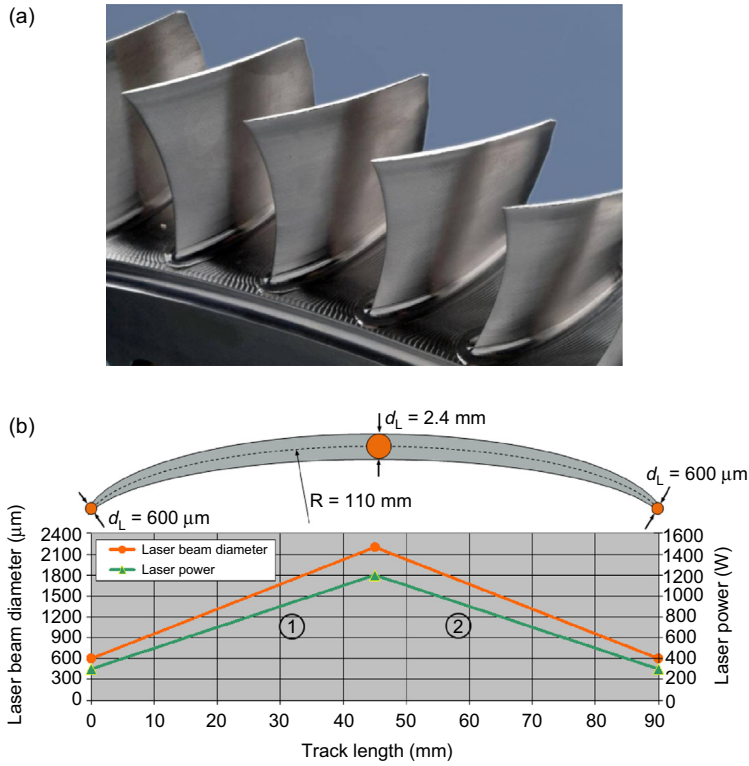

Figure 3 (a) Blisks. (b) The cross-sectional profile and deposition strategy for rebuilding a blisk with variable laser beam diameter and power [15].

Trends in powder bed technology

The powder bed or selective laser melting (SLM) technology was invented by Fraunhofer ILT in mid 1990s and is now one of the fastest growing AM technologies globally. The Wohlers report [6] indicates that in 2015, some 800 metal AM machines—of which 90% were laser based—were sold globally. This represents a growth of approximately 50% compared with that in 2014 and over 200% compared with that in 2013. It is now not only being explored but also adopted in production in the aerospace, biomedical, defense, automotive, and many other industries because of the benefits it offers (discussed above) compared with conventional manufacturing. Illustrated in Fig. 6 is a Ti64 spinal disc designed and manufactured at the RMIT Advanced Manufacturing Precinct that was implanted in a patient in 2015.

The process, illustrated in Fig. 7, involves a layer of spherical metal powder (typically 20–45 µm in diameter and 30–100 µm thick) spread uniformly across a metal platform. A laser beam scans across it using high-speed XY galvanometers based on the computer-generated tool path. The focused laser beam fully melts the powder

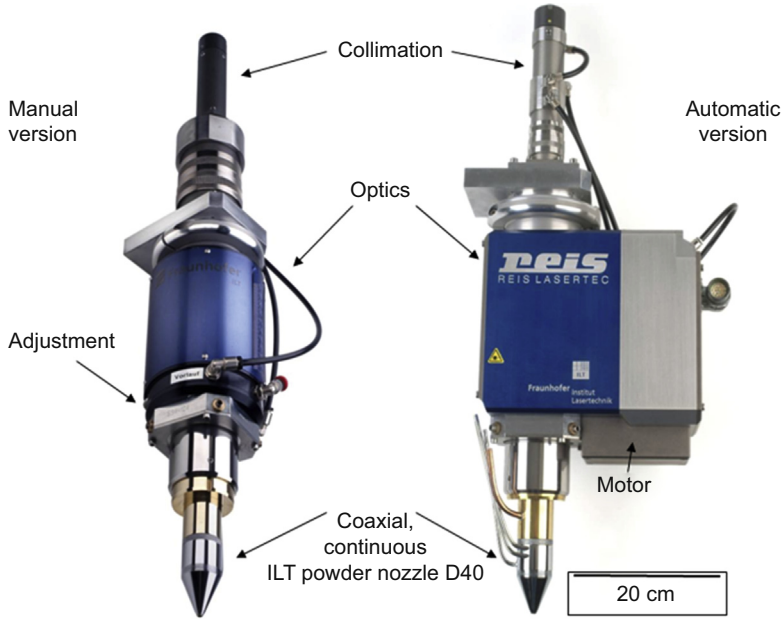

Figure 4 Zoom optics for adaptive additive manufacturing. Manual version (left) and automatic, numerically controlled version (right) [16].

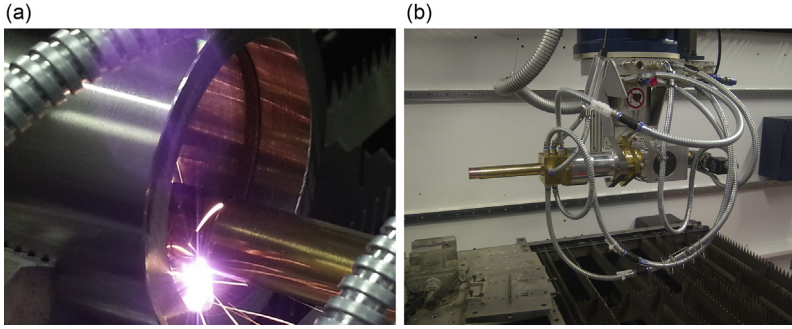

Figure 5 (a) Internal cladding repair of a part. (b) Internal cladding head at RMIT Advanced Manufacturing Precinct mounted on a TRUMPF 7020 system.

and fuses it to the layer below, after which the platform descends one layer thickness and the whole process is repeated until the part is manufactured.

The build platform is located inside a metal chamber and is protected with a homogenous flow of inert gas (argon, nitrogen) during processing to prevent melt pool oxidation and assist in removing generated metal vapor. Depending on the orientation of the part and the angles relative to normal that need to be built, support structures are generally required to be incorporated for part angles typically larger that 50 degrees. Illustrated in Fig. 8 are the steps in the manufacturing of a part.

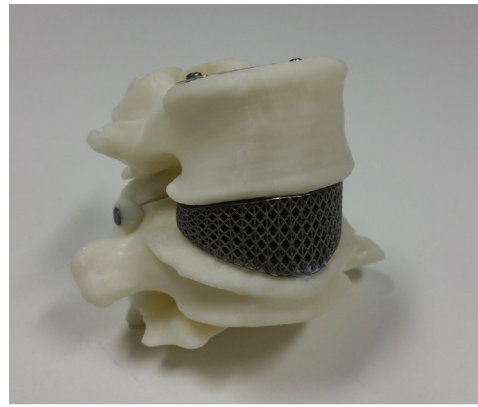

Figure 6 Titanium spinal disc in a model of deformed lumbar vertebrae. Disc design is based on a complex lattice structure designed to both take the load and allow X-ray computed tomography monitoring after the operation.

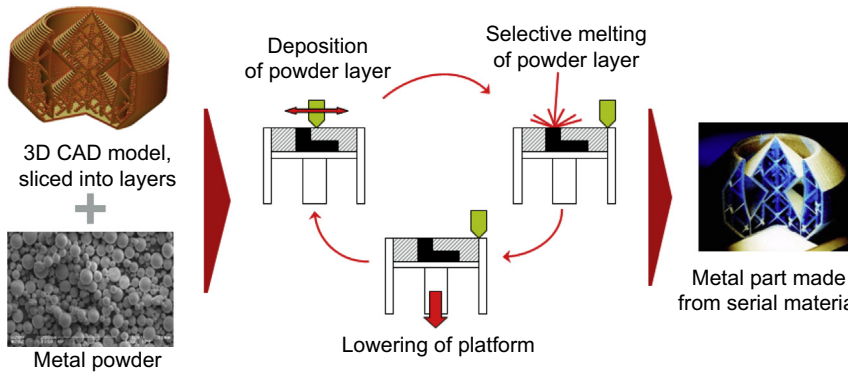

Figure 7 Schematic of the powder bed process. *3D*, three-dimensional; *CAD*, computer-aided design. Courtesy of Fraunhofer ILT.

The manufacturing process itself is very complex, with many variables, such as laser power, scan speed, hatch spacing (center-to-center distance between single tracks), powder particle size morphology, distribution, layer thickness, and scan strategy, all playing important roles in producing fully dense, metallurgically sound parts with minimal internal stress. The complexity of the process is discussed in depth in Chapter 2 by Sun, Brandt and Easton.

In the early days of the technology [5], low-power (on the order of 50−100 W) CO_2 and Nd:YAG lasers with focused spot sizes on the order of 200−300 μm in diameter were used as heat sources to melt the powder and manufacture parts. The machine build volume was also relatively small, on the order of $50 \times 50\ mm^2$ by $50 \times 100 \times 100\ mm^3$. At these laser power levels and build volumes, only small and relatively porous parts could be manufactured because of the partial melting of the alloy powder. The growth of the technology and its following applications can

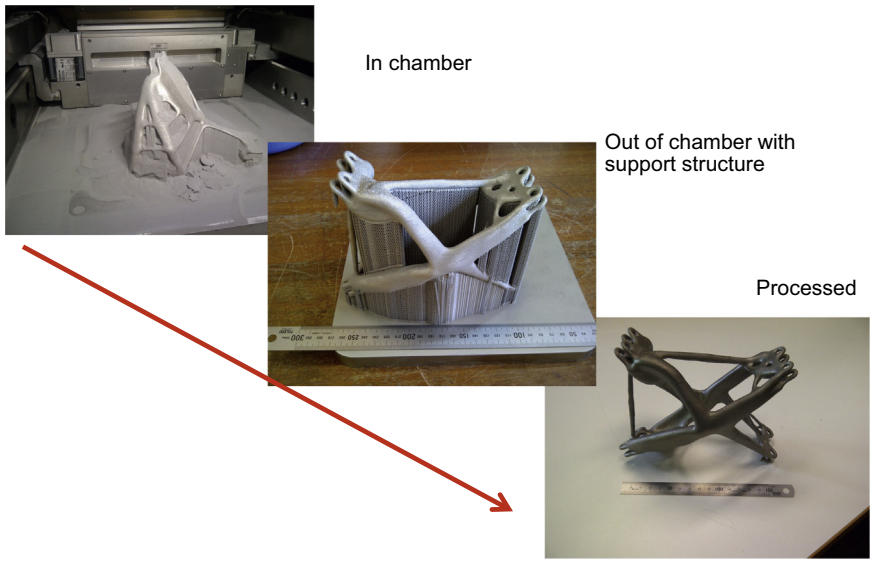

Figure 8 Steps involved in part manufacture from in the chamber to the final part. Note the support structure necessary when manufacturing parts using selective laser melting. Courtesy RMIT Centre for Additive Manufacturing.

be linked to the development of a high-power fiber laser, the ytterbium fiber laser, in the mid 2000s, with low-order modes producing spot sizes typically 80 μm in diameter on the powder-bed surface. This has also driven developments in beam scanning technology and platform/volume size, with the largest commercial volumes today being the Concept X2000 [17], at $800 \times 400 \times 500\ mm^3$ with up to two 1-kW lasers, and the SLM Solutions SLM 500 HL, with a volume size of $500 \times 280 \times 325\ mm^3$ [18] and various laser configurations up to 1 kW. Illustrated in Fig. 9 is the SLM Solutions Group's history of development of SLM technology. This is similar to those of other major powder-bed equipment manufacturers, such as Concept Laser, EOS, and Renishaw.

Illustrated in Fig. 10 is the associated increase in build speed with increasing volume size, number of laser sources, and laser power.

In addition to increasing the volume size and laser power to increase the build rate, a new build strategy has been developed because of the increase in the output power of laser sources. This involves manufacturing a number of "skins," or the surfaces of the part layers, first using a finer powder layer thickness, typically 30–50 μm, followed by a single "core" layer thickness depending on the total number of skin layers. This allows the part to be manufactured with a relatively low surface roughness but at a higher speed. The processing strategy is illustrated in Fig. 11.

Compared with other laser-based AM technologies, the powder-bed technology is evolving rapidly because of its potential, and many research groups are currently focusing their attention in the area. The laser technology is one area involving process

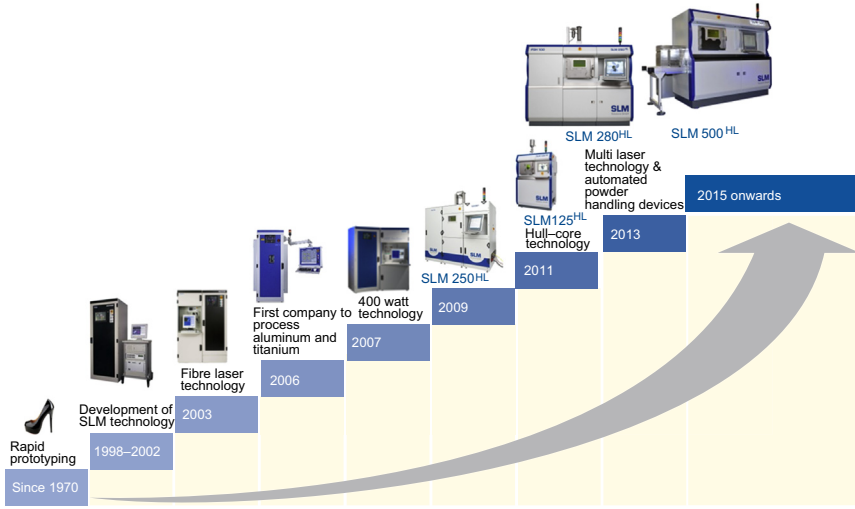

Figure 9 SLM Solutions Group developments in selective laser melting (SLM) technology. Courtesy SLM Solutions.

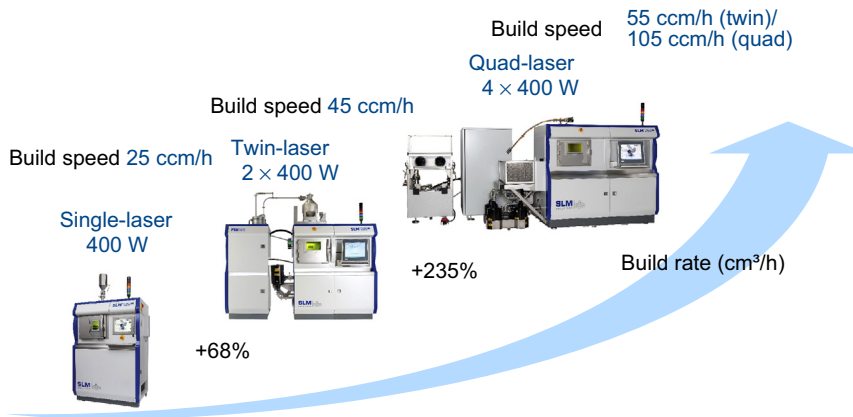

Figure 10 Increase in productivity from different SLM Solutions manufacturing platforms. Courtesy SLM Solutions.

monitoring and control, handling of metal powder for the mass production of parts, control of microstructure in situ, and design of factories for the mass manufacturing of parts. These are illustrated in Fig. 12. Although all these areas of research are challenging and exciting in their own right, the one that stands out in my view is the concept of an integrated laser and powder scanning head involving diode bars. The head would cover the full width of a powder-bed platform and include a linear array of diode lasers of sufficient intensity, individually addressable in order to print the part.

(a)

Procedure

1. Deposition of "skin layer" (50 μm)
2. SLM of skin area
3. Re-iteration until core layer thickness is reached (eg, 4 times if core layer thickness is up to 200 μm)
4. SLM of core area
5. Repetition of steps 1–4

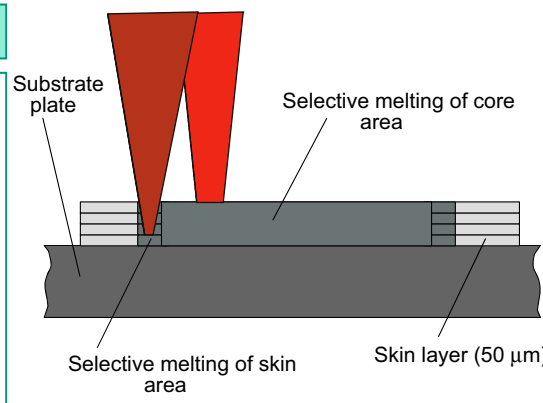

(b)

- Tool insert for injection mould
- Conformal cooling channels
- Layer thickness ratio of 1:4
- Skin core overlap 0.75 mm
- Density ~100%
- Core dep. rate: 16.8 mm³/s
- Skin dep. rate: 3 mm³/s
- Average dep. rate: 10.2 mm³/s

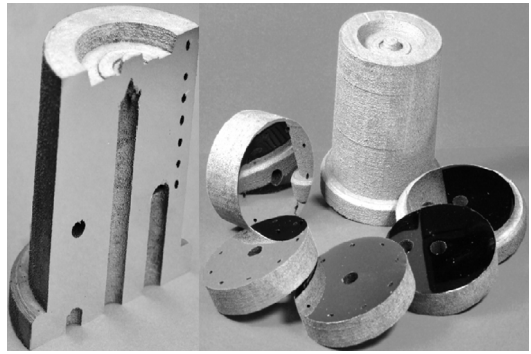

Figure 11 (a) The skin-core part manufacturing strategy. (b) A skin-core-manufactured demonstration. *Dep*, deposition; *SLM*, selective laser melting. Courtesy Fraunhofer ILT.

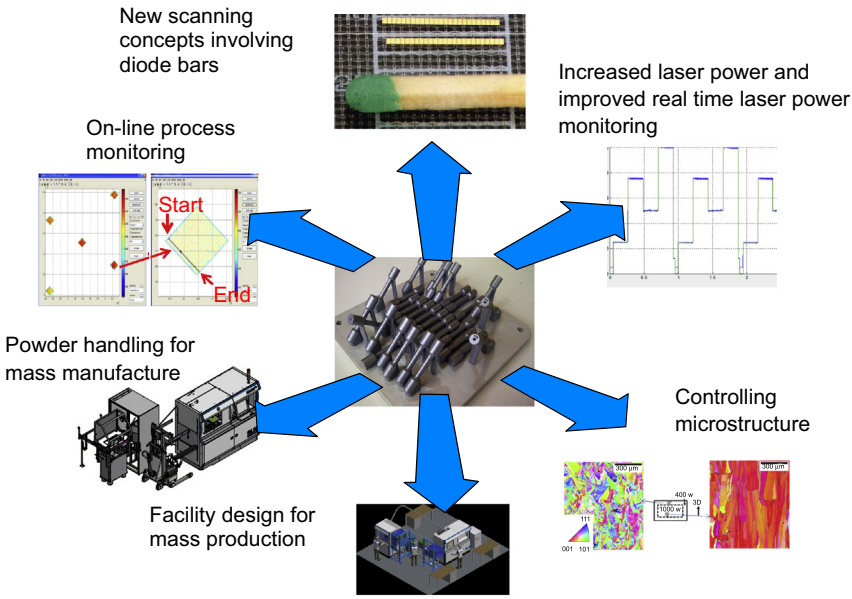

Figure 12 Current major areas of research involving powder-bed technology.

Summary

Undeniably, the laser has played a key role in the growth of laser-based AM globally and will continue to do so in the future. Technology developments in terms of output wavelength, beam quality, output power, optical efficiency, and beam delivery have all contributed to this growth and in particular in metal-based AM. New innovations in beam delivery concepts that are on the horizon, in particular for the powder-bed process, to speed up the build rates present opportunities for the laser to remain a pace-setting technology for AM.

This book presents trends and recent developments in the area of laser AM. The chapters are written by some of the leading researchers in the field and capture and highlight research in both the powder-fed and powder-bed laser technologies, design for AM and process planning, lattice structures, materials for AM, increased process productivity, and fundamental aspects of deposit and part metallurgy through process and material manipulation, as well as specific applications both commercial and currently under development. This and other, similar research in laser technology and laser-based AM processes will continue to drive the growth and adoption of this technology by industry in the future.

References

[1] T.H. Maiman, Stimulated optical radiation in ruby, Nature 187 (1960) 493−494.
[2] W.M. Steen, J. Mazumder, Laser Material Processing, fourth ed., Springer, London, 2010.
[3] R. Poprawe, K. Boucke, Tailored Light 1: High Power Lasers for Production, Springer, Berlin, 2012.
[4] E. Kannatey-Asibu Jr., Principles of Laser Materials Processing, Wiley, USA, 2009.
[5] I. Yadroitsev, Selective Laser Melting, Lambert Academic Publishing, Germany, 2009.
[6] T. Wohler, et al., Additive Manufacturing and 3D Printing State of the Industry − Annual Worldwide Progress Report, Wohlers Associates, Inc., 2016.
[7] www.3ders.org, April 2015.
[8] J. Coykendall, M. Cotteleer, J. Holdowsky, M. Mahto, 3D Opportunity in Aerospace and Defence, Deloitte University Press, 2013.
[9] D. Belforte, Industrial Laser Solutions, January/February, 2016.
[10] G.G. Gladush, I. Smurov, Physics of Laser Materials Processing, Springer, Berlin, 2011.
[11] W.E. King, A.T. Anderson, R.M. Ferencz, N.E. Hodge, C. Kamath, S.A. Khairallah, et al., Laser powder bed fusion additive manufacturing of metals; physics, computational and material challenges, Applied Physics Reviews 2 (2015).
[12] M. Brandt, S. Sun, N. Alam, P. Bendeich, A. Bishop, Laser cladding repair of turbine blades in power plants: from research to commercialisation, International Heat Treatment and Surface Engineering 3 (3) (September 2009) 105−114.
[13] I. Kelbassa, A. Gasser, W. Meiners, G. Backes, B. Müller, High-speed LAM, in: 37th MATADOR Conference on Advanced Manufacturing, The University of Manchester, Manchester, UK, 2012. Paper 3386.
[14] I. Kelbassa, Qualifizieren des Laserstrahl-Auftragschweißens von BLISKs aus Nickel- und Titanbasislegierungen (Dissertation), RWTH Aachen University, Aachen, 2006.

[15] C. Hong, B. Burbaum, A. Gasser, I. Kelbassa, Advantages of laser metal deposition by using zoom optics and MWO, in: 30th International Congress on Applications of Lasers and Electro-Optics ICALEO, Laser Institute of America, LIA, Orlando, FL, 2011. Paper 507.
[16] I. Kelbassa, T. Wohlers, T. Caffrey, Quo vadis, laser additive manufacturing? Journal of Laser Applications, JLA 24 (5) (2012). Cover Story.
[17] www.concept-laser.de/.
[18] www.stage.slm-solutions.com/.

Laser-aided direct metal deposition of metals and alloys

1

J. Mazumder
The University of Michigan, Ann Arbor, MI, United States

1.1 Introduction

The well-known adage that the "early bird gets the worm" is true for any industry in this era of information technology. The cycle of consumer taste for a product is shortening, and therefore the need for an industry to go to the market with a shorter lead time is becoming more of a necessity than a desire. Concurrently, a desire for improved performance at a cheaper cost puts conflicting demands on design engineers. For example, more people want cheaper and safer air travel, which requires lighter planes with lower fuel consumption plus a higher load-carrying capacity. It is not smart to just scale up an existing design to increase capacities. Thinking out of the box is a must in order to engineer materials with properties to match the performance desired by modern consumers. Synthesis of topological design, heterogeneous computer-aided design (CAD), and direct metal deposition (DMD) offer opportunities to engineer material properties to match desired performance. Additive manufacturing has caught the imagination worldwide for the fabrication of 3D components with a desired geometry and properties. *Economist* magazine identified additive manufacturing as a "third industrial revolution" on the cover of the April 2012 issue [1].

1.1.1 What is direct metal deposition?

DMD is a solid free-form fabrication (SFF) technique that enables the production of realistic components with 0.01-in. accuracy and properties similar to wrought materials, with close to 100% density. Recent advances in laser-based SFF manufacturing have made possible "one-step" fabrication of useful tools for the metals and plastics industries directly from metal powders. Closed-loop DMD is a synthesis of multiple technologies including lasers, sensors, a computer numerical controlled (CNC) work handling stage, CAD/computer-aided manufacturing software and cladding metallurgy. DMD, developed in the Center for Laser-Aided Intelligent Manufacturing at the University of Michigan [2], is a laser-cladding-based process that makes fully dense free-form metallic parts layer by layer (Fig. 1.1). The key characteristic of the DMD process, which distinguishes it from other similar laser-cladding-based SFF processes, is the integrated feedback system. This system actively maintains a uniform deposition thickness, thus saving precious time after machining. In the DMD process, sensors collect light from the interaction zone and use it as a feedback to control laser power and other process parameters. The closed-loop DMD process is creating

Laser Additive Manufacturing. http://dx.doi.org/10.1016/B978-0-08-100433-3.00001-4
Copyright © 2017 Elsevier Ltd. All rights reserved.

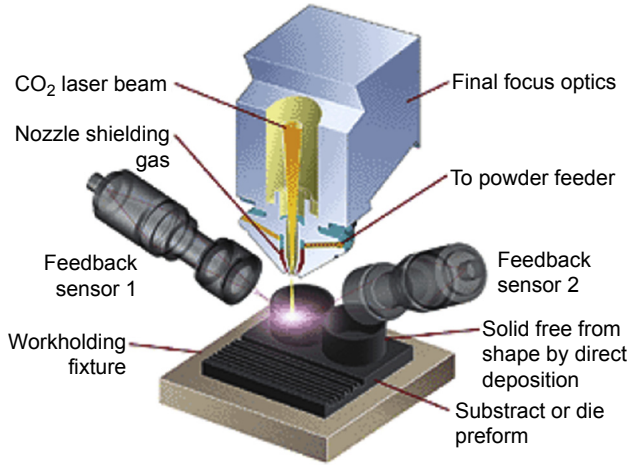

Figure 1.1 Direct metal deposition process with an active height controller.

considerable contemporary interest because of its capability to deliver "CAD to part." DMD can significantly reduce the lead time for "concept to product" by eliminating several intermediate steps. Moreover, many performance parameters such as heat transfer in a mold or a die can be enhanced by tailoring the properties of material to the function needed, since DMD can deposit different materials in different pixels. For example, the surface of a die can be made of tool steel for better wear resistance, whereas internal sections of that same die can incorporate conductive materials and conformal cooling channels for improved heat transfer.

Currently, it is not unusual for large, complicated dies to take weeks, even months, before they are ready to manufacture a product. Stereolithography has helped in the design process by visualizing a component produced directly from a CAD database and by curing polymers with lasers. Most manufacturers are looking for a device that can make a product directly from a CAD drawing with a designed macro- and micro-structure. Repair procedures are also needed that do not change the material properties of the metals or result in a reduced life of the product. DMD offers a solution for all of these challenges.

A number of research efforts have been conducted to explore and extend the capability of DMD technology in processing various materials, manufacturing molds and dies, repairing/remanufacturing parts, synthesizing designed materials, and so on. The range of these efforts can be found in Refs. [2−14].

The closed-loop DMD process ensures close dimensional tolerance and enables the fabrication of components with multiple materials. A mold flow analysis revealed that an injection-molding die with conformal cooling and a copper heat sink can reduce the cycle time up to 50% or more. DMD has already demonstrated the capability of fabricating three-dimensional (3D) 100% dense metal components with functional designs. Popular engineering alloys such as H13 and S7 tool steels, Stellite 21 and 6 cobalt alloys, and nickel alloys such as Inconel 718 are already reported in the literature. DMD can be adapted directly to the digital data from CAD, magnetic resonance

imaging, and X-ray tomography. Conceptually, DMD is capable of fabricating a wide variety of metallic parts with internal features. This chapter critically reviews the state of the art of DMD and also speculates how DMD may affect manufacturing technology in the future. We believe three areas seem to be most promising:

1. **Designed materials**: This capability can be used to create a new class of optimally "designed materials," a class of artificial materials with properties and functions that do not yet exist. In other words, a material system can be designed and fabricated for a chosen performance.
2. **Integrated design and manufacturing**: Another potential impact of closed-loop DMD is the integration of design and manufacturing. In the integrated approach, customer-desired performance can be implemented throughout the design concept stage to the manufacturing realization stage. This not only reduces lead time for concept to product but also offers materials with properties and functions that do not yet exist.
3. **Remote manufacturing**: Modern communication methods are improving the Internet's capability to transfer large volumes of data in a relatively short time. Mathematical and optical methods of data compression enhance this capability even further. This will enable seamless communication between design and manufacturing teams in industry. It is conceivable that a design team can send their design data electronically, observe the fabrication from a remote site, and even edit it online. Of course, to realize this scenario, synthesis and enhancement of various technologies not directly related to DMD are needed.

DMD is an extension of laser-cladding technology. It is, in principle, a multilayer laser-cladding process with feedback control. The following section briefly reviews the laser-cladding process.

1.2 Review of the laser-cladding process

1.2.1 What is laser-cladding technology?

Laser cladding by a powder injection technique has been widely used in industrial applications such as rapid manufacturing, parts repair, surface coating, and innovative alloy development [2,14−18]. The capability to mix two or more types of powders and to control the feed rate of each powder flow makes laser cladding a flexible process for fabricating heterogeneous components or functionally graded materials. This technology also allows the material gradient to be designed at a microstructure level because of small localized fusion and strong mixing motion in the melt pool of laser cladding. Thus materials can be tailored for a flexible functional performance in particular applications. The inherently rapid heating and cooling rates associated with the laser-cladding process enable extended solid solubility in the metastable or nonequilibrium phases of production, offering the possibility of creating new materials with advanced properties.

1.2.2 Novel materials and applications enabled by laser cladding

A wide variety of microstructures can be generated by the laser-cladding technique, including extended solid solutions and amorphous phases. Many surface-related

failures, such as corrosion, oxidation, wear, and fatigue, may be minimized or eliminated using these techniques. Strategies for nonequilibrium synthesis by laser cladding include the selection of phases, elements, and process parameters [17,18]. Selection of phases is important to achieve desired mechanical properties. A face-centered cubic structure, for example, is known to have better ductility because of its large number of available slip planes, whereas brittle noncubic phases provide hardness and resistance to wear as a result of the limited numbers of available slip planes. The duplex phase, which is the combination of the latter two phases, can provide adequate toughness as well as reasonable resistance to wear. Elemental additions can promote certain phases or improve resistance against chemical degradation at high temperatures and reduce the material density. For example, aluminides of titanium, nickel, and iron in the form of X_3Al are good candidate materials for advanced gas-turbine engines. Chromium promotes a body-centered cubic phase for ferrous alloys [19]. Cr_2O_3 forms passive layers to inhibit corrosion at temperatures up to 800°C [20]. Reactive elements with a high atomic 6 number such as yttrium and hafnium are known to be able to stabilize the resistance of Al_2O_3 to oxidation at high temperatures [21,22]. However, their dissolution in other materials is difficult [23]. The most effective method to realize such alloys is extending the solid solution by atom trapping. As explained earlier, this is enabled by the high cooling rate and strong convection inherent to the laser-cladding process. A combination of the knowledge of phase transformation kinetics and processing transport phenomena is required to determine the process parameters that will result in a desired phase and composition.

Considerable literature has been published regarding materials tailor-made by laser-cladding techniques. Many researchers reported various systems of metastable laser-clad alloys, including Fe-Cr-Mn-C [24] for improved resistance to wear, Ni-Cr-Al-Fe-Hf [38], Ni-Cr-Al-Hf on Inconel 718 [25], and Ni-Cr-Al-Hf on nickel [26] for improved oxidation resistance. Mg-Zr and Mg-Al systems for corrosion-resistant materials were studied as well [27−30]. Various conventional metals and alloys have been laser clad for applications where an improved material performance is desired, such as a Co base alloy on a Cr-Ni-Ti base metal of nuclear valve seats [31], Hastelloy C-22 (Ni-Cr-Mo base) on a Cu-Zn-based alloy for marine propeller repairing [32], a WC−Ni metal matrix composite coating on H13 tool steel for improved resistance of molds and dies to abrasive wear [33], an Fe-Al-Ti-C powder mixture on an austenitic stainless steel substrate for better resistance to wear at high-temperatures [34], and an Ni-Cr_3C_2 composite on a 0.2% C martensitic stainless steel for improving the erosive-corrosive wear performance [35].

Quasicrystal was discovered in a rapidly cooled sample of an aluminum-manganese alloy by Shechtman et al. [36] in 1982. Quasicrystals are stable phases of condensed matter that exhibit crystalline features such as symmetry and repeating patterns of unit cells; unlike a crystal, however, the unit cells are more than one type in large-scale order. Quasicrystals have been found to be common structures in aluminum alloys with such metals as cobalt, iron, and nickel. Quasicrystal materials have demonstrated many favorable characteristics such as high hardness, low friction coefficient, and low thermal and electrical conductivities, which give these materials great potential in applications where low friction and resistance to wear are required. However, the

use of the quasicrystalline material in bulk form is difficult because of the brittleness that these materials exhibit at room temperature. A possible alternative is to synthesize quasicrystalline coatings that exhibit the favorable properties of these materials. Composite quasicrystalline coatings of an Al-Cu-Fe mixture have been developed by laser cladding [37].

1.2.3 Modeling of laser cladding

Laser cladding by an coaxial powder injection technique involves complex physical phenomena such as laser–powder interactions, heat transfer, fusion, fluid flow, solidification, and, in the case of high-power lasers, accompanying evaporation and plasma formation. Understanding the formation of cladding geometry and how it is determined by complex processing parameters such as laser power, powder feed rate, and laser scanning speed provides the means for accurate dimensional control. In a multiconstituent material cladding process, solute concentrations in the solidified layer can be distributed by solving the species transportation equation with appropriate solute partitioning conditions at the solidification interface.

1.2.3.1 Laser–powder interaction

In the one-step laser-cladding process, powder can be delivered into the melt pool either coaxially around the laser beam or laterally from the side of the laser beam. Either way, the laser light travels through and interacts with the cloud of powder particles before it reaches the workpiece. The powder particles can absorb the laser energy, and their temperature may increase under irradiation by the laser. Meanwhile, the cloud of the powder particles attenuates the laser energy. When the laser passes through it, a part of the laser energy is absorbed and reflected, reducing its intensity and changing its distribution. A semiempirical method of evaluating the laser energy redistribution during CO_2 laser cladding with lateral powder injection was reported by Gedda et al. [38]. Lin [39,40] studied laser attenuation and powder temperature distribution in a focused coaxial powder stream both experimentally and theoretically. A Gaussian distribution of coaxial powder concentration was used in his calculations and verified by experimental observation. Liu and Lin [41] studied, using a numerical model, the heating, melting, and evaporation processes of a single spherical powder particle when irradiated by a CO_2 laser beam in coaxial powder flow cladding process.

1.2.3.2 Heat transfer and fluid flow models

Heat transfer and hydrodynamic flow in a laser-induced melt pool are the two most important transport phenomena in many laser processes, including laser welding, cladding, or surface alloying, and they have been exhaustively studied from a modeling point of view [42]. In the past decade, several analytical and numerical models have been developed for laser cladding, revealing the process's dependence on related parameters. The early models were mostly based on heat transfer with necessary consideration of phase transformations (ie, melting and solidification), but few models incorporated fluid flow calculations because of the complexity involved. Picasso et al. [43] proposed a

simple but realistic model for laser cladding, incorporating the attenuation of laser power owing to the powder particles as well as the dependence of workpiece absorption with respect to clad geometry. The melt pool shape was simply computed using a 3D analytical solution that assumed a predeposited layer of powder on the substrate. Jouvard et al. [44] studied the relation between the laser power and the cladded mass through the calculation of energy distribution in laser cladding. They suggested a method to evaluate two power thresholds, of which the first is the power required to melt the substrate and the second is the threshold power when the coaxial powder is melted directly by the beam and is, therefore, a liquid when contacting the substrate.

Hoadley and Rappaz [45] developed a two-dimensional (2D) finite element model to obtain the quasi-stationary temperature field in a clad layer. They took into account the melting of powders in the liquid pool and updated the shape and position of the liquid-free surface conforming to the thermal field. However, in their model the height and length of the melt pool have to be predefined. Yevko et al. [46] modeled the preplaced powder cladding process by solving a 3D heat transfer equation numerically. Kaplan and Groboth [47] modeled a 3D quasi-steady laser-cladding process considering laser−powder interactions. Their model is simplified with the assumption that the dimensions of the melt pool remain similar to pure surface melting in the absence of a clad layer. The cladding shape in their model is defined by parameterized functions. Toyserkani et al. [48] developed a 3D transient finite element model considering laser power attenuation through a blown powder stream. They used modified thermal conductivity to take into account the thermocapillary phenomena of the liquid metal without calculating the fluid flow. The clad geometry was obtained by continuously stacking tiny layers of deposited mass in the melt pool area. Zhao et al. [49] proposed a quasi−steady state laser-cladding model using a 3D finite element method that is similar to Hoadley's model but focused on dilution control. Huang et al. [50] recently developed a 3D transient laser-cladding model in which fluid flow is fully solved with an energy equation in a coupled manner. A solid/liquid continuum model [51] was used to predict the melting and solidification phenomena. They used a simple indicative variable method to update the growth of the molten pool free surface without calculating accurate surface geometry for curvature-dependent flow.

1.2.3.3 Mass transfer models

Mass or species transfer plays an important role in the laser-cladding process. A uniform solute distribution or material phase distribution in the solidified cladding layer is desired, since large random variations in local composition make compositional control in the laser-cladding process difficult and could seriously affect the mechanical or chemical performance of the cladded material. When laser cladding with multiple materials, the uniformity of mixing and the resultant average compositions in the liquid state are primarily determined by the nature and level of diffusion and convection established in the molten pool. Hence knowledge of the mechanisms and characteristics of material redistribution within the molten pool is desirable to better understand solidified alloy formation in laser cladding. During solidification, the partitioning phenomenon of solute elements at the solid−liquid interface also needs to be considered. Especially

under nonequilibrium conditions associated with a high cooling rate ($>10^4$ K/s), the uniformity of the solute distribution is highly dependent on the partitioning kinetics at the solidifying interface. Chande and Mazumder [52] developed a numerical model that solved the 2D transient equation for convection of added species in the melt pool using an alternate diagonally implicit method. The surface of the melt pool was assumed to be flat in order to simplify the surface boundary condition. Mass transport by diffusion was negligible compared with that of convection.

Considerable models can be found in the literature on nonequilibrium segregation of solute during rapid solidification. For concentrated solutions, Aziz [53] performed theoretical studies and derived an expression for the nonequilibrium partition coefficient by correcting the fluxes and driving forces in a previously developed continuous growth model [54]. Kar and Mazumder [55] analyzed the laser-cladding process with a one-dimensional heat and mass transfer model. They solved governing equations analytically and predicted the extended solubility in clad with the continuous growth model [54]. Kar and Mazumder [56] later developed a model to partition solute in concentrated solutions, which is related to the solidification growth rate as well as mushy zone dimensions. Chakraborty and Dutta [57] recently studied a laser surface alloying process with a 3D transient numerical model. They assumed a fixed, flat top surface on the molten pool and solved the governing equations for heat, momentum, and mass transfer in a coupled manner. Their solution for species concentration distribution was based on a modified nonequilibrium partition coefficient on account of solutal undercooling.

1.2.3.4 Self-consistent 3D transient model

A self-consistent 3D transient model was developed for a coaxial powder injection laser-cladding process [58–60]. Physical phenomena including heat transfer, melting/solidification phase change, mass addition, liquid metal flow, and species transportation were modeled and solved with a controlled-volume finite difference method. Interactions between the laser beam and the coaxial powder flow were also considered in this model, which encompasses the attenuation of beam intensity and increase in powder temperature. The level-set method was implemented to track precisely the growth and evolution of the liquid-free surface during a continuous cladding process. The solute concentration distribution in the cladding layer was determined using a nonequilibrium partition coefficient model. Fig. 1.2 demonstrates the sequential temperature fields of continuous low-carbon steel cladding track formation in a 120-ms period with a laser power of 600 W. It can be observed that a 0.5-mm-long and 0.3-mm-wide molten pool is formed after the laser beam passes by 1.0 mm in the x-direction. The maximum temperature in the melt pool is 2001.6K. Because of the large surface temperature gradient, the liquid in the molten pool flows outward from the center area. This motion, combined with the scanning speed, "piles up" the continuously added material behind the molten pool and subsides the molten pool surface. The maximum velocity magnitude is 1.12 m/s when the molten pool is fully developed. The strong fluid flow inside the molten pool causes fluctuations to form in the cladding surface. The solute concentration results with use of a laser beam of 500

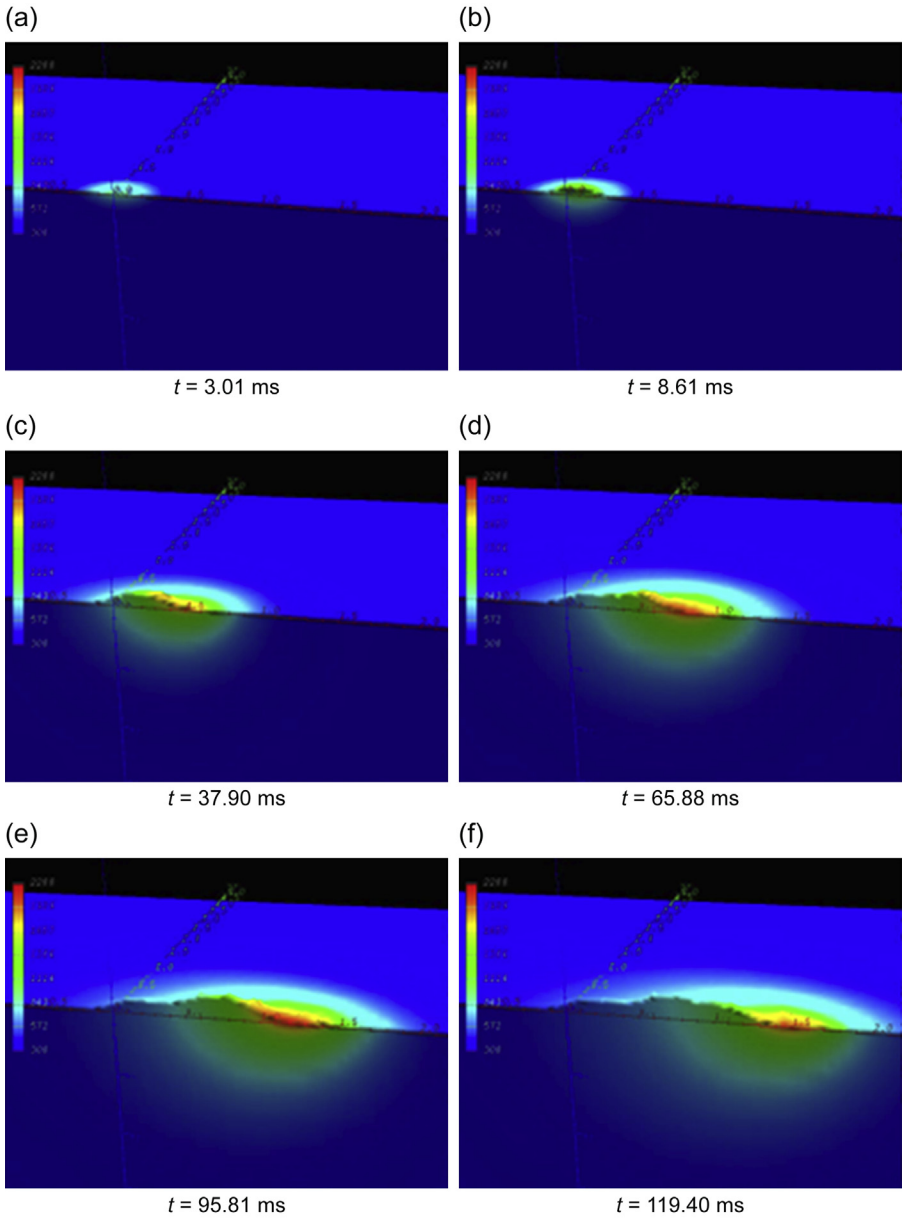

Figure 1.2 Sequential temperature fields as in the evolution of a continuous low-carbon steel cladding track with a laser power of 600 W, scanning speed of 12.7 mm/s, powder feed rate of 6.0 g/min, and a laser spot size of 0.6 mm.

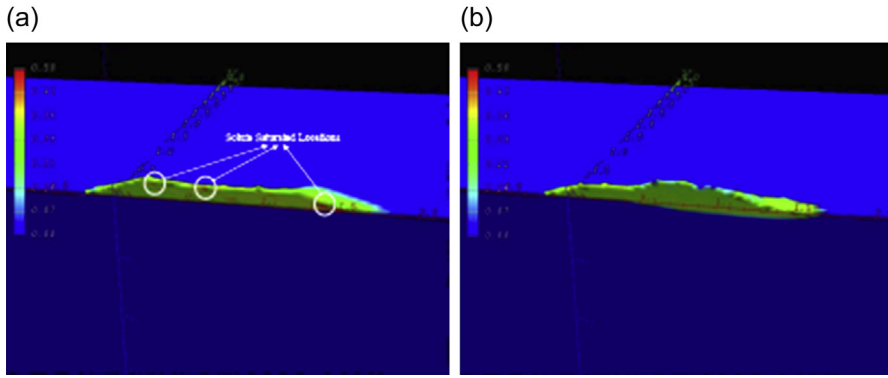

Figure 1.3 Solute concentration field obtained using (a) an equilibrium partition coefficient and a laser power of 500 W; (b) a nonequilibrium partition coefficient and a laser power of 600 W.

and 600 W are shown in Fig. 1.3(a) and (b), respectively. An equilibrium partition coefficient was used in the case of a 500-W laser power, whereas a nonequilibrium partition model [56] was used for the result shown in Fig. 1.3(b). The substrate starts melting as the laser beam moves to 0.5 mm in the *x*-direction. The diluted layer in the substrate has a concentration as uniform as that of the cladding layer, which is contributed by the solute diffusion and convection flow in the melt pool. Good metallurgical bonding is formed in this case.

1.2.4 What is solid free-form fabrication?

Today, several novel technologies are capable of producing complex, solid free-form objects directly from CAD models without the use of conventional tooling. These manufacturing methods are normally characterized as additive processes and have been termed "solid free-form fabrication," otherwise known as layer manufacturing or rapid prototyping/manufacturing.

The SFF method can be traced back to two early techniques: topography and photosculpture. The topography technique was patented in 1892 by Blanther [61], who suggested a layer-based plate-stacking method for making topographic relief maps. Similar to this technique, photosculpture involves using the 2D contours of an object photographed at equally divided angles in circumferential directions to create a 3D replica. The concept of building a 3D object with a set of discrete 2D profiles is still being used in modern SFF manufacturing methods, where objects are normally built up layer by layer. With the fast development of CNC technologies and other computer tools in the past two decades, more complex prototyping products could be made by machines in a shorter processing time. To date, more than 20 different SFF techniques have emerged [62].

The processing methods used in current SFF techniques can be generally classified into four categories:

- Photo-curing
- Cutting and gluing/joining
- Melting and solidifying/fusing
- Joining/binding

Table 1.1 Coefficients of thermal expansion for materials used in direct metal deposition

Material	Coefficient of thermal expansion (10^{-6} cm/cm/°C)
Invar	1.54
Chromium	6.0
1020 steel	12.0
Nickel	13.0
Copper	16.6
Aluminum	25.0

Materials that have been processed in SFF include paper, polymers, nylon, wax, resins, metals, and ceramics. The form of input material covers a wide range, including solid sheet, wire, powder, liquid, droplet, and gas/vapor. Application fields of SFF technology can be grouped into (1) product design, (2) engineering analysis and production planning, and (3) tooling and manufacturing. SFF technologies have benefited a wide range of industries such as aerospace, automotive, biomedical, consumer, electrical and electronics. Many publications [62–64] provide comprehensive reviews of emergent SFF technologies.

The key parameters that characterize an SFF technique are the build rate and the build envelope, the ability to make parts of different materials, dimensional accuracy, and minimum feature size. Table 1.1 summarizes the key technical characteristics of the popular SFF processes that are capable of processing metals and have been successfully commercialized today.

Among the various SFF techniques, the powder-based laser-cladding technique seems to have achieved a high level of commercialization because of its flexibility and accuracy. This process involves either a powder bed (two-step cladding; eg, selective laser sintering) or a powder flow injection (one-step cladding; eg, DMD, laser engineering net-shape). Compared with the powder injection process, laser cladding with a powder bed process can usually achieve better deposit resolution. However, it has the major limitations of long processing times and small build envelops as a result of the powder-paving steps. Moreover, it lacks the flexibility to build heterogeneous materials/structures within one layer.

1.3 Material microstructure design and realization

The requirements of material performance in current industrial applications are becoming more and more stringent and complicated. In some applications, conventional single-phase materials can barely meet various engineering requirements such as the high toughness of tool die surfaces and the creep and oxidation resistance of a turbine

blade. To reduce the cost of production without sacrificing the quality of products, mass-efficient designs are desired in contemporary industrial production. Being able to tailor materials for particular physical properties such as bulk, shear, or anisotropic elastic moduli and conductivity, transport, or thermal expansion coefficients has become the most important challenge in material design.

Designed materials may be defined as a class of artificial materials synthesized by incorporating dissimilar constituent materials to meet certain desired product performances. This synthesis allows material properties or functions to be tailored according to specific design requirements. A material with a periodic cellular body can be considered as a simple example of a designed material comprising solids and voids. This is the case for the material model used in structural topology optimization [65]. It is a revolutionary design method different from conventional parameter-based structural optimization design (eg, designs optimizing size or shape). Unlike conventional methods, which represent a structural shape with parametric size or shape functions, the underlying principle of topology optimization is to represent the geometry of a structure with an element-based image. In other words, shape optimization problems are transformed into material distribution problems in a fixed design domain [66]. This technique can usually achieve greater savings on structural mass and design improvements than mere size or shape optimization. Topological optimization is enabled by a mathematically rigorous method, that is, the homogenization method [67], which allows us to calculate the effective properties of periodic composite materials without imposing limitations on the geometry of the given composite.

Topology optimization combined with the numerical homogenization method has been used to tailor material microstructures with prescribed elastic properties [68]. This material design method is a departure from conventional material selection methods where material performance is limited by available materials. The topology optimization method has been used to design materials with specific mechanical [69], thermomechanical [70,71], piezoelectric [72], and thermal conductivity properties [73]. Unusual material properties such as a negative Poisson ratio [80] and negative thermal expansion coefficients [70,74] have been designed using the topology optimization method.

In the following section we briefly describe the homogenization design method (HDM) along with closed-loop DMD, needed for the production of "designed materials." The overall system architecture is shown in Fig. 1.4.

1.3.1 Homogenization design method

The homogenization design method was originally developed to determine the optimal topology and layout of a macroscale structural component subjected to a set of loading and support constraints before creating a CAD model [65,75–78]. In other words, the shape and topology were not created by the designer, but by HDM. By means of geometric modeling techniques, the HDM output was converted into a CAD model. HDM has since been extended to design the microstructure of composite materials to achieve desired material performance. Instead of using existing materials, this new approach enables materials—more specifically material constituents—that can perform as intended (within the bounds of physics) for specific structural components.

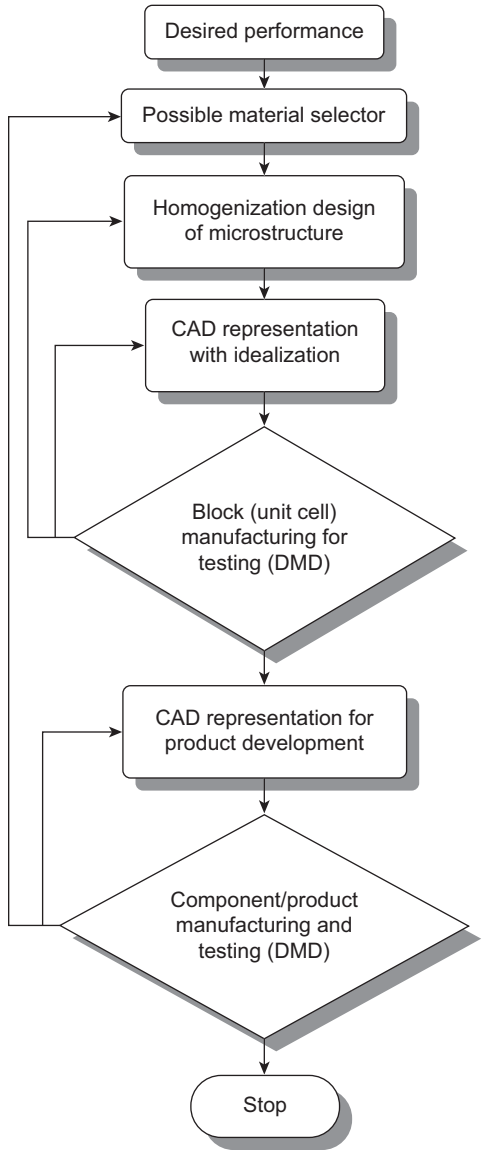

Figure 1.4 Overall system architecture. *CAD*, computer-assisted design; *DMD*, direct metal deposition.

As typical examples of materials design, by generating microscale (possibly even nanoscale or mesoscale) voids within a given metallic/polymeric/ceramic material whose Poisson ratio is positive, we have shown several different microstructures ending with a negative Poisson ratio as composites (ie, a mixture of solid materials and voids). Solving an appropriately defined objective function with specified material characterization, such microstructures can be determined mathematically.

This enhanced HDM can be used for material design to control Young's moduli, shear moduli, Poisson ratios, and even thermal expansion coefficients [68,79–81]. As expected, this mathematical method requires sophisticated computational methods because of the massive calculations needed to determine an optimum microstructure layout. An optimization algorithm is used at the core, while a large-scale homogenization procedure is applied at each design stage.

1.4 Experimental procedure

The system at the University of Michigan includes a 6-kW radiofrequency-excited CO_2 laser integrated with a 5-axes workstation controlled by an Allan Bradley 8400 controller. The laser has the capability to operate between 0 and 6 kW, and the workstation has a traverse speed range of 0–400 ipm (0–169.3 mm/s). It has a work envelop of 1–0.5–0.5 m and carries up to half a ton. Fig. 1.5 shows a sketch of the closed-loop DMD system.

Powder can be delivered either from the side with an independent nozzle or with a concentric nozzle where the beam and powder come through the same nozzle. The concentric nozzle designed is based on a patent [82] and offers equal deposition rates in any direction. Inert gas flown through the nozzle helps both to deliver powder and to shield the deposit from oxidation. This shielding strategy obtains a delicate balance between powder delivery and adequate disbursement of ambient air, without causing excessive disturbance at the melt pool. A side injection nozzle can build up volume rapidly, whereas a concentric nozzle can provide better resolution. In an ideal system, a rotating head with both types of nozzles would be available.

Control of the deposit thickness or height is a critical issue because it affects the quality of the product. Visualization and measurement of the surface deformation of the melt pool is possible by the reflective topography technique developed at the University of Illinois [83]. To control the deposit dimensions, a feedback loop to control the process parameters was designed and executed [84]. This feedback loop can also be adapted to monitor composition in an open loop.

The basic function of the height controller is to limit the maximum height of metal deposition. The following is a simple example of the controller function. Fig. 1.6

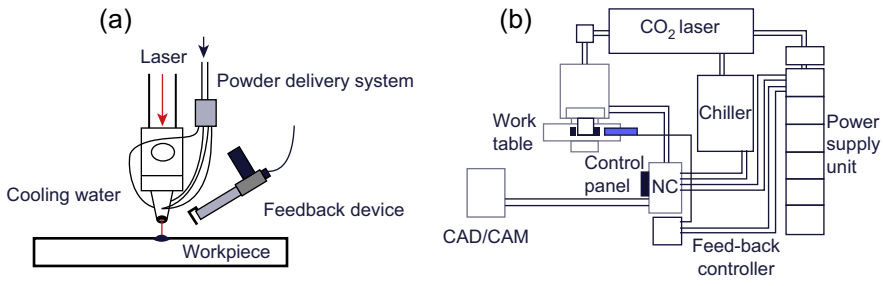

Figure 1.5 (a) Schematic of the direct metal deposition (DMD) process. (b) A DMD system. *CAD*, computer-assisted design; *CAM*, computer-assisted manufacturing.

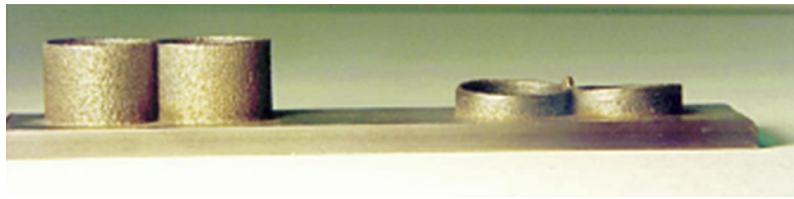

Figure 1.6 Example of fabrication with a height controller (left) and with no height controller (right).

shows two samples produced by laser cladding, each of which has a deposition path of two overlapping circles. After multiple cladding, in which layers are placed one at a time on top of previous layers, a pair of overlapping cylinders are fabricated. The sample on the right is produced without any height control, and it can be seen that there is excess cladding built up where the circles overlap. The overall height at this location is approximately twice that of the cylinders' height because the laser cladding passes this point twice per layer, laying down the same amount of material during each pass. In areas other than the overlap, it can be seen that the overall height is uneven. The sample on the left in Fig. 1.6 was fabricated using a height controller, which has the ability to sense when the cladding layer is building up higher in the overlapping region. The controller shuts off the laser until it passes the area of excess buildup. In this case the layer thickness was set at 0.1778 mm, and 100 layers were subsequently built up from the substrate. As a result, the overall height was held to 17.78 mm with a variation of less than 0.075 mm. For this reason, a height controller is a necessity to fabricate accurate macroscopic shapes.

The scientific challenge is to control the dimensions and properties of the designed materials. Close control of dimension results in substantial cost savings in machining after processing for surface finishing. Substantial cost reduction is also possible if desired properties can be achieved through process control and thus minimize heat treatment after processing. Control of the melt pool size and solidification time can offer both desired dimension (by limiting the melt pool volume) and desired properties (through microstructure manipulation by controlling the cooling rate). This requires a quantitative understanding of the relationship between independent process parameters (laser power speed, powder deposition rate, etc.), dimension, cooling rate, microstructure, and properties by developing a fundamental understanding of the associated transport phenomena. Strategies for online process control are also required to achieve the desired melt pool volume and cooling rate.

One can use either one sensor or multiple sensors for closed-loop feedback control of the deposit height. Multiple sensors will overcome any problem related to the field of view with respect to the cladding direction for a single sensor. Fig. 1.7 shows a top view of the ideal layout of the three sensors that are spaced equally 120 degrees apart. For the actual layout of the sensors for this study, the second sensor was only 90 degrees from the first sensor. This uneven spacing did not cause any problems, since the sensors are effective up to 180 degrees. Since two or more sensors were added to the system, the signal processor also had to be modified. To input one signal into the

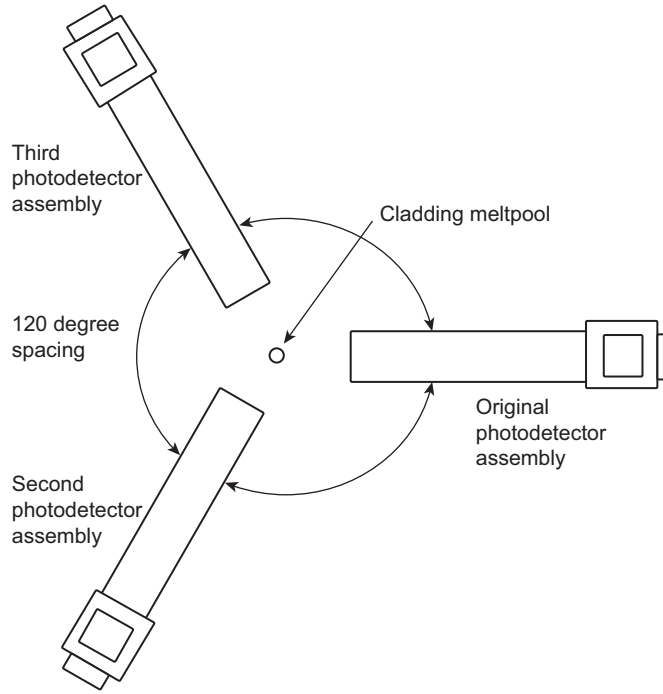

Figure 1.7 Multiple-sensor layout (top view).

processor, the three sensor signals were combined through several logic gates before they were sent to the processor. The new flow diagram for the height controller is shown in Fig. 1.8.

Two major areas of DMD processing were investigated. The first area studied was the laser processing parameters and how they affect the multiple characteristics of the fabricated samples. The other area studied was the effect of multiple height control sensors on the characteristics of the final parts. Effects of some controller parameters

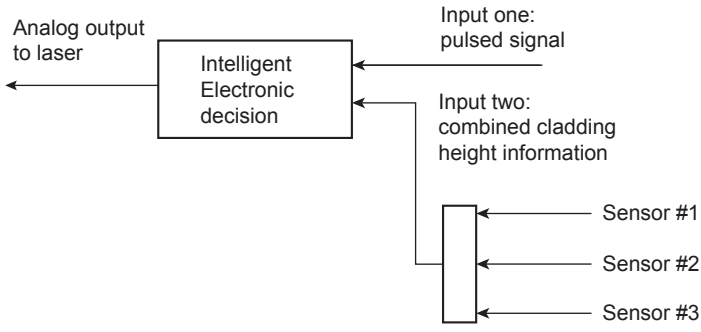

Figure 1.8 Height controller with multiple sensor inputs.

on material processing were also investigated. A statistically designed experimental matrix was used for this study. The basic process parameter information is subsequently used for the fabrication of designed macro- and microstructures.

1.4.1 Negative coefficient of thermal expansion experiments

A negative coefficient of thermal expansion (CTE) structure experiment was done in conjunction with three other research groups from the University of Michigan. A student provided the optimized design and another student converted it from a series of elements to lines defining the regions of the two different materials (Fig. 1.9). This model, in IGES format, could then be imported into SurfCAM and tool paths could be generated. The last group tested the structure for its CTE. Three challenges remained before the structure could be built. First, the two materials had to be chosen; second, a tool path needed to be created; and third, optimal process parameters needed to be found through experiments.

1.4.2 Material selection

The key to the functioning of the negative CTE structure is the difference in the thermal expansion coefficient of the two constituents. The two materials act as a type of bimetallic strip, whereby when one material expands more than the other, the net result is bending. This in turn leads to a net contraction, as shown in Fig. 1.10. While choosing two materials for the structure, their particular identity was of less importance than their CTEs. The greater the difference in CTE, the more pronounced the contraction would be. The target ratio of the two materials' CTEs was between 2 and 3. Also taken into consideration was the miscibility between the materials, since some mixing

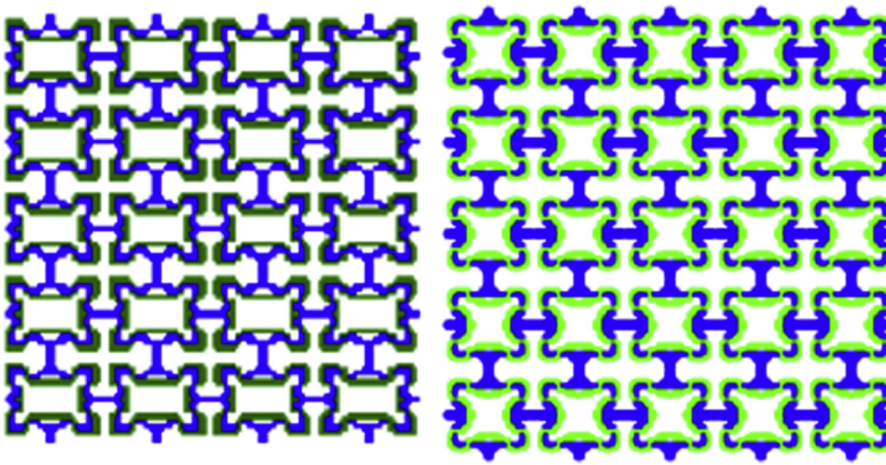

Figure 1.9 Negative coefficient of thermal expansion structure: homogenization design method model (left); IGES file after smoothing (right; gray, nickel; dark gray, chromium).

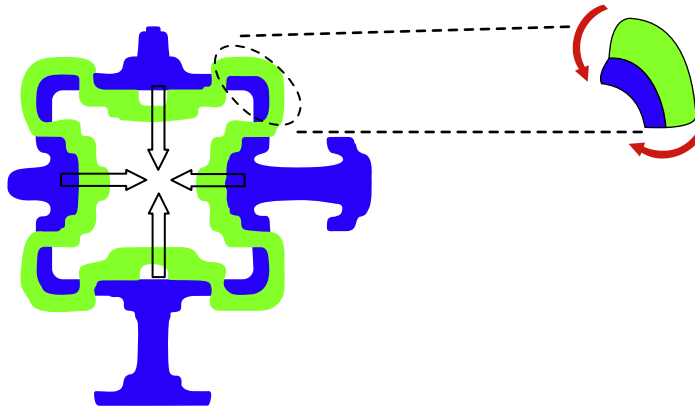

Figure 1.10 Contraction mechanism of negative coefficient of thermal expansion structure.

would be necessary at the interface to ensure a solid bond. Table 1.1 lists materials that were considered as candidates either because they were previously used for DMD or they were considered attractive for the project.

From Table 1.1, it can be seen that many materials that are commonly used for DMD, such as copper, steel, and nickel, all have very similar CTEs. Aluminum has a much higher CTE but forms brittle intermetallics with many of the other materials. Invar has a very low CTE, of course, but has problems with cracking during DMD processing. Chromium is the only material that remains. In excess of 40% by weight, it is miscible with nickel at 1300°C, and it has a CTE that is less than half that of nickel. Therefore it was chosen for the low-expansion phase of the structure, and nickel was chosen for the high-expansion phase.

Fig. 1.11 shows two of the key dimensions of the unit cell tool paths labeled. These two dimensions are the spacing between the nickel and chromium tool paths around the perimeter of the cell itself, and the spacing between the chromium tool paths in the actual cell and the bridge tool paths. These values for the five different tool paths are also listed in Table 1.2. To put the values in perspective, for a 600-μm-wide deposition track, a spacing of 0.012 inches is equivalent to a 50% overlap between the tracks, and 0.024 in. of spacing means there is no overlap.

1.5 Results and discussion

Our initial work on the development of the DMD process was driven by industrial needs. The main foci were (1) to provide aluminum components with low enough oxidation that they retain mechanical properties [84,85], and (2) to provide mechanically sound H13 tool steel components. The emphasis is the demonstration of the strength of the DMD technique; both were successful [2,86–88]. Mechanical properties of aluminum and H13 tool steel components fabricated by DMD were found to be almost the same as the wrought materials [2,84,85]. The cooling rate can be varied by

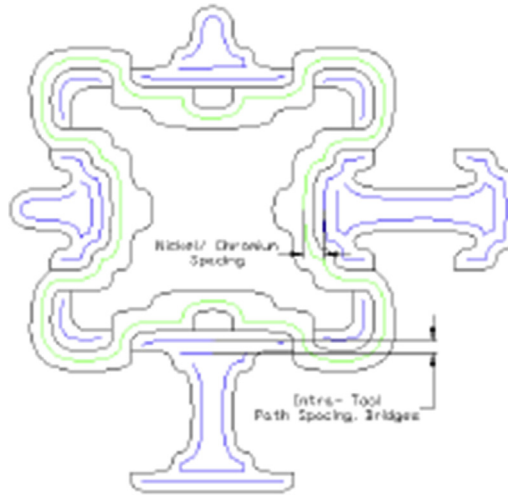

Figure 1.11 Two primary dimensions of unit cell tool paths.

Table 1.2 Descriptions of five tool path

Tool number	Path design	Chromium intratool path spacing (in.)	Chromium−nickel tool path spacing (in.)
1	1	0.012	0.024
2	2	0.014	0.024
3	2	0.014	0.024
4	2	0.0174	0.025
5	2	0.0174	0.030

adapting the deposition layer thickness and adjusting the specific energy [4]. Control the cooling rates enables one to control the dendrite arm spacing and refine the microstructure.

Within the power, velocity, and powder mass flow rate study, the wall profile roughness averages were found to vary between 13 and 51 μm, whereas the wall maximum peak-to-valley distances ranged from 75 to 275 μm [4]. These roughness values were found to be directly related to the layer thickness. The wall roughness can be reduced significantly by making the deposition layers thinner. The wall surface gets rougher as the layer thickness increases because the beam diameter varies as a result of defocusing. As the layers become thicker, the beam diameter has a longer distance to diverge. Therefore the width of cladding is larger at the bottom of the cladding pass in comparison to the top of the cladding pass. By reducing the layer thickness, this beam diameter variation is also reduced and therefore the specimen wall roughness is minimized.

A problem occurred with wall quality in cases with higher deposition velocities. With higher velocities, the cladding at the sample edges sometimes did not catch as much powder as the internal sample cladding. Eventually, the cladding was unable to build up fast enough to compensate for this condition, creating gaps in the cladding passes at the sample edges. By reducing the traverse speed of the deposition around the outline of the part, enough time was obtained for the clad to build to the required height, eliminating any defects.

The three-sensor systems proved to be effective in reducing the average surface roughness of the fabricated parts by approximately 14%. In other words, from an average of seven different specimen sets (five different build patterns and two more with higher pass overlap), the three-sensor configurations reduced the average profile roughness from 44 to 38 μm. At the same time, this sensor configuration reduced the average maximum profile roughness height from 270 to 210 μm, or a 22% improvement. As stated earlier, the maximum profile roughness height is the maximum surface peak-to-valley measurement.

Strict control of laser power and beam quality demonstrates that a wide range of deposition rates and geometrical resolutions may be possible by DMD. Using CO_2 lasers, a lateral resolution of 500 μm and a vertical resolution of 25 μm have been achieved. Fig. 1.12 shows an IMS-Tl sample fabricated with H13 tool steel using DMD. This is a benchmark design used to validate any rapid prototyping process.

DMD laser systems interfaced with CAD/CAM systems for one or two materials in sequence (eg, copper cooling channels and heat sinks in injection-molding die), as in Fig. 1.13, has also been demonstrated. As shown in Fig. 1.14, a conformal cooling channel with a copper heat sink has the potential for improved thermal conductivity with a copper chiller block, and 3D calculation shows that the time cycle can be reduced considerably.

A conformal cooling channel can be made using sacrificial materials [88] with a lower melting point than the material of interest. Fig. 1.13 shows a radiograph of a conformal cooling channel formed in an H13 tool steel die. In an injection-molding die, 75% of the cycle time is devoted to cooling, as shown in Fig. 1.15. Fig. 1.16 shows

Figure 1.12 IMS-T1 sample process parameters.

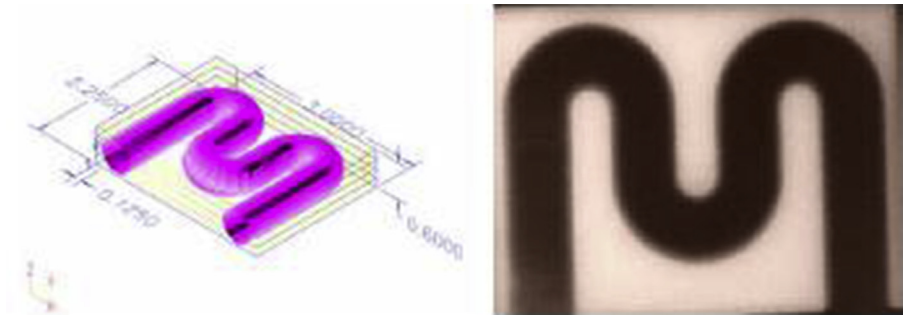

Figure 1.13 Left: An H13 sample with a 0.5-inch channel. Right: A radiographic image of the sample, showing a consistent diameter throughout.

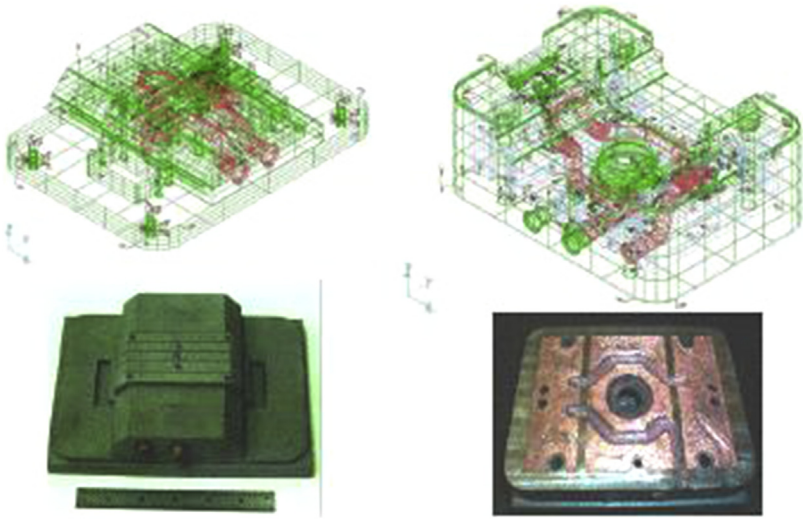

Figure 1.14 Images of the core and cavity of injection molding dies [computer-assisted design images (top) and final fabricated parts (bottom)].

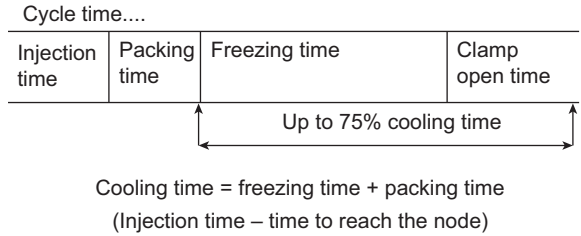

Figure 1.15 In an injection-molding die, 75% of the cycle time is devoted to cooling.

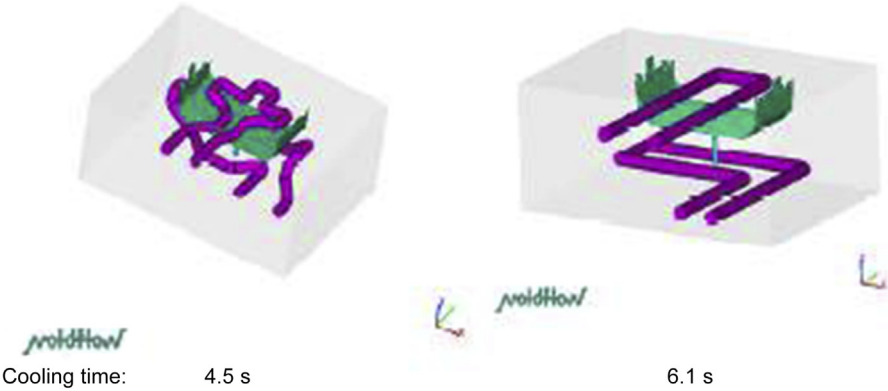

Figure 1.16 A conventional straight-line cooling channel (right) and conformal cooling channels (left) used for the "fuse cover die," with a 26% quicker cooling time.

Table 1.3 Mold flow calculation for cycle time for a straight-line cooling channel and a conformal cooling channel

Geometry	Straight-line cooling (s)	Conformal cooling (s)	Time saved in seconds (%)
Semicylinder	6.6	4.1	38
U-plate	10.4	3.4	67
Hemisphere	14	5.4	61
Relay cover	6.1	4.5	26

the conventional straight-line cooling channel and conformal cooling channels used for the "fuse cover die." Theoretical calculation shows a potential time savings of 26%. A benchmark experiment carried out by one of the users showed 9% savings without any optimization of the flow. Potential time savings increase with the complexity of the shape, as shown in Table 1.3. This type of macrostructure design has already attracted considerable industrial interest.

Closed-loop DMD opens up a new horizon for designed materials when integrated with the HDM and heterogeneous CAD. This methodology of producing performance-based designed materials has the potential to change manufacturing paradigms. This methodology will provide materials with properties that do not occur in nature. Fig. 1.17(a) shows an example of a designed material with a negative coefficient of expansion using the HDM [65]. Fig. 1.17(b) shows the component fabricated by the homogenization DMD technique using a combination of nickel and chromium. Fig. 1.18 shows a designed component similar to a turbine blade that has 50% less mass but has a similar mechanical strength when compared with conventional blade designs. Fig. 1.19 shows creep test data for a component fabricated with Inconel 738. The implication of a 50% reduction in mass in a turbine is a proportional reduction in fuel lost.

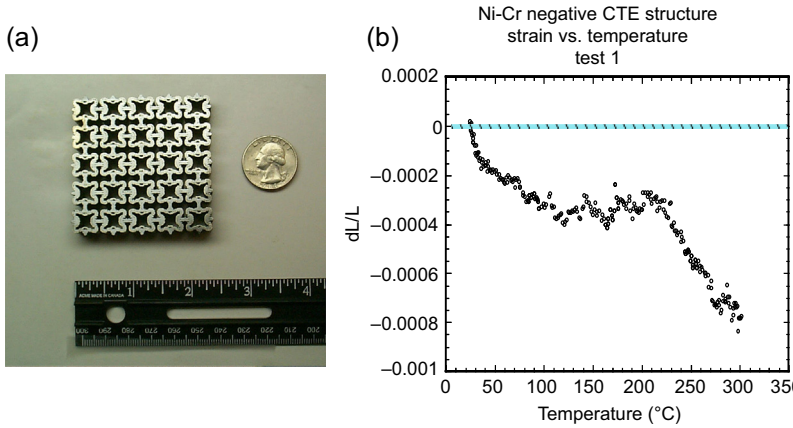

Figure 1.17 (a) A negative coefficient of thermal expansion (NCTE) specimen. (b) Behavior of negative strains of the NCTE structure in the *y*-direction from a heating test in a precisely controlled furnace.

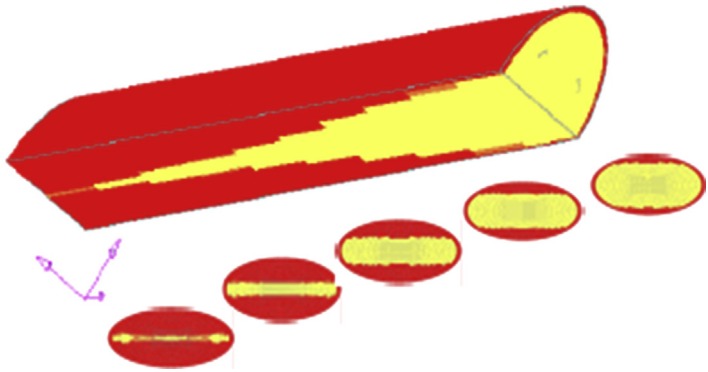

Figure 1.18 A cavity monotonically increases from the fixed to the free end.

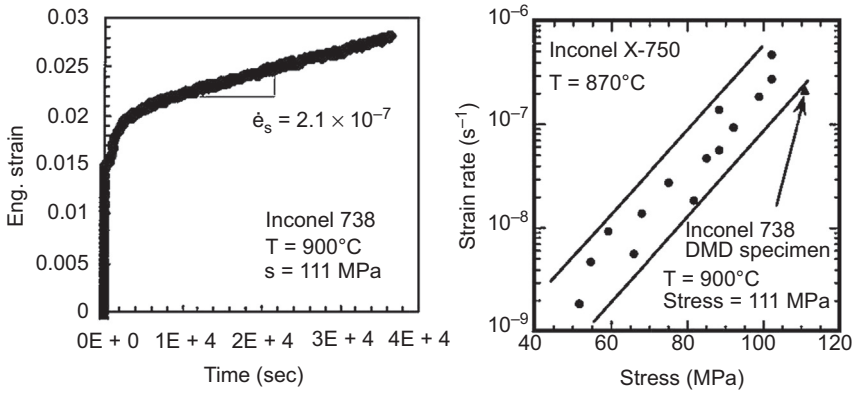

Figure 1.19 Creep results: Engineering strain versus time plot for an Inconel 738 specimen fabricated by direct metal deposition (left). Comparison with Inconel X-750 (right).

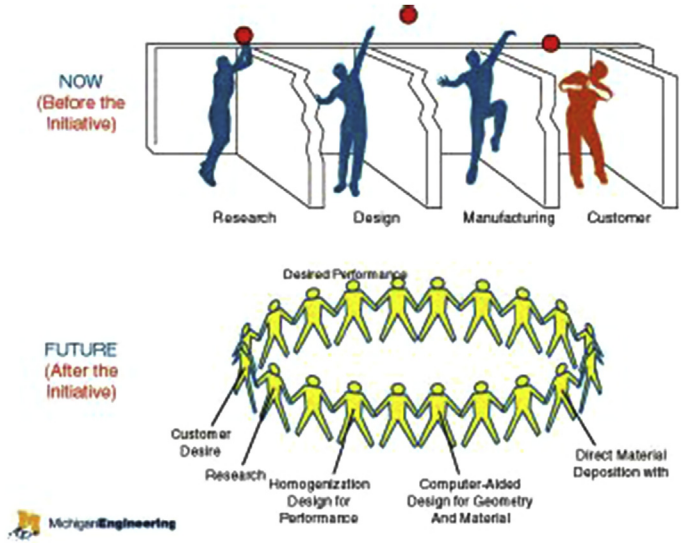

Figure 1.20 Synergy of integrated design and manufacturing for designed materials.

1.5.1 Integrated design and manufacturing

Imagine the impact of designed materials on society and the environment. One can foresee a new paradigm of manufacturing driven by the customer's desire instead of the best available practice. Fig. 1.20 illustrates the synergy this methodology can create compared with current practice.

1.5.2 Remote manufacturing

Modern communication methods are improving the Internet's ability to transfer large volumes of data in a relatively short time. Mathematical and optical methods of data compression are enhancing this capability even further. This will enable seamless communication between design and manufacturing teams in industry. It is conceivable that a design team can send their design data electronically and observe fabrication from a remote site and even edit it online [89]. Of course, to realize this scenario, various technologies must be synthesized and enhanced. Fig. 1.21 shows the process already made possible at POM Group Inc. (acquired by DM3D Technology, LLC). This has the potential to become a global manufacturing platform. An advantage for such platforms will be paperless technology transfer across the globe. At the same time, it will protect the intellectual property of the inventor by reducing the paper trail. Electronic data transfer can be encrypted and thus reduce the potential for unwanted exposure.

1.5.3 Process control and quality-assured manufacturing system (QAMS)

Recent advances have developed the capability to monitor and control (1) geometry, (2) temperature, (3) composition, and (4) microstructure. Microstructure control was not available to the scientific and engineering communities until this invention was filed for a patent [90].

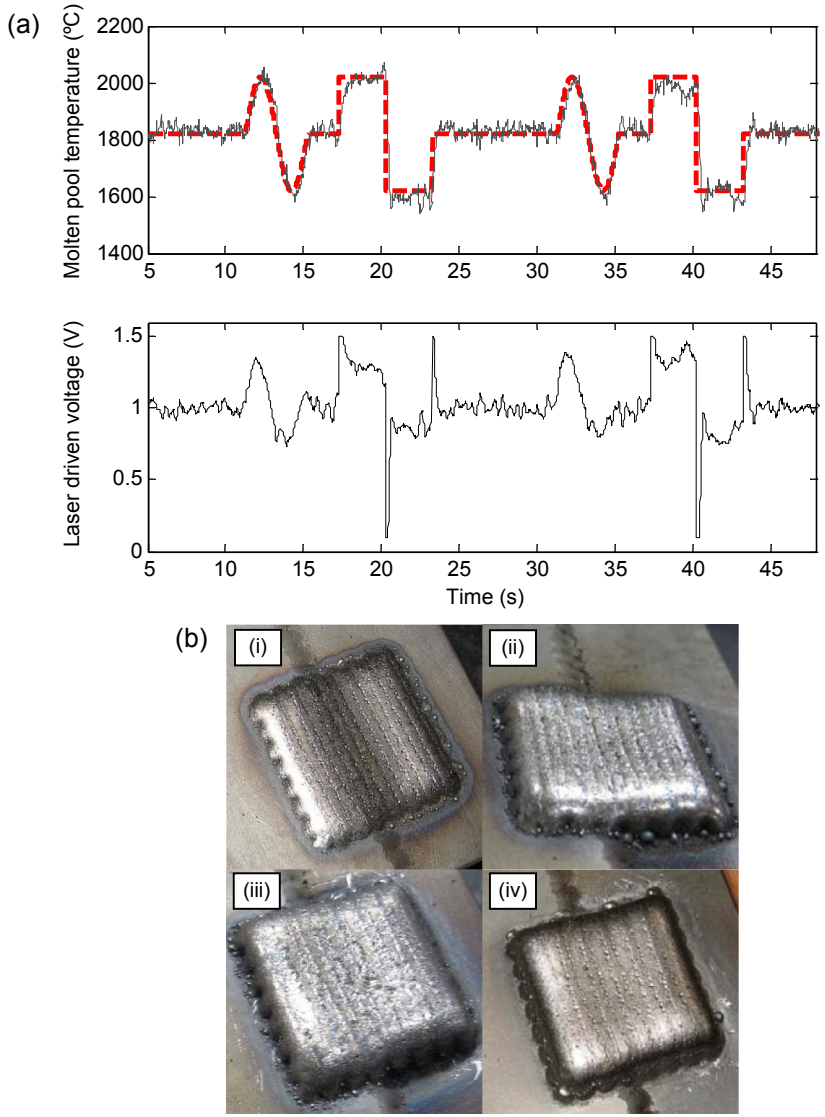

Figure 1.21 (a) Experimental results of tracking the melt pool temperature to sinusoidal-shaped and square temperature profiles. The red curve represents the preset temperature profile; the black curve shows the experimental results. (b) Photographs of the deposition at (i) 10th layer, (ii) 20th layer, (iii) 30th layer and (iv) 40th layer.

1.5.3.1 Geometry control

The basic function of the height controller is to limit the maximum height of metal deposition. The cladding height is monitored using three lenses that are located at 120 degrees spacing in the *x*-*y* plane and 45 degrees corresponding to the laser beam [3,84]. The three collecting lenses are fiber-pigtailed to three high-speed

charge-coupled device cameras, which is used to obtain the cladding images. The image-processing unit includes setting a detection threshold for the pixel brightness and calculating the centroids of the cladding height from the images obtained from each camera. The building height at each layer is a preset value. The three calculated cladding heights are compared with the reference height. The robustness of the height detection is fulfilled by the logic that "overbuilding" is determined by the results of the two of three cameras. A thin-walled figure-8 deposition using this controller, with a dramatically improved dimensional accuracy compared with the one without controller, is shown in Fig. 1.6.

1.5.3.2 Temperature and cooling rate control

A dual-color pyrometer with a selected wavelength away from that of the laser radiation has been used to monitor the melt pool temperature. The measured temperature can be used to provide feedback to a real-time controller to track the melt pool temperature to a preset value. During the DMD process, the controller calculates the optimized control value and sends a control signal to adjust the laser power each time it obtains an updated melt pool temperature.

Fig. 1.21(a) shows the controlled temperatures and the laser actions using a generalized predictive control algorithm that was implemented in a real-time controller during a laser-cladding process on H13 tool steel. The melt pool temperature was successfully tracked to the preset temperature profile. This controller has been used to control the heat input during laser cladding on an uneven surfaced substrate. The controller was able to compensate the cladding on the lower side, as shown in Fig. 1.21(b). By monitoring the temperature as a function of time, we can calculate the cooling rate. Microstructure evolution is dependent on the cooling rate. In situ monitoring of the cooling rate will enable us to control the microstructure and thus the properties by using cooling rate as the input to a closed-loop controller to modify laser power and speed [91]. A hybrid two-input and one-output control system that combines the geometry control and temperature together was also implemented for the DMD process [92]. The system is able to control the heat input for complex geometries to prevent the problems of underfilling or overfilling. Improved geometric accuracy was obtained using this closed-loop control system.

1.5.3.3 Composition sensor

During DMD, a plasma plume is generally a by-product because of the laser-induced plasma. Therefore, real-time spectroscopic analysis can be used to predict composition by evaluating the generated plasma using optical emission spectroscopy; further, a full spatial compositional evaluation of the manufactured products can be obtained. During DMD of an H13 tool steel material, both chromium and iron atomic emission lines are observed. When comparing the H13 tool steel spectral lines with the emission lines of pure chromium and pure iron, the chromium and iron lines are easily identified. Fig. 1.22(a) shows the calibration curves using two different chromium neutral atomic lines and two iron neutral atomic lines [93]. Second-order polynomial fittings were used to form the calibration curves. By measuring the plasma line intensity ratios

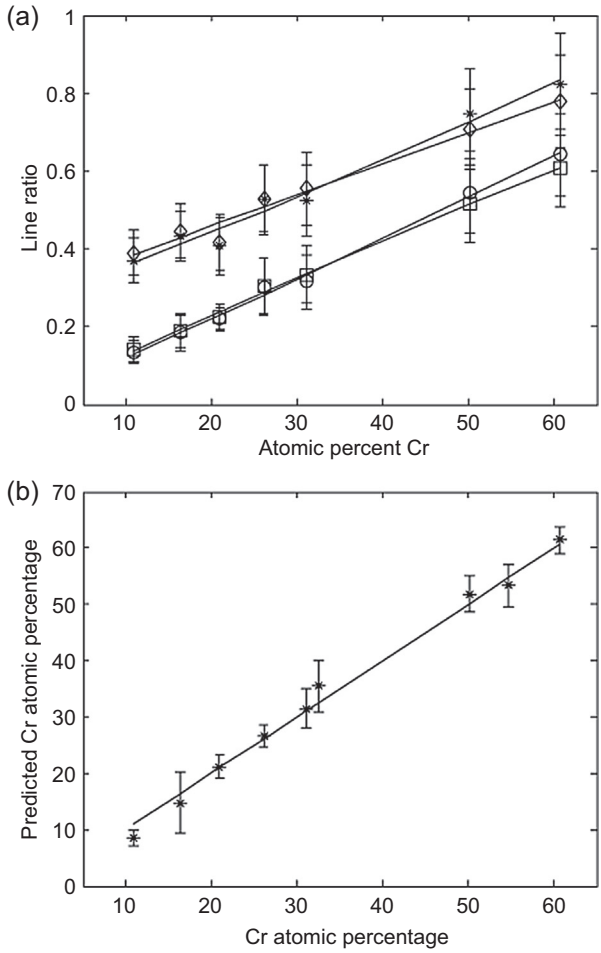

Figure 1.22 (a) A calibration curve using Cr-I/Fe-I line intensity ratios (*star*: Cr-I 428.97/Fe-I 430.8 nm; *diamond*: Cr-I 428.97/Fe-I 432.6 nm; *circle*: Cr-I 434.45/Fe-I 430.8 nm; *square*: Cr-I 434.45/Fe-I 432.6 nm). (b) Predicted chromium percentage using line intensity ratio calibration curves formed by five chromium lines and three iron lines.

and comparing them with the calibration curve, the composition ratio of different elements can be obtained. To improve the prediction accuracy, an average of seven predictions using seven different calibration curves were used (Fig. 1.22(b)).

1.5.3.4 Microstructure sensor

During the DMD process, powders of different elements melt into the molten pool and solidify on the substrate. Different elemental combinations experience different phase changes and form different microstructures, depending on the composition, cooling rate, and heat treatment. We discovered that there exists a strong correlation between the physical parameters of a plasma plume and the final microstructures. Therefore,

we believe that the spectral line acquired from the plasma immediately before solidification can be a valid indicator of the crystal structure. Electron populations at different energy states and the transition probability of the emission lines affect the plasma parameters. This relationship can be used to predict the microstructure from the plasma characterization. For example, Fig. 1.23 shows the correlation between Ti/Fe line ratios

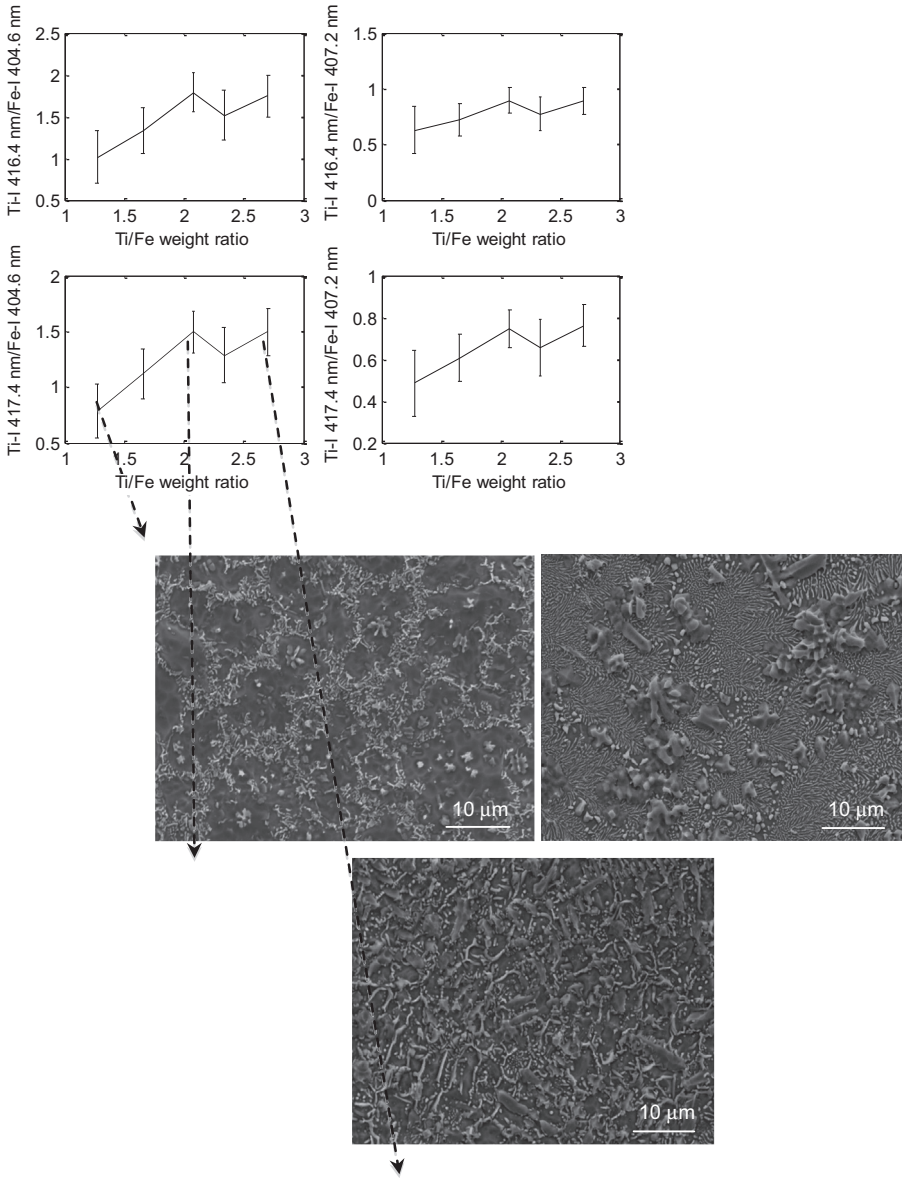

Figure 1.23 Relationship between the four Fe-I/Ti-II line ratios and titanium weight percentage and the corresponding microstructure.

and the microstructure of the Ti−Fe alloys with different weight ratios. We can see that the line intensity has an odd point when a eutectic microstructure was obtained [90].

The changes to the plasma characteristics caused by the microstructure can be used to predict the phase change. Therefore, a spectroscopic sensor that monitors phase changes during the process can be developed based on the observations described in this section.

1.6 Summary and conclusion

Recent advances in DMD system control offer the capability to monitor and control geometry, temperature, composition, and microstructure from the light collected at the laser−material interaction zone. Never in the history of manufacturing was in situ monitoring of phase transformation possible. These monitoring sensors will enable products with desired properties to be produced directly from the CAD data. By integrating the homogenization method, DMD with closed-loop control can also produce meta-materials such as metallic structures with negative CTEs [1]. POM Group Inc. recently built a DMD machine capable of remote manufacturing [16]. Conceptually, one can seat in Manchester (UK) and manufacture in Rochester, New York (USA). Such systems will be a natural choice for a global "economic space." For the research community it will open frontiers for creating alloys with microstructures required for desired performance characteristics.

This chapter presents how closed-loop DMD can be used to fabricate parts with improved performance. It also presents a methodology to use digital information along with HDM and heterogeneous CAD to produce designed materials with desired performance. The latter is a revolutionary departure from the traditional material selection method. This technology can also integrate design and manufacturing to provide products based on performance needed by society.

Readers should also note from the references that although additive manufacturing has been identified as a "third industrial revolution" [1], research on the topic began from 1980s (Fig. 1.24).

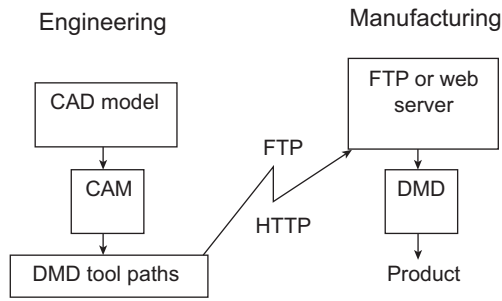

Figure 1.24 Internet operability for remote engineering and manufacturing. *CAD*, computer-assisted design; *DMD*, direct metal deposition; *FTP*, file transfer protocol.

Acknowledgments

This chapter presents multiple years of group effort and funding from DARPA, NSF, ONR, AFOSR, General Electric, POM Group Inc., and several industrial partners and colleagues, including Professors Kikuchi, Dutta, and Ghosh. Present and past CLAIM group members include Justin Koch, Andrew Schifferer, Joohyun Choi, Jollin DeSouza, Eric Stiles, Huan Qi, Lijun Song, and Xiuli He.

References

[1] A Third Industrial Revolution, The Economist, April 12, 2002.
[2] J. Mazumder, J. Choi, K. Nagarathnam, J. Koch, D. Hetzner, The direct metal deposition of H13 tool steel for 3-D components, Journal of the Minerals, Metals and Materials Society 49 (5) (1997) 55−60.
[3] J. Mazumder, A. Schifferer, J. Choi, Direct materials deposition: designed macro and microstructure, Materials Research Innovations 3 (3) (1999) 118−131.
[4] J. Mazumder, D. Dutta, N. Kikuchi, A. Ghosh, Closed loop direct metal deposition: art to part, Optics and Lasers in Engineering 34 (4−6) (2000) 397−414.
[5] J. D'souza, Laser-Aided Direct Metal Deposition of Three Dimensional Components (Master thesis), Mechanical Engineering Department, the University of Michigan, 2001.
[6] E. Stiles, The Fabrication of Designed Materials Using Direct Metal Deposition (Master thesis), Mechanical Engineering Department, the University of Michigan, 2000.
[7] M. Ma, Z. Wang, D. Wang, X. Zeng, Control of Shape and performance for direct laser fabrication of precision large-scale metal parts with 316L Stainless Steel, Optics and Laser Technology 45 (2013) 209−216.
[8] K. Zhang, S. Wang, W. Liu, X. Shang, Characterization of stainless steel parts by laser metal deposition shaping, Materials and Design 55 (2014) 104−119.
[9] T. Amin, J.W. Newkirk, F. Liou, An investigation of the effect of direct metal deposition parameters on the characteristics of the deposited layers, Case Studies in Thermal Engineering 3 (2014) 21−34.
[10] A.J. Pinkerton, Advances in the modeling of laser direct metal deposition, Journal of Laser Applications 27 (S15001) (February 2015).
[11] S. Wen, Y.C. Shin, Modeling of transport phenomena during the coaxial laser direct deposition process, Journal of Applied Physics 108 (2010) 044908.
[12] X. He, G. Yu, J. Mazumder, Temperature and composition profile during double-track laser cladding of H13 tool steel, Journal of Physics D: Applied Physics 43 (2010).
[13] M. Sachs, J. Cima, P. Williams, D. Brancazio, J. Cornie, Three dimensional printing: rapid tooling and prototypes directly from a CAD model, Journal of Engineering for Industry-Transactions of the ASME 114 (4) (1992) 481−488.
[14] B. Dutta, S. Palaniswamy, J. Choi, L. Song, J. Mazumder, Direct Metal Deposition, Advanced Materials and Processes (5) (May 2011) 33−36.
[15] R. Vilar, Laser alloying and laser cladding, Lasers in Materials Science 301 (1999) 229−251.
[16] O. Milewski, G.K. Lewis, J. Fonseca, R.B. Nemec, Laser powder deposition of a near net shape injection mold core − a case study, Materials and Manufacturing Processes 15 (2) (2000) 247−258.
[17] J. Mazumder, Laser assisted surface coatings, in: K. Stern (Ed.), Metallurgical and Ceramic Protective Coatings, Chapman and Hall, London, 1996, pp. 74−111.

[18] J. Mazumder, O. Conde, M. Steen, R. Vilar (Eds.), Laser Processing: Surface Treatment and Film Deposition, Ser. NATO ASI Series E, vol. 307, Kluwer Academic Publishers, 1996, pp. 47−75.
[19] A.A. Levin, D.C. Meyer, A. Gorbunov, A. Mensch, W. Pompe, P. Paufler, Phase transformations after long-time annealing in metastable Fe-Cr alloy films prepared by pulsed laser deposition, Journal of Alloys and Compounds 360 (1−2) (2003) 107−117.
[20] A.A. Ashary, R.C. Tucker, Electrochemical and long-term corrosion studies of several alloys in bare condition and plasma sprayed with Cr_2O_3, Surface and Coatings Technology 43−44 (1−3) (1990) 567−576.
[21] J.K. Tien, F.S. Pettit, Mechanism of oxide adherence on Fe-25Cr-4Al (Y or Sc) alloys, Metallurgical Transactions 3 (6) (1972) 1587.
[22] G.C. Wood, F.H. Stott, Directions for future-research in high-temperature corrosion, Oxidation of Metals 44 (1−2) (1995) 375−397.
[23] P. Nash, D.R.F. West, Phase-equilibria in Ni-rich region of Ni-Al-Hf system, Metal Science 15 (8) (1981) 347−352.
[24] J. Singh, J. Mazumder, Microstructure and wear properties of laser clad Fe-Cr-Mn-C alloys, Metallurgical Transactions A-Physical Metallurgy and Materials Science 18 (2) (1987) 313−322.
[25] J. Singh, J. Mazumder, Effect of extended solid-solution of Hf on the microstructure of the laser clad Ni-Fe-Cr-Al-Hf alloys, Acta Metallurgica 35 (8) (1987) 1995−2003.
[26] J. Singh, K. Nagarathnam, J. Mazumder, Laser cladding of Ni-Cr-Al-Hf on Inconel 718 for improved high-temperature oxidation resistance, High Temperature Technology 5 (3) (1987) 131−137.
[27] J. Singh, J. Mazumder, Microstructure of laser clad Ni-Cr-Al-Hf alloy on a Gamma'-strengthened Ni-base superalloy, Metallurgical Transactions A-Physical Metallurgy and Materials Science 19 (8) (1988) 1981−1990.
[28] S. Raja, J. Singh, J. Mazumder, Laser cladding of Zr on Mg for improved corrosion properties, Journal of Metals 40 (7) (1988). A22−A22.
[29] R. Subramanian, S. Sircar, J. Mazumder, Laser cladding of zirconium on magnesium for improved corrosion properties, Journal of Materials Science 26 (4) (1991) 951−956.
[30] A.A. Wang, S. Sircar, J. Mazumder, Laser cladding of Mg-Al alloys, Journal of Materials Science 28 (19) (1993) 5113−5122.
[31] S. Shi, Q. Zheng, G. Fu, X. Wang, Comparison study on resistance to wear and abrasion of high-temperature sliding strike of laser and plasma spray layer on the stainless steel surface, Nuclear Engineering and Design 231 (1) (2004) 121−126.
[32] J.D. Kim, K.H. Kang, J.N. Kim, Nd:YAG laser cladding of marine propeller with hastelloy C-22, Applied Physics A-Materials Science and Processing 79 (4−6) (2004) 1583−1585.
[33] S.W. Huang, M. Samandi, A. Brandt, Abrasive wear performance and microstructure of laser clad WC/Ni layers, Wear 256 (11−12) (2004) 1095−1105.
[34] Y. Chen, H.M. Wang, High-temperature wear resistance of a laser clad TiC reinforced FeAl in situ composite coating, Surface and Coatings Technology 179 (2−3) (2004) 252−256.
[35] D.W. Zhang, T.C. Lei, The microstructure and erosive-corrosive wear performance of laser-clad Ni-Cr_3C_2 composite coating, Wear 255 (2003) 129−133.
[36] D. Shechtman, I. Blech, D. Gratias, J.W. Cahn, Metallic phase with long-range orientational order and no translational symmetry, Physical Review Letters 53 (20) (1984) 1951−1953.
[37] K. Biswas, R. Galun, B.L. Mordike, K. Chattopadhyay, Laser cladding of quasicrystal forming Al-Cu-Fe on aluminum, Journal of Non-Crystalline Solids 334 (2004) 517−523.

[38] H. Gedda, J. Powell, G. Wahlstrom, W.B. Li, H. Engstrom, C. Magnusson, Energy redistribution during CO_2 laser cladding, Journal of Laser Applications 14 (2) (2002) 78−82.
[39] J. Lin, Laser attenuation of the focused powder streams in coaxial laser cladding, Journal of Laser Applications 12 (1) (2000) 28−33.
[40] J. Lin, Temperature analysis of the powder streams in coaxial laser cladding, Optics and Laser Technology 31 (8) (1999) 565−570.
[41] C.Y. Liu, J. Lin, Thermal processes of a powder particle in coaxial laser cladding, Optics and Laser Technology 35 (2) (2003) 81−86.
[42] J. Mazumder, P. Mohanty, A. Kar, Mathematical modelling of laser materials processing, International Journal of Materials and Product Technology 11 (3−4) (1996) 193−252.
[43] M. Picasso, C.F. Marsden, J.D. Wagniere, A. Frenk, M. Rappaz, A simple but realistic model for laser cladding, Metallurgical and Materials Transactions B-Process Metallurgy and Materials Processing Science 25 (2) (1994) 281−291.
[44] J. Jouvard, D. Grevey, F. Lemoine, A. Vannes, Continuous wave Nd:YAG laser cladding modeling: a physical study of track creation during low power processing, Journal of Laser Application 9 (1) (1997) 43−50.
[45] A.F.A. Hoadley, M. Rappaz, A thermal-model of laser cladding by powder injection, Metallurgical Transactions B-Process Metallurgy 23 (5) (1992) 631−642.
[46] V. Yevko, C. Park, G. Zak, T. Coyle, B. Benhabib, Cladding formation in laser-beam fusion of metal powder, Rapid Prototyping Journal 4 (4) (1998) 168−184.
[47] A.F.H. Kaplan, G. Groboth, Process analysis of laser beam cladding, Journal of Manufacturing Science and Engineering-Transactions of the ASME 123 (4) (2001) 609−614.
[48] E. Toyserkani, A. Khajepour, S. Corbin, Three-dimensional finite element modeling of laser cladding by powder injection:effects of powder feedrate and travel speed on the process, Journal of Laser Applications 15 (3) (2003) 153−160.
[49] G. Zhao, C. Cho, J. Kim, Application of 3-D finite element method using Lagrangian formulation to dilution control in laser cladding process, International Journal of Mechanical Science 45 (2003) 777−796.
[50] Y.L. Huang, D.N. Zou, G.Y. Liang, J.Y. Su, Numerical simulation on cladding track, fluid flow field and temperature field in laser cladding process with powder feeding, Rare Metal Materials and Engineering 32 (5) (2003) 330−334.
[51] W.D. Bennon, F.P. Incropera, A continuum model for momentum, heat and species transport in binary solid liquid-phase change systems I model formulation, International Journal of Heat and Mass Transfer 30 (10) (1987) 2161−2170.
[52] T. Chande, J. Mazumder, Two-dimensional, transient model for mass-transport in laser surface alloying, Journal of Applied Physics 57 (6) (1985) 2226−2232.
[53] M.J. Aziz, Dissipation-theory treatment of the transition from diffusion-controlled to diffusionless solidification, Applied Physics Letters 43 (6) (1983) 552−554.
[54] M.J. Aziz, Model for solute redistribution during rapid solidification, Journal of Applied Physics 53 (2) (1982) 1158−1168.
[55] A. Kar, J. Mazumder, One-dimensional diffusion-model for extended solid-solution in laser cladding, Journal of Applied Physics 61 (7) (1987) 2645−2655.
[56] A. Kar, J. Mazumder, Model for nonequilibrium partitioning during rapid solidification of binary concentrated-solutions, Acta Metallurgica et Materialia 40 (8) (1992) 1873−1881.
[57] S. Chakraborty, P. Dutta, Numerical modeling of heat and mass transfer in laser surface alloying: non-equilibrium solidification effects, Materials and Manufacturing Processes 17 (4) (2002) 455−468.

[58] H. Qi, H. Ki, J. Mazumder, Numerical simulation of multi-material laser cladding by coaxial powder injection, in: ICALEO, San Francisco, 2004.
[59] H. Qi, Synthesis of Designed Materials by Laser-Based Direct Metal Deposition Technique: Experimental and Theoretical Approaches (Ph.D. thesis), University of Michigan, 2005.
[60] H. Qi, J. Mazumder, H. Ki, Numerical simulation of heat transfer and fluid flow in coaxial laser cladding process for direct metal deposition, Journal of Applied Physics 100 (2) (July 2006).
[61] J. Blanther, Manufacture of Contour Relief Maps, 1892. US Patent 473901.
[62] C. Chua, K. Leong, C. Lim, Rapid Prototyping: Principles and Applications, second ed., World Scientific, Singapore, 2003.
[63] L. Lü, J. Fuh, Y. Wong, Laser-Induced Materials and Processes for Rapid Prototyping, Kluwer Academic Publishers, 2001.
[64] D.T. Pham, R.S. Gault, A comparison of rapid prototyping technologies, International Journal of Machine Tools and Manufacture 38 (10−11) (1998) 1257−1287.
[65] M. Bendsøe, N. Kikuchi, Generating optimal topologies in structural design using a homogenization method, Computer Methods in Applied Mechanics and Engineering 71 (1988) 197−224.
[66] M. Bendsøe, Optimal shape design as a material distribution problem, Structural and Multidisciplinary Optimization 1 (1989) 193−202.
[67] N.S. Bakhvalov, G. Panasenko, Homogenizaiton: Averaging Processes in Periodic Media: Mathematical Problems in the Mechanics of Composite Materials, Kluwer Academic Publishers, Dordrecht, Boston, London, 1989.
[68] O. Sigmund, Materials with prescribed constitutive parameters − an inverse homogenization problem, International Journal of Solids and Structures 31 (17) (1994) 2313−2329.
[69] O. Sigmund, Tailoring materials with prescribed elastic properties, Mechanics of Materials 20 (4) (1995) 351−368.
[70] O. Sigmund, S. Torquato, Design of materials with extreme thermal expansion using a three-phase topology optimization method, Journal of the Mechanics and Physics of Solids 45 (6) (1997) 1037−1067.
[71] B.-C. Chen, E.C.N. Silva, N. Kikuchi, Advances in computational design and optimization with application to MEMS, International Journal for Numerical Methods in Engineering 52 (1−2) (2001) 23−62.
[72] E.C. Silva, J.S.O. Fonseca, N. Kikuchi, Optimal design of periodic piezocomposites, Computer Methods in Applied Mechanics and Engineering 159 (1−2) (1998) 49−77.
[73] J. Haslinger, J. Dvorak, Optimum composite material design, RAIRO Mathematical Modelling and Numerical Analysis 29 (1995) 657−686.
[74] O. Sigmund, S. Torquato, Design of smart composite materials using topology optimization, Smart Materials and Structures 8 (1999) 365−379.
[75] R.V. Kohn, G. Strang, Optimal design and relaxation of variational problems, 1, Communications on Pure and Applied Mathematics 39 (1) (1986) 113−137.
[76] R.V. Kohn, G. Strang, Optimal design and relaxation of variational problems, 2, Communications on Pure and Applied Mathematics 39 (2) (1986) 139−182.
[77] R.V. Kohn, G. Strang, Optimal design and relaxation of variational problems, 3, Communications on Pure and Applied Mathematics 39 (3) (1986) 353−377.
[78] K. Suzuki, N. Kikuchi, A homogenization method for shape and topology optimization, Computer Methods in Applied Mechanics and Engineering 93 (3) (1991) 291−318.
[79] B.C. Chen, Optimal Design of Material Microstructures and Optimization of Structural Topology for Design-Dependent Loads (Ph.D. thesis), The University of Michigan, 2000.

[80] R. Lakes, Foam structures with a negative Poisson's ratio, Science 235 (4792) (1987) 1038−1040.
[81] G.W. Milton, Composite-materials with Poisson ratios close to -1, Journal of the Mechanics and Physics of Solids 40 (5) (1992) 1105−1137.
[82] A. Hammeke, Laser Spray Nozzle and Method, 1988. US Patent 4724299.
[83] J. Mazumder, D. Voekel, Method and Apparatus for Noncontact Surface Contour Measurement, 1995. US Patent 5446549.
[84] J.L. Koch, J. Mazumder, Apparatus and Methods for Monitoring and Controlling Multilayer Laser Cladding, 2000. US Patent 6122564.
[85] J. Koch, J. Mazumder, Rapid prototyping by laser cladding, in: P. Denney, I. Miyamoto, B.L. Mordike (Eds.), ICALEO '93, vol. 77, 1993, pp. 556−565.
[86] J. Mazumder, J. Koch, K. Nagarathnam, J. Choi, Rapid manufacturing by laser aided direct deposition of metals, in: Advances in Powder Metallurgy and Particulate Materials (MPIF), 1996, pp. 107−118.
[87] J. Choi, K. Nagarathnam, J. Koch, D. Hetzner, J. Mazumder, Microstructure and properties of laser clad material for rapid tooling manufacturing, in: International Conference on Powder Metallurgy and Particulate Materials, Chicago, IL, 1997.
[88] J. Mazumder, T. Skszek, J. Kelly, J. Choi, Production of Overhang, Undercut, and Cavity Structures Using Direct Metal Depostion, 2002. US Patent 6410105.
[89] J. Mazumder, System and Method for Remote Direct Material Deposition, 2003. US Patent 6580959.
[90] L.J. Song, C. Wang, J. Mazumder, In-situ identification and control of microstructure produced by phase transformation of a material, in: J. Mazumder, L. Song, C. Wang (Eds.), USPTO 13/159955 (Pending Patent).
[91] L.J. Song, J. Mazumder, Feedback control of melt pool temperature during laser cladding process, IEEE Transactions on Control Systems Technology 19 (6) (2011) 1349−1356.
[92] L.J. Song, et al., Control of melt pool temperature and deposition height during direct metal deposition process, International Journal of Advanced Manufacturing Technology 58 (1−4) (2012) 247−256.
[93] L.J. Song, J. Mazumder, Real time Cr measurement using optical emission spectroscopy during direct metal deposition process, IEEE Sensors Journal 12 (5) (2012) 958−964.

Powder bed fusion processes: an overview

2

S. Sun, M. Brandt, M. Easton
RMIT University, Centre for Additive Manufacturing, Melbourne, VIC, Australia

2.1 Process characteristics

The laser-based powder bed fusion process is schematically illustrated in Fig. 2.1. A laser beam scans at a controlled speed the selected locations of the powder bed and fuses the powder to the solid material underneath by either full melting [selective laser melting (SLM)] or partial melting [selective laser sintering (SLS)]. The powder bed is lowered by the defined layer thickness and a new layer of powder is dropped and levelled after laser radiation in one layer is completed. The process repeats until the part is completely built. The laser scanning path in each layer is defined by the part geometry at the corresponding z location and the selected scanning strategy.

The built chamber is protected with the flow of inert gas (argon, nitrogen) during processing to prevent oxidation. Because the gas flow also helps to remove the condensate that is produced by melting the powder, homogeneous gas flow across the build area plays an important role in the quality and properties of SLM-processed parts [2].

Based on the process description, it is important to achieve a homogeneous thickness of powder in each layer to control the quality of the part built by powder bed

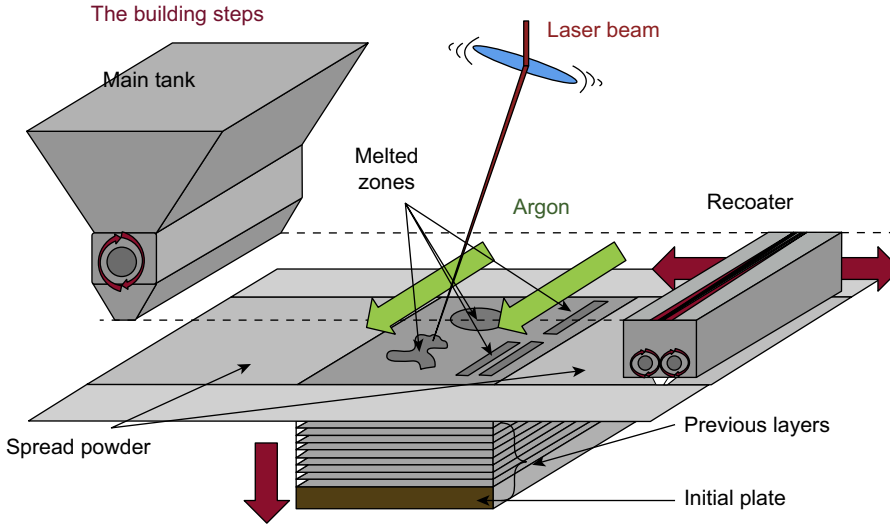

Figure 2.1 Schematic illustration of the laser-based powder bed fusion process [1].

Laser Additive Manufacturing. http://dx.doi.org/10.1016/B978-0-08-100433-3.00002-6
Copyright © 2017 Elsevier Ltd. All rights reserved.

processes. Various methods have been developed to provide and level the powder in each layer before laser scanning.

Sufficient powder for building each layer can be supplied by dropping a controlled volume through a recoater or a hopper, or by lifting the feed cartridge to a controlled height. The powder is then spread uniformly over the build platform by a counter-rotating roller, wiper or doctor blade. A powder delivery system should maximize the ability of the powder to flow, minimize the formation of a particle cloud and minimize the shear forces over the previous layer of the build.

2.2 Processing parameters

The processing parameters in the powder bed fusion processes include layer thickness (t), laser power (P), laser scanning speed (v) and scanning path strategy, hatching space (h) and laser spot size (d), particle size and distribution, platform pre-heating temperature and laser beam scanning strategy (see Fig. 2.2).

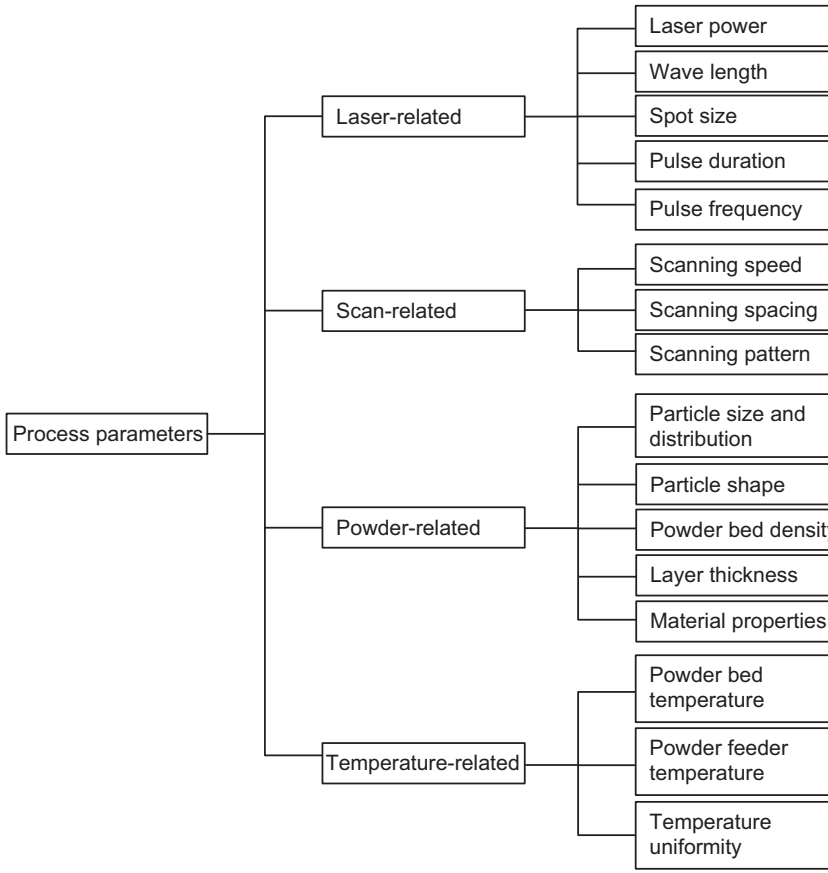

Figure 2.2 The principal processing parameters involved in the selective laser melting process [3].

Almost all metals can be processed by SLM [4]. However, processing windows and, consequently, their difficulty can vary because of differences in chemical composition, laser absorption, surface tension and viscosity of the melt and thermal conductivity.

2.2.1 Definition of the combined processing parameters

A number of key variables defined by the processing parameters can be used to characterize the process:

1. Volumetric energy density (E_V, Joules/millimeter cubed) [4–8]:

$$E_V = \frac{P}{v \cdot h \cdot t} \tag{2.1}$$

2. Linear input energy density (E_I, Joules/millimeter cubed) [9]:

$$E_I = \frac{4P}{\pi v \cdot d^2} \tag{2.2}$$

3. Surface energy density (E_S, Joules/millimeter squared) is the energy density applied to the surface of the powder bed [10,11]:

$$E_S = \frac{P}{vd} \tag{2.3}$$

4. Liner energy density (LED) is the power input per unit speed (E_L, Joules/millimeter) [11–17]:

$$E_L = \frac{P}{v} \tag{2.4}$$

The optimal hatching space is [18]:

$$h = 0.7 \cdot w \tag{2.5}$$

where w is the beam waist.

2.2.2 Morphology and size of particles

The morphology and size of feedstock powders are important factors for powder bed fusion processes because they affect powder flowability, laser energy absorption and the thermal conductivity of the powder bed.

A higher packing density of the powder bed is preferred for powder bed fusion processes because of the lower internal stresses, part distortion, porosity and surface roughness in the built part [19–21]. The packing density of the powder bed is significantly affected by the particle morphology, size and distribution [20,22,23]. A higher

powder bed packing density can be achieved with a wider distribution of particle size, as the gaps between larger particles can be filled in with smaller particles [11].

A spherical particle morphology improves the flowability of the powder to achieve a high packing density in the powder bed, which improves the final quality of the SLM-processed parts [20]. Hence gas-atomized powders with a spherical shape are widely used as the feedstock for additive manufacturing processes.

On the other hand, the flow of powder with a non-spherical shape is obstructed because the particles tend to interlock mechanically and entangle with each other. Hence non-homogeneous layers of powder with varying packing densities form on the top of the previously built solid surface, which may lead to the formation of defects such as porosity and/or incomplete melting [20,24].

A reduction in particle size results in (1) an increase in surface area, which favours the absorption of laser energy to increase the melt pool temperature [25]; (2) an increase in the gap in the powder bed, which may lead to high porosity in the consolidated part if the gap is too large [11]; (3) an increase in the tendency for particle agglomeration [23,25]; and (4) a reduction in powder flowability.

The thermal conductivity of loose powder is primarily determined by the packing density of the powder bed [26,27] and, less significantly, by the properties of the powder material. In general, the thermal conductivity of powder beds formed by irregular particles or by those with a wide size distribution is higher than that formed by monodisperse spherical powders at the same density [27,28].

The incident laser power is absorbed by the powder layer by multiple reflections through the gaps among the particles [29−32]. Hence the absorption of laser energy by the powder bed is significantly higher than the absorption by a flat surface of a solid metal with the same composition [30,33−35]. The effect of multiple reflections on absorption is more significant for highly reflective metals (such as aluminium and copper) than for moderately absorptive metals (such as iron and titanium); therefore the dependence of absorptivity on powder array and powder feed system is more pronounced for highly reflective metals [30]. The percentage of the incident energy absorbed by the substrate or the previously built solid underneath the powder layer decreases with an increase in the optical thickness of the powder layer [34,36] and a decrease in particle size [36].

2.3 Characteristics of the melt pool

A very small melt pool is produced as a result of laser radiation on the surface of the powder bed during SLM. It has various characteristics:

1. Melt pool temperature: The maximum temperature significantly increases with a general increase in laser power [37−39] or linear energy density [14,16], but it slightly decreases with an increase in laser scanning speed [38,39].
2. Temperature gradient: The temperature gradient in the melt pool increases linearly with an increase in the applied laser power [37,40]. The temperature gradient is more pronounced in materials with low thermal conductivity [41].

3. Melt lifetime: The liquid lifetime is the duration from the time powder particles in the local region start to melt until they eventually solidify. It is found to increase with an increase in the laser power and a decrease in the laser scanning speed [40].
4. Melt pool dimensions: The melt pool dimensions including length, width and depth increase with an increase in LED [16] or laser power [36,39,40]. The influence of LED on the melt pool length and width is more significant than that on melt pool depth [16]. However, the melt pool length increases and the width of the melt pool decreases with an increase in laser scanning speed [11,18,36,42,43].
5. Melt viscosity: The viscosity of a melt decreases with an increase in linear energy density as a result of the increase in the melt pool temperature [42]. Dynamic viscosity should be balanced so that its low enough that the melt pool can be spread properly on a formerly processed layer and high enough to prevent balling phenomena [44,45].
6. Melt flow: Mass transfer in the melt pool occurs as a result of the thermocapillary flow; Marangoni convection occurs as the result of surface tension gradient. The direction of the melt flow is determined by the sign of the surface tension gradient of the melt, as shown schematically in Fig. 2.3. A shallow and broad melt pool is produced if the flow is radially outward when $\frac{d\gamma_{LV}}{dT} < 0$ (as for pure metals and many alloys) [40], as in Fig. 2.3(a). A narrow/deep melt pool is formed if the flow is radially inward when $\frac{d\gamma_{LV}}{dT} > 0$ (as for alloys containing a sufficiently large amount of surface-active elements) [46], as shown in Fig. 2.3(b). Surface tension at the edge of a melt pool can be dramatically reduced by surface oxidation during SLM of iron and tungsten; this changes the sign of the surface tension gradient and the melt flow from the cooler melt at the edge (lower relative surface tension due to oxidation) toward the area near the center of the melt pool (higher surface tension) [46,47]. The velocity

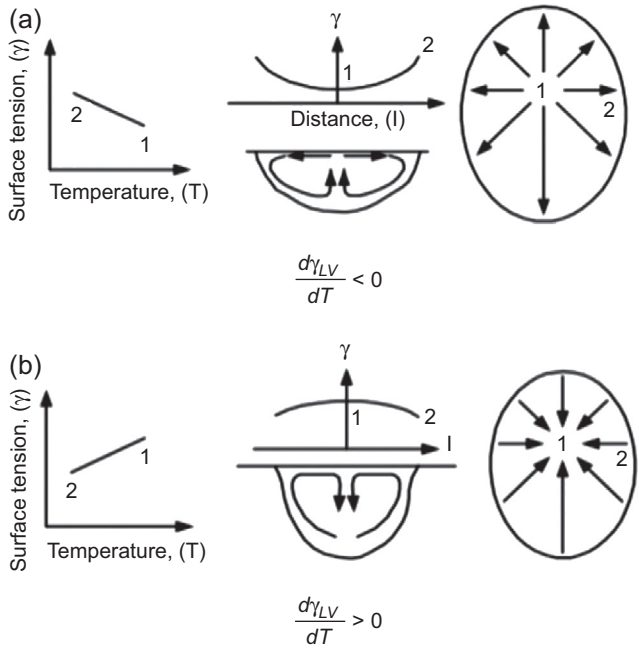

Figure 2.3 Schematic illustration of the effect of the surface tension gradient on Marangoni convection in a melt pool [47]. (a) $\frac{d\gamma_{LV}}{dT} < 0$. (b) $\frac{d\gamma_{LV}}{dT} > 0$. 1 represents the centre of the melt pool, 2 represents the edge of the melt pool.

of the melt flow increases with an increase in laser scanning speed and powder layer thickness [48], which results in melt splashing at high laser scanning speeds [8,48,49].

7. Stability of the melt pool: A melt pool is stable at a range of scanning speeds for a given laser power. The range of the stable zone increases with an increase in laser power, and it becomes narrower for materials with a higher thermal conductivity at a given laser power and layer thickness [42]. The melt pool stability is critical for the quality of SLM-fabricated parts; melt pool instability results in an irregular and/or discontinuous track, which leads to high surface roughness and volumetric porosity due to balling in the fabricated parts [12].
   a. Hydrodynamic instability of a melt is driven by the Marangoni effect and becomes increasingly important with an increase in the LED because of a relativity high laser power or a low scanning speed [5,42].
   b. Capillary (Rayleigh) instability of a melt occurs when the total surface of the melt pool is larger than that of a sphere with the same volume and when the viscosity is too low [14,44].
8. Balling: Balling is a phenomenon where the molten track shrinks and breaks up into a row of spheres to reduce the surface energy by the surface tension if the molten material does not wet the underlying substrate [50,51]. The balling effect can lead to high surface roughness and porosity in the as-built parts, and it might even jeopardize the powder-laying process if the size of the balls is large enough to obstruct the movement of the paving roller or recoater [51]. An ellipsoidal ball with a diameter of about 500 μm is detrimental to the quality of the SLM-processed part. However, spherical balls with a diameter of about 10 μm have no obvious detrimental effect on the quality of the SLM-processed part [51].
9. Sputtering: Sputtering is caused by overheating the melt pool [52], and the intensity of sputtering increases with an increase in input energy density [9]. Liquid droplet and non-melted powder particles around the melt pool are expulsed by the recoil pressure generated on the melt pool as the result of the melt evaporating [9,52]. The sputter caused by melt expulsion is spherical and much larger than the particle size of the feed powders [9,52]. Oxides a few micrometres in size on the sputter surface are the result of the oxidation of the most volatile elements in the alloys that are enriched on the surface of the sputters [52]. The sputter caused by the expulsion of non-melted particles is also known as a satellite [53] and has a microstructure similar to that of the feed powder alloy [3].

Balling is attributed to (1) the capillary instability of a melt pool [42,49,50]; (2) hydrodynamic instability driven by the Marangoni effect [42]; (3) splashing of the melt pool as a result of a high melt pool surface temperature [14,16], a high velocity of the melt flow [48] and a turbulent liquid solidification front [14]; (4) high oxygen content in the atmosphere due to deteriorated wettability at the interface, with the oxidation of the melt pool [8] and the increasing tendency to the larger radially inward Marangoni flow caused by the larger positive value of the surface tension gradient of liquid, with higher dissolved oxygen content in iron [46,50,51,54] and tungsten [47,55]; (5) rapid solidification before the melt is properly spread, driven by capillary flow when processing materials with high thermal conductivity, such as tungsten [47]; and (6) lack of contact between the molten powder and the substrate because of insufficient melting of substrate.

Balling occurs as a result of capillary instability (Fig. 2.4) to reduce the surface free energy [50]. Therefore it is critical to control the ratio of the length of the melt to the width of the melt to meet:

$$\frac{l}{d} < 2.1 \text{ [50]} \tag{2.6}$$

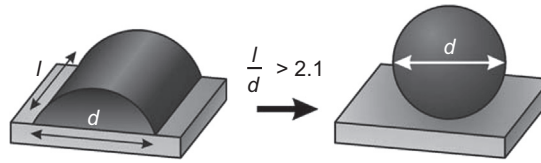

Figure 2.4 Balling caused by capillary instability as a half cylinder transitioning to a sphere, depending on the dimensions of the melt pool [50].

$$\frac{l}{d} < \frac{\pi}{\sqrt{2}}\sqrt{\frac{2\phi(2+\cos 2\,\phi)-3\sin 2\,\phi}{\phi(1+\cos 2\,\phi)-\sin 2\,\phi}} \quad \text{when} \quad \phi > \frac{\pi}{2}\,[42] \tag{2.7}$$

where ϕ is the contact angle. Hence optimal laser processing parameters are required to make the length-to-width ratio of the melt pool as small as possible in order to eliminate the balling effect [16].

Balling can be eliminated to a certain extent with surface remelting provided by a second laser scan [47,51] and proper selection of laser exposure time to achieve a balanced viscosity [47]. The density of SLM-processed parts can be improved by laser surface remelting after the first scan [47,56–58].

2.4 Microstructural features

The microstructure of additively manufactured alloys is significantly different from that of conventionally processed alloys because of the fast and directional cooling achieved during the additive manufacturing processing. Several significant characteristics of additively manufactured alloys via laser based process are summarized in this section.

2.4.1 Texture

Because of the unidirectional heat transfer and cooling (heat is primarily conducted away vertically through the previously built part to the platform [59]), a strong morphological and crystallographic texture has been observed in columnar structures in Ti6Al4V [60], nickel superalloys [61,62], 1Cr18Ni9Ti stainless steel [63], NiCr alloy [64], AlSi10Mg [65], CoCrMo steel [66] and Al-12Si (AlSi12) [7,67] processed by layer-based additive manufacturing processes. The columnar structures are the elongated grains that grow across the layers in the direction roughly parallel to the build direction because of the epitaxial grain growth at the partially remelting grains on the previously solidified layers and directional solidification [68].

The dominant {100} texture in the direction of grain growth is developed in SLM-processed Inconel alloy [61] as the result of the preferential {100} growth direction of cubic crystals [60], which results in the columnar structure shown in Fig. 2.5.

In the SLM-processed Ti6Al4V, the average length of prior β grains is in the order of millimetres. This shows that prior β grains grow through tens of layers along a

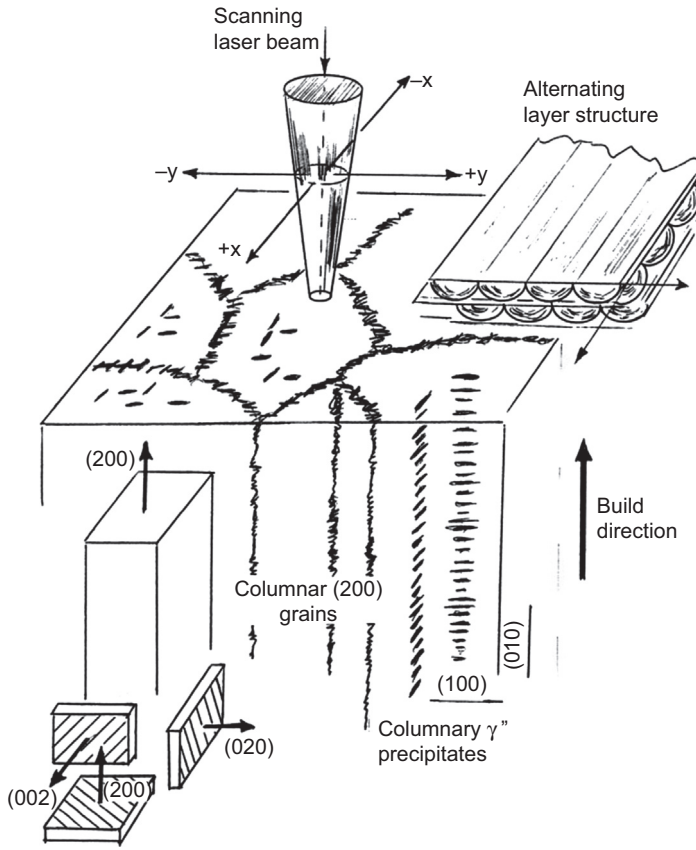

Figure 2.5 Schematic illustration of columnar γ grains formed by unidirectional solidification, γ'' precipitate arrays and the melt pool/layer structure in Inconel 718 processed by selective laser melting [69].

direction tilted at an angle about 20 degree from the build direction (z-axis) [5,60,70]. The inclined angle is attributed to the rotation of the scan direction in each layer. The acicular martensite α' laths, characterized by high vanadium content and a high dislocation density, are primarily orientated at inclinations of about ± 45 and 90 degree to the build direction [60,70].

The texture can be changed by applying different laser-scanning strategies [68]. A reduction in texture can be achieved by rotating a 90 degree laser scanning vector between the two adjacent layers or rotating the scanning vector within one layer (the checkerboard or island scanning method) [68].

2.4.2 Non-equilibrium microstructure

An out-of-equilibrium microstructure is normally produced in the SLM process as a result of a high cooling rate. The cooling rate in the SLM process is approximated

within the range of 10^3-10^8 K/s [10,40,71–73], which is fast enough to fabricate bulk metallic glass for certain alloy compositions [74–78].

Very fine acicular martensite (α') is normally obtained in SLM-processed Ti6Al4V [5,60,79–81] and commercially pure titanium (cpTi) [44] as a result of the phase transformation $\beta \rightarrow \alpha'$ at a high cooling rate. In addition to defects, the hard and brittle nature of metastable martensite is partially attributed to the higher strength and lower ductility of SLM-processed Ti6Al4V compared with conventionally forged/annealed Ti6Al4V parts in which stable/ductile alpha (α) plus beta (β) phases are produced. However, $\alpha + \beta$ phases have been reported in SLM-processed Ti6Al4V with appropriate energy input [82] and double laser scanning on each layer [83] as a result of the in situ decomposition of the martensite α' phase induced by heating and cooling during the build of the subsequent layers caused by the following phase transformations:

$$\alpha' \rightarrow \beta \quad \text{during heating}$$

$$\beta \rightarrow \alpha + \beta \quad \text{during cooling}$$

The phase obtained in SLM-processed cpTi is reported to be dependent on laser scanning speed (v) [14] because of the following phase transformations:

$$\beta \rightarrow \alpha \quad \text{when} \quad v = 100 \text{ mm/s}$$

$$\beta \rightarrow \alpha\prime \quad \text{when} \quad v \geq 200 \text{ mm/s}$$

The microstructure of Al12Si processed by SLM consists of an extremely fine, supersaturated, Al-rich cellular structure along with residual Si at the cellular boundaries (as networked walls with a thickness of about 200 nm at an LED of 0.22 J/mm [67] or particles with a size around 10–100 nm at an LED of 0.4 J/mm [84]); this is caused by the high cooling rate and extended solid solubility of Si in α-Al. The latter results in a smaller amount of free residual Si and Al matrix supersaturated in Si in SLM-processed Al12Si compared with the equilibrium concentration or lower cooling rate in processes such as casting in the same alloy [67,84]. The refined microstructure is attributed to the high heating and cooling rates that induce superheating and undercooling; hence the nucleation rate is enhanced and grain growth is suppressed [84].

2.4.3 Residual stresses, cracking and distortion of SLM-processed parts

Similar to welding processes, residual stresses are produced in SLM-processed parts as a result of high temperature gradients, large amounts of thermal expansion and shrinkage or non-uniform plastic deformation during the heating and cooling cycle [45,85,86]. The substantial shrinkage of the moving melt pool during cooling and solidification is constrained by the cooler underlying previously processed layers [87].

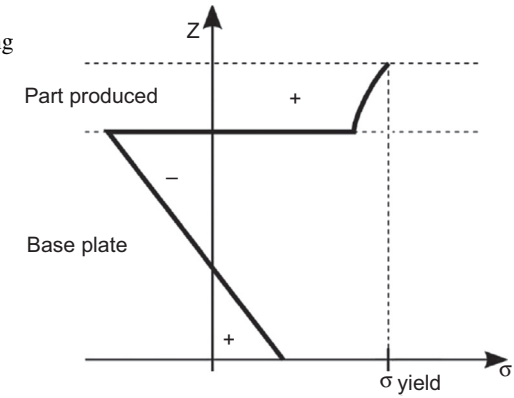

Figure 2.6 Distribution of residual stresses in a base plate and built part along the building direction [86].

The thermal shrinkage rate for a given powder material increases with an increase in laser power or a decrease in laser scanning speed (ie, an increase in linear energy density) [88].

An SLM-built part is under tension, and the maximum stress is located at the surface of the part and can reach the yield stress, as shown in Fig. 2.6. The final residual stress increases with the number of layers that have been built [41,85].

The effect of processing parameters on the development of residual stress during the SLM process can be assessed by measuring the curling angle (α) of the bridge [86] or cantilever [89] structures after the built structures are removed from the base plate.

It has been reported that the anisotropic behaviour of Ti6Al4V processed by SLM is significantly affected by residual stresses [87]. Residual stresses result in:

1. Part distortion [86].
2. Cracking [14,18,81,90].
3. Delamination of the part [41].

Interlayer thermal cracks have been reported in SLM-processed cpTi as a result of tensile residual stresses between two neighbouring layers [14]. However, intergranular cracks (with lengths of a few microns up to 100 μm and more) are always found to propagate along a large-angle grain boundary along the build direction in SLM-processed IN738LC [18].

Crack density is more significantly dependent on laser power because the temperature profile is more strongly dependent on laser power than laser scanning speed; hence steeper temperature gradients produced at higher laser powers result in an increase in the magnitude of thermal stress and therefore increase hot cracking [72].

Because the average residual stress in the laser scanning direction is about two times higher than the stress in the direction perpendicular to the laser scanning direction [41,91], residual stresses can be reduced by shortening the scan track using an island/checkerboard scanning strategy [86,92]. More homogeneous stress distribution can be achieved by changing the stress anisotropy from one layer to the next, scanning with a rotating scan pattern [87].

Rescanning by the laser beam with the lower energy density is reported to effectively stop crack propagation during SLM fabrication of $Al_{85}Ni_5Y_6Co_2Fe_2$ bulk metallic glass composites, probably as a result of part distortion [77].

Distortion caused by internal stresses can be reduced by using elemental powders instead of a pre-alloyed powder. The in situ alloying of two or more elemental powdered materials during manufacturing can lower the solidification temperature by forming various combinations of eutectic/hypoeutectic/hypereutectic alloys. The processed alloy is able to remain in a semi-solid or stress-reduced state throughout the build with the assistance of powder bed being pre-heated at the elevated temperature. Much longer overhangs without support can be built using a mixture of elemental powders [93].

Residual stresses and distortion of the SLM-processed part can be reduced by applying (1) stress relief heat treatment [85,94,95], (2) re-scanning by the laser beam [77,94] and (3) increasing in the powder bed temperature [89,94]. However, residual stresses are not always disadvantageous [85]; the retention of a reasonable level of residual stress in SLM-processed parts favours enhanced hardness [96].

2.4.4 Defects and density of SLM-/SLS-processed parts

Defects such as porosity, lack of fusion and cracks are often produced in additively manufactured materials. These defects adversely affect the properties and performance of these materials because the defects reduce the part density and act as stress risers. The defects include:

1. Gas pores: Gas pores are formed by trapped gases [17] and are normally spherical. The gas pores are inherited from a gas-atomized powder [3] or moisture on the powder particle surface and the dissolved hydrogen in the powder, which are the primary contributors to the formation of porosity in SLM-processed aluminium alloys [97]. These are not significant contributors to the porosity of SLM-processed Ti6Al4V samples since the porosity depends on the processing parameters [98].
2. Keyhole pores: Keyhole pores are produced by the collapse of a steep and deep melt pool that is formed at the start/end points of the scan tracks [65] or when the linear energy density is too high [17].
3. Incomplete melting or lack-of-fusion: Some un-melted particles can be trapped inside the pores if the energy is insufficient to melt all the powder, which has a statistically geometric shape [97,99]. This type of defect is located at the interlayers and is also known as an elongated pore [100]. The plane of this type of defect is perpendicular to the build direction.
4. Unstable melt pool: Irregular pores can be formed at low laser scanning speeds as a result of hydrodynamic instability of the melt pool at a high energy density [5] and because of melt flow instability at a high laser scanning speed. The instability of melt flow during SLM is attributed to the Marangoni force and recoil pressure produced by the evaporation of the melt pool. The instability of melt flow, which increases with an increase in laser scanning speed and powder layer thickness [48,101], results in small liquid droplets splashing onto the solid built surface [3,48].
5. Lack of overlap: Intra-layer porosity is produced as a result of the large hatching space [3].

Porosity or relative density in the SLM-fabricated part is strongly dependent on linear energy density [13,15,72]. The velocity of gaseous bubbles in the melt pool

increases with an increase in linear energy density and reaches a maximum value at an optimal LED at which the highest density of the part is achieved. Further increases in linear energy density result in the formation of a rotational pattern of the flow vortex, which tends to entrap gaseous bubbles and reduce their velocity. This leads to the formation of high porosity in the consolidated parts [16].

Four melting zones have been defined on a laser power versus laser scanning speed map for SLM of Ti6Al4V [102−104]: 'fully dense' (zone I), 'over-melting' (zone II), 'incomplete melting' (zone III) and 'over-heating' (zone OH), as shown in Fig. 2.7(a). Defects in the samples produced in zone II have a spherical shape, whereas the morphology of defects in the samples produced in zone III is irregular.

At a laser power, the density decreases/porosity increases with an increase in laser scanning speed [71,100,105], as shown in Fig. 2.7(c). However, reducing the porosity with an increase in laser scanning speed up to a threshold (the upper limit of zone II) has been reported at a given high level of laser power [98,104,106], as shown in Fig. 2.7(b).

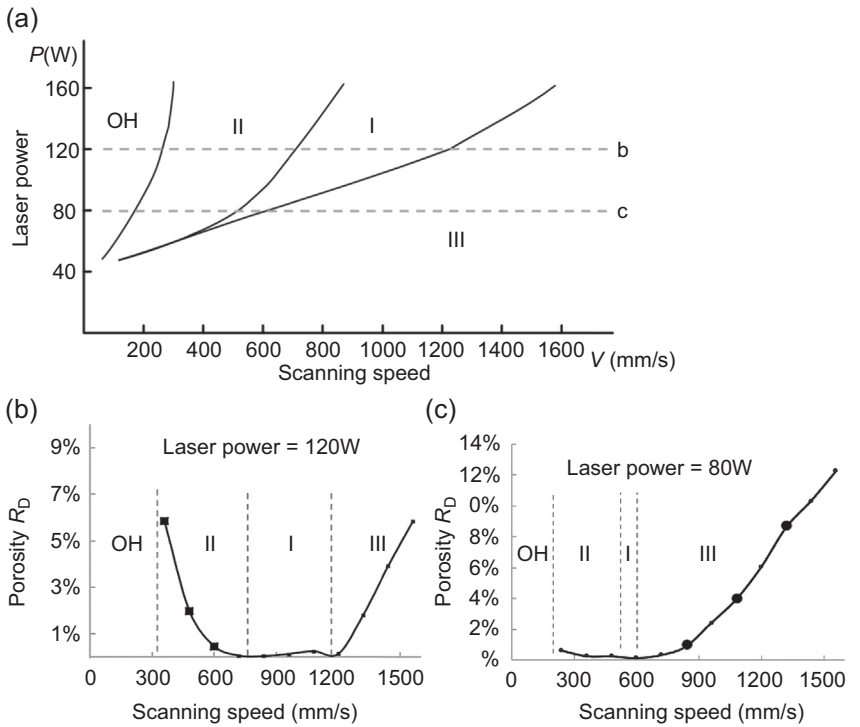

Figure 2.7 (a) Four zones on a laser power versus laser scanning speed map. (b) and (c) Graphs of the dependence of porosity on laser scanning speed at two levels of laser power in selective laser melting−fabricated Ti6Al4V [104]. [The graphs in (b) and (c) correspond with the b and c levels in (a)].

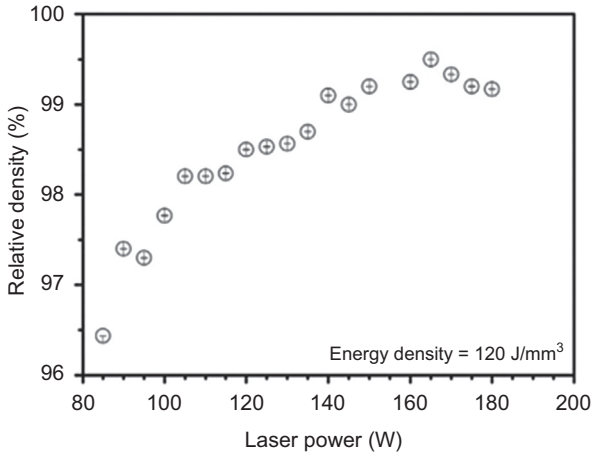

Figure 2.8 Effect of laser power on the relative density of selective laser melting—fabricated commercially pure titanium at a constant energy density of 120 J/mm^3 [44].

It has been reported that the density of the SLM-/SLS-fabricated part (ρ) increases with an increase in energy density (E_V), as described by [6]:

$$\rho = C_1 - C_2 \exp(-KE_V) \tag{2.8}$$

However, significant density variations can be found at the same level of energy density (as shown in Fig. 2.8) because some combinations of laser power and laser scanning speed may cause (1) incomplete melting of powder; (2) instability of the melt pool; (3) overheating of the powders and (4) balling effects [44]. At the same energy density level of 120 J/mm^3, the density of the additively manufactured part increases with an increase in laser power and laser scanning speed and reaches a maximum value at the laser power of 165W; a further increase in laser power results in a slight reduction in density [44,107,108]. The porosity produced at the combination of higher laser power and higher scanning speed is smaller and more circular in shape and is attributed to the balling effect and high thermal stress cracking, whereas the porosity produced at the combination of lower laser power and lower scanning speed is filled with un-melted powders because of insufficient melting [107]. However, the balling effect has also been observed in a sample that was produced at a low laser power and scanning speed [44].

The density of SLM-processed AlSi10Mg parts can be significantly increased by applying a double laser scan on each layer, with the first scan using a lower laser power for pre-sintering and the second scan using a higher laser power to fully consolidate the pre-sintered layer [3].

2.5 Mechanical properties of SLM-processed metallic parts

Mechanical properties of SLM-processed metallic parts are strongly dependent on the microstructure and the relative density of the parts. As in castings, the strength,

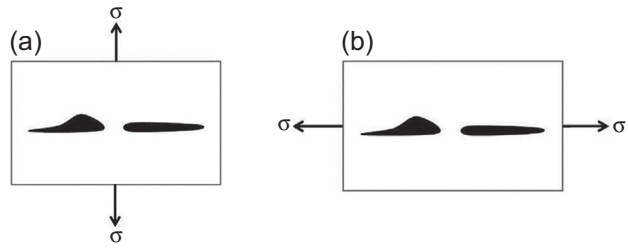

Figure 2.9 Relation of loading direction to the orientation of the planar defects showing the loading along the axis of (a) vertically and (b) horizontally built samples [100].

ductility and fatigue life of SLM-processed parts decrease with an increase in porosity, especially when the size and fraction of pores exceed the critical values.

In general, mechanical properties of SLM-processed metallic parts when loading is perpendicular to the layer plane are lower than those when loading is parallel to build plane. No significant effect of build orientation on the strength of SLM-processed aluminium samples has been reported [67,109].

The ductility of SLM-processed samples is lower when loading is parallel to the build direction than when loading is perpendicular to the build direction [23], which is attributed to:

1. More borderline porosity being formed in the *z*-oriented tensile samples [110]
2. Stress concentration effect caused by the loading direction being perpendicular to the orientation of the planar defects (lack of fusion) [80,100], as shown in Fig. 2.9(a)
3. Effect of texture [111]
4. Track and layer interfaces [111].

An increase in yield strength and ultimate tensile strength with an increase in scan speed during SLM processing of an NiCr alloy is attributed to the growth of columnar grains [64].

Both the fracture strain and strength (yield strength and ultimate tensile strength) of the cpTi samples fabricated by SLM at the same energy density increase with an increase in laser power and laser scanning speed. The former is attributed to higher-density parts and the latter to the grain refinement and the formation of a martensitic α' structure. The fracture behaviour of the additively manufactured samples is significantly affected by the incompletely melted particles and porosity [44].

In general, the strength (yield strength and ultimate tensile strength) of SLM-processed aluminium alloys, titanium alloys and 316L stainless steel samples is higher than or comparable to those processed by conventional manufacturing processes (eg, forging, casting), mainly because of a refined and metastable microstructure; however, the ductility of SLM-processed metallic samples is poorer [79–81,109,112,113]. Great scatter in the mechanical properties is reported and is attributed to the defects in the SLM-processed metallic samples [7,95].

Both the yield strength and ultimate tensile strength are lower and ductility is higher or similar in SLM-fabricated Inconel 718 samples compared with those of aged wrought samples [61,69,114,115], This is attributed to the precipitation of a brittle

Laves phase in the interdendritic regions and a lack of the strengthening effects of γ'' and γ' precipitates in the SLM-processed samples [115].

A coarser microstructure has been observed at the layer and track boundaries in SLM-processed aluminium alloys [65,67,84,93,111] because of the slower solidification rate and localised partial heat treatment of the remelted zone. The brittle and coarser Si-phases at the layer boundaries decrease the ductility when loading occurs vertical to the layer plane [111].

The orientation of the planar defects also plays an important role in the anisotropy in impact toughness [116]; the lower impact toughness in the vertically built samples is attributed to a reduction in the load-bearing cross section. If the layers are well bonded without the existence of directional defects at the layer boundaries, the fracture toughness is not affected by the build orientation with respect to the loading direction [117].

The performance of SLM-processed parts under fatigue is also strongly susceptible to the defects and residual stresses in the parts [95,99,118], the pre-heating temperature of plate [119] and the build orientation [118,119]. The fatigue life of SLS-/SLM-fabricated samples is longer when the loading direction is perpendicular to the build direction.

Cracking during fatigue testing initiates from a rounded depression when an unmelted powder particle attaches to the as-built surface [112] or a defect (especially a lack-of-fusion defect) at the subsurface [99]. It was reported that cracking initiates from pores that are larger than 50 μm in diameter and located within 250 μm from the outer surface during cyclical loading [7].

Superior fatigue life and a combination of strength and ductility have been achieved in SLM-processed Ti6Al4V samples with an ultrafine, lamellar $\alpha + \beta$ microstructure, which is obtained through the in situ decomposition of acicular martensitic α' in SLM with an appropriate energy input [82,120].

2.6 Concluding remarks

As one of the most popular and fastest growing additive manufacturing technologies, the laser-based powder bed fusion process involves a large number of processing parameters, which makes optimizing the process difficult.

Like other additive manufacturing processes, the laser-based powder bed fusion process also provides research opportunities and manufacturing capacities in various fields:

1. Fast alloy design and development
2. Formation of meta-stable phases during solidification under extreme cooling conditions
3. Design, manufacturing and characterization of parts with novel structures (such as multi-material structures) and complex geometry, including cellular structures.

Further fundamental research into the SLM process, its numerical modelling analyses and in situ quality monitoring are still required to make this technology more robust and reliable for the manufacture of parts for structural applications.

References

[1] O. Rigo, C. Engel, Selective Laser Melting versus Electron Beam Melting, 2013. http://www.slideshare.net/carstenengel/selective-laser-melting-versus-electron-beam-melting.

[2] B. Ferrar, L. Mullen, E. Jones, R. Stamp, C.J. Sutcliffe, Gas flow effects on selective laser melting (SLM) manufacturing performance, Journal of Materials Processing Technology 212 (2012) 355−364.

[3] N.T. Aboulkhair, N.M. Everitt, I. Ashcroft, C. Tuck, Reducing porosity in AlSi10Mg parts processed by selective laser melting, Additive Manufacturing 1−4 (2014) 77−86.

[4] J.P. Kruth, P. Mercelis, J. Van Vaerenbergh, L. Froyen, M. Rombouts, Binding mechanisms in selective laser sintering and selective laser melting, Rapid Prototyping Journal 11 (2005) 26−36.

[5] L. Thijs, F. Verhaeghe, T. Craeghs, J.V. Humbeeck, J.-P. Kruth, A study of the microstructural evolution during selective laser melting of Ti−6Al−4V, Acta Materialia 58 (2010) 3303−3312.

[6] A. Simchi, H. Pohl, Effects of laser sintering processing parameters on the microstructure and densification of iron powder, Materials Science and Engineering: A 359 (2003) 119−128.

[7] S. Siddique, M. Imran, E. Wycisk, C. Emmelmann, F. Walther, Influence of process-induced microstructure and imperfections on mechanical properties of AlSi12 processed by selective laser melting, Journal of Materials Processing Technology 221 (2015) 205−213.

[8] D. Gu, Y. Shen, Balling phenomena in direct laser sintering of stainless steel powder: metallurgical mechanisms and control methods, Materials & Design 30 (2009) 2903−2910.

[9] Y. Liu, Y. Yang, S. Mai, D. Wang, C. Song, Investigation into spatter behavior during selective laser melting of AISI 316L stainless steel powder, Materials and Design 87 (2015) 797−806.

[10] M. Das, V.K. Balla, D. Basu, S. Bose, A. Bandyopadhyay, Laser processing of SiC-particle-reinforced coating on titanium, Scripta Materialia 63 (2010) 438−441.

[11] S. Kumar, Selective laser sintering/melting, in: Comprehensive Materials Processing, 2014, pp. 93−134.

[12] I. Yadroitsev, P. Bertrand, I. Smurov, Parametric analysis of the selective laser melting process, Applied Surface Science 253 (2007) 8064−8069.

[13] Q. Jia, D. Gu, Selective laser melting additive manufacturing of Inconel 718 superalloy parts: densification, microstructure and properties, Journal of Alloys and Compounds 585 (2014) 713−721.

[14] D. Gu, Y.C. Hagedorn, W. Meiners, G. Meng, R.J.S. Batista, K. Wissenbach, R. Poprawe, Densification behavior, microstructure evolution, and wear performance of selective laser melting processed commercially pure titanium, Acta Materialia 60 (2012) 3849−3860.

[15] Y. Zhou, S.F. Wen, B. Song, X. Zhou, Q. Teng, Q.S. Wei, Y.S. Shi, A novel titanium alloy manufactured by selective laser melting: microstructure, high temperature oxidation resistance, Materials & Design 89 (2016) 1199−1204.

[16] D. Dai, D. Gu, Thermal behavior and densification mechanism during selective laser melting of copper matrix composites: simulation and experiments, Materials & Design 55 (2014) 482−491.

[17] K. Kempen, L. Thijs, J.V. Humbeeck, J.P. Kruth, Processing AlSi10Mg by selective laser melting: parameter optimisation and material characterisation, Materials Science and Technology (United Kingdom) 31 (2015) 917−923.
[18] M. Cloots, P.J. Uggowitzer, K. Wegener, Investigations on the microstructure and crack formation of IN738LC samples processed by selective laser melting using Gaussian and doughnut profiles, Materials & Design 89 (2016) 770−784.
[19] J.P. Kruth, G. Levy, F. Klocke, T.H.C. Childs, Consolidation phenomena in laser and powder-bed based layered manufacturing, CIRP Annals − Manufacturing Technology 56 (2007) 730−759.
[20] H.J. Niu, I.T.H. Chang, Selective laser sintering of gas and water atomized high speed steel powders, Scripta Materialia 41 (1999) 25−30.
[21] A.B. Spierings, N. Herres, G. Levy, Influence of the particle size distribution on surface quality and mechanical properties in AM steel parts, Rapid Prototyping Journal 17 (2011) 195−202.
[22] N.P. Karapatis, G. Egger, P.-E. Gygax, R. Glardon, in: 10th International Solid Freeform Fabrication Symposium − an Additive Manufacturing Conference, SFF 1999, The University of Texas at Austin, USA, 1999, pp. 255−264.
[23] D. Manfredi, F. Calignano, M. Krishnan, R. Canali, E.P. Ambrosio, E. Atzeni, From powders to dense metal parts: characterization of a commercial AlSiMg alloy processed through direct metal laser sintering, Materials 6 (2013) 856−869.
[24] H. Attar, K.G. Prashanth, L.-C. Zhang, M. Calin, I.V. Okulov, S. Scudino, C. Yang, J. Eckert, Effect of powder particle shape on the properties of in situ Ti−TiB composite materials produced by selective laser melting, Journal of Materials Science & Technology 31 (2015) 1001−1005.
[25] A. Simchi, The role of particle size on the laser sintering of iron powder, Metallurgical and Materials Transactions B 35 (2004) 937−948.
[26] A.V. Gusarov, T. Laoui, L. Froyen, V.I. Titov, Contact thermal conductivity of a powder bed in selective laser sintering, International Journal of Heat and Mass Transfer 46 (2003) 1103−1109.
[27] M. Rombouts, L. Froyen, A.V. Gusarov, E.H. Bentefour, C. Glorieux, Photopyroelectric measurement of thermal conductivity of metallic powders, Journal of Applied Physics 97 (2005).
[28] M. Rombouts, L. Froyen, A.V. Gusarov, E.H. Bentefour, C. Glorieux, Light extinction in metallic powder beds: correlation with powder structure, Journal of Applied Physics 98 (2005).
[29] C.X. Wang, T. Laoui, J. Bonse, P.J. Kruth, B. Lauwers, L. Froyen, Direct selective laser sintering of hard metal powders: experimental study and simulation, International Journal of Advanced Manufacturing Technology 19 (2002) 351−357.
[30] W.E. King, A.T. Anderson, R.M. Ferencz, N.E. Hodge, C. Kamath, S.A. Khairallah, A.M. Rubenchik, Laser powder bed fusion additive manufacturing of metals; physics, computational, and materials challenges, Applied Physics Reviews 2 (2015) 041304.
[31] A. Foroozmehr, M. Badrossamay, E. Foroozmehr, S.I. Golabi, Finite element simulation of selective laser melting process considering optical penetration depth of laser in powder bed, Materials & Design 89 (2016) 255−263.
[32] A.V. Gusarov, J.P. Kruth, Modelling of radiation transfer in metallic powders at laser treatment, International Journal of Heat and Mass Transfer 48 (2005) 3423−3434.
[33] S.C. Stacy, X. Zhang, M. Pantoya, B. Weeks, The effects of density on thermal conductivity and absorption coefficient for consolidated aluminum nanoparticles, International Journal of Heat and Mass Transfer 73 (2014) 595−599.

[34] A.V. Gusarov, I. Smurov, Modeling the interaction of laser radiation with powder bed at selective laser melting, Physics Procedia 5 (Part B) (2010) 381−394.
[35] N.K. Tolochko, Y.V. Khlopkov, S.E. Mozzharov, M.B. Ignatiev, T. Laoui, V.I. Titov, Absorptance of powder materials suitable for laser sintering, Rapid Prototyping Journal 6 (2000) 155−161.
[36] B. Zhang, C. Coddet, Selective laser melting of iron powder: observation of melting mechanism and densification behavior via point-track-surface-part research, Journal of Manufacturing Science and Engineering, Transactions of the ASME 138 (2016).
[37] Y. Li, D. Gu, Parametric analysis of thermal behavior during selective laser melting additive manufacturing of aluminum alloy powder, Materials and Design 63 (2014) 856−867.
[38] I. Yadroitsev, P. Krakhmalev, I. Yadroitsava, Selective laser melting of Ti6Al4V alloy for biomedical applications: temperature monitoring and microstructural evolution, Journal of Alloys and Compounds 583 (2014) 404−409.
[39] R. Li, Y. Shi, J. Liu, H. Yao, W. Zhang, Effects of processing parameters on the temperature field of selective laser melting metal powder, Powder Metallurgy and Metal Ceramics 48 (2009) 186−195.
[40] P. Yuan, D. Gu, Molten pool behaviour and its physical mechanism during selective laser melting of TiC/AlSi10Mg nanocomposites: simulation and experiments, Journal of Physics D: Applied Physics 48 (2015) 035303.
[41] I. Yadroitsev, I. Yadroitsava, Evaluation of residual stress in stainless steel 316L and Ti6Al4V samples produced by selective laser melting, Virtual and Physical Prototyping 10 (2015) 67−76.
[42] I. Yadroitsev, A. Gusarov, I. Yadroitsava, I. Smurov, Single track formation in selective laser melting of metal powders, Journal of Materials Processing Technology 210 (2010) 1624−1631.
[43] N.T. Aboulkhair, I. Maskery, C. Tuck, I. Ashcroft, N.M. Everitt, On the formation of AlSi10Mg single tracks and layers in selective laser melting: microstructure and nano-mechanical properties, Journal of Materials Processing Technology 230 (2016) 88−98.
[44] H. Attar, M. Calin, L.C. Zhang, S. Scudino, J. Eckert, Manufacture by selective laser melting and mechanical behavior of commercially pure titanium, Materials Science and Engineering A 593 (2014) 170−177.
[45] D.D. Gu, W. Meiners, K. Wissenbach, R. Poprawe, Laser additive manufacturing of metallic components: materials, processes and mechanisms, International Materials Reviews 57 (2012) 133−164.
[46] M. Rombouts, J.P. Kruth, L. Froyen, P. Mercelis, Fundamentals of selective laser melting of alloyed steel powders, CIRP Annals − Manufacturing Technology 55 (2006) 187−192.
[47] X. Zhou, X. Liu, D. Zhang, Z. Shen, W. Liu, Balling phenomena in selective laser melted tungsten, Journal of Materials Processing Technology 222 (2015) 33−42.
[48] C. Qiu, C. Panwisawas, M. Ward, H.C. Basoalto, J.W. Brooks, M.M. Attallah, On the role of melt flow into the surface structure and porosity development during selective laser melting, Acta Materialia 96 (2015) 72−79.
[49] D. Gu, Y. Shen, Balling phenomena during direct laser sintering of multi-component Cu-based metal powder, Journal of Alloys and Compounds 432 (2007) 163−166.
[50] J.P. Kruth, L. Froyen, J. Van Vaerenbergh, P. Mercelis, M. Rombouts, B. Lauwers, Selective laser melting of iron-based powder, Journal of Materials Processing Technology 149 (2004) 616−622.

[51] R. Li, J. Liu, Y. Shi, L. Wang, W. Jiang, Balling behavior of stainless steel and nickel powder during selective laser melting process, International Journal of Advanced Manufacturing Technology 59 (2012) 1025−1035.
[52] M. Simonelli, C. Tuck, N.T. Aboulkhair, I. Maskery, I. Ashcroft, R.D. Wildman, R. Hague, A study on the laser spatter and the oxidation reactions during selective laser melting of 316L stainless steel, Al-Si_{10}-Mg, and Ti-6Al-4V, Metallurgical and Materials Transactions A: Physical Metallurgy and Materials Science 46 (2015) 3842−3851.
[53] I. Yadroitsev, P. Krakhmalev, I. Yadroitsava, S. Johansson, I. Smurov, Energy input effect on morphology and microstructure of selective laser melting single track from metallic powder, Journal of Materials Processing Technology 213 (2013) 606−613.
[54] H.J. Niu, T.H. Chang, Instability of scan tracks of selective laser sintering of high speed steel powder, Scripta Materialia 41 (1999) 1229−1234.
[55] P. Regenfuss, A. Streek, L. Hartwig, S. Klötzer, T. Brabant, M. Horn, R. Ebert, H. Exner, Principles of laser micro sintering, Rapid Prototyping Journal 13 (2007) 204−212.
[56] E. Yasa, J. Deckers, J.P. Kruth, The investigation of the influence of laser re-melting on density, surface quality and microstructure of selective laser melting parts, Rapid Prototyping Journal 17 (2011) 312−327.
[57] E. Yasa, J.P. Kruth, Microstructural investigation of selective laser melting 316L stainless steel parts exposed to laser re-melting, Procedia Engineering 19 (2011) 389−395.
[58] E. Yasa, J.P. Kruth, J. Deckers, Manufacturing by combining selective laser melting and selective laser erosion/laser re-melting, CIRP Annals − Manufacturing Technology 60 (2011) 263−266.
[59] I.A. Roberts, C.J. Wang, R. Esterlein, M. Stanford, D.J. Mynors, A three-dimensional finite element analysis of the temperature field during laser melting of metal powders in additive layer manufacturing, International Journal of Machine Tools and Manufacture 49 (2009) 916−923.
[60] M. Simonelli, Y.Y. Tse, C. Tuck, On the texture formation of selective laser melted Ti-6Al-4V, Metallurgical and Materials Transactions A: Physical Metallurgy and Materials Science 45 (2014) 2863−2872.
[61] J. Strößner, M. Terock, U. Glatzel, Mechanical and microstructural investigation of nickel-based superalloy IN718 manufactured by selective laser melting (SLM), Advanced Engineering Materials 17 (2015) 1099−1105.
[62] L.N. Carter, C. Martin, P.J. Withers, M.M. Attallah, The influence of the laser scan strategy on grain structure and cracking behaviour in SLM powder-bed fabricated nickel superalloy, Journal of Alloys and Compounds 615 (2014) 338−347.
[63] M. Ma, Z. Wang, M. Gao, X. Zeng, Layer thickness dependence of performance in high-power selective laser melting of 1Cr18Ni9Ti stainless steel, Journal of Materials Processing Technology 215 (2015) 142−150.
[64] B. Song, S. Dong, P. Coddet, H. Liao, C. Coddet, Fabrication of NiCr alloy parts by selective laser melting: columnar microstructure and anisotropic mechanical behavior, Materials & Design 53 (2014) 1−7.
[65] L. Thijs, K. Kempen, J.-P. Kruth, J. Van Humbeeck, Fine-structured aluminium products with controllable texture by selective laser melting of pre-alloyed AlSi10Mg powder, Acta Materialia 61 (2013) 1809−1819.
[66] X. Zhou, K. Li, D. Zhang, X. Liu, J. Ma, W. Liu, Z. Shen, Textures formed in a CoCrMo alloy by selective laser melting, Journal of Alloys and Compounds 631 (2015) 153−164.
[67] K.G. Prashanth, S. Scudino, H.J. Klauss, K.B. Surreddi, L. Löber, Z. Wang, A.K. Chaubey, U. Kühn, J. Eckert, Microstructure and mechanical properties of Al−12Si produced by selective laser melting: effect of heat treatment, Materials Science and Engineering A 590 (2014) 153−160.

[68] L. Thijs, B. Vrancken, J.P. Kruth, J. Van Humbeeck, in: Materials Science and Technology Conference and Exhibition 2013, MS and T 2013, 2013, pp. 21−28.
[69] K.N. Amato, S.M. Gaytan, L.E. Murr, E. Martinez, P.W. Shindo, J. Hernandez, S. Collins, F. Medina, Microstructures and mechanical behavior of Inconel 718 fabricated by selective laser melting, Acta Materialia 60 (2012) 2229−2239.
[70] M. Simonelli, Y.Y. Tse, C. Tuck, Effect of the build orientation on the mechanical properties and fracture modes of SLM Ti-6Al-4V, Materials Science and Engineering A 616 (2014) 1−11.
[71] D. Buchbinder, H. Schleifenbaum, S. Heidrich, W. Meiners, J. Bültmann, High power selective laser melting (HP SLM) of aluminum parts, Physics Procedia 12 (Part A) (2011) 271−278.
[72] N.J. Harrison, I. Todd, K. Mumtaz, Reduction of micro-cracking in nickel superalloys processed by selective laser melting: a fundamental alloy design approach, Acta Materialia 94 (2015) 59−68.
[73] L.-E. Loh, C.-K. Chua, W.-Y. Yeong, J. Song, M. Mapar, S.-L. Sing, Z.-H. Liu, D.-Q. Zhang, Numerical investigation and an effective modelling on the selective laser melting (SLM) process with aluminium alloy 6061, International Journal of Heat and Mass Transfer 80 (2015) 288−300.
[74] H.Y. Jung, S.J. Choi, K.G. Prashanth, M. Stoica, S. Scudino, S. Yi, U. Kühn, D.H. Kim, K.B. Kim, J. Eckert, Fabrication of Fe-based bulk metallic glass by selective laser melting: a parameter study, Materials & Design 86 (2015) 703−708.
[75] X.P. Li, C.W. Kang, H. Huang, L.C. Zhang, T.B. Sercombe, Selective laser melting of an $Al_{86}Ni_6Y_{4.5}Co_2La_{1.5}$ metallic glass: processing, microstructure evolution and mechanical properties, Materials Science and Engineering: A 606 (2014) 370−379.
[76] S. Pauly, L. Löber, R. Petters, M. Stoica, S. Scudino, U. Kühn, J. Eckert, Processing metallic glasses by selective laser melting, Materials Today 16 (2013) 37−41.
[77] X.P. Li, C.W. Kang, H. Huang, T.B. Sercombe, The role of a low-energy−density re-scan in fabricating crack-free $Al_{85}Ni_5Y_6Co_2Fe_2$ bulk metallic glass composites via selective laser melting, Materials & Design 63 (2014) 407−411.
[78] X.P. Li, M. Roberts, Y.J. Liu, C.W. Kang, H. Huang, T.B. Sercombe, Effect of substrate temperature on the interface bond between support and substrate during selective laser melting of Al−Ni−Y−Co−La metallic glass, Materials & Design 65 (2015) 1−6.
[79] M. Brandt, S. Sun, M. Leary, S. Feih, J. Elambasseril, Q. Liu, High-value SLM aerospace components: from design to manufacture, Advanced Materials Research 633 (2013) 135−147.
[80] T. Vilaro, C. Colin, J.D. Bartout, As-Fabricated and heat-treated microstructures of the Ti-6Al-4V alloy processed by selective laser melting, Metallurgical and Materials Transactions 42A (2011) 3190−3199.
[81] L. Facchini, E. Magalini, P. Robotti, A. Molinari, S. Höges, K. Wissenbach, Ductility of a Ti-6Al-4V alloy produced by selective laser melting of prealloyed powders, Rapid Prototyping Journal 16 (2010) 450−459.
[82] W. Xu, M. Brandt, S. Sun, J. Elambasseril, Q. Liu, K. Latham, K. Xia, M. Qian, Additive manufacturing of strong and ductile Ti−6Al−4V by selective laser melting via in situ martensite decomposition, Acta Materialia 85 (2015) 74−84.
[83] M. Simonelli, Y.Y. Tse, C. Tuck, The formation of $\alpha + \beta$ microstructure in as-fabricated selective laser melting of Ti-6Al-4V, Journal of Materials Research 29 (2014) 2028−2035.
[84] X.P. Li, X.J. Wang, M. Saunders, A. Suvorova, L.C. Zhang, Y.J. Liu, M.H. Fang, Z.H. Huang, T.B. Sercombe, A selective laser melting and solution heat treatment refined Al−12Si alloy with a controllable ultrafine eutectic microstructure and 25% tensile ductility, Acta Materialia 95 (2015) 74−82.

[85] P. Mercelis, J.P. Kruth, Residual stresses in selective laser sintering and selective laser melting, Rapid Prototyping Journal 12 (2006) 254−265.
[86] J.P. Kruth, J. Deckers, E. Yasa, R. Wauthlé, Assessing and comparing influencing factors of residual stresses in selective laser melting using a novel analysis method, Proceedings of the Institution of Mechanical Engineers, Part B: Journal of Engineering Manufacture 226 (2012) 980−991.
[87] B. Vrancken, V. Cain, R. Knutsen, J. Van Humbeeck, Residual stress via the contour method in compact tension specimens produced via selective laser melting, Scripta Materialia 87 (2014) 29−32.
[88] H.H. Zhu, L. Lu, J.Y.H. Fuh, Study on shrinkage behaviour of direct laser sintering metallic powder, Proceedings of the Institution of Mechanical Engineers, Part B: Journal of Engineering Manufacture 220 (2006) 183−190.
[89] D. Buchbinder, W. Meiners, N. Pirch, K. Wissenbach, J. Schrage, Investigation on reducing distortion by preheating during manufacture of aluminum components using selective laser melting, Journal of Laser Applications 26 (2014).
[90] R. Engeli, T. Etter, S. Hövel, K. Wegener, Processability of different IN738LC powder batches by selective laser melting, Journal of Materials Processing Technology 229 (2016) 484−491.
[91] A.V. Gusarov, M. Pavlov, I. Smurov, Residual stresses at laser surface remelting and additive manufacturing, Physics Procedia 12 (Part A) (2011) 248−254.
[92] M.F. Zaeh, G. Branner, Investigations on residual stresses and deformations in selective laser melting, Production Engineering 4 (2010) 35−45.
[93] P. Vora, K. Mumtaz, I. Todd, N. Hopkinson, AlSi12 in-situ alloy formation and residual stress reduction using anchorless selective laser melting, Additive Manufacturing 7 (2015) 12−19.
[94] M. Shiomi, K. Osakada, K. Nakamura, T. Yamashita, F. Abe, Residual stress within metallic model made by selective laser melting process, CIRP Annals − Manufacturing Technology 53 (2004) 195−198.
[95] S. Leuders, M. Thöne, A. Riemer, T. Niendorf, T. Tröster, H.A. Richard, H.J. Maier, On the mechanical behaviour of titanium alloy TiAl6V4 manufactured by selective laser melting: fatigue resistance and crack growth performance, International Journal of Fatigue 48 (2013) 300−307.
[96] D. Gu, W. Meiners, Microstructure characteristics and formation mechanisms of in situ WC cemented carbide based hardmetals prepared by selective laser melting, Materials Science and Engineering: A 527 (2010) 7585−7592.
[97] C. Weingarten, D. Buchbinder, N. Pirch, W. Meiners, K. Wissenbach, R. Poprawe, Formation and reduction of hydrogen porosity during selective laser melting of AlSi10Mg, Journal of Materials Processing Technology 221 (2015) 112−120.
[98] C. Qiu, N.J.E. Adkins, M.M. Attallah, Microstructure and tensile properties of selectively laser-melted and of HIPed laser-melted Ti−6Al−4V, Materials Science and Engineering: A 578 (2013) 230−239.
[99] Q. Liu, J. Elambasseril, S. Sun, M. Leary, M. Brandt, P.K. Sharp, The effect of manufacturing defects on the fatigue behaviour of Ti-6Al-4V specimens fabricated using selective laser melting, Advanced Materials Research 891-892 (2014) 1519−1524.
[100] C. Qiu, N.J.E. Adkins, M.M. Attallah, Selective laser melting of Invar 36: microstructure and properties, Acta Materialia 103 (2016) 382−395.
[101] C. Panwisawas, C.L. Qiu, Y. Sovani, J.W. Brooks, M.M. Attallah, H.C. Basoalto, On the role of thermal fluid dynamics into the evolution of porosity during selective laser melting, Scripta Materialia 105 (2015) 14−17.

[102] H. Gong, K. Rafi, H. Gu, T. Starr, B. Stucker, Analysis of defect generation in Ti-6Al-4V parts made using powder bed fusion additive manufacturing processes, Additive Manufacturing 1−4 (2014) 87−98.
[103] H. Gong, K. Rafi, T. Starr, B. Stucker, in: 24th International SFF Symposium − an Additive Manufacturing Conference, SFF 2013, 2013, pp. 424−439.
[104] H. Gong, K. Rafi, N.V. Karthik, T. Starr, B. Stucker, in: 24th International SFF Symposium − an Additive Manufacturing Conference, SFF 2013, 2013, pp. 440−453.
[105] B. Song, S. Dong, H. Liao, C. Coddet, Process parameter selection for selective laser melting of Ti6Al4V based on temperature distribution simulation and experimental sintering, International Journal of Advanced Manufacturing Technology 61 (2012) 967−974.
[106] G. Kasperovich, J. Hausmann, Improvement of fatigue resistance and ductility of TiAl6V4 processed by selective laser melting, Journal of Materials Processing Technology 220 (2015) 202−214.
[107] H. Gu, H. Gong, D. Pal, K. Rafi, T. Starr, B. Stucker, in: 24th International SFF Symposium − an Additive Manufacturing Conference, SFF 2013, Austin, TX, USA, 2013, pp. 474−489.
[108] L.C. Zhang, D. Klemm, J. Eckert, Y.L. Hao, T.B. Sercombe, Manufacture by selective laser melting and mechanical behavior of a biomedical Ti−24Nb−4Zr−8Sn alloy, Scripta Materialia 65 (2011) 21−24.
[109] N. Read, W. Wang, K. Essa, M.M. Attallah, Selective laser melting of AlSi10Mg alloy: process optimisation and mechanical properties development, Materials & Design 65 (2015) 417−424.
[110] K. Kempen, L. Thijs, J. Van Humbeeck, J.P. Kruth, Mechanical properties of AlSi10Mg produced by selective laser melting, Physics Procedia 39 (2012) 439−446.
[111] D. Buchbinder, W. Meiners, K. Wissenbach, R. Poprawe, Selective laser melting of aluminum die-cast alloy—correlations between process parameters, solidification conditions, and resulting mechanical properties, Journal of Laser Applications 27 (2015) S29205.
[112] K.S. Chan, M. Koike, R.L. Mason, T. Okabe, Fatigue life of titanium alloys fabricated by additive layer manufacturing techniques for dental implants, Metallurgical and Materials Transactions A 44 (2013) 1010−1022.
[113] A. Mertens, S. Reginster, H. Paydas, Q. Contrepois, T. Dormal, O. Lemaire, J. Lecomte-Beckers, Mechanical properties of alloy Ti-6Al-4V and of stainless steel 316L processed by selective laser melting: influence of out-of-equilibrium microstructures, Powder Metallurgy 57 (2014) 184−189.
[114] Z. Wang, K. Guan, M. Gao, X. Li, X. Chen, X. Zeng, The microstructure and mechanical properties of deposited-IN718 by selective laser melting, Journal of Alloys and Compounds 513 (2012) 518−523.
[115] D. Zhang, W. Niu, X. Cao, Z. Liu, Effect of standard heat treatment on the microstructure and mechanical properties of selective laser melting manufactured Inconel 718 superalloy, Materials Science and Engineering A 644 (2015) 32−40.
[116] M.W. Wu, P.H. Lai, J.K. Chen, Anisotropy in the impact toughness of selective laser melted Ti-6Al-4V alloy, Materials Science and Engineering A 650 (2016) 295−299.
[117] E. Yasa, J. Deckers, J.P. Kruth, M. Rombouts, J. Luyten, Charpy impact testing of metallic selective laser melting parts, Virtual and Physical Prototyping 5 (2010) 89−98.
[118] P. Edwards, M. Ramulu, Fatigue performance evaluation of selective laser melted Ti−6Al−4V, Materials Science and Engineering: A 598 (2014) 327−337.

[119] E. Brandl, U. Heckenberger, V. Holzinger, D. Buchbinder, Additive manufactured AlSi10Mg samples using selective laser melting (SLM): microstructure, high cycle fatigue, and fracture behavior, Materials & Design 34 (2012) 159−169.
[120] W. Xu, S. Sun, J. Elambasseril, Q. Liu, M. Brandt, M. Qian, Ti-6Al-4V additively manufactured by selective laser melting with superior mechanical properties, JOM 67 (2015) 668−673.

Hybrid laser manufacturing

3

F. Brückner[1], *C. Leyens*[2]
[1]Fraunhofer IWS, Dresden, Germany; [2]Fraunhofer IWS, Dresden, Germany, and Technische Universität Dresden, Dresden, Germany

3.1 Introduction

Additive manufacturing (AM) yields a paradigm shift in manufacturing technologies for specific parts; this shift is caused by:

- increased material utilization ("buy-to-fly ratio")
- reduced production time and costs
- improved quality and precision
- high functionality combined with a high complexity
- availability of parts
- beneficial flexibility of production

Laser-based processes, such as laser metal deposition (LMD) or selective laser melting, concentrate the heat input to a small, localized process zone. Hence, high precision is achieved and the remaining distortion is low compared with other manufacturing technologies such as plasma transfer arc (PTA). The precise control of power also yields limited dilution and well-adjusted properties layer by layer.

However, benefits of AM can be completely negated by certain drawbacks along the process chain. One important impact may be caused by materials that are difficult to weld and related defects in the added material, for example, cold or hot cracking, porosity, lack of fusion, or microstructure variations due to process instabilities.

Cracking in particular greatly restricts the spectrum of suitable materials. One major reason for this is found in thermal contractions of molten material during cooling to an ambient temperature. Residual stresses yield plastic deformation, distortion, and even cracking and delamination in the case of brittle materials. Unfavorable phase transformations (eg, martensitic formation) might also increase such adverse effects. The cracking propensity can be reduced by additional heat sources, and thus a larger variety of available materials can extend the applicability of the technology. Hybrid laser manufacturing is meant to include additional heat sources as well as process technologies to overcome current limitations in laser-based AM and to use the synergistic effects of both heat sources. The additional energy sources are often cheaper than laser sources, but they are less precise.

Various hybrid laser manufacturing technologies have already been considered in the field of science and industrial applications of laser-based AM:

- The interaction of two or more laser beams with differing focus allows additional laser energy to be used to increase the build-up rate through increased surface temperatures and hence the absorptance [1].

Laser Additive Manufacturing. http://dx.doi.org/10.1016/B978-0-08-100433-3.00003-8
Copyright © 2017 Elsevier Ltd. All rights reserved.

Table 3.1 Advantages and disadvantages of hybrid laser manufacturing

Pros	Cons
• Weldability of challenging materials • Advanced material properties • Avoidance of material defects (eg, cracks) • Modification and/or displacement of distortion • Reduction of residual stress states • Synergy effects of combined processes • Improved use of process energy • Higher productivity (build-up rates, process speed)	• Complex process development • Higher investment costs • Geometrical restrictions (accessibility of energy sources) • Lack of know-how and experience • Increased effort for standardization • Quality control effort • Sophisticated simulation • Greater effort required for process stability and robustness • Synchronization between energy sources • Changed process chain

- A plasma or flame can be used to preheating the process zones or to rapidly build up areas with low precision. One solution is the combined use of PTA and LMD [2]. In fact, this is not considered fully hybrid because of heat sources are used consecutively.
- Another thermal hybrid manufacturing possibility is the combination of laser energy and induction. As a result of the deep penetration of electromagnetic energy, high laser-induced temperature gradients and the resulting residual stress states are greatly reduced. Absorptance is also enhanced by the increased substrate temperature.

Hybrid manufacturing possibilities do not yield only beneficial process behaviors, as shown in Table 3.1. Major drawbacks of hybrid technologies are related to increased and more cost-intensive process development and equipment. In some cases the accessibility of additional energy sources might be reduced. However, various applications only become possible by means of hybrid processing and if the mentioned additional effort is taken into account.

3.2 Overview of possible hybrid laser manufacturing procedures

In principle, different kinds of energy sources can be used for hybrid laser manufacturing, as seen in Fig. 3.1. Examples of these sources include

- the combination of several laser beams (possibly with varying wavelengths)
- electromagnetic sources to influence melt pool characteristics
- mechanical impacts (eg, by simultaneous hammering or laser shock peening)
- thermal support of the melt pool (eg, with a flame)
- support of the process zone by a plasma

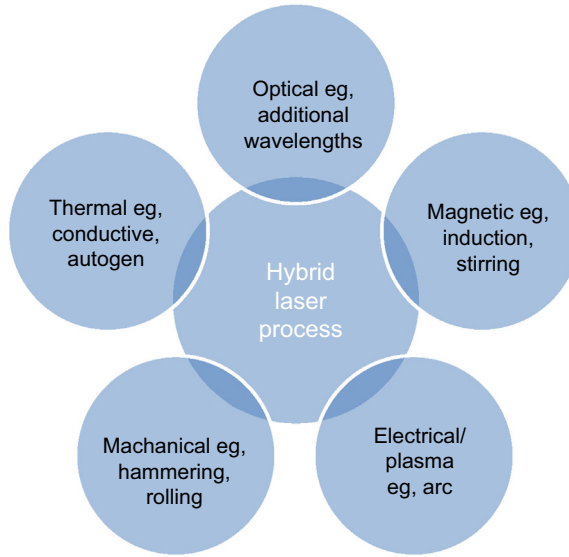

Figure 3.1 Selected energy sources for hybrid laser manufacturing.

Independent from the energy source, most hybrid approaches focus on modifying the thermal regime during processing. The aim is to overcome current process limitations related to usable materials and to increase process performance by modifying residual stress states. More detailed explanations about the formation of residual stress, cracking, and possible configurations of added materials are given in Section 3.3.

In a broader sense, laser-based AM in combination with finishing technologies such as milling can be considered hybrid laser manufacturing, but the process regime actually has a sequential characteristic of the combined processes. These quasi-hybrid laser manufacturing processes are briefly described in Section 3.4.

3.3 Improving process performance by adding thermal heat sources

Each heat treatment yields residual stresses caused by the inhomogeneous heating of the work piece. Laser-based methods in particular are characterized by high temperature gradients and high related stress states. In powder bed processing and LMD, such stress states are primarily based on the various effects:

- The added material is placed in a molten state onto a subjacent solid material.
- The molten filler material contracts while cooling. This might even occur after the temperature equalizes in the case of different coefficients of thermal expansion (CTEs) between the filler material and the underlying substrate.
- Irreversible phase transformations can yield residual deformations and thereby intrinsic stress caused by local density changes.

- Additional stresses can be formed by plastic deformation (especially at high temperatures) by exceeding the yield strength.
- If the tensile stress exceeds the local tensile strength, rudiments for cracking might be formed.

Therefore high temperature differences and related temperature gradients between the placed material and the already solidified subjacent material (substrate) have to be reduced. Different implementations of thermal heat sources can be used to do this.

3.3.1 Reducing stress by adding beam sources

The described reduction of temperature gradients between placed material (in the molten state) and the subjacent part at lower temperatures can be achieved by adding beam sources such as additional plasma or laser beams [3]. Hügel and Graf [1] describe the reduction of cracking with pre- and postheating by means of a laser−laser coupling with a double focus. Another example was studied by Habedank et al. [4], who enlarged the process window using an additional laser source. Hu and Hehmann [5] used a configuration of two or more additional laser beams to prevent cracking in the repair of damaged guide vanes and rotor blades of stationary gas turbines.

However, additional beam sources in combination with laser-based AM only penetrate metals up to several atom layers and can consequently reduce high-temperature gradients only in near-surface regions. By contrast, preheating deeper into the subjacent volume of the part using a furnace/chamber or by induction couples also reduces temperature gradients in deeper regions of the work piece. As a result, preheating in a furnace or by induction is more helpful in reducing stress levels and the danger of cracking.

3.3.2 Preheating of the whole part in a furnace or by induction

As described, the deep penetration of heat has a significant influence on the reduction of temperature gradients and cooling rates. Hence fully preheating the part in a furnace or heated chamber strongly reduces initial temperature differences between molten and already solidified material and thereby reduces plastic deformation, which has to be compensated for until an ambient temperature is reached. In the case of high preheating temperatures, the ultimate elongation that might yield cracking is not reached, even in crack-sensitive materials. A harmful effect might occur while cooling in the case of materials with large differences in the CTE. Preheating the whole part during material deposition can be defined as hybrid processing and represents a valid tool for the prevention of cracking. However, technological integration as well as a strong impact on the full part (eg, when combined with unwanted diffusion processes) are drawbacks of this technology. Therefore the preheating temperature has to be as high as necessary but as low as possible.

A more suitable solution can be realized by induction: Induction heating is applied to accessible areas of the part and relevant process zones are indirectly preheated. Compared with local induction (see Section 3.3.3), inductors do not have to be configured to dimensions of welding areas close to the process zone. Depending on the

specific part and the process, this procedure may offer improved flexibility for the integration of preheating. Compared to a furnace or a heated chamber, this procedure may yield shorter response times and improved heat management, especially in the case of rotational symmetric parts where heat can be uniformly distributed.

3.3.3 Hybrid laser manufacturing using local pre- and postheating by induction

Local induction is a rather comfortable, partially flexible, and effective hybrid process support. The surrounding process area is heated without contact using directly integrated inductors (eg, integrated into processing heads). Both induction and laser exposure act simultaneously during material deposition. The heat input is higher compared with conventional laser-based processes such as LMD but is less compared with heating the whole part in a furnace or chamber. Hence, a huge thermal modification or damage of the part can be avoided.

The combination of local induction with the laser beam yields a tailored temperature regime that consists of a broad base with low temperature gradients at temperatures below the preheating temperature and a steep temperature peak caused by the laser beam (see Fig. 3.2). The maximal preheating temperature must be high enough that significant residual stress forms only below this temperature while cooling down.

In addition to avoiding high temperature gradients, "costly" laser-related energy is compensated for by the "less expensive" energy provided by an induction generator, and the absorptance is increased, which saves laser power and increases build-up rates.

There are several ways to integrate inductive devices into laser-based AM. An inductor heating the whole part has already been described (see Fig. 3.3(a)). Another highly efficient possibility to heat the work piece can be achieved by the electromagnetic field going through an induction coil (see Fig. 3.3(b)). Another geometric variation of inductors uses the electromagnetic field surrounding the induction coil (see Fig. 3.3(c)). However, the geometries of the inductors have to be adjusted to the specific task and might not be fully independent of omnidirectional movements. By contrast,

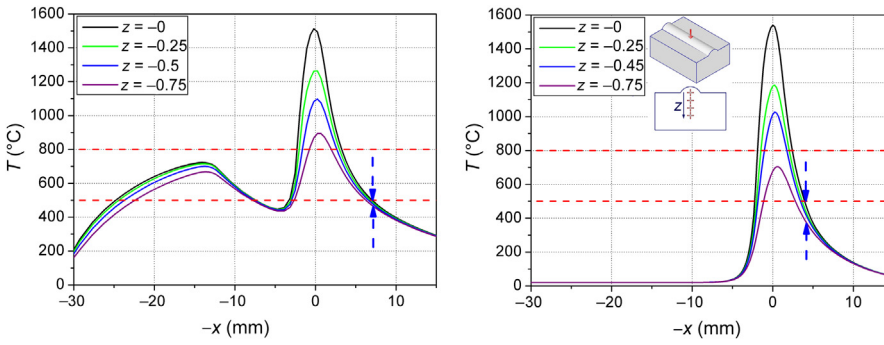

Figure 3.2 Temperature profiles in varying distances z from the part surface in laser metal deposition with inductive preheating (left) and without preheating (right) [6].

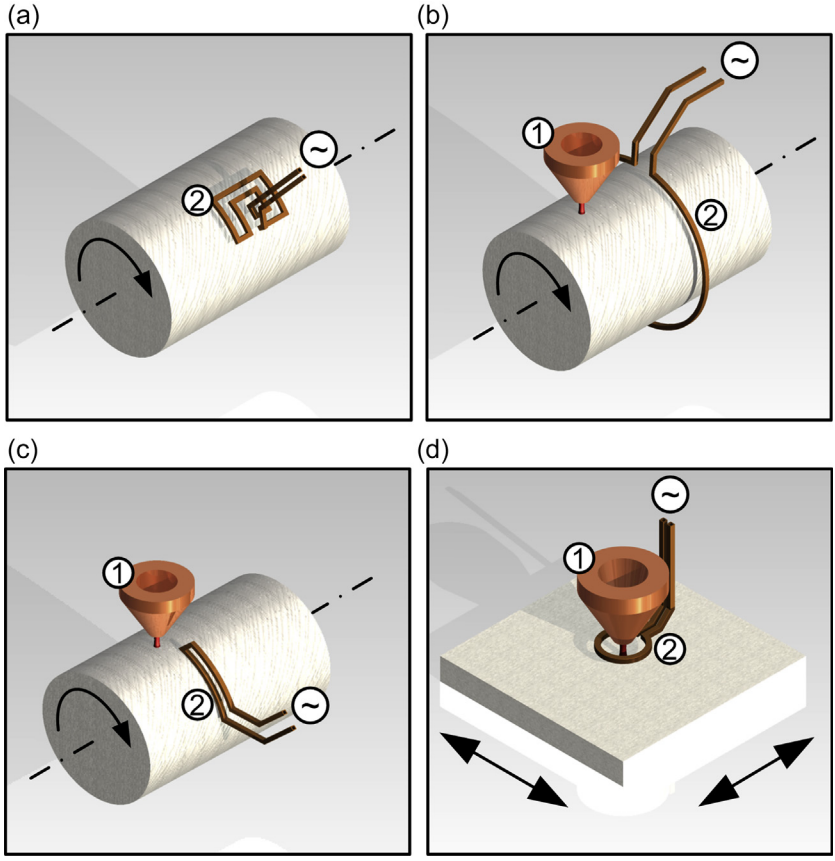

Figure 3.3 Variants of heating by induction in, for example, LMD: (a) preheating the whole part by induction, (b) local pre- and postheating using the inner field of the inductor, (c) local inductive pre- or postheating using the outer field of the inductive device, and (d) pre- and postheating by a ring inductor enabling omnidirectional movements of the melt pool. ① processing unit with laser beam, ② inductor.

implementing an induction coil around the process zone (eg, around the nozzle in LMD) may allow more flexibility by simultaneous omnidirectional pre- and post-heating (see Fig. 3.3(d)). Whereas the scheme shown in Fig. 3.3(d) yields good performance in the case of crack-sensitive materials, variations shown in Fig. 3.3(b) and (c) might be more suitable for directional build-ups with high deposition rates.

Fig. 3.4 shows an example of a processing head with an integrated inductor as schematically pictured in Fig. 3.3(d).

Basic experimental trials of hybrid processing in LMD using induction were carried out in the early 1990s. Brenner and colleagues [7–12] could deposit hard nickel-base alloys such as Deloro 60 onto various case hardening steels, heat-treatable steels, and cold work steels. In their studies, sequential as well as simultaneous preheating by induction was used. Preheating times ranging from 9 to 14 s and a maximal preheat temperature around 700°C were used to fully prevent primary cracking by means of inner

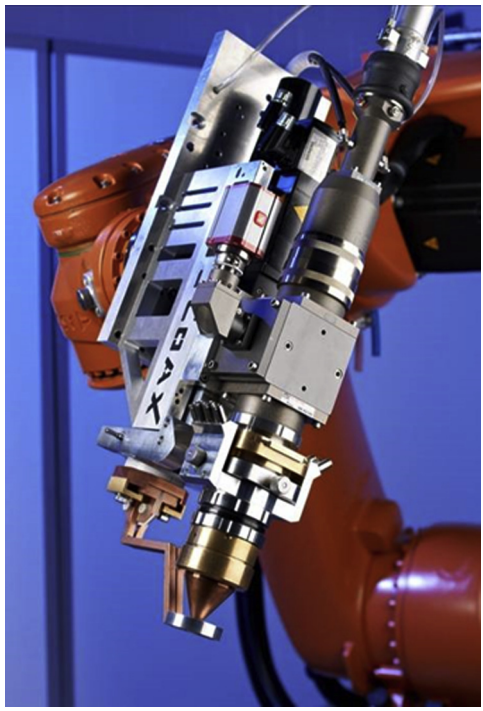

Figure 3.4 A coaxial laser metal deposition processing unit with an integrated ring inductor below the nozzle tip.
Photo courtesy of Fraunhofer IWS.

electromagnetic fields. Materials with maximal hardness around 60 HRC (Rockwell hardness C) could be built up free of defects even with increased deposition rates. Later studies by Zhang et al. [13] showed no disadvantages of inductive preheating related to the wear behavior.

3.3.4 Effect of substrate preheating and comparison of different thermal effects

As described earlier, the major cause for cracking in laser-based AM is related to the large difference between the solidification temperature of the added material and the temperature of the substrate. The difference in thermal expansion has to be compensated for by elastic and inelastic deformation (eg, plastic deformation) in the added material and/or the original substrate as well as by corresponding distortion. In brittle materials the plasticity limit might be exceeded and cracking may occur (see additional information in Fig. 3.5).

Plastic deformation, which is caused by distortion and is necessary to compensate for differences in thermal strains of the added and substrate materials, is partially transferred to the more ductile base material. However, this effect is significantly lower for base materials that show an increase in hardness during welding. This is attributed to the formation of martensite, which is linked to a considerable expansion in volume combined with a substantial lower plastic deformability as a result of its high yield stress.

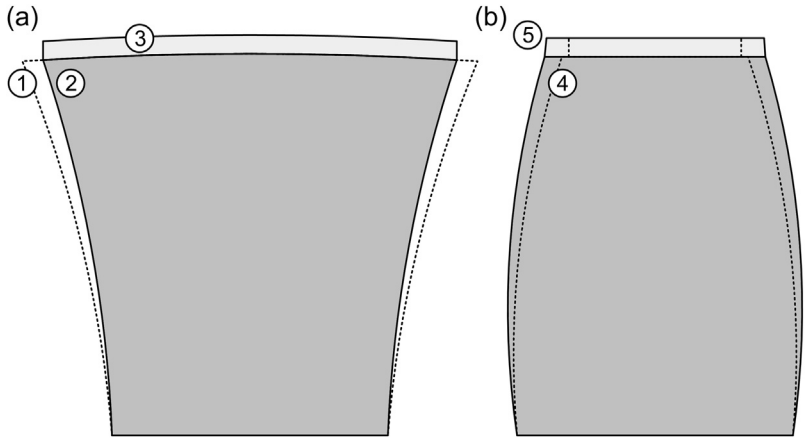

Figure 3.5 Schematic of stress relief by distortion in laser metal deposition: (a) near-surface areas of already solidified material (substrate) are heated and hence expanded by heat conduction or inductive heating (①). Because of the restraint of the expansion of the surrounding material, compressive stress and plastic deformation form; this is schematically shown by the stretched boundary (②). The molten material placed on top of the surface (③) fits to this shape (called fluid flow strain). (b) Added material and the heated part of the solid subjacent substrate contract differently while cooling (④). Elastic and plastic deformations in both areas keep the consistency of neighboring volume elements and determine the final contour (⑤).

To decrease the danger of cracking, the plastic deformation of a weld must be controlled; this can be managed by considering the following effects:

- The temperature range between the solidifying weld and the initial temperature of the base material is minimized by controlled oven heating or component-specific induction heating (see the preceding section). This reduces the gradient in thermal expansion between the weld and the base material, which must be compensated for after cooling to an ambient temperature. Additional differences due to the use of materials with different CTEs that occur during the cooling process cannot be compensated for.
- The application of selective heating in the near-surface area of the base material induces temporary compressive stresses. At sufficiently high temperatures the latter leads to a plastic deformation that shortens the directions parallel to the surface. If the aforementioned effect is superposed with build-up welding, compensation for the mismatch in expansion upon cooling may be balanced by distortion. This means that the plastic deformation that is essential for stress relief is partially shifted from the weld to the base material. Selective heating in the near-surface field can be achieved either by thermal conduction as an effect of the build-up welding process itself or, more efficiently, by applying process-integrated induction heating as already described.
- Application of this process-integrated induction heating determines a temporary and locally limited elongation of the near-surface field. The filler material that is transferred in a molten state is able to adapt the plastic deformation of the base material until it solidifies. This so-called fluid flow strain is preserved during solidification and decreases the existing inelastic contraction of the weld after cooling.

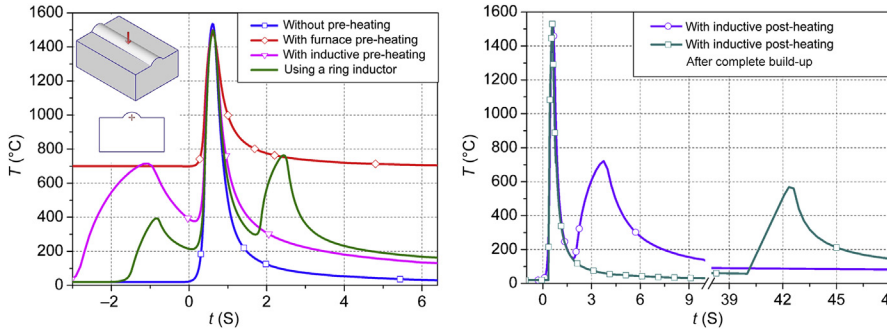

Figure 3.6 Temperature-time relations for laser metal deposition welding with powder influenced through the application of an additional heat source. The characteristic curves belong to the intersection point of the center line and the fusion line between the weld und the base material (Stellite 21 on AISI1045; maximum preheating or post−heat treatment temperature: ∼700°C; maximum temperature of the base material: $T_{\text{Martensite}}$ +30 K; feed rate: 0.6 m/min).

Targeted temperature control in terms of preheating and/or subsequent heat treatment can modify the rate of cooling in the regions of the weld that are particularly sensitive to the formation of austenite. This means that the formation of unfavorable phases (eg, martensite, with a considerable expansion in volume) can be suppressed or at least be adjusted during the welding of different materials. The latter can be achieved by applying a tempering process that reduces the expansion in volume and increases plastic deformability. To achieve this effect with inductive post−heat treatment, the treatment temperature, the penetration depth, and the duration must be particularly adapted to the specific requirements of the materials used.

These procedures for preventing crack formation drastically influence the temperature field that is generated by the laser during additive layer manufacturing. This can be seen in Fig. 3.6, which shows typical temperature-time relations for oven heating, inductive preheating, or inductive post−heat treatment, their combined application with an inductor ring, as well as an inductive heat treatment after the weld is completed.

3.3.5 Crack formation and delamination in LMD processes

Compared with other methods such as PTA, LMD causes much higher temperature gradients and cooling rates. This requires higher tensile stresses that can provoke cracks during welding processes or over the lifetime of the component.

Brittle fracture can be caused in materials that can only be stressed elastically during cooling from molten to solid states. Therefore, in LMD processes, materials that are reasonably ductile are preferred in order to reduce tensions caused by plastic deformations.

Defects such as crystal defects or accidental inclusions can lead to local stress concentrations in ductile materials. These stress concentrations have to be reduced by fortified plastic deformations. In this case dislocation pile-ups constraining plastic deformations can occur. This effect leads to increasing flow stress. Thus micro cracks are generated at locations where the stress level exceeds the local reduced strength. In the case of proceeding crack growth, the cavities increase and join other cavities. A crack can grow quickly in mechanically weaker areas, and thus delamination occurs. The risk of cracking depends on the current stress levels and the history of the process.

Every material tolerates a certain degree of plastic deformation. Therefore the direction of the tension is not very important. The relative accumulated plastic deformation is comparable to the uniaxial plastic deformation, as in tensile tests [6]. This deformation increases with every plastic deformation. Therefore it could be assumed to be a proportion of dislocation density in deformed volumes. The maximum it can reach is the specified strain of rupture. Many alloys with high hardness and wear resistance are not suited for laser-based AM as LMD because of their low strain of rupture.

Dislocation density and the risk of crack growth can be reduced by thermally induced regeneration at higher temperatures [14]. These effects also occur during progressive deformations. Similar effects can be observed in diffusion-driven phase transformations that take place at higher temperatures [15]. Hence, it is obviously advantageous to compensate for long periods of high temperatures by, for example, preheating the completely affected zone.

Contamination and corrosion can reduce strength, particularly at grain boundaries and other boundary surfaces. Hydrogen is able to quickly diffuse and accumulate in critical areas for this reason reduces the strength and plasticity. It is imported by water vapor or organic substances if no precautions are taken. In sensitive materials cracks can be prevented by shielding the process zone using atmospheres.

Cracks can also result from triaxial stress conditions at lower tensions if one tension exceeds the threshold tension. Further, these stress conditions promote the diffusion of atomic hydrogen and other corrosive elements.

The highest tensions caused by LMD occur along the bead and at its edges (caused by the notch effect). This may result in transverse cracking within beads and/or delamination at the edges.

3.3.6 Influence of pre- and postheating on residual stresses at single and overlapping beads

Related tensions during the cooling of plastic deformable layers are equal or nearly equal to the current flow stress [6]. This also occurs in LDM combined with oven preheating. The need for plastic deformation can be reduced by the application of additional energy sources to compensate for the difference in thermal dilatation between the layer and the substrate. The resulting lower yield stress also leads to lower stresses within the layer. The additional reduction of tensions within the layer caused by further

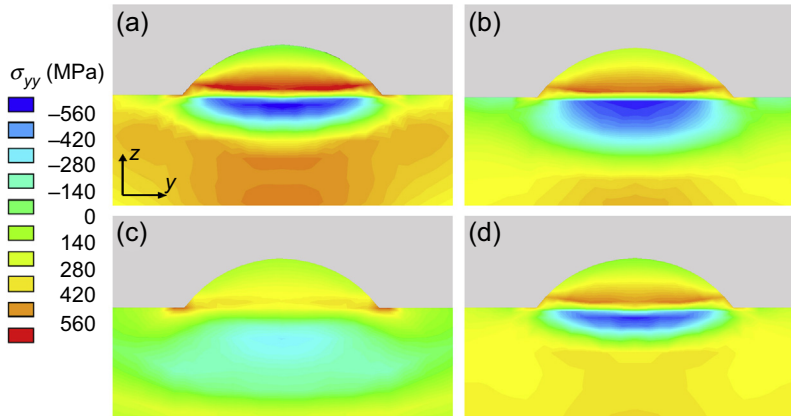

Figure 3.7 Transverse stress distribution σ_{yy} of a laser metal deposition−generated bead without pre- and postheating (a), with local preheating up to 720°C by an integrated inductor (b), with preheating of the entire component up to 700°C by an oven (c), and with local postheating up to 720°C (d) (Stellite 21 on AISI1045; feed rate: 0.6 m/min; bead bright: 2.0 mm; bead height: 0.5 mm; substrate thickness: 20 mm; circular inductor diameter: 20 mm; distance laser beam. Inductor: 11 mm).

energy sources is the result of decreased plastic deformations. A slight reduction of flow stress leads to a larger reduction of plastic deformations and cracking propensity.

As finite element simulations show [6], there are no fundamental differences between stress distributions within the bead, but a significant reduction is caused by additional energy sources, especially preheating in a chamber or furnace.

As an example, for an AISI1045 substrate material, the austenitic zone increases only slightly by inductive preheating and much more in case of preheating in an oven. After inductive preheating (Fig. 3.7(b)), the austenite converts partly to bainite or martensite, which yields a broad area of reduced residual stress. After oven preheating (Fig. 3.7(c)), austenite converts to perlite. As a result, compressive stresses within the substrate are reduced. An extended region of slight residual tensile stress adjoins. The residual tensile stress is caused by plastic deformation during preheating and also can be applied to massive components. In the case of oven preheating this zone extends deeply into the workpiece.. During postheating (Fig. 3.7(d)) the martensite is a function of dwell time. Hence the area of compressive stress is as wide as that without any inductive support, and the compressive stress can be reduced as a function of postheating temperature and dwell time. A further area of tensile stress and plastic deformation adjoins, as occurs with preheating; this contributes to stress relief in the substrate after cooling. Postheating is favorable in the case of an increase in laser-based hardness in substrates caused by unwanted phase transformations.

These considerations are transferable to layers that consist of multiple overlapping beads. Oven preheating reduces the difference of thermal distention between the layer and substrate of all beads. In inductive heating the inductor integrated into process heads heats every track, yielding oscillating time dependencies of the temperature

(Fig, 3.8, left). The local dwell time is extended at any passage of process head (Fig. 3.8(a)). This leads to higher temperatures in the process zone, deeper penetration, and reduced temperature gradients. Fig. 3.8 shows four time-dependent temperature distributions of overlapping beads for the position at the ground of the third bead, as shown in Fig. 3.8(a) for an LDM process. It shows distributions with and without inductive pre- or postheating and corresponding residual transverse stress. The maxima of tensile stress arise at the same position in all cases but can be enormously reduced by additional heat. Preheating increases the temperature of the last applied bead. Hence tensile stresses are widely distributed over several weld beads, and the

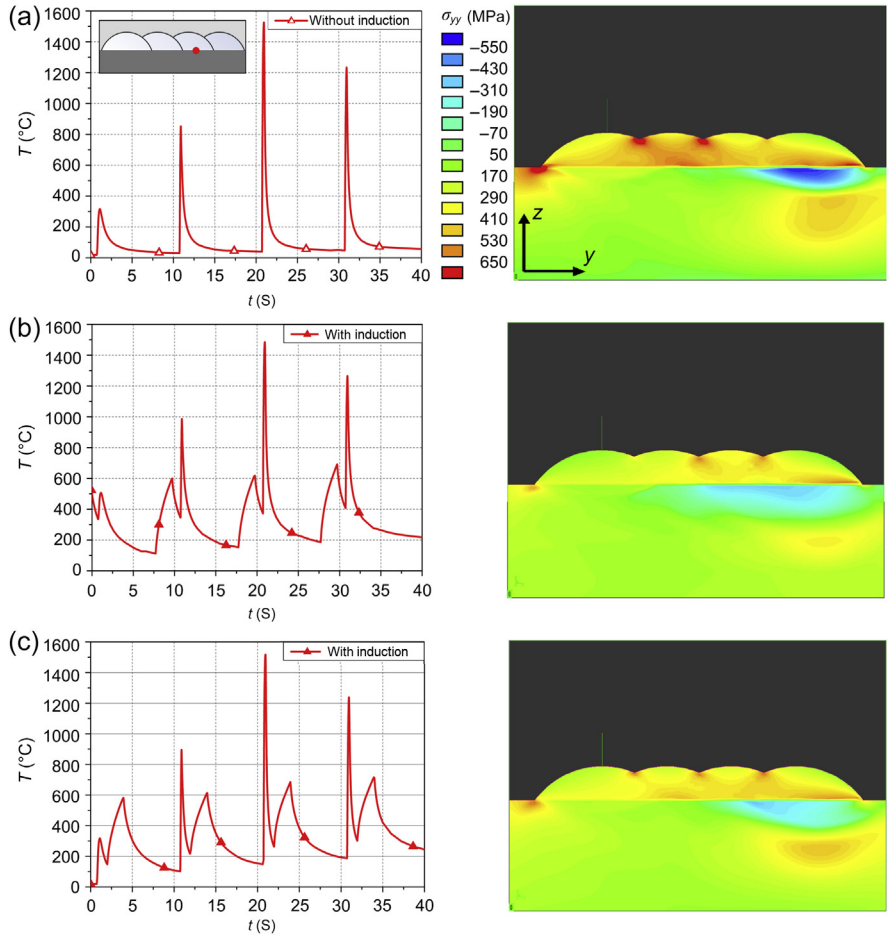

Figure 3.8 Finite element calculations of temperature distributions and transverse stresses at four overlapping beads without preheating (a), with inductive preheating (b), and with inductive postheating up to 700°C (c) (Stellite 21 on AISI1045; substrate thickness: 20 mm; layer height: 0.5 mm; overlap per track: 0.4; feed rate: 0.6 m/min; frequency: 10 kHz; inductor length: 20 mm; distance from laser beam to inductor: 11 mm).

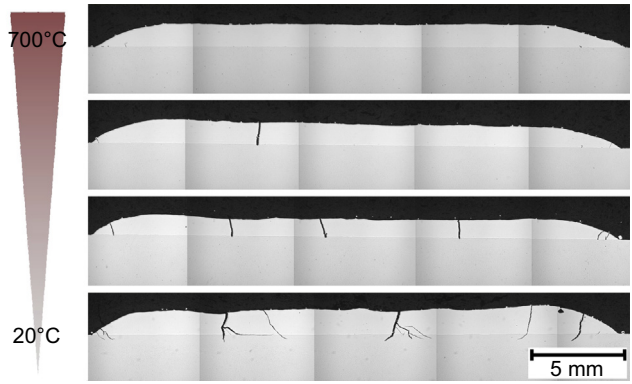

Figure 3.9 Transverse cracks in single laser metal deposition weld beads fabricated from Stellite 20 combined with inductive preheating at varying maximum temperatures (feed rate: 0.6 m/min; laser beam spot: 4 mm; build-up height: 1 mm; substrate thickness: 10 mm; inductor length: 100 mm; inductor width: 20 mm).

maxima of tensile stress at overlapping regions are reduced. In the case of postheating this effect is lower, but the impact caused by martensitic formation is reduced. In the simulation example, the postheating duration of this example was 2 s, which corresponds to an inductor length of 2.0 cm at a feed rate of 0.6 m/min.

Corresponding to previously described simulations, Fig. 3.9 shows the positive impact of hybrid processing by means of inductive preheating. The combination can significantly reduce the risk of cracking and delamination.

Even materials with a high tendency to cracking under heat can be added without any defects, as shown in Fig. 3.10. Typical cavities with molten materials enclosed between dendritic structures are prevented.

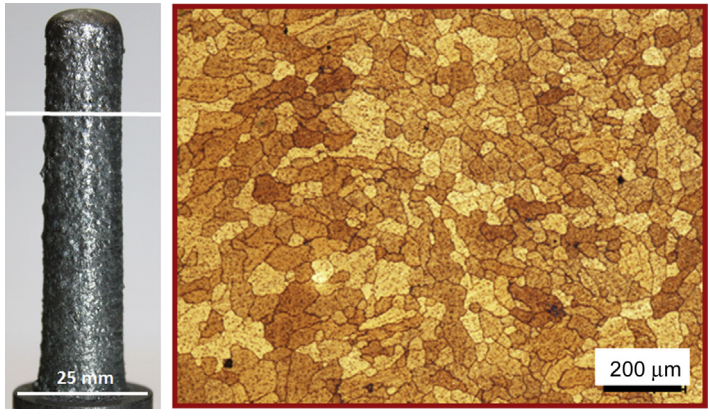

Figure 3.10 Cross section of a nickel-base superalloy test specimen (MarM247) fabricated by hybrid laser-based additive manufacturing.

3.3.7 Geometry and position of the integrated inductor

The shape and size of the inductor must be adapted to the component geometry to reach maximum efficiency. For inductor shapes with line and hairpin geometries, the dwell time to get the component appropriately heated and the depth of penetration are mainly determined by the inductor length. Fig. 3.11 shows maximum values of the accumulated malleable-related and adapted deformations within the layer (Fig. 3.11(a)). This further shows the maximum values of the related tensile stresses within the layer and the compressive stresses within the substrate during preheating in relation to the inductor length.

Although the tensile stresses are constant, plastic deformation is reduced by increasing inductor length because of the depth of penetration of the temperature field. For long inductors the injected heat reduces the cooling rate so strongly that austenite is transformed into bainite instead of martensite.

In addition to inductor shape and size, its position relative to the component and the laser beam is important. The air gap between the component and the inductor should be as small as possible to ensure maximum injection. The distance between the laser beam and the postheating inductor should be as low as possible, too, to prevent thermal stresses caused by high cooling rates. This generally also has to be considered for the distance between the laser beam and the preheating inductor. However, a minimum distance, dependent on the inductor geometry, is necessary to realize adequate preheating that allows enough time for the heat to spread within the component. Fig. 3.12 shows an example of a minimum of transverse stress within a bead as a function of distance from the inductor. The optimum distance is typically a few millimeters. In practice the optimal distance is determined by the process head dimensions.

Line- and hairpin-shaped inductors inject energy along straight tracks and cannot be used for applications with curved tracks or tracks that frequently change direction. In these cases a ring-shaped inductor mounted coaxially to the process head is used

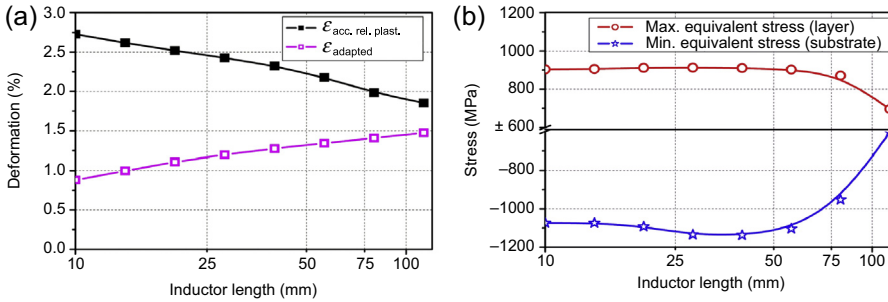

Figure 3.11 Dependence of maximum accumulated related plastic and adapted deformations within a layer (a) and maximum values of related tensile stresses within in a layer and compressive stresses within the substrate (b) as a function of inductor length during preheating by a line-shaped inductor (Stellite 21 on AISI1045; layer thickness: 1 mm; board thickness: 10 mm; feed rate: 0.6 m/min; maximum preheating temperature: 700°C; inductor width: 10 mm).

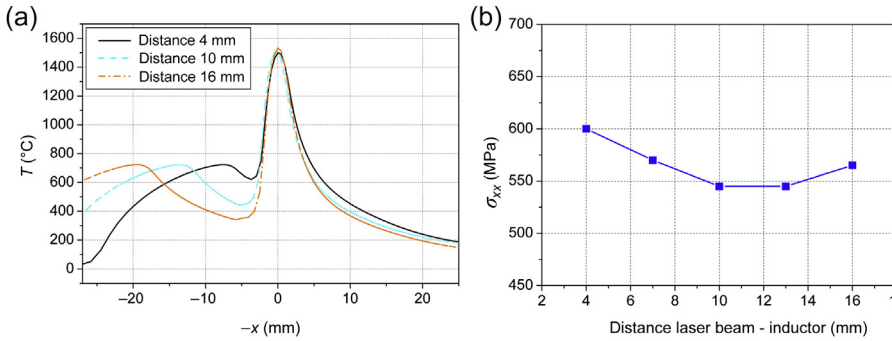

Figure 3.12 Optimum distance between the laser beam and a circular inductor with a 20-mm diameter: (a) temperature profile along the feed direction in a symmetry plane of the substrate surface; (b) maximum transverse stress within a bead as a function of inductor distance (Stellite 21 on AISI1045; maximum preheating temperature: ∼700 °C; feed rate: 0.6 m/min; bead width: 2.0 mm; bead height: 0.5 mm).

because it has no preferred direction. Fig. 3.13(a) compares a simulated magnetic field in the air gap and preheated surface areas of a line- and a ring-shaped inductor.

Ring-shaped inductors combine the advantages of pre- and postheating very well. But there are some disadvantages. For example, uneven surface structures prevent optimum injection of heat near the bead, and therefore the effect of preheating is low.

- Injected heat beside the track only warms the component and has less effect on the development of stresses.
- Increasing the inductor diameters for a larger induction region causes a loss of energy to the surrounding area (Fig. 3.13(a)).

The use of a magnetic field inside the inductor is beneficial to coat axisymmetric components at high coating rates. Here the ring-shaped inductor surrounds the component and can be moved beside the process head in an axial direction. Efficient use of ring-shaped inductors is constrained to the coating deposition of axisymmetric components and applications where frequent changes in direction occur.

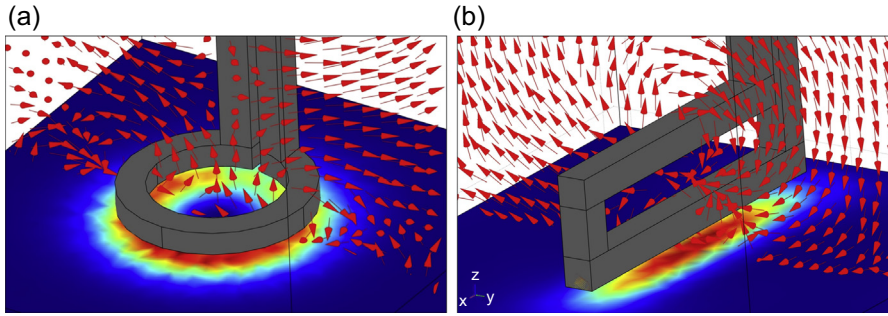

Figure 3.13 Streamlines of the magnetic field (*red arrows*) and injected heat in a ring-shaped (a) and line-shaped (b) inductor.

3.4 Hybrid approaches using mechanical impacts

Although mechanical impacts have been of only marginal interest in laser-based AM so far, some hybrid approaches yield mainly low distortion, reduced stress levels, and, in the broader sense, the final net shape of parts.

3.4.1 Reduction of distortion and stress by mechanical forces

Distortion and stress states are not only reduced by tailored temperature regimes; well-directed additional forces can be applied to counteract distortion and stresses originating from the process zone. One solution is an indirect force by outer induction: Because of the thermal expansion of heated regions far from the process zone, mechanical forces may yield compressive stress onto molten material [16]. By contrast, direct, exactly defined mechanical forces or clamping devices may act to weld areas, lowering distortion or stress. However, the latter mainly focuses on simple parts with good accessibility and can be carried out by, for example, compressive stress coming from directly coupled rollers. Also, laser-generated shock waves (laser shock peening) and hammering have also been considered [17–19]. Here tensile stress in the surface regions up to ~ 1 mm can be transformed into compressive stress. However, taking these methods into account may yield to changed distortion and stress states in unaffected areas of the part.

3.4.2 Combined finishing and laser-based AM

In the broadest sense the combination of finishing and laser-based AM is considered a hybrid process in the literature and the relevant press. In fact, we may not talk directly about hybrid processing because of the sequence of interacting process steps. However, several machine manufacturers already have combined machines available on the market [20,21]. Such machines are characterized by automated tool changes and corresponding software considering subtractive as well as additive manufacturing strategies. Advantages of these machine concepts are expected to be related to the manufacturing of geometrically complex parts that require intermediate machining during AM because of the limited accessibility of the machined areas once the part is completed. Moreover, for operations with limited lot sizes, extracting an almost ready-to-use part can be advantageous.

3.5 Conclusions and outlook

Different combinations of hybrid laser manufacturing are addressed in this chapter. Current hybrid processes within laser-based AM mainly take into account thermal heat sources to overcome current material restrictions and to increase process performance (see Section 3.3).

In laser-based AM the added material placed in a molten state yields high laser-related temperature gradients and high heating and cooling rates. Thermo-metallurgical strain causes high residual stresses and strong plastic deformation. In the case of hard and brittle materials, the strain to rupture might be exceeded and hence cracking and delamination can occur during the AM process or later in service. Careful selection of process parameters is the first step in preventing weld defects. However, many materials used in laser-based AM require an extension of the substrate surface by simultaneous (local) preheating. Hence, molten material is placed on top of the "stretched" substrate (fluid flow strain), and cracking is prevented by reduced plastic deformation while cooling. Additional thermal sources implemented in the deposition process can also reduce unwanted phase transformation, which increases high tensile stress in the added material because of its volume expansion.

Heating the entire part is the safest way to prevent cracking and can be classified as a hybrid procedure because of its simultaneous character. However, the full part might be damaged and annealed. In addition, the procedure is often time-consuming and costly. Hence preheating in a chamber or furnace may yield technological and application-related disadvantages.

Hybrid processing using a ring inductor in combination with a coaxial nozzle makes changes in direction easier. However, well-defined inductors (eg, line inductors) are more effective to prevent cracking. In all cases of local induction, the inductor and the fabricated part have to be adjusted to each other, which sometimes makes the fabrication of specific inductors difficult. The higher pre- and postheating temperature and duration, and the higher the skin depth, the better the reduction of stress and the danger of cracking by local induction. Hence significant parameters are the power used, the excitation frequency, and the shape and size of the inductor.

In general it is not possible to overcome stress and distortion at the same time and location. Therefore preventing distortion using thermal or mechanical hybrid procedures makes sense only with rather ductile materials. Otherwise these efforts may yield intolerable cracking.

We have reached some conclusions regarding the use of additional thermal heat sources. Compared with hybrid processing with integrated flames or additional laser beams, induction or full preheating in a chamber penetrates deeper into the already fabricated piece and thereby improves crack prevention and increases the build-up efficiency.

The higher the pre- or postheating temperature, the higher the resulting effect. However, temperature has to be kept as low as possible to avoid unwanted structural changes and defects.

Preheating temperatures can partially be reduced by increasing the depth of penetration. For example, increased the heating duration or decreasing the excitation frequencies can be useful.

In the case of the substrate material AISI1045, simulations have shown no additional effect in case of preheating times longer than 10 s. For hardening materials, technologies allowing postheating might be preferred to avoid unwanted microstructure states.

Hybrid laser manufacturing can be also useful to avoid defects in the deposited material.

Acknowledgments

The authors gratefully acknowledge contributions by Dr. Stephan Hunze, Mirko Riede, and André Seidel.

References

[1] H. Hügel, T. Graf, Laser in der Fertigung, Vieweg+Teubner, GWV Fachverlage GmbH, Wiesbaden, 2009.
[2] S. Nowotny, U. Berners, A. Gasser, R. Gnann, T. Heptner, M. Jurca, K. Kramm, A. Ott, R. Pfeifer, A. Popp, B. Stimper, Oberflächenbeschichten und formgebendes Auftragschweißen mit laserbasierten hybriden Fertigungsverfahren – FAVOR, Fraunhofer IRB Verlag, 2004.
[3] M. Förster, Einsatz der Verfahrenskette Laser-, Plasmaauftragschweißen undFräsen zur Reparatur, Oberflächenschutz und Rapid Tooling von Bauteilen, Diplomarbeit, Hochschule für Technik und Wirtschaft Dresden, 2003.
[4] G. Habedank, C. Theiler, M. Grupp, H. Kohn, G. Sepold, F. Vollertsen, Laser beam cladding of steel with high power diode lasers, in: Proceedings of the Second International WLT-Conference on Lasers in Manufacturing, 2003, pp. S. 45–50.
[5] Y. Hu, W. Hehmann, Multi-Laser Beam Welding High Strength Superalloys, Patent US6972390B2, 2005.
[6] F. Brückner, Modellrechnungen zum Einfluss der Prozessführung beim induktiv unterstützten Laser-Pulver-Auftragschweißen auf die Entstehung von thermischen Spannungen, Rissen und Verzug (Ph.D. thesis), Dresden University of Technology, 2011.
[7] B. Brenner, V. Fux, A. Wetzig, S. Nowotny, Induktiv unterstütztes Laserauftragschweißen - eine Hybridtechnologie überwindet Anwendungsgrenzen, in: Proceedings of the Sixth European Conference on Laser Treatment of Materials ECLAT, vol. 1, 1996, pp. S. 469–476.
[8] B. Brenner, V. Fux, A. Wetzig, Induktiv Unterstütztes Laserauftragschweißen – Eine Hybrid-technologie Eröffnet Neue Möglichkeiten, vol. 52 (4), Härterei-Technische Mitteilungen, 1997, pp. S. 221–225.
[9] B. Brenner, V. Fux, Induktiv unterstütztes Laserauftragschweißen – ein neues Verfahren zur effektiven Erzeugung hochverschleißbeständiger Randschichten, vol. 4, Stahl Formen Fügen Ferti-gen, 1999, pp. S. 48–50.
[10] V. Fux, B. Brenner, Leistungsfähige Beschichtungsprozesse durch induktiv unterstütztes La-serauftragschweißen, vol. B297, Freiberger Forschungshefte, 1999, pp. S. 121–130.
[11] A. Wetzig, B. Brenner, V. Fux, E. Beyer, Induction assisted laser-cladding: a new and effective method for producing high wear resistant coatings on steel components, in: Proceedings of the Laser Materials Processing Conference ICALEO'98, Orlando, USA, 1998.
[12] H. Stiele, B. Brenner, Kombinierte Wärmebehandlung Laser – Induktionserwärmung, vol. 6, Stahl, 2002, pp. S. 40–42.
[13] Y. Zhang, Z. Xianghua, Y. Xiangkai, Elimination of laser cladding cracks; thermal control and stress analysis, in: Proc. ICALEO, 2001, p. S. 705.
[14] K. Lange, Umformtechnik, Springer-Verlag Berlin, Heidelberg, NewYork, 1984.
[15] SYSWELD - Handbuch, SYSWELD User Manual, 2008.

[16] Gunther Göbel, Erweiterung der Prozessgrenzen beim Laserstrahlschweißen heißrissgefährdeter Werkstoffe (Ph.D. thesis), Technische Universitaet Dresden, 2008.
[17] A. Mehlhorn, Laser-Pulver-Auftragschweißen von Spritzgusswerkzeugen aus Gusseisen, Großer Beleg, Technische Universität Dresden, 2008.
[18] K. Ding, L. Ye, Laser Shock Peening: Performance and Process Simulation, 2006.
[19] A.H. Clauer, Laser shock peening for fatigue resistance, in: J.K. Gregory, H.J. Rack, D. Eylon (Eds.), Surface Performance of Titanium, TMS, Warrendale, PA, 1996, pp. S. 217−230.
[20] F. Lell, Additive Manufacturing in finished part quality by means of hybrid processing, Proc. of the International Symposium of Additive Manufacturing, Dresden, February. 25−26, 2015.
[21] P. Mognol, L. Jègou, M. Rivette, B. Furet, High speed milling, electro discharge machining and direct laser metal sintering: a method to optimize these processes in hybrid metal tooling, The International Journal of Advanced Manufacturing Technology 29 (2006) 35−40.

Surface roughness optimisation for selective laser melting (SLM): accommodating relevant and irrelevant surfaces

4

M. Leary
RMIT University, Centre for Additive Manufacturing, Melbourne, VIC, Australia

4.1 Introduction

Additive manufacturing (AM) provides a significant opportunity for the manufacture of innovative products. In particular, AM allows the manufacture of geometries that include complex features that are not possible with traditional manufacturing methods, and the opportunity to economically manufacture short production runs without significant cost penalty. In particular, AM is suited to the manufacture of:

- *prototype components*, for design validation before large-volume manufacture
- *low-volume production components*, especially during the initial deployment of a specific design, to allow rapid implementation of design changes, as required
- *high-volume customised components* for which the geometry of each component is subject to variation and is therefore not compatible with fixed-tooling methods
- *components that are not technically feasible with traditional methods*, for example, complex lattice structures and components with internal voids

For these scenarios, it is likely that surface roughness is a highly relevant design attribute. For AM, surface roughness is highly dependent on the specific attributes of the AM process used, the associated process parameters, and the orientation of the component within the available build volume.

To provide AM components that are acceptable for a specific purpose, a quantified surface roughness is highly desirable; the available literature includes work that seeks to address this issue, including experimental investigation of surface roughness of selective laser melting (SLM) [1−6], fused deposition modelling [7−10], and selective laser sintering [11]. The orientation of the component can be used to optimise the average surface roughness. Orientation is optimised by reference to either pre-selected [7,12] or continuously variable orientations [13−15]. This work contributes to the available literature by providing:

- *New material roughness data*: To provide useful design data, the surface roughness versus build inclination of SLM Ti64 is experimentally assessed and reported in detail, including high-magnification microscopy and associated surface roughness statistics of the upper and lower surfaces for a comprehensive array of specimen inclinations.

Laser Additive Manufacturing. http://dx.doi.org/10.1016/B978-0-08-100433-3.00004-X
Copyright © 2017 Elsevier Ltd. All rights reserved.

- *Visualisation of roughness objectives versus orientation*: An infinite number of feasible orientations of a component exist within the build volume. Visualisation of the roughness objectives within the assessed orientations aids identification of the optimal orientation(s) within the available optimisation time.
- *Novel surface roughness objectives*: The available literature on orientation optimisation considers only the minimisation of average surface roughness. This research proposes novel surface roughness objectives, including:
  - *peak roughness avoidance*, which is appropriate when a specific roughness type violates an inflexible design constraint.
  - *weighted roughness*, which is appropriate when a non-linear correlation exists between specific roughness types and performance.
- *Filtering of irrelevant surfaces*: It is common for a manufactured product to include surfaces that are irrelevant in terms of associated surface roughness. For example, commercial products consist of *visible* and *hidden* surfaces. Hidden surfaces are not relevant to the aesthetic value associated with the product. Engineering components may have critical roughness tolerances associated with key surfaces, but not all surfaces are functionally relevant. The method proposed in this research enables the discrimination of relevant and irrelevant surfaces when assessing the associated surface roughness objective.

These contributions have been used to enable novel design outcomes for a number of engineering applications of SLM technologies (Section 4.4):

- *A surgical implant*, whereby an orientation map of average roughness is presented for feasible orientations to identify the optimal implant orientation for surgical objectives
- *Low-volume prototype cover*, whereby a custom roughness weighting is applied to discourage facets with high roughness from occurring on visible surfaces
- *Hydraulic valve assembly*, whereby surfaces of relevance to functional objectives are assessed to enable robust identification of optimal build orientation

4.2 Additive manufacturing

AM is defined by the ASTM [16] as the 'process of joining materials to make objects from 3D model data, usually layer upon layer, as opposed to subtractive manufacturing methodologies, such as traditional machining'. AM begins with a computer-assisted design (CAD) representation of the intended component geometry. This data are then converted to stereolithographic (STL) format to be compatible with AM processes (Fig. 4.1). The STL format represents the CAD data with a discrete number of triangular facets and their associated surface norms (Table 4.1). The STL representation is processed as required to provide specific tool path and processing instructions for the specific AM method [17,18].

AM processes can be characterised according to the method by which support is provided, the resolution of the manufactured geometry to the intended geometry, and the relevant processing parameters of manufacture [18–20]. Of the AM processes of commercial interest, SLM is extremely important because it allows the manufacture of large-scale functional components with engineering-grade metals with high complexity and a relatively low unit cost [21]. This research focuses specifically on the optimisation of SLM components with specific surface finish objectives; however, the associated methods are generally applicable to any AM processes.

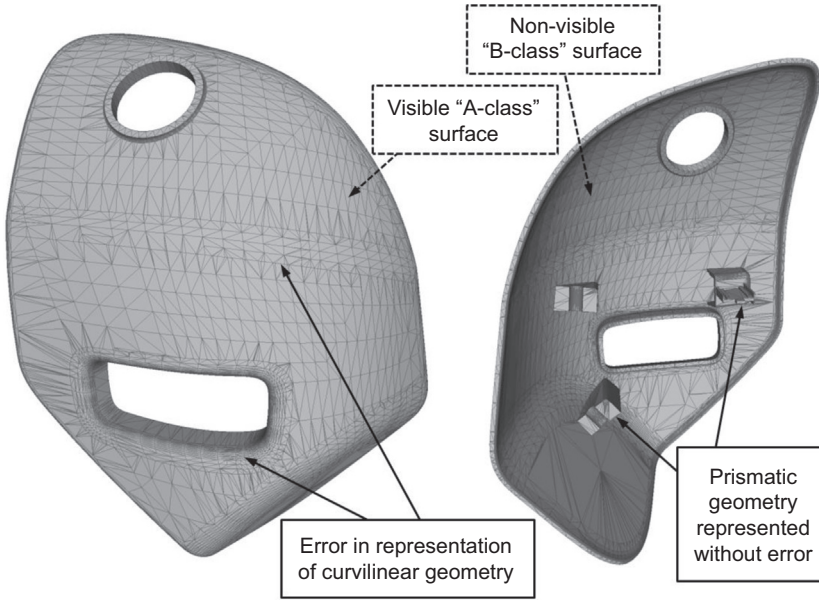

Figure 4.1 Computer-assisted design model (shaded) and associated stereolithographic representation (wireframe facets). This model of a low-volume prototype cover indicates visible (A-class) and non-visible (B-class) surfaces, which inherently have different surface roughness objectives.

Table 4.1 Binary stereolithographic file standard

Element	Content	Size
Header	Component information	80 bytes
n	Number of facets	32-bit unsigned integer
Facet *1*	Vertex 1 Cartesian coordinates	32-bit floating point
	Vertex 2 Cartesian coordinates	32-bit floating point
	Vertex 3 Cartesian coordinates	32-bit floating point
	Facet normal vector	32-bit floating point
	Attribute byte count	2-byte unsigned integer
…	…	…
Facet *n*	Vertex 1 Cartesian coordinates	32-bit floating point
	Vertex 2 Cartesian coordinates	32-bit floating point
	Vertex 3 Cartesian coordinates	32-bit floating point
	Facet normal vector	32-bit floating point
	Attribute byte count	2-byte unsigned integer

4.2.1 Selective laser melting

SLM refers to the fusion of metal powder with a laser power source to incrementally manufacture an intended product [22]. SLM is an important commercial AM process because it [21,23]:

- enables the manufacture of a range of fusible ferrous and non-ferrous metals
- readily accommodates support structures to enable manufacture of acute overhang geometry
- provides high structural integrity of manufactured components
- has relatively low fixed and variable costs
- has a reasonably short build time

Despite the particular advantages associated with SLM, the associated surface roughness may introduce technical challenges because of the layered nature of AM and the associated process parameters and powder morphology.

Control of surface roughness is of particular importance for commercial applications because of the associated implications on product aesthetics, structural integrity and geometric tolerance. Surface roughness is fundamentally the result of some source of geometric error.

4.2.2 Sources of geometric error

Geometric error refers to a discrepancy between the CAD representation of the intended product and the geometry of the actual manufactured product. Geometric error in AM can be attributed to either error in the STL representation of the CAD geometry or error in the AM manufacture of the STL representation (Fig. 4.2).

4.2.2.1 Error in STL representation of CAD data

Because of the discrete nature of the STL format, error may occur in the representation of the original CAD data. If the original CAD data are prismatic, the discrete facets of the STL represent the CAD data without error (Fig. 4.1). If the original CAD data are

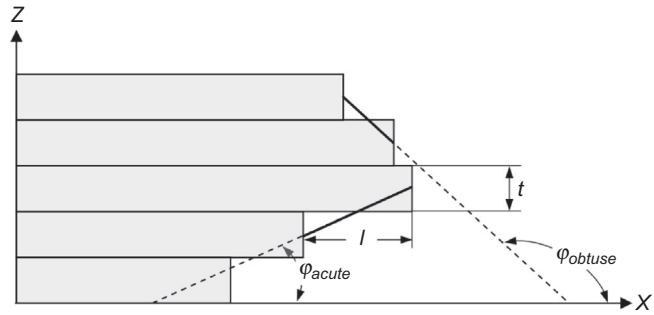

Figure 4.2 Layered approximation of computer-assisted design (CAD) geometry, indicating a loss of fidelity between the CAD and the manufactured geometry as a result of staircase error [24].

curvilinear, the STL representation of the original CAD data includes some approximation error (Fig. 4.2); this error diminishes with an increasing number of facets [6]. It is desirable to minimise the number of facets to reduce computational demands; if possible, however, the number of facets should be sufficiently high that the associated STL representation error is negligibly small.

4.2.2.2 Error in manufacture of the STL representation

AM involves the successive addition of material to manufacture an intended geometry. The AM process introduces manufacturing error in the representation of the STL data as a result of:

1. machine precision and repeatability [25]
2. distortion and part shrinkage [6]
3. *staircase* errors [9,26], which introduce roughness caused by the discrete layers associated with AM (Fig. 4.2)
4. Roughness introduced by process parameters, the laser scan path [6], and the powder morphology [4]

4.3 Roughness

Roughness refers to a geometric deviation from a reference datum. Numerous measures of roughness have been proposed [27]. To be compatible with other contributions in this field, the arithmetic average roughness, R_a, is used, where R_a measures the arithmetic average deviation of the measured profile from the centre line of the measured profile (Eq. (4.1)):

$$R_a = \frac{1}{n}\sum_{i=1}^{n} |y_j| \tag{4.1}$$

where y_j is the vertical distance from the mean line to the jth data point and i is the facet of interest.

4.3.1 Experimental results

Specimens were fabricated to quantify the roughness of a commercial SLM method versus inclination angle[1] (Table 4.2, Fig. 4.3). Optical macroscopy was recorded (Fig. 4.5) and R_a recorded for the upper and lower surfaces (Fig. 4.6).

Inspection of the sample macroscopy (Fig. 4.5) and measured surface roughness (Fig. 4.6) identifies distinct topology regions associated with the inclination angle Φ:

- For inclinations approaching horizontal ($\phi \rightarrow 0$ degree), staircase effects dominate, and the observed roughness asymptotes towards peak values. For inclinations below the

[1] Note, the inclination angle, ϕ, used in this work seems to be the most common nomenclature reported in the literature; however, $\theta = \pi/2 - \phi$, for example, is also used [8].

Table 4.2 Process parameters associated with the samples shown in Fig. 4.4

Parameter		Value
Machine	Specification	SLM Solutions 250HL
	Layer thickness	30 μm
	Ambient temperature	90°C
	Process parameters	As in Ref. [28]
Powder	Material	Ti64
	Size distribution	See Fig. 4.4

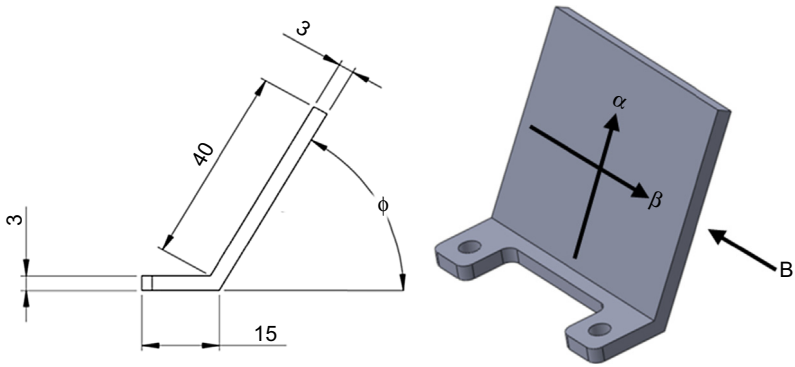

Figure 4.3 Standard specimens to assess surface roughness versus inclination angle, ϕ. α and β refer to the perpendicular direction of roughness measurement.

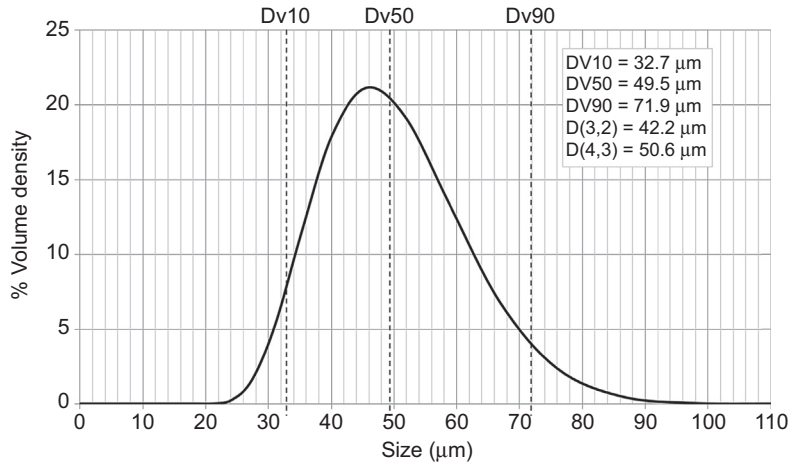

Figure 4.4 Ti64 powder distribution.

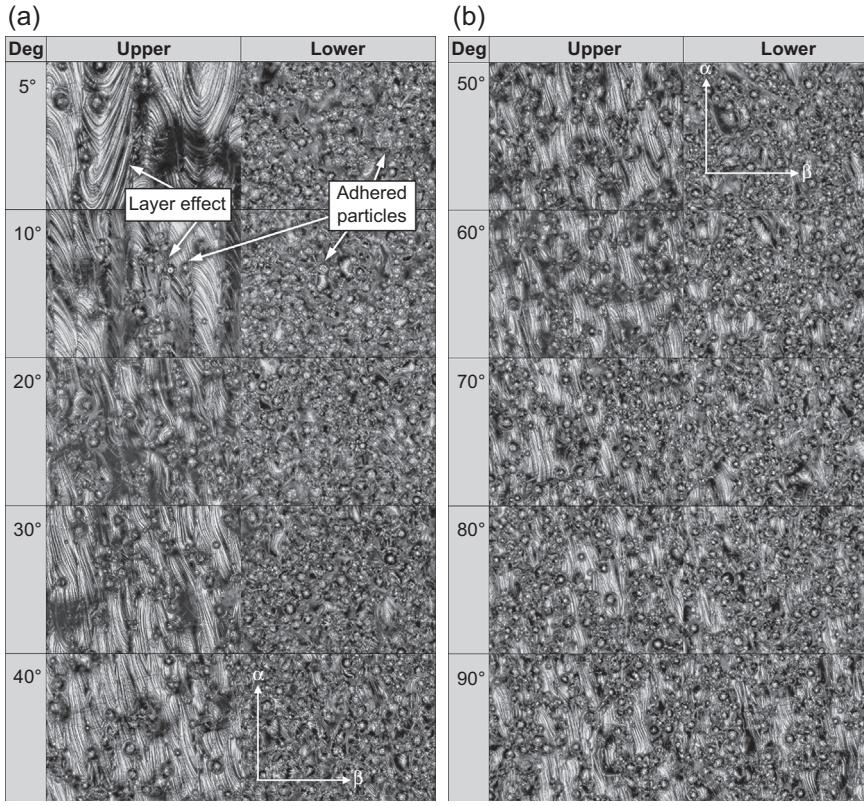

Figure 4.5 Macroscopy of SLM samples at inclination angles ϕ of 0−40 degrees (a) and 50−90 degrees (b). Orientation α and β are as defined in Fig. 4.4.

self-supporting inclination angle, supporting structures may be desirable to reduce error during manufacturing.

- As the surface tends towards a vertical orientation, $\phi \rightarrow 90$ degrees, the staircase effects coalesce, and observed roughness seems to be predominantly the result of the presence of adhered, partially melted particles.
- Of the curve fit options considered (linear, exponential, power, and logarithmic), the correlation of the logarithmic curve provides the best match for both the upper and lower surfaces (Table 4.3); although the variability associated with the logarithmic curve fit shown in Fig. 4.6 is relatively high, it does provide a useful insight into observed roughness trends.
- The observed roughness in the lower surface is always larger than that of the upper surface, and often significantly larger. The rationale for this observation is that heat transfer through the inclined specimen causes elevated temperatures at downward-facing (lower) surfaces, resulting in greater thermal distortion and particle adhesion. Surface damage to downward-facing surfaces can also occur where supporting structures are physically removed from the surface, although no supporting structures were used to generate the coupons used in this research.

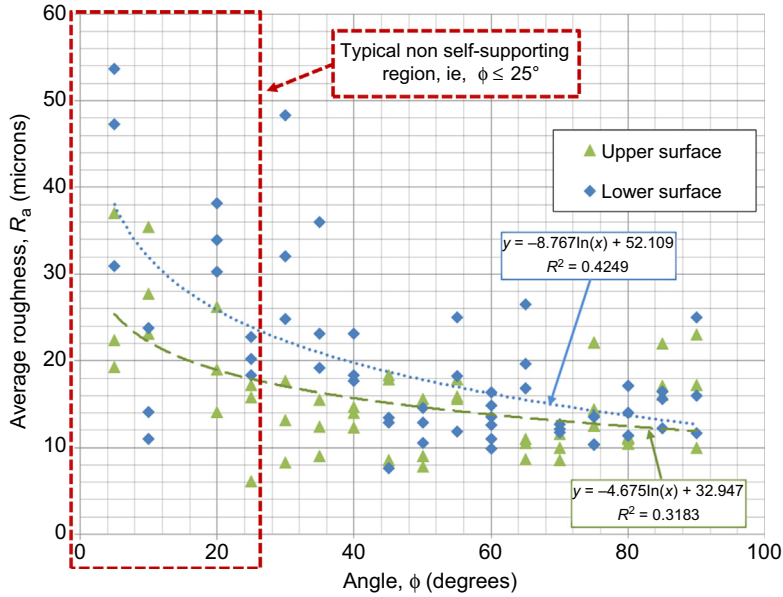

Figure 4.6 Surface roughness R_a versus the specimen inclination angle ϕ for the upper and lower surfaces with directions α and β (Fig. 4.4).

Table 4.3 Linear, exponential, power, and logarithmic curve fit options and associated correlation coefficients (R^2) for upper and lower surfaces shown in Fig. 4.6

	Linear	Exponential	Power	Logarithmic[a]
Upper surface	0.167	0.117	0.234	0.318
Lower surface	0.318	0.350	0.372	0.425

[a]Logarithmic provides the highest correlation coefficient for both the upper and lower scenarios.

By accommodating these observations of surface roughness versus surface inclination and by rotating the intended component according to the spatial rotations shown in Fig. 4.7, the associated surface finish can be optimised for the specific design objectives.

4.3.2 Roughness objectives

To achieve robust surface roughness outcomes in AM, it is critically important to apply a surface roughness objective that is appropriate for the intended functional and aesthetic objectives. In addition to the area-weighted average roughness, R_{a_ave}, that is reported in the literature, this section presents a series of novel surface roughness objectives that are of specific relevance to AM.

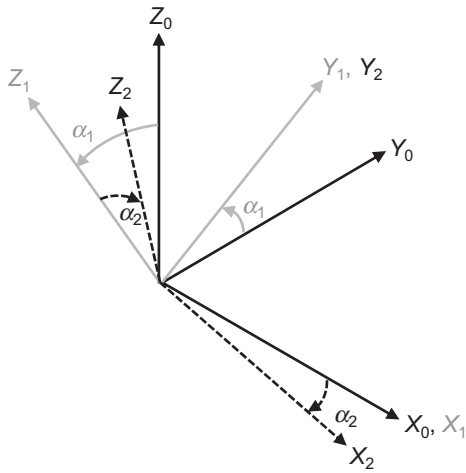

Figure 4.7 Standard spatial rotations, α_1 and α_2, used to define the rotation of a component's geometry in space [24].

4.3.2.1 Average roughness

Average roughness, R_{a_ave}, refers to the area-weighted average roughness of each facet within the component geometry (Eq. (4.2)). The area, A, associated with each facet may be assessed by the Cartesian coordinates of the associated vertices (Eq. (4.3)) or by Heron's rule with reference to the facet side lengths (a, b, and c) (Eq. (4.4)).

$$R_{a_ave} = \frac{\sum_{i=1}^{n} R_{a,i}(\emptyset)A}{\sum_{i=1}^{n} A} \tag{4.2}$$

$$A = \frac{1}{2}|x_1y_2 - x_1y_3 + x_2y_3 - x_2y_1 + x_3y_1 - x_3y_2| \tag{4.3}$$

$$A = \sqrt{1/16[(a+b+c)(-a+b+c)(a-b+c)(a+b-c)]} \tag{4.4}$$

The literature associated with the surface roughness of AM specimens universally reports R_{a_ave} as the objective function (for example, Refs. [9,10,14,15,29]). Although the average roughness is useful in determining the quality of a manufactured component in terms of roughness, it is not the only parameter of relevance. This work extends the available literature associated with surface roughness by accommodating additional roughness objectives, including peak roughness avoidance, the roughness of relevant surfaces only and weighted average roughness.

4.3.2.2 Peak roughness avoidance

Peak roughness avoidance, R_{a_pa}, returns ∞ when the orientation results in any facet roughness value that exceeds the reference limit, R_{a_limit}, and thereby identifies

orientations (if they exist) that avoid the inclusion of excessive roughness (Eq. (4.5)). R_{a_pa} is useful to avoid roughness types that violate some fundamental design constraint. For example, R_{a_pa} may be used to identify orientations that do not require supporting structures by setting R_{a_limit} to the minimum self-supporting build angle (Fig. 4.5).

$$R_{a_pa} \begin{array}{l} = \infty, \text{for } \max\left(R_{a,i}\right)_{i=1}^{n} > R_{a_limit} \\ = R_{a\text{-}ave}, \text{otherwise} \end{array} \tag{4.5}$$

4.3.2.3 Roughness of relevant surfaces

The roughness of relevant surfaces, R_{a_r}, is dependent only on facets that are relevant ($r_i = 1$) to the functionality of the intended component. Facets that are functionally or aesthetically irrelevant ($r_i = 0$) do not contribute to R_{a_r} (Eq. (4.6)). The roughness of relevant surfaces provides a useful surface roughness objective for scenarios that have geometric tolerances assigned to mating surfaces (Section 4.4.1) or aesthetic restrictions of surface roughness on visible surfaces only. The R_{a_r} approach is applied in case study 2 to identify orientations that meet the functional requirement for selected surfaces within a prototype cover (Section 4.4.2) and a hydraulic housing (Section 4.4.3).

$$R_{a_r} = \frac{\sum_{i=1}^{n} r_i R_{a,i}(Ø) A_i}{\sum_{i=1}^{n} A_i r_i} \tag{4.6}$$

4.3.2.4 Weighted roughness

Weighted roughness, R_{a_w}, applies a roughness weighting $\lambda(\phi)$ to the measured surface roughness of each facet to optimise the desired surface roughness distribution in the finished component (Eq. (4.7)).

$$R_{a_w} = \frac{\sum_{i=1}^{n} \lambda(Ø) R_{a,i}(Ø) A_i}{\sum_{i=1}^{n} A_i} \tag{4.7}$$

Weighted roughness is a useful roughness objective because it allows the presence of high roughness facets (unlike for R_{a_pa}), on the condition that their associated surface area is correspondingly low. For example, in response to the roughness profile observed in Fig. 4.6, the hypothetical roughness weighting shown in Fig. 4.8 is applied in Section 4.4.3 to discourage facets that have high roughness or are not robustly self-supporting.

4.3.2.5 Weighted roughness of relevant surfaces

Weighted roughness of relevant surfaces, $R_{a_w_r}$, applies a roughness weighting $\lambda(\phi)$ to the measured surface roughness of each facet to promote the desired surface roughness distribution in the finished component (Eq. (4.8)). As for R_{a_r}, facets are defined as either relevant ($r_i = 1$) or irrelevant ($r_i = 0$) to the associated surface roughness

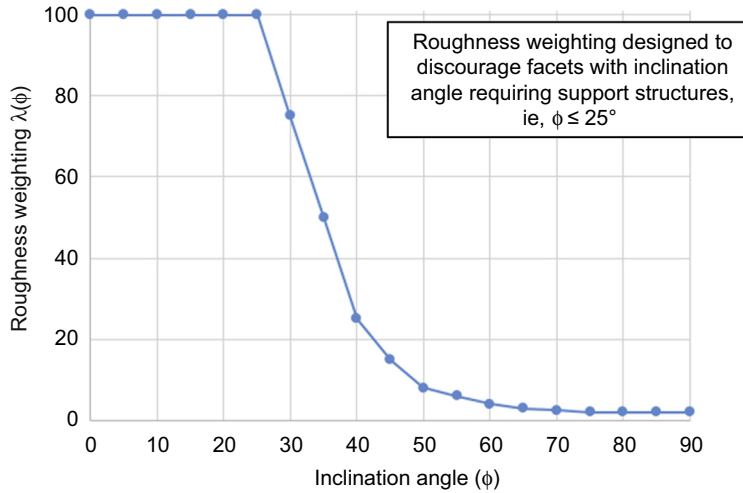

Figure 4.8 Roughness weighting $\lambda(\phi)$ to discourage facets with and inclination angle requiring support structures (ie, $\phi \leq 25$ degrees) (Fig. 4.6).

objective. The $R_{\text{a_w_r}}$ approach is applied in case study 2 to identify orientations that avoid high roughness values for relevant surfaces (Section 4.4.2).

$$R_{\text{a_w_r}} = \frac{\sum_{i=1}^{n} r_i \lambda(\emptyset) R_a(\emptyset) A_i}{\sum_{i=1}^{n} A_i r_i} \tag{4.8}$$

4.4 Case studies

Case studies are presented for a surgical implant, a low-volume prototype cover, and a functional hydraulic housing. These case studies demonstrate the enhanced design outcomes that are achievable by the material data and surface roughness objectives developed in this research.

4.4.1 Case study 1: surgical implant design

AM provides significant application in the manufacture of high-value, patient-specific surgical implants [28,30]. Surgical implants have both surgical and biological requirements for specific surface roughness targets. For example, the proposed surgical implant is to be fastened with a surgical-grade screw of predetermined geometry at a vector defined a priori by the surgical team. Based on these inputs, corresponding screw clearance envelopes are specified geometrically (Fig. 4.9). It is highly desirable that the implant surface roughness be determined versus orientation within the build volume such that orientations that avoid high roughness values are avoided, and that screw clearance envelopes be self-supporting such that no post-processing

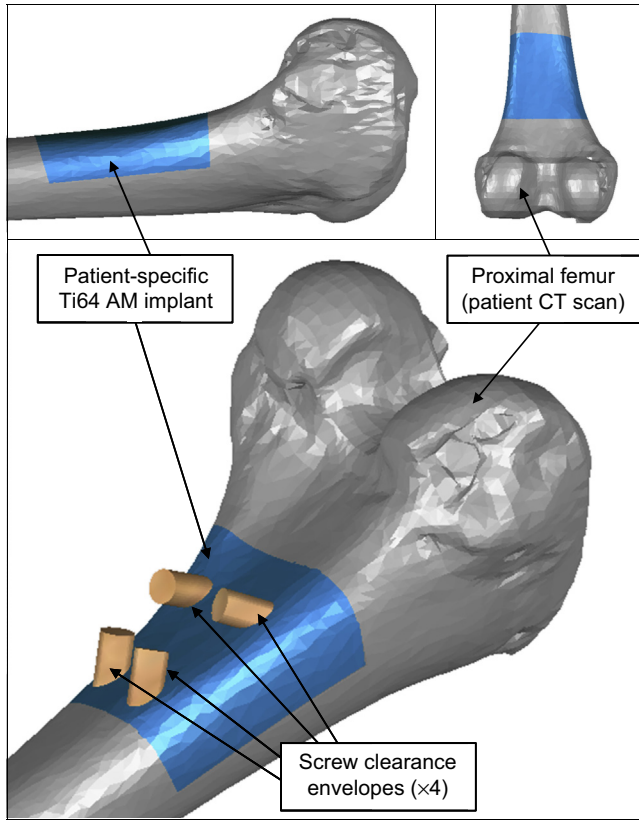

Figure 4.9 Rear, side and isometric views of the proximal femur, including the zone identified for patient-specific Ti64 additive manufacturing (AM) implant and associated screw clearance envelopes (×4). *CT*, computed tomography.

operation is required to remove internal support material. These orientation maps (Fig. 4.10) allow the identification of optimal implant orientation to meet surgical requirements; however, it is apparent that the identification of global optima requires analysis with a relatively small orientation angle increment, $\Delta\alpha$.

4.4.2 Case study 2: low-volume prototype cover

A low-volume prototype cover is to be manufactured for an automotive concept vehicle (Fig. 4.2). Minimisation of average surface roughness, R_{a_ave}, is a useful roughness objective; however, it does not fully represent the requirements of this application. In particular, it is necessary to accommodate aesthetic and post-processing roughness requirements:

- The prototype housing is an interior product with visible 'A-class' surfaces that are critical to customer perception. Surfaces that are not visible to the customer are not relevant in terms of

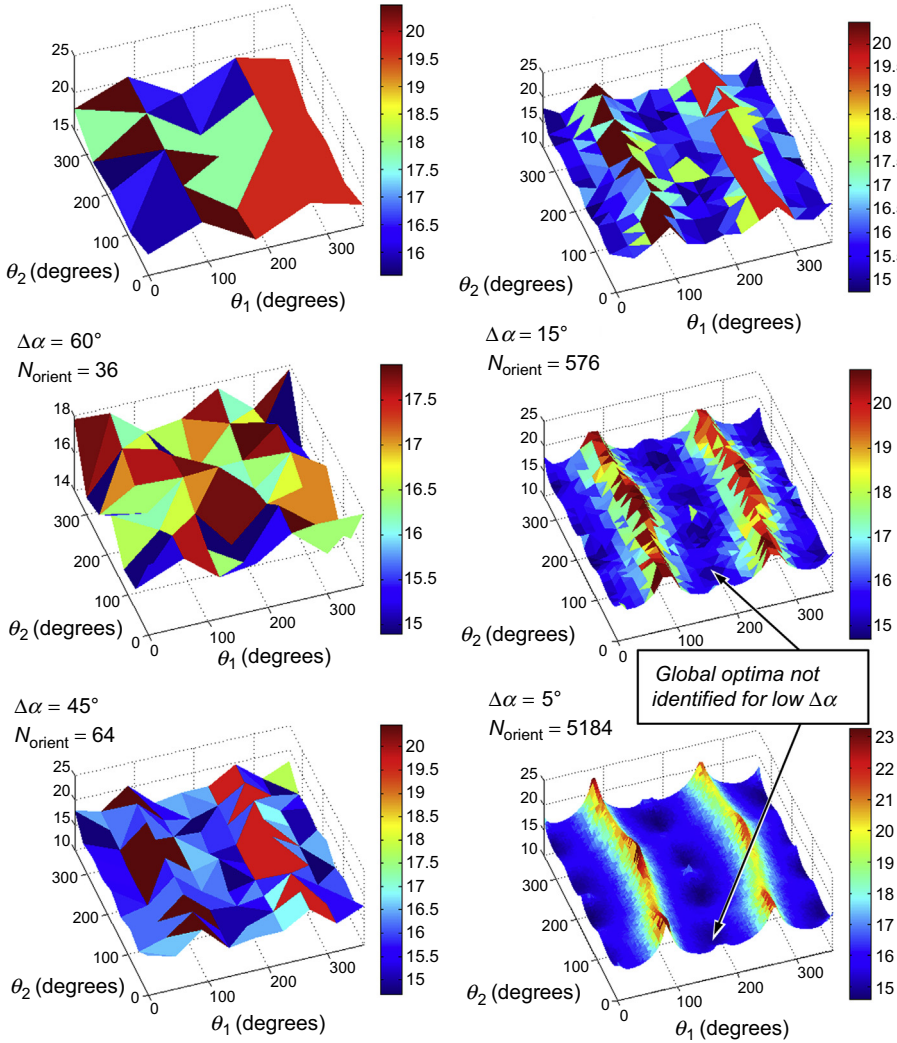

Figure 4.10 Orientation maps of weighted roughness, R_{a_w}, of selective laser melting titanium implant versus orientation for $\Delta\alpha = 90$, 60, 30, 15, and 5 degrees. Note that local optima are not identified until the number of orientations (and associated computational time) is increased.

surface roughness and are defined as 'B-class' surfaces. To meet this roughness requirement, B-class surfaces are not included in the surface roughness analysis (Fig. 4.2). The associated roughness of relevant surfaces, R_{a_r}, of the prototype component is presented in Fig. 4.11 (left).

- It is necessary to avoid high roughness values that occur as a result of low inclination angles and geometry that is not self-supporting. To meet this roughness objective, a custom roughness weighting was developed (Fig. 4.8). Weighted roughness of relevant surfaces, $R_{a_w_r}$, is presented for the prototype component in Fig. 4.11 (right).

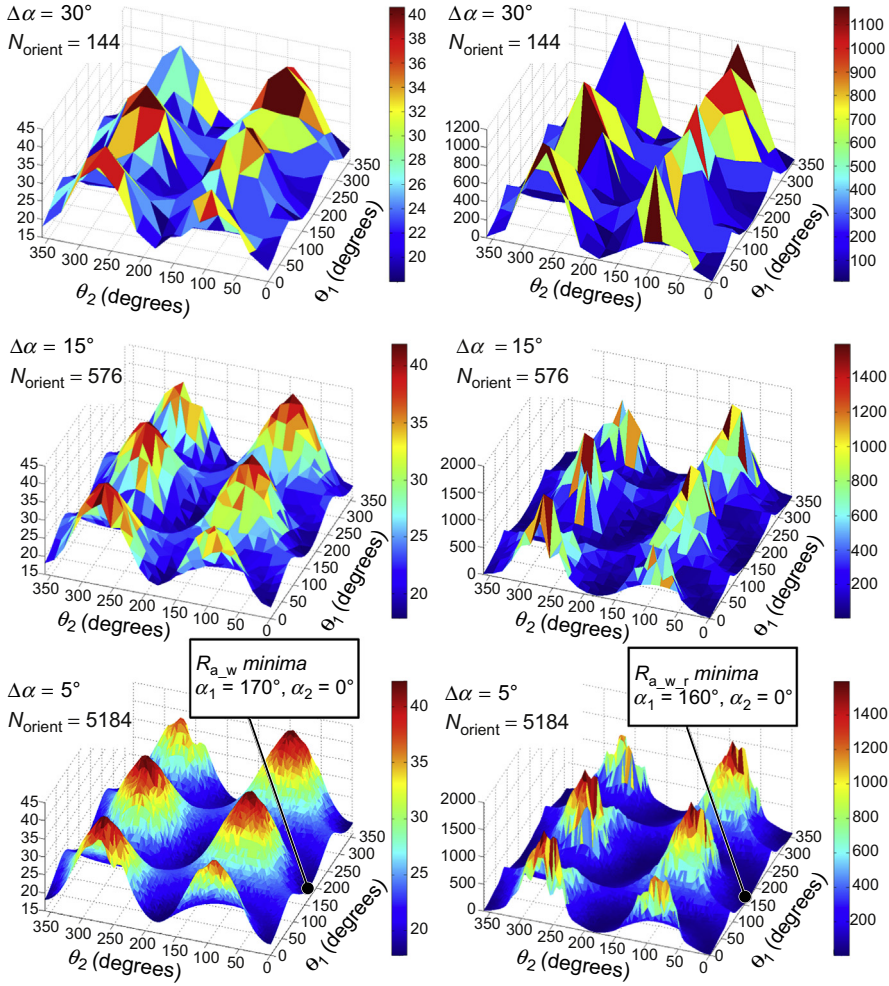

Figure 4.11 Orientation map of weighted average roughness, R_{a_w} (left), and weighted roughness of relevant surfaces, $R_{a_w_r}$ (right), for all facets of the prototype housing (Section 4.4.2) for $\Delta\alpha = 30$,15, and 5 degrees.

The orientation map of R_{a_r} and $R_{a_w_r}$ provides design guidance on the effect of component orientation on the surface roughness objective. The orientation map clearly identifies global minima and maxima and enables an informed trade-off when compromising between competing objectives such as build time and support material consumption. It is apparent that the minima for both R_{a_r} ($\alpha_1 = 170$ degrees, $\alpha_2 = 0$ degree) and $R_{a_w_r}$ ($\alpha_1 = 160$ degrees, $\alpha_2 = 0$ degree) occur at slightly different locations, indicating that the $R_{a_w_r}$ successfully identifies a more favourable orientation for the design objectives.

4.4.3 Case study 3: functional hydraulic housing for an engineering application

The hydraulic housing shown in Fig. 4.13 is to be manufactured by SLM for low- to medium-volume production. For this functional engineering application, there are no aesthetic requirements for surface finish. However, it is technically necessary that the surface finish of the mating features and mounting holes be minimised to ensure robust technical function.

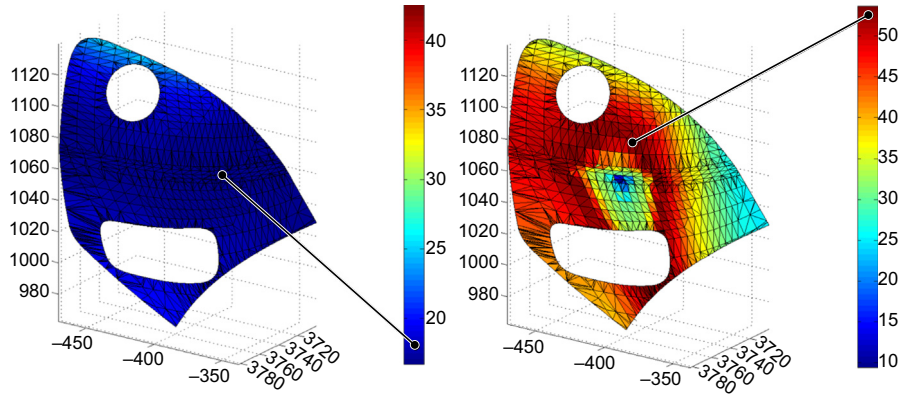

Figure 4.12 Cover component orientation for minimum weighted roughness, R_{a_w} (left). For comparison, the orientation for the maximum $R_{a_w_r}$ is included (right). Note the difference in scale.

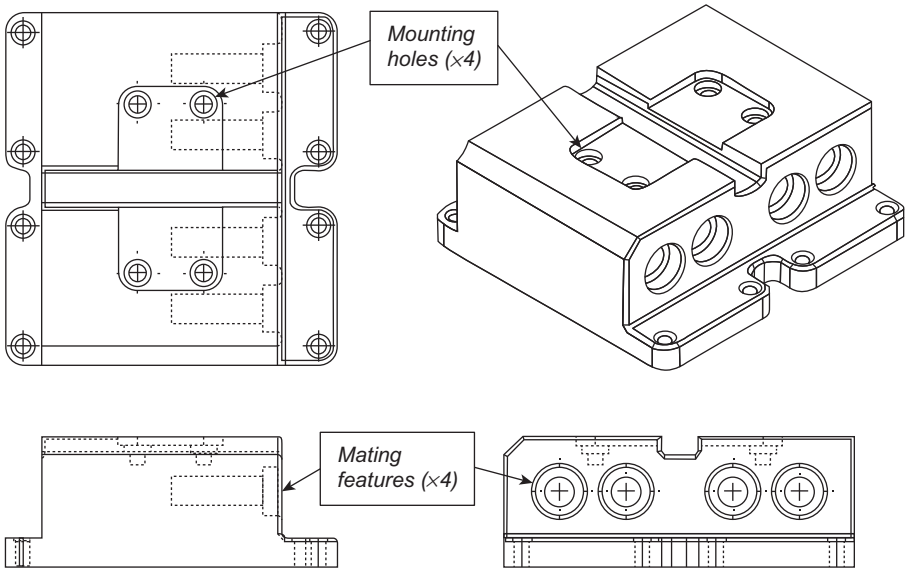

Figure 4.13 Functional housing for an engineering application, indicating mounting holes (×4) and features (×4) that contribute to the surface roughness objective.

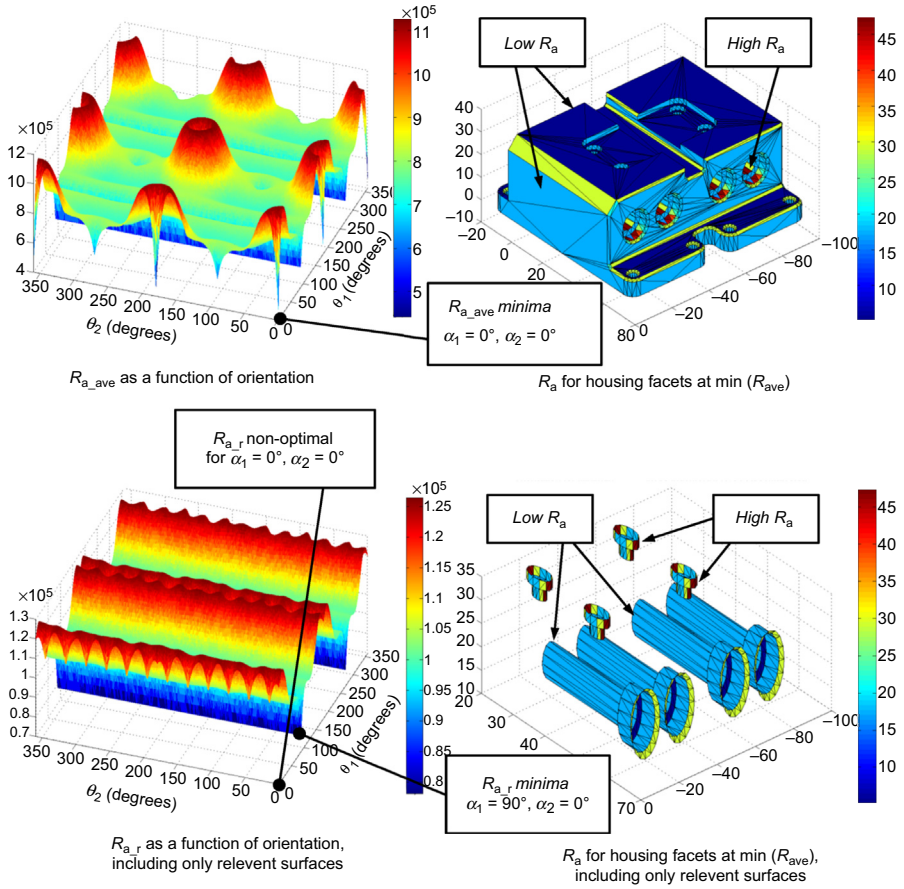

Figure 4.14 Average surface roughness, R_{a_ave}, and facet R_a at min (R_{a_ave}) for functional housing: all surfaces (upper), relevant surfaces only (lower). $\Delta\alpha = 2$ degree.

For this scenario, the average surface roughness, R_{a_ave}, is not an appropriate surface roughness objective because the surface roughness of features other than the mating features is inconsequential to component function. For example, minimising average surface roughness of the entire component results in a minima of R_{a_ave} at $\alpha_1 = \alpha_2 = 0$ degrees (Fig. 4.14). This minima repeats with a period of 180 degrees and results in low R_a facets on the large planar surfaces and mounting holes (however with large R_a facets on cylindrical mounting holes). However, when only relevant surfaces are considered, the global minima for R_{a_r} occurs at $\alpha_1 = 90$ degrees and $\alpha_2 = 0$ degree (ie, the minima orientation for R_{a_ave} does not exist), and low R_a facets occur on the cylindrical mating features (Fig. 4.12, lower). Note that for the orientation that is optimal for minimising average surface roughness over the entire component ($\alpha_1 = \alpha_2 = 0$ degree; Fig. 4.14, top), the R_{a_ave} of relevant facets only is not optimal

(Fig. 4.11, bottom). This case study demonstrates that the use of R_{a_ave} as the surface roughness objective can result in erroneous design guidance when the component consists of surfaces that are irrelevant to component function.

4.5 Conclusions

To provide greater insight into the optimal component orientation for AM, this work contributes various outcomes to the available literature:

- To ensure robust design data, the surface roughness versus build inclination of SLM-manufactured Ti64 was assessed experimentally and reported in detail, including measured roughness data and high-resolution macroscopy for upper and lower surfaces. Based on these data, correlations between the orientation and the observed surface roughness are presented, including the dominance of staircase effects and adhered particles on observed roughness when inclination tends towards horizontal ($\phi \rightarrow 0$ degree) and vertical ($\phi \rightarrow 90$ degrees), respectively.
- Manufactured products typically include surfaces that are not relevant to customer satisfaction or function. For example, consumer products consist of visible and hidden surfaces, and engineered components have critical roughness tolerances associated with key surfaces. The methods proposed in this research enable the discrimination of relevant and irrelevant surfaces when assessing the associated surface roughness objective. It was shown that this method can avoid erroneous design guidance when the component consists of surfaces that are irrelevant to component function.
- The available literature considers only the minimisation of average surface roughness. This work proposes novel surface roughness objectives, including penalty avoidance and penalty weighting, to avoid specific roughness types. When applied to optimise the orientation of a low-volume prototype cover, the proposed penalty-weighting method identified a more favourable orientation than optimisation methods based on average surface roughness only.
- An infinite number of component orientations exist. The orientation maps presented in this work clearly identify global minima and associated trends, enabling an informed trade-off when compromising between competing objectives such as build time and support material consumption.

Nomenclature

α_1	(degrees)	Rotation angle about the X_0 axis between $\{X_0, Y_0, Z_0\}$ and $\{X_1, Y_1, Z_1\}$
α_2	(degrees)	Rotation angle about the Y_1 axis between $\{X_1, Y_1, Z_1\}$ and $\{X_2, Y_2, Z_2\}$
$\Delta\alpha$	(degrees)	Orientation angle increment
ϕ	(degrees)	Filament inclination angle
$_i$	–	Facet index

Continued

n	−	Number of facets within a component
A	(m^2)	Facet area
$R_{a,i}$	(μm)	Average roughness of facet i
R_{a_ave}	(μm)	Area-average roughness
R_{a_pa}	(μm)	Peak avoidance surface roughness
R_{a_limit}	(μm)	Maximum allowable R_a value for peak avoidance
R_{a_r}	(μm)	Surface roughness accommodating relevant surfaces
R_{a_w}	(μm)	Weighted surface roughness
$R_{a_w_r}$	(μm)	Weighted surface roughness accommodating relevant surfaces
t	(m)	Layer thickness
l	(m)	Overhang distance
y_j	(m)	Vertical distance from the mean line to the data point
N_{orient}	−	Number of assessed orientations
p	−	Unit vector oriented vertically downwards to the platen

References

[1] D. Dai, D. Gu, Tailoring surface quality through mass and momentum transfer modeling using a volume of fluid method in selective laser melting of TiC/AlSi10Mg powder, International Journal of Machine Tools and Manufacture 88 (2015) 95−107.

[2] M. Leary, M. Mazur, J. Elambasseril, M. McMillan, T. Chirent, Y. Sun, M. Qian, M. Easton, M. Brandt, Selective laser melting (SLM) of AlSi12Mg lattice structures, Materials and Design 98 (2016) 344−357.

[3] K. Mumtaz, N. Hopkinson, Top surface and side roughness of Inconel 625 parts processed using selective laser melting, Rapid Prototyping Journal 15 (2) (2009) 96−103.

[4] A.B. Spierings, N. Herres, G. Levy, Influence of the particle size distribution on surface quality and mechanical properties in AM steel parts, Rapid Prototyping Journal 17 (3) (2011) 195−202.

[5] S. Van Bael, G. Kerckhofs, M. Moesen, G. Pyka, J. Schrooten, J.P. Kruth, Micro-CT-based improvement of geometrical and mechanical controllability of selective laser melted Ti6Al4V porous structures, Materials Science and Engineering: A 528 (24) (2011) 7423−7431.

[6] E. Yasa, J. Deckers, T. Craeghs, M. Badrossamay, J.P. Kruth, Investigation on occurrence of elevated edges in selective laser melting, in: International Solid Freeform Fabrication Symposium, Austin, TX, USA, August 2009, pp. 673−685.

[7] W. Cheng, J.Y.H. Fuh, A.Y.C. Nee, Y.S. Wong, H.T. Loh, T. Miyazawa, Multi-objective optimization of part-building orientation in stereolithography, Rapid Prototyping Journal 1 (4) (1995) 12−23.

[8] D. Ahn, J.-H. Kweon, S. Kwon, J. Song, S. Lee, Representation of surface roughness in fused deposition modelling, Journal of Materials Processing Technology 209 (2009) 5593−5600.
[9] P. Sreedhar, C. MathikumarManikandan, G. Jothi, Experimental investigation of surface roughness for fused deposition modeled part with different angular orientation, International Journal of Advanced Design and Manufacturing Technology 5 (3) (June 2012) 21.
[10] K. Thrimurthulua, P.M. Pandey, N.V. Reddya, Optimum part deposition orientation in fused deposition modelling, International Journal of Machine Tools and Manufacture 44 (6) (May 2004) 585−594.
[11] P.B. Bacchewar, S.K. Singhal, P.M. Pandey, Statistical modelling and optimization of surface roughness in the selective laser sintering process, Proceedings of the Institution of Mechanical Engineers, Part B: Journal of Engineering Manufacture 221 (1) (2007) 35−52.
[12] D. Frank, G. Fadel, Expert system based selection of the preferred direction of build for rapid prototyping, Journal of Intelligent Manufacturing 6 (1994) 334−339.
[13] L. Aijun, Z. Zhuohui, W. Daoming, J. Yang, Optimization method to fabrication orientation of parts in fused deposition modeling rapid prototyping, in: 2010 International Conference on Mechanic Automation and Control Engineering (MACE), Wuhan, China, 26−28 June 2010, 2010.
[14] H.-S. Byun, K.H. Lee, Determination of the optimal part orientation in layered manufacturing using a genetic algorithm, International Journal of Production Research 43 (13) (2005) 2709−2724.
[15] S.K. Singhal, P.K. Jainb, P.M. Pandey, A.K. Nagpala, Optimum part deposition orientation for multiple objectives in SL and SLS prototyping, International Journal of Production Research 47 (22) (2009) 6375−6396.
[16] ASTM F2792−12a, Standard Terminology for Additive Manufacturing Technologies, ASTM International, West Conshohocken, 2012.
[17] A. Gebhardt, Understanding Additive Manufacturing Rapid Prototyping, first ed., Hanser Publications, Cincinatti, 2011.
[18] G.N. Levy, R. Schindela, J.P. Kruth, Rapid manufacturing and rapid tooling with layer manufacturing (LM) technologies, state of the art and future perspectives, CIRP Annals − Manufacturing Technology 52 (2) (2003) 589−609.
[19] M. Brandt, S. Sun, M. Leary, S. Feih, J. Elambasseril, Q. Liu, High-value SLM aerospace components: from design to manufacture, Advanced Materials Research 633 (2013) 135−147, http://dx.doi.org/10.4028/www.scientific.net/AMR.633.135. Trans Tech Publications, Switzerland.
[20] N. Hopkinson, R. Hague, P. Dickens, Rapid Manufacturing: An Industrial Revolution for the Digital Age, John Wiley and Sons, Hoboken, 2005.
[21] O. Rehme, C. Emmelmann, Rapid manufacturing of lattice structures with selective laser melting, in: Lasers and Applications in Science and Engineering, International Society for Optics and Photonics, February 2006, p. 61070K.
[22] W. Meiners, K. Wissenbach, A. Gasser, Shaped Body Especially Prototype or Replacement Part Production, DE Patent 19, 1998.
[23] Y. Zhai, D.A. Lados, J.L. LaGoy, Additive manufacturing: making imagination the major limitation, JOM 66 (5) (2014) 808−816.
[24] M. Leary, M. Babaee, M. Brandt, A. Subic, Feasible build orientations for self-supporting fused deposition manufacture: a novel approach to space-filling tesselated geometries, Advanced Materials Research 633 (2013) 148−168, http://dx.doi.org/10.4028/www.scientific.net/AMR.633.148. Trans Tech Publications, Switzerland.

[25] R.J. Hocken, Machine tool accuracy (No. UCRL-52960-5), Technology of Machine Tools, vol. 5, California Univ., Livermore (USA), 1980 (Lawrence Livermore Lab).
[26] L.M. Galantucci, F. Lavecchia, G. Percoco, Experimental study aiming to enhance the surface finish of fused deposition modeled parts, CIRP Annals − Manufacturing Technology 58 (2009) 189−192.
[27] Japanese Industrial Standard, JIS B 0601:2013, Geometrical Product Specifications (GPS) − Surface Texture: Profile Method − Terms, Definitions and Surface Texture Parameters, Japanese Industrial Standard/Japanese Standards Association, 2013.
[28] M. Mazur, M. Leary, S. Sun, M. Vcelka, D. Shidid, M. Brandt, Deformation and failure behaviour of Ti-6Al-4V lattice structures manufactured by selective laser melting (SLM), The International Journal of Advanced Manufacturing Technology (2015) 1−21.
[29] J. Giannatsis, V. Dedoussis, Decision support tool for selecting fabrication parameters in stereolithography, The International Journal of Advanced Manufacturing Technology 33 (7−8) (2007) 706−718.
[30] X. Wang, S. Xu, S. Zhou, W. Xu, M. Leary, P. Choong, et al., Topological design and additive manufacturing of porous metals for bone scaffolds and orthopaedic implants: a review, Biomaterials 83 (2016) 127−141.

Mechanical properties of Ti6Al4V and AlSi12Mg lattice structures manufactured by Selective Laser Melting (SLM)

5

M. Mazur, M. Leary, M. McMillan, S. Sun, D. Shidid, M. Brandt
RMIT University, Centre for Additive Manufacturing, Melbourne, VIC, Australia

5.1 Introduction

Cellular materials offer unique functional characteristics, allowing design freedom beyond the capability of solid materials. These characteristics include high specific strength and stiffness, enhanced absorption of mechanical energy and heat transfer control [1]. Cellular materials are formed by periodic or stochastic arrangements of open or closed cell types, with either two-dimensional cell configurations (such as honeycomb) or three-dimensional polyhedral layouts (such as lattice structures) [2].

The mechanical performance of cellular structures is dependent on factors such as cell topology; number of cells; geometric parameters, including strut diameter and cell size; material and manufacturing process characteristics; as well as structural boundary and loading conditions [3,4]. Adjustment of the cell topology and size allows the characteristic properties of the cellular material to be manipulated to achieve desired application requirements.

Mechanical properties such as compressive strength and stiffness are particularly dependent on whether the cell exhibits bending-dominated or stretch-dominated behaviour during loading [5]; stretch-dominated structures typically show superior strength, and bending-dominated structures show superior compliance. For example, stochastic open-cell materials, such as foams, typically exhibit cell element bending during loading, whereas ordered open-cell lattice structures can show either stretch- or bending-dominated behaviour, depending on cell topology [6]. Lattice structures are therefore of particular interest; by selecting the cell topology they can address a range of structural requirements, from high compliance (for dampening or energy absorption) to high specific strength (for light-weight structural materials).

Additive manufacturing techniques provide an exceptional opportunity for the manufacture of cellular material such as lattice structures tailored to dedicated applications [7,8]. Selective laser melting (SLM) is an additive manufacturing process in which part geometry is progressively built up by selectively melting subsequent layers of metal powder, using a scanning laser beam under an inert gas atmosphere [9]. SLM can process a range of a metals, including light-weight titanium and aluminium alloys such as Ti6Al4V and AlSi12Mg, respectively, which are desirable for applications

Laser Additive Manufacturing. http://dx.doi.org/10.1016/B978-0-08-100433-3.00005-1
Copyright © 2017 Elsevier Ltd. All rights reserved.

requiring high specific strength [10]. SLM processes can produce geometrically complex periodic cellular structures with robust control over uniformity and repeatability. In comparison, traditional metal cellular structure manufacturing processes are limited to stochastic foam production with comparatively low uniformity, or wire mesh lattices with a high cost and comparatively lower manufacturable geometric complexity and range of achievable mechanical properties [11].

However, SLM is subject to specific process limits, such as a minimum manufacturable feature size and inclination angle for a given build material [12]. These process limits impose constraints on manufacturable geometries [13] and require experimentation to quantify manufacturable lattice design configurations [14]. Furthermore, the application of lattice structures requires that their mechanical properties and failure modes be quantified for varying geometric conditions. Although prior work has contributed to the understanding of the behaviour of SLM-manufactured lattice structures, there remain uncertainties in the literature, and as such has been applied by the authors. Ti6Al4V and AlSi12Mg alloys (Section 5.2.1), which offer attractive material properties for use in lattice structures that have not been fully exploited, such as high specific strength, resistance to corrosion, bio-compatibility (Ti6Al4V) and high thermal diffusivity (AlSi12Mg) [12,15–18].

The aim of this work is to provide insight into the influence of cell topology, cell size, number of unit cells and boundary conditions on the deformation and failure behaviour of SLM-manufactured Ti6Al4V and AlSi12Mg alloy lattice structures under compressive loading. This is achieved through the following contributions:

- investigation of the manufacturability of lattice structures, including the influence of strut diameter and inclination on manufacturability and dimensional accuracy (Section 5.3.3).
- characterization of deformation and failure modes for a broad range of cell topologies and cell sizes (Section 5.4.3).
- characterization of the cell number at which mechanical properties (in particular modulus and compressive strength) converge to a steady value representative of multi-cell structure properties, in particular for varying cell topologies and unit cell sizes (Section 5.4.1.1).
- quantification of loading and unloading moduli for varying cell topologies and cell sizes (Section 5.4.1).
- investigation of the effect of boundary conditions on the compressive mechanical properties of lattice specimens (Section 5.4.1).
- numerical investigation of experimental compressive testing results for manufactured sample geometry (Section 5.4.2.1).
- characterization of lattice sample manufacturing fidelity through computed tomography (CT) of manufactured samples (Section 5.3.5.2).
- experimental observation of deformation behaviour and failure modes at macro and micro scales (Section 5.4.3).

5.2 Lattice structures

The mechanical properties of lattice structures, in particular compressive strength and modulus, are dependent on factors such as cell topology, geometric parameters, material properties, structural boundary and loading conditions and the relative

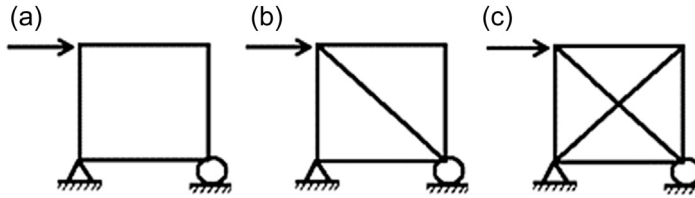

Figure 5.1 Examples of two-dimensional under-stiff (a), just-stiff (b) and over-stiff (c) lattice structures.

density (ρ/ρ_s) of the lattice density (ρ) to the solid material density (ρ_s) [19,20]. Mechanical properties are particularly influenced by whether the cell topology results in a loading response of lattice struts that is dominated by either stretch or bending [20]. It is possible to gain insight into the type of expected loading response by considering the degree of strut connectivity and associated degrees of freedom present in a lattice cell. These can be quantified by the Maxwell number (M) Eq. (5.1), which quantifies the expected mechanical behaviour in a lattice consisting of a number of interacting struts, s, pin-jointed at a number of nodes, n [21] (Fig. 5.1).

$$\begin{aligned} M &= s - 2n + 3 = 0 \quad \text{For two-dimensional truss} \\ M &= s - 3n + 6 = 0 \quad \text{For three-dimensional truss} \end{aligned} \tag{5.1}$$

- An *under-stiff* lattice structure ($M < 0$) occurs when a lattice has too few struts to be statically determinant and acts as a mechanism unless moments are transferred at nodes (eg, Fig. 5.1(a)). An under-stiff lattice shows *bending-dominated* behaviour and has high compliance and relatively low strength [22].
- A *just-stiff* lattice structure ($M = 0$) occurs when a lattice has the minimum number of struts required for it to be statically determinant (eg, Fig. 5.1(b)). A just-stiff lattice does not require the transmission of moments at nodes to maintain structural integrity, and strut loads can be determined analytically by reference to the equations of equilibrium. A just-stiff lattice has relatively low compliance (high stiffness) and relatively high strength. Such a structure exhibits *stretch-dominated* behaviour and has high structural efficiency.
- An *over-stiff* lattice structure ($M > 0$) occurs when a lattice has an excess of struts required to achieve static equilibrium (eg, Fig. 5.1(c)). An over-stiff structure does not require the transmission of moments at nodes to maintain structural integrity, and strut loads can only be calculated by assessing the effect of strut stiffness. An over-stiff lattice has high stiffness and strength as a result of the reinforcing effect of the redundant strut elements [23]. Such structures exhibit *stretch-dominated* behaviour [3].

The Maxwell number increases with an increasing number of struts per joint, which can imply higher strut interconnectivity and therefore higher cell rigidity. The Maxwell criteria can thereby aid in identifying lattice cell topologies which either maximize load-bearing efficiency by ensuring stretch-dominated behaviour or maximize compliance by ensuring bending-dominated behaviour (Table 5.1). However, the criteria provide necessary but not sufficient conditions for determining cell rigidity, since they can allow strut configurations which do not contribute to lattice rigidity to influence the Maxwell number [5]. Furthermore, the influence of loading direction on cell rigidity

Table 5.1 Maxwell number for unit cell candidate lattice structures

Cell type	BCC	FCCZ	FBCCZ	FBCCXYZ	BCCZ	FCC
Struts, s	8	20	28	44	12	16
Joints, n	9	12	13	15	9	12
Maxwell number, M	−13	−10	−5	5	−9	−14
Strut aligned to load direction	No	Yes	Yes	Yes	Yes	No

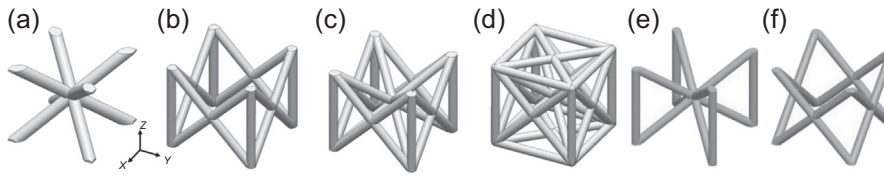

Figure 5.2 Lattice structure unit cells: (a) Body-centred cubic (BCC); (b) face-centred cubic with vertical struts (FCCZ); (c) FCC and BCC with vertical axis struts (FBCCZ); (d) FCC and BCC with horizontal and vertical axis struts (FBCCXYZ); (e) BCC vertical axis and struts (BCCZ); (f) FCC.

is also not accommodated despite the potentially significant effect on load capacity. For example, for the cell in Fig. 5.2(b), the compressive load capacity is expected to be higher when the load is aligned in the z-axis compared to loading in the x- or y-directions, yet such effects are not captured by the Maxwell criteria. Additionally, the desired cell topology according to the Maxwell criteria may be limited by manufacturability constraints (Section 5.3.3). Despite the identified limitations, the Maxwell criteria provide a useful tool for preliminary insights into the expected performance of varying lattice topologies, and as such has been applied by the authors.

In this work a number of periodic lattice structures were selected for analysis (Fig. 5.2). The lattice structures were selected for the following range of expected properties (Table 5.1, Fig. 5.2):

- Body-centred cubic (BCC) (Fig. 5.2(a)): High compliance [i.e., highly under-stiff ($M = -13$)].
- Face-centred cubic (FCC) with vertical (z-axis) struts (FCCZ) (Fig. 5.2(b)): Theoretically under-stiff (ie, $M = -10$), but high compressive strength and stiffness in the z-direction because of the presence of vertical struts.
- FCC and BCC with vertical (z-axis) struts (FBCCZ) (Fig. 5.2(c)): Theoretically under-stiff (i.e., $M = -5$), high strength and stiffness in the z-direction, body centred struts provide stiffness against loads in x and y-directions.

- FCC and BCC with vertical and horizontal struts (FBCCXYZ) (Fig. 5.2(d)): Theoretically over-stiff (ie, $M = 5$). High strength and stiffness with isotropic cell topology. Manufacturability may be compromised by constraints associated with horizontal truss members (Section 5.3.3) (Investigated only for Ti6Al4V alloy; see Section 5.3.4.)
- BCC with vertical (z-axis) struts (BCCZ) (Fig. 5.2(e)): Theoretically under-stiff (ie, $M = -9$), but high compressive strength and stiffness in the z-direction as a result of the presence of vertical struts. (Investigated only for AlSi12Mg alloy; see Section 5.3.4.)
- Face Centred Cubic (FCC) (Fig. 5.2f): High compliance [i.e., highly under-stiff ($M = -14$)]. (Investigated only for AlSi12Mg alloy; see Section 5.3.4.)

Orientations are defined per the axes presented in Fig. 5.2. Cell names are based on conventions in crystallography according with the approach taken by other investigators of SLM lattice structures eg, [24–26]. Additional designations denoting the presence of X, Y and Z struts (per the orientations in Fig. 5.2) are adopted in this work.

With regard to the relative density of lattice cells, mechanical properties such as the relative strength σ/σ_s (where σ denotes the compressive strength of the lattice structure and σ_s, that of the solid material) and relative modulus E/E_s typically exhibit a positive power relationship with the relative density (ρ/ρ_s) (where ρ denotes the density of the lattice, and ρ_s that of the solid) [1]. Bending-dominated structures also typically exhibit proportionally lower values of specific compressive strength and modulus compared to stretch-dominated structures; specific relationships are described in Section 5.4.

5.2.1 Selective-laser-melting-manufactured lattice structures: background

Previous studies have assessed the manufacturability and mechanical properties of SLM-manufactured lattice structures. These studies are typically for stainless steel and titanium lattice structures, as summarized below. The authors are aware of no formal experimental data on aluminium lattice manufacturability and testing.

Rehme and Emmelman [24] evaluated the SLM manufacturability and compressive strength of varying lattice cell topologies at different strut diameters and cell sizes in DIN 1.4404/ASTM 316L stainless steel. Manufacturability was assessed in terms of an *aspect ratio* metric, defined as the ratio of cell edge length to strut diameter. Manufacturable aspect ratios were found to vary depending on cell topology and ranged from 3.36 for comparatively low-density cells to 22.9 for high-density cells. The work suggested that manufacturability is higher for cell topologies with comparatively shorter strut span lengths; this observation is also made in this chapter (Section 5.3.3). Compressive testing of lattice specimens was conducted on cubic $10 \times 10 \times 10$ (ie, 10^3) cell specimens only, in a single cell size (2.5 mm) and strut diameter (0.5 mm). Compressive test parameters such as specimen strain rate and boundary conditions were not reported; however, an FCCZ lattice was found to offer the highest specific compressive strength in vertical compression.

Shen et al. [27] tested the compressive strength of SLM-manufactured 316L stainless steel lattice structures in three configurations: BCC, BCCZ (ie, BCC with vertical struts) and BCC with carbon-fibre reinforced epoxy skin plates at the upper and lower specimen surfaces. The specimens were 8^3 cell cubes with a unit cell size of 2.5 mm and a strut diameter of 0.2 mm. BCCZ structures were found to offer the highest

absolute and specific compressive strengths. The BCC and BCCZ structures were found to offer increased compressive strength of approximately 25% with high strain rates (150 s^{-1}) compared to quasistatic strain conditions (8E-4 s^{-1}). The reinforced end plates for the BCC specimen were reported to increase the compressive strength by a factor of two, which was attributed to the increased resistance of lattice struts at the platen interface against horizontal sliding during compressive loading. However, based on the published SEM images, the strut diameter appeared close to the limit of resolution of the applied SLM processes, resulting in low dimensional accuracy of strut geometric parameters such as cylindricity and linearity, particularly in inclined build directions [28]. It is expected that such low uniformity may propagate to stochastic variation in the mechanical properties of tested specimens.

Brenne et al. [26] studied the response of SLM-manufactured Ti6Al4V BCC lattice structures under quasi-static and cyclic compressive loading for as-built and annealed heat treatment conditions. The results showed increased ductility and fatigue life, with reduced compressive strength for annealed specimens. Compressive testing was carried out on cubic 10^3 cell specimens of a single cell size (2 mm), BCC topology and a 0.2 mm strut diameter. Shear failure was observed along diagonal specimen planes.

Although prior work has contributed to quantifying a number of aspects of the behaviour of SLM-manufactured lattice structures, there remain uncertainties in the literature, in particular associated with Ti6Al4V and AlSi12Mg alloys. The aim of this chapter is to address some of the limitations of the literature and to provide insight into the influence of cell topology and geometry on the deformation and failure behaviour of SLM-manufactured Ti6Al4V and AlSi12Mg lattice structures under compressive loading, specifically:

- Quantification of the influence of the number of cells in a lattice specimen array on the convergence of mechanical properties (in particular elastic modulus and compressive strength). Existing studies are predominantly based on a single test specimen size and the authors are not aware of any existing numerical or experimental studies that explicitly assess the effect of lattice specimen array size on mechanical properties.
- Characterization of deformation and failure modes for a broad range of cell topologies and cell sizes. The available studies are limited by considering only single cell sizes or topologies.
- Comparison of loading and unloading moduli for varying cell topologies and cell sizes. Note that although unloading moduli are regularly reported for metallic foams [6], we are not aware of data for unloading moduli of SLM lattice structures.
- Investigation of the effect of boundary conditions in compressive loading of lattice specimens. Studies presented in the literature predominately conduct compressive testing with sliding boundary conditions at the platen interface. Sliding boundary conditions have low resistance to lateral strut deformation and may present a different mechanical response to a fixed boundary condition with high rigidity.
- Quantification of the manufacturability and mechanical properties of AlSi12Mg lattice specimens. We are not aware of published experimental data for SLM-manufactured aluminium alloy lattice specimens.
- Quantification of the elastic modulus and compressive strength of lattice specimens with larger cells for applications in bulk components (specimens with >50 mm edge length).
- Characterization of lattice sample manufacturing fidelity through computed tomography (CT) of manufactured samples and numerical investigation of compressive loading response for manufactured sample geometry obtained from CT data.

5.3 Selective laser melting manufacturability

5.3.1 Identification of selective laser melting parameters

SLM is a highly complex multi-physics process, due to: large thermal gradients [29]; complex three-dimensional geometries [30]; local overheating [31]; local heat transfer paths that are temporally and spatially transient [32]; and, thermal powder bed resistance that is poorly understood and subject to significant experimental uncertainty [33,34]. SLM is highly dimensional, with nearly 130 variables of influence on final component quality [24].

Processing parameters that determine the laser energy density E_d (Eq. (5.2)) are laser power P, laser scanning speed v, hatch spacing h and the layer thickness t. The required laser input energy varies for different build materials, and experimentation is required to determine a suitable parameter set [35].

$$E_d = \frac{P}{h \cdot v \cdot t} \tag{5.2}$$

where E_d, energy density (J/mm^3); P, laser power (W); v, scan speed (mm/s); t, layer thickness (mm); h, hatch spacing (mm).

5.3.2 Selective laser melting processing parameters for Ti6Al4V and AlSi12Mg

An experimental study was conducted to identify a desirable set of Ti6Al4V and AlSi12Mg processing parameters suitable for the SLM process used in this work. All SLM manufacturing was carried out with a SLM250HL machine (SLM Solutions) with a variable-power 400-W fibre laser. Powder for both materials was provided by SLM Solutions GmbH. X-ray Computed Tomography (CT) was used to evaluate the porosity of cubic test specimens built with a 4-mm side length. Test specimens were manufactured with varying laser power P and scanning speed v, corresponding to a range of energy densities Ed. Processing parameters listed in Table 5.2 produced low porosity and high build quality [36]. These parameters were used in the manufacture of the lattice structures used in this work.

5.3.3 Lattice strut manufacturability

SLM process limitations constrain the range of feasible geometries [12]. Particular constraints are imposed by overhanging geometry and geometry that has excessive resistance to heat transfer, resulting in overheating during manufacture [37–39]. SLM processes often require support structures to achieve the robust builds. Support structures increase the range of feasible geometries; however, the use of support material can increase surface roughness, extend manufacturing time, and compromise part functionality when manual removal is constrained by access, as in lattice structures. To avoid the need for support structures and to identify the associated manufacturable lattice structure topology, it is necessary to limit the inclination angle of overhanging geometries to angles which are buildable without support

Table 5.2 Optimal Ti6Al4V and AlSi12Mg selective laser melting processing parameters

Material	Laser energy density, E (J/mm^3)	Laser power, P (W)	Hatch spacing, h (mm)	Focal offset (mm)	Scan speed, v (mm/s)	Layer thickness, t (μm)	Relative density (%)
Ti6Al4V	68.5	173	0.12	2	710.00	30	99.10
AlSi12Mg	40.0	350	0.19	2	921.05	50	98.86

[40]. Additionally, the manufacturable cell topology is constrained by the minimum SLM manufacturable feature size, which dictates the achievable lattice strut diameter [24].

To establish a feasible build angle and feature size relevant for Ti6Al4V and AlSi12Mg, SLM cantilever strut test specimens were manufactured with a broad design of experiments (DOE) analysis of manufacturability versus strut diameter and associated inclination.

A full-factorial DOE analysis was completed to establish the manufacturability of cantilever strut elements based on strut diameter (0.3−1.0 mm, in increments of 0.1 mm) and inclination angle (0−60 degrees, in 10 degrees increments) (Fig. 5.3). The resulting test specimens were evaluated and ranked for manufacturability. The results are summarised in Table 5.3 for cantilever struts.

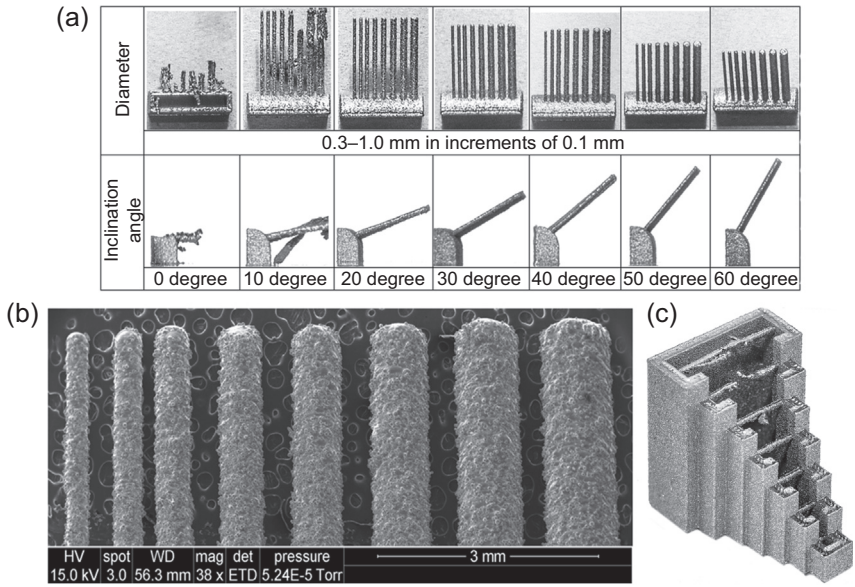

Figure 5.3 (a) Manufactured Ti6Al4V cantilever strut test block specimens for range of inclination angles and strut diameters of 0.3-1.0 mm in increments of 0.1mm (b) Sample Ti6Al4V SEM image of manufactured strut elements. (c) Example Ti6Al4V manufactured strut span test specimen for 0.6 mm strut diameter.

Table 5.3 Manufacturability of Ti6Al4V and AlSi12Mg cantilever strut inclination specimens at varying diameters and build angles. Ranking indices: L = Major flaws, M = Some flaws, H = Manufactured successfully.

Material		Ti6Al4V										AlSi12Mg									
Diam. (mm)		0.1	0.2	0.3	0.4	0.5	0.6	0.7	0.8	0.9	1.0	0.1	0.2	0.3	0.4	0.5	0.6	0.7	0.8	0.9	1.0
Angle (degrees)	0	L	L	L	L	L	L	L	L	L	L	L	L	L	L	L	L	L	L	L	L
	10	L	L	M	M	M	M	M	L	L	L	L	L	L	L	L	M	M	M	M	M
	20	L	L	H	H	H	H	H	H	H	H	L	L	L	L	L	M	M	M	M	M
	30	L	M	H	H	H	H	H	H	H	H	L	L	L	M	H	H	H	H	H	H
	40	L	H	H	H	H	H	H	H	H	H	L	L	L	H	H	H	H	H	H	H
	50	L	H	H	H	H	H	H	H	H	H	L	L	L	H	H	H	H	H	H	H
	90	L	H	H	H	H	H	H	H	H	H	L	L	L	H	H	H	H	H	H	H

For a unit cell with equal side lengths, there exist four possible strut inclination angles: 0, 35.26, 45, and 90 degrees. As such, the identified cantilever manufacturability thresholds indicate the robust manufacture of struts within the lattice structures considered in Section 5.2 for all lattice topologies, excluding 0 degree inclination struts (FBCCXYZ). However, it was observed that if strut elements are supported at both ends, and if the strut span is sufficiently small, lattice struts can be manufactured horizontally. To establish the manufacturability limits for supported struts, a series of span test specimens (Fig. 5.3. (c) and Table 5.4) were manufactured with varying span lengths and strut diameters for both Ti6Al4V and AlSi12Mg. The test specimens were evaluated for manufacturability and the results summarised in

Table 5.4 Manufacturability of Ti6Al4V and AlSi12Mg span strut inclination specimens at varying diameters and build angles. Ranking indices: L = Major flaws, M = Some flaws, H = Manufactured successfully.

Material		Ti6Al4V										AlSi12Mg									
Diam. (mm)		0.1	0.2	0.3	0.4	0.5	0.6	0.7	0.8	0.9	1.0	0.1	0.2	0.3	0.4	0.5	0.6	0.7	0.8	0.9	1.0
Span (mm)	1	L	M	H	M	H	H	H	H	H	H	L	L	L	L	H	L	H	H	H	H
	2	L	M	H	H	H	H	H	H	H	H	L	L	L	L	H	H	H	H	H	H
	3	L	M	H	H	H	H	H	H	H	H	L	L	L	L	H	H	H	H	H	H
	4	L	L	M	H	H	H	H	H	H	H	L	L	L	L	H	H	H	H	H	M
	5	L	M	M	M	H	H	H	H	H	H	L	L	L	L	H	M	H	H	H	M
	7.5	L	L	L	L	L	M	L	M	L	L	L	L	L	L	M	M	M	M	H	H
	10	L	L	L	L	L	L	L	L	L	L	L	L	L	L	M	M	M	M	M	M

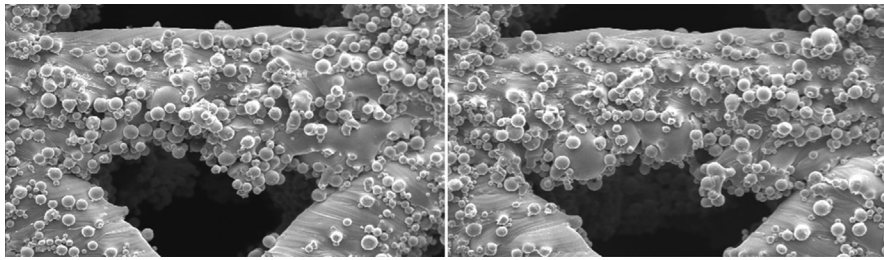

Figure 5.4 Manufactured Ti6Al4V horizontal struts in FBCCXYZ lattice specimens with a 2-mm cell size.

Table 5.4. However, although horizontal struts are manufacturable if supported at both ends, SEM revealed noticeably oversized strut diameters and high levels of partially melted particle adhesion (Fig. 5.4). This flaw is attributed to additional powder being captured by the melt pool during SLM manufacturing of layers of overhanging surfaces [13,41].

5.3.4 Lattice specimen manufacture and testing objectives

Based on the material-specific experimental study of strut manufacturability, a series of manufacturable lattice structures with varying parameters (such as topology, Maxwell number and strut alignment to the loading direction) were selected for experimental testing to assess mechanical performance under compressive loading for both Ti6Al4V (Table 5.5) and AlSi12Mg (Table 5.6) materials.

The lattice specimens manufactured and tested for Ti6Al4V and AlSi12Mg varied because of different testing objectives. The objectives for testing Ti6Al4V lattice specimens were (Section 5.4.1):

- comparison of loading and unloading moduli for varying cell topologies and cell sizes
- investigation of different boundary conditions in compressive loading of lattice specimens
- quantification of the influence of the number of cells in a lattice array on the convergence of mechanical properties (in particular the elastic modulus and compressive strength) (Section 5.4.1.1)
- characterization of deformation and failure modes for a range of cell topologies as well as cell sizes (Section 5.4.3)

The objectives for testing AlSi12Mg lattice specimens were (Section 5.4.2):

- characterization of lattice sample manufacturing fidelity through CT of manufactured samples (Section 5.3.5.2)
- quantification of the elastic modulus and the compressive strength of lattice specimens with larger cell sizes (edge length >50 mm) compared with Ti6Al4V for applications in large components (Section 5.4.2)
- numerical investigation of compressive loading response for manufactured sample geometry (Section 5.4.2.1)
- characterization of deformation and failure modes for an extensive range of cell topologies for a fixed cell size (Section 5.4.3)

Because of the different experimental objectives and associated constraints, not all lattice topologies were manufactured and tested in both Ti6Al4V and AlSi12Mg alloys. FBCCXYZ cells were limited to Ti6Al4V alloys because the high relative density and large size of a FBCCXYZ AlSi12Mg specimen was expected to exceed the compressive strength of the test equipment (100kN) (Section 5.4). BCCZ and FCCZ lattice cell testing was restricted to AlSi12Mg alloys. Testing additional BCCZ and FCCZ topologies in Ti6Al4V would have exceed the experimental budget on account of the significantly higher number of Ti6Al4V specimens used for investigations of convergence of mechanical properties (Section 5.4.1.1).

5.3.4.1 *Ti6Al4V lattice specimens*

A series of Ti6Al4V lattice test specimens were manufactured for compressive testing (Figs 5.5 and 5.6). The manufactured specimens (Table 5.5) use the minimum manufacturable strut diameter (0.3 mm) and vary in cell topology and cell size (2 or 3 mm).

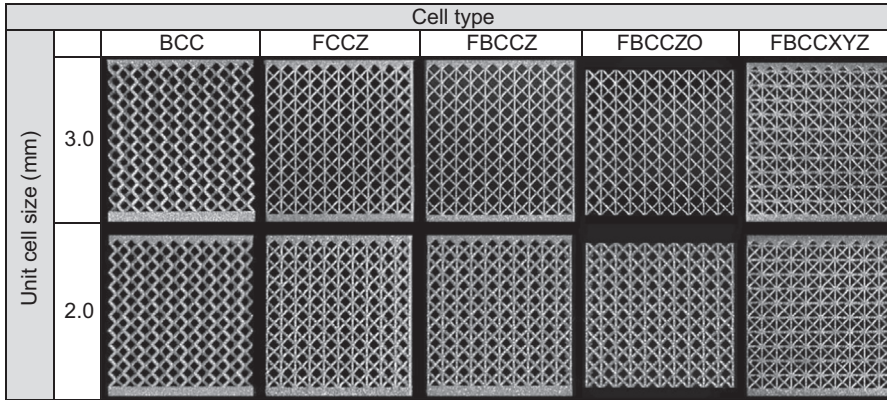

Figure 5.5 Manufactured Ti6Al4V lattice specimens with varying lattice topology and cell size: body-centred cubic (BCC), face-centred cubic (FCC) with vertical struts (FCCZ), FCC and BCC with vertical axis struts (FBCCZ), FCC and BCC with vertical axis struts and no end plates (FBCCZO) and FCC and BCC with horizontal and vertical axis and struts (FBCCXYZ).

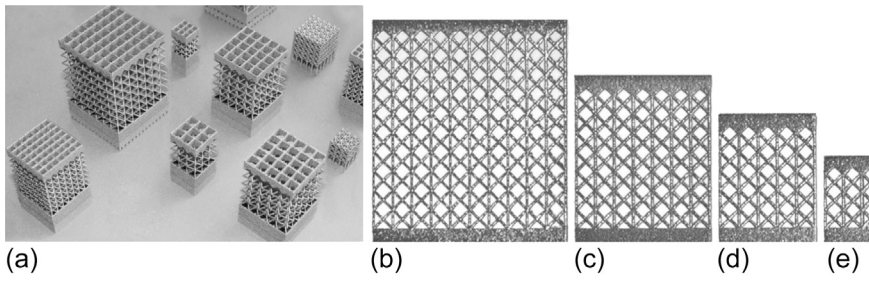

Figure 5.6 (a) Manufactured Ti6Al4V lattice test specimens with and without node-connecting webs. (b–e) FCCZ specimens with a varying number of 3-mm unit cells: 10-unit cubic cell (b), 7-unit cubic cell (c), 5-unit cubic cell (d) and 3-unit cubic cell (e).

Table 5.5 Ti6Al4V lattice test specimen details

Cell topology	Cell size (mm)	Strut diameter (mm)	Aspect ratio[a]	Specimen size (no. of cells)	Unit cell theoretical relative density $\left(\frac{\rho_c}{\rho_s}\right)$ (%)
BCC	3	0.3	10	3^3, 5^3, 7^3, 10^3	4.1
	2		6.67	3^3, 5^3, 7^3, 10^3	8.0
FCCZ	3		10	3^3, 5^3, 7^3, 10^3	9.1
	2		6.67	3^3, 5^3, 7^3, 10^3	17.7
FBCCZ and FBCCZO	3		10	3^3, 5^3, 7^3, 10^3	12.8
	2		6.67	3^3, 5^3, 7^3, 10^3	24.7
FBCCXYZ	3		10	3^3, 5^3, 7^3, 10^3	20.6
	2		6.67	3^3, 5^3, 7^3, 10^3	39.7

[a]The aspect ratio is the ratio of cell size to strut diameter.

The cell topology was selected based on the rationale outlined in Section 5.2. Additionally, two different cell sizes were selected to investigate the influence of cell size on mechanical properties for a given cell topology and strut diameter. Values for the corresponding nominal (based on idealized computer-assisted design (CAD) geometry) unit cell relative density (ρ_c/ρ_s) are presented in Table 5.5. The relative density values and corresponding manufacturing fidelity of the manufactured lattice specimens are presented in Fig. 5.8.

Specimen size (i.e., the number of cells) was selected to achieve an increasing number of cells (with a cubic distribution of 3^3, 5^3, 7^3, and 10^3 cells) in order to identify the number of cells at which cell-specific mechanical properties (in particular the elastic modulus and compressive strength) converge to constant values that are representative of an infinite array of lattice cells. For stochastic cellular solids (such as metal foams) under compressive loading, it has been reported that specimens which feature a minimum of 7 unit cells in each direction and a height-to-thickness ratio exceeding 1.5 exhibit convergence of mechanical properties [6]. However, for periodic lattice structures, in particular the topologies considered in this work, there has not been a clear characterization of convergence established in the literature (Section 5.1).

Studies presented in the literature predominately conduct compressive testing with sliding boundary conditions at the platen interface. Sliding boundary conditions have low resistance to lateral strut deformation and may present a different mechanical response to a fixed boundary condition with high rigidity. To assess the influence of boundary conditions on the mechanical properties of the lattice specimens under compressive loading, Ti6Al4V FBCCZ specimens were manufactured with two boundary configurations. In the first boundary configuration (as also used for all other tested cell topologies), test specimens were manufactured with connected webs on the upper and lower specimen faces (Figs 5.5 and 5.6) to constrain boundary

struts against lateral sliding. These were used in combination with rigid, high-friction plates made from hardened tool steel, which were inserted between the compressive platens of the axial testing machine. The second boundary configuration (used only for FBCCZO specimens) was devoid of node-constraining web structures, and specimens were placed on lubricated platens. The two different configurations result in lattice specimen boundary conditions with comparatively low or high lateral rigidity. The majority of test specimens had high rigidity conditions; these constraints reflect the intended applications for the lattices as space-filling structures within enclosed volumes, in which lattice structure boundaries are rigidly connected to stiff end supports.

For brevity, where multiple cell and specimen sizes are used (Ti6Al4V lattice specimens only), the lattice specimens are denoted in this work with the following naming convention: cell topology (as defined in Section 5.2), end condition (O for open with no end webs), cell size in millimetres (S) and the number of cells along the edge of a specimen (N). For example, FBCCZO-S2N7 designates a specimen with an FBCCZ cell topology and no end webs, a cell size of 2 mm, and 7^3 specimen cells. Where a single specimen configuration is used or summary data averaged over multiple specimen sizes are presented, only the cell topology name is used as a reference and the corresponding material identified in the associated text.

5.3.4.2 AlSi12Mg lattice specimens

AlSi12Mg lattice structures were successfully manufactured (Fig. 5.4) with the previously identified processing parameters (Table 5.2). A strut diameter of 1.0 mm was selected to provide a similar aspect ratio as that used for Ti6Al4V specimens and because of manufacturability constraints; 10 cells were specified with a cell size of 7.5 mm, such that the overall lattice structure size (75 mm^3) allowed all specimens to be manufactured concurrently on one 250-mm square SLM machine build plate.

Table 5.6 AlSi12Mg lattice test specimen details

Cell topology	Cell size (mm)	Strut diameter (mm)	Specimen size (no. of cells)	Aspect ratio[a]	Unit cell theoretical relative density, ρ_c/ρ_s (%)	Specimen theoretical relative density, ρ (%)
BCC	7.5	1.0	10^3	7.5	8.5	8.5
BCCZ					10.8	9.7
FCC					11.6	7.5
FCCZ					14.7	8.7
FBCCZ					20.6	16.1

[a]The aspect ratio is the ratio of cell size to strut diameter.

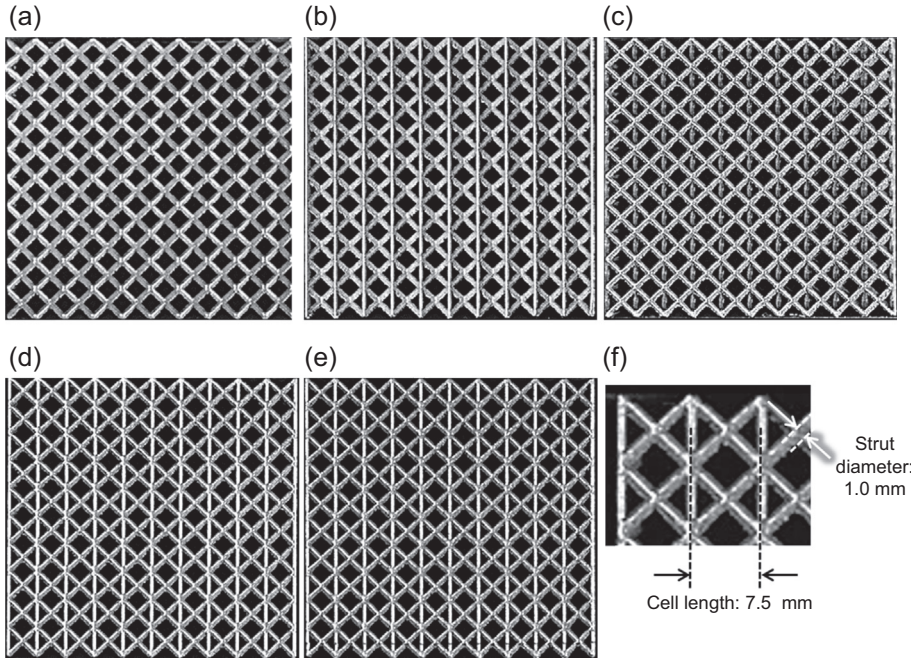

Figure 5.7 As-manufactured AlSi12Mg lattice specimens: (a) body-centred cubic (BCC), (b) BCC with Z struts (BCCZ), (c) face-centred cubic (FCC), (d) FCC with Z struts (FCCZ), (e) FCC and BCC with Z struts (FBCCZ). (f) Typical cell dimensions.

5.3.5 Geometric fidelity of as-manufactured lattice geometry

The complex transient thermal effects, layer-wise geometry and stochastic effects characteristic of SLM manufacturing of aluminium result in variation between the intended CAD geometry (Table 5.5) and the as-manufactured geometry. To provide insight into variation of lattice geometry, two distinct analysis approaches were applied for Ti6Al4V and AlSi12Mg manufactured lattice specimens.

5.3.5.1 Selective laser melting manufacturing fidelity of Ti6Al4V lattice specimens

To gain insight into the general fidelity of manufactured lattice specimens, the manufactured Ti6Al4V lattice specimens were measured to determine the manufactured relative density values $\frac{\rho}{\rho_s}$ (Eq. (5.3)) and the general percentage deviation from the nominal CAD geometry. The measurement was based on weighing the manufactured samples, comparing the measured weight with the expected theoretical weight for the given material according to CAD model geometry and then determining the relative density of the manufactured samples based on the measured weight difference (percentage). Fig. 5.8 presents the results for a solid Ti6Al4V material density of $\rho_s = 4430\ \text{kg/m}^3$ [42].

$$\rho = \frac{V}{V_s}\rho_s \left[\frac{\text{kg}}{\text{m}^3}\right] \tag{5.3}$$

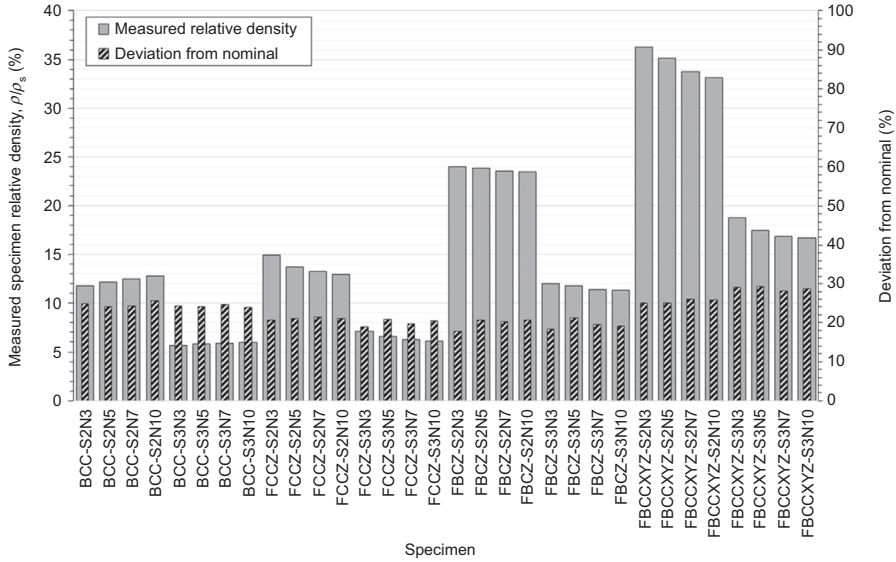

Figure 5.8 Manufactured Ti6Al4V lattice specimen relative density and deviation from nominal CAD geometry.

where ρ, density of the lattice specimen (kg/m^3); $\frac{V}{V_s}$, lattice cell solid volume fraction (percentage); ρ_s, lattice material density (equivalent to 4430 kg/m^3 for Ti6Al4V).

The results of Fig. 5.8 indicate that the relative density of the manufactured parts is larger compared with the nominal geometry by between 20% and 30%. This difference can most likely be attributed to geometric deviations and material added by partially fused particle adhesion observed in the manufactured specimens (Fig. 5.24).

The manufactured relative density measurement technique applied for Ti6Al4V samples can be carried out rapidly; however, it is subject to errors associated with not directly measuring the sample volume, such as not accounting for the nature of the distribution of material in the sample or any enclosed porosity. For more accurate measurement, the Archimedes method can be applied, although it can be subject to longer measurement times and potential measurement errors associated with rough surfaces caused by surface tension effects creating entrapped air bubbles [43]. Alternative techniques such as CT can also be applied to measure density, although with a higher cost, long measurement times and limitations on achievable scan resolution with large parts [43]. CT analysis can, however, provide high-resolution information about the dimensional characteristics of manufactured parts and was applied to assess AlSi12Mg lattice specimens.

5.3.5.2 Geometric fidelity of AlSi12Mg lattice specimens

Manufactured AlSi12Mg specimens were inspected using CT to provide quantitative insight into cell morphology based on a 2 × 2 × 2 cell array. In particular, CT analysis indicates that (Fig. 5.9):

- Downward-facing surfaces consistently display higher-than-average surface roughness; specific analysis of strut surface roughness was completed to quantify the effect of geometry and inclination on strut roughness (Section 5.2).

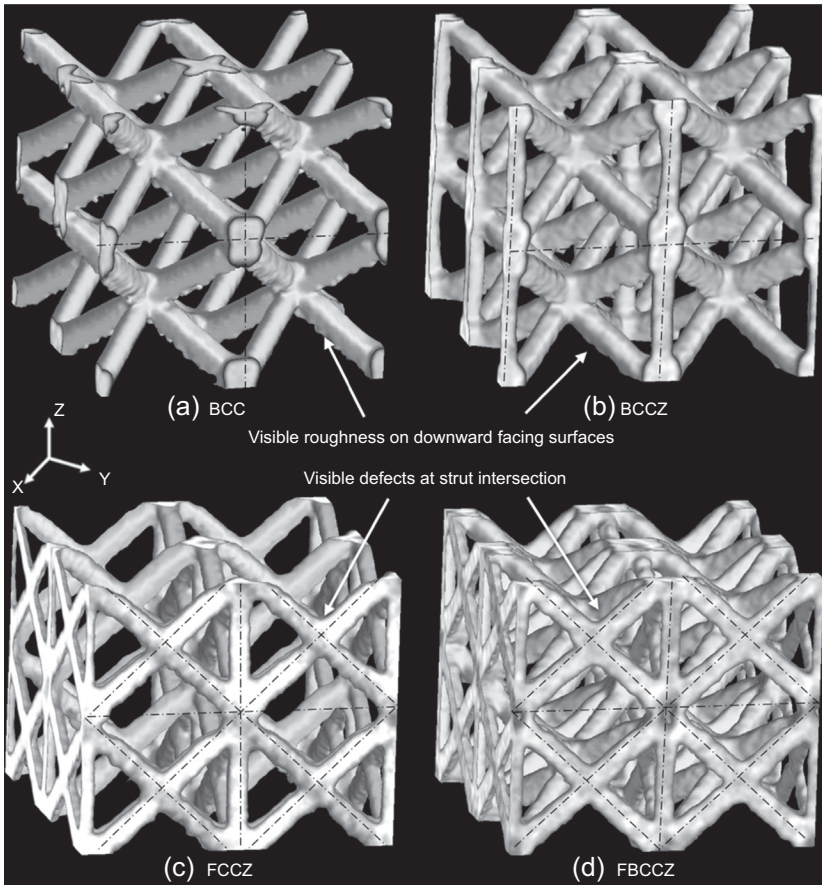

Figure 5.9 AlSi12Mg computed tomography data of a 2 × 2 × 2 array subset of the manufactured lattice specimen array.

- Visible geometric defects occur when struts intersect at nodes. These defects appear to be asymmetric, even for lattice structures with nominally symmetric geometry. The effect of node geometry on structural integrity has been assessed by computational analysis of the CT data (Section 5.4.2.1).

5.3.5.3 AlSi12Mg lattice strut surface roughness evaluation

The struts of AlSi12Mg cell topologies assessed in this work exhibit build angles of 35.26, 45 and 90 degrees to the build plate (Table 5.5). To assess the associated surface roughness, three struts were mechanically removed from the manufactured lattice array for each build angle. An optical microscope (5× magnification) was used to capture a shadow profile as an image with a nominal surface length of 1.41 mm (Fig. 5.10). Four angular orientations of interest were assessed: *upper* and *lower* surfaces have the normal surface oriented away from and toward the platen, respectively; *side* surfaces have the normal surface parallel to the platen.

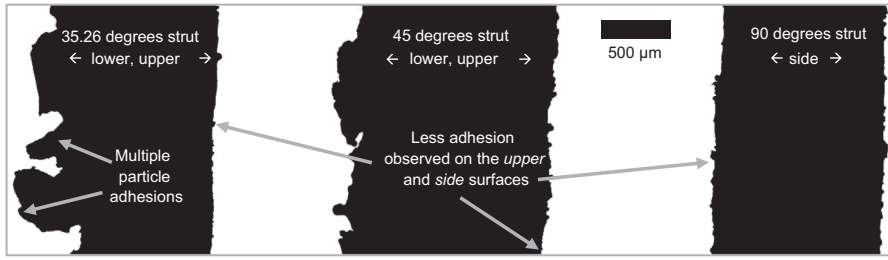

Figure 5.10 AlSi12 Mg lattice strut representative optical microscopy image of the lower and upper faces of 35.26, 45 and 90 degrees AlSi12Mg lattice struts.

Note the 90 degrees struts do not exhibit *upper* or *lower* faces, and the reported result is the average of all four measured perpendicular faces. Average roughness R_a and peak-to-peak roughness R_z were assessed for each orientation. Two positions were measured for three struts, resulting in six samples for every combination of angle and orientation (Table 5.7).

$$R_a = \frac{1}{N}\sum_{i=1}^{N}|y_i| \tag{5.4}$$

where y_i is the distance between the local position of the surface and the nominal surface.

Table 5.7 AlSi12Mg lattice strut average roughness R_a and peak-to-peak roughness R_z of strut elements (Fig. 5.11)

	Build angle (degrees)		
	35.26	**45**	**90**
R_a lower	120.2	43.5	–
SD	39.7	20.6	–
R_a sides	8.1	9. 2	8.2
SD	3.7	1.9	3.0
R_a upper	8.8	8.9	–
SD	2.6	1.5	–
R_z lower	456.5	235.5	–
SD	113.6	118.2	–
R_z sides	56.2	57.2	48.9
SD	22.1	15.3	11.8
R_z upper	53.0	60.5	–
SD	10.3	16.0	–

SD, standard deviation. Measurements are in micrometres.

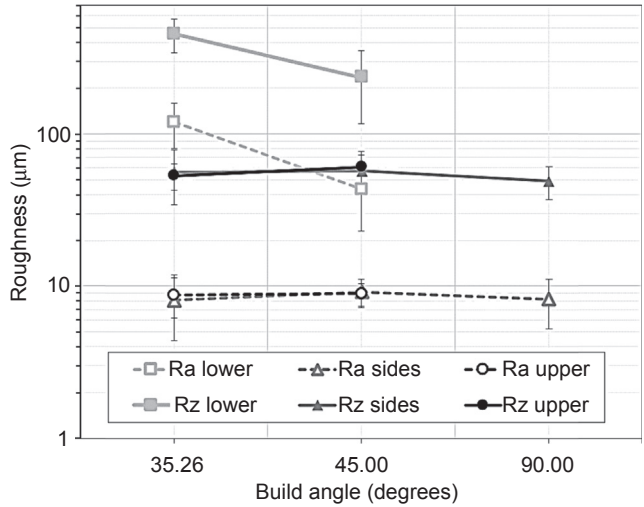

Figure 5.11 Summary surface roughness data for AlSi12Mg lattice struts (error bars indicate ±1 standard deviation).

$$R_t = \max(y_i) - \min(y_i) \tag{5.5}$$

$$R_z = \frac{1}{j}\sum_{i=1}^{j} R_{ti} \tag{5.6}$$

where R_{ti} is each unique value of R_t samples.

Inspection of the surface roughness data (Fig. 5.11) indicates • lower strut surfaces have an order of magnitude higher surface roughness than the other sampled surfaces. The increased roughness is due to preferential particle adhesion on downward facing surfaces on account of limited heat transfer between the powder bed and solid material [37]. The average, R_a, and peak-to-peak, R_z, roughness of lower surfaces is highest for 35.26° struts. For example (Table 5.8), for 35.26° struts, $R_a = 120.2 \pm 39.7$ µm and $R_z = 456.5 \pm 113.6$ µm; for 45° struts, $R_a = 43.52 \pm 20.56$ µm and $R_z = 235.5 \pm 118.2$ µm. Side and upper surfaces have average and peak-to-peak surface roughness that is statistically indistinguishable.

5.4 Compressive testing results

The manufactured Ti6Al4V and AlSi12Mg lattice specimens were tested under compressive loading to quantify the compressive strength and modulus according to the testing objectives defined in Section 5.3.4.

The manufactured lattice structures were tested under quasi-static uniaxial compression to assess mechanical properties as well as deformation and failure modes. The uniaxial compressive tests were conducted on an MTS 100-kN universal testing machine. A

strain rate of 1E-3 mm/mm s was used according to corresponding compressive testing standards [44], with strain calculated from the testing machine head displacement. The engineering compressive stress for each lattice specimen was calculated based on the applied compression load and the initial cross-sectional area of the base of each test specimen, where the cross-sectional area is in the XY plane of the specimen.

5.4.1 Ti6Al4V lattice specimen compressive testing results

Tests for Ti6Al4V lattice specimens were conducted with two repetitions of each lattice specimen variant:

- Test 1: A *high-strain test* to a compressive strain of 80%; this data were used to characterize elastic and yield properties as well as plastic high strain behaviour and failure modes (Section 5.4.1). The loading conditions consisted of three loading stages and two unloading stages to measure the loading and unloading elastic moduli. The first and second loading/unloading stages were conducted at 2% and 4% engineering strain, respectively. The final loading stage compressed the specimen to 80% strain.
- Test 2: A *low-strain test* to a strain of 1−2% beyond the compressive strength (peak load before collapse); this data were used to obtain high-magnification images of initial plastic deformation and fracture of strut elements (Sections 5.4.3). Loading/unloading was conducted at 2% strain to capture modulus values.

Uniaxial compressive stress-strain curves for lattice specimens with 10^3 unit cells are shown in Figs 5.12 and 5.13 for 2- and 3-mm cell sizes, respectively. The specimens exhibited a range of compressive strengths and loading responses. Furthermore, notable differences are present in the ratio of collapse stress to the plateau stress (average stress after the initial peak). In 3-mm cells (Fig. 5.12), most specimens showed a comparatively high initial strength followed by significant softening after the onset of the initial collapse. The exception was BCC structures, which exhibited a plateau stress similar in average magnitude to the initial peak. In 2-mm cells, however, the FBCCZ/FBCCZO specimens exhibited behaviour similar to BCC specimens, where the magnitude of the average plateau stress was comparable to the initial peak. The behaviour of BCC structures is characteristic of typical bending-dominated cellular structures in which the bending deformation mechanism leads to gradual structural collapse. For structures with a high ratio of collapse stress to plateau stress, the deformation behaviour is typically dominated by tension and compression (and associated buckling), where failure leads to more abrupt structural collapse [20].

Fig. 5.14 shows a more detailed view of an observed stress-strain curve which identifies Young's modulus and the loading and unloading moduli at 2% and 4% strain for an FBCCZ-S3N7 specimen. Fig. 5.14 is typical of the response seen in the tested lattice specimens; however, for a number of specimens (predominantly high-stiffness specimens such as FBCCXYZ), the 4% modulus occurred beyond the peak stress. Because the 4% modulus values were not consistently in the elastic region, the resulting measurements are not considered further. The 2% modulus values are taken to be representative of the modulus in the elastic region (Fig. 5.16).

Fig. 5.15(a) shows the relative modulus (E/E_s) for 2% strain against the measured relative density (ρ/ρ_s) for the tested lattice specimens. Similarly, Fig. 5.15(b) shows

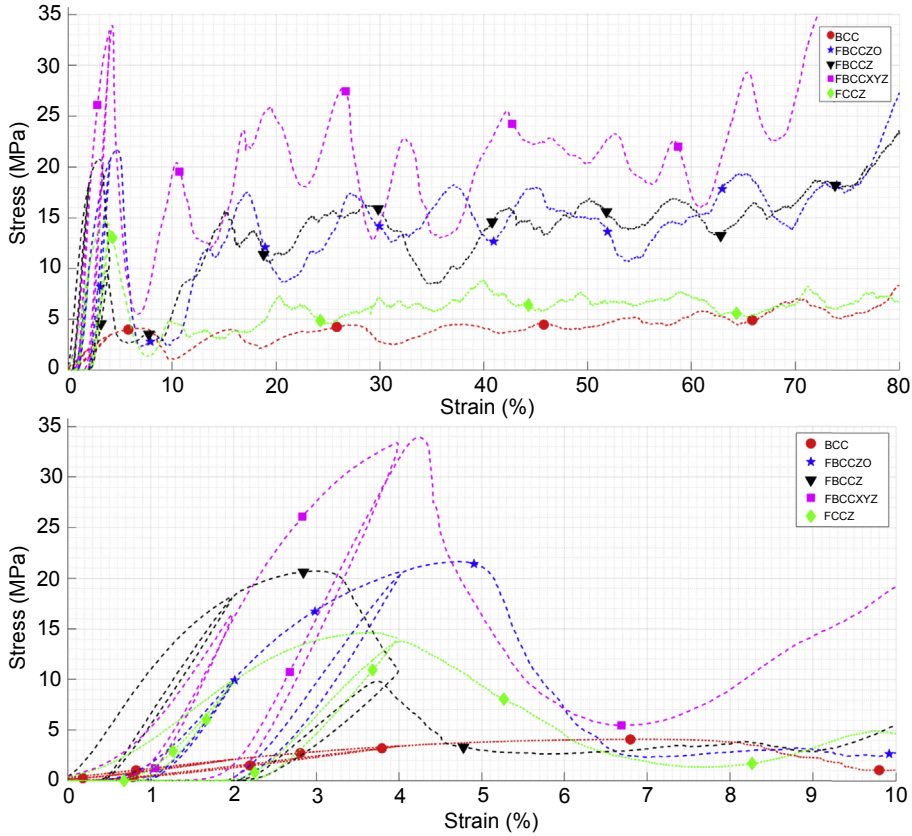

Figure 5.12 Stress−strain response of Ti6Al4V 3-mm cell size lattice structures for 10^3 cell specimens. Top: Complete stress-strain curve to 80% strain. Bottom: Detailed view of the initial portion of the stress-strain response.

the relative compressive strength (σ/σ_s) against the measured relative density (ρ/ρ_s). Both figures show the observed average trend for measured specimens, as well as expected theoretical trends for bending- and stretch-dominated cellular structures [1]. In both graphs the observed average trend shows a positive power relationship with the density for a given lattice cell topology; that is, 2-mm cell specimens have a higher relative density than 3-mm cell specimens and a correspondingly higher modulus and compressive strength. Furthermore, although some statistical variation is present in the measured results, notable differences are observed between lattice topologies. These are predominantly in regards to the presence of vertical axis struts aligned with the compressive loading direction. Topologies devoid of vertical axis struts (BCC) show a trend which corresponds to the theoretically expected behaviour exhibited by bending-dominated structures. The remaining topologies (FCCZ, FBCCZ and FBCCXYZ), which all include vertical struts aligned with the loading direction, exhibit trends which correspond more closely with the expected behaviour of stretch-dominated structures. Comparing this behaviour against the predicted response

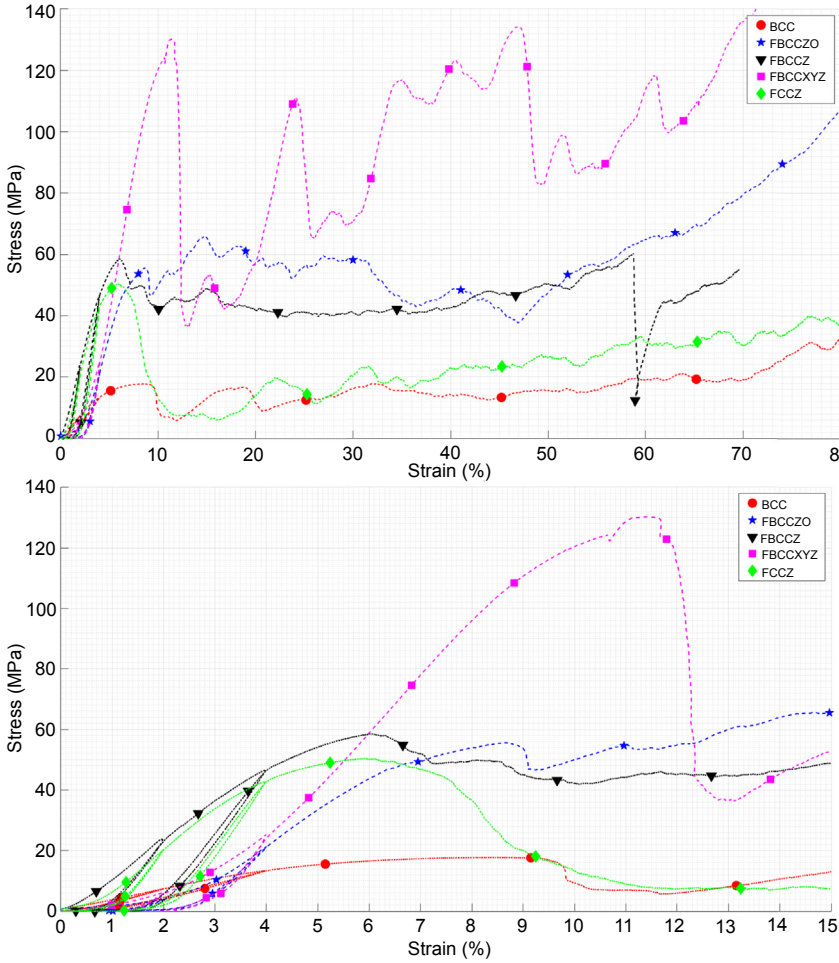

Figure 5.13 Stress−strain response of Ti6Al4V 2-mm cell size lattice structures for 10^3 cell specimens. Top: Complete stress-strain curve to 80% strain. Bottom: Detailed view of the initial portion of the stress-strain response.

according to the Maxwell stability criteria (Section 5.2), the BCC topology corresponds well to the expected bending-dominated trend. The remaining topologies include both bending-dominated (FCCZ and FBCCZ) and stretch-dominated (FBCCXYZ) behaviour (Table 5.1), according to the Maxwell criteria. However, the experimentally measured trend for the bending-dominated topologies is observed to be closer to the expected stretch-dominated response, suggesting that the topologies are more subject to stretch-dominated deformation mechanisms. As stated in Section 5.2, the Maxwell criteria do not accommodate the significant effect of loading direction on cell rigidity, which highlights that the criteria are a necessary but not sufficient condition for predicting mechanical response.

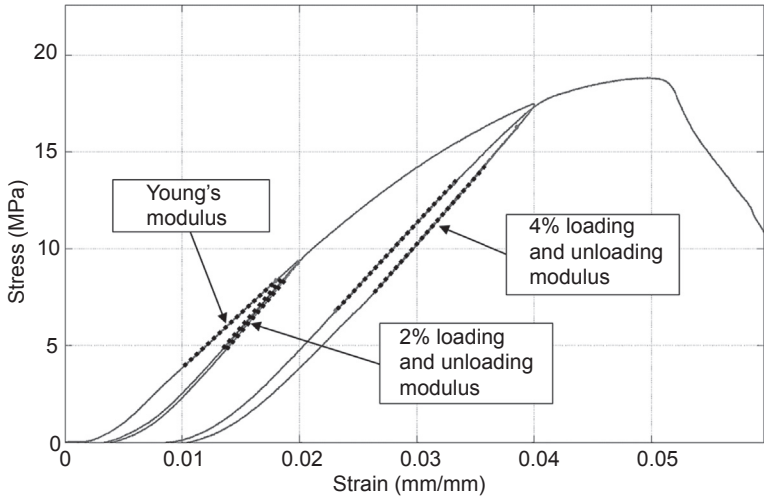

Figure 5.14 Stress−strain response of the Ti6Al4V FBCZ-S2N7 specimen.

Fig. 5.16(a) summarizes the average Young's and 2% strain moduli for each cell type and cell size. Loading and unloading moduli were averaged for the summary data presented in this work. Fig. 5.16(b) shows the corresponding relative standard deviation (RSD), that is, the ratio of standard deviation to mean value. The RSD is calculated across all tested specimens for a given topology and cell size, that is, specimens with N3, N5, N7 and N10 cells with two repetitions (ie, low-strain and high-strain specimens, as detailed in Section 5.4), for a total of eight specimens per set. The RSD is an indicator of the general variation in modulus and compressive strength seen across a specimen set in which the number of cells varies.

Fig. 5.17(a) and (b) summarize the average lattice compressive strength and associated RSD, respectively. The 2% strain specific modulus, defined as the ratio of the modulus to the lattice density ρ (Table 5.5), and the specific compressive strength (ratio of the compressive strength to ρ) are shown in Figs 5.16(c) and 5.17(c), respectively, to compare lattice efficiency for light-weight design. To allow a relative comparison of the mechanical properties of the tested lattice topologies, the data from Figs 5.16 and 5.17 are averaged across all specimens with a specific topology and number of cells.

Summary observations of the data in Figs 5.16 and 5.17 are presented here:

- Fig. 5.16(a) shows that the Young's modulus is always lower than the moduli at 2%. This observation indicates that localized plasticity is occurring in the lattice specimens at stresses below the compressive strength. This outcome is compatible with observations for metallic foams (eg, [1]), but this work confirms this phenomena in additively manufactured lattice structures. A number of publications focused on additively manufactured lattices associate the Young's modulus with the expected in situ stiffness of lattice structures (eg, [4,45,46]). However, as demonstrated in this chapter, the Young's modulus may underestimate the lattice stiffness under repeated elastic loading. An accurate estimate of the modulus is particularly important in applications aimed at the use of SLM lattice structures for

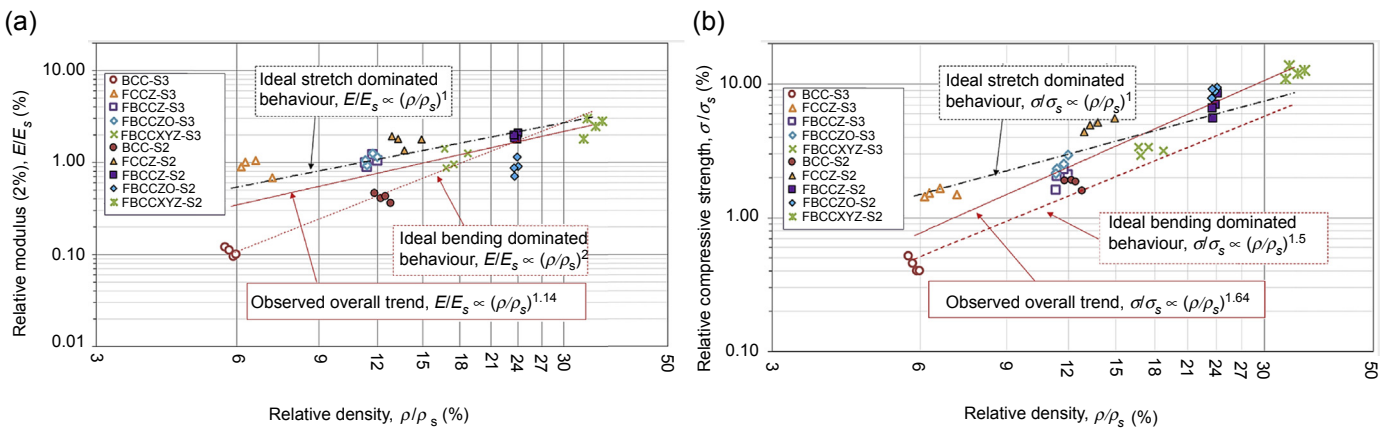

Figure 5.15 Ti6Al4V relative modulus (2% strain) (a) and relative compressive strength (b) versus the relative density for tested lattice cell specimens, including the observed trend and typical trends for bending- and stretch-dominated cellular structures.

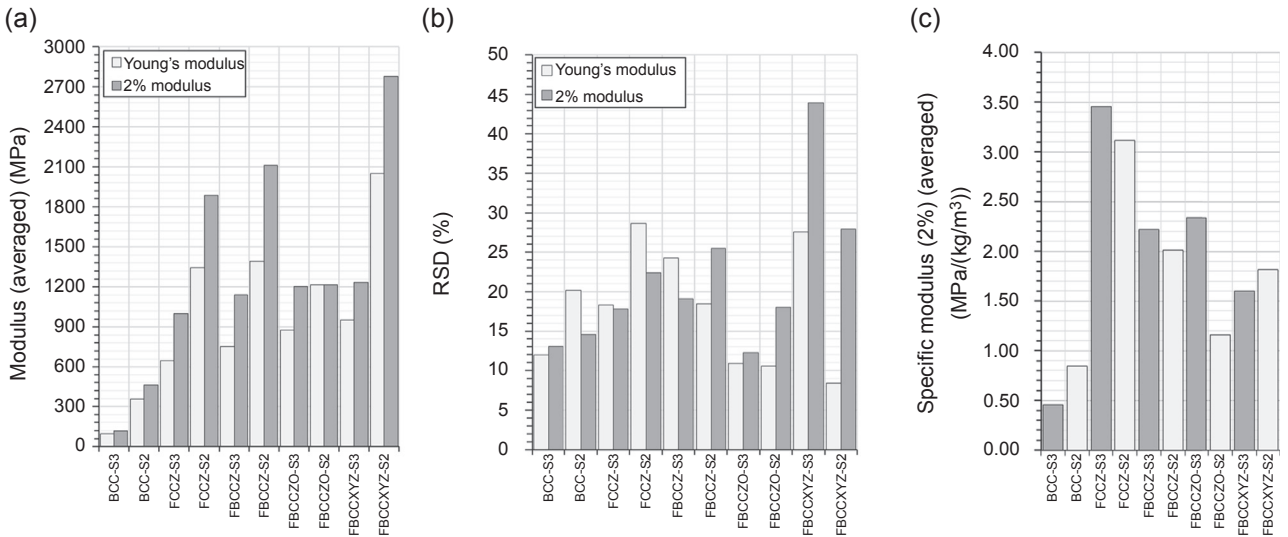

Figure 5.16 (a) Young's and 2% moduli averaged over all Ti6Al4V specimens of indicated topology and cell size. (b) Relative standard deviation (RSD) of modulus values. (c) Specific modulus (2%) averaged over loading and un-loading values and all Ti6Al4V specimens of indicated topology.

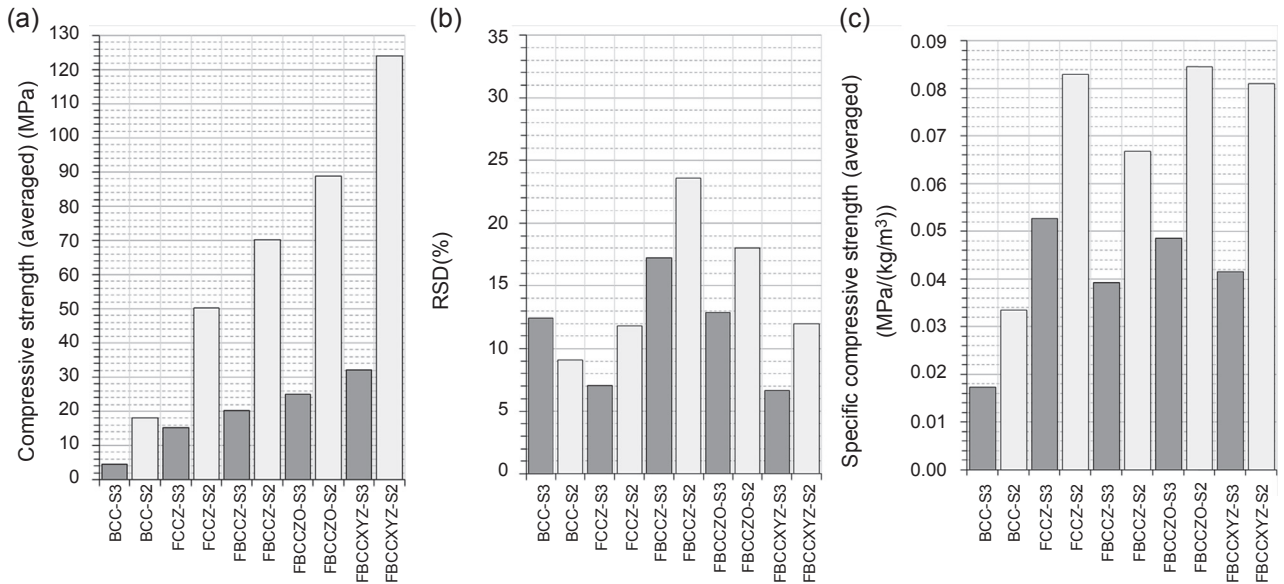

Figure 5.17 (a) Compressive strength averaged over all Ti6Al4V specimens of indicated topology and cell size. (b) Relative standard deviation (RSD) of compressive strength. (c) Specific compressive strength averaged over all Ti6Al4V specimens of indicated topology and cell size.

orthopaedic implants, where lattice structures which match bone stiffness are critical for avoiding stress shielding effects that lead to bone resorption and weakening [47].

- BCC structures have the lowest observed moduli, which is indicative of their high structural compliance caused by under-stiff behaviour and low relative density (Section 5.2).
- The highest observed moduli was exhibited by the FBCCXYZ-S2 structures, which correspond to the robust, over-stiff behaviour of the lattice topology and correspondingly high density (Section 5.2).
- Although the FBCCXYZ lattice has the highest modulus of the tested specimens, the FCCZ has the highest specific modulus for both 2- and 3-mm cell sizes (Fig. 5.16(a)) for closed-end specimen boundary conditions. This outcome indicates that, of the tested lattice structures, FCCZ provides superior performance for compressive load scenarios that attempt to optimize the stiffness-to-weight ratio.
- It is interesting to note that the absolute modulus of the FCCZ and FBCCZ lattices is greater for the 2-mm cell size than for the 3-mm cell size. However, the specific modulus of the 3-mm cell size is marginally higher than that of the 2-mm cell size. This outcome indicates that although larger cell size tends to increase compliance, the associated reduction in lattice density may compensate for this increase in stiffness-limited light-weight design.
- The influence of FBCCZ boundary conditions on modulus showed mixed results. For 3-mm cells, the absence of end webs marginally increases the modulus, whereas for the 2-mm specimen, the absence of end webs reduces the modulus. The compressive strength increased for both 2- and 3-mm cells in the absence of end webs.
- BCC structures exhibit the lowest overall compressive strength. The highest compressive strength was achieved by FBCCXYZ specimens. It is apparent that increasing cell size significantly reduces the associated compressive strength for all topologies; that is, for all scenarios investigated, the compressive strength for 3-mm cell size is significantly lower than for the 2-mm cells. This outcome corresponds with the reduction in density between the 3- and 2-mm specimens and the expected reduction in compressive strength according to expected theoretical trends (Fig. 5.15(b)).
- Similarly, BCC structures exhibit the lowest specific compressive strength of the scenarios investigated. The highest absolute value of specific compressive strength was achieved by FBCCXYZ with a 2-mm cell size. It is interesting to note that, for a 3-mm cell size, the FBCCXYZ has poor specific compressive strength, and of the scenarios investigated, only the BCC lattice was lower.
- The RSD values for Young's modulus and 2% unloading modulus (Fig. 5.16(b)) and compressive strength (Fig. 5.17(b)) generally range between 10% and 30%.

5.4.1.1 *Convergence of mechanical properties for Ti6Al4V lattice specimens*

The compressive strength for varying Ti6Al4V specimen and cell sizes is shown as a function of cross-sectional area in Fig. 5.18(a). Modulus values for varying specimen and cell sizes are shown in Fig. 5.18(b). The values are presented as a ratio of the response of the largest specimen (10^3 cells) in order to observe the convergence of values with increasing specimen size. The results are averaged for a sample set of two specimens (Section 5.4).

In general, lower-density BCC and FCCZ structures with both 2- and 3-mm cells show comparatively better convergence than higher-density FBCCZ and FBCCXYZ

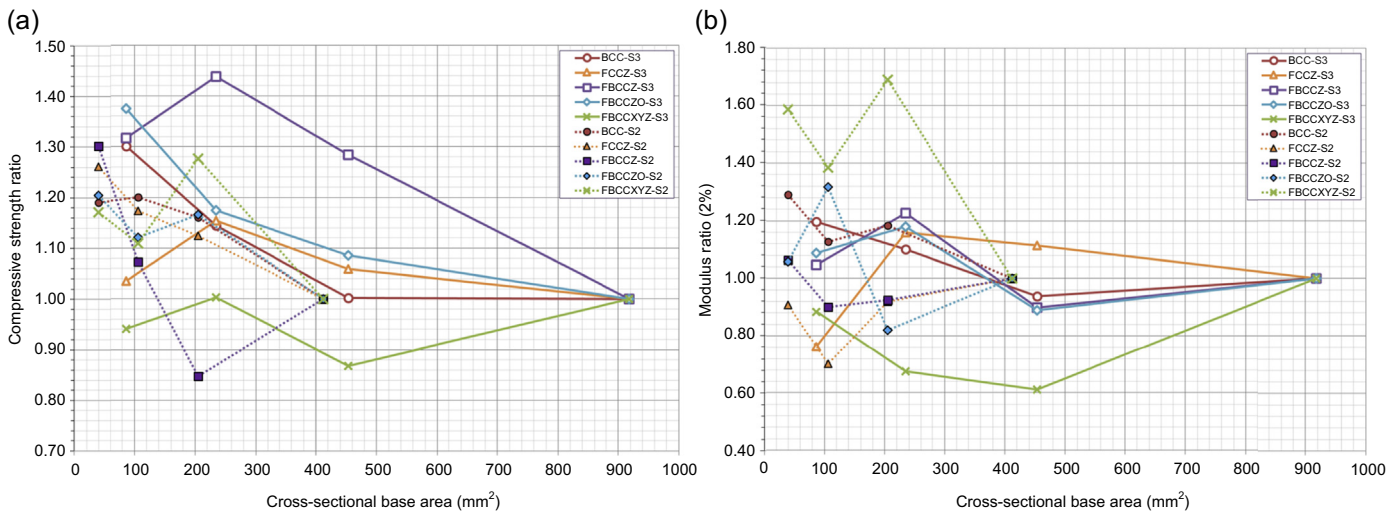

Figure 5.18 (a) Compressive strength versus base area of Ti6Al4V lattice specimens as a ratio with the largest specimen. (b) Modulus (2% strain) versus base area of Ti6Al4V lattice specimens as a ratio with the largest specimen. All values average for a sample set of two.

specimens. Comparatively higher variation is seen in the modulus values. As such, for FBCCZ, FBCCZO and FBCCXYZ specimens, more than 10^3 cells may be required for the specimen to reach values that converge to constant values that are expected to be representative of an infinite array of lattice cells. However, testing larger samples may be limited by SLM machine build volume constraints and testing equipment capabilities.

5.4.2 Compressive testing results for AlSi12Mg lattice specimens

Tests were conducted on two repetitions of each AlSi12Mg lattice specimen:

- Test 1: Compression to 15% strain; the data were used to characterize the compressive strength.
- Test 2: Compression to the onset of collapse (approximately 1−2% strain beyond peak stress); test results were used to characterize the Young's, 1% strain and 2% strain moduli and to obtain images of failure mode associated with collapse (Fig. 5.19). The modulus values were measured at 1% and 2% compared with 2% and 4% in Ti6Al4V specimen tests; as 4% was previously found to be beyond the peak compressive stress for a number of tested specimens (Section 5.4.1).

Fig. 5.20 summarizes compressive strength and modulus results (including specific values) for all tested AlSi12Mg lattice specimens.

Fig. 5.21(a−c) compares the relative Young's, 1% and 2% strain moduli (E/E_s) against the theoretical relative density (ρ/ρ_s) for the tested AlSi12Mg lattice specimens. The relative compressive strength (σ/σ_s) is compared against the measured

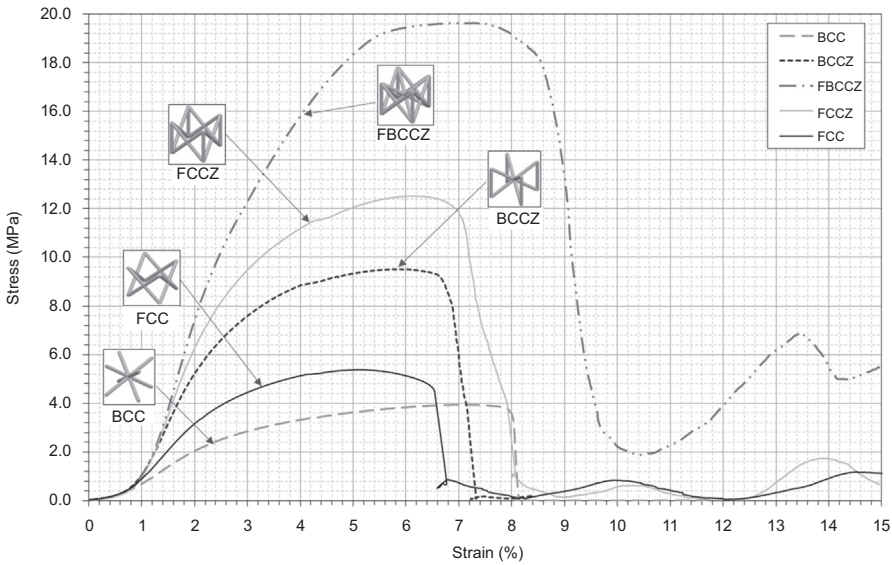

Figure 5.19 Uniaxial compression stress−strain responses of tested AlSi12Mg lattice specimens.

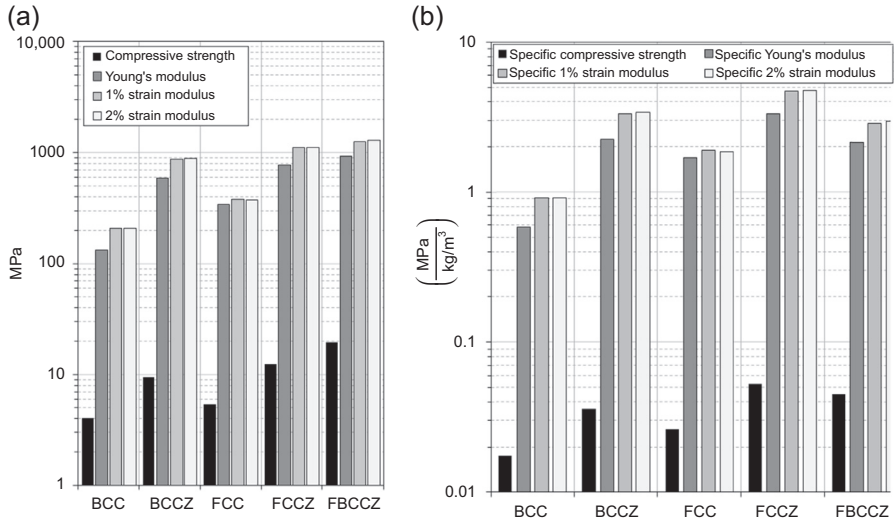

Figure 5.20 Mechanical properties of tested AlSi12Mg lattice specimens. (a) Absolute compressive strength and modulus. (b) Specific compressive strength and specific modulus.

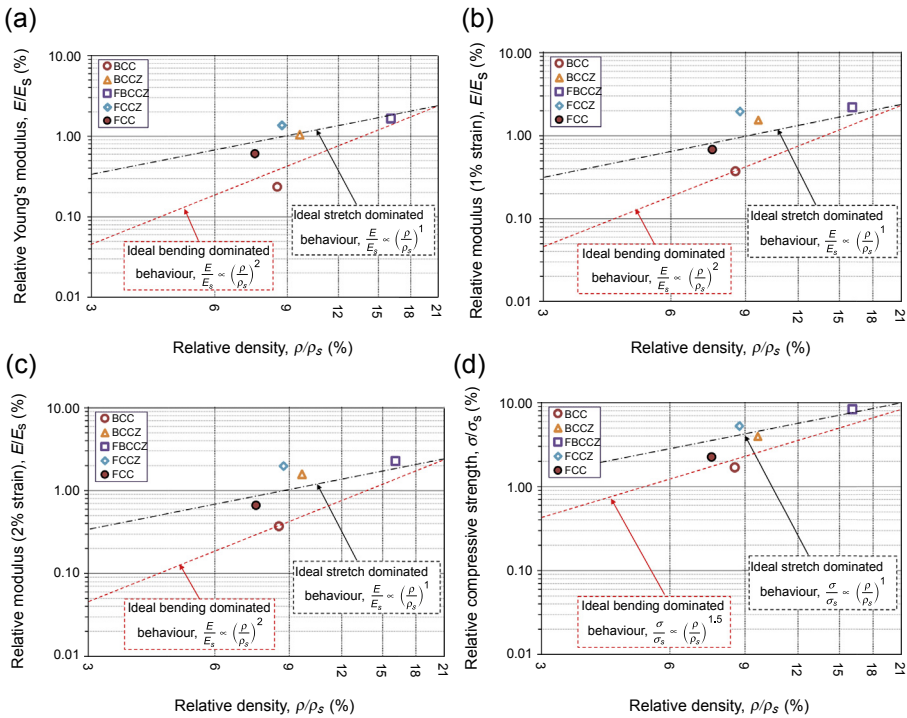

Figure 5.21 Relative modulus and relative compressive strength versus relative density for tested AlSi12Mg lattice cell specimens, including typical trends for bending- and stretch-dominated cellular structures. (a) Relative Young's modulus, (b) relative modulus (1% strain), (c) relative modulus (2% strain), (d) relative compressive strength.

relative density (ρ/ρ_s) in Fig. 5.21d. Expected theoretical trends are presented for bending- and stretch-dominated cellular structures in which mechanical properties show a positive power relationship with the relative density [1].

5.4.2.1 Numerical analysis of AlSi12Mg specimens

Numerical analysis of CT data was completed on the AlSi12Mg specimens to provide insight into the fundamental deformation and failure mechanisms and associated mechanical property trends, and to allow comparison with observed experimental data.

Cell boundary conditions vary significantly depending on boundary conditions imposed on the external lattice boundary as well as on cell position within the bulk cellular array. For example, a unit cell within a bulk cellular array will be constrained by interaction with neighbouring cells, whereas a unit cell on a lattice boundary may be unconstrained, depending on its specific location. To gain insight into the possible cell response, the following extremes in boundary conditions were assessed individually:

- *Constrained* boundary condition, whereby nodes on the lateral lattice boundary are constrained to disallow lateral translation. The constrained scenario represents lattice cells fully within bulk lattice structures as well as external lattice structures that are subject to rigid external constraints.
- *Unconstrained* boundary condition, whereby nodes on the lateral lattice boundary are free to translate. The unconstrained scenario represents lattice cells on the external lattice surface that are not subject to external constraints.

For both cases, linear-elastic analysis was completed with solid elements loaded to a strain of 5% of total cell size, based on CT data (Section 5.3.5); von Mises stress and relative stiffness k_R are shown (Table 5.8), normalized to results for BCC, which displays the lowest stiffness of all assessed topologies. Numerical and experimental data are compared in terms of relative compressive strength and relative density in Fig. 5.22.

The numerical analysis results indicate that:

- Higher stiffness is associated with lattices including vertical struts aligned with the loading direction, confirming the associated high resistance to compressive loads observed in Section 5.4.2.
- Stress concentrations are present at the intersection of diagonal struts because of the presence of small fillet radii. Increased filleting may improve strength by reducing stress concentrations, particularly in lattice structures without vertical struts, where stress concentrations are particularly noticeable as a result of pronounced bending at intersecting strut nodes.
- Specimens with constrained boundaries exhibit expectedly higher stiffness values than unconstrained specimens. The results for constrained boundary conditions are in general closer to the experimental results, suggesting the constrained boundary conditions are more representative of experimental conditions.
- The loading response trends in Fig. 5.22 generally align with theoretically expected trends for stretch- and bending-dominated cellular structures in which compressive strength increases with relative density [1].

Table 5.8 Numerical analysis of candidate lattice structures[a]

	Unconstrained	Constrained
BCC	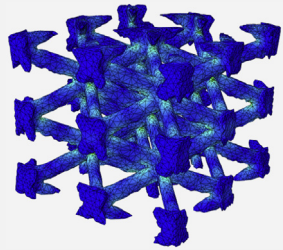	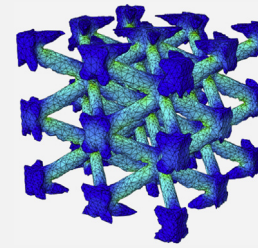
k_R	1.0	3.5
BCZ	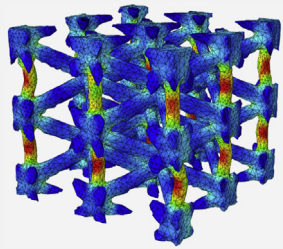	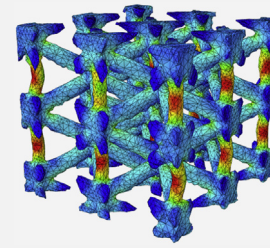
k_R	8.1	11.1
FBCZ	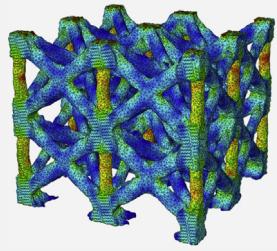	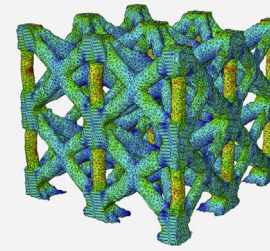
k_R	9.6	15.3
FCZ	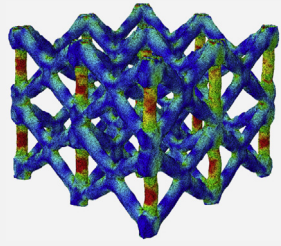	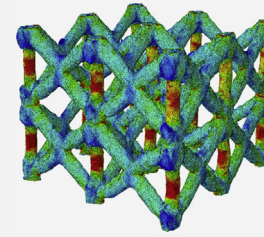
k_R	8.0	10.9

Continued

Table 5.8 Continued

	Unconstrained	Constrained
FC	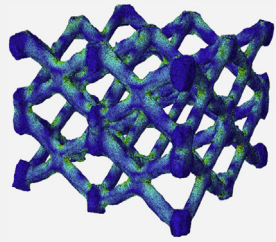	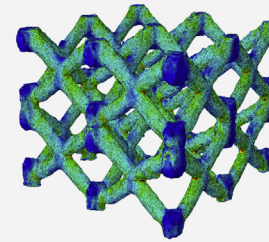
k_R	1.5	6.2

[a]The images show von Mises stress and relative stiffness k_R, both normalized to data for unconstrained BCC.

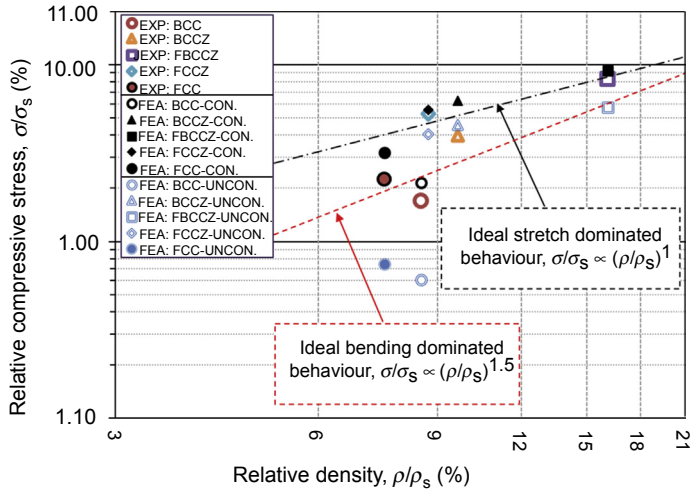

Figure 5.22 Relative compressive stress versus relative density for experimental (EXP) and numerical (FEA) results. Numerical results include constrained (CON.) and unconstrained (UNCON.) boundary conditions.

5.4.2.2 Discussion of AlSi12Mg lattice specimen experimental results

The following characteristics are observed for the experimental and numerical AlSi12Mg lattice specimen test results:

- BCC specimens exhibit the lowest absolute compressive strength and moduli of all candidate lattice cell structures. Similarly, low values are exhibited by FCC specimens (Fig. 5.20). These results align with the expected high structural compliance of the BCC and FCC lattice topologies because of their under-stiff behaviour, lack of struts aligned in the loading direction and low relative density (Section 5.2).

- The low compliance of BCC and FCC specimens corresponds to a stress concentration at the strut−node intersection in the associated numerical results (Table 5.8). Of the highly compliant lattice topologies, FCC specimens show notably higher specific compressive strength and modulus values compared with BCC specimens, indicating superior structural efficiency but lower ductility (Fig. 5.19).
- The highest overall compressive strength and observed modulus was achieved by FBCCZ specimens (Fig. 5.20), attributable to their increased strut connectivity, the presence of z-axis struts aligned with the loading direction and a correspondingly high density. Numerical analysis indicates that peak stresses occur in the z-struts in the FBCCZ lattice; however, it is apparent that the BCC and FCC elements within the FBCCZ lattice assist in supporting the z-struts, as the associated stress concentration is lower than for either FCCZ and BCCZ specimens (Table 5.8).
- When observing specific strength and moduli values (Fig. 5.11(b)), FCCZ specimens show the highest specific strength and modulus relative to other specimens, despite having lower absolute values compared with FBCCZ specimens (Fig. 5.20(a)). This outcome indicates that FCCZ provides superior performance for compressive load scenarios aimed at maximizing strength- and stiffness-to-weight ratios. Similar performance was noted for titanium lattice structures (Section 5.4.1).
- The ductility of the tested specimens was approximately 6−8%, and all specimens showed a large ratio of collapse stress to plateau stress (average stress post initial peak), where a high initial strength is followed by a drastic collapse after reaching a maximum compressive strength (Fig. 5.7).
- Young's modulus was found to be always lower than the moduli at 1% and 2% strain (Fig. 5.20), indicating that localized plasticity is occurring in the lattice specimens at stresses below the compressive strength. Similar observations have been made for metallic foams (eg, [1]) and in the Ti6Al4V alloy SLM lattice structures tested in Section 5.4.1. This outcome is particularly important because a number of publications relevant to additively manufactured lattices associate the Young's modulus with the expected in situ lattice stiffness (eg, [4,45,46]), despite the observation demonstrated in this work that the Young's modulus may underestimate stiffness for repeated elastic loading of lattice structures.
- The response of tested lattice specimens exhibits trends in relative density, relative modulus and compressive strength which are associated with the presence of vertical z-struts aligned with the compressive loading direction (Fig. 5.21 and Fig. 5.22). Lattice topologies which include vertical struts (BCCZ, FCCZ and FBCCZ) correspond with the expected behaviour of stretch-dominated structures (suggesting that the topologies are more subject to stretch-dominated deformation mechanisms), whereas lattice topologies without vertical axis struts (BCC, FCC) do not adhere to this trend.

5.4.3 Deformation behaviour and failure modes

A series of time-lapse images were acquired during compressive testing of Ti6Al4V and AlSi12Mg lattice specimens to record the deformation response of specimens under loading, as well as the associated failure modes. Figs 5.23 and 5.25 show an acquired image sequence for a series of 10^3 specimen states comprising the initial state, elastic preload, initial failure, progressed failure and gross failure. Additional details for AlSi12Mg specimens can be seen in Fig. 5.26. Highlights indicate notable

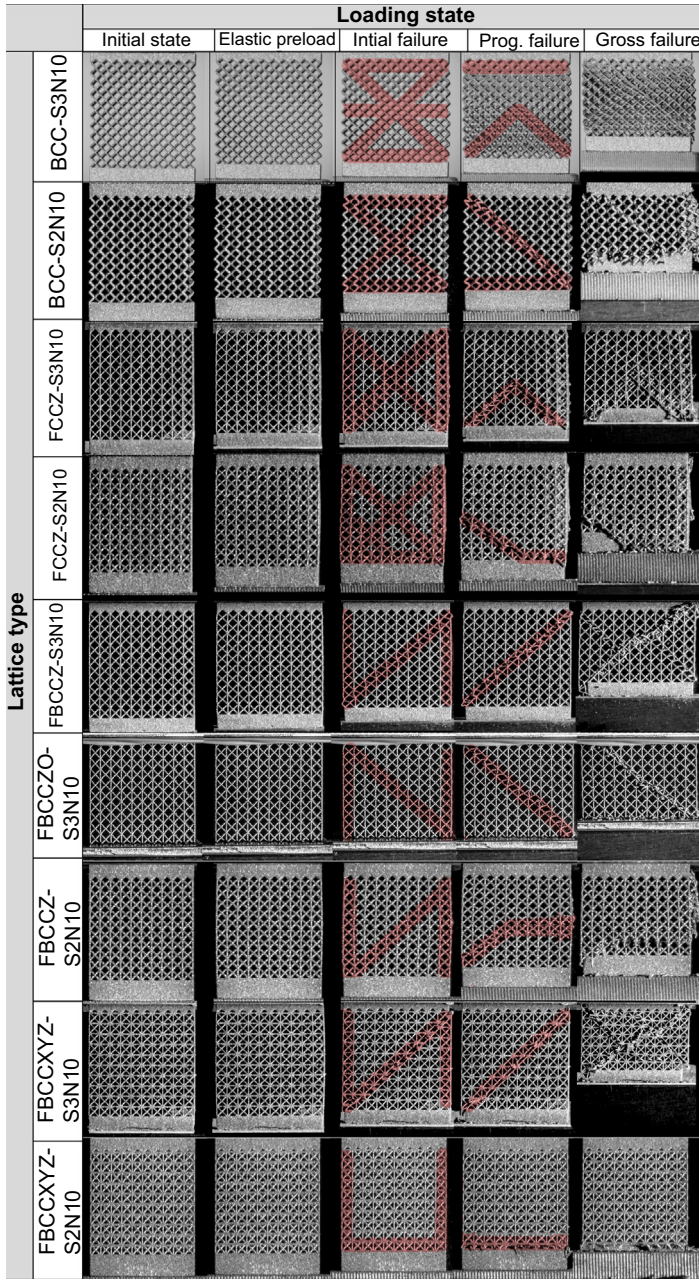

Figure 5.23 Failure modes of tested Ti6Al4V lattice specimens.

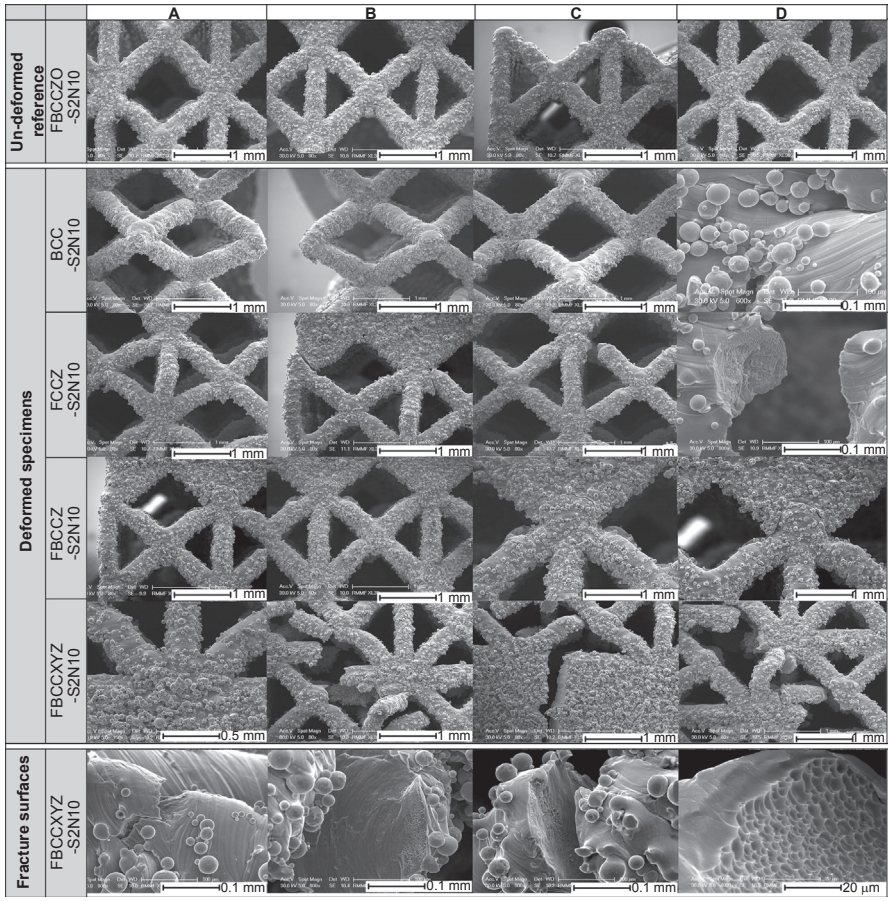

Figure 5.24 Failure modes of tested lattice Ti6Al4V specimens. Un-deformed reference specimen is shown in row 1. Deformed specimens are shown in rows 2−5. Fracture surfaces are shown in row 6.

regions of deformation or failure and are discussed below. General observations associated with the deformation response include:

- BCC structures show comparatively large compliance upon loading on account of their under-stiff topology (Sections 5.2 and 5.4.1). Deflection occurs through pronounced strut bending at lattice joints, followed by fracture and subsequent lattice cell collapse. In Ti6Al4V specimens with end webs, prominent deflection was observed across diagonal bands at 45 degrees to the loading direction, as well as horizontal deformation bands at the specimen top, bottom and mid-height. The dominant failure mode for BCC-S3 specimens was by horizontal layer collapse near the top of the specimen, as well as diagonal shear collapse. Collapse in BCC-S2 structures was a combination of diagonal and horizontal layer collapse across the specimen's lower half.
- FCCZ structures show vertical strut buckling and fracture leading to lattice cell collapse. Dominant buckling was observed across diagonal shear bands of the specimen. The collapse

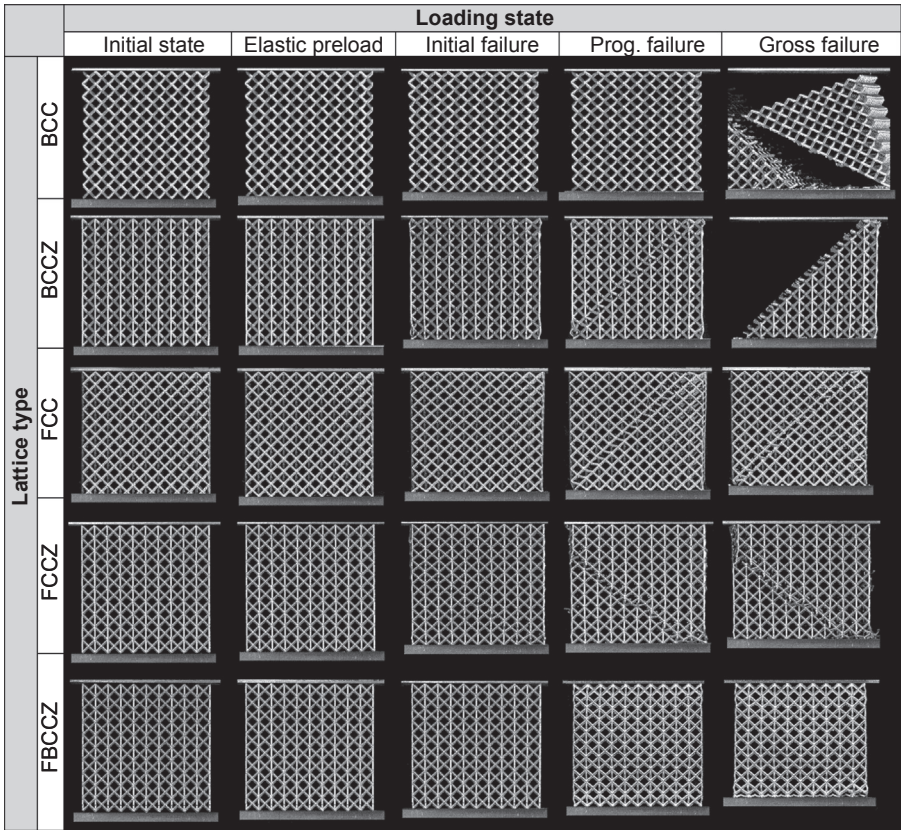

Figure 5.25 Failure modes of tested AlSi12Mg lattice specimens.

mode for the FCCZ-S3 specimen was by bi-directional diagonal layer collapse in the lower half of the specimen.

- FBCCZ structures exhibited buckling across diagonal shear bands of the specimen. The collapse mode for FBCCZ-S3 specimens was by diagonal layer failure. FBCCZ-S2 specimen failure initiated in a similar manner; however, further compression resulted in a path adjustment, whereby the diagonal shear band was transformed into a diagonal-horizontal shear band propagating through the specimen.
- FBCCXYZ structures showed similar behaviour to FBCCZ specimens. However, although FBCCXYZ-S3 failed by diagonal shear failure akin to FBCCZ-S3, FBCCXYZ-S2 failure was by horizontal layer collapse at the base of the specimen. This outcome suggests that, for a 2-mm cell size, the X and Y struts are able to resist diagonal shear failure in the structure. This behaviour is useful for energy-absorbing applications where progressive layer collapse is desirable, rather than diagonal shear.
- All specimens tested with end web structures presented a pronounced barrel shape under loading, attributable to the increased lateral resistance provided by the webs against horizontal deformation. FBCCZO specimens devoid of end webs exhibited more uniform horizontal deflection.

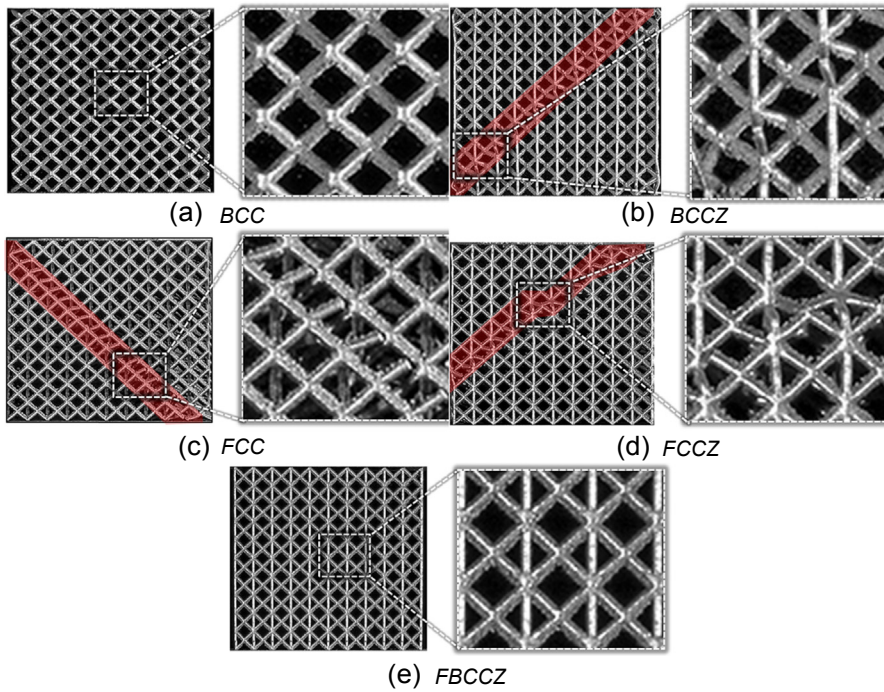

Figure 5.26 Details of observed deformation and failure modes of tested AlSi12Mg lattice specimens at collapse.

Fig. 5.24 presents detailed images of lattice specimen structures acquired through SEM. Images were taken of 2-mm cell specimens before testing (FBCCZ-S2N10) as well as following compression up to the onset of collapse (Section 5.4). Observing the un-deformed specimens in Fig. 5.24, row 1, reveals non-uniformities associated with the manufactured lattice geometry:

- Diagonal lattice struts show an increased diameter compared with the model geometry. This is attributed to additional powder being captured by the melt pool during SLM layer manufacture of overhanging surfaces [48]. Possible compensation for the diameter increase in diagonal struts could be achieved in future builds by an appropriate reduction of the strut diameter in CAD model files.
- Partially melted particles have adhered to the strut surface; this is compatible with other observations, especially on downward-facing surfaces with an acute inclination angle caused by overheating [13,49].
- Diagonal struts in some specimens exhibit diameter reduction at the strut intersection (eg, Fig. 5.24 D1) and an offset in the strut central axis (images B1 and D1). This effect reduces the load capacity of the strut, and the fundamental cause of this effect requires further investigation. Possible compensation for the diameter reduction could be achieved by an appropriate increase of the strut diameter in CAD model files at the affected location.

The deformed specimens in Fig. 5.24, rows 2−5, show a number of notable effects:

- BCC specimens exhibit pronounced strut bending at lattice joints, reflecting the expected bending-dominated behaviour (Section 5.2) and associated high compliance seen during testing (Section 5.4.1).
- FCCZ specimens show vertical strut buckling and fracture. Fracture predominately occurs in joints incorporating vertical struts rather than on diagonal strut face joints.
- FBCCZ structures exhibited similar buckling to FCCZ specimens. Fracture was observed at the interface between the lattice and the boundary web structures (Fig. 5.24 images C4 and D4).
- FBCCXYZ specimens showed similar behaviour to FCCZ and FBCCZ structures. Fracture was also observed through the web structures at the base of the FBCCXYZ specimen.
- The observed fracture surfaces (Fig. 5.24 row 6) shows micro-voids and dimples characteristic of ductile fracture.

5.5 Concluding remarks

This chapter addressed a range of current uncertainties associated with SLM-manufactured Ti6Al4V and AlSi12Mg lattice structures by providing insight into the influence of material, cell topology, cell size, number of unit cells and boundary conditions on the deformation and failure behaviour of lattices under compressive loading. The chapter identifies various key outcomes:

- Limitations of Ti6Al4V and AlSi12Mg lattice manufacturability were documented, including minimum strut diameter and allowable inclination angle for the proposed processing parameters. Based on these identified processing limits, a number of relevant lattice structures were defined, including structures with a low Maxwell number (intending to provide high compliance) as well as structures with a higher Maxwell number and struts aligned in the loading direction (these lattice elements provide high compressive strength and stiffness).
- Experimental observation of the compressive loading of lattice specimens indicates that Young's modulus is always lower than the moduli at 1% and 2% strain. This effect is caused by local plasticity not observed in bulk materials, and although typically reported for metallic foams, it does not seem to be commonly reported for AM structures. This observation is therefore particularly important for AM lattice designers and researchers because the reported Young's modulus may underestimate stiffness for in-service loading.
- BCC structures show the lowest observed moduli, attributable to their high structural compliance caused by under-stiff behaviour. The highest observed moduli were exhibited by FBCCXYZ (for Ti6Al4V) and FBCCZ (for AlSi12Mg) structures. However, the highest specific modulus was exhibited by FCCZ structures, indicating superior performance for compressive-loaded scenarios that attempt to optimize the stiffness-to-weight ratio. For Ti6Al4V FCCZ, FBCCZ and FBCCXYZ structures, it was found that although a larger cell size tends to increase compliance, the specific modulus remained similar for 2- and 3-mm cells. This characteristic, where a reduction in lattice density may compensate for reduced stiffness, may be desirable in light-weight design scenarios.
- BCC structures exhibit the lowest overall and specific compressive strengths. For Ti6Al4V, FBCCXYZ and FCCZ structures showed high overall and specific strength values,

respectively. For AlSi12Mg, FBCCZ and FCCZ structures showed high overall and specific strength values, respectively.

- Analysis of the convergence of mechanical properties with an increase in the specimen size showed that for FBCCZ and FBCCXYZ structures, specimens comprising more than 10^3 cells may be required for the specimen to reach values that converge to constant values. Convergence trends for modulus values are similar to those for compressive strength but have comparatively higher variation.
- Failure modes of tested lattices structures under compression occurred through pronounced bending of diagonal struts and buckling of vertical struts, followed by strut fracture and subsequent lattice cell collapse predominantly across diagonal shear bands. For topologies with a low Maxwell number and no struts aligned in the loading direction, notably BCC and FCC, significant deflection occurred before failure; these topologies may be appropriate for the design of intentionally compliant structures. For topologies with a high lateral stiffness, notably FBCCZ in AlSi12Mg and FBCCXYZ in Ti6Al4V, failure was observed by horizontal layer crushing; these topologies may be appropriate for energy-absorbing structures.
- The observed response of lattice structures aligned with the theoretical response of stretch- and bending-dominated structures. However, topologies which were classified as bending-dominated according to the Maxwell stability criteria (FCCZ and FBCCZ) were found to correspond with stretch-dominated behaviour trends. The result was attributed to the presence of vertical struts aligned with the loading direction, which exhibited stretch-dominated deformation mechanisms. Similar results were observed in the numerical analysis of lattice specimens. The results highlighted that the Maxwell criteria are a necessary but not necessarily sufficient condition for predicting mechanical response, particularly because they do not accommodate the significant effect of loading direction on cell rigidity.

Nomenclature

Abbreviations

Term	Definition
AM	Additive manufacturing
BCC	Body-centred cubic unit cell
BCCZ	Body-centred cubic unit cell with vertical struts
CT	Computed tomography
DOE	Design of experiments
FBCCXYZ	Face-centred and body-centred cubic unit cell with vertical and horizontal struts
FBCCZ	Face-centred and body-centred cubic unit cell with vertical struts
FBCCZO	Face-centred and body-centred cubic unit cell with vertical struts and no end webs
FCCZ	Face-centred cubic unit cell with vertical struts

Continued

FEA	Finite element analysis
RSD	Relative standard deviation
SLM	Selective laser melting
Symbols	
Term	**Definition**
E	Lattice specimen modulus (MPa)
E_s	Solid material modulus (MPa)
h	Hatch spacing (μm)
j	Roughness sample index
k_R	Relative stiffness
M	Maxwell number
n	Number of nodes
N	Number of roughness measures per sample, number of test specimens
ρ	Lattice specimen density (kg/m^3)
ρ_c	Unit cell density (kg/m^3)
ρ_s	Solid material density (kg/m^3)
P	Laser power (W)
s	Number of struts
σ	Lattice specimen compressive strength (MPa)
σ_s	Solid material compressive strength (MPa)
t	Layer thickness (mm)
v	Scan speed (mm/s)
V	Lattice cell solid material volume (mm^3)
V_s	Lattice cell enclosed volume (mm^3)
E_d	Laser energy density (J/mm^3)

References

[1] L.J. Gibson, M.F. Ashby, Cellular Solids: Structure and Properties, Cambridge University Press, 1999.
[2] M. Scheffler, P. Colombo, Cellular Ceramics: Structure, Manufacturing, Properties and Applications, Wiley, 2005.
[3] M.F. Ashby, Cellular Ceramics, FRG: Wiley-VCH Verlag GmbH & Co. KGaA, Weinheim, 2005.

[4] J. Wieding, A. Wolf, R. Bader, Numerical optimization of open-porous bone scaffold structures to match the elastic properties of human cortical bone, The Journal of the Mechanical Behavior of Biomedical Materials 37 (September 2014) 56−68.
[5] V.S. Deshpande, M.F. Ashby, N.A. Fleck, Foam topology bending versus stretching dominated architectures, Acta Materialia 49 (2001) 1035−1040.
[6] M.F. Ashby, A.G. Evans, N.A. Fleck, L.J. G, Metal Foams: A Design Guide, Butterworth-Heinemann Limited, Woburn, MA, 2000.
[7] S.L. Campanelli, N. Contuzzi, A. Angelastro, A.D. Ludovico, Capabilities and performances of the selective laser melting process, New Trends in Technologies: Devices, Computer, Communication and Industrial Systems (2010) 233−252.
[8] M. Rombouts, J.P. Kruth, L. Froyen, P. Mercelis, Fundamentals of selective laser melting of alloyed steel powders, CIRP Annals − Manufacturing Technology 55 (1) (2006) 187−192.
[9] I. Yadroitsev, I. Smurov, Surface morphology in selective laser melting of metal powders, Physics Procedia 12 (2011) 264−270.
[10] S. Bremen, W. Meiners, A. Diatlov, Selective laser melting, Laser Technik Journal 9 (2) (2012) 33−38.
[11] H. Altenbach, A. Oechsner, Cellular and Porous Materials in Structures and Processes, Springer Verlag, 2011.
[12] M. Brandt, S.J. Sun, M. Leary, S. Feih, J. Elambasseril, Q.C. Liu, High-value SLM aerospace components: from design to manufacture, Advanced Materials Research 633 (2013) 135−147.
[13] D. Wang, Y. Yang, Z. Yi, X. Su, Research on the fabricating quality optimization of the overhanging surface in SLM process, The International Journal of Advanced Manufacturing Technology 65 (9−12) (June 2012) 1471−1484.
[14] Z. Doubrovski, J.C. Verlinden, J.M.P. Geraedts, Optimal design for additive manufacturing: opportunities and challenges, in: ASME 2011 International Design Engineering Technical Conferences and Computers and Information in Engineering Conference, 2011, pp. 635−646.
[15] P.A. Kobryn, S.L. Semiatin, The laser additive manufacture of Ti-6Al-4V, JOM 53 (9) (2001) 40−42.
[16] J. Imanishi, P.F.M. Choong, Three-dimensional printed calcaneal prosthesis following total calcanectomy, International Journal of Surgery Case Reports 10 (2015) 83−87.
[17] J.R. Davis, J.R. Davis, Aluminum and Aluminum Alloys, ASM International, 1993.
[18] K.J. Maloney, K.D. Fink, T.A. Schaedler, J.A. Kolodziejska, A.J. Jacobsen, C.S. Roper, Multifunctional heat exchangers derived from three-dimensional micro-lattice structures, International Journal of Heat and Mass Transfer 55 (9−10) (2012) 2486−2493.
[19] M. Scheffler, P. Colombo, Cellular Ceramics: Structure, Manufacturing, Properties and Applications, Wiley, 2006.
[20] M.F. Ashby, The properties of foams and lattices, Philosophical Transactions of the Royal Society, A: Mathematical, Physical & Engineering Sciences 364 (1838) (January 2006) 15−30.
[21] V.S. Deshpande, N.A. Fleck, M.F. Ashby, Effective properties of the octet-truss lattice material, Journal of the Mechanics and Physics of Solids 49 (8) (August 2001) 1747−1769.
[22] W.F. Chen, E.M. Lui, Principles of Structural Design, Taylor & Francis, 2005.
[23] D.L. Schodek, Structures, Prentice-Hall Inc., Englewood Cliffs, NJ, 1980.
[24] O. Rehme, C. Emmelmann, Rapid manufacturing of lattice structures with selective laser melting, Proceedings of SPIE − The International Society for Optical Engineering 6107 (February 2006), 61070K. 1−61070K. 12.

[25] R.A.W. Mines, S. Tsopanos, Y. Shen, R. Hasan, S.T.T. McKown, Drop weight impact behaviour of sandwich panels with metallic micro lattice cores, International Journal of Impact Engineering 60 (2013) (October 2013) 120−132.
[26] F. Brenne, T. Niendorf, H.J.J. Maier, AM cellular structures − impact on microstructure and local strains, monotonic, cyclic behavior − uniaxial and bending load, PDF, Journal of Materials Processing Technology 213 (2013) 1558−1564.
[27] Y. Shen, S. Mckown, S. Tsopanos, C.J. Sutcliffe, R.A.W. Mines, W.J. Cantwell, The mechanical properties of sandwich structures based on metal lattice architectures, Journal of Sandwich Structures and Materials 12 (2) (June 2009) 159−180.
[28] H.S. Byun, K.H. Lee, Determination of the optimal build direction for different rapid prototyping processes using multi-criterion decision making, Robotics and Computer-Integrated Manufacturing 22 (1) (2006) 69−80.
[29] L. Facchini, Microstructure and Mechanical Properties of Biomedical Alloys Produced by Rapid Manufacturing Techniques, 2010.
[30] J.P. Kruth, P. Mercelis, J. Van Vaerenbergh, T. Craeghs, Feedback Control of Selective Laser Melting, 2007, pp. 1−7.
[31] E. Foroozmehr, R. Kovacevic, Effect of path planning on the laser powder deposition process: thermal and structural evaluation, International Journal of Advanced Manufacturing Technology 51 (5−8) (2010) 659−669.
[32] T. Craeghs, S. Clijsters, J.-P. Kruth, F. Bechmann, M.-C. Ebert, Detection of process failures in layerwise laser melting with optical process monitoring, Physics Procedia 39 (2012) 753−759.
[33] M.R. Alkahari, T. Furumoto, T. Ueda, A. Hosokawa, R. Tanaka, M.S. Abdul Aziz, Thermal conductivity of metal powder and consolidated material fabricated via selective laser melting, Key Engineering Materials 523−524 (2012) 244−249.
[34] A.V. Gusarov, T. Laoui, L. Froyen, V.I. Titov, Contact thermal conductivity of a powder bed in selective laser sintering, International Journal of Heat and Mass Transfer 46 (6) (2003) 1103−1109.
[35] B. Baufeld, O. Van der Biest, R. Gault, Additive manufacturing of Ti-6Al-4V components by shaped metal deposition: microstructure and mechanical properties, Materials & Design 31 (2010) S106−S111.
[36] Q.C. Liu, J. Elambasseril, S.J. Sun, M. Leary, M. Brandt, P.K. Sharp, The effect of manufacturing defects on the fatigue behaviour of Ti-6Al-4V specimens fabricated using selective laser melting, Advanced Materials Research 891 (2014) 1519−1524.
[37] J.P. Kruth, L. Froyen, J. Van Vaerenbergh, P. Mercelis, M. Rombouts, B. Lauwers, Selective laser melting of iron-based powder, Journal of Materials Processing Technology 149 (1−3) (2004) 616−622.
[38] G. Adam, D. Zimmer, Design for additive manufacturing—element transitions and aggregated structures, CIRP Journal of Manufacturing Science and Technology 7 (1) (January 2014) 20−28.
[39] M. Leary, L. Merli, F. Torti, M. Mazur, M. Brandt, Optimal topology for additive manufacture: a method for enabling additive manufacture of support-free optimal structures, Materials & Design 63 (November 2014) 678−690.
[40] M. Leary, M. Babaee, M. Brandt, A. Subic, Feasible build orientations for self-supporting fused deposition manufacture: a novel approach to space-filling tesselated geometries, Advanced Materials Research 633 (2013) 148−168.
[41] D. Thomas, The Development of Design Rules for Selective Laser Melting, 2010.
[42] SLM Solutions, SLM Material Data − SLM 250 HL, 2012.

[43] A.B. Spierings, M. Schneider, R. Eggenberger, Comparison of density measurement techniques for additive manufactured metallic parts, Rapid Prototyping Journal 17 (2011) 380−386.
[44] ASTM Standard E9-09, Standard test methods of compression testing of metallic materials at room temperature, Annual Book of ASTM Standards 3.01 (1) (2012) 92−100.
[45] C. Yan, L. Hao, A. Hussein, D. Raymont, Evaluations of cellular lattice structures manufactured using selective laser melting, International Journal of Machine Tools and Manufacture 62 (November 2012) 32−38.
[46] O. Cansizoglu, O. Harrysson, D. Cormier, H. West, T. Mahale, Properties of Ti-6Al-4V non-stochastic lattice structures fabricated via electron beam melting, Materials Science and Engineering: A 492 (1−2) (September 2008) 468−474.
[47] M.H. Elahinia, M. Hashemi, M. Tabesh, S.B. Bhaduri, Manufacturing and processing of NiTi implants: a review, Progress in Materials Science 57 (5) (June 2012) 911−946.
[48] G. Strano, L. Hao, R.M. Everson, K.E. Evans, A new approach to the design and optimisation of support structures in additive manufacturing, International Journal of Advanced Manufacturing Technology 66 (9−12) (2012) 1247−1254.
[49] D. Thomas, The Development of Design Rules for Selective Laser Melting, University of Wales Institute (2010). Cardiff.

Laser additive manufacturing of ceramic components: materials, processes, and mechanisms

6

Y. Hagedorn
Aconity3D, Aachen, North Rhine-Westphaila, Germany

6.1 Introduction

Additive manufacturing (AM) methods have attracted interest in the field of product development because of their extended capabilities compared with conventional production methods. Main advantages of AM are the fast and tool-less generation of complex net-shaped geometries. One drawback in the industrial dissemination of these AM techniques, however, is the limited choice of applicable materials.

However, the rising demands of modern engineering disciplines require superior material strength and thermal and wear resistance. Material characteristics such as biocompatibility and esthetics are required for various medical applications. Ceramics especially are capable of fulfilling all these increased demands. Limitations on the geometry and shrinking during the conventional sintering process hinder the use of these high-strength ceramics in various applications. In addition, High costs are generated during the manufacturing process by conventional production methods such as milling as a result of high tool wear and little material yield. These limitations may be overcome by using AM for ceramics. This approach allows for layer-wise generation of complexly shaped components with high densities and material strengths. With regard to this issue, various AM techniques for processing ceramics are currently developed and partially industrially applied. Approaches for additive manufacturing of ceramics exist, but their use depends on the applied material and AM technique, however, some are readily applied in industrial applications.

6.2 Ceramic materials and conventional fabrication

Technical ceramics are mainly classified into oxides, carbides, and nitrides, as depicted in Fig. 6.1.

Oxides represent the widest applied ceramic family, and aluminum oxide (Al_2O_3) is the most important structural ceramic with applications as electric insulators and biocompatible medical devices, as well as technical uses resulting from its high chemical and thermal resistance [1,2]. Oxides are also applied in lambda sensors (ZrO_2), high-temperature shielding ($Al_2O_3TiO_2$), crucibles (MgO), and actuators

Laser Additive Manufacturing. http://dx.doi.org/10.1016/B978-0-08-100433-3.00006-3
Copyright © 2017 Elsevier Ltd. All rights reserved.

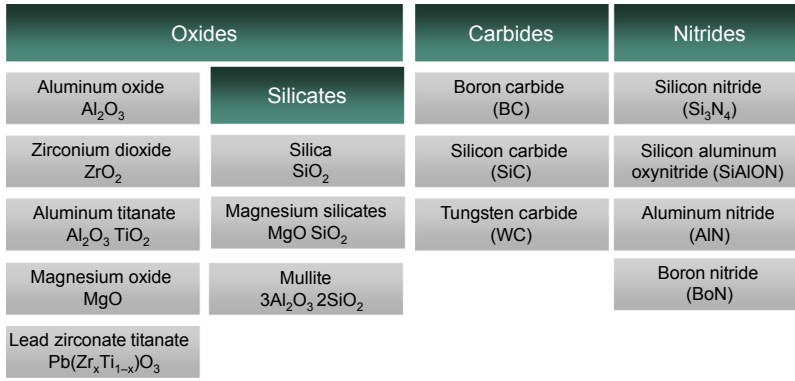

Figure 6.1 Commonly applied technical ceramics (extract).

$(Pb[Zr_xTi_{1-x}])O_3$. For these applications their second-order electrical conductivity at elevated temperatures, high resistivity to thermal shocks, and piezoelectric effect are exploited. One subcategory of oxides are silicates, with applications in the glass industry (SiO_2), as food additives ($MgOSiO_2$), and as porcelain ($3Al_2O_32SiO_2$).

Nitrides and carbides exhibit high strength, hardness, thermal stability (BC, WC, Si_3N_4, SiAlON, BN) (see Fig. 6.1 for abbreviations), and semiconductivity (SiC), qualifying their use in cutting tools and for waver production. Piezoelectric capabilities (AlN) allow for their application as radiofrequency filters in the telecom industry.

Ceramics are difficult to process with conventional manufacturing methods such as milling and casting because of their comparatively high hardness and melting temperatures. As a consequence, most ceramic components are attained by applying multiple treatments, as schematically depicted in Fig. 6.2.

Thus, after the initial step of powder synthesis, basic or complex geometries are created in the master forming process; an optional soft machining step follows.

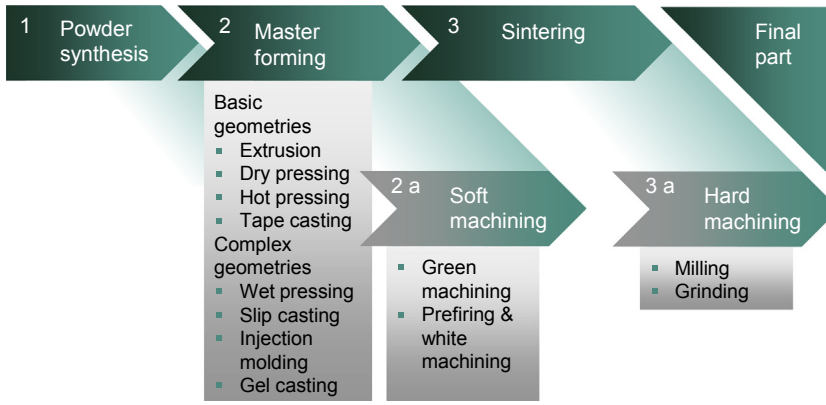

Figure 6.2 Schematic illustration of conventional manufacturing routes for ceramics.

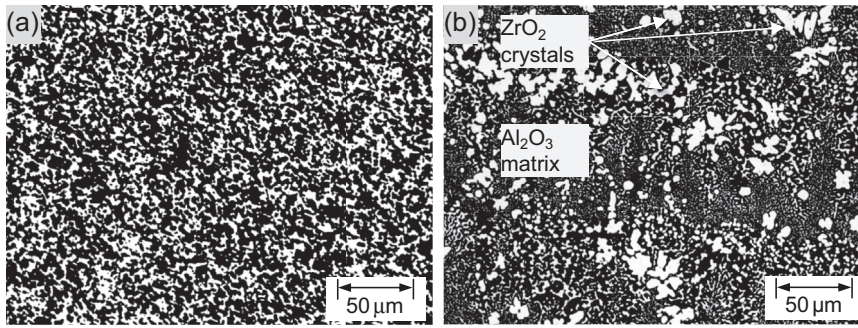

Figure 6.3 Microstructure of ceramic composite with an Al_2O_3 matrix (*black*) and ZrO_2 crystals (*bright*) [3]: (a) sintered material; (b) melt-grown material.

Sintering yields a dense structure that may be subject to further hard machining before the final part is achieved.

The melting temperature of the material components is not exceeded during sintering, becoming dense by means of diffusion processes that are dependent on pressure, temperature, and time. A sintered microstructure is distinguished by a homogenously distributed grain size compared with melt-grown microstructures, which exhibit dendritic crystals; an example is shown in Fig. 6.3 for an Al_2O_3–ZrO_2 composite [3].

Different microstructures have a crucial impact on macroscopic characteristics such as wear resistance and high-temperature creep in favor for melt-grown ceramics [4].

6.3 AM processes for ceramics

Typically, ceramics can be additively manufactured by means of *indirect* and *direct manufacturing* routes, as depicted in Fig. 6.4.

Accordingly, for indirect manufacturing, AM technologies are applied for the master forming process, resulting in a green body. Similar to conventional manufacturing routes, a dense structure is achieved by debinding and final sintering, before optional post-processing provides the final finish. Conventional AM techniques may also be applied to fabricate molds for the traditional preparation of ceramics by means of gel casting or slip casting.

Figure 6.4 Schematic illustration of two different manufacturing routes for preparing ceramics by means of additive manufacturing.

Further, AM techniques yield the possibility of direct manufacturing of ceramics. At this the steps of master forming and sintering are combined, and thus shrinkage due to final densification is avoided.

6.3.1 Indirect laser-based additive manufacturing techniques for ceramics

Indirect AM techniques exploit the presence of a fugitive polymer-based binder that is heavily loaded with ceramic filler material, yielding a green body suitable for handling and further processing. The applicable materials comprise oxides, nitrides, borides, and silicates, provided that the ceramic filler material does not interfere with the laser-based processing of the polymer-based binder. Final densification is accomplished by conventional sintering, and mechanical strengths comparable to those achieved with conventional manufacturing techniques such as gel casting or injection molding can be achieved. The most prominent laser-based AM techniques for generating such presintered green bodies are *stereolithography (STL)*, *laminated object manufacturing (LOM)*, *indirect selective laser sintering (SLS)*, and *layer-wise slurry deposition (LSD)*.

6.3.1.1 Stereolithography

STL is based on exposure of an ultraviolet-curing photopolymer (resin) that is deposited layer-wise by a sweeper before the cross section is scanned by a focused laser beam according to three-dimensional (3D) computer-assisted design3D (CAD) data. Typical layer thicknesses of 5−20 μm are generated by a downward movement of the build platform. Because overhangs are not supported by the slurry, additional supporting structures are necessary to produce complex parts.

The basic setup for STL is illustrated schematically in Fig. 6.5.

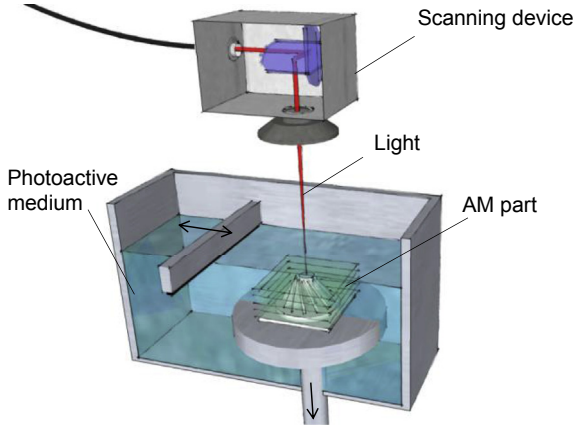

Figure 6.5 Schematic illustration of the stereolithography process. *AM*, additive manufacturing.

Patented in 1986 [5], STL represents one of the first AM methods used for manufacturing 3D objects. The technology was commercialized by 3D Systems [6] in the late 1980s and has since been subject to constant advancements concerning the scope of processable materials [7,8] and the hardware [9].

Early investigations of STL for ceramics show that the final density is crucially affected by the content of ceramic particles loaded into the polymer resin. Ceramic loading is supposed to be in the range of 45−70 vol% [8,10]. Such high solid loading increases the viscosity of the resin to values above 3000 mPa/s, indicating the threshold for proper layer deposition. In addition, for solid loadings, the refractive index of the slurry is increased, which implies a severe effect on the photocuring ability and curing depth. This has crucial implications on defects such as delamination and porosity. The scattering of the incident light at the surface of the solid particles also decreases the dimensional accuracy of ceramic parts produced via STL [10−12].

As a consequence, intense research has studied slurry development for the ceramic STL process, focusing on both the rheological slurry behavior and the scope of ceramic filler material. Toward this purpose, investigations of processing slurries with a solid loading of Al_2O_3 [7−16], ZrO_2 [8,16], and SiO_2 [10,17] have been conducted. For medical applications, bioglass, β-tricalcium phosphate, and hydroxyapatite (HA) have been investigated [7,8]. The flexural strength of the sintered parts is comparable to that of uniaxially pressed ceramics, yielding a strength of ∼400 MPa for Al_2O_3 and >1100 MPa for ZrO_2 and achieving relative densities of more than 99% after full densification. The dimensional accuracy of the green parts is typically about 200 μm before sintering [12]. The sintered parts, however, yield anisotropic shrinkage between 15% and 25%, which naturally limits the dimensional accuracy and complexity of the final part and may also cause cracks to form.

A recent study about the main factors influencing fabrication accuracy identified processing parameters such as hatch spacing and layer thickness as having a major impact during STL, whereas the drying process and sintering temperature have a major impact during post-processing. The surface roughness has been identified as depending on the inclination angle caused by the step effect, and Ra values range between 2 and 15 μm [17].

Among established AM techniques, STL yields high surface qualities, which also qualifies this process for micro-STL [29] and other high-tech applications such as functional heating bodies used for the Mars rover *Curiosity*, launched by the NASA in 2011 [18]. Commercial fabrication of functional parts for biomedical, luxury, and technical applications are provided by contractors such as 3DCeram [19].

6.3.1.2 Selective laser sintering

SLS was invented at the University of Texas at Austin and patented by Carl Deckard in 1989 [20]. During processing, thin layers of powder material <100 μm are repetitively deposited by a wiper onto the build platform before the layer information is selectively sintered according to the 3D CAD data, as schematically depicted in Fig. 6.6.

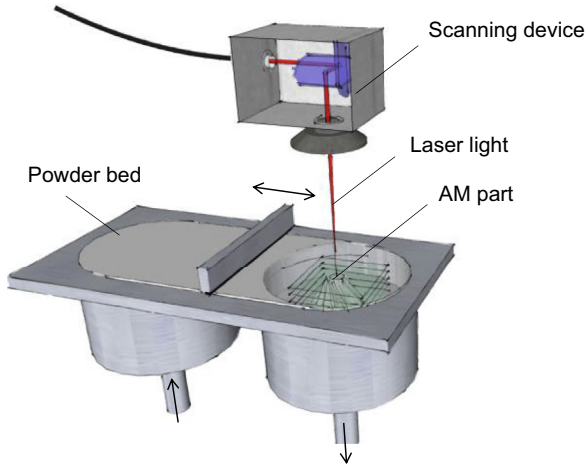

Figure 6.6 Schematic illustration of the selective laser sintering process. *AM*, additive manufacturing.

Early studies by Bourell et al. [21] discuss the different consolidation mechanisms of viscous flow and low-melting-point phases during laser processing for both metals and ceramics. Depending on the applied raw material, SLS is categorized into *direct* and *indirect SLS*: the latter exploits the presence of a fugitive binder with low melting point for consolidation of the green part. Post-processing by thermal treatment or infiltration yields the final dense parts.

Indirect SLS exploits the presence of a sacrificial binder with low melting point, which serves as a matrix phase, drastically improving the densities of the green parts compared with direct SLS. Because the high-melting phase is not thermally affected, silicates and nitrides may also be processed without dissolving, achieving full density and compensating for shrinkage after post-heat treatment and infiltration with pure silicon (Si) [22,23]. The fugitive binder also allows for elastic deformation during laser sintering, preventing crack formation in the ceramic part. For producing highly dense structural ceramics, however, the green density of ceramic parts is limited to the packing density of the powder bed and may reach ~50%. Early investigations of SLS for Al_2O_3 yielded structures with an interconnected porosity of 50% after debinding and sintering, resulting in flexural strengths of 2−8 MPa [24]. To increase the strength, extensive research has been launched to make the green parts more dense in any post-processing steps applied.

Investigations by Deckers et al. [25] resulted in increasing the density of the initial green body from 48% to 71% by infiltrating the prefired part with an Al_2O_3 slurry before subsequent sintering; this increased density is accompanied by a linear shrinkage of 23%. Further improvements in the final density (to 88%) were achieved by processing Al_2O_3 particles in the submicron domain for improved sintering. The flexural strength of such structures is still limited to 255 MPa, however, restricting the field of applications [26].

6.3.1.3 Layer-wise slurry deposition

LSD was introduced to overcome the drawback of insufficient densities of SLS parts as a result of unpacked powder layers. This process exploits the increased packing density of ceramic slurries, which are loaded with up to 87 wt% solid particles in the submicron domain for increased sintering dynamics [27]. However, rapid contraction of the slurry during laser processing causes crack formation [28]. Hence an additional drying step to decrease the liquid content to values beneath 3 wt% before laser processing is necessary [29]. The range of applicable materials for this technology varies from HA for bone scaffolds [30], Al_2O_3/SiO_2 blends for manufacturing dental restorations [27,31], and porcelain for structural low-strength ceramics [32–34]. Typical densities of up to 97% may be achieved after sintering, achieving mechanical properties close to the ones obtained via conventional manufacturing techniques.

Further work toward additively manufacturing complex 3D structures out of ceramics is based on slight alterations to the LSD process discussed above. Yen [35] applied a ceramic slurry of 40–41 wt% SiO_2, deposited in thin (30 μm) layers, before heating to 1200°C; this caused the whole layer to gel. Subsequent scanning of the two-dimensional information by a laser beam renders only the scanned sections water insoluble. Washing off the remaining gel yields green parts with the potential for improved densities and surface qualities compared with conventional LSD parts [35].

Similarly, Tang et al. [36] applied LSD to an aqueous slurry with a solid loading of >50 wt% Al_2O_3. By adding a polymer coating to the ceramic particles, the density of the final sintered parts increased to 98%, thus yielding flexural strengths of 363.5 MPa.

6.3.1.4 Laminated object manufacturing

LOM allows for additively building parts by stacking subsequent layers of a material sheets on top of each other. Each layer is cut to its shape by a knife or laser beam, according to the 3D CAD data, before it is laminated by a thermoplastic adhesive on top of the previous layer. The adhesive is activated by a heated roller, which laminates the layers at a temperature between 60°C and 80°C and a pressure of 10–30 MPa [37]. Excessive material is used as supporting structures for overhangs, inhibiting the generation of internal structures and cavities. During fabrication, excessive material is sliced and cubed to facilitate manual extraction of the part. Still, post-processing is time intensive and often requires special tools, rendering the production of filigree structures inadequate for this technology. Because LOM is a hybrid between additive and subtractive processing methods, a relatively low material yield is achieved. Green ceramic tapes are typically used for LOM of ceramics; hence, ceramic parts are subject to post-processing steps such as debinding and sintering.

Fig. 6.7 gives a schematic illustration of the LOM process.

The first investigations of LOM of complex-shaped ceramics were conducted by Griffin et al. [38] using Al_2O_3 tapes as the raw material; they achieved densities

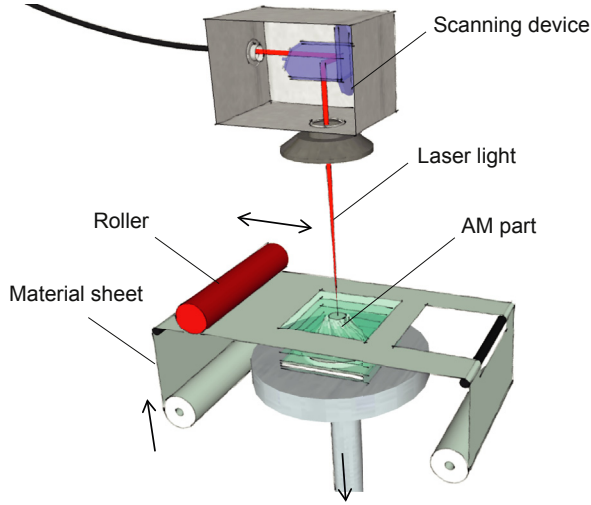

Figure 6.7 Schematic illustration of the laminated object manufacturing process. *AM*, additive manufacturing.

of ~99% after post-processing. The mechanical properties are comparable to those of conventionally pressed Al_2O_3 ceramics, showing a flexural strength of ~310 MPa, a Vickers hardness of 20.1 GPa, and a fracture toughness of ~4 MPa $\sqrt{m}$, while having an overall shrinkage of 14.1% [38].

Investigations into other materials include the manufacturing of ZrO_2 and Al_2O_3–ZrO_2 compounds [39], silicates such as SiC [40] and ceramic composites such as Si/SiC [41].

The density of the sintered ceramic part greatly depends on the lamination pressure and the porosity of the green ceramic tape, reaching up to 57% [42]. Hence a strong anisotropy in the sintered parts, resulting in a decrease of the flexural strength by up to 50% in lateral directions compared with the z-direction, prevail, although this renders the part susceptible to crack formation [43]. This drawback limits the technical applications for LOM and is overcome by the development of cold pressure laminated object manufacturing, allowing for objects to be manufactured at room temperature with decreased pressures, avoiding inhomogeneous densification and rendering complex-shaped micro electron mechanical systems possible [37].

The surface qualities of LOM parts greatly depend on the thickness of the ceramic tapes, which typically range from 190 to 200 μm, causing a distinct step effect. Hence surface qualities reach values between 2 and60 μm for Ra, depending on the surface angle and the layer thickness [44]. By applying two-step cutting before and after the lamination of each layer, the step effect and the decubing of the manufactured part are drastically reduced [45]. Further developments have also included investigations of LOM on curved surfaces [46], rendering this AM technology suitable for the economic production of a large scope of different applications.

6.3.1.5 Conventional AM techniques for mold fabrication

Because the conventional AM techniques discussed above are not capable of directly producing high-strength ceramics with high accuracy, AM manufacturing methods are also applied to create lost molds for conventional gel casting. The applied AM techniques include conventional ones, such as SLS [47], STL [48], and variations between additive and subtractive processes like mold shape deposition manufacturing, which additively builds up a wax mold before it is cut into a shape [49]. Combining AM with conventional gel casting allows for complex structures to be created with mechanical properties comparable to those of structures resulting from conventional manufacturing methods.

6.3.2 Direct laser-based AM techniques for ceramics

Direct laser-based AM techniques combine the steps of *forming* and *densification* by directly generating functional parts without the need for post-heat treatment for final densification. Such techniques are *direct SLS*, which generates only porous ceramic structures directly from the ceramic raw material, and *selective laser melting (SLM)*, which is capable of generating dense melt-grown structures.

6.3.2.1 Direct selective laser sintering

Densities of the green parts produced by direct SLS are in the range of the packing density of the powder bed [24]. Small particles of a medium diameter (<10 μm) increase the packing density and improve sintering, but agglomeration impedes an even powder deposition, which also is a precondition for high densities. Hence SLS of ZrO_2 yields densities up to 56%, which cannot be further densified by post-heat treatment or infiltration because the structures are already sintered and the porosity is not interconnected. Rapid temperature–time cycles of $\sim 10^4$–10^6 K/s further weaken the structure by forming microcracks as a result of thermally induced stresses [50]. Similarly, in situ reaction sintering of yttria (Y_2O_3) stabilized ZrO_2 with the addition of 20 wt% aluminum and/or Al_2O_3 in variable atmospheres of oxygen and argon led to parts with large pores (>100 μm) along with the appearance of cracks [51]. Consequently, insufficient mechanical properties restrict this technology to foundry applications [52] requiring post-processing because of typical surface roughness of $Ra = 12$ μm [53].

One approach for improving densities and surface quality is laser microsintering, introduced by Regenfuss et al. [54] in 2003. This approach deposits powders of a medium diameter (≤ 10 μm) in concordant layer thicknesses to manufacture complex microstructures out of oxides (SiO_2, Al_2O_3), silicates (SiC), and suboxides (silicon monoxide, SiO) [55]. The energy input is delivered in the q-switched regime, partially melting the processed material and achieving theoretical densities of up to 98%; the minimal resolution is improved from 150 to 80 μm for Al_2O_3 parts, exhibiting a surface roughness of $Ra = 10$ μm [56]. By applying two wiper systems, this approach shows great potential for the production of multimaterial parts.

However, the build time and the formation of cracks remain central issues for laser microsintering of functional ceramics.

6.3.2.2 Selective laser melting

Another approach for direct manufacturing of high-strength oxide ceramics is SLM, which was initially introduced by Meiners [57] in the mid-1990s for processing metallic materials without the addition of any binder. In this process the raw material is completely melted by means of a focused laser beam, yielding relative part densities of up to 100%.

Ceramics that sufficiently absorb the applied laser source and also exhibit a melt pool during ambient pressure conditions can also be processed via SLM. Because of their brittle nature, however, most ceramics are susceptible to thermally induced crack formation. Accordingly, initial studies for SLM of ZrO_2 specimens show severe microcracking, which reduces flexural strength to values <20 MPa. Post-heat treatment and infiltration with SiO_2 allows these values to increase to >150 MPa [58].

Further, application of high-temperature preheating above 1700°C reduces thermal tension during selective melting and thus suppresses microcracks. This yields a flexural strength of up to 1100 MPa for a eutectic Al_2O_2/ZrO_2 mixture, which is comparable to that of conventionally sintered specimens. Because homogenous preheating is a precondition, these results are limited to specimens $<3-10$ mm in height, drastically reducing the field of possible applications. For demonstration purposes, filigree ceramic dental restorations have been manufactured, yielding a surface roughness value of $Rz < 70$ µm and a dimensional accuracy of ± 150 µm. These results, and poor build-up rates of <0.2 mm^3/s, are attributed to the preheating and render SLM of $Al_2O_3-ZrO_2$ alloys insufficient for industrial application with the current state of the art [3,58].

6.3.2.3 Laser-engineered net shaping

Balla et al. [59] used laser-engineered net shaping technology to additively generate structures from Al_2O_3. The process resembles laser cladding, with powder material being added to a laser-induced melt pool by a nozzle. The work discusses grain size as dependent on the temperature gradient and the cooling rate. The densities of the as-fabricated parts reach 94% but are further increased to 97% by post-heat treatment. Some specimens are crack free and reach the strength of conventionally manufactured parts. Dimensional resolution, however, is limited to the spot size of the applied laser (1.5-mm diameter), with anisotropic deviations in the achievable resolution of 10% and 17% in the lateral and build directions, respectively [59].

6.4 Applications of additive manufactured ceramics

Ceramics can be applied in nearly all engineering fields and are chosen based on their material properties. Accordingly, for the aerospace and automotive industries, physical properties such as low thermal conductivity and high thermal resistivity, combined with low specific material density, are exploited for use in engine components and

heat-resistant tiles for space shuttles. The high specific material strength is also exploited for ballistic shields used for both military applications and to protect aircrafts from space debris. Because of the possibility of generating complex parts in small lot sizes, AM yields exceptional potential in extending these fields of applications.

Ceramics are also of great interest in biomedical applications because of their biocompatible nature. A mixture of β-tricalcium phosphate and polylactid in particular features biodegradability that, in combination with an interconnected porosity, can fully restore bone defects [60,61]. Such an implant manufactured via indirect SLS is shown in Fig. 6.8.

Furthermore, high resistance to wear allows ceramics to be applied as, for example, acetabular cups in hip prostheses, and their favorable esthetics compared with metals makes them useful as dental restoration frameworks. The natural similarity of HA to human bone also allows it to be applied as a bone scaffold, minimizing stress shielding accompanied by bone reduction, which is typically examined for conventional titanium implants. Because most medical applications require a lot size of one, AM shows great potential in the efficient manufacturing of patient-specific solutions.

In electronics, depending on the type applied, ceramics can be used as insulators, transducers, capacitors, and integrated circuit packages. These applications are mostly not prone to high mechanical load, and therefore indirect AM techniques for manufacturing complex structures also show great potential.

Further, Engineering ceramics mostly exploits their high mechanical strength, low thermal expansion at exceptionally high temperature, wear resistance, or optical properties. However, for applications as bearings made of Si_3N_4, disc brakes made of SiC, and optical components made of sapphire (Al_2O_3), available AM techniques cannot be applied yet because of the ceramics' insufficient strength and poor surface qualities.

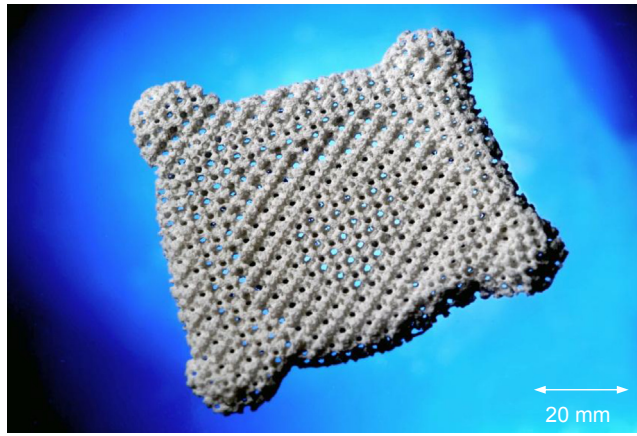

Figure 6.8 Photograph of a β-tricalcium phosphate/polylactid biodegradable bone implant produced via indirect selective laser sintering.
From L. Jauer, Fertigung von Bioresorbierbaren Implantaten mittels Selective Laser Melting, Fraunhofer Institute for Laser Technology, 2011; S. Hoeges, Entwicklung des Selective Laser Melting für die Verarbeitung bioresorbierbarer medizinischer Werkstoffe (Ph.D. thesis), RWTH-Aachen, 2010.

Furthermore, simple geometries and large lot sizes hinder the economic application of AM for these products.

The increased freedom in the complexity of 3D structures opens up new possibilities for manufacturing complex molds for conventional casting processes. Molds may be directly produced from porous ceramics using conventional AM techniques such as SLS [62–64] or LSD [65]. This allows for casting metals with increasingly complex internal structures and interconnected porosity, as is the case for orthopedic implants [62]. Approaches by Das [66] and Halloran et al. [67] created ceramic cores for investment casting of turbine blades. In these approaches, a ceramic-loaded resin is photocured by laser light applied through SLS or by continuous projection of high-resolution bitmaps by means of large-area maskless photopolymerization [68].

Still, for indirect AM techniques, post-heat treatment and complete densification are accompanied by severe shrinkage of up to 20%, depending on the solid loading of the slurry; this may cause cracks to form. Hence the final complexity of ceramic parts remains restrained by variations in the wall thickness, which causes different amounts of shrinkage and subsequent crack formation. This still limits the use of complex ceramics for high-strength applications.

6.5 Conclusion and outlook

Table 6.1 summarizes the medium dimensional accuracies, surface roughness, maximum densities, flexural strength, and build rate for different indirect and direct laser-based AM techniques.

Accordingly, the different techniques differ largely in their process characteristics. Indirect laser-based AM techniques yield comparatively high densities accompanied by high flexural strengths after post-heat treatment. Also, the build rates are

Table 6.1 Summary of main process characteristics of the different laser-based additive manufacturing techniques

AM technique	Dimensional accuracy (μm)	Surface roughness, Ra (μm)	Maximum density (%)	Flexural strength	Build rate (mm^3/s)
Indirect techniques (post-heat treatment required)					
STL	200 [12]	2–15 [17]	99 [12]	High	>50
LSD	>200	10–12 [53]	98 [36]	Medium	<20
LOM	200 [69]	2–60 [44]	99 [38]	Medium	>200
Direct techniques					
SLS	150 [56]	10–12 [56]	98 [56]	Low	>50
SLM	150 [3]	~16 [3]	>99 [58]	High	<20
LENS	>200 [59]	10–30	97 [59]	High	>200

AM, additive manufacturing; *LENS*, laser-engineered net shaping; *LOM*, laminated object manufacturing; *LSD*, laser-wise slurry deposition; *SLM*, selective laser melting; *SLS*, selective laser sintering; *STL*, stereolithography.

comparatively high because of the maturity of most polymer-based AM techniques, which represent the basis for most indirect laser-based AM techniques. Final densification by means of post-heat treatment, however, yields the caveat of anisotropic shrinkage in the *z*- and lateral *x*- and *y*- dimensions as a result of layer-wise build-up. Anisotropic shrinkage may negatively influence the dimensional accuracies of final parts and cause crack formation.

Table 6.2 provides an overview of the characteristics of the established laser-based AM techniques for ceramics.

Table 6.2 Characteristics of the established laser-based additive manufacturing techniques for ceramics

AM technique	Initial material	Advantages (✓) and disadvantages (✗)
Indirect techniques (post-heat treatment required)		
STL (Solidification by laser beam/ultraviolet radiation)	Photocurable resin loaded with ceramic particles	✓ High accuracy ✓ Low surface roughness ✗ Supporting structures
LOM (Lasercutting and adhesive bonding)	Casted tapes loaded with ceramic particles	✓ No supporting structures ✗ Anisotropy ✗ Surface quality ✗ Limited complexity
LSD (Solidification/ sintering by laser beam)	Ceramic slurry with optional addition of polymer binder	✓ High strength before sintering ✗ Low productivity
Direct techniques		
SLS (Sintering of ceramic powder bed)	Ceramic powder with optional addition of binder material	✓ Complex geometries ✓ No supporting structures ✗ High surface roughness
SLM (Melting of ceramic powder bed)	Ceramic powder	✓ High mechanical strength ✗ Low productivity ✗ High surface roughness ✗ Limited part sizes
LENS (Melting of ceramic powder stream by means of a nozzle)	Ceramic powder	✓ High mechanical strength ✓ Applicable on complex surfaces ✓ High productivity ✗ Low density ✗ High surface roughness

AM, additive manufacturing; *LENS*, laser-engineered net shaping; *LOM*, laminated object manufacturing; *LSD*, laser-wise slurry deposition; *SLM*, selective laser melting; *SLS*, selective laser sintering; *STL*, stereolithography.
Data from A. Gebhardt, Grundlagen des rapid prototyping, RTejournal - Forum für Rapid Technologie 8 (2011) 1−5, http://www.rtejournal.de/ausgabe8/aufsaetze/Grundlagen/.

Thus different AM techniques are suited for diverging applications. For applications that do not exploit the ceramic material's full strength but require rather smooth surface qualities, STL is a good approach because one can benefit from a mature technology. On the contrary, for applications that exploit ceramics' high material strength, direct laser-based AM techniques are a good approach. For example, LENS allows for complex structures to be repaired because it uses a nozzle-based approach, which is capable of dispensing molten ceramic material onto complex surfaces if attached to a robotic arm. Approaches such as SLM allow high mechanical strength to be generated directly from the AM process, albeit at the cost of surface quality and overall size of generated parts because of the need for homogenous, high-temperature preheating.

In conclusion, AM of ceramics is still a fairly new research topic, with many promising approaches. Generating high-strength structures either by indirect or direct AM techniques is on the verge of having industrial applications and shows great potential in extending the scope of applicable ceramics for highly demanding medical and engineering applications.

References

[1] J. Cawley, W. Lee, Oxide Ceramics, Vol. 11 of Materials Science and Technology, Wiley-VCH, Weinheim, 2005.
[2] K.D. Linsmeier, Technische Keramik, Landsberg: Moderne Industrie, 2010.
[3] Y. Hagedorn, Additive Manufacturing of High Performance Oxide Ceramics via Selective Laser Melting (Ph.D. thesis), RWTH-Aachen, 2013.
[4] J. Llorca, V.M. Orera, Directionally solidified eutectic ceramic oxides, Progress in Materials Science 51 (2006) 711−809.
[5] C.W. Hull, Apparatus for Production of Three-Dimensional Objects by Stereolithography (U.S. Patent 4.575.330), 1986.
[6] 3D Systems. http://www.3dsystems.com/, 2014.
[7] R. Felzmann, S. Gruber, G. Mitteramskogler, P. Tesavibul, A.R. Boccaccini, R. Liska, J. Stampfl, Lithography-based additive manufacturing of cellular ceramic structures, Advanced Engineering Materials 1 (2012) 1−7.
[8] C. Chaput, T. Chartier, Fabrication of ceramics by stereolithography, RTejournal − Forum für Rapid Technologie 4 (2007) 1−5. http://www.rtejournal.de/ausgabe4/1163.
[9] S. Gruber, J. Stampfl, R. Felzmann, S. Springer, R. Liska, Lithographiebasierte fertigung keramischer bauteile, RTejournal − Forum für Rapid Technologie 8 (2011) 1−5. http://www.rtejournal.de/ausgabe8/3027.
[10] M.L. Griffith, J.W. Halloran, Freeform fabrication of ceramics via stereolithography, Journal of the American Ceramic Society 79 (10) (1996) 2601−2608.
[11] C. Hinczewski, S. Corbel, T. Chartier, Ceramic suspensions suitable for stereolithography, Journal of the European Ceramic Society 18 (6) (1998) 583−590.
[12] T. Chartier, C. Chaput, F. Doreau, M. Loiseau, Stereolithography of structural complex ceramic parts, Journal of Materials Science 37 (2002) 3141−3147.
[13] G.A. Brady, J.W. Halloran, Stereolithography of ceramic suspensions, in: Proceedings of the 6th International Conference on Rapid Prototyping and Manufacturing, 1997.

[14] C. Provin, S. Monneret, Complex ceramic-polymer composite microparts made by microstereolithography, IEEE Transactions on Electronics Packaging Manufacturing 25 (1) (2002) 59−63.
[15] A. Bertsch, S. Jiguet, P. Renaud, Microfabrication of ceramic components by microstereolithography, Journal of Micromechanics and Microengineering 14 (2004) 197−203.
[16] A. Licciulli, C.E. Corcione, A. Greco, V. Amicarelli, A. Maffezzoli, Laser stereolithography of ZrO_2 toughened Al_2O_3, Journal of the European Ceramic Society 25 (2005) 1581−1589.
[17] X. Tian, D. Li, Z. Chen, W. Zhou, Study on the fabrication accuracy of ceramic parts by direct stereolithography, Virtual and Physical Prototyping 1 (2012) 1−8.
[18] Technology Assessment and Transfer Inc. (TA&T), CMD − Ceramic Stereolithography, 2012. http://www.techassess.com/technologies/ceramic-micro-devices/ceramic-stereolithography.
[19] 3DCeram, Ceramic Customized Implant, 2012. http://3dceram.com/wp-content/uploads/2010/07/ceram_book.pdf.
[20] C.R. Deckard, Method and Apparatus for Producing Parts by Selective Sintering (U.S. Patent 4.863.538, 1), https://utexas.influuent.utsystem.edu/en/publications/selective-laser-sintering-of-metals-and-ceramics.
[21] D.L. Bourell, H.L. Marcus, J.W. Barlow, J.J. Beaman, Selective laser sintering of metals and ceramics, International Journal of Powder Metallurgy (Princeton, New Jersey) 28 (4) (1992) 369−381.
[22] T. Gill, K. Hon, Experimental investigation into the selective laser sintering of silicon carbide polyamide composites, Proceedings of the Institution of Mechanical Engineers, Part B: Journal of Engineering Manufacture 218 (10) (2004) 1249−1256.
[23] R.S. Evans, D.L. Bourell, J.J. Beaman, M.I. Campbell, Rapid manufacturing of silicon carbide composites, Rapid Prototyping Journal 11 (1) (2005) 37−40.
[24] K. Subramanian, N. Vail, J. Barlow, H. Marcus, Selective laser sintering of alumina with polymer binders, Rapid Prototyping Journal 1 (2) (1995) 24−35.
[25] J. Deckers, J.-P. Kruth, K. Shahzad, J. Vleugels, Density improvement of alumina parts produced through selective laser sintering of alumina-polyamide composite powder, CIRP Annals − Manufacturing Technology 61 (1) (2012) 211−214.
[26] Z. Liu, J. Nolte, J. Packard, G. Hilmas, F. Dogan, M. Leu, Selective laser sintering of high-density alumina ceramic parts, in: S. Hinduja, K.-C. Fan (Eds.), Proceedings of the 35th International MATADOR Conference, Springer, London, 2007, pp. 351−354.
[27] A. Gahler, J.G. Heinrich, J. Guenster, Direct laser sintering of Al_2O_3/SiO_2 dental ceramic components by layer-wise slurry deposition, Journal of the American Ceramic Society 89 (10) (2006) 3076−3080.
[28] C. Ader, Untersuchungen Zum Lasersintern Keramischer Suspensionen (Ph.D. thesis), RWTH-Aachen, 2006.
[29] J.-P. Kruth, G. Levy, F. Klocke, T.H.C. Childs, Consolidation phenomena in laser and powder-bed based layered manufacturing, Annals of the CIRP 56 (2) (2007) 730−759.
[30] Z. Sadeghian, Laser Sintering of Hydroxyapatite by Layer-Wise Slurry Deposition (Ph.D. thesis), TU Clausthal, 2005.
[31] J. Heinrich, A. Gahler, J. Guenster, M. Schmuecker, J. Zhang, D. Jiang, M. Ruan, Microstructural evolution during direct laser sintering in the Al_2O_3 − SiO_2 − system, Journal of Materials Science 42 (2007) 5307−5311.
[32] J. Guenster, S. Engler, J.G. Heinrich, Forming of complex shaped ceramic products via layer-wise slurry deposition (LSD), Bulletin of the European Ceramic Society 1 (2003) 1−4.

[33] X. Tian, J. Guenster, J. Melcher, D. Li, J.G. Heinrich, Process parameters analysis of direct laser sintering and post treatment of porcelain components using Taguchi's method, Journal of the European Ceramic Society 29 (10) (2009) 1903−1915.
[34] X. Tian, B. Sun, J.G. Heinrich, D. Li, Stress relief mechanism in layer-wise laser directly sintered porcelain ceramics, Materials Science and Engineering: A 527 (2010) 1695−1703.
[35] H.-C. Yen, A new slurry-based shaping process for fabricating ceramic green part by selective laser scanning the gelled layer, Journal of the European Ceramic Society 32 (12) (2012) 3123−3128.
[36] H.-H. Tang, M.-L. Chiu, H.-C. Yen, Slurry-based selective laser sintering of polymer-coated ceramic powders to fabricate high strength alumina parts, Journal of the European Ceramic Society 31 (8) (2011) 1383−1388.
[37] K. Schindler, A. Roosen, Manufacture of 3D structures by cold low pressure lamination of ceramic green tapes, Journal of the European Ceramic Society 29 (5) (2009) 899−904.
[38] C. Griffin, J. Daufenbach, S. McMillin, Solid freeform fabrication of functional ceramic components using a laminated object manufacturing technique, in: H.L. Marcus, J.J. Beaman, J.W. Barlow, D.L. Bourell, R.H. Crawford (Eds.), Solid Freeform Fabrication Symposium, 1994.
[39] C. Griffin, D. Marshall, Rapid prototyping of functional ceramic composites, American Ceramic Society Bulletin 75 (7) (1996) 65−68.
[40] N. Travitzky, H. Windsheimer, T. Fey, P. Greil, Preceramic paper-derived ceramics, Journal of the American Ceramic Society 91 (11) (2008) 3477−3492.
[41] D. Klosterman, R. Chartoff, G. Graves, N. Osborne, A. Lightman, G. Han, A. Bezeredi, S. Rodrigues, Automated fabrication of monolithic ceramics and ceramic matrix composites (CMCs) using a novel rapid prototyping method, in: 22nd Annual Conference on Composites, Advanced Ceramics, Materials, and Structures: A, 1998.
[42] M. Cho, A. Roosen, A. Stiegelschmitt, D. Schwanke, F. Bechtold, In-situ shrinkage measurements of LTCC multilayers by means of an optical dilatometer, in: Key Engineering Materials I, Euro Ceramics VII, 2002, pp. 1281−1284.
[43] Y. Zhang, X. He, S. Du, J. Zhang, Al_2O_3 ceramics preparation by LOM (laminated object manufacturing), The International Journal of Advanced Manufacturing Technology 17 (2001) 531−534.
[44] D. Ahn, J.-H. Kweon, J. Choi, S. Lee, Quantification of surface roughness of parts processed by laminated object manufacturing, Journal of Materials Processing Technology 212 (2) (2012) 339−346.
[45] I. Cho, K. Lee, W. Choi, Y.-A. Song, Development of a new sheet deposition type rapid prototyping system, International Journal of Machine Tools and Manufacture 40 (12) (2000) 1813−1829.
[46] D. Klosterman, R. Chartoff, N. Osborne, G. Graves, A. Lightman, G. Han, A. Bezeredi, S. Rodrigues, Development of a curved layer LOM process for monolithic ceramics and ceramic matrix composites, Rapid Prototyping Journal 5 (2) (1999) 61−71.
[47] K. Cai, D. Guo, Y. Huang, J. Yang, Solid freeform fabrication of alumina ceramic parts through a lost mould method, Journal of the European Ceramic Society 23 (6) (2003) 921−925.
[48] H. Wu, D. Li, Y. Tang, B. Sun, D. Xu, Rapid fabrication of alumina-based ceramic cores for gas turbine blades by stereolithography and gelcasting, Journal of Materials Processing Technology 209 (2009) 5886−5891.

[49] J. Stampfl, H.-C. Liu, S.W. Nam, K. Sakamoto, H. Tsuru, S. Kang, A.G. Cooper, A. Nickel, F. Prinz, Rapid prototyping and manufacturing by gelcasting of metallic and ceramic slurries, Materials Science and Engineering A334 (2002) 187−192.
[50] P. Bertrand, F. Bayle, C. Combe, P. Goeuriot, I. Smurov, Ceramic components manufacturing by selective laser sintering, Applied Surface Science 254 (2007) 989−992.
[51] I. Shishkovsky, I. Yadroitsev, P. Bertrand, I. Smurov, Alumina-zirconium ceramics synthesis by selective laser sintering/melting, Applied Surface Science 254 (2007) 966−970.
[52] H. Wirtz, Selektives Lasersintern von Keramikformschalen für Giessanwendungen (Ph.D. thesis), RWTH-Aachen, 2000.
[53] F. Klocke, C. Ader, Direct selective laser sintering of ceramics, in: Deutsche Keramische Gesellschaft (Jahrestagung), 2002.
[54] P. Regenfuss, A. Streek, F. Ullmann, C. Kühn, L. Hartwig, M. Horn, R. Ebert, H. Exner, Laser micro sintering of ceramic materials, part 2, Interceram 57 (1) (2008) 6−9.
[55] P. Regenfuss, A. Streek, F. Ullmann, T. Suess, L. Hartwig, M. Horn, C. Kühn, R. Ebert, H. Exner, Laser micro sintering of ceramics − reaction models and results, Ceramic Forum International/Ber. DKG 85 (13) (2008) 65−72.
[56] H. Exner, P. Regenfuss, R. Ebert, L. Hartwig, A. Streek, S. Kloetzer, H. Horn, Laser-mikrosintern von keramischen materialien, RTejournal − Forum für Rapid Technologie 3 (2006) 1−5. http://www.rtejournal.de/ausgabe3/347?searchterm=kerami.
[57] W. Meiners, Direktes Selektives Laser Sintern Einkomponentiger MetallischerWerkstoffe (Ph.D. thesis), RWTH-Aachen, 1999.
[58] J. Wilkes, Selektives Laserschmelzen zur Generativen Herstellung von Bauteilen aus Hochfester Oxidkeramik (Ph.D. thesis), RWTH-Aachen, 2009.
[59] V.K. Balla, S. Bose, A. Bandyopadhyay, Processing of bulk alumina ceramics using laser engineered net shaping, International Journal of Applied Ceramic Technology 5 (3) (2008) 234−242.
[60] L. Jauer, Fertigung von Bioresorbierbaren Implantaten Mittels Selective Laser Melting, Fraunhofer Institute for Laser Technology, 2011.
[61] S. Hoeges, Entwicklung des Selective Laser Melting für die Verarbeitung Bio-resorbierbarer Medizinischer Werkstoffe (Ph.D. thesis), RWTH-Aachen, 2010.
[62] A. Curodeau, E. Sachs, S. Caldarise, Design and fabrication of cast orthopedic implants with freeform surface textures from 3-D printed ceramic shell, Journal of Biomedical Materials Research 53 (5) (2000) 525−535.
[63] N.R. Harlan, R. Reyes, D.L. Bourell, Building better bones, Foundry Management & Technology 1 (2000) 82−83.
[64] N.R. Harlan, R. Reyes, D.L. Bourell, J.J. Beaman, Titanium castings using laser-scanned data and selective laser-sintered zirconia molds, Journal of Materials Engineering and Performance 10 (4) (2001) 410−413.
[65] T. Krause, S. Engler, J. Guenster, J.G. Heinrich, Process and a Device for Producing Ceramic Molds (U.S. Patent 6.827−988), 2004.
[66] S. Das, Direct Digital Manufacturing of Airfoils via Large Area Maskless Photo-polymerization, 2012. http://ddm.me.gatech.edu/page8/page8.html.
[67] J.W. Halloran, V. Tomeckova, S. Gentry, S. Das, P. Cilino, D. Yuan, R. Guob, A. Rudraraju, P. Shao, T. Wu, T.R. Alabi, W. Baker, D. Legdzina, D. Wolski, W.R. Zimbeck, D. Longd, Photopolymerization of powder suspensions for shaping ceramics, Journal of the European Ceramic Society 31 (2011) 2613−2619.

[68] D. Yuan, K. Kambly, P. Shao, A. Rudrarju, P. Cilio, V. Tomeckoa, Experimental investigations on photocurable ceramic materials systems for large area maskless photopolymerization (LAMP), in: H.L. Marcus, J.J. Beaman, J.W. Barlow, D.L. Bourell, R.H. Crawford (Eds.), Solid Freeform Fabrication Symposium, 2009.
[69] E. Grenda, Printing the Future: The 3D Printing and Rapid Prototyping Source Book, Castle Island Company, 2006. http://books.google.de/books?id= FTeLNAAACAAJ.
[70] A. Gebhardt, Grundlagen des rapid prototyping, RTejournal - Forum für Rapid Technologie 8 (2011) 1−5. http://www.rtejournal.de/ausgabe8/aufsaetze/Grundlagen/.

Powder bed fusion of polymers

7

R. Goodridge[1], *S. Ziegelmeier*[2]
[1]University of Nottingham, Nottingham, United Kingdom; [2]BMW Group, Munich, Germany

7.1 Introduction

Powder bed fusion (PBF) is a subset of additive manufacturing (AM) whereby a heat source (eg, laser, thermal print head) is used to consolidate material in powder form to form three-dimensional (3D) objects. The heat source is applied to particles contained within a powder bed, which gradually indexes down as each layer is completed and new powder is spread over the build area.

PBF techniques share the basic principles of all AM techniques (eg, layer-by-layer fabrication directly from 3D model data) as well as common advantages such as cost-effective customization and reduced assembly. However, polymer PBF processes have a significant advantage over many other AM processes in that they do not require support structures, since overhangs and unconnected islands are supported by the surrounding unfused powder bed (Fig. 7.1). This allows more complex geometries to be produced, as removal of support structures after the build does not need to be considered.

The lack of support structures also means that parts can be stacked freely in the powder bed, increasing the number of parts that can be produced in each build and thus increasing the productivity (Fig. 7.2). However, there are some design limitations in terms of the removal of unfused powder from trapped volumes (eg, enclosed pores) and fine channels. Another advantage of PBF techniques is the wide range of materials that can potentially be processed: Any material that can be melted and resolidified can, in theory, be used with PBF techniques. In practice, however, this is not currently the case; the reasons for this are discussed throughout this chapter.

Laser sintering is currently the most established PBF technique for polymers and is the main focus of this chapter. However, an increasing number of variants have started to emerge, and these are discussed in the final section of this chapter.

7.2 Laser sintering: basic principles

Laser sintering is one of the most common and widely accepted AM process. It produces parts by selectively fusing individual layers of powdered material using a laser (typically a carbon dioxide laser) (Fig. 7.3).

A STL file of the part to be fabricated is sliced into cross-sectional layers. A layer thickness of 100 to 150 μm is commonly used. Powder is spread over the build platform and levelled using a roller, recoating blade or alternative device. Before

Laser Additive Manufacturing. http://dx.doi.org/10.1016/B978-0-08-100433-3.00007-5
Copyright © 2017 Elsevier Ltd. All rights reserved.

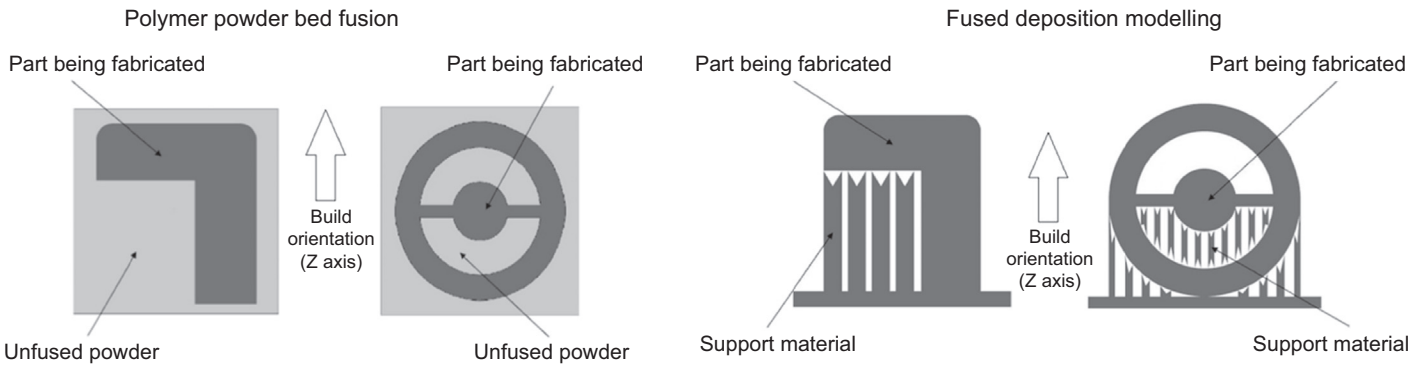

Figure 7.1 Schematic illustrating the ability of polymer powder bed fusion to produce parts with overhangs and unsupported islands without support structures (left) compared with other AM processes, for example, fused deposition modelling (right), in which these structures must be supported during the build process.

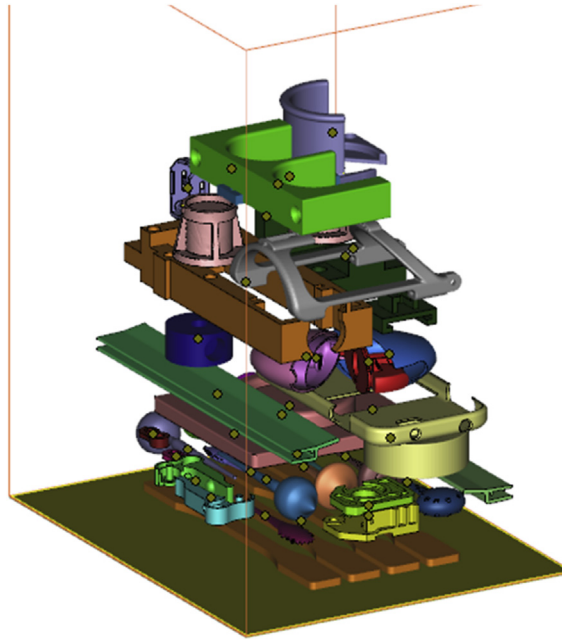

Figure 7.2 A typical laser sintering build set-up consisting of multiple individual parts. Because no support structures are required, parts can be placed freely in the entire build volume without to be connected to the part below.

commencing fabrication of a part or series of parts, the powder bed is normally heated gradually from room temperature to the desired processing bed temperature, typically over a period of 1−2 h, depending on the final temperature to be reached. This is known as the 'warm-up' phase. The powder bed continues to be heated during the

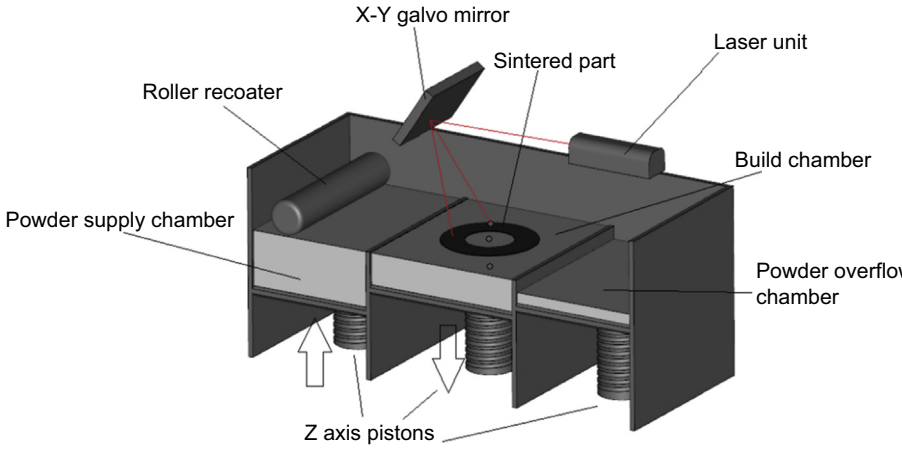

Figure 7.3 Schematic of the laser sintering process.

processing phase. Processing begins with the build platform, which is moveable in the z-direction, indexing down by one layer thickness and the spreading of a thin layer of powder over the build area. Selected regions of this powder layer are fused by the laser according to the cross-sectional data from the STL file. The platform is lowered and a fresh layer of powder is spread over the previously scanned layer. A scan corresponding to the next cross-sectional layer of the part causes powder particles to fuse to each other within that layer and to the underlying layer, where required. These processing steps are repeated until the 3D part is completed. During part production, laser sintering does not require structures to support overhangs because the un-melted powder within the powder bed supports the melted polymer.

Upon completion of the parts, the powder bed and the parts contained within it (often referred to as the 'part cake') are allowed to cool before being removed from the build chamber. The un-sintered powder can be reused to a certain extent depending on the type of polymer (see Section 7.7.3). The manufactured parts can now be used or refined in conformance to their proposed application.

A number of different process parameters can be modified, including laser parameters (eg, laser power and scan speed) and build parameters (eg, layer thickness). The most commonly modified parameters are described in Table 7.1; the effects of modifying them are discussed in Section 7.6.

It is common for several parts to be produced together within the same build, meaning that each powder layer may contain cross-sectional layers of multiple parts. In this instance, the laser may scan each part in turn before recoating, or it may scan full x or y vectors. Scan patterns and strategies are discussed further in Section 7.6.

Commercial suppliers of polymer laser sintering systems include 3D Systems (USA), EOS (Germany), ASPECT (Japan) and Hunan Farsoon (China). These systems differ in two key ways: the method used to spread the powder and the type and location of the heaters used to heat the build area [1]. These differences have a significant effect on

Table 7.1 Laser sintering process parameters

Parameter	Description
Laser power	Applied power of the laser as it scans the area of each layer
Scan speed	Velocity at which the laser beam travels as it traverses a scan vector
Scan spacing	Distance between parallel laser scans
Scan count	Number of times the laser beam traverses a scan vector per layer
Scan strategy	Pattern of the laser as it scans over a layer, in combination with the laser parameters used in each specific area
Layer thickness	The distance the build platform lowers for spreading of a new layer of powder
Build temperature	The temperature of the process chamber and/or part bed

the processing of some polymers, which is discussed in Sections 7.4 and 7.5, respectively. There is also an increasing number of low-cost systems starting to appear on the market, including Sintratec and ShareBot. To lower costs, the Sintratec system uses a diode laser and therefore requires dark-coloured materials. Most commercial systems are able to heat the build area to around 180°C, except for the EOSINT P800, which can heat up to 385°C. EOS also uses dual lasers on its larger systems to speed up processing.

7.3 Materials for laser sintering

The most common polymers used in laser sintering are semi-crystalline thermoplastics, typically polyamides (PAs; nylon) 12 and 11, which make up more than 95% of the current market [2]. A polypropylene, polyetheretherketone and high-density polyethylene are also commercially available, along with a small number of thermoplastic elastomers and some filled polyamides. In addition to semi-crystalline polymers, amorphous polymers such as polystyrene can also be processed using laser sintering. Because of their wide softening range, amorphous thermoplastics lead to less dense parts and inferior mechanical properties and are therefore less frequently used in laser sintering. Compared with conventional manufacturing methods where thousands of different grades are available for a wide range of polymers, there is currently a much smaller choice of materials for laser sintering.

In theory, any material able to be produced in powder form can be used in the laser sintering process. This is a distinct advantage over some other AM techniques that require specific classes of polymers (eg, ultraviolet-curable). However, in practice, this is not currently the case, or at least not for producing multi-layer parts with properties sufficient to meet the requirements of industrial applications. This is mainly a result of the complex thermal properties of polymers coupled with the lack of control of current laser sintering systems. As a result, the benefits of laser sintering are frustrated, to some extent, by the current repertoire of available polymers; significant research is being undertaken by industry and academia to increase the number and variety of polymers available for the laser sintering process.

The ability to process a given material and its resultant part properties depend on four main criteria [3,4]:

1. the material's physical properties (eg, particle size, particle shape, bulk density)
2. the material's thermal properties (glass transition, melting and crystallization temperatures, specific heat and thermal conductivity)
3. the laser sintering process parameters, including laser parameters (eg, laser power, spot size), scan parameters (eg, scan speed, scan spacing and scan strategy) and build parameters (eg, layer thickness, bed/chamber temperature)
4. the material's behaviour during processing (in powder form and in a molten state)

The influence of these factors are discussed in the next sections. It should be noted at this point that many current theories for the processing of polymers are based on the experience of processing polyamides and a handful of other materials. Therefore caution is required in assuming all polymers will process by laser sintering in a similar way.

7.4 Material properties: physical

For laser sintering, the material must be in powder form, and the physical properties of the powder (particle size, size distribution, shape, surface morphology etc.) affect powder deposition, ease of processing and final part properties.

Particles between 45 and 90 μm are usually preferred, with commercial laser sintering powders having a relatively narrow distribution around 50−60 μm. In general, the smaller the particle size, the better the part density, surface quality and accuracy of the laser-sintered part. However, if the particles are too small, static forces and particle coagulations resulting from the relatively large specific surface area can cause the particles to adhere to surfaces and cohesion between contacting particles, making spreading of the powder difficult. In addition, during sintering, because small particles coalesce faster than larger particles, unwanted fusing of particles adjacent to the desired area is more likely to occur. Particles outside of this range can be processed and have in some cases been shown to have reasonable mechanical properties [1]; however, for optimum processing and mechanical properties, a particle size within this range is preferred. The maximum particle size is limited by the layer thickness. A layer thickness of 100−150 μm is typically used, equivalent to two to three times the recommended average particle size. This ensures that most particles receive direct contact from the laser rather than relying on particle-to-particle conduction. If this ratio between layer thickness and particle size is decreased (either by increasing the particle size or decreasing the layer thickness), the particles tend to move and separate during deposition. The use of multimodal powders (ie, mixing different particle size fractions) can lead to better particle packing in the powder bed. However, smaller particles require less laser energy to melt compared with larger particles, and therefore larger particles may be left with an un-melted core or parts may be left with porosity as a result of the over-melting of small particles.

Spherical or near-spherical powders are desired to aid flow and thus deposition of the powder over the build area, to reduce the surface area-to-volume ratio and to improve packing efficiency. Irregular-shaped particles tend to interlock with each other, forming cakes, arches and voids inside the bulk, which results in higher cohesive behaviour and shear stresses [5,6].

Compared with near-spherical particles, irregular-shaped particles have been shown to decrease the mechanical properties of some laser sintering materials [7], with elongation-to-fracture particularly affected [9].

In laser sintering, the powder is spread over the build area using a roller or blade, but it does not undergo any additional compaction. Therefore, achieving good powder flow and a high packing density is important because these factors are known to have a significant effect on the mechanical properties of the final part [4]. Inorganic powdered additives such as hydrated silicas and metallic stearates may be added to improve powder flow; however, these can compromise mechanical properties and therefore should be added in minimal quantities. Flow properties are also affected by moisture and temperature − these are discussed in more detail in Section 7.5.

A number of standard laboratory tests are available to provide an indication of a powder's flow properties; however, there currently exists no single technique that characterizes powder flow using a method that directly represents the laser sintering process. Attempts have been made to develop tests with a more direct link to laser sintering, but further developments must take into account all relevant factors (eg, temperature) as well as differences in the deposition/recoating methods used in different laser sintering machines. As defined by Prescott and Barnum [10], powder flowability is 'the ability of powder to flow in a desired manner in a specific piece of equipment'; therefore true flowability can currently only be determined when using a specific laser sintering system. The deposition method has a significant influence on the laser sintering process, with rollers or recoating blades most commonly used. Counter-rotating rollers are able to compact the powder to a small degree. Building a part on a system with a recoating blade is more likely to fail if there is an imperfection in the powder bed because the blade is likely to dislodge the part, whereas a roller may just pass over it and compact it. However, it could be argued that recoating blades therefore prevent the production of sub-optimum parts that would go undetected in an automated production process. This may be critical for some end-use AM applications. Machines that use overflow bins generate more powder that needs to be recycled; the drawbacks to this are described in Section 7.7.3. However, in comparison to machines that spread the same powder back and forth and therefore can re-introduce agglomerates or imperfections back into the build area, with overflows these are quickly removed.

The morphology of the individual particles and their flow properties influence the density of the powder bed and, as a result, the density of the laser-sintered parts. Table 7.2 lists the three most commonly used commercially available laser sintering PA12 powders.

Duraform PA12 and EOS PA2200 are both based on VESTOSINT produced by Evonik [11]; however, they contain different size fractions. Orgasol has slightly more spherical particles compared with the two materials based on Vestosint, the latter consisting of particles that are frequently referred to as 'potato-shaped'. Orgasol also has a much narrower distribution in the volume and number of particles; this results in

Table 7.2 Three most commonly used laser sintering polyamide 12 powders

	Supplier	Source	Reported production method
Duraform PA12	3D Systems	Evonik (VESTOSINT)	Solution-precipitation process in ethanol at elevated temperatures [11]
PA2200	EOS	Evonik (VESTOSINT)	Solution-precipitation process in ethanol at elevated temperatures [12]
Orgasol Invent Smooth	Arkema	Arkema	Emulsion polymerization [13]

denser parts and superior surface quality compared with the Vestosint materials [11]. Cryogenic grinding is a common method of producing powders; however, these powders tend to have irregular-shaped particles with a high proportion of fines and are therefore less suitable for the laser sintering process. However, it is not just the physical properties but also the thermal properties of a material that affect processability, which is largely influenced by molecular structure, in particular the viscosity and crystallinity of the polymer.

7.5 Material properties: thermal

In the laser sintering process, the laser rapidly scans across the powder bed, and the primary fusion of the particles takes place over a short time period with no mechanical pressure applied. The part is then cooled slowly, usually over a number of hours; a complex series of events affects the exact cooling rate of each part. The combination of these factors can make consolidation of many polymers challenging.

For semi-crystalline materials, the powder bed is typically heated to just below the melting temperature and held at this temperature throughout the process (often referred to as the 'bed temperature'). This means that during exposure, the laser is only required to contribute the remaining amount of energy needed to exceed the phase transition and thus selectively melt the material. It also helps to prevent early crystallization of the molten polymer, which could result in localized shrinkage and part distortion [14].

It was noted in Section 7.3 that PAs are the most widely used laser sintering materials, largely because of their ease of processing. A typical differential scanning calorimetry (DSC) thermogram for a commercial PA12 laser sintering powder can be seen in Fig. 7.4. The reason that PA12 processes so well by laser sintering is thought to be the relatively large difference between the onset of melting and the onset of crystallization, reducing the risk of early crystallization.

This difference is an indication of the thermal 'processing window', although it should be noted that the full processing window also depends on laser parameters (see Section 7.6). Because PA12 has a large thermal processing window, it is more stable despite fluctuations in heating and cooling during the laser sintering process. Materials with a smaller processing window (or, in fact, no standard thermal processing window) can be processed; however, they usually require a more precise set of processing parameters and therefore can be more challenging to process. Therefore DSC is often used when screening new materials for their potential use in the laser sintering process, with a significant difference between the onset of melting and the onset of crystallization considered ideal for semi-crystalline laser sintering materials. DSC is also used to gain an initial indication of the processing parameters used. It should be noted that DSC is performed at constant heating and cooling rates (typically 10°C/min), whereas in an laser sintering system there is significantly more variation that is not currently controllable or is not, in fact, fully known. Therefore precise parameters are normally gained on a trial-by-error basis, using DSC as a guide.

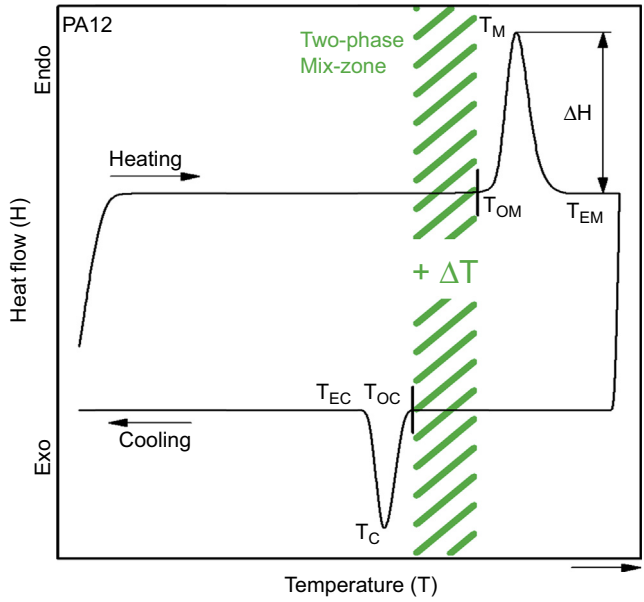

T_{OM} Onset of melting
T_M Peak temperature of melting (melting point)
T_{EM} End of melting
ΔH Enthalpy of fusion
T_{OC} Onset of crystallization
T_{EC} End of crystallization

Figure 7.4 Schematic representation of a differential scanning calorimetry run and the delta between the onset of melting and the onset of crystallization for polyamide 12 (PA12).

To reduce thermal gradients and prevent early crystallization, it is desirable to use a bed temperature as close to the melting temperature as possible. Too low a temperature can cause the edges of the part to bend upwards as a result of early crystallization, a phenomenon referred to as 'curling'. Severe curling causes builds to fail since the recoating blade or roller cannot pass without dislodging the part from its desired location. Shrinkage upon crystallization is a particular problem for semi-crystalline polymers. On the other hand, too high a temperature can result in the surrounding powder becoming hard and difficult to recycle with clean-up (eg, removal of the supporting powder from around the produced part when it is removed from the part cake at the end of the build) also being more difficult). A temperature close to the melting onset is generally used. Therefore, a material that has a sharp melting point is desirable so that the temperature used can be as close to the melting temperature as possible and, when the laser is applied, complete melting can occur (see Fig. 7.5). A high enthalpy of fusion is also desired to prevent the conduction of heat which melts excess powder particles adjacent to those intended to be fused by the laser.

Whereas parts produced by injection moulding are cooled and solidified in just a few seconds, in laser sintering there is a much more complex cooling rate. The

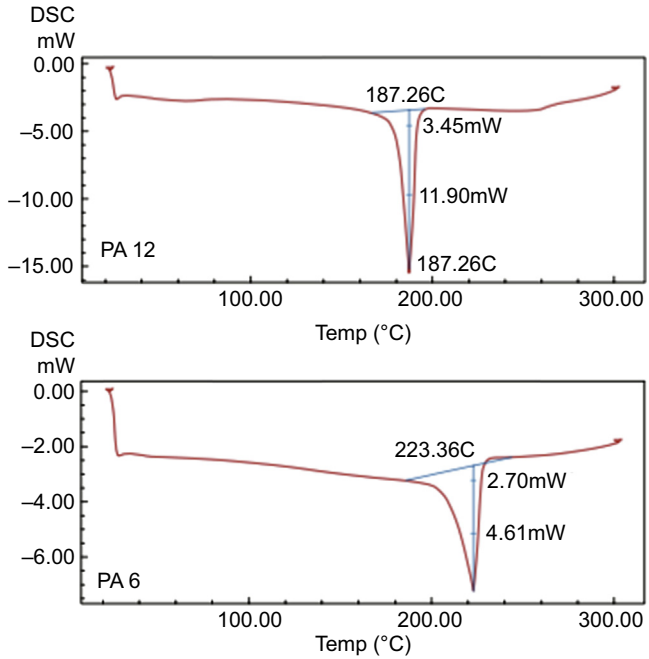

Figure 7.5 Differential scanning calorimetry curve of a polyamide (PA) 12 (top) compared with a PA6 (bottom) [8]. Note the smaller melting range and melting temperature of PA12 compared with those of PA6, offering an explanation as to why PA12 is easier to process by laser sintering than PA6.

processed material mainly cools and solidifies at the end of the build; however, in-process cooling also occurs. In-process cooling is often non-uniform and based on a number of factors, making it difficult to predict and measure. Once the laser has passed over a layer, the scanned area is partially cooled by the new layer of powder being spread over it. Despite some cooling, the starting temperature of the powder bed is likely to be at an elevated temperature in these select areas; the degree to which it is raised depends on the laser parameters used and the composition of the build (eg, size and number of parts). These are discussed in Sections 7.6 and 7.7, respectively.

Depending on the location of the heaters that control the temperature of the powder bed, it may then be further cooled as it gradually moves away from the heaters. For this reason, machine design makes a significant difference. For example, piston heaters reduce in-process cooling compared with systems that have only overhead heaters. The number and size of other parts in the powder bed also affects in-process cooling, as the scanning of subsequent layers of a part is delayed while other parts in the build are scanned.

In general, cooling rates are slow because of the reliance on conduction through the powder bed and the low thermal conductivity of polymer powders [15].

Most models for the laser sintering process do not take into account in-process cooling and instead assume that the powder bed is cooled as a whole at the end of the build.

Crystallization is related to time and temperature. Therefore, these slow cooling rates are associated with the formation of different crystalline structures compared with the same materials processed by traditional manufacturing techniques. For example, for PAs, α(monoclinic) phases are more prevalent following slow cooling rates or high temperatures, whilst γ (hexaganol) phases occur more often in parts that have undergone fast cooling rates or low temperatures [16]. For polypropylene, which has three crystalline structures (α, β, and γ), the slow cooling rates increase the proportion of the γ-phase [17].

If a commercial laser sintering PA12, for example, Duraform PA (3D Systems), is compared with a standard injection-moulded PA12, such as Grilamid PA12 (Ems Chemie), the distance between melting and crystallization onset – that is, the thermal processing window – is larger on the first heating run (although the melting temperature is diminished in the second run) [11] (see Fig. 7.6). The increase in melting temperature and decrease in crystallization temperature have been purposely altered during powder production to make the thermal processing window larger. There are also differences between different laser sintering PA12s; for example, Duraform (Evonik) has a wider thermal processing window than Orgasol (Arkema).

High coalescence rates are achieved when surface tension is high and viscosity is low. Zero-shear viscosity is considered to be the most significant factor when establishing a material's suitability for the laser sintering process. The melt flow rate is often used to give an indication of viscosity; however, as explained by [18], it is not representative of zero shear since it is influenced by many factors, including the material's viscosity. Steady and oscillatory shear methods have been used more recently. Because long sampling times at lower frequencies are required for oscillatory

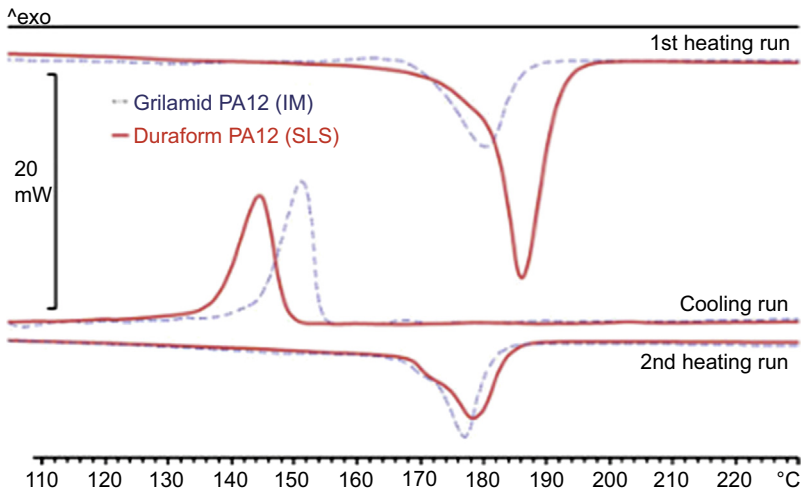

Figure 7.6 Differential scanning calorimetry curves for an injection-moulding polyamide (PA) 12 (Grilamid) and a laser-sintering PA12 (Duraform), showing enlargement of the thermal processing window for the laser-sintering material [11].

measurements, steady shear conditions are thought to be more appropriate [18]. Hot-stage microscopy is also used to visualize coalescence.

Three of the commonly used laser sintering PA12 materials were discussed in Section 7.4. PA2200 has been found to demonstrate significant postcondensation behaviour, especially at higher temperatures. This is in contrast to PA12-Orgasol, which did not show any change in viscosity, suggesting that the polymer chains were stabilized by, for example, end-capping [18]. For PA2200, when a higher temperature was used, the crystallization onset was delayed. Postcondensation results in increased molecular weight and melt viscosity, which has both advantages and disadvantages in laser sintering. On the one hand, a higher molecular weight delays the onset of crystallization and leads to improved mechanical properties. However, recycling the supporting powder becomes more difficult. Powders are rarely used in an as-received 'virgin' state; instead they are usually mixed with 'used' powder — in other words, powder that has already been through the laser sintering system as the supporting powder bed of from the overflow chambers. The effects this has on viscosity and coalescence are discussed in more detail in Section 7.7.3.

7.6 Processing parameters

Laser sintering processing parameters (defined in Table 7.1) can be divided into three groups:

- laser parameters (eg, laser power, spot size)
- scan parameters (eg, scan speed, scan spacing and scan strategy)
- build parameters (eg, layer thickness, build temperatures)

In practical terms, however, they are best considered together since they work in combination to determine both the ease of processing and the final part properties.

7.6.1 Layer thickness

As described in Section 7.2, the 3D model file of the desired part is sliced into a series of layers. The thickness of these layers can be altered, with thicker layers increasing the production speed and thinner layers reducing surface roughness and improving dimensional accuracy. The maximum layer thickness is restricted by the depth of penetration of the laser energy into the powder, which is determined from the energy density, particle size, powder density, thermal conductivity, compaction and specific heat of the material. The minimum layer thickness is determined by the size of the powder particles. A layer thickness of 100−150 μm is typically used, equivalent to two to three times the recommended average particle size, in order to ensure the powder spreads sufficiently over the build area with good powder bed packing (see Section 7.4).

7.6.2 Build temperatures

In the sequence of processing, the build temperatures are next to be considered. Depending on the laser sintering system being used, these may include the temperature

of the powder bed, the temperature of the build chamber and, in some cases, the temperature of the chamber from which fresh powder is being fed. Whilst most systems have the ability to control bed and chamber temperatures, only certain machines have the capability to heat the powder before spreading over the build area. This has advantages and disadvantages: Heating the powder before spreading it over the build platform reduces the mismatch between the powder bed and fresh layer of powder, potentially reducing issues with interlayer cooling; however, it also means that the powder is held longer at elevated temperatures, which may have an effect on the material's recyclability.

The ideal build temperatures are unique to each material. If the temperatures used are too high, powder spreading is difficult, forming an uneven powder bed. If the build temperatures are too low, premature crystallization can lead to curling of the part.

Despite setting a constant bed temperature, it is common for the temperature to vary slightly across the powder bed; on commercial machines this is typically 1−2°C, but on some bespoke machines the variation is higher. Bourell et al. [14] attributed this variation to four causes:

1. conduction from previously heated powder layers
2. inconsistent powder bed heating caused by irregular heating elements
3. conduction through the part cake walls
4. thermal convection channels that form in the nitrogen atmosphere above the part bed

Although relatively small, this variation can have a significant effect on the processing of some polymers, particularly those with a small processing window, leading to inconsistent part properties. Although thermal control of industrial laser sintering systems is improving, there are often variations between different systems. Therefore it is necessary to determine the exact build temperatures for each polymer on the specific system that is going to be used.

7.6.3 Laser and scan parameters

A number of different laser and scan parameters can be specified, the most common being laser power, scan speed and scan spacing (also referred to as hatch distance). These terms are defined in Table 7.1. Increasing laser power, decreasing scan speed and decreasing scan spacing all result in an increase in part density and tensile strength up to a certain point, after which these properties decrease as a result of the degradation of the polymer.

To quantify the amount of energy provided by the laser, a simplified relationship between the different parameters when the energy is introduced is often used; this is described by the so-called Andrew number and is also referred to as area-related energy density (E_A), shown in Eq. (7.1):

$$E_A = \frac{P_L}{v_s \times H} \tag{7.1}$$

where E_A is the area-related energy density, P_L is the laser power, v_s is the scan speed, and H is the hatch distance.

The E_A thereby describes the nominal power introduced on the surface of the powder bed by the laser, independent of the material processed.

To take into account the influence of the layer thickness, the E_A can be extended to a volume-related energy density considering the variable for layer thickness, as shown in Eq. (7.2):

$$E_V = \frac{P_L}{v_s \times H \times d_{layer}} \tag{7.2}$$

where E_V is the energy density based on volume, P_L is the laser power, v_s is the scan speed, H is the hatch distance, and d_{layer} is the layer thickness.

The approach is often criticized because amongst other parameters the absorbance of the laser energy throughout the layer is dependent on various parameters such as the packing density of the material, and it assumes the penetration depth of the laser complies with the thickness of the produced layer, which is generally not the case.

Moreover, because of the Gaussian temperature distribution of the laser beam, the heat introduced into the powder bed is not homogenous throughout the laser diameter, since the highest temperature would occur at the innermost region (Fig. 7.7(a)). Thus the particles being hit by the centre (targeted area) of the laser beam are exposed to higher temperatures than the ones at the edges.

Considering Eq. (7.1) in combination with Fig. 7.7(b), it can be observed that, depending on the diameter of the laser beam and the hatch distance, there is an overlap of the single scan paths of the moving heat source (laser spot), and therefore some points get exposed multiple times. This overlap is represented by the area shown between the curves at $t = 0$ and $t = 1$ for constant scan speed a. If the beam is moving with an increased scan speed ($a + x$; where x is positive), the overlapping area

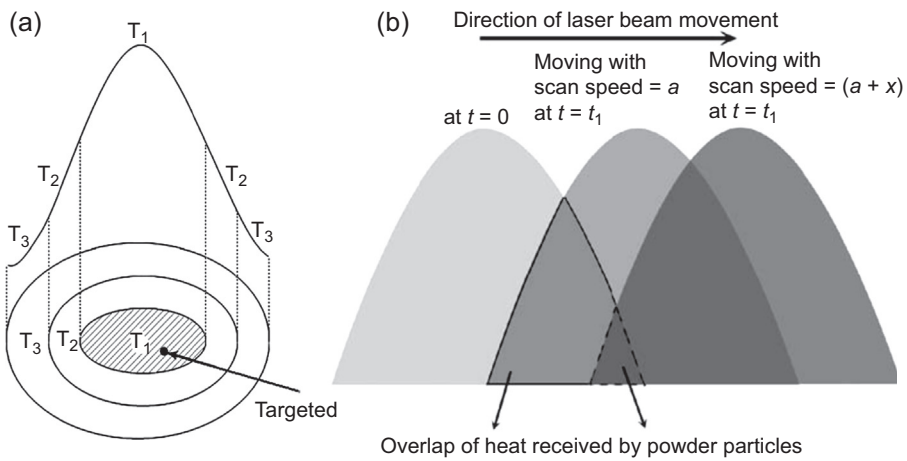

Figure 7.7 Temperature distribution of a carbon dioxide laser beam (a) and a sintering model of a moving laser beam (b) [19].

decreases as a result of the reduced time the powder is exposed to the laser. As a result of these effects, it becomes clear that the equations are simplified and limit the direct correlation to the real process, as the build temperature was treated as a constant parameter and the time of exposure was only described in the E_V approach, dependent on laser power, hatch space, scan speed and layer thickness.

Another important influential factor is the size of the exposed area, since the heat conduction within large melt pools is slower compared with smaller melt spots. As a result, the polymer melt in the larger pool is capable of flowing for a longer period of time, thus building a more homogenous film and connecting the underlying layer. Consequently, the heating and cooling rates of the exposed areas are dependent on the size of the corresponding cross section. According to Scholten and Christoph [20] the specific amount of heat loss resulting from convection and radiation, as well as the incoming rate of heat flux of the part bed heater, the cylinder heater and the piston heater, are negligible compared with the high-intensity laser radiation during exposure of the material. During pre-heating and applying a new layer, as well as during the time between the exposure phases, though, the rate of heat loss from convection and radiation as well as the incoming rate of heat flux do play a dominant role. Therefore a temperature gradient should only be present during exposure to the laser; in any other case an even energy balance is desired. The balancing of the heat flows can be represented simply in Eq. (7.3):

$$\underbrace{\dot{q}_a + \dot{q}_{\text{Part Bed Heater}} + \dot{q}_{\text{Cylinder Heater}} + \dot{q}_{\text{Piston Heater}}}_{\text{Incoming Heat Flux}} = \underbrace{\dot{q}_{HC} + \dot{q}_{con} + \dot{q}_{rad}}_{\text{Amount of Heat Loss}} \tag{7.3}$$

where $\dot{q}_a$ is the absorbed laser radiation; $\dot{q}_{\text{Part Bed Heater}}$ is the absorbed radiation of the part bed heater; $\dot{q}_{\text{Cylinder Heater}}$ is the absorbed radiation of the cylinder heater; $\dot{q}_{\text{Piston Heater}}$ is the absorbed radiation of the piston heater; $\dot{q}_{HC}$ is the rate of conductive heat loss; $\dot{q}_{con}$ is the rate of convective heat loss; and $\dot{q}_{rad}$ is the rate of radiation heat loss.

Although the effects of varying build chamber temperature on the mechanical properties of sintered parts have been proven, they often have not been quantified. Starr et al. [21] used a total-energy approach to describe the effect of the build temperature dependent on the material properties, as shown in Eq. (7.4). The aim of the study was to measure not only the effect of energy introduction by the laser but also the energy introduced by the infrared heater, as well as the influence of material parameters on the mechanical properties of the laser-sintered specimen, and to determine the range of conditions that provide consistent mechanical performance. For that purpose, the energy melt ratio was created to put the volume-based energy density (Eq. (7.2)) in relation to the energy needed to fuse a single layer (energy to melt layer).

$$\text{EMR} = \frac{E_V}{\text{EML}} \tag{7.4}$$

where EMR is the energy melt ratio, E_V is the energy density based on volume, and EML is the energy to melt layer.

Despite its limitations, however, the area-related energy density, E_A, remains the most commonly stated parameter by researchers in the field. Higher energy densities have been found to improve particle fusion and mechanical properties; however, this is only up to a certain point; if this point is exceeded, the polymer degrades. The increase in part density and tensile strength has been attributed to a decrease in the viscosity of the material, which reduces porosity and increases density. Each material has its own optimum energy density, which at present is determined on a trial-by-error basis in combination with the evaluation of an optimum build temperature and scan strategies.

7.6.4 Scan strategy

Scan strategy includes consideration of the scan count and the scan pattern and the allocation of laser parameters to a specific area in the scanning of a layer.

On commercial systems, when the laser scans a given layer of a part, it usually scans the contours of the part, then raster scans the area within it (or vice versa). Different parameters can be assigned to the contour compared with the main infill area. The infill scan is usually performed in straight lines in the direction of either the *x*- or *y*-axis. Alternating between the two directions in sequential layers has been found to improve the mechanical properties of a part. In addition, altering the scan pattern — for example, scanning from the centre of the part out to the contours — has been found to enable the processing of some materials [23]. At present, however, there are only a limited variety of scan patterns that can be used on commercial laser sintering systems. With current systems and software it is also difficult to allocate different processing parameters to specific areas in a given layer. However, varying the laser parameters across a layer can counteract thermal inconsistencies and delay time effects (see section 7.7.1).

'Scan count' refers to the number of times a layer is scanned by a laser before a fresh layer of powder is spread over it. Typically a scan count of 1 is used; that is, the layer is scanned once before being recoated. This ensures the fastest production speed. However, for certain geometries, for example, thin-walled components, it is advantageous to scan the contours of the part twice to improve their strength. In addition, some materials have been found to require multiple scanning of the entire cross section to put the required energy more gradually into the powder layer. Using a lower laser power in conjunction with multiple scanning (typically 'double scanning', that is, a scan count of 2) has been found to prevent the accumulation of stress and to minimize dimensional inaccuracies in parts produced from materials with a small processing window [22].

7.7 Processing Effects

7.7.1 Delay time

'Delay time' refers to the period of time between scanning a specific point on a cross-sectional area in a given layer and the same point in the next adjoining layer.

Following the scanning of each cross-sectional area, there is a delay whilst a new layer of powder is spread over the build area and the chamber temperatures return to their set value, before the next layer is scanned by the laser. Each material has an optimum delay time, and the degree by which a material is affected by different delay times is also dependent on the material. If the period of time is too long, excess in-process cooling occurs, causing delamination of the layers or curling of the parts as a result of premature crystallization. If the delay time is too short, degradation can occur as a result of a large build-up of heat. Whilst there is an optimum delay time for each material, control of the delay time is difficult in practice since delay time is affected by the size (and, to a lesser degree, the shape) of the part and the process parameters being used (in particular scan speed and scan count, although processing temperatures and laser power can also have an effect) [1]. It is also dependent on the laser sintering system's deposition methods and control. It is common practice for several parts to be produced in the same build (as illustrated in Fig. 7.2). The increase in time while the laser scans the other parts in the layer can also contribute to a delay time effect.

7.7.2 Part orientation and placement in the build area

The resulting properties of parts manufactured using laser sintering are influenced not only by the material properties and the process parameters applied but also by the orientation of the parts in the build and its geometry. Because laser sintering is an additive process, the parts built consist of (depending on their size) many individual layers, between which delamination (detachment of single layers) could occur, as indicated by Fig. 7.8. The probability of delamination thereby increases proportionally with the amount of layers. This effect, though, is superimposed by notch effects emerging at the borders of the parts, which are caused by the layer-by-layer structure (step effect) and the Gaussian intensity distribution of the laser, as shown in Fig. 7.8. Analogous to the delamination effect, the notch effect — and therefore a potential component failure — increases proportionally with the number of layers. Moreover, the surface roughness, which has a direct impact on the mechanical strength of the part, is affected by the step effect, which in turn is most significant at curved or angled areas.

Advances in system control and scan strategies have reduced anisotropy in recent years; however, laser sintering materials normally exhibit some level of anisotropic behaviour. This is also because of the layer-by-layer nature of laser sintering and is explained in Fig. 7.9.

Initially the laser scans powder particles in a single vector, achieving optimum consolidation (Fig. 7.9(a)). When it scans the next parallel vector, whilst the degree of necking between particles in that vector will be similar to that experienced in the first vector, the necking between particles in the two vectors will be reduced (Fig. 7.9(b)). This is a result of the particles in the previous vector having cooled slightly while waiting for the second vector to be scanned. The process of spreading a fresh layer of powder over each sintered layer means that the bonding between particles in different layers will be reduced even further (Fig. 7.9(c)). Therefore the

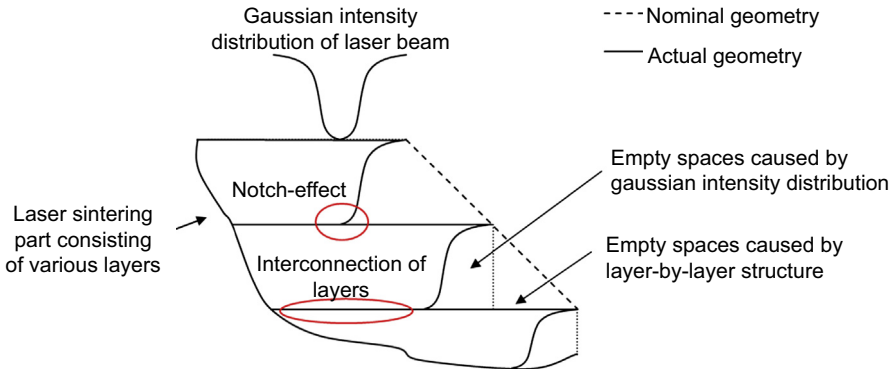

Figure 7.8 Layer-by-layer structure of a laser-sintered (LS) part, indicating areas of notch effect and interconection between the layers at which delamination could occur.
Adapted from Kaddar, Die generative Fertigung mittels Laser-Sintern:Scanstrategien, Einflüsse verschiedener Prozessparameter auf die mechanischen und optischen Eigenschaften beim laser sintering von Thermoplasten und deren Nachbearbeitungsmöglichkeiten, in: Universität Duisburg-Essen, Duisburg, 2010.

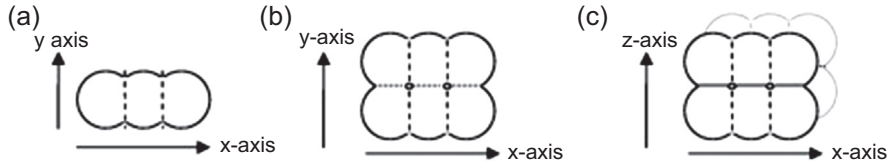

Figure 7.9 Schematic of particle consolidation during the laser-sintering process, showing (a) necking between particles in a single vector, (b) necking between two parallel vectors and (c) necking between different layers [1].

weakest properties are experienced when stress is applied perpendicular to this layer-to-layer bonding. The anisotropic nature of laser-sintered materials is in part connected to delay time. Small cross sections retain more heat to contribute to forming stronger bonds with the new layer than those where a long delay time is experienced. Whilst for PA12 this seems to be a minimal effect, materials that are significantly affected by delay time will experience greater anisotropy.

7.7.3 Powder reuse

In theory, any powder that has not been consolidated into a part during the laser sintering process (eg, supporting powder) can be recycled and used again in subsequent builds. In practice, however, this is not always the case. During laser sintering, the polymer in the powder bed spends hours at a temperature close to the crystalline melting point and is therefore exposed to high thermal loads. Although the process is running in an almost inert atmosphere, it ages the polymer powder, hindering its reuse in subsequent production cycles. The ageing or degradation effects manifest themselves in the decomposition of the polymer. Chemical changes caused by ageing

are even further supported by the oxygen and water molecules contained within the polymers. Kühnlein et al. [25] described the ageing process of polyamides that tend towards chain scission, as well as chain branching or cross-linking, undergoing recombination processes, starting with the formation of radicals at temperatures close to the melting point. The radicals emerging in this so-called auto-oxidation process can continue to react in different ways and build out cross-linking or chain scission. When two radicals recombine, it comes to cross-linking that coincides with an increase in molecular weight and termination of the reaction. Accordingly, a shift in crystallization and crystalline melting temperatures was determined; these are two key parameters for stable processing of semi-crystalline polymers in laser sintering. Depending on the type of polymer applied, chain breaking or cross-linking dominate the oxidation process. In general, chemical and physical ageing processes are manifested in changing the melting, crystallization and flow characteristics of the polymer melt. These changes affect the ability to process the material in subsequent builds.

For economic reasons, it is not desirable to use new powder for each build. However, if all the material is continually reused, a poor surface finish, often referred to as 'orange peel', is rapidly evident, and more shrinkage occurs [26]. Moreover, mechanical properties of the manufactured specimens have been found to decrease with increasing processing cycles. A study by Wegner and Witt [27] investigated the ageing of PA12 in the laser sintering process over four ageing cycles in an EOS Formiga P100. The effects on the powder properties were measured with the Hausner ratio (HR) on a bulk scale, melt flow was analyzed by means of melt volume rate (MVR) and mechanical properties were measured using a tensile test. A significant increase in MVR with an increasing number of processing cycles was found as a result of cross-linking and reactions after polymerization. The sharpest drop in MVR, at around 200 cm^3/10 min, equalling 55% of the initial value of the virgin powder, was reached in the first ageing cycle that lasted 25 h. This significant decrease in the MVR over ageing cycles is the result of cross-linking and reactions after polymerization. After a processing time of 75 h, the value of the MVR decreased to a lesser extent and levelled off at 60 cm^3/10 min. In characterizing the powder flow, they found a continuous increase in HR that exceeded the threshold from high flowability to reduced flowability at a value of 1.25 in the second ageing cycle. Similar to the MVR results, the most rapid increase in HR took place from virgin material to powder that was processed one time. The observed changes in the flow behaviour were explained by the change in particle size distribution and particle shape. Moreover, they found that the mechanical properties of the manufactured specimen changed with increasing processing cycles. Depending on the energy density applied, the ultimate tensile strength for specimens built in the *x*-*y*-direction dropped more or less rapidly from 50 N/mm^2 (virgin material) to 30 N/mm^2 (four times the processed material); so did the Young's modulus, which decreased from 1800 N/mm^2 to 1100 N/mm^2.

This correlates with another study, published by Kühnlein et al. [25], investigating the effects on mechanical properties of PA12 (PA2200 by EOS) being conditioned at building temperatures for different periods. The Young's modulus and the percentage elongation at break decreased over multiple processing cycles because of the ageing-

induced changes of the material, such as a shift in the crystalline melting point towards higher temperatures, leading to insufficient melting.

Similar experiments examining the changing powder and part properties of PA12 (DuraForm PA by 3D Systems) over a build time of 300 h under the influence of varying laser power (high, medium, low) were carried out by Choren et al. [28]. The objective was to determine the maximum powder life cycle. An increase in the laser power relative to its ageing state aimed to maintain part quality. The laser power was increased with additional ageing cycles to reach a constant degree of melting as viscosity increased. They found that the notched impact strength increased up to an ageing duration of 168 h, then dropped significantly after exceeding this point, even at higher levels of laser power, marking the point at which the ageing-induced effects dominate the possibilities of energy input.

Most studies of the deterioration of powders during laser sintering have been performed on PA12. In a study of the ageing of thermoplastic elastomers in laser sintering, Ziegelmeier et al. [29] showed that with increasing processing cycles (powder reuse), slight changes in molecular weight were present, indicating chain scission caused by thermal stresses. It was found that this change in molecular weight led to enhanced flowability of the polymer melt, allowing for less porous parts but reduced elongation at break of the tensile specimens. In terms of the powder's physical properties, a significant decrease in bulk density was observed; this was a result of the changing particle size distributions that could potentially affect processability. The polymers did not show systematic changes when examining the chemical changes caused by thermal loads, and hence showed overall good performance in terms of powder life, with some restrictions that have to be taken into account on the powder side.

To achieve more consistent part properties, 'virgin' (as-supplied) and 'used' (previously run through an laser sintering system but not consolidated) powders are commonly combined in a ratio referred to as the 'refresh rate'. The optimum refresh rate is polymer-specific; some commercial powders claim almost full recyclability, and some are unable to be recycled at all.

One of the difficulties with recycling powder is the variance in degradation of the powder. Variations are evident even with powder that has been through the same number of processing cycles, for example, depending on whether the used powder was close to the parts being consolidated or at the edge, or whether it was simply spread and immediately deposited into the overflow. The MFR is therefore commonly measured in an attempt to quantify the quality of the powder.

7.8 Other polymer powder bed fusion systems

Alternative PBF systems have primarily focused on reducing processing costs compared with laser sintering, increasing productivity and/or allowing multiple materials to be used during the process. In laser sintering, the cross section of each layer of a part is raster scanned from 'point to point'. Methods that fuse an entire layer of the part simultaneously, or at least a complete horizontal or vertical line of the part, are being

sought to increase production speeds and decrease the negative effects of delay time (see Section 7.5). In addition, because of the relatively high costs of carbon dioxide lasers, alternative heat sources have been considered. This section describes five alternative PBF systems for polymers: selective mask sintering, high-speed sintering, selective inhibition sintering, selective heat sintering and multi-jet fusion.

7.8.1 Selective mask sintering

In this process, infrared thermal energy is applied to the powder bed though a mask outline of the desired cross section of the part. The entire layer is exposed to the infrared heater at once, thus reducing the time taken to complete the layer to approximately 1 s. Because of the use of an infrared heating source, polymers must be able to absorb light in the infrared region, limiting material choice mostly to dark-coloured materials.

7.8.2 High-speed sintering

In high-speed sintering, a radiation-absorbing material (RAM) is selectively deposited directly on to the powder bed surface by an inkjet printer in the pattern required for each layer of the part. An infrared lamp is used to irradiate the entire build area, with the areas containing the RAM absorbing sufficient energy for consolidation, while the areas without RAM do not and therefore remain unconsolidated. Again, materials are limited to dark colours, typically grey or black.

7.8.3 Selective inhibition sintering

This process works in the opposite way to high-speed sintering, in that an inhibitor is printed in the areas of the powder bed that are not required for that particular layer of the part, before exposing the layer to infrared radiation. Whilst the unused powder in this process is more difficult to recycle, it does mean that the part itself does not contain RAM.

7.8.4 Selective heat sintering

Selective heat sintering uses a thermal print head to consolidate the powder. Whilst selective heat sintering systems do not currently match the speed and mechanical properties of laser sintering, they offer a low-cost alternative to industrial laser sintering systems.

7.8.5 Multi-jet fusion

Multi-jet fusion technology prints chemical agents into the powder bed using an HP Thermal Inkjet array, which passes from left to right (or vice versa) across the build area. A second carriage that combines the layering and energy processes then passes from top to bottom (or vice versa), consolidating the part and spreading the next layer

of powder over the build area. Multiple agents are applied, including a fusing agent for areas where consolidation is required and a detailing agent for reducing or amplifying consolidation.

7.9 Conclusion

The key advantage of polymer laser sintering is that the process does not require support structures, which allows increased design freedom and less effort during post-processing compared with other AM techniques where overhangs must be supported and support structures either be built into the design or be able to be removed at the end of the build. However, removal of supporting powder from internal structures must be considered. The dominance of PA12 and, to a lesser extent, PA11, as materials for laser sintering is in part because of their established history and availability in powder form but predominantly a result of their relative stability in complex and fluctuating thermal conditions, a property contributed to by their low initial zero-shear viscosity and the relatively large difference between the onset of melting and crystallization, which prevents early crystallization.

The current understanding of polymer processing by laser sintering is based largely on the processing of PAs. To further understand the processing of polymers by laser sintering, and subsequently to increase the number and variety of polymers available for use with this technique, greater consideration of other polymers is required. Furthermore, focus must not be limited to the single-layer phenomenon but must consider the whole part and build. Improved process monitoring and control will contribute to this.

To allow for laser sintering to compete with conventional manufacturing such as injection moulding, not only does the variety of available polymers need to increase, but the cost for the raw materials has to decrease, since it is the main driver in the cost of laser sintering. In addition, controllability in terms of machine and process capability has to be confirmed for the application of the technology within industrial series production. In addition, there is still a need to qualify specific and suitable quality assurance measures during and after processing for the approval of a build.

Acknowledgements

The authors are grateful to J. White, University of Nottingham, for Figs. 7.1–7.3.

References

[1] R.D. Goodridge, C.J. Tuck, R.J.M. Hague, laser sintering of polyamides and other polymers, Progress in Material Science 57 (2012) 229–267.
[2] Wohlers Report 2009, Wohlers Associates, 250 pp.

[3] I. Gibson, D. Shi, Materials properties and fabrication parameters in selective laser sintering process, Rapid Prototyping Journal 3 (1997) (Forum Rapid Technol).
[4] S. Ziegelmeier, P. Christou, F. Wollecke, C. Tuck, R. Goodridge, R. Hague, E. Krampe, E. Wintermantel, An experimental study into the effects of bulk and flow behavior of laser sintering polymer powders on resulting part properties, Journal of Materials Processing Technology 215 (2015) 239−250.
[5] G. Lumay, F. Boschini, K. Traina, S. Bontempi, J.-C. Remy, R. Cloots, N. Vandewalle, Measuring the flowing properties of powders and grains, Powder Technology 224 (2012) 19−27.
[6] C. Nystrom, G. Alderborn, M. Duberg, P.-G. Karehill, Bonding surface area and bonding mechanism: two important factors for the understanding pf powder comparability, Drug Delivery and Industrial Pharmacy 19 (1993) 2143−2196.
[7] R.D. Goodridge, M.L. Shofner, R.J.M. Hague, M. McClelland, M.R. Schlea, R.B. Johnson, C.J. Tuck, Processing of a polyamide-12/carbon nanofibre composite by laser sintering, Polymer Testing 30 (1) (2011) 94−100.
[8] J.-P. Kruth, G. Levy, F. Klocke, T.H.C. Childs, Consolidation phenomena in laser and powder bed based layered manufacturing, CIRP Annals 56 (2) (2007).
[9] S. Griessbach, R. Lach, W. Grellmann, Structure-property correlations of laser sintered nylon 12 for dynamic dye testing of plastic parts, Polymer Testing 29 (2010) 1026−1030.
[10] J.K. Prescott, R.A. Barnum, On powder flowability, Pharmaceutical Technology (2000) 60−84.
[11] M. Schmid, A. Amado, K. Wegener, Materials perspective of polymers for additive manufacturing with selective laser sintering, Journal of Materials Research 29 (17) (2014) 1824−1832.
[12] H. Scholten, W. Cristoph, Use of a Nylon-12 for Selective Laser Sintering, US Patent 6245281, 2001.
[13] K. Loyen, H. Senff, F.X. Pauly, Process for the Manufacture of Polyamide-12 Powder With a High Melting Point, US Patent 8124686, 2012.
[14] D.L. Bourell, T.J. Watt, D.K. Leigh, B. Fulcher, Performance limitations in polymer laser sintering, Physics Procedia 56 (2014) 147−156.
[15] M. Yuan, D. Bourell, T. Diller, Thermal conductivity measurements of polyamide 12, in: Proceedings of the Solid Freeform Fabrication Symposium, 2011, pp. 427−437.
[16] H.-K. Huang, B. Wang, W.-W. Zhou, Polymorphism in polyamide 6 and polyamide 6/clay nanocomposites molded via water-assisted injection moulding, Composites: Part B 43 (2012) 972−977.
[17] W. Zhu, C. Yan, Y. Shi, S. Wen, J. Liu, Y. Shi, Investigation into mechanical and microstructural properties of polypropylene manufactured by selective laser sintering in comparison with injection molding counterparts, Materials and Design 82 (2015) 37−45.
[18] L. Verbelen, S. Dadbakhsh, M. Van den Eynde, J.-P. Kruth, B. Goderis, P. Van Puyvelde, Characterisation of polyamide powders for determination of laser sintering processability, European Polymer Journal 75 (2016) 163−174.
[19] F.E. Wiria, K.F. Leong, C.K. Chua, Modeling of powder particle heat transfer process in selective laser sintering for fabricating tissue engineering scaffolds, Rapid Prototyping Journal 16 (2009) 12.
[20] H. Scholten, W. Cristoph, Verwendung eines Polyamids 12 fur selektives Las-Sintern und Polyami 12 Pulver, European Patent EP0911142 B1, 1998.
[21] T.L. Starr, T.J. Gornet, J.S. Usher, The effect of process conditions on mechanical properties of laser sintered nylon, Rapid Prototyping Journal 17 (2011) 6.

[22] R.D. Goodridge, R.J.M. Hague, C.J. Tuck, An empirical study into laser sintering of ultra-high molecular weight polyethylene (UHMWPE), Journal of Materials Processing Technology 210 (1) (2010) 72−80.
[23] R.D. Goodridge, Internal Report, University of Nottingham, 2014.
[24] Kaddar, Die generative Fertigung mittels Laser-Sintern:Scanstrategien, Einflüsse verschiedener Prozessparameter auf die mechanischen und optischen Eigenschaften beim LS von Thermoplasten und deren Nachbearbeitungsmöglichkeiten, in: Universität Duisburg-Essen, Duisburg, 2010.
[25] F. Kühnlein, D. Drummer, D. Rietzel, A. Seefried, Degradation behavior and mechanical properties of PA12-plastic powders processed by powder based additive manufacturing technologies, in: 3rd International Conference, Nova Gorica, Slovenia, 2010.
[26] D.T. Pham, K.D. Dotchev, W.A.Y. Yusoff, Deterioration of polyamide powder properties in the laser sintering process, Proceedings of the Institution of Mechanical Engineers − Part C − Journal of Mechanical Engineering Science 222 (2008) 2163−2176.
[27] A. Wegner, G. Witt, Betrachtung zur Pulvernutzungsdauer beim Laser-Sintern und Einfluss der Prozessfuhrung auf die Entstehung von Ausschussbauteilen, Rapid Prototyping Journal (2012) 21.
[28] J. Choren, V. Gervasi, T. Herman, S. Kamara, J. Mitchell, SLS powder life study, in: Solid Freeform Fabrication Symposium, Austin, TX, 2001, pp. 39−44.
[29] S. Ziegelmeier, F. Wollecke, C.J. Tuck, R.D. Goodridge, R.J.M. Hague, Aging behavior of thermoplastic elastomers in the laser sintering process, Journal of Materials Research 29 (17) (2014) 1841−1851.

Polymer nanocomposites for laser additive manufacturing

8

J.H. Koo [1,2], R. Ortiz [1], B. Ong [1], H. Wu [1]
[1]The University of Texas at Austin, Austin, TX, United States; [2]KAI, LLC, Austin, TX, United States

8.1 Introduction

8.1.1 Overview of selective laser sintering

Selective laser sintering (SLS) is one of the main processes in the rapidly evolving additive manufacturing field. Specifically, it is a rapid prototyping method capable of producing complex parts and geometry from a computer-aided design (CAD) model in a relatively short amount of time. This is accomplished by analyzing the model file and breaking it into cross sections of small thicknesses, typically less than 0.25 mm. These cross sections are then used as layers of a part build. The build medium is usually very fine powder, and this is distributed onto a central platform using a feed-and-roller system. Once the powder is deposited, a laser is used to sinter it together into contours of the preestablished layers. Upon completion, the layer is lowered, covered by new powder, and the process is repeated until all of the model cross sections have been finished [1,2]. An illustration of this procedure can be seen in Fig. 8.1.

8.1.2 Selective laser sintering build parameters

This procedure has several key build characteristics that affect the formulation of a part. In regards to the machine and build parameters, the primary variable involved is the laser energy imparted into the build material. This energy is derived from the laser power, the scan speed, and the scan spacing. The laser power is specifically the energy directed onto the part bed, as supposed to the total wattage input into the laser. The scan speed is the velocity that the laser moves across the part profile. The scan spacing refers to the physical gap between each scanning sweep [1]. These three factors combined define energy density, which can be deduced using the following equation:

$$[\text{Energy density}] = \frac{[\text{Laser power}]}{[\text{Scan speed}][\text{Scan spacing}]} \tag{8.1}$$

Energy densities that are too great typically result in poor dimensional tolerances, which in turn can cause a myriad of problems during the mechanical operations inside

Laser Additive Manufacturing. http://dx.doi.org/10.1016/B978-0-08-100433-3.00008-7
Copyright © 2017 Elsevier Ltd. All rights reserved.

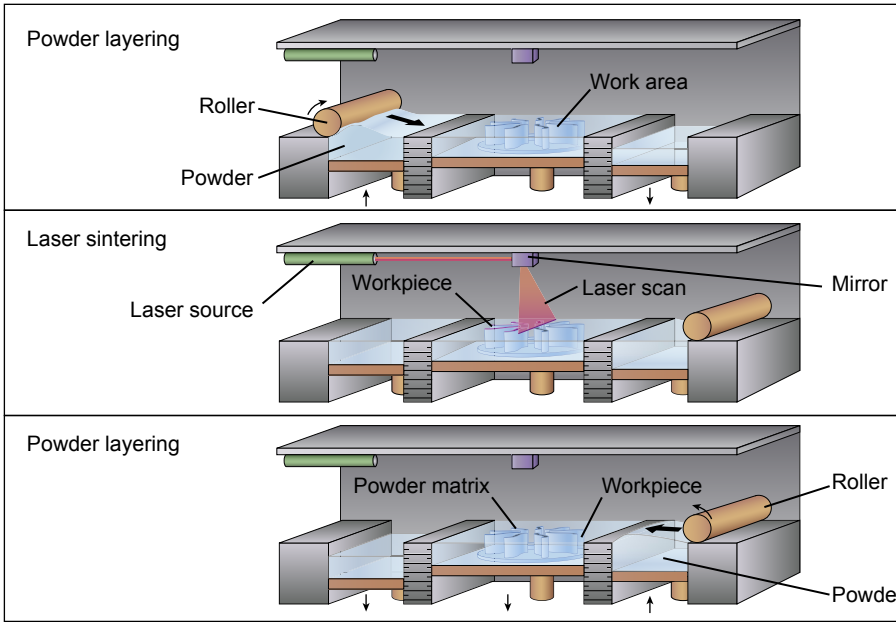

Figure 8.1 Basic selective laser sintering procedure.
© 2012 Encyclopedia Britannica, Inc.

the build chamber. Energy densities that are too low result in improper particle adhesion and eventual delamination or disintegration of parts [3].

Another important factor in the build is the temperature control. With a standard SLS machine, the operator is given control of the part bed temperatures and the feed bin temperatures, and these must be carefully maintained within the build medium's tolerable range to produce successful parts. Failure to adequately preheat the powder reservoirs or the workspace can lead to poor adhesion. Overheating produces the opposite effect, possibly leading to oversintering more material than is desired and producing parts with poor dimensional tolerances. In addition, improperly regulating heat distribution of the layers may result in curling, a phenomenon in which the gradient of layers undergoes irregular thermal contraction and physically bends the part structure. This often forces a build to be aborted if it occurs mid-procedure [3]. Cooling the build too quickly after the procedure can also possibly lead to curling, which typically results in the delamination of a part (Fig. 8.2). Fig. 8.2(a) shows the top view of a curled SLS mechanical test specimen of an dogbone, and Fig. 8.2(b) shows the cross-sectional view of a curled SLS mechanical property test specimen.

8.1.3 Materials used in selective laser sintering

The most common material used in SLS processing is polyamide (PA), specifically PA11 and PA12. Technically, a standard-constructed SLS machine is capable of loading and using any type of polymer powder; however, most builds are limited to

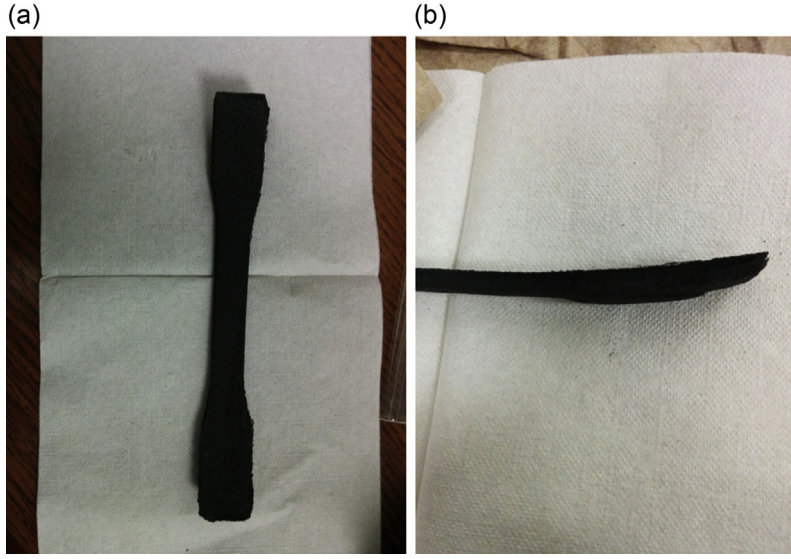

Figure 8.2 Photographs of a tensile specimen subjected to curling: top view (a) and cross-sectional view (b).

just PA because of current understandings of material properties and how they behave with various temperatures and laser energies [2].

This material restriction is one of the largest impairments to the advancement of SLS technology. While there have been a few commercial applications of additive manufacturing with PA parts, in most cases there is a demand for more robust and stronger materials. In response to this, research in the field of polymer nanocomposites has recently expanded dramatically, such as SLS of clay-reinforced PA. Typically, this involves polymers infused with small filler materials designed to enhance the overall strength, stiffness, thermal conductivity, flame retardancy, and/or other properties [2,4]. The additives involved can be as small as the nanometer scale (10^{-9} m) and are usually chosen because they improve a composite's properties with low weight percentages [3]. While numerous formulations and material additives have been explored, this study focuses on the effectiveness of multiwalled carbon nanotubes (MWNTs) in PA11.

One procedure for manufacturing composite powder parts is to simply load a powdered mixture of the base polymer and nanoscale additive during the sintering process. While this powder−powder mixture produces composite parts, the additives are not mixed at the particulate level and simply line the outer edges of the polymer powders during the sintering process. Extra steps must be taken to ensure the highest quality composite mixtures. A more thorough process entails cryogenically grinding an extruded mixture of base polymer and additive. The extrusion process melts both the base polymer and additive together, while the subsequent grinding phase allows the additive to be thoroughly implanted within the individual particulates of the powder, facilitating good dispersion in the final material [3,4].

8.2 Experimental approach

8.2.1 Materials

8.2.1.1 Base polymer

The polymer used for all the experiments discussed in this study was Rilsan® PA11 manufactured by Arekema (Lacq, France). Specifically, the extrusion grade is PA11 PCG LV. This base powder was selected to facilitate the continuation of experiments originally performed by Johnson and Koo [4] at the University of Texas at Austin, and the material is recognized for its good heat, chemical, and creep resistances, as well as its ease of use in additive manufacturing.

8.2.1.2 Nanocomposite formulation

In the electrical conductivity studies, the two additives used for initial material characterization were MWNTs and nanographene platelets (NGPs). For the preliminary tests on sintered parts, this study was narrowed to concern only the MWNT additive because of machine constraints with experimental materials. The study used 3 wt% loading and C150 P Baytube MWNTs. The mixture was first melt-compounded using a twin screw extrusion process and then cryogenically ground by Vortec Products Company (Long Beach, CA). As mentioned earlier, this procedure was carried out to maximize dispersion and produce the highest quality formulation for use in the SLS parts. Provided initial builds and tests are successful, further experimentation is planned for PA11-NGP.

The flame-retardant (FR) studies use the same Arkema PA11 PCG LV grade (Lacq, France), which was dried at 80°C for 24 h before processing. Clariant International Ltd. (Germany) provided the FR additive Exolit OP1312. Kraton Polymers, Inc. (Houston, TX) provided the Kraton FG1901 G. Both OP1312 and FG1901 G were used as received.

A total of six formulations were melt-blended with different concentrations, as shown in Table 8.1, using a Process 11 Parallel Twin Screw Extruder from Thermo Scientific. The materials were melted and mixed at 195°C at a speed of 220 rpm.

Table 8.1 Flame-retardant polyamide 11 composite matrix

Formulation	Flame retardant (wt%)	Kraton (wt%)	Nylon 11 (wt%)
1	–	–	100
2	20	0	80
3	20	5	75
4	20	10	70
5	20	15	65
6	20	20	60

To ensure a homogenous dispersion, each formulation was mixed by physical stir mixing before melt-compounding. The extruded formulations were air cooled before injection-molding in a Mini-jector injection molding system with a 216°C barrel temperature and a 90°C mold temperature.

8.2.2 Fabrication of selective laser sintering test specimens

This study primarily used two SLS machines: a Sinterstation 2000 HiQ and a Sinterstation 2500-plus HiQ. Both are DTM models manufactured by 3D Systems (Rock Hill, SC). The older of the two, the Sinterstation 2000, was used primarily for preliminary part fabrication to verify the established temperature parameters. The newer model, the Sinterstation 2500, was used to create a prototype of and produce the final test specimen. The primary differences between the two machines are their maximum laser power and heating/temperature control. The Sinterstation 2000, property of the University of Texas at Austin, used a bed-mounted heating and measurement system to regulate the temperatures in the machine bays. The Sinterstation 2500, provided by Advanced Laser Materials in Temple, TX, had been outfitted with a new, overhead-mounted, multicoil heating system that allowed for superior temperature control. It also had double the potential laser power (100 W) of the Sinterstation 2000. For our builds, we used a range of laser powers between 50 and 60 W, as prescribed by Advanced Laser Materials, a scan speed of 500 mm/s, and a scan spacing of 0.006 mm.

8.2.3 Characterizing properties

8.2.3.1 Thermogravimetric analysis

Thermal stability is a substance's resistance to permanent property changes caused solely by heat. Decomposition temperature is a commonly used metric to assess thermal stability. The thermal decomposition of each blend was assessed by a TGA-50 (Shimadzu Scientific Instruments), which measures the mass of the sample as a function of temperature in a closed nitrogen environment. The samples were heated in a nitrogen environment from room temperature to 1000°C at a heating rate of 10°C/min. The nitrogen flow was 20 mL/min. A single thermogravimetric analysis (TGA) test was performed on each blend and used to determine the 10% and 50% mass loss decomposition temperatures ($T_{10\%}$ and $T_{50\%}$, respectively).

To identify the ideal heating parameters for the nanocomposite formulation and to observe the decomposition trends exhibited, a battery of TGA tests was conducted for each of the three materials: PA11 with NGPs, PA11 with MWNTs, and neat PA11. The main focus of this study concerns PA11-MWNT, but the same tests were performed on two similar materials for reference and further experimentation will be conducted in the future. Each material was tested at four different heating rates: 5, 10, 20, and 40°C/min, all in a nitrogen atmosphere with the same testing parameters. These tests were conducted to observe the decomposition trends exhibited by each material. Kinetics calculations can be determined using an isoconversion technique with these data [4].

To better understand the decomposition rates, the data were converted to DTG (derivative of TGA) format. The rate of mass loss is critical to future SLS materials research. The data range observed, particularly the 10% decomposition point of each material, will set the temperature boundaries for the differential scanning calorimetry (DSC) tests.

8.2.3.2 Differential scanning calorimetry tests

To evaluate a specific temperature range around which to build the SLS heating parameters, DSC tests were performed on powdered samples of PA11, PA11 with NGPs, and PA11 with MWNTs. Two full heating and cooling cycles were conducted for each test battery to erase any potential material working history that would interfere with the evaluated melting temperature.

8.2.3.3 Electrical conductivity

It is known in the literature that certain additives, particularly MWNTs, can be added to increase the electrical conductivity of insulative polymers. This allows the material to be better suited for applications requiring adequate static dissipation or for sensing devices [5–9]. The testing procedure for this property involved careful application of silver wiring onto flat, nonconductive panels. By placing a rectangular sample of sintered material between the two wire bands and measuring the resistivity of the sample, conductivity could be evaluated using the inverse of the resistivity measured. The resistivity of each sample was evaluated using a digital resistance meter attached to silver wire leads. The electrostatic dissipation (ESD), a key benchmark, was measured against. The threshold for this cutoff is $10^{11}\ \Omega$ cm and indicates a point where a material is deemed safe for use in industry [2].

8.2.3.4 Flammability

Different test protocols and methods, such as UL 94 (the Standard for Flammability of Plastic Materials for Parts in Devices and Appliances) [10] and microscale combustion calorimetry (MCC), have been developed to quantify the "degree of difficulty" required to initiate and perpetuate combustion in plastics.

Microscale combustion calorimetry

An MCC-2 Microscale Combustion Calorimeter (Govmark, Inc.) was used to measure the thermal combustion properties according to ASTM D7309-2007 [11]. The combustor temperature was held constant at 900°C and the heating rate of the pyrolysis was 1°C/s. The percentage of oxygen concentration was measured to calculate the heat release.

UL 94 test

UL 94 is a standard, small-scale test of the flammability of plastic materials that determines the material's tendency to either self-extinguish or to spread the flame once ignited [10]. This test is a preliminary indication of a plastic's acceptability for use as a device or appliance component. It is important to note that UL 94 does not

represent the material's hazards under actual fire conditions; it is simply a preliminary step toward obtaining recognition under the "Plastics—Component" section of the UL's "Recognized Component Directory." Three ratings—V-2, V-1, and V-0—indicate that the material was tested in a vertical position, the time it took to self-extinguish, and whether the test specimen dripped flaming particles that ignited a cotton indicator below the sample. Of these three ratings, V-0 is the best.

For this study, the UL 94 testing requirements and procedures were followed even though our lab is not officially certified for UL 94 testing. As a consequence, the results serve only as a screening tool. Materials were conditioned for 48 h at 25°C and 50% relative humidity. Five repetitions were conducted for each blend.

8.2.3.5 Mechanical properties

The tensile tests were performed using an Instron 5966. The crosshead speed was 5 mm/min and the gauge length was 50 mm. The samples were conditioned at 25°C and 50% relative humidity for 48 h before testing. The average values and standard deviations of the tensile properties were calculated by testing five specimens of each formulation.

8.3 Results and discussion

Two studies are described in this chapter: (1) electrical conductive polymer nanocomposites and (2) FR polymer nanocomposites for SLS applications.

8.3.1 Electrical conductive selective laser sintering polymer nanocomposites

8.3.1.1 Thermal properties

TGA, DTG (derivative of TGA), kinetics parameters, and DSC data are included in this section. From the data in Table 8.2, several trends can be observed. At 5°C/min, all three 10% decomposition temperatures are similar. Significant differences appear at higher heating rates, but PA11 is consistently the lowest of the three. PA11-NGP and PA11-MWNT show only slight variances at this decomposition point, and neither is consistently higher than the other.

A similar pattern is evident at the 50% decomposition point. PA11 again has the lowest decomposition temperature, whereas PA11-NGP and PA11-MWNT show only slight differences. The following plots (Figs. 8.3, 8.5, and 8.7) show the results of the TGA experiments on the three materials. Table 8.2 shows a collective list of the decomposition temperatures at 10% and 50% mass loss.

Figs. 8.3 and 8.4 show the TGA and DTG data, respectively, of the virgin PA11 at four heating rates (5, 10, 20, and 40°C/min) under a nitrogen atmosphere. As expected, thermal stability increases with heating rate in nitrogen, shown by the thermogravimetric curve moving to the right (higher temperature). Figs. 8.5 and 8.6 show the TGA and

Table 8.2 Decomposition temperature data at 10% and 50% mass losses

	PA11		PA11-NGP		PA11-MWNT	
Heating rate (°C/min)	**Decomposition (%)**	**Temperature (°C)**	**Decomposition (%)**	**Temperature (°C)**	**Decomposition (%)**	**Temperature (°C)**
5	10	392	10	387	10	389
	50	419	50	430	50	429
10	10	400	10	417	10	407
	50	429	50	445	50	441
20	10	415	10	417	10	425
	50	443	50	453	50	458
40	10	433	10	437	10	438
	50	461	50	467	50	473

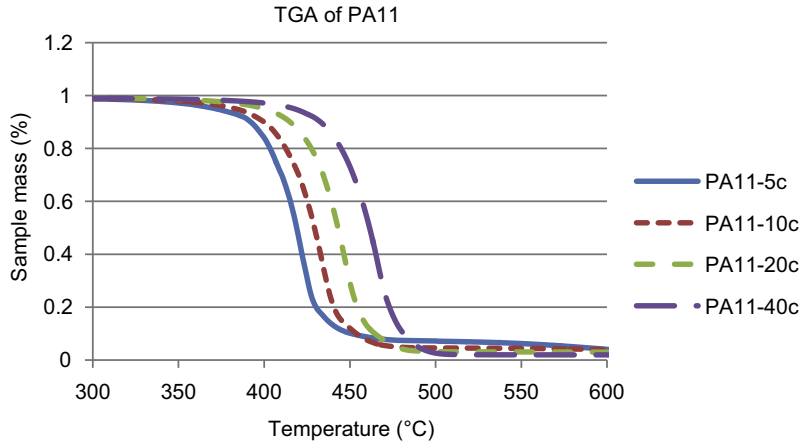

Figure 8.3 Thermogravimetric analysis data of polyamide 11 (PA11) at 5, 10, 20, and 40°C/min in nitrogen.

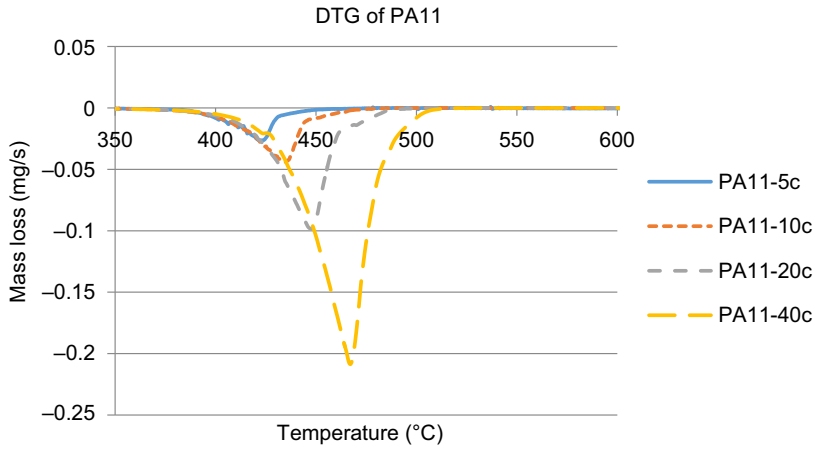

Figure 8.4 DTG data of polyamide 11 (PA11) at 5, 10, 20, and 40°C/min in nitrogen.

DTG data, respectively, of the PA11-MWNT nanocomposites at the same four heating rates under the same atmosphere. As expected, thermal stability also increases with the heating rate in nitrogen: the thermogravimetric curve moves to the right (higher temperature). Figs. 8.7 and 8.8 show the TGA and DTG data, respectively, of the PA11-NGP nanocomposites under the same conditions. The thermal stability also increases with heating rate in nitrogen: the TG curve again moves to the right (higher temperature).

In Fig. 8.6, note the second peak that occurs between 450 and 500°C. This indicates a second reaction caused by the inherent composition of the material. In this case it is likely to be influenced from the carbon infused into the PA11.

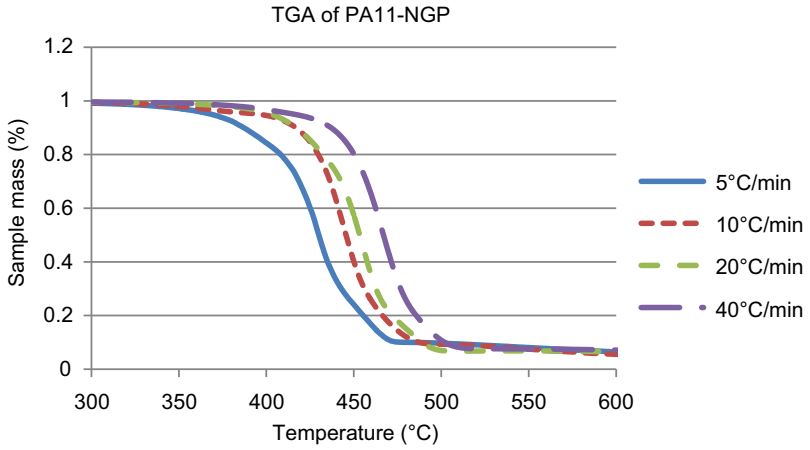

Figure 8.5 Thermogravimetric analysis data of polyamide 11 with nanographene platelets at 5, 10, 20, and 40°C/min in nitrogen.

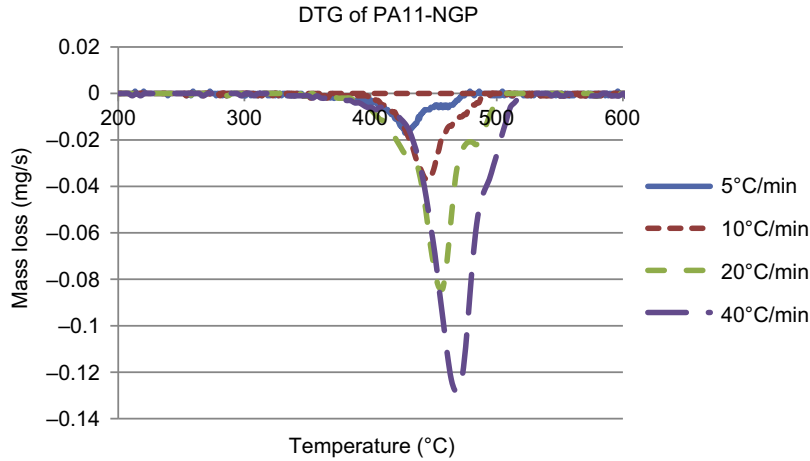

Figure 8.6 DTG data of polyamide 11 with nanographene platelets at 5, 10, 20, and 40°C/min in nitrogen.

In Fig. 8.8, a second peak occurs between 475 and 525°C. As before, this indicates a second reaction, likely the result of the carbon in the material. This second peak forms at a higher temperature than the second peak in the PA11-NGP (see Fig. 8.6). A comparison of these peaks is more evident in the later plots (Figs. 8.9–8.12).

On the comparison plots (Figs. 8.9–8.12) the TGA data curves support what is shown in Table 8.2. PA11 has the earliest decomposition, reaching 0% at a lower temperature than the other two materials. PA11-NGP and PA11-MWNT express similar characteristics at all heating rates, with no consistent significant difference between the material decomposition.

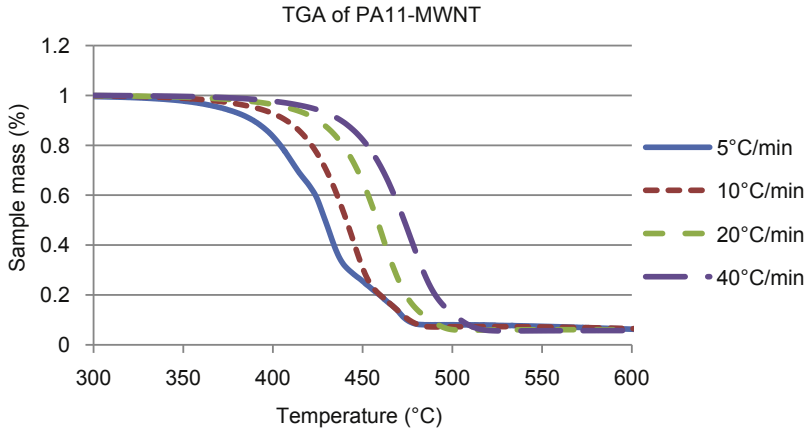

Figure 8.7 Thermogravimetric analysis data of polyamide 11 with multiwalled carbon nanotubes at 5, 10, 20, and 40°C/min in nitrogen.

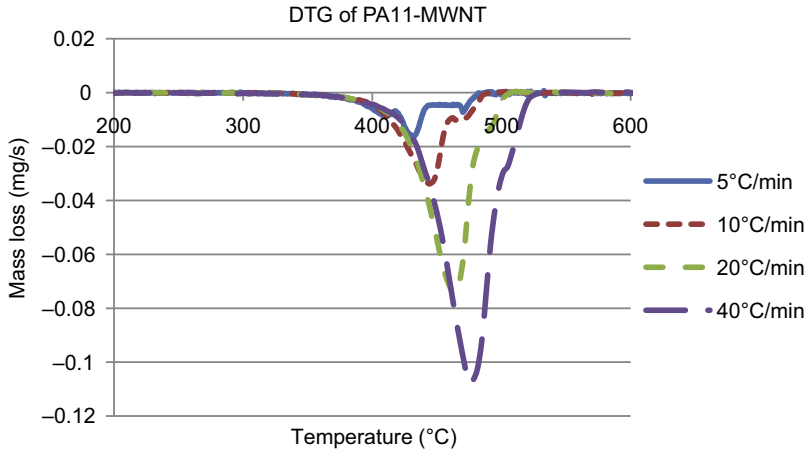

Figure 8.8 DTG data of polyamide 11 with multiwalled carbon nanotubes at 5, 10, 20, and 40°C/min in nitrogen.

The DTG comparisons (Figs. 8.13–8.16) show that PA11 consistently has the highest mass loss rate. At the lower heating rates of 5 and 10°C/min, PA11-NGP and PA11-MWNT have similar peaks, but it is evident that NGP loses mass more quickly at the higher heating rates. Note the second peaks that appear in the PA11-NGP and PA11-MWNT plots. It is clear from these comparison plots that the second peak occurs at a higher temperature in the PA11-MWNT and that the magnitude of the second peak is much larger.

The DSC data of PA11, PA11-MWNT, and PA11-NGP are shown in Figs. 8.17–8.22. The full DSC data for two heating and cooling cycles and an isolated second cycle of each material are shown.

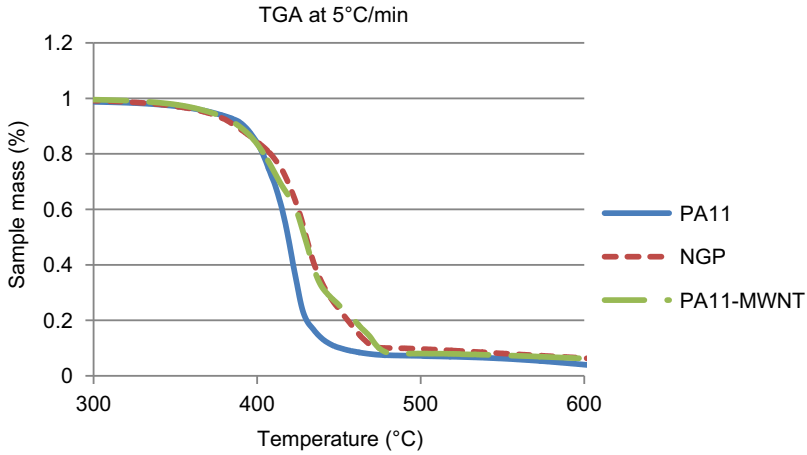

Figure 8.9 Thermogravimetric analysis comparing polyamide 11 (PA11), PA11 with nanographene platelets (PA11-NGP), and PA11 with multiwalled carbon nanotubes (PA11-MWNT) at 5°C/min in nitrogen.

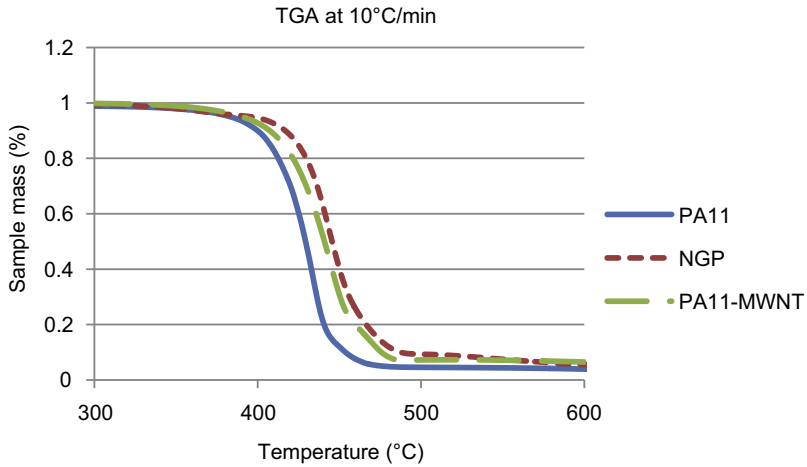

Figure 8.10 Thermogravimetric analysis comparing polyamide 11 (PA11), PA11 with nanographene platelets (PA11-NGP), and PA11 with multiwalled carbon nanotubes (PA11-MWNT) at 10°C/min in nitrogen.

Observing the second heating curves for each case, the melting temperature of each material could be deduced by verifying the temperature of the peaks: 190, 189, and 189°C for PA11-MWNT, PA11-NGP, and base PA11, respectively. The consistency of this melting temperature indicates that the additives did not have a significant role in altering the melting temperature of the overall composites; therefore the SLS build parameters were planned to accommodate the 189°C melting point.

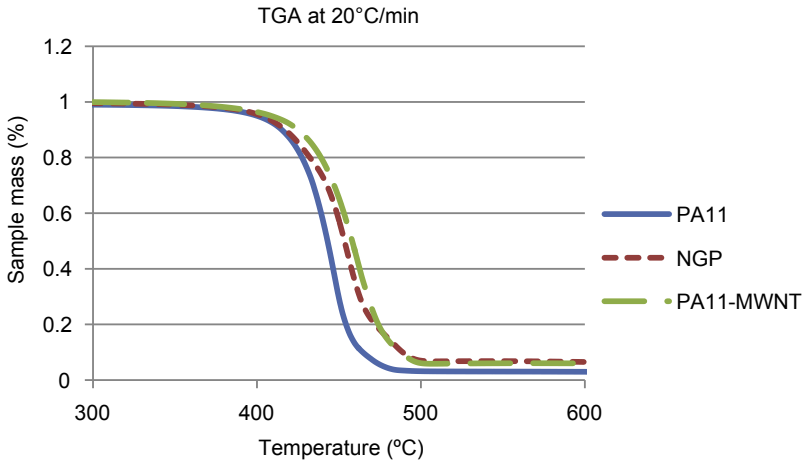

Figure 8.11 Thermogravimetric analysis comparing polyamide 11 (PA11), PA11 with nanographene platelets (PA11-NGP), and PA11 with multiwalled carbon nanotubes (PA11-MWNT) at 20°C/min in nitrogen.

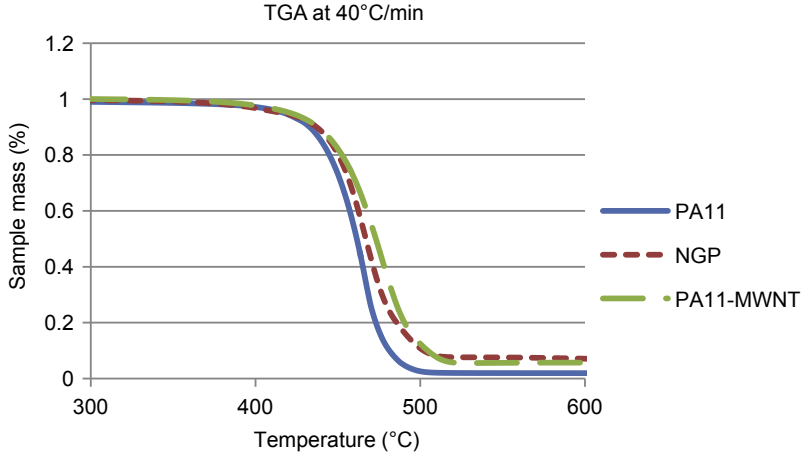

Figure 8.12 Thermogravimetric analysis comparing polyamide 11 (PA11), PA11 with nanographene platelets (PA11-NGP), and PA11 with multiwalled carbon nanotubes (PA11-MWNT) at 40°C/min in nitrogen.

8.3.1.2 Density evaluation

Overall, density is used as a general estimate of sintering quality. Particles that are sintered appropriately tend to adhere better to adjacent particles, and optimizing build parameters can result in the ideal scenario of tightly layered cross sections. Conclusively, samples with a higher density indicate a superior build with stronger mechanical properties. The density of our initial samples over various laser powers is shown in Fig. 8.23. Five samples were fabricated for each energy density, though some of them

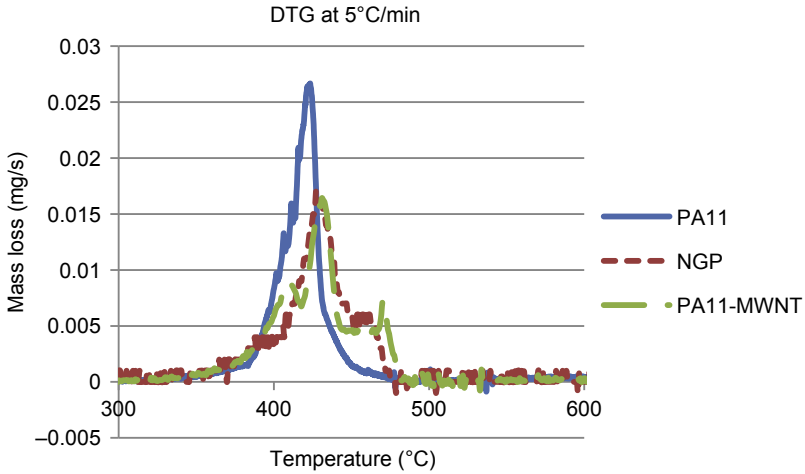

Figure 8.13 DTG comparing polyamide 11 (PA11), PA11 with nanographene platelets (PA11-NGP), and PA11 with multiwalled carbon nanotubes (PA11-MWNT) at 5°C/min in nitrogen.

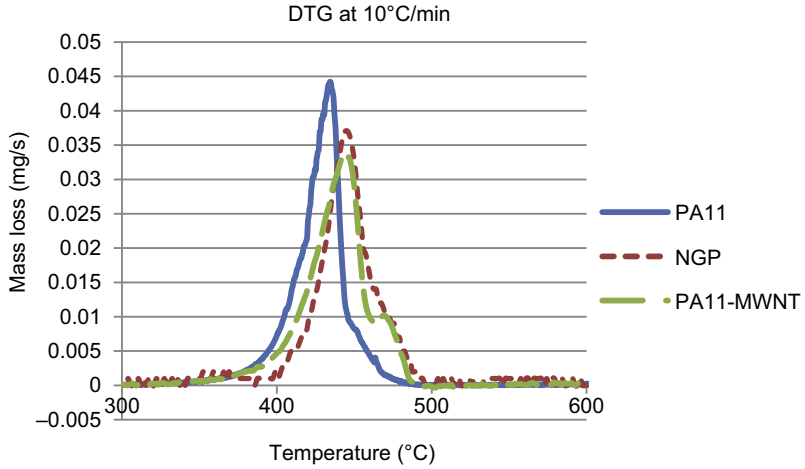

Figure 8.14 DTG comparing polyamide 11 (PA11), PA11 with nanographene platelets (PA11-NGP), and PA11 with multiwalled carbon nanotubes (PA11-MWNT) at 10°C/min in nitrogen.

had to be discarded because of significant imperfections in the final print. The error used to represent these sets with fewer samples is set to 5%.

Previous research indicates that neat PA11 has a typical density of 1.04 g/cm^3, which is only marginally higher than the densities of our samples [4]. The data show that at higher energy densities, the density of our specimens increased slightly; the highest value of 1.01 g/cm^3 occurred at an energy density of 0.0295 J/mm^2. To obtain accurate data, two samples were fabricated for each laser power over a window of 50−60 W, and the tensile data for each pair was averaged. While this positive trend between specimen density and energy density is evident here, other research with

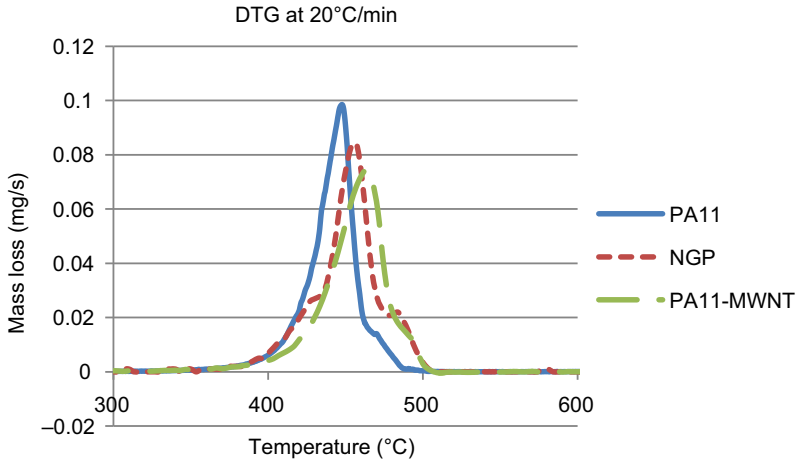

Figure 8.15 DTG comparing polyamide 11 (PA11), PA11 with nanographene platelets (PA11-NGP), and PA11 with multiwalled carbon nanotubes (PA11-MWNT) at 20°C/min in nitrogen.

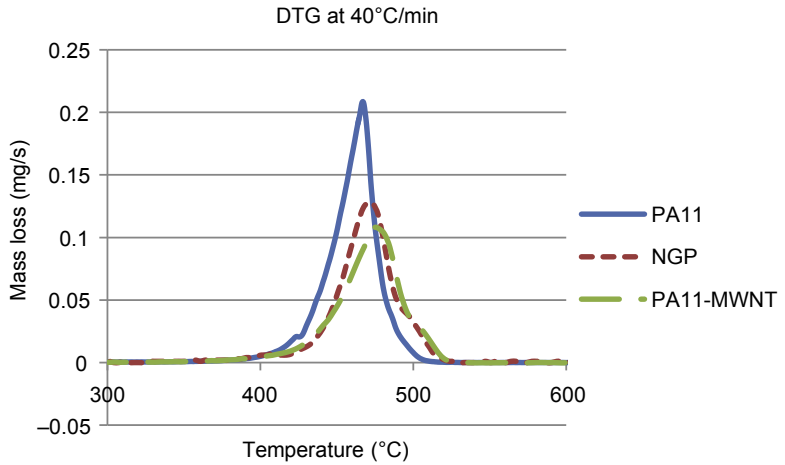

Figure 8.16 DTG comparing polyamide 11 (PA11), PA11 with nanographene platelets (PA11-NGP), and PA11 with multiwalled carbon nanotubes (PA11-MWNT) at 40°C/min in nitrogen.

different materials suggests this trend may reverse itself once certain energy densities are reached [6,7]. The high density displayed by the specimens indicates very good sintering with our temperature parameters, confirming the conclusions garnered from visual observations.

During a second build, to observe whether there were diminishing density gains over a wider range of energy densities, several sets of density cube specimens were made. Each set was sintered at a different laser power—30, 40, 50, and 60 W—which corresponded to energy densities of 0.0158, 0.0211, 0.0264, and 0.03 J/mm^2, respectively. Five specimens were made in each set. The resulting densities of these cubic

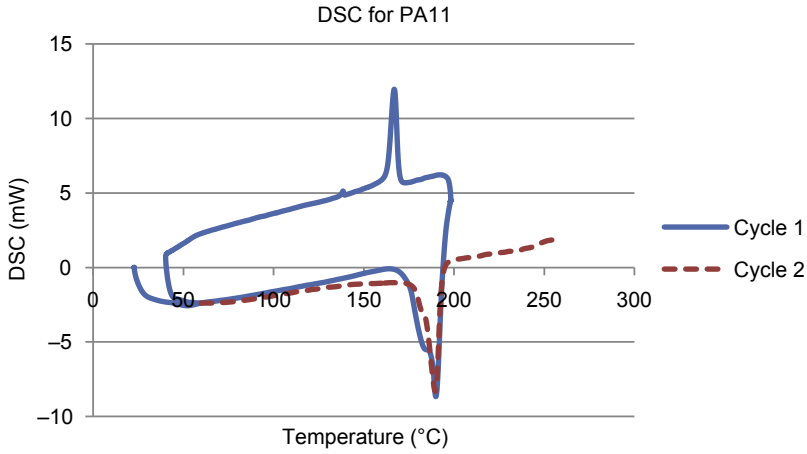

Figure 8.17 Full differential scanning calorimetry data for polyamide 11.

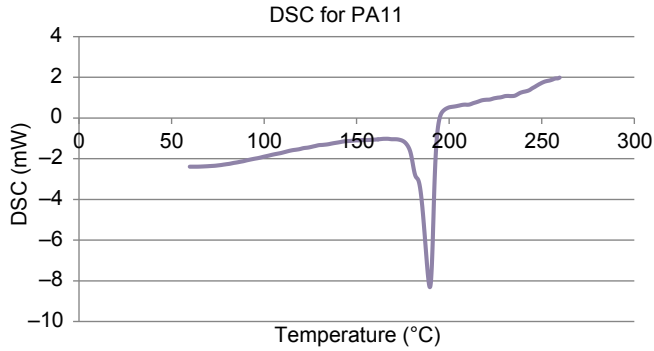

Figure 8.18 Isolated second differential scanning calorimetry cycle for polyamide 11.

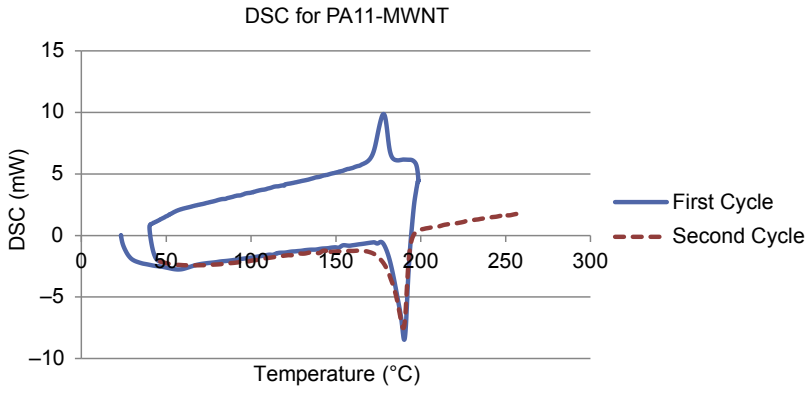

Figure 8.19 Full differential scanning calorimetry data for polyamide 11 with multiwalled carbon nanotubes.

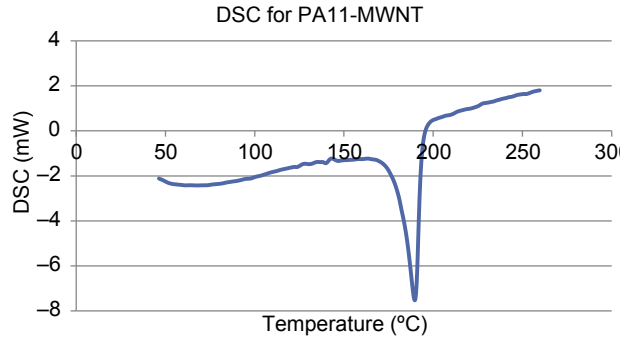

Figure 8.20 Isolated second differential scanning calorimetry cycle for polyamide 11 with multiwalled carbon nanotubes.

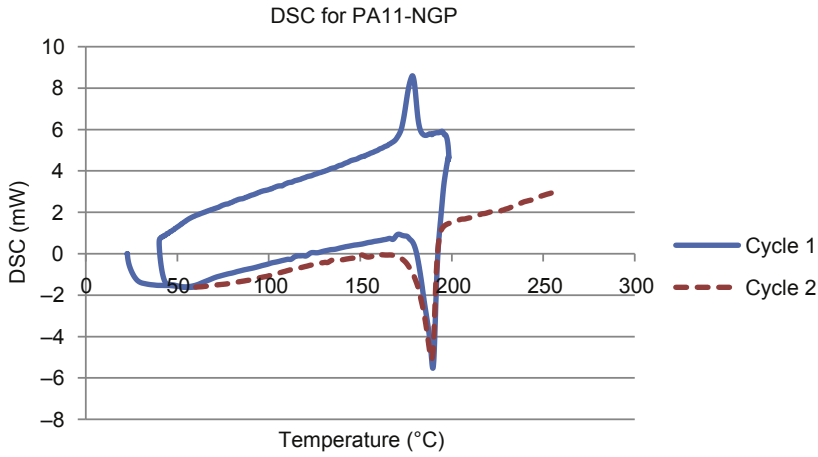

Figure 8.21 Full differential scanning calorimetry data for 11 with nanographene platelets.

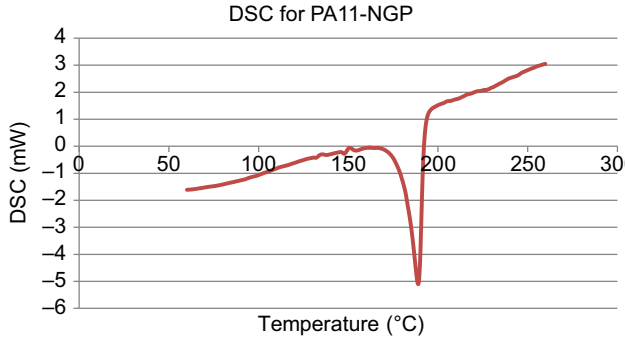

Figure 8.22 Isolated second differential scanning calorimetry cycle for 11 with nanographene platelets.

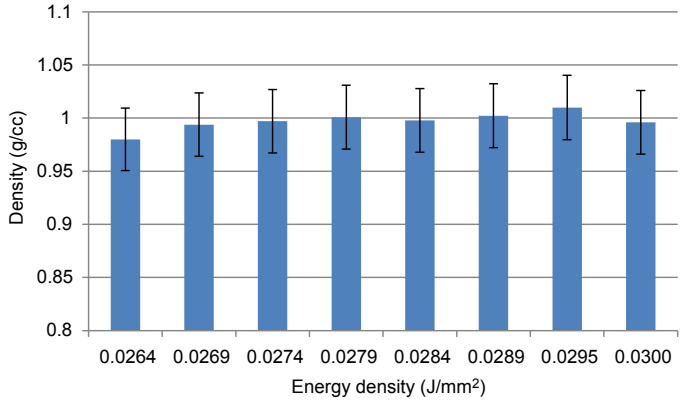

Figure 8.23 Average density of samples sintered at various energy densities.

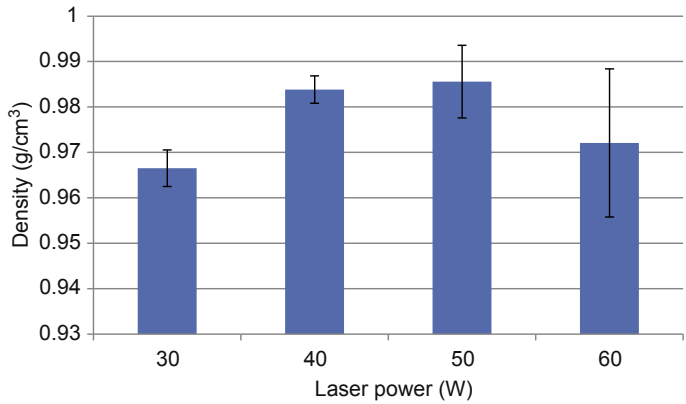

Figure 8.24 Specimen densities at different laser powers.

specimens were then measured by determining the mass of each specimen and dividing this value by its size. The determined densities can be observed in Fig. 8.24.

The change in density from set to set is very small, though in general the density was lowest in the 30-W samples, increased up through the 50-W samples, then decreased slightly at 60 W. The results for the 50- and 60-W specimens were similar to those observed in the previous build, with all densities being only marginally smaller than the ideal of 1.04 g/cm^3.

A significant detail not immediately observable from Fig. 8.24 is the size deviations from sample set to sample set. The samples sintered at the highest laser power had more notable instances of swelled or slightly deformed parts. Specifically, roughly 20% of the 60-W samples were removed from the evaluation because of this deformity, whereas only 10% of the 50-W samples and none of the 40- and 30-W samples had to be removed. Once the deficient samples had been removed from the set, the remaining sample data were plotted in Fig. 8.25.

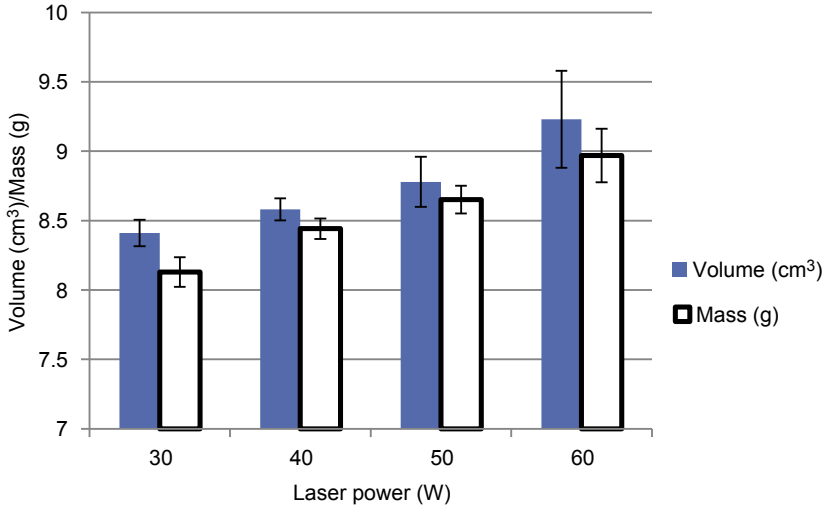

Figure 8.25 Comparison of masses and volumes of samples made using different laser powers.

An interesting trend can be observed from this set of data. With progressively higher laser powers, the samples notably increased in volume, with semiproportional increases in mass. This extra volume could be confirmed with visual observation, as the higher laser power samples developed slightly larger profiles than their counterparts using lower laser power. As all the sample sets were input to be the same size and printed on the same lateral z layer with even heating, so only the difference in the applied wattage was a variable. One theory we proposed for the observed phenomenon was that the material was more susceptible to bleed-over heating effects during the build phase. This suggested that higher laser powers incidentally caused more powder to be sintered together as a result of the inability of the composition to adequately cool in the proper form. This also explains why the samples created using higher laser power had more occurrences of deformation and swelling.

8.3.1.3 Mechanical properties

Tensile strength and modulus, elongation at break, Izod impact, and heat deflection temperature (HDT) data are described in this section. Tensile tests are typically used to determine a material's strength and stiffness [1]. For this we used an Instron Tensile Tester. Per ASTM D638 adapted in this study, the testing procedure for this machine involves first conditioning specimens at a controlled temperature and humidity for 40 h to decrease inconsistency. Next, a specimen is mounted between two crossheads, which apply tensile loading until the specimen is destroyed. The elongation and force measurements recorded during the procedure allow the Young's modulus, ultimate tensile strength, and elongation at break to be calculated, along with other properties not critical to this study [1,5]. Five specimens were created at each energy density, though as with the previous test some specimens had to be discarded because of imperfections. It is worth noting that during every test the tensile specimens were

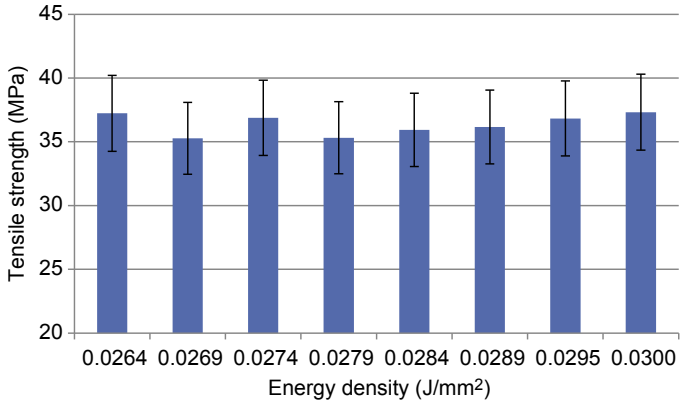

Figure 8.26 Average tensile strengths of samples sintered at varying energy densities.

oriented such that the tensile loading was applied along the *x* build direction. This was done to maximize the strength of the samples, as all of the samples were fabricated in the *x*-*y* plane. Because of the manner in which the SLS machine sinters layers together vertically in the *z* direction, the *z*-axis becomes the weakest direction in a sintered part, and any tests performed on this axis would not be indicative of the composite's strength. Results of these tensile tests are shown in Figs. 8.26–8.28.

Referencing Johnson and Koo's [4] previous builds using an unaltered PA11 base polymer, the base polymer alone featured a tensile strength of 47 MPa and a Young's modulus of 1.4 GPa. Comparing the data shown in Figs. 8.27 - 8.29 with the previously noted mechanical properties of the PA11 base polymer, it can be observed that the addition of the MWNTs in our sintering process resulted in specimens with a lower tensile strength and a lower Young's modulus. For the range of energy densities used, there does not seem to be an observable trend in the data. It is possible that the experimentation window was too narrow and that a trend could be observed if a wider range of energy densities were sampled. Further tests to evaluate this phenomenon are planned.

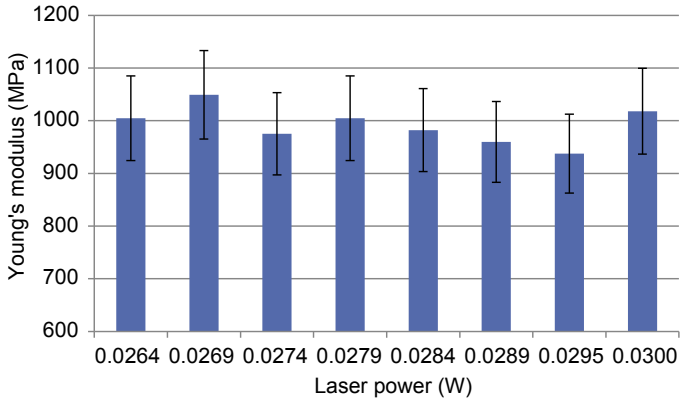

Figure 8.27 Average Young's moduli of samples sintered at varying energy densities.

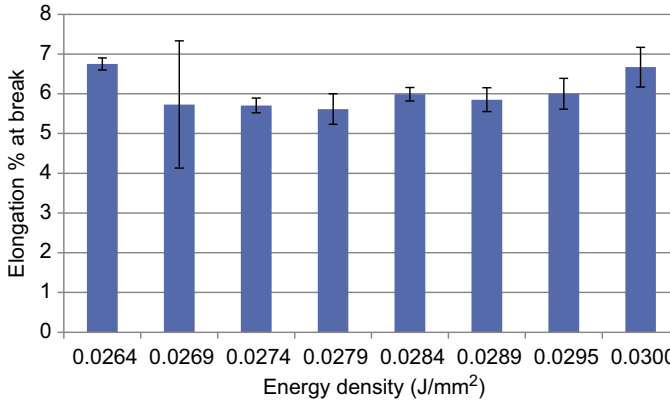

Figure 8.28 Average elongation at break of samples sintered at varying energy densities.

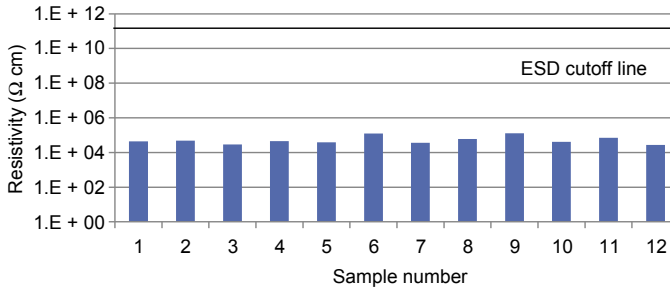

Figure 8.29 Resistivity of various samples tested. *ESD*, electrostatic dissipation.

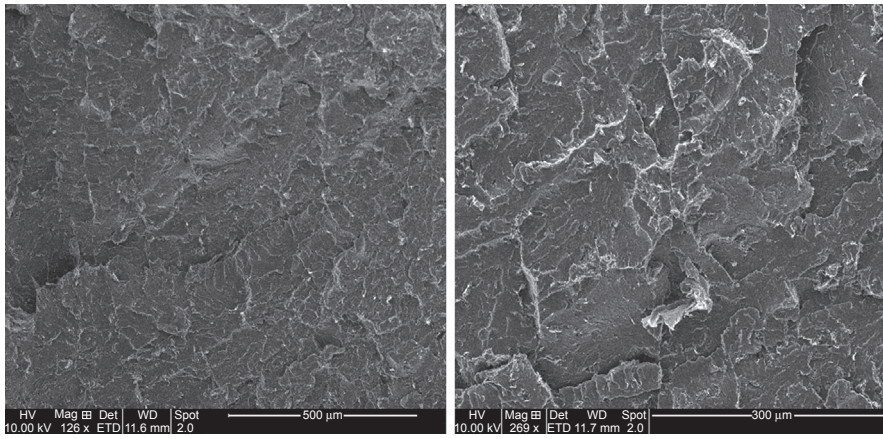

Figure 8.30 Scanning electron microscopy images of the *x*-direction cross section in progressive magnification.

8.3.1.4 Izod impact testing

To determine material resistance, notch-A Izod impact strength tests were conducted in accordance with ASTM D256. Several impact specimens were sintered using a laser power of 50 W, then subsequently filed and sanded to the correct testing parameters, if necessary. Once all five samples were of appropriate dimensions, as prescribed in the D256 standard, a 2.56-mm notch was created in each specimen using a motorized notch cutter. Each specimen was then mounted in the Izod impact tester and subsequently struck using a standard cantilever beam-weight configuration. The resulting energy absorbed by the specimen before breakage was recorded using the energy difference of the pendulum. Averaging the results of each sample, it was determined that the Izod impact strength had a mean of 0.754 J/cm^2 with a standard deviation of 0.0425 J/cm^2.

8.3.1.5 Heat deflection temperature testing

HDT tests were performed per ASTM D648 to further characterize the material. This entailed subjecting specimens to increasing temperatures while under three-point bending loading to observe what temperature causes a 0.25-mm deflection. The sintered samples were sent to Intertek (Pittsfield, MA), and all the samples were evaluated at a load of 1.80 MPa (264 psi). Intertek returned testing values with an average HDT of 165°C. However, Intertek noted that a few problems occurred with two of the samples they attempted to test: complete deterioration and subsequent melting of the sample without a deflection reading. We requested they return the problematic samples so we could conduct scanning electron microscopy (SEM) on them to obtain a better understanding of what happened.

8.3.1.6 Electrical conductivity

ESD properties are described in this section. It is known in the literature that certain additives, particularly MWNTs, can be added to insulative polymers to increase their electrical conductivity. This allows the material to be better suited for applications requiring adequate static dissipation or for sensing devices [6,8,9]. The testing procedure for this property involved careful application of silver wiring onto flat, nonconductive panels. By placing a rectangular sample of sintered material between the two wire bands and measuring the resistivity of the sample, conductivity could be evaluated using the inverse of the resistivity measured. The resistivity of each sample was evaluated using a digital resistance meter attached to silver wire leads.

A key benchmark measured against was the ESD property. The threshold for this cutoff is 10^{11} Ω cm and indicates a point where a material is deemed safe for use in industry [2]. Note that, as shown in Fig. 8.29, every PA11-MWNT sample tested demonstrated resistivity rates below the ESD cutoff. This indicates that the conductivity of the samples was far above the necessary minimum prescribed. For comparison, neat PA11 samples tested resulted in resistivity values of 1.0E + 14 and higher and would have not made the ESD cutoff.

8.3.1.7 Microstructural analysis

As a secondary method of verifying the degree of sintering attained, SEM images were obtained. A sintered tensile specimen was sectioned along the *x* (parallel to the neck of

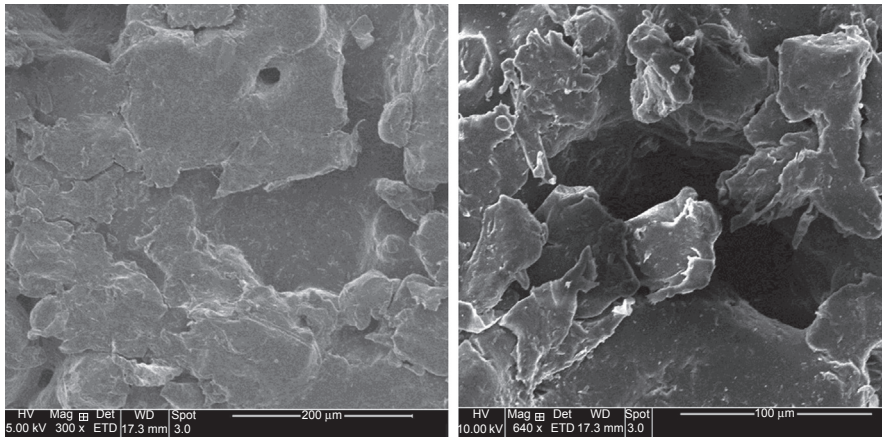

Figure 8.31 Scanning electron microscopy images of the *y*-direction cross section in progressive magnification.

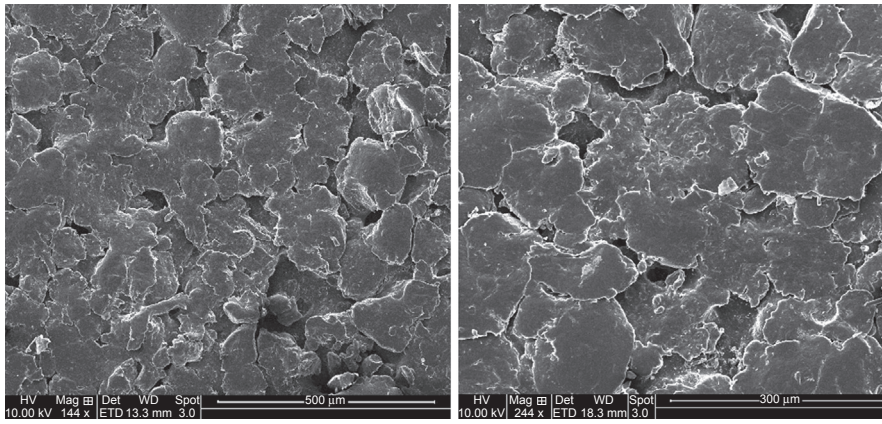

Figure 8.32 Scanning electron microscopy images of the *z*-direction cross section in progressive magnification.

the specimen), *y* (parallel with the layering direction of the specimen), and *z* (parallel to the build direction of the specimen) directions. The images included in this chapter are of relatively low magnifications, used to check the general form of the sintered particles. From Figs. 8.30–8.32, it is evident that despite the good densification observed earlier, the sintering process left several voids during the build. A closer view of one of such voids can be observed in Fig. 8.31. This suggests that the build parameters used were not yet optimized, which would account for the observed losses in tensile strength noted earlier.

8.3.1.8 Summary of the product technical data sheet

Compiling the data gathered from these builds based on Johnson and Koo's [4] previous experimentation, a summary of a product technical data sheet containing the

Table 8.3 Summary of PA11−multiwalled carbon nanotube material properties

Property	Test method	Metric
Color/appearance	Visual	Black
Density	ASTM D792	1.01 g/cc
Elongation at break (XY)	ASTM D638	6.03%
Flexural modulus	ASTM D790	
Tensile modulus	ASTM D638	991 MPa
Tensile strength (XY)	ASTM D638	45 MPa
Izod impact strength (method A, notched)	ASTM D256	0.754 J/cm^2
Heat deflection temperature @ 264 psi	ASTM D648	165°C
Heat deflection temperature @ 64 psi	ASTM D648	
50% Mass loss temperature	TGA	403°C
10% Mass loss temperature	TGA	373°C
Thermal conductivity (40°C)	Hot Disk TPS 500	0.3 W/m K
Surface finish	Ra	
Electrical volume resistivity	Hioki megaohmmeter	3.46×10^9 Ω cm
Electrical surface resistivity	Hioki megaohmmeter	2.68×10^7 Ω cm
Surface ESD	Hioki megaohmmeter	Pass
Volume ESD	Hioki megaohmmeter	Pass

ESD, electrostatic dissipation; *TGA*, thermogravimetric analysis.

material characterization data is shown in Table 8.3. Also included in the table are characterizations we plan to conduct or are currently in progress.

8.3.2 Flame retardant selective laser sintering polymer nanocomposite

8.3.2.1 Thermal stability

The definitions of N is nylon 11 (PA11), F is FR additive, E is elastomer (Kraton), and C is nanoclay are introduced in Figs. 8.33 and 8.34, and Tables 8.4 and 8.5. In Fig. 8.33, 70N_15F_10E_5C represents 70% of nylon, 15% of FR, 10% of elastomer, and 5% of nanoclay by weight. TGA data are included in this section. TGA was performed on neat PA11 and FR/Kraton/Nanoclay-reinforced PA11 under nitrogen using scan rates of 10°C/min, as shown in Fig. 8.33. The data gathered for formulation 70N_20F_10E from our previous study is plotted against our new results for comparison; a 10% concentration of Kraton was kept constant in all of the formulations. The

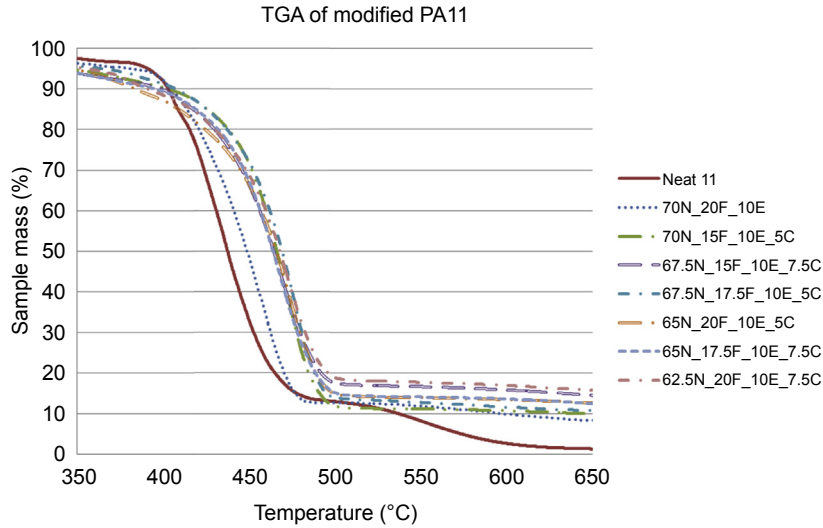

Figure 8.33 Sample mass (percentage) of neat polyamide 11 (PA11) and reinforced PA11 (thermogravimetric analysis; scan rate, 10°C/min in nitrogen).

Table 8.4 Decomposition temperatures of reinforced PA11

Formulation	$T_{10\%}$ (°C)	$T_{50\%}$ (°C)	Residue mass at 1000°C (%)
Neat PA11	403	438	0.88
70N_20F_10E	405	448	7.5
70N_15F_10E_5C	403	466	9.5
67.5N_15F_10E_7.5C	399	465	12.8
67.5N_17.5F_10E_5C	407	469	10.6
65N_20F_10E_5C	383	466	12.2
65N_17.5F_10E_7.5C	396	463	10.8
62.5N_20F_10E_7.5C	391	468	15.3

$T_{10\%}$, decomposition temperature for 10% mass loss; $T_{50\%}$, decomposition temperature for 50% mass loss. N is nylon 11 (PA11), F is FR additive, E is elastomer (Kraton), and C is nanoclay.

results of the TGA indicate that all formulations with FR additives and nanoclay have higher degradation curves when compared with PA11 and formulation 70N_20F_10E. All FR/Kraton/Nanoclay-reinforced PA11 formulations have slightly different degradation curves, as can be seen in Fig. 8.33. It can also be seen that FR/Kraton/Nanoclay-reinforced PA11 formulations degrade at a faster rate at the beginning compared with neat PA11 and 70N_20F_10E. The $T_{10\%}$ and $T_{50\%}$ are summarized in Table 8.4. The $T_{10\%}$ for neat PA11 and formulation

70N_20F_10E is 403 and 405°C, respectively; these values are higher than those for the rest of the formulations, except 67.5N_17.5F_10E_5C; 65N_20F_10E_5C is the lowest at 383°C. The $T_{50\%}$ for neat PA11 is 438°C, which is lower than all other formulations. Similarly, $T_{50\%}$ for 70N_20F_10E, although higher than that of neat PA11, is lower than all FR/Kraton/Nanoclay-reinforced PA11 formulations by about 20°C. After heating the materials to 1000°C, neat PA11 has only 0.089% of char residue left, whereas the amount of char residue for all other formulations was significantly increased. The nanoclay did have an effect in char residue. The formulation without nanoclay had a char residue of 7.5%, whereas the ones with nanoclay had an increase in char residue ranging from 9.5% to 15.3%. The concentration of nanoclay and fire retardant also increase the char residue of the material. Formulations with higher concentrations of fire retardant, nanoclay, or both had higher char residue; formulation 62.5N_20F_10E_7.5C had the most.

8.3.2.2 Flammability

MCC and UL 94 data are included in this section.

Heat release rates using microscale combustion calorimetry

Advanced Laser Materials has a commercially available fire-retardant PA11 powder for SLS. This material was compared with our FR/Kraton and FR/Kraton/Nanoclay-reinforced PA11 formulations. Fig. 8.34 shows that the formulation without nanoclay and only 20% fire retardant significantly decreases the peak heat release rate of neat PA11 by about 50%. On average, the formulation without nanoclay has a lower peak heat release rate than 70N_15F_10E_5C. The addition of nanoclay seems to slightly reduce the peak heat release rate and heat release capacity of the formulations when compared with those without nanoclay. Advanced Laser Materials's formulation has a heat release rate of about 540 J/g K and a peak heat release rate of about 605 W/g,

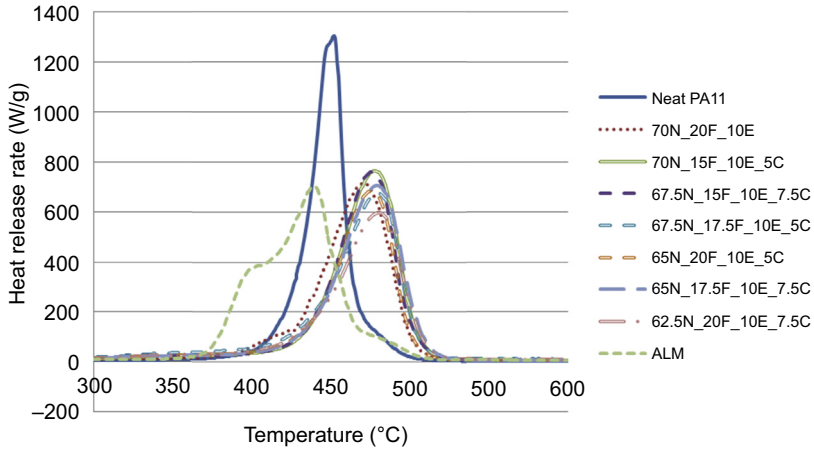

Figure 8.34 Heat release rate of modified polyamide 11.

Table 8.5 Summary of microscale combustion calorimetry results

Formulation	Heat release capacity (SD) (J/g K)	Peak heat release rate (SD) (W/g)
Neat PA11	1112 (50)	1277 (46)
70N_20F_10E	616 (9)	718 (10)
70N_15F_10E_5C	648 (6)	756 (8)
67.5N_15F_10E_7.5C	599 (10)	699 (11)
67.5N_17.5F_10E_5C	581 (41)	679 (47)
65N_20F_10E_5C	605 (32)	640 (39)
65N_17.5F_10E_7.5C	604 (18)	705 (21)
62.5N_20F_10E_7.5C	563 (27)	605 (28)
Advanced laser materials	540 (27)	605 (28)

which is relatively better than most of our formulations (except 62.5N_20F_10E_7.5C). These results correlate with our TGA results. The higher concentration of fire retardant, nanoclay, or both seems to yield a lower peak heat release rate and heat release capacity. Table 8.5 summarizes the heat release rate of the modified PA11 formulations.

UL 94 results

Table 8.6 summarizes the UL 94 test results of the formulations. From the data gathered, none of the formulations met the V-0 requirements. In addition, the results from the

Table 8.6 Summary of UL 94 test results

Formulation	Average first-burn flaming combustion duration (s)	Averaged second-burn flaming combustion duration (s)	Flaming drip	UL 94 rating
Neat PA11	4	–	Yes	V-2
70N_20F_10E	14.6	12.4	No	V-1
70N_15F_10E_5C	30	10	No	V-1
67.5N_15F_10E_7.5C	30	11	No	V-1
67.5N_17.5F_10E_5C	23.6	6.6	No	V-1
65N_20F_10E_5C	15.6	7.4	No	V-1
65N_17.5F_10E_7.5C	18.5	6.4	No	V-1
62.5N_20F_10E_7.5C	13	18	No	V-1

MCC do not correlate well with the UL 94 results; 70N_20F_10E was almost rated V-0 and had a significantly higher heat release capacity than most of the formulations with nanoclay. One thing to note is that all formulations, with the exception of 62.5N_20F_10E_7.5C, seem to have a longer combustion duration of first-burn flaming.

8.3.2.3 *Mechanical properties*

Tensile strength, tensile modulus, and elongation at break are described in this section. Table 8.7 summarizes the mechanical properties at room temperature of blends containing Kraton, fire retardant, and nanoclay. It is known from previous studies that the main impact of the fire retardant on mechanical properties lies in the elongation at break, which is typically decreased by more than 90% [12]. Our previous research showed that 20% fire retardant reduces the elongation at break to 6% [13,14]. The addition of 10% Kraton increased the elongation back to 17%. It was of interest to see how the elongation at break would be affected by the nanoclay, since it is also known that nanoclay has a negative effect on elongation at break [12]. The addition of nanoclay improved the modulus by almost 50%; 62.5N_20F_10E_7.5C had the highest modulus. The tensile strength does not change with different concentrations of fire retardant and nanoclay. However, elongation at break was drastically affected by the addition of nanoclay. Fig. 8.35 shows that the higher concentration of nanoclay, the lower the elongation at break, with reading as low as 3%, which is even lower than the 6% obtained from our previous study [13,14].

Fig. 8.36 shows the samples after the UL 94 test was conducted, which visually correlates with the time it took each sample to self-extinguish. From all these formulations, it can be concluded from both the time it took each formulation to self-extinguish, and it is clear from Fig. 8.36 that formulation 70N_20F_10E is the best in this test.

Table 8.7 Summary of tensile test results

Formulation	Tensile strength (SD) (MPa)	Modulus (SD) (MPa)	Elongation at break (SD) (%)
Neat PA11	49 (3)	1380 (41)	164 (74)
70N_20F_10E	34 (1)	1320 (67)	17 (2)
70N_15F_10E_5C	36 (2)	1920 (47)	8 (1)
67.5N_15F_10E_7.5C	37 (2)	2310 (44)	3 (0)
67.5N_17.5F_10E_5C	35 (1)	2050 (67)	8 (1)
65N_20F_10E_5C	34 (1)	2060 (142)	7 (1)
65N_17.5F_10E_7.5C	34 (5)	2310 (106)	3 (1)
62.5N_20F_10E_7.5C	34 (2)	2460 (132)	3 (0)

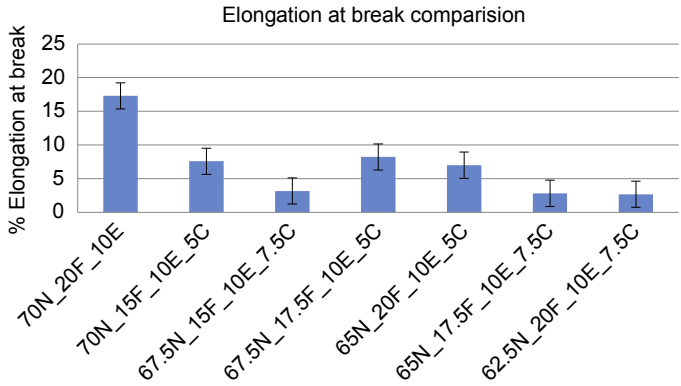

Figure 8.35 Comparison of elongation at break for different polyamide 11 compositions.

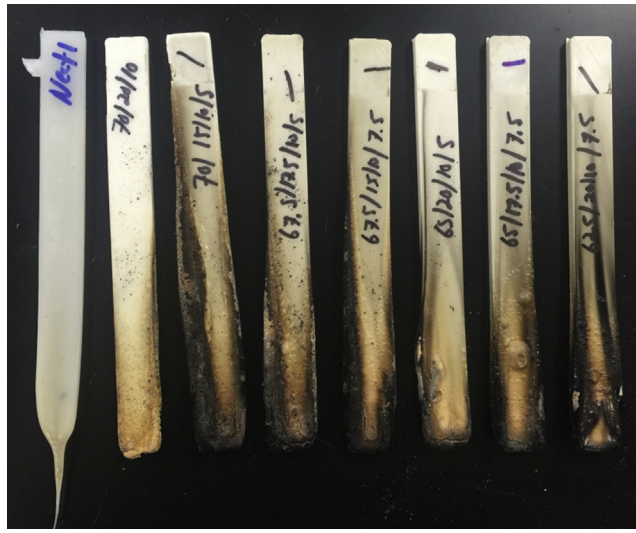

Figure 8.36 UL 94 samples (from left to right): neat polyamide 11, 70N_20F_10E, 70N_15F_10E_5C, 67.5N_17.5F_10E_5C, 67.5N_15F_10E_7.5C, 65N_20F_10E_5C, 65N_17.5F_10E_7.5C, and 62.5N_20F_10E_7.5C.

8.4 Summary and conclusions

The laser power and scan speed will be adjusted for future PA11-MWNT builds to sample a wider range of energy densities to study the full effects of energy density on the sintering process of this material. Additional characterization, including the heat deflection temperature at 66 psi and the flexural modulus, is planned for additional composites once appropriate specimens have been fabricated. Using the parameters established in this study, similar tests are planned for PA11-NGP to observe how

the SLS parts of this polymer nanocomposite perform compared with the PA11-MWNT parts. Last, once the build parameters of the material have been optimized, higher-magnification SEM images will be created to check the dispersion of the additives in the material. FR PA11 composites will be processed and fabricated into SLS test specimens to characterize their material properties.

A feasibility study was performed to explore the potential of using SLS as a fabrication method for polymer nanocomposites made using a fire-retardant additive, an elastomer, and nanoclay [15]. Thermal, FR, and mechanical properties of FR/Kraton/Nanoclay-reinforced PA11 nanocomposites were compared by first preparing the formulations via the twin screw melt mixing method and then injection molding specimens. It is important to note that SLS specimens have not yet been made using any of the FR formulations discussed in this chapter. These formulations have not reached the desired mechanical and FR properties via injection molding; hence making specimens via SLS is not yet economically feasible.

Based on this set of results, the addition of nanoclay and the fire-retardant additive gives more char residue when compared with neat PA11. In addition, nanoclay brought the peak heat release and heat release capacity lower and close to the commercially available PA11 powder from Advanced Laser Materials, with 62.5N_20F_10E_7.5C being the best formulation in this set of experiments. Unfortunately, none of the formulations achieved a V-0 rating, even though the MCC results seemed promising when compared with the ALM formulation. In addition, all the formulations with nanoclay performed poorly with regard to the elongation at break. Microstructure analysis is still in progress. We are interested to determine the degree of dispersion of the elastomer and nanoclay in the polymer matrix and how this might have affected our results.

In a recent study, Ortiz reported by blending a multi-component of FR additive, elastomer, nanoclay, and MWNT with PA11 through twin-screw extrusion processing, a PA11 nanocomposite formulation with an elongation at break of 30% and a UL 94 V-0 rating was achieved [16].

Acknowledgments

The authors would thank KAI, LLC, for providing material and financial support for the duration of this study. The authors also credit Advanced Laser Materials for the use of their facilities and the assistance of their staff during the SLS build phases. Last, the authors thank Intertek (Pittsfield, MA) for their assistance with the HDT testing.

References

[1] P. Jain, P. Pandey, P.V.M. Rao, Selective laser sintering of clay-reinforced polyamide, Polymer Composites 31 (4) (2009) 733−738.

[2] R.D. Goodridge, M.L. Shofner, et al., Processing of a polyamide-12/carbon nanofibre composite by laser sintering, Polymer Testing 30 (1) (2011) 94−96.

[3] C. Yan, L. Hao, L. Xu, Y. Shi, Preparation, characterization and processing of carbon fibre/polyamide-12 composites for selective laser sintering, Composites Science and Technology 71 (16) (2011) 1834−1841.
[4] B.A. Johnson, J.H. Koo, Analysis of the selective laser sintering process using nanocomposite materials, in: Proc. SAMPE 2012 ISSE, SAMPE, Covina, CA, May 2012.
[5] S.R. Athreya, K. Kalaitzidou, S. Das, Processing and characterization of carbon-black-filled electrically conductive nylon-12 nanocomposite produced by selective laser sintering, Materials Science and Engineering 527 (10−11) (2010) 2637−2642.
[6] G.V. Salmoria, R.A. Paggi, Microstructural and mechanical characterization of Pa12/MWCNTs nanocomposite manufactured by selective laser sintering, Polymer Testing 30 (6) (2011) 611−615.
[7] S.R. Athreya, K. Kalaitzidou, S. Das, Mechanical and microstructural properties of nylon-12/carbon black composites: selective laser sintering versus melt compounding and injection molding, Composites Science and Technology 71 (4) (2011) 506−510.
[8] C. Wei, D. Srivastava, K. Cho, Thermal expansion and diffusion coefficients of carbon nanotube-polymer composites, Nano Letters 2 (2002), http://dx.doi.org/10.1021/nl025554.
[9] B. Caulfield, P.E. McHugh, S. Lohfeld, Dependence of mechanical properties of polyamide components on build parameters in the SLS process, Journal of Materials Processing Technology 182 (1−3) (2007) 482−485.
[10] UL 94, Tests for Flammability of Plastic Materials for Parts in Devices and Appliances, Underwriters Laboratories Inc. (UL), Northbrook, IL, 1996.
[11] ASTM D7309-07, Standard Test Method for Determining Flammability Characteristics of Plastics and Other Solid Materials Using Microscale Combustion Calorimetry, ASTM International, West Conshohocken, PA, 2007. www.astm.org.
[12] S. Lao, J.H. Koo, A. Morgan, H. Jor, G. Wissler, L. Pilato, Z.P. Luo, Flammability intumescent polyamide 11 nanocomposites, in: Proc. SAMPE 2007 ISTC, Covina, CA, 2007.
[13] R. Ortiz, H. Wu, J.H. Koo, Flame-retardant polyamide 11/elastomer blends for SLS: processing and characterization, in: Proc. CAMX 2015, Dallas, TX, Oct 26−29, 2015.
[14] R. Ortiz, H. Wu, T. Correa, E. Lui, J.H. Koo, Fire-retardant polyamide 11 nanocomposites/elastomer blends for selective laser sintering: further studies, in: AIAA SciTech 2016, San Diego, CA, Jan. 4−7, 2016.
[15] H. Wu, M. Krifa, J.H. Koo, Flame retardant polyamide 6/elastomer blends: processing and characterization, in: Proc. SAMPE 2014, Seattle, WA, June 2014.
[16] R. Ortiz, Fire Retardant Polyamide 11 Nanocomposites/Elastomer Blends for Selective Laser Sintering, M.S. thesis, in: The University of Texas at Austin, Dept. of Mechanical Engineering, Austin, TX, May 2016.

Laser additive manufacturing using nanofabrication by integrated two-photon polymerization and multiphoton ablation

9

W. Xiong [1,2], *L.J. Jiang* [1], *T. Baldacchini* [3], *Y.F. Lu* [1]
[1]University of Nebraska-Lincoln, Lincoln, NE, United States; [2]Huazhong University of Science and Technology, Wuhan, Hubei, China; [3]Newport Corporation, Irvine, CA, United States

9.1 Introduction

9.1.1 Brief review of laser direct writing for micro/nanofabrication

Methods of micro-/nanofabrication of three-dimensional (3D) structures are of increasing interest because of their importance for the creation of compact 3D devices and their assembly into functional 3D systems. Recent years have witnessed a phenomenal increase in 3D micro-/nanofabrication techniques from diversified fields, such as microelectromechanical systems (MEMS)/nanoelectromechanical systems (NEMS), nanoelectronics, micro-/nanophotonics, biomedical engineering, bio-inspired architectures, and micro-/nanofluidics, with the aim of developing neoconceptual and high-value-added products [1−8]. Most current 3D micro-/nanofabrication techniques are based on traditional two-dimensional (2D) fabrication techniques such as photolithography, using layer-by-layer strategies [1−8]. However, such 3D micro-/nanofabrication techniques provide only limited 3D micro-/nanofabrication capabilities [1−8]. Broad applications of such 3D micro-/nanofabrication are limited because of expensive facilities, a time-consuming layer-by-layer strategy, high cost, low throughput, and the inability to fabricate 3D micro-/nanostructures of arbitrary geometry and increased complexity [1−8]. Some applications would be extremely challenging using conventional micro-/nanofabrication techniques, such as the controlled introduction of defects into 3D photonic crystals to achieve required functionality, fabricating 3D movable components in MEMS/NEMS devices, and constructing micro-/nanofluidic devices [1−8]. Therefore, a 3D micro-/nanofabrication technique that is capable of fabricating 3D micro-/nanostructures of arbitrary geometry at a nanometric resolution using a cost-effective process is highly desirable.

Laser Additive Manufacturing. http://dx.doi.org/10.1016/B978-0-08-100433-3.00009-9
Copyright © 2017 Elsevier Ltd. All rights reserved.

Femtosecond laser direct writing (FsLDW) is a precise, laser-based 3D micro-/nanofabrication method and has been recently recognized as a promising candidate to address existing challenges [9–14]. In FsLDW, a tightly focused laser beam penetrates a bulky material without obvious loss of absorptive energy; it scans according to a designed pattern from the bottom slice to the upside slice or vice versa until the entire 3D structure is fabricated [14]. Because of the extremely high transient power density, photons are absorbed in a nonlinear manner at the focal point in a volume much smaller than the cubic wavelength, λ^3, achieving high spatial resolution beyond the optical diffraction limit [14]. Therefore, FsLDW can be simply understood as a laser direct writing technique that involves nothing more than converting a 3D digital design into a target material. FsLDW also distinguishes itself from other micro-/nanofabrication methods as a universal tool applicable to diversified materials, including organic materials, biomaterials, dielectrics, metals, and semiconductors, only if a proper photon-material strategy is determined [14]. Compared with conventional 3D nanofabrication techniques, FsLDW demonstrates several advantages, including (1) single-step, noncontact, and mask-free direct 3D fabrication; (2) capability to fabricate arbitrary geometries and irregular structures; (3) capability to fabricate movable components; (4) realization of real 3D nanofabrication; (5) capability to work on a broad range of materials such as polymers, ceramics, metals, and hybrid materials; and (6) easy fabrication of voids, channels, and holes inside a bulk material [14].

This chapter introduces our research efforts in 3D micro-/nanofabrication based on FsLDW. Two different 3D micro-/nanofabrication strategies are demonstrated, including the additive 3D micro-/nanofabrication by two-photon polymerization (TPP) and the subtractive 3D micro-/nanofabrication by multiphoton ablation (MPA). The advantages and disadvantages for both fabrication techniques are shown and analyzed. Finally, a comprehensive 3D micro-/nanofabrication method by seamless integration of the additive TPP and subtractive MPA is demonstrated. The established comprehensive 3D fabrication method not only inherits the merits of both TPP and MPA in achieving ultrahigh writing resolution beyond the diffraction limit and features of sharp and clean edges, but it also offers the possibility to produce novel device structures that are difficult to be fabricated by either TPP or MPA alone.

9.1.2 Linear and nonlinear optical absorption in laser direct writing

In TPP an intensity laser threshold exists below which no polymerization occurs. In the specific case of resins that polymerize through a radical mechanism, the presence of this threshold is a direct consequence of the chemical nature of the resins' components. The growth of macromolecular chains within the resin depends greatly on the delicate ratios of the rate constants among several processes that occur at the same time: initiation, propagation, recombination, and termination. If radicals are not continuously

generated during the initial stages of the polymerization reaction, no chains will be formed. In polymerization induced by light absorption, this mechanism results in the presence of an intensity threshold.

In the first approximation, the accumulated exposure dose D of a single voxel induced for an N-photon-absorption process can be described as:

$$D \propto (P - P_{\text{th}})^N t, \tag{9.1}$$

where P is the laser average power, P_{th} is the laser threshold power, and t is the exposure time [15].

According to this model, in one-photon polymerization ($N = 1$) the exposure dose is linearly proportional to the laser average power. In TPP ($N = 2$) the exposure dose becomes proportional to the square of the average laser power. To take advantage of this model from an experimental point of view, a series of voxels are fabricated using different values of both laser average powers and exposure times. Among these voxels there will be some with identical widths that are created with different combinations of laser average powers and exposure times. Assuming that identical voxels are fabricated when the same exposure dose is used, a log−log plot of exposure times and laser average powers used to create identical feature sizes can reveal the value of N in Eq. (9.1). Hence, careful dosimetry experiments such as the ones described in the previous section not only produce useful information regarding writing conditions to use when performing high resolution TPP; they can also offer insightful evidence on the nature of the light absorption process that starts polymerization.

9.1.3 Challenges and opportunities

All of the grand goals for nanoscience are dependent upon reliable ways to fabricate nanostructures. Methods that use a laser direct writing process to achieve these goals show promising results in the fabrication of various nanomaterials and micro-/nanostructures of various dimensions, which are challenging to fabricate via conventional fabrication methods. Although TPP is almost ready to be implemented in a complimentary fashion with other more conventional microfabrication methods for industrial production, there are still three challenges that need to be addressed. The first is scalability. Being a serial process, TPP can produce only one object at a time slowing manufacturing progress and increasing its cost. The second challenge is the limited range of nonlinear photosensitive resins available for TPP, which seriously limits the functionality of the as-fabricated 3D micro-/nanostructures. The third challenge is the lack of comprehensive femtosecond laser 3D micro-/nanofabrication techniques combining both subtractive and additive fabrication capabilities. It is then imperative to focus future research activities to solve these three challenges in order to fully unleash the potential of 3D laser micro-/nanofabrication for various industrial applications such as MEMS/NEMS, 3D electronics, integrated optics, lab-on-a-chip, biomimetics, and metamaterials.

9.2 Additive nanofabrication using two-photon polymerization

9.2.1 Characterization of two-photon polymerization

TPP is one of the additive FsLDW techniques making use of photosensitive resins in 3D micro-/nanofabrication. Compared with other micro-/nanofabrication approaches, additive TPP offers both high resolution and relatively high throughput. TPP lithography is a typical nonlinear optical effect that, in general, requires a femtosecond laser to provide short pulses with photon energy well below the one-photon absorption edge of a photoresist. The photoresist polymerizes if the light intensity is high enough for two-photon absorption inside the material, which is in the focal volume of a microscope objective. This process causes a chemical and/or physical change of the photoresist within a small-volume pixel ("voxel"). This voxel typically is of ellipsoidal shape and is the basic building block in the 3D fabrication process. By moving the sample relative to the fixed focal position, arbitrary paths can be written into the photoresist. It can be simply described as using a laser beam to inscribe 3D nanostructures. Because of the threshold behavior and nonlinear nature of the process, a resolution far beyond the diffraction limit can be realized by controlling the laser power and scanning speed. As a result, the technique provides much better structural resolution and quality than conventional stereolithography.

9.2.1.1 Characterization of voxel dimensions

The "voxel" of a polymer is the basic building block of TPP. To obtain the highest fidelity of fabrication when writing a complex 3D microstructure by TPP, it is of uttermost importance to characterize the voxel's lateral and axial dimensions. One experimental technique used to retrieve this information is the so-called ascending method. Separate voxels are fabricated on the substrate's surface, keeping all writing conditions the same but positioning the laser focal volume in reference to the substrate−resin interface. Because a polymerized voxel will have a defined length, some of the voxels will be fully anchored to the substrate, whereas others will lay sideways because of their weak adhesion to the substrate. By imaging these latter voxels using scanning emission microscopy (SEM), it is possible to measure both their length and diameter. Although this method has the advantage of reveling in one image both dimensions of a voxel, it has the drawback of not giving a direct measure of the voxel size when performing TPP. In almost all cases, TPP occurs by moving either the sample around a fixed laser beam or the laser beam within a fixed resin. In both cases the microstructure is fabricated with a continuous overlap of voxels. Hence a more direct way to get information on the feature size used in TPP is to fabricate lines suspended from the substrate by means of tall supports. These lines, generated by a single laser passes, can reveal both the width and length of the polymerized feature size when imaged by SEM at different angles. An example of such a study is shown in Fig. 9.1.

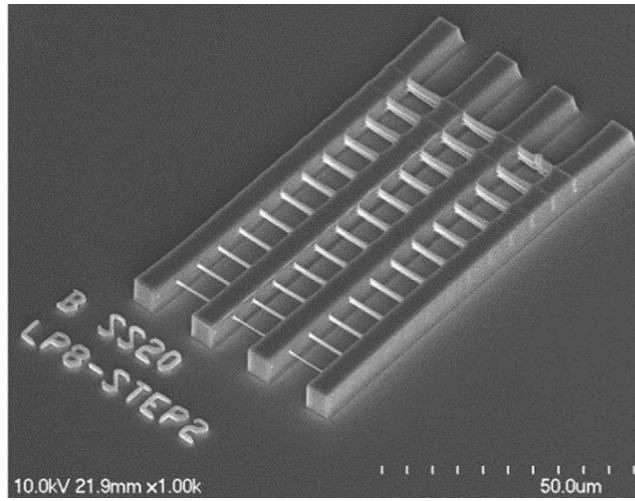

Figure 9.1 Characterization of voxel sizes in the two-photon polymerization process: scanning emission microscopy image of a test microstructure used to measure the width and the length of suspended lines.

9.2.1.2 Raman spectroscopy of TPP

Although TPP has become an enabling technology for several applications, there are still some fundamental aspects that have not yet been fully characterized. One of these is the influence of the scanning pattern on the mechanical properties of the microstructures. Even if the same object can be realized using different writing strategies, some approaches are better than others in producing accurate and dimensionally robust microstructures. Another aspect of TPP that requires a better understanding is the influence of the developing process on polymer swelling and solvent inclusion, which might have a large impact on the structural integrity of the microstructures. To answer these and other questions, an analytical technique capable of investigating the materials used in TPP at the molecular level is required before and after laser processing. Raman spectroscopy is a formidable tool for the characterization of microstructures fabricated by TPP. It allows for in situ and nondestructive monitoring of specific molecular bond vibrations with high spectral resolution and minimal sample preparation [16].

Raman spectroscopy provides comprehensive information about the vibrational modes of molecules using light scattering. The Raman-scattered light from the molecules in the probed sample is shifted in the frequency domain relative to the excitation light center frequency, and it contains information about the vibrational frequencies and anisotropy of molecular vibrations. Vibrational modes are like fingerprints of molecules. Therefore, Raman scattering is endowed with the sensitivity to discern different molecular species. Raman spectroscopy has broad applications, ranging from fundamental physical chemistry, inorganic chemistry, biochemistry, art, and archaeology to highly practical forensic examinations.

Most TPP has been performed using acrylic-based resins that are composed mainly of two molecular components: a photoinitiator and a mixture of monomers/oligomers [17]. The first one is the molecule capable of undergoing excitation by two-photon absorption and of generating active species (radicals) that start the polymerization process. In the presence of excited photoinitiators, the monomer/oligomer mixture forms a complex linked network − a polymer. Monomers and oligomers are present in the resin in much larger numbers than photoinitiators. Radicals generated during laser irradiation react with the monomer/oligomer mixture to form high-molecular-weight materials through a chain growth mechanism. Several reactions with different rates for initiation, propagation, chain transfer, and termination occur at the same time. In chain polymerization monomers and oligomers react only with the propagating reactive center, not with other monomers and oligomers, and chain addition ceases when the active species are depleted by a number of termination reactions. The molecular weight of chain polymers increases rapidly during polymerization and monomer/oligomer-to-polymer conversion (degree of conversion) can widely range between 20% and 90%, depending on the chemical nature of the monomers and oligomers. In acrylic monomers and oligomers, chain addition takes place in the carbon−carbon double bonds (C═C) present in molecules' ester moiety. Thus, during TPP, the number of C═C bonds diminishes in favor to the formation of new intermolecular carbon−carbon single bonds (C−C).

The Raman spectra of a typical resin used in TPP before and after polymerization are shown in Fig. 9.2. Two distinctive peaks are observed at 1635 and 1723 cm^{-1}, which

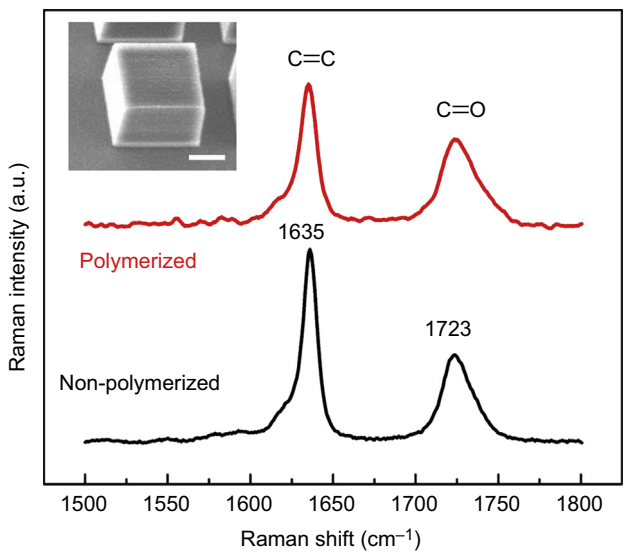

Figure 9.2 Raman spectra of a typical acrylic-based resin used in two-photon polymerization (TPP) before and after polymerization. The inset shows a scanning electron micrograph of a solid cube created by TPP and used to perform Raman spectroscopy (scale bar: 5 mm) [16]. a.u., arbitrary units.

are ascribed to the vibrational modes of C═C and the carbonyl (C═O) groups of the monomer, respectively. As a consequence of the diminished concentration of the C═C bonds following polymerization, the intensity of the peak at 1635 cm^{-1} in the polymerized resin is smaller than in the unpolymerized resin. On the other hand, the intensity of peak at 1723 cm^{-1} remains the same before and after polymerization because the carbonyl group does not participate in the chain reaction. The area of a peak in a Raman spectrum is proportional to the concentration of the oscillators responsible for that particular Raman active mode. Thus, spectra such as the ones in Fig. 9.2 can be used to measure the degree of conversion (DC) in resins following TPP. DC represents the number of C═C bonds consumed during polymerization and is a major factor influencing the mechanical properties of the ultimate microstructure; the higher the DC, the stronger the polymer. Since the number of carbonyl groups in the resin remains the same before and after polymerization, the peak at 1723 cm^{-1} can be used as internal reference for DC estimation. The percentage of DC is obtained using Eq. (9.2):

$$\mathrm{DC} = \left[1 - \frac{A_{C=C}/A_{C=O}}{A'_{C=C}/A'_{C=O}}\right] \tag{9.2}$$

where $A_{C=C}$ and $A_{C=O}$ are the integrated intensities of the 1635 and 1720 cm^{-1} peaks in the polymerized resin, respectively, whereas $A'_{C=C}$ and $A'_{C=O}$ are the integrated intensities of the same peaks in the unpolymerized resin.

A series of microcubes were fabricated first and then characterized using a confocal Raman microspectrometer. An SEM image of a microstructure used in the study is shown in the inset of Fig. 9.2. The microcubes were fabricated using several laser average powers and writing speeds. For each microstructure, Raman spectra like the ones in Fig. 9.2 were recorded and then used to measure DCs with Eq. (9.2). The results are shown in Fig. 9.3. At constant writing speeds, DC values monotonically increase with increasing average laser power. The highest DC value is around 43%; larger DCs are not attainable because the resin starts to boil if higher average laser powers were used. During TPP, highly cross-linked macromolecules are formed that can severely limit molecular mobility. The probability that an unreacted C═C bond will encounter a radical is dramatically reduced with the evolving polymerization, and a complete conversion (DC = 100%) is not achieved.

9.2.2 Additive nanofabrication of 3D micro-/nanostructures

Fig. 9.4 shows a schematic and a photo of a typical 3D lithography system (Photonic Professional; Nanoscribe GmbH), which mainly consists of a femtosecond laser, a piezoelectric 3D scanning stage for fast writing of small-area structures, and a motor-driven linear positioning system. The laser is a compact femtosecond-fiber laser (T-Light II; Menlo Systems) with 65-mW average power, 780-nm center wavelength, a pulse duration <120 fs, and a repetition rate of 100 MHz. The piezo positioning system, with *x*-*y*-*z* axes, provides a maximum travel distance of 300 μm in each direction. The Zeiss optical microscope equipped with a charge-coupled device camera enables real-time process monitoring. The whole system is installed on a

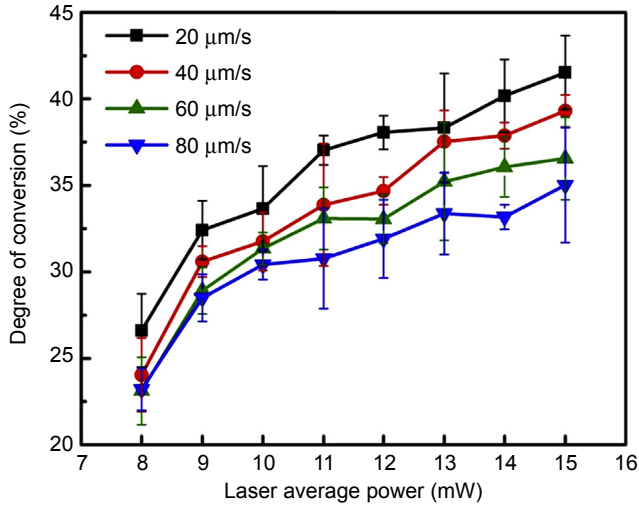

Figure 9.3 Polymeric degree of conversion of microstructures fabricated by two-photon polymerization using Raman spectroscopy [16].

vibrational isolation table from Thorlabs Inc. Table 9.1 summarizes the specifications of the 3D lithography system.

TPP micro-/nanofabrication generally requires three steps. First, a glass substrate is coated with a layer of photoresist and loaded into the lithography system. The second step is structure programming using a specialized GWL. Alternatively, the structure data can be also imported from a computer-assisted design or a stereolithography file. The 3D lithography system visualizes the loaded structure data and automatically approaches the designated samples and adjusts the focus to the interface. Third, the 3D lithography system conducts the TPP process by tightly focusing the laser beam inside the photoresist and making a 3D scan according to the geometry design. After the TPP lithography, the samples are developed and processed for further experiments.

In addition to the calibration of voxel dimensions with different laser powers and scanning speeds, laser scanning modes should be optimized. Practical applications of micro optical devices, such as microlenses, generally require high-quality surface profile and sufficient smoothness. Therefore it is important to optimize the TPP process for the fabrication of 3D micro-/nanostructures with sufficient surface smoothness. In the TPP process, we found that conventional parallel linear scanning mode hardly achieves a high-quality surface. In fact, during parallel linear scanning the width of the fabricated line not only deforms the circle dimension but also causes protrusions at the edges of the lens surface, as shown in Fig. 9.5(a)–(c). To obtain a smooth microlens with better optical performance by TPP lithography, an annular scanning mode coordinated with continuous variable scanning steps was adopted. Using this new scanning method, a spherical microlens with a high surface quality was readily produced in a shorter processing time (see Fig. 9.5(d)).

Figs. 9.6 and 9.7 show a variety of 3D photonic crystal structures fabricated using the additive TPP technique, including woodpile and spiral photonic crystal structures

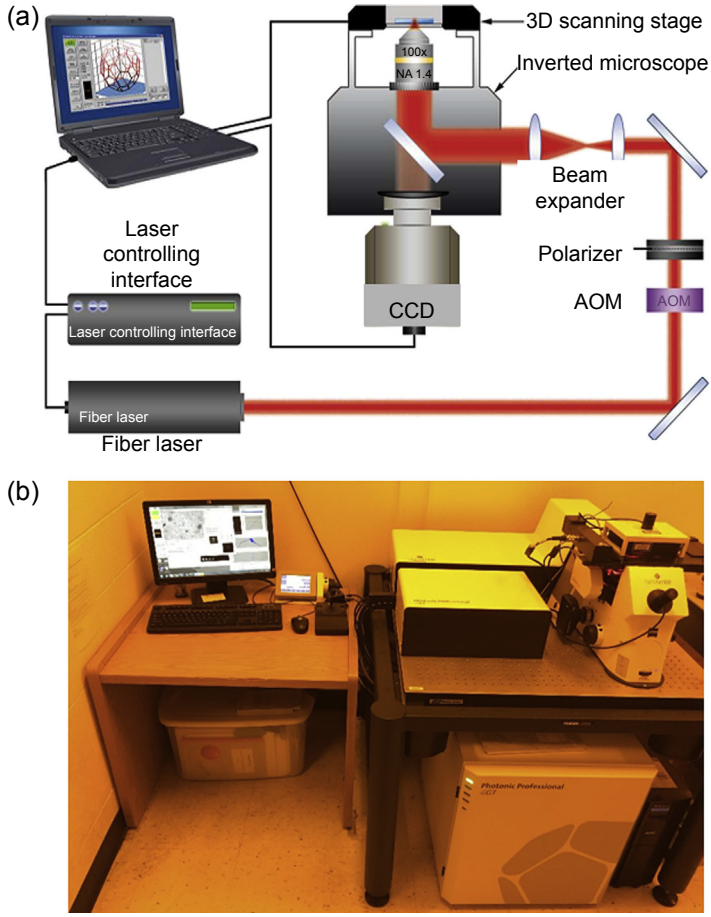

Figure 9.4 (a) Schematic of the two-photon polymerization three-dimensional (3D) lithography system (Nanoscribe GmbH). (b) Photo of the Photonic Professional 3D lithography system installed in the Laser-Assisted Engineering Lab.

Table 9.1 Specifications of the 3D lithography system

Lateral feature size	150 nm	Piezo range	300 × 300 × 30 0 μm
Maximum writing speed	2 mm/s	Maximum laser power	100 mW
Positioning accuracy	<5 nm	Laser wavelength	780 nm
Positioning repeatability	2 nm	Working distance	160 μm to 4 mm

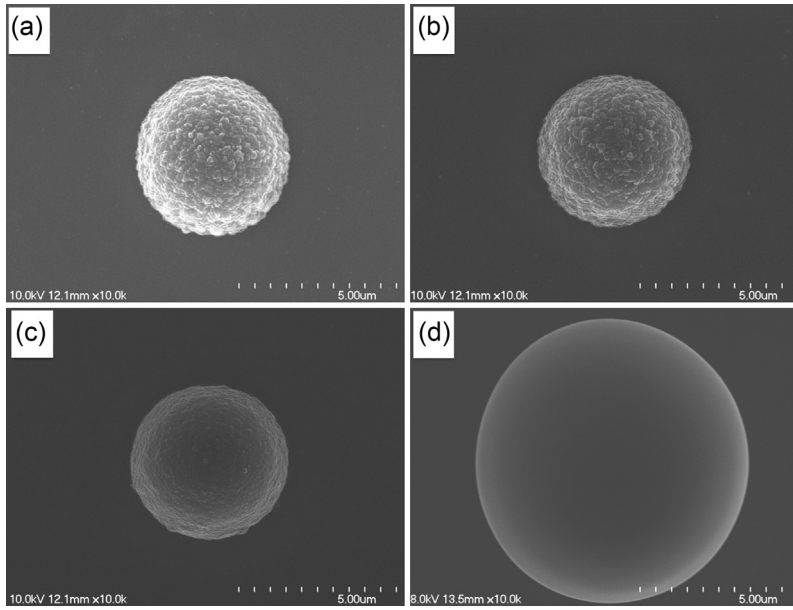

Figure 9.5 Comparison of TPP fabrication results with different laser scanning parameters: (a) parallel linear scanning mode, 200-nm step; (b) parallel linear scanning mode, 100-nm step; (c) parallel linear scanning mode, 20-nm step, 1-h processing time; (d) annular scanning mode, 10-nm step, 20-min processing time.

with a spatial resolution around 150 nm. Compared with 2D photonic crystals, 3D photonic crystals provide the ability to manipulate light regardless of the polarization direction because of their omnidirectional photonic band structures coming from corresponding solid network structures [18]. Therefore, 3D photonic crystals can avoid many disadvantages of 2D photonic crystals. However, such 3D photonic crystals are very challenging and costly to fabricate using conventional approaches. It was demonstrated that TPP provides a powerful tool in the convenient fabrication of functional 3D photonic crystals. Other than 3D photonic crystal structures, many other 3D optical components and structures were successfully fabricated using the additive TPP fabrication process. Figs. 9.8 and 9.9 demonstrate scanning electron micrographs of microlens arrays, optical cavity structures, and various complex 3D micro-logos. The fabrication results demonstrate the capability of the TPP method in precisely fabricating 3D micro-/nanostructures of complicated geometries.

9.3 Subtractive micro-/nanofabrication using multiphoton ablation

MPA is another typical FsLDW technique that has been established as a useful subtractive manufacturing technology in 3D micro-/nanostructuring of solid materials

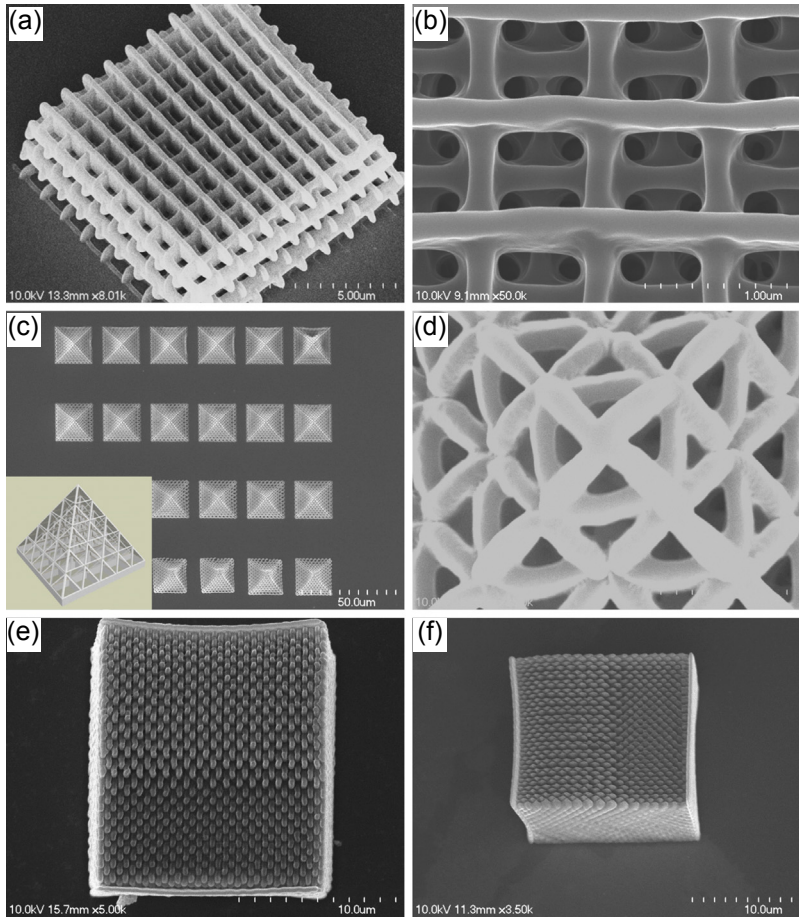

Figure 9.6 (a, b) Woodpile structures, (c, d) pyramid structures, and (e, f) slanted-pore structures.

by direct ablative writing [19–21]. MPA requires the simultaneous absorption of multiple photons in a single quantum event to initiate the ablation [22]. Multiphoton absorption produces initial free electrons that are further accelerated by the femtosecond laser electric field [22]. These electrons induce avalanche ionization and optical breakdown and generate localized plasma [22]. The subsequent expansion of the localized plasma results in the fabrication of a void structure at the focal point [22]. Because of the nature of nonlinear interaction, a high resolution beyond the diffraction limit can be obtained [22]. A variety of micro-/nanostructures have been fabricated by the MPA process. Chichkov et al. [22] reported the fabrication of a photonic crystal structure with a defect cavity at the center by creating periodic nanostructures in sapphire using MPA. Sun et al. [23] reported the fabrication of 3D photonic crystals within silica. Zhou and Gu [24] fabricated the first void-dot face-centered

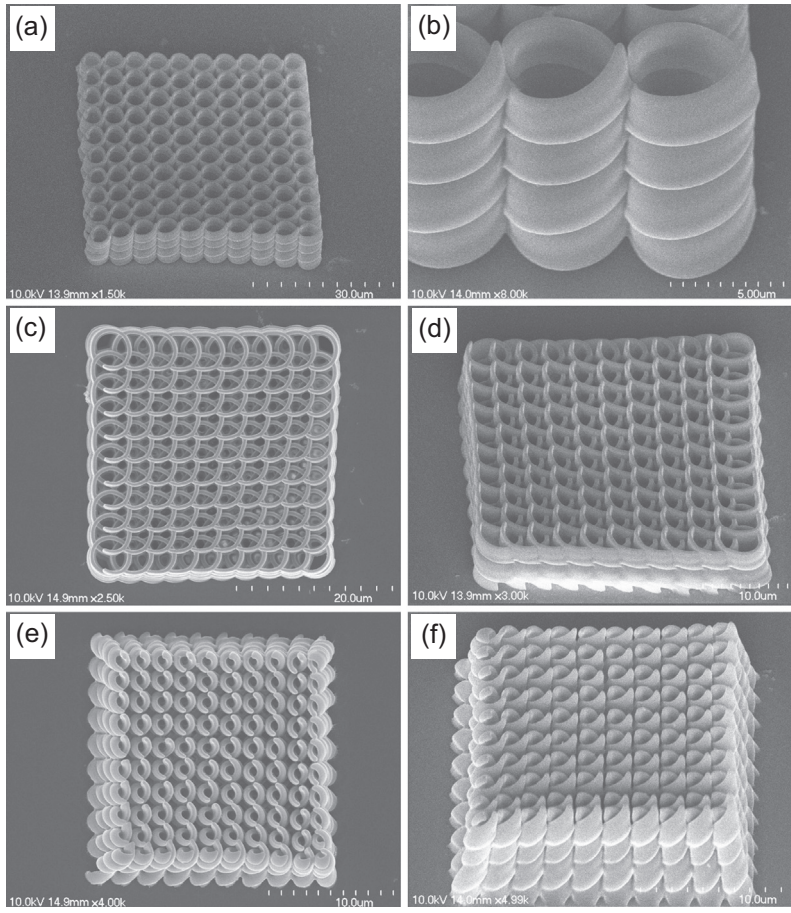

Figure 9.7 (a, b) Single-spiral, (c, d) overlapped single-spiral, and (e, f) double-spiral structures.

cubic 3D photonic crystal in lithium niobate with a pronounced high-order stop gap at a 1.5−2-μm wavelength. It is noteworthy that, because of the femtosecond pulse duration, electron−photon interactions ranging in the picosecond regime are minimized, and thus thermal effects are almost negligible with minimal edge effects [20]. Therefore, MPA is especially capable in fabricating structures such as channels, holes, and voids in various materials [19−21,25−27].

We used the same laser lithography system to carry out subtractive MPA fabrication. The experimental setup is similar to the TPP fabrication process, as described in Section 2.2, except significantly higher laser powers than the TPP process (two to seven times higher) are required. Cured (IP-L, a trademark name of a photo-resist from Nanoscribe GmbH) polymers were used as the raw material, which promises a high spatial resolution beyond the diffraction limit. Because of the short pulse duration of the femtosecond laser (120 fs), which is much shorter than the electron-phonon coupling time ($\sim$1 ps) [28], there is limited heat exchange between the irradiated

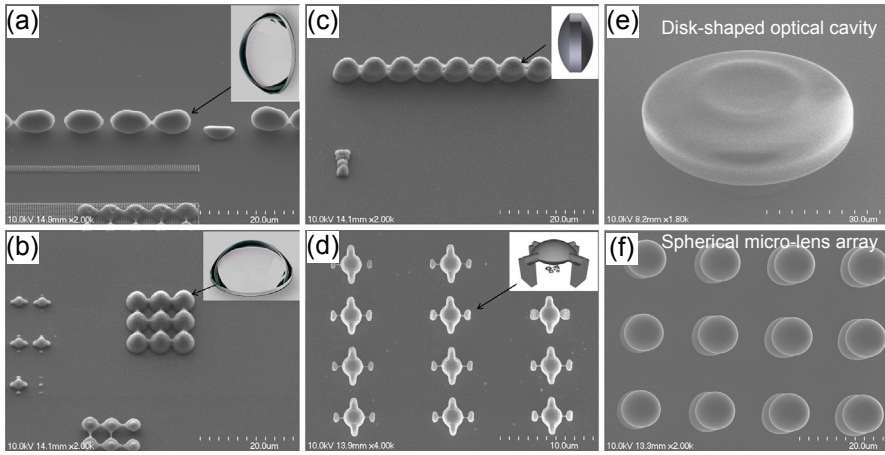

Figure 9.8 Scanning electron micrographs of microlens arrays and optical cavity structures fabricated by three-dimensional lithography. (a) A vertically aligned aspheric lens array. (b) A horizontally aligned aspheric lens array. (c) A vertically aligned biconvex lens array. (d) A horizontally aligned biconvex lens array. (e) A disk-shaped optical cavity for dye laser application. (f) A spherical microlens array.

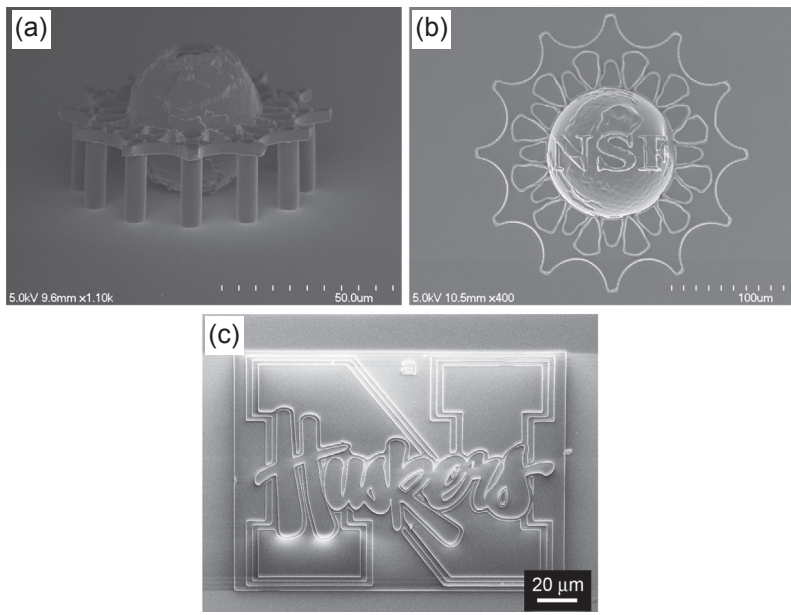

Figure 9.9 Scanning electron micrographs of some examples of complex three-dimensional (3D) structures fabricated by two-photon polymerization lithography. (a) Side view of a 3D National Science Foundation (NSF) logo. (b) Top view of a 3D NSF logo. (c) 3D logo of the University of Nebraska Cornhuskers.

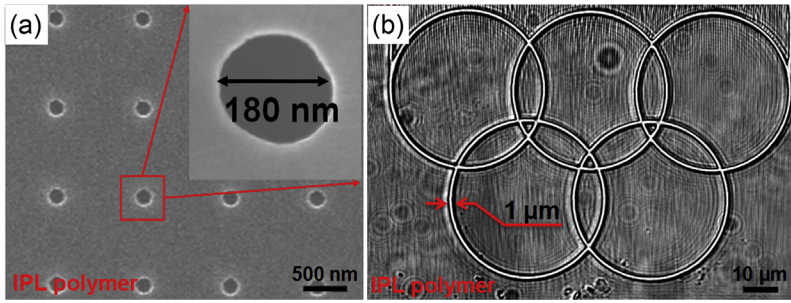

Figure 9.10 Micro-/nanostructures fabricated by the subtractive multiphoton ablation (MPA) process in cured IP-L (the trademark name of a photo-resist from Nanoscribe GmbH) polymer films. (a) Scanning electron micrograph of nano holes; the inset is a magnified image of a hole with a sharp edge and a pore diameter of 180 nm. (b) Optical image of five micro-sized interconnected hollow rings resembling the Olympic pings embedded in a cured IP-L polymer film created by MPA.

area and the surroundings during the subtractive MPA process, resulting in stable and reproducible subtractive fabrication with minimized thermal stress and collateral damage. Fig. 9.10(a) shows an array of holes created by MPA in a 200-nm-thick IP-L film. A magnified image of one hole is shown in the inset of Fig. 9.10(a). The diameter of the holes is around 180 nm, far beyond the diffraction limit of the laser beam. In addition, Fig. 9.10(b) shows five interconnected hollow rings resembling the Olympic rings created inside a cured IP-L polymer film. The channel width is 1 μm, with sharp and clean ablation edges.

9.4 Comprehensive 3D micro-/nanofabrication

Although both additive and subtractive micro-/nanofabrication methods are established separately, they have been largely isolated. Fabricating advanced devices of complex 3D geometries calls for the use of both additive and subtractive processes. For example, a seamless spherical shell is difficult to fabricate using either an additive or subtractive process. In additive processes the solid shell of the sphere prevents the unexposed photoresist from dissolving inside the sphere and producing a void. In subtractive processes, a solid sphere has to be created before subtracting the inner part to make a hollow shell. Therefore, a comprehensive 3D micro-/nanofabrication method possessing both additive and subtractive functionalities is not only desirable but also in demand for advanced device fabrication.

We successfully integrated an additive (TPP) and a subtractive (MPA) process into a single femtosecond laser direct writing system in which process conditions could be precisely controlled. The integrated fabrication method not only inherits the merits of both TPP and MPA, such as writing resolution smaller than the diffraction limit and features with sharp and clean edges, but also offers the possibility to produce novel device structures that are difficult to fabricate using either TPP or MPA alone.

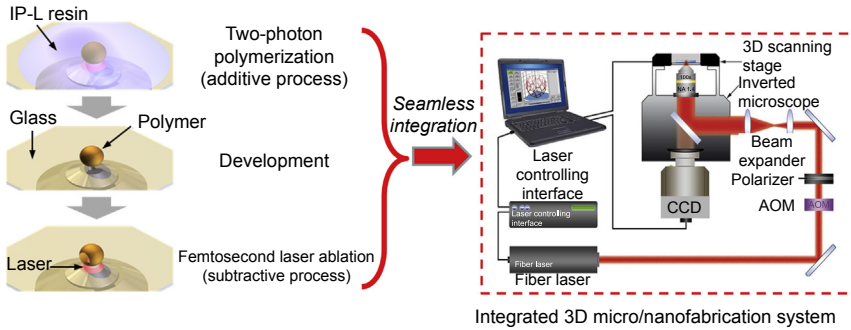

Figure 9.11 Schematic diagram of the comprehensive three-dimensional micro-/nanofabrication combining additive two-photon polymerization and subtractive multiphoton ablation processes.

Fig. 9.11 shows a schematic of an integrated 3D micro-/nanofabrication system combining both additive TPP and subtractive MPA processes. The whole fabrication process consists of three steps. First, TPP is used to fabricate solid 3D microstructures inside the negative photoresist of IP-L (Nanoscribe GmbH). Second, the unsolidified IP-L photoresist is washed away by rinsing the sample in isopropyl alcohol (99.5%; BDH Chemicals) for 20 min. Third, a subtractive process based on MPA is carried out in air to tailor the cured IP-L to a desired 3D geometry. Depending on the size of the desired structure, TPP is performed by using average laser powers that vary between 3.5 and 8 mW. Instead, MPA requires an average laser power that is two to seven times higher than that used for TPP. The laser beam is generated by a mode-locked femtosecond-fiber laser (780-nm central wavelength, 100-MHz repetition rate, and 120-fs pulse duration) and is tightly focused within the sample by an oil-immersion objective lens (numerical aperture: 1.4; Magnification: 100). Writing in both additive and subtractive processes is achieved by moving the sample around a fixed laser beam by means of a computer-controlled XYZ piezo stage.

To demonstrate the capabilities of the "TPP + MPA" method in 3D micro-/nanofabrication, we fabricated two kinds of device structures. The first one is shown in Fig. 9.12; it consists of arrays of microstructured polymer fibers with different diameters. The TPP process was used to fabricate these structures with 2-, 1-, and 0.5-μm line widths, as shown in Fig. 9.12(a,c,e), respectively. The average laser power and stage scanning speed used for TPP were 7 mW and 100 μm/s, respectively. And the different line widths of the fibers were achieved by controlling the number of laser passes in fabricating a single polymer fiber. Upon polymerization, the refractive index of IP-L increases to a value of 1.52. Therefore the polymer fibers could be used as light waveguides for integrated optics [29]. Following TPP, a subtractive MPA process was performed with an average laser power of 26 mW, laser exposure time of 5 ms/spot, and a stage scanning speed of 100 μm/s. Periodic hole patterns with a ~500-nm diameter were fabricated along the polymer fibers to form Bragg grating structures in waveguides, as shown in Fig. 9.12(b,d,f). The diameter and the periodicity of the holes were tunable by adjusting the average laser power, exposure time, and scanning

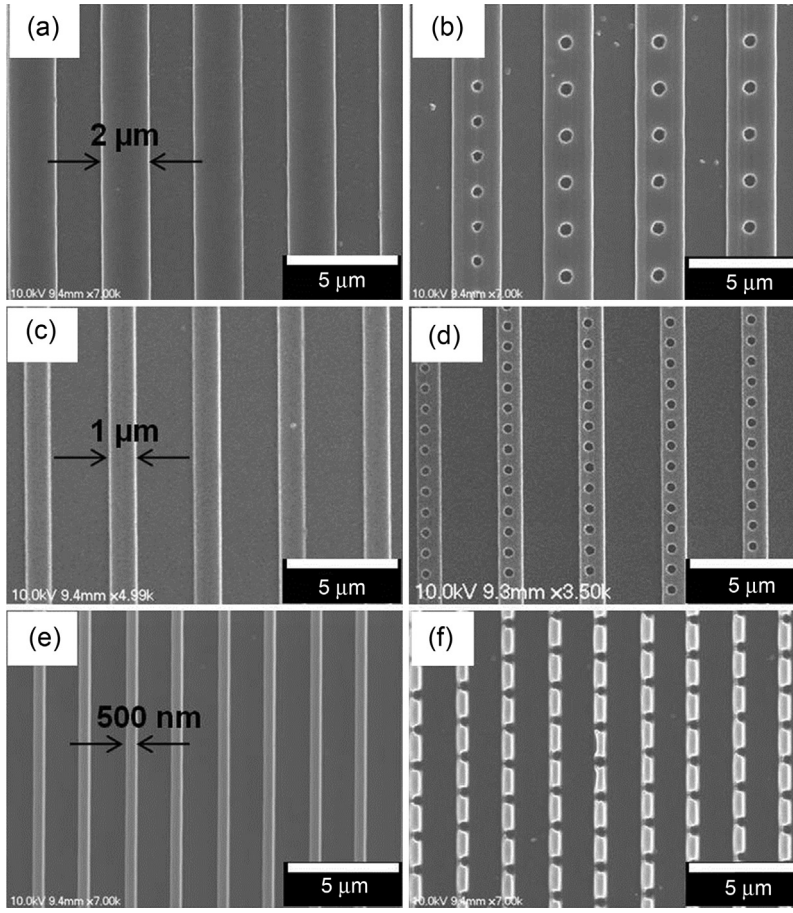

Figure 9.12 Scanning electron microscopy images of polymer fibers fabricated by the comprehensive three-dimensional micro/nanofabrication method combining additive two-photon polymerization (TPP) and subtractive multiphoton ablation (MPA) processes.(a, c, e) the arrays of fibers created by TPP with 2, 1 and 0.5 mm in diameters,respectively; (b, d, f) the arrays of fibers with periodic hole patterns after the TPP and MPA process. [30].

speed. It is noteworthy that the fiber Bragg gratings shown in Fig. 9.12 are difficult to fabricate using either TPP or MPA alone.

The second type of device structures fabricated by implementing TPP and MPA is shown in Figs. 9.13 and 9.14, where meshed and spiral microfluidic channel systems are represented, respectively. First, polymer cubic structures were fabricated on glass substrates using the additive process of TPP. Then, interconnected microchannels were directly written within the polymer microstructures via the subtractive process of MPA. The average laser power and the scanning speed used to create the channels were 26 mW and 50 μm/s, respectively. Fig. 9.13(a,b) clearly shows the typical micro-channels created by MPA. The diameter of a channel is about 1 μm, according to the

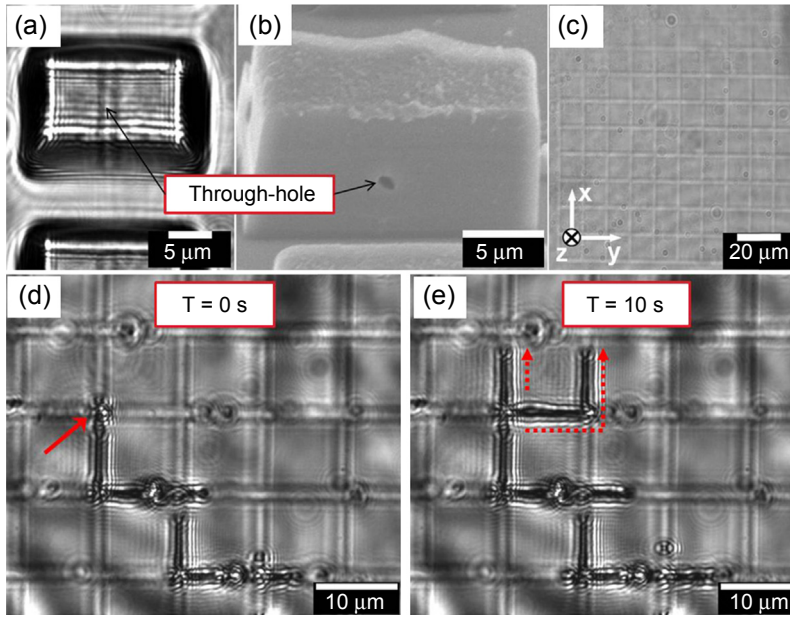

Figure 9.13 Two-dimensional meshed microfluidic channels inside an IP-L polymer fabricated by the "two-photon polymerization + multiphoton ablation" method: (a) optical micrograph of a typical microfluidic channel inside a polymer cube; (b) a cross-sectional scanning electron micrograph of the microfluidic channel; (c) an optical micrograph of the fabricated mesh microfluidic channels. (d) and (e) demonstrate the liquid flow inside the meshed channels at $t = 0$ s and $t = 10$ s, respectively. The dashed line shows the pathway of liquid flow through the mesh microfluidic channels [30].

SEM characterization. Fig. 9.13(c) shows the meshed microfluidic channel system created inside the IP-L polymer cube. Liquid flowing through the meshed channels can be clearly observed in Fig. 9.13(d,e), which verifies the hollow structure and the connectivity of the microfluidic channels. In addition to the 2D meshed channels, 3D spiral microchannels were also successfully fabricated inside the IP-L polymer. Fig. 9.14(a) shows the schematic structure of a 3D spiral channel inside a polymer cube. The labels of "A" and "B" in Fig 9.14 refer to two points that are the highest and the lowest in the z direction, respectively. The optical microscopy image of the spiral channel changes as the focal plane of observation shifts from low to high, as shown in Fig. 9.14(b−d), which indicates the 3D characteristics of the spiral microfluidic channel created inside the IP-L polymer. By using the TPP + MPA method, arrays of the spiral microfluidic channels with a user-defined spacing can be readily fabricated, as shown in Fig. 9.14(e). Compared with the mainstream technique of soft lithography for fabricating microfluidic systems [31], the TPP + MPA method holds several advantages. First, it is a mask-free process. It provides an unparalleled convenience and freedom in prototype design using a computer-aided design program, without the need to fabricate replica molds, as is always required by the soft

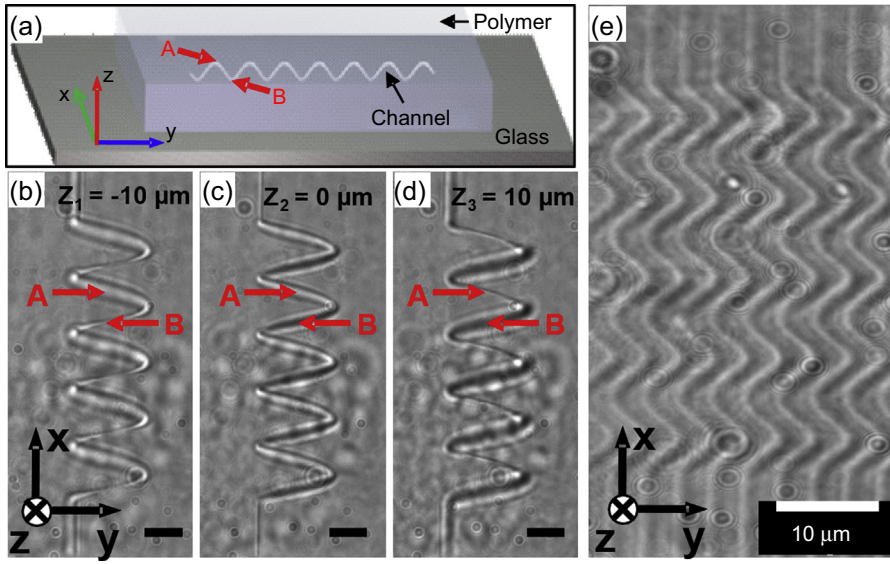

Figure 9.14 Three-dimensional (3D) spiral microfluidic channels inside a IP-L polymer cube fabricated by the "two-photon polymerization + multiphoton ablation" method: (a) schematic of the 3D spiral microfluidic channel. (b), (c), and (d) show the *x-y* cross-sectional view of a spiral channel under a transmission-mode optical microscope at different focal planes (scale bar: 10 μm). The coil diameter of the spiral channel is 20 μm. (e) An array of spiral microfluidic channels fabricated inside a polymer cube with a coil diameter of 5 μm and an inter-channel spacing of 3 μm [30].

lithography method. Second, it is a truly 3D fabrication method, in contrast to soft lithography, which is inherently limited to 2D processing because of the requirement of molding. Third, it needs no sealing of microchannels, which is a necessary fabrication step in the soft lithography process.

9.5 Conclusions

Research efforts have been extended to 3D micro-/nanofabrication based on the FsLDW method. A truly 3D laser direct writing platform has been established. Both additive TPP and subtractive MPA techniques for 3D micro-/nanofabrication have been demonstrated separately based on this platform. Process optimization by studying the dependence of the voxel dimension and the surface roughness on various laser scanning parameters has been obtained. Raman spectroscopy has been proven to be a reliable tool for DC characterization in TPP. The successful fabrication of a wide range of 3D micro-/nanostructures by either TPP or MPA processes, including 3D photonic crystals, optical lenses, disk cavities, hole arrays, and embedded channels, have proven the usefulness and efficiency of TPP and MPA in 3D micro-/nanofabrication.

Moreover, a comprehensive and versatile 3D micro-/nanofabrication method has been developed by integrating both additive TPP and subtractive MPA processes into a single FsLDW framework. The nonlinear characteristics of the fabrication processes offer a writing resolution <200 nm, far beyond the optical diffraction limit. In addition, this method also inherits the virtues of MPA in creating sharp and clean processing edges as a result of the minimized thermal stress and collateral damages. Results show that the combination of additive and subtractive fabrication processes enables the fabrication of complex 3D micro-/nanostructures that are difficult for either TPP or MPA alone. It is believed that this new 3D micro-/nanofabrication method paves the way for the development of advanced devices such as integrated optical circuits and lab-on-a-chip devices.

References

[1] C.J. Dixon, O.W. Curtines, Nanotechnology: Nanofabrication, Patterning, and Self Assembly, Nova Science Publishers Incorporated, 2009.
[2] B.D. Gates, Q.B. Xu, J.C. Love, D.B. Wolfe, G.M. Whitesides, Unconventional nanofabrication, Annual Review of Materials Research 34 (2004) 339−372.
[3] B.D. Gates, Q.B. Xu, M. Stewart, D. Ryan, C.G. Willson, G.M. Whitesides, New approaches to nanofabrication: molding, printing, and other techniques, Chemical Reviews 105 (2005) 1171−1196.
[4] D. Mailly, Nanofabrication techniques, European Physical Journal-Special Topics 172 (2009) 333−342.
[5] C.R.K. Marrian, D.M. Tennant, Nanofabrication, Journal of Vacuum Science & Technology A 21 (2003) S207−S215.
[6] C.R.K. Marrian, E.A. Dobisz, O.J. Glembocki, Nanofabrication − how small can devices get, R&D Magazine 34 (1992) 123.
[7] J.M. Tour, V. Yong, Theoretical efficiency of nanostructured graphene-based photovoltaics, Small 6 (2010) 313−318.
[8] B.J. Wiley, D. Qin, Y.N. Xia, Nanofabrication at high throughput and low cost, ACS Nano 4 (2010) 3554−3559.
[9] T.C. Chong, M.H. Hong, L.P. Shi, Laser precision engineering: from microfabrication to nanoprocessing, Laser & Photonics Reviews 4 (2010) 123−143.
[10] R.R. Gattass, E. Mazur, Femtosecond laser micromachining in transparent materials, Nature Photonics 2 (2008) 219−225.
[11] K.S. Lee, D.Y. Yang, S.H. Park, R.H. Kim, Recent developments in the use of two-photon polymerization in precise 2D and 3D microfabrications, Polymers for Advanced Technologies 17 (2006) 72−82.
[12] L.J. Li, J.T. Fourkas, Multiphoton polymerization, Materials Today 10 (2007) 30−37.
[13] S.H. Park, D.Y. Yang, K.S. Lee, Two-photon stereolithography for realizing ultraprecise three-dimensional nano/microdevices, Laser & Photonics Reviews 3 (2009) 1−11.
[14] Y.L. Zhang, Q.D. Chen, H. Xia, H.B. Sun, Designable 3D nanofabrication by femtosecond laser direct writing, Nano Today 5 (2010) 435−448.
[15] M. Thiel, J. Fischer, G. Von Freymann, M. Wegener, Direct laser writing of three-dimensional submicron structures using a continuous-wave laser at 532 nm, Applied Physics Letters 97 (2010).

[16] L.J. Jiang, Y.S. Zhou, W. Xiong, Y. Gao, X. Huang, L. Jiang, T. Baldacchini, J.F. Silvain, Y.F. Lu, Two-photon polymerization: investigation of chemical and mechanical properties of resins using Raman microspectroscopy, Optics Letters 39 (2014) 3034−3037.
[17] T. Baldacchini, C.N. Lafratta, R.A. Farrer, M.C. Teich, B.E.A. Saleh, M.J. Naughton, J.T. Fourkas, Acrylic-based resin with favorable properties for three-dimensional two-photon polymerization, Journal of Applied Physics 95 (2004) 6072−6076.
[18] A. Feigel, M. Veinger, B. Sfez, A. Arsh, M. Klebanov, V. Lyubin, Three-dimensional simple cubic woodpile photonic crystals made from chalcogenide glasses, Applied Physics Letters 83 (2003) 4480−4482.
[19] D. Gomez, F. Tekniker, I. Goenaga, I. Lizuain, M. Ozaita, Femtosecond laser ablation for microfluidics, Optical Engineering 44 (2005).
[20] F. Korte, J. Serbin, J. Koch, A. Egbert, C. Fallnich, A. Ostendorf, B.N. Chichkov, Towards nanostructuring with femtosecond laser pulses, Applied Physics A-Materials Science & Processing 77 (2003) 229−235.
[21] R. Suriano, A. Kuznetsov, S.M. Eaton, R. Kiyan, G. Cerullo, R. Osellame, B.N. Chichkov, M. Levi, S. Turri, Femtosecond laser ablation of polymeric substrates for the fabrication of microfluidic channels, Applied Surface Science 257 (2011) 6243−6250.
[22] B.N. Chichkov, C. Momma, S. Nolte, F. Vonalvensleben, A. Tunnermann, Femtosecond, picosecond and nanosecond laser ablation of solids, Applied Physics A-Materials Science & Processing 63 (1996) 109−115.
[23] H.B. Sun, Y. Xu, S. Juodkazis, K. Sun, M. Watanabe, S. Matsuo, H. Misawa, J. Nishii, Arbitrary-lattice photonic crystals created by multiphoton microfabrication, Optics Letters 26 (2001) 325−327.
[24] G.Y. Zhou, M. Gu, Direct optical fabrication of three-dimensional photonic crystals in a high refractive index $LiNbO_3$ crystal, Optics Letters 31 (2006) 2783−2785.
[25] P. Fischer, A. Mcwilliam, L. Paterson, C.T.A. Brown, W. Sibbett, K. Dholakia, M.P. Macdonald, Two-photon ablation with 1278 nm laser radiation, Journal of Optics A-Pure and Applied Optics 9 (2007) S19−S23.
[26] M. Gu, B.H. Jia, J.F. Li, M.J. Ventura, Fabrication of three-dimensional photonic crystals in quantum-dot-based materials, Laser & Photonics Reviews 4 (2010) 414−431.
[27] A. Waldbaur, H. Rapp, K. Lange, B.E. Rapp, Let there be chip-towards rapid prototyping of microfluidic devices: one-step manufacturing processes, Analytical Methods 3 (2011) 2681−2716.
[28] J.R. Goldman, J.A. Prybyla, Ultrafast dynamics of laser-excited electron distributions in silicon, Physical Review Letters 72 (1994) 1364−1367.
[29] H.P. Zappe, Fundamentals of Micro-Optics, Cambridge University Press, Cambridge; New York, 2010.
[30] W. Xiong, Y.S. Zhou, X.N. He, Y. Gao, M. Mahjouri-Samani, L. Jiang, T. Baldacchini, Y.F. Lu, Simultaneous additive and subtractive three-dimensional nanofabrication using integrated two-photon polymerization and multiphoton ablation, Light-Science & Applications 1 (2012) e6.
[31] D. Qin, Y.N. Xia, G.M. Whitesides, Soft lithography for micro- and nanoscale patterning, Nature Protocols 5 (2010) 491−502.

Design for laser additive manufacturing

10

C. Emmelmann [1,2], D. Herzog [1], J. Kranz [1]
[1]Hamburg University of Technology (TUHH), Hamburg, Germany; [2]LZN Laser Zentrum Nord GmbH, Hamburg, Germany

10.1 Introduction

According to Pahl and Beitz [1], it is the engineer's task to develop solutions for technical problems. To do so, it is necessary to consider material-, technological-, and economic-related boundary conditions and restrictions. The products designed usually have to fulfill multiple requirements to be successful in their respective markets. Responding not only to customers' demands but also to restrictions imposed on the product by the design and manufacturing process is necessary. Manufacturing processes greatly influence feasible geometries and product functionalities especially.

Laser additive manufacturing (LAM) is a repeating layer-wise manufacturing process that uses a laser beam to melt and solidify material in a powder bed according to slices of a corresponding three-dimensional (3D) computer-aided design (CAD) model. Stepwise production reduces complex 3D geometries into simpler two-dimensional manufacturing steps, thus also reducing manufacturing restrictions [2,3]. Because of the high geometric freedom it provides, LAM facilitates new impulses for the design of functional parts by having the potential to manufacture geometries that are impossible to manufacture using other processes. The geometric freedom enables the designer to realize complex hollow structures, overhangs, and lattice structures [4]. This chapter gives an overview over the most basic design guidelines for LAM and describes product functionalities that exploit the geometric freedom of LAM.

10.2 Design restrictions of LAM

The stepwise production in LAM reduces complex 3D geometries into simple two-dimensional manufacturing steps and enables the production of highly complex parts. In general, it is important to consider design restrictions of manufacturing processes that impede product design from the early stages on. Otherwise cost-intensive iteration cycles toward a design suitable for production to obtain stable manufacturing processes can be necessary. Temporal delays and only barely calculable additional costs can result. In general, part costs in LAM are primarily determined by a part's volume and not the complexity of its shape.

Laser Additive Manufacturing. http://dx.doi.org/10.1016/B978-0-08-100433-3.00010-5
Copyright © 2017 Elsevier Ltd. All rights reserved.

10.2.1 Geometric resolution

Minimizing a part's volume can significantly reduce manufacturing time and costs. Manufacturing time can be reduced further by minimizing the buildup height and thus the layers to be applied and exposed by the laser. A part's orientation in the building chamber does not only influence manufacturing time. Because of the layer-wise buildup, directional dependencies in terms of geometric accuracy have to be considered as well. The layer thickness (LT) significantly determines the geometric resolution of the part and affects the manufacturing time and the realizable surface qualities. The layer-wise production process leads to a "staircase effect" at angled surfaces that is the result of a limited geometric resolution (see Fig. 10.1). Thus only an approximation of the ideal part contour is possible. Compared with high layer thicknesses, low thicknesses facilitate a higher geometric resolution but lead to an increase in manufacturing time by increasing the overall layers to be built and exposed. Typical layer thicknesses vary between 20 and 60 µm and depend on the distribution of the material-specific powder grain size. Moreover, the machine setup as well as the recoater concept also influence the suitable layer thickness [2,3].

10.2.2 Surface quality and support structures

Compared with conventional manufacturing, in LAM the dependence of the achievable surface roughness on orientation is a process-specific feature that needs to be considered when designing parts. In general, the higher a surface's angular alignment toward the building platform, the rougher the surface is. Surpassing a critical angle leads to an increased droplet effect on down-facing surfaces and finally to an erroneous buildup of the layers, caused by a reduced heat flux into the powder bed, compared to completely solidified metal. This results in the process being aborted and, in general, the loss of the part. Figs. 10.2 and 10.3 show the typical characteristics of the surface qualities' dependence on part alignment (angle relative to the build direction) adverse the building platforms surface normal.

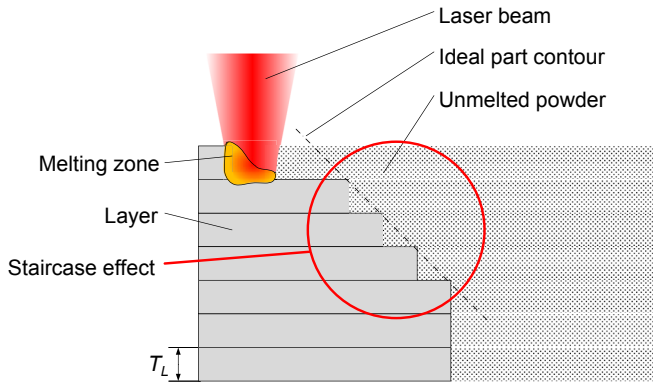

Figure 10.1 A simplified illustration showing layers composed using laser additive manufacturing.

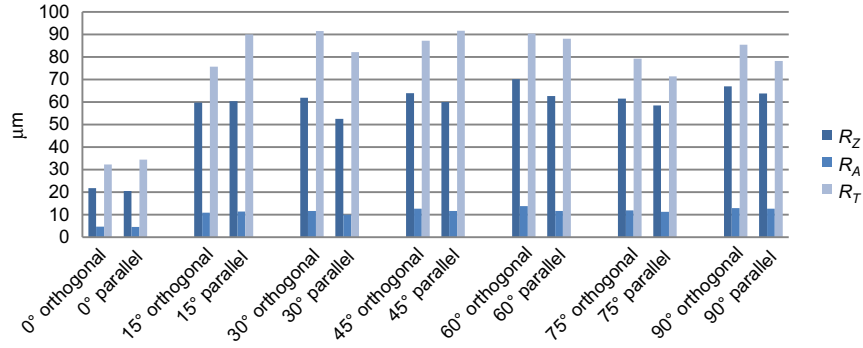

Figure 10.2 Roughness of up-facing surfaces versus angular alignment toward the building platform; orthogonal/parallel indicate measurement orientation toward the direction of exposure. Material: $TiAl_6V_4$, EOS M270xt, retail powder and parameters (see Table 10.1). $R_{Z,}$ average distance between the highest peak and lowest valley in each sampling length of five samples; $R_{A,}$ arithematic mean value; $R_{T,}$ maximum height of the profile.

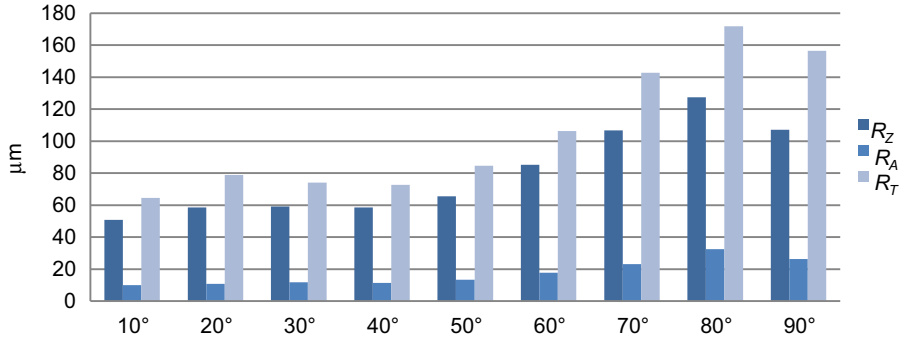

Figure 10.3 Roughness of down-facing surfaces versus angular alignment toward the building platform. Material: $TiAl_6V_4$, EOS M270xt, retail powder and parameters (see Table 10.1).

The use of support structures (Fig. 10.4) can counteract material fall-in at overhanging sections and part warpage caused by thermal-induced stresses; support structures are recommended above critical angles of typically 45 degree ± 10 degree [5–7]. The critical angle is, however, highly dependent on the machine and material used.

Support structures such as those shown in Fig. 10.4 typically consist of thin, lattice-like structures and are intended to be removed after the part is built up. Manifold support structures are available and must be chosen according to the part's demands. Parts manufactured by LAM always have to be connected to the building platform, either directly or by support structures.

To reduce the need for postprocessing, it may be suitable to reduce the number of overhanging structures in a part's geometry and to include angular and round sections instead (see Fig. 10.5). Parts should be designed with easy support removal in mind.

Figure 10.4 A lightweight bracket with perforated support structures.

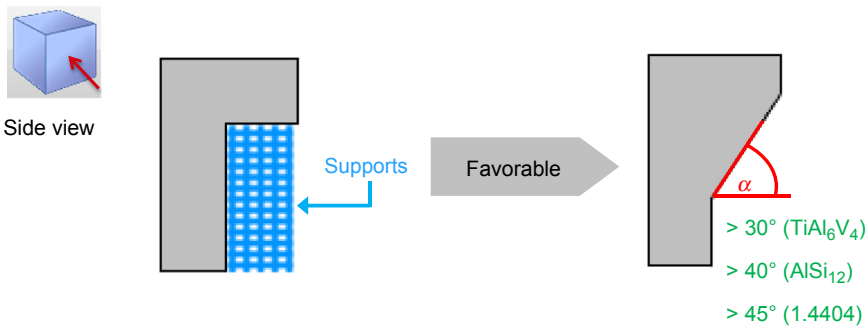

Figure 10.5 Reducing support structures through suitable part geometry.

10.2.3 Geometric features

Because of LAM's layer-wise manufacturing principle and the laser focus diameter determining the effective melt track width, there are geometric restrictions to consider in terms of feasible geometries. The effective values strongly depend on the chosen material and manufacturing system.

10.2.3.1 Bores and holes

Bores are an essential design feature. Engineering parts often incorporate interfaces in the form of rivets or screws, which requiring bores in the parts to allow them to be connected. Recent developments show the potential for integrating functions in the form of internal cooling channels or fluid ducting [8].

Bores and holes should already be incorporated in the part design to minimize the part volume that must be built up and thereby the manufacturing and postprocessing costs. Bore buildup is subject to geometric limitations. Small bore dimensions may cause a lower temperature flux compared with larger ones, leading to internal powder adhesion and bore blocking. Achievable minimum dimensions greatly depend on the material and machine setup. Bores with a minimum dimensions of 3 mm were successfully manufactured from $TiAl_6V_4$ [9].

The highest geometric accuracy can be achieved with horizontally (orthogonal to build direction) bore geometry features (see Fig. 10.6). Bores oriented horizontally (orthogonal to build direction) show material that has fall in on the bore's upper side as a result of a curling of the upper sections of the bore shortly before connecting the layers that close the bore's cross section (compare with [9,10]). The use of support structures with large bore diameters might thus be necessary. In $TiAl_6V_4$, bores smaller than 12 mm were successfully built up free of supports (see Ref. [9]). Strategies allowing a support-free buildup by designing bores that outrun sharply to the top were developed by Thomas [10].

Bore accuracy is also influenced by the staircase effect, especially at small dimensions. The stronger a bore's axis aligns toward a substrate platform's normal surface, the more obvious is the geometric deviation from the CAD ideal. The influence greatly depends on the chosen layer thickness (see Figs. 10.1 and 10.7). Bores built up with an axis alignment perpendicular to the substrate platform generally show a higher geometric accuracy than those aligned horizontally.

10.2.3.2 Minimum wall thickness

The producible minimum wall thickness depends on several parameters. The focus spot's form in the building plane determines the minimal melting track width and

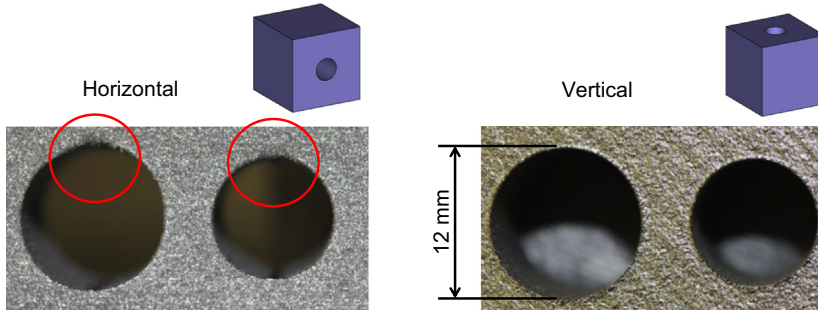

Figure 10.6 Horizontal (orthogonal to build direction) and vertical (in build direction) bores adverse the building platform.

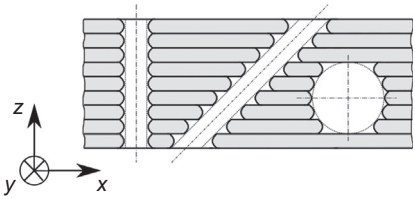

Figure 10.7 Staircase effect on bores and holes.

thus defines the lower boundaries in terms of the feasible geometric resolution in the building plane itself. Moreover, the external or internal mechanical loads introduced in the walls to be built up influence their in-process buildup behavior and thus the minimum thickness that can be manufactured. During the recoating process of each layer, the recoater device moves over each individual layer. Contact between the just-exposed layer and the recoater device can induce forces in the wall. Moreover, the layer-wise melting and solidification of the powdered raw material causes thermal-induced stresses. These mechanical loads also influence the thinnest walls that are safely producible. Producible wall thicknesses strongly depend on the machine setup and material. The thinnest wall usable for parts made of $TiAl_6V_4$ is 0.4 mm [9,11].

10.2.4 General restrictions

Maximum part dimensions are limited by the machine's building envelope. Available dimensions largely differ between machine concepts and should be considered in the early stages and on. Parts exceeding the available building chamber dimensions can be scaled or separated and then be joined later in postprocessing [9,11]. In terms of hybrid manufacturing, the substrate plate can be implemented into the part to reduce the volume to be built up.

Powder not exposed during the manufacturing process can be reused after additional sieving. Its removal from manufactured parts is an essential element of postprocessing in LAM. In particular, special care is needed at hollow structural sections, holes, or gaps to ensure powder-free parts. The consideration of holes allowing access to hollow sections for powder removal is necessary and should be already incorporated into the part design. A sufficient number and size of access holes for powder removal can help optimize postprocessing efforts.

Applying new powder layers is one part of the iterative LAM process. During this process, it is possible that the recoater device induces mechanical loads into the part to be built up by direct contact that usually corresponds to the line of contact (see Fig. 10.8). In general, the longer the line of contact, the larger the potential forces that could be induced in the part. When critical values are extended, a part can failure and/or the recoater device can be blocked. Thus the appropriate angular alignment of the part should be considered from the early design stages to minimize the line of contact between the part slices and the recoater device.

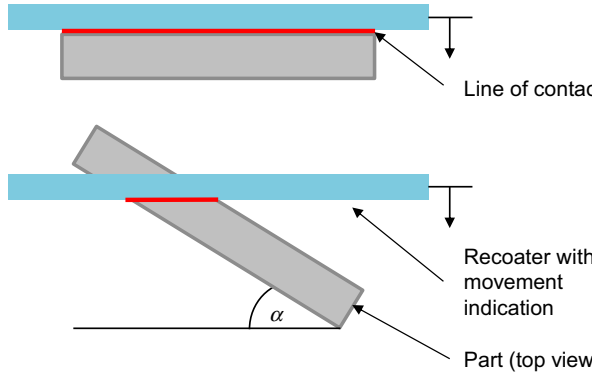

Figure 10.8 Part alignment toward the recoater device.

10.2.4.1 Final machining

That LAM is a manufacturing process free of processing after machining is a widespread conception. Yet building $TiAl_6V_4$ parts on building platforms requires later separation. High demands on surface roughness and part tolerances can also oblige a designer to consider conventional manufacturing processes for postmachining. The restrictions inherent in the process can significantly influence the freedom of design. Incorporating the most basic design guidelines for conventional manufacturing processes into a design guideline for LAM thus is a necessity because it raises the designer's awareness of the holistic manufacturing chain. Typical postmachining processes for lightweight brackets primarily incorporate wire eroding and milling.

10.2.5 Basic guideline catalogue

This chapter summarizes some of the most basic design guidelines in form of a catalogue (see Table 10.1). Design catalogues allow more solutions and easier synthesis of activities that frequently occur in product development and design. Especially in fields of recurring design challenges, such as manufacturing restrictions, the creation of design catalogues can support efficient product development. The catalogue presented here was created in line with the VDI 2222 guideline [12]. For clarity, it is separated in several columns. The classification section on the left is divided according to basic geometries, part design, and final machining. The sections are colored in order of ease of handling. The main part incorporates pictures showing preferable design solutions according to the manufacturing challenge. Columns on the right provide comments and more detailed information on the specific restrictions. For a more comprehensive overview see Ref. [9].

10.3 Product design approaches for LAM

LAM's toolless and layer-wise nature can provide significant benefits for product functionalities if they are designed accordingly. In general, LAM's application is feasible if

Table 10.1 **Catalogue of guidelines for laser additive manufacturing of $TiAl_6V_4$**

Structure			Unfavourable	Favourable	Explanation	Restrictions and recommendations
Design process – $TiAl_6V_4$ / General geometry/part form	General part size	General		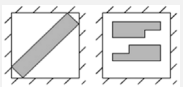	• Part size must consider substrate plate dimensions • Rotate, scale or separate parts if necessary	Max. part dimensions incl. substrate plate: x = ca. 250 mm, y = ca. 250 mm, z = ca. 215 mm (see machine manufacturers for more information; larger machines available)
		Inclusion of substrate platform			• Integration of substrate platform into part possible • Reduction of manufacturing time and costs • Hybrid manufacturing approach	
					• Radii at the interface part / substrate platform prevent part strip off during manufacturing process	• The larger the interfaces layer, the larger the radius should be • R = 3–5 mm suitable for $TiAl_6V_4$
		Height		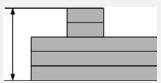	• Part heigth in build up direction should equal multiple layer thicknesses	Layer thickness: 20 – 50 µm $TiAl_6V_4$: 30 µm (see manufacturing machine documentation)
	Integration of functions		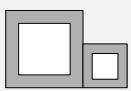	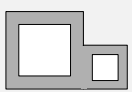	• Prefere integral part design • Reduction of manufacturing time	
	Cavities	Volume			• Use cavities in order to reduce the part volume to be exposured • Reduction of manufacturing time and cost	
		Design	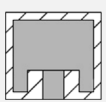	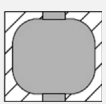	• Avoid powder nesting by designing simple cavity geometries	

Structure			Unfavourable	Favourable	Explanation	Restrictions and recommendations
Design process – $TiAl_6V_4$	General geometry/part form	Walls – Thin walls	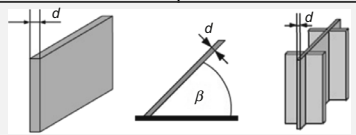		• Consider minimum wall thickness for part design • Use additional ribs for wall stabilization if necessary	Minimum wall thickness: 90° ≥ β > 30°: min. wall thickness 0.4 mm β = 30°: min. wall thickness 0.3 mm • Walls 10 mm wide and high
		Radii	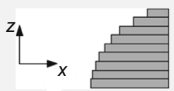		• Avoid staircase effect by adequate part orientation (z-axis represents building direction)	
		Bores – Part design	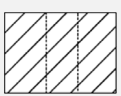	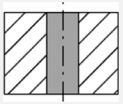	• Bores should be incorporated into part design in order to reduce final machining	• Consider allowance for final machining
		Bore type			• Prefere through-holes towards blind holes	
		Min. size	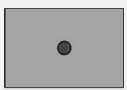		• Bores below minimum diameter show powder adhesion	• Minimal bore diameter: 2 mm ($TiAl_6V_4$)
		Max. size	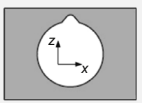	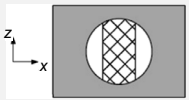	• Bores with an axis close to the substrate plate plane show curling and defects in the upper bore section • The use of supports can reduce this effect	• Use supports above a diameter of 12 mm • Lower radii may lead to higher form accuracy and surface quality
			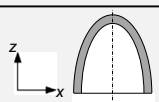	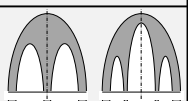	• Large crosssections incorporating bore like structures can be realized without supports by implementing multiple sub structures reducing the effective diameter at upper bore areas	

Continued

Table 10.1 Continued

Structure			Unfavourable	Favourable	Explanation	Restrictions and recommendations
Design process – $TiAl_6V_4$	General geometry/part form	Overhangs	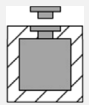	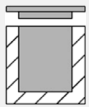	• Avoid overhangs in order to minimize necessity for support structures	
			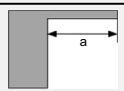		• Horizontal overhangs tend to bend upwards and can lead to part imperfections or building failure • Stay below recommended length	• Max. overhang without support: a ≤ 0.3 mm
	Support-structures	Access	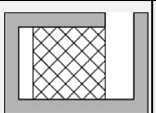	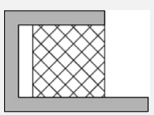	• Part design should allow easy support structure removal • Guarantee accessibility for final machining	
		Avoidance	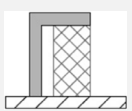	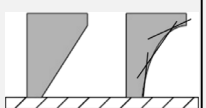	• Avoid support structures by adequate strcutural transitions • The tangient angle of the overhang defines the necessity of supprts	
		Critical angle	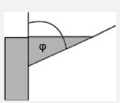	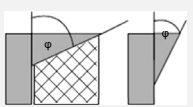	• Support structures are necessary above the critical angle φ	• φ > 50°: supports recommended • φ > 80°: supports necessary
		Bores	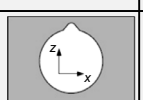	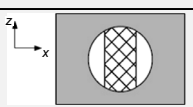	• Bores with an axis close to the substrate plate plane show curling and defects in the upper bore section (see left)	• Use supports above a diameter of 12 mm • Lower radii may lead to higher form accuracy and surface quality
		General remarks	• Always connect parts with the building platform directly or with supports • Always carefully support the lowest part section • Consider block supports for large surfaces		• Consider point support for small features or surfaces • Connect supports with the part at large dimensions without breacking teeth	• Directly connect large structures with the building platform • Minimize support usage • Strengthen large and filigree supports by additional small beams

Structure			Unfavourable	Favourable	Explanation	Restrictions and recommendations
Design process – $TiAl_6V_4$	Final machining	Necessary for final machining	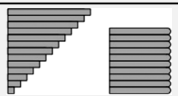 As built	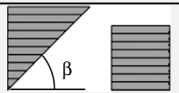 Machined	• Surfaces with high demands on accuracy and/or a low roughness require final machining • Already consider demands on surface quality in part design and define the part orientation adequately	• Averaged roughnesses for $TiAl_6V_4$ **Orientation** / **Angle β** / **Roughness Ra** Upside: 0° – 3 – 5 µm; 10° – 90° – 10 – 13 µm Downside: 0° – 40° – 10 – 12 µm; > 50° – > 13 µm; > 70° – 23 µm < Ra < 32 µm
	Surface quality					
	Part alignment	Surfaces	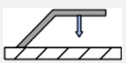	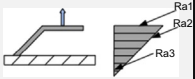	• Consider alignment influence on surface quality as built • Surface qualities: Ra1 > Ra3 > Ra2	• Can vary with part, material and machine
	Part placement	Overhang	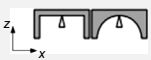		• Avoid overhangs and droplet effects by adequate part placement and orientation	
		Orientation			• Minimize build heigth • Reduction of manufacturing time and costs	
		Recoater			• Consider a part orientation of ca. 30° towards the recoater device in order to minimize forces induced into the part	

Continued

Table 10.1 Continued

Structure			Unfavourable	Favourable	Explanation	Restrictions and recommendations
Design process – $TiAl_6V_4$	Part placement	Part alignment – Filigree parts	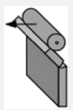		• Place thin walls perpendicular towards recoater • Do not place large filigree crosssections parallel to the recoater	
		Part alignment – General	Typical target figures: • Max. support area • Min. contact with supports • Min. roughness of interfaces • Min. support volume			
		Package density	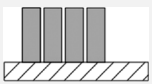	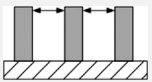	• Consider free space between manufactured parts in order to ease final machining • Too close packaging can lead to thermal interaction of parts	• Sufficient distance between parts minimizes thermal influences • $TiAl_6V_4$: ca. 5 mm; no powder bed heater

Guideline constraints			• Guidelines strongly depending on chosen material, machine concept and process parameters
			• Test specimens were manufactured on:
			  • EOS M270xt
			  • Concept laser M2
			  • See explanation section for parameter setups
			• See section 2 for further remaks on the methodical approach for the guidelines presented			

Machine	EOS M270 XT	Concept laser M2
Material	$TiAl_6V_4$, retail powder	$TiAl_6V_4$, retail powder
Layer thickness (µm)	30	30
Laser power (W)	Core: 170; skin: 120	Core: 180; skin: 200
Scan velocity (mm/s)	Core: 1250; skin: 1000	1250
Hatch distance (mm)	0.1	0.15
Exposure type	Stripe	Stripe

the amortization of fix tool costs is impeded by small lot sizes. Moreover, LAM can help reduce the costs of parts with a highly complex geometry. Whereas the costs of conventional manufacturing processes are primarily dependent on part complexity, LAM's manufacturing costs are mostly determined by the volume to be built up and mostly independent of the part's topology. Moreover, expensive and conventionally hard-to-machine materials, such as $TiAl_6V_4$, can be used to manufacture near- or net-shape geometries directly by LAM in order to reduce manufacturing costs [2,13−15]. LAM also reduces consistent product revisions because the process is tool-less and the need for time- as well as cost-intensive adaptations of the manufacturing equipment no longer exists. This can be a significant benefit, especially for fast-moving industrial sectors. LAM also facilitates the realization of mass production of customized products with a high complexity and a high diversity of variants in the product lineup [5,16].

Currently, a major field of application is the medical sector. Because of the demand for individualized solutions, this market is predestined to benefit from LAM's specific advantages. Already realized at an industrial scale is the manufacturing of patient-specific dental bridges or implants by LAM [17]. Medical products manufactured by LAM are often fitted to patient-specific geometric restrictions and demands. Computer tomography and scanning data can be directly used to model products such as hip or dental implants (see Fig. 10.9).

The field of lattice-based osseointegrative interfaces that are conventionally not manufacturable shows an increase in applications [8]. These structures consist of small latticed structures made of filigree bar elements that optimize bone growth (see Fig. 10.9). The application of such structures is also suitable for lightweight structures and crash absorbers. By substituting massive part sections with lattice structures, a part's volume to be manufactured can be reduced. In addition to functional benefits, manufacturing time and costs can be reduced as a result of implementing latticed structures into products.

As mentioned before, LAM facilitates parts with a highly complex geometry. Hence it is promising for lightweight design based on structural optimization and bionics since these approaches in general yield to part architectures with a highly complex geometry. The resulting geometries are usually a combination of complex

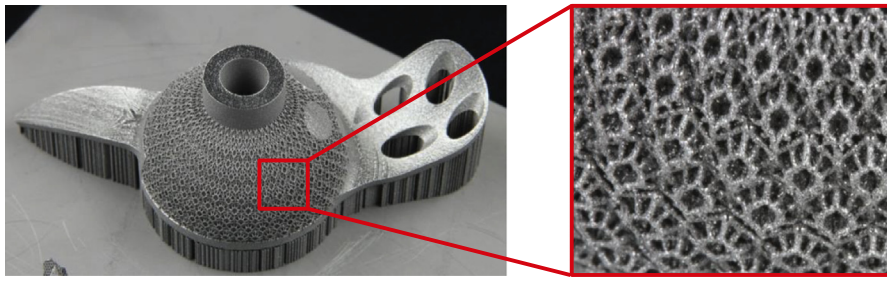

Figure 10.9 A hip implant with lattice structures manufactured by laser additive manufacturing. Cell size of the lattice approx. 1 mm. [18].

freeform surfaces, hollow structures, and undercuts. Conventional manufacturing processes, with their inherent restrictions, often prevent the direct conversion of theoretically optimized structural designs. Therefore deviations from the optimal structures to less optimal structures imposed by manufacturing restrictions are required and the greatest possible exploitation of the lightweight potential is missed.

Methods for optimizing structure are manifold. Fig. 10.10 shows the most basic principles based on the example of a simple bridge. The "choice of design" includes the consideration of truss construction or compound structures. Furthermore, whether the part's design will be integral or differential must be determined. During the "choice of materials," the materials themselves are the design variables that have to be chosen according to the case-specific requirements. The preceding methods of structural optimization were of an analytical nature. With the advent of affordable and highly capable personal computers, numerical methods for optimizing structures are being increasingly used. The major methods are described briefly in the following.

The "topology optimization" goal is the determination of the fundamental optimal part structure in the form of the distribution of the structurally relevant material. The "shape optimization" is the adaptation of local geometry according to the part load in order to reduce local stress peaks. By contrast, the "parameter optimization" is the simplest numerical method. Its goal is to adapt wall thicknesses or profiles according to a part's loads. Because the results of topology optimization are the most radical, it is the decisive method in combination with LAM and is described in more detail.

A common method for optimizing topology is the "solid-isotropic-material-with-penalization" method (see Fig. 10.11), which is described in the following with the help of a simple bar. It is based on an iterative process that begins with the discretization of design space, which includes the modeling of the design space and the

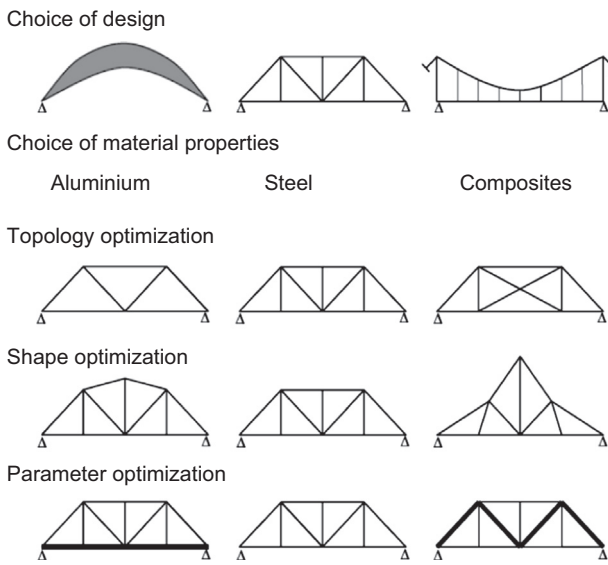

Figure 10.10 Differentiation of structural optimization problems by design variables [19].

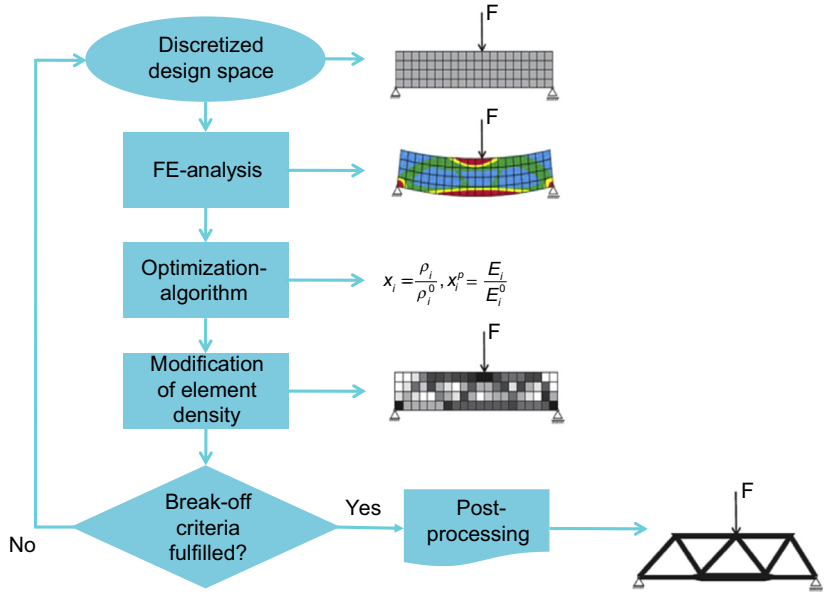

Figure 10.11 Process of topology optimization according to the solid isotropic material with penalization method [20].

definition of the finite element method problem (eg, forces, mesh, constraints) [20]. The optimization problem is then defined by the declaration of design variables, the definition of objective function (eg, weighted compliance or a volume reduction of 85%), and the definition of manufacturing constraints. Thereafter a finite element analysis is performed to determine the stress distribution within the part. The optimization algorithm is adapted from the element density by a fictional material law during the iterative optimization process. Elements with a high structural relevance are assigned a density <1, and elements with a negligible structural relevance, >0. During the break-off criteria examination, the model is checked to determine whether the change of the objective function lies below a specific value, otherwise a further iteration will start. The consequence of this process is a constantly evolving structurally relevant volume during the iterations.

Fig. 10.12 shows an application of topology optimization and potential biological lightweight structures. By optimizing topology during the development process of "designed-for-LAM" parts, the following characteristics can be achieved [20]:

- minimized weight
- reduced peak stresses
- homogeneous stress distribution
- reduced production waste.

Using the explained methods, Emmelmann et al. [20,21] optimized the part design and production of an aluminium bracket in an A380 Airbus (see Fig. 10.13). This

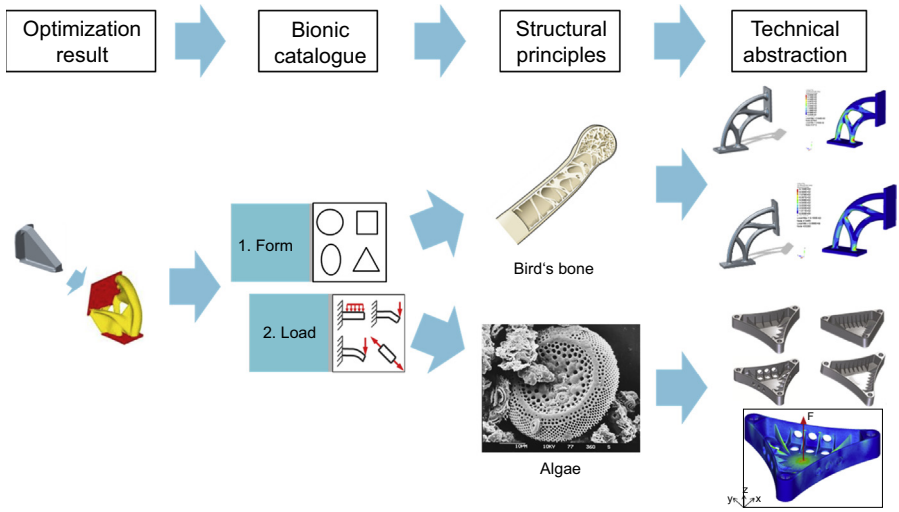

Figure 10.12 Application of topology optimization and potential bionic lightweight structures.

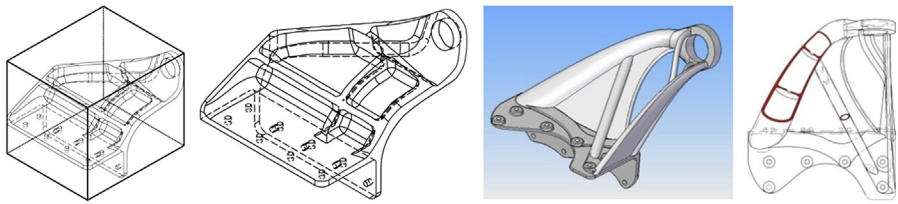

Figure 10.13 Left: The raw part and the conventionally manufactured bracket. Right: A bracket with a bamboo structure and optimized topology [21].

bracket is a part use to fix the crew rest compartment to the aircraft's primary hull. Overall, more than 25,000 brackets fulfill similar functions in a typical aircraft. In contrast to the counterparts manufactured by LAM shown here, the majority are milled from massive material of which a high volume percentage is removed during the machining step. High material waste and energy consumption during the part production results. The incorporation of bionic bamboo beams facilitated a very stiff and light bracket design that is not manufacturable by any other process (see Fig. 10.13). An overall weight reduction of 50% could be realized as a result of the freedom of design through LAM and by changing the material to titanium.

Even though a simple manufacturing process substitution combined with a redesign can achieve a tremendous weight reduction, the potential of LAM for lightweight design goes far beyond this and needs far more radical approaches to be fully exploited. In addition to bionic and optimized design, further lightweight potential could be successfully achieved by integrating functions with the help of another A350 bracket design that was initially directly attached to the honeycomb (see Fig. 10.14). The force offset from the neutral axis generated a momentum and

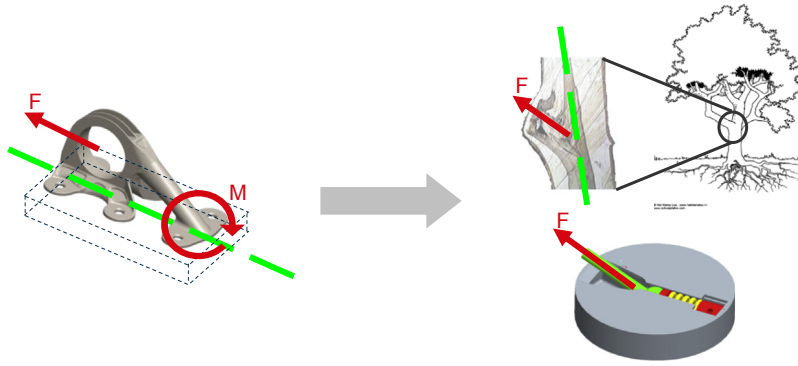

Figure 10.14 Adapted bracket design incorporating the integration of functions and loading.

additional loads that had to be considered during the design phase. Aiming for an improved lightweight design and an optimized load input, the initial bracket and the honeycomb insert plate were combined, following the bionic analogy of a tree and its load transfer from branches to the trunk (see Fig. 10.14). Gluing the part directly into the sandwich compound induces a direct load into the neutral axis.

Fig. 10.15 summarizes the results of weight reductions for the different designs of the analyzed A380 bracket. The initial design was manufactured by milling and weighs 330 g, the insert plate (including fasteners) weighs ~1,400 g. In comparison, the bionic bracket designed for a manufacturing process substitution shows a weight reduction of 41%, whereas the radical approach of an integrated design reduces by more than 80%.

	Original design	**Bionic design**	**Integrated design** ("bracket" directly glued into honeycomb)
	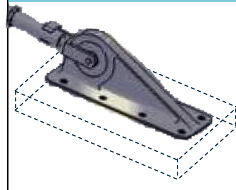	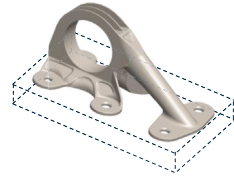	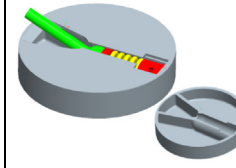
Bracket weight	330 g	195 g	0 g
Assembly weight	1,400 g incl. fiber mount and HiLocks	1,265 g incl. fiber mount and HiLocks	300 g
Dimensioning load case	35 kN	35 kN	35 kN
Weight saving		135 g per bracket −41%	1,100 g per assembly >−80%

Figure 10.15 Comparison of different design alternatives for aircraft brackets.

Figure 10.16 A lightweight bracket manufactured by laser additive manufacturing for use in an Airbus A350 XWB [22].

New design and manufacturing approaches often have to assert themselves in real applications in order to be adopted at an industrial scale. In addition to theoretical studies, a recent design project showed the potential of LAM for real end use in lightweight applications. Fig. 10.16 shows a lightweight bracket used in an Airbus A350 XWB. The goal of the design was to minimize the part weight and exploit the geometric freedom allowed by LAM. Structural tests and a first flight test were successful, showing the potential of LAM for end-use applications in the aviation industry.

Another major field of LAM application is rapid tooling that takes advantage of the geometric freedom of LAM by facilitating tool designs with complex internal cooling ducts that are not conventionally manufacturable [2]. The highly complex injection molds are often produced as single units or in small lot sizes. They are driven by high time and cost pressures because of customer demands for a short time to market and difficult competition with the tooling industry in low-wage countries. An innovation by tool manufacturers to reduce lead time and costs is the integration of additional functions into existing components [23].

The Institute of Laser and System Technologies at Hamburg University of Technology, together with Werkzeugbau Siegfried Hofmann and Concept Laser, developed an ejection system operating with pressurized air (see Fig. 10.17). This system completely replaces classic ejector pins. The integration of air ejectors into a laser additive manufactured tool insert with conformal cooling has no impact on costs. The lead time of the insert is not changed by the additional system. No additional investments are required by molding companies because injection molding machines are already equipped with the valves to operate the air ejector system. By using an integrated air ejector system, the expenses of the entire mechanical ejector package are reduced. This results in a reduction in lead time for and costs of the injection molding tool [23,24].

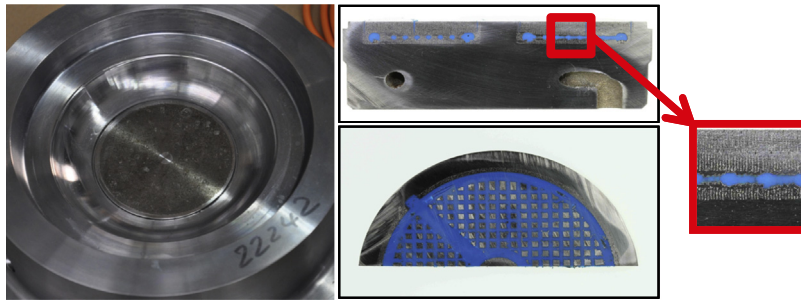

Figure 10.17 An air ejector system manufactured by laser additive manufacturing [23].

Figure 10.18 Complex cooling structures manufactured using laser additive manufacturing by Werkzeugbau Siegfried Hofmann GmbH.

Part warpage and cycle times in injection molding can also be reduced by close hollow structures with a complex contour in the mold tool (see Fig. 10.18). Manufacturing by conventional processes is often impossible [9].

Moreover, a part of the liquid oxygen systems tubing for the Eurofighter has successfully been applied in the military aviation sector. Complex internal structures allow liquid oxygen to flow according to the system's demands. The LAM design can be made of only one part, whereas the conventionally manufactured counterpart consisted of welded subassemblies. The approach facilitated a reduction in system leakage and optimized flow, with an only marginal increase in costs [25]. For a comprehensive overview of the state of the industry of additive manufacturing in particular, see the regular reports by Wohlers [8].

10.4 Summary and conclusion

Compared with conventional manufacturing processes, LAM offers a new freedom in design. The potential for new approaches in product design is immense. Yet, because the novelty of LAM, knowledge of its design restrictions is only marginal. Against this background, this chapter presented the most basic design rules that should be considered when designing parts for LAM and summarized it in a compact overview. Finally, the reader was given an overview over some already successfully realized design approaches for parts specifically designed for LAM in order to show the potential of the process in industrial applications. The studies show that it is already possible to successfully use parts designed for and manufactured by LAM in a competitive market if a suitable benefit for the product functionalities can be achieved. With the productivity gained by future machine concepts, the economic applications of LAM as an industrial-scale manufacturing process will increase.

References

[1] K. Pahl, W. Beitz, Konstruktionslehre − Grundlagen Erfolgreicher Produktentwicklung, Methoden und Anwendung, seventh ed., Springer, Berlin, 2007.
[2] A. Gebhardt, Understanding Additive Manufacturing, Carl Hanser, Munich, 2011, p. 89.
[3] I. Gibson, D. Rosen, B. Stucker, Additive Manufacturing Technologies, Springer, New York, 2010.
[4] M. Mazur, M. Leary, S. Sun, M. Vcelka, D. Shidid, M. Brandt, Deformation and failure behaviour of Ti-6Al-4V lattice structures manufactured by selective laser melting (SLM), The International Journal of Advanced Manufacturing Technology 84 (5) (May 2016) 1391−1411, http://dx.doi.org/10.1007/s00170-015-7655-4.
[5] O. Rehme, Cellular Design for Laser Freeform Fabrication (Ph.D. thesis), Hamburg University of Technology, 2008.
[6] K. Schmidtke, F. Palm, A. Hawkins, C. Emmelmann, Process and mechanical properties: application of a scandium modified Al-alloy for laser additive manufacturing, in: Proceedings of the International WLT-Conference on Lasers in Manufacturing, Munich, Germany, May 23−26, 2011, 2011.
[7] E. Wycisk, J. Kranz, C. Emmelmann, Fatigue strength of light weight structures produced by laser additive manufacturing in $TiAl_6V_4$, in: Proceedings of 1st International Conference of the International Journal of Structural Integrity, Porto, June 15−28, 2012, 2012.
[8] T. Wohlers, Wohlers Report 2013—State of the Industry, Wohlers Associates, Fort Collins, CO, 2013.
[9] J. Kranz, D. Herzog, C. Emmelmann, Design guidelines for laser additive manufacturing of lightweight structures in $TiAl_6V_4$, Journal of Laser Applications 27 (S1) (Februar 2015).
[10] D. Thomas, The Development of Design Rules for Selective Laser Melting (Ph.D. thesis), University of Wales, Cardiff, 2009.
[11] C. Aumund-Kopp, F. Petzold, Laser sintering of parts with complex internal structures, in: Paper Presented at the 2008 World Congress on Powder Metallurgy and Particulate Materials, Washington, 8−12 June 2008, 2008.

[12] NN, VDI Richtlinie 2222: Konstruktionsmethodik—Erstellung und Anwendung von Konstruktionskatalogen, Beuth, Berlin, 1982.
[13] N. Hopkinson, R.J.M. Hague, P.M. Dickens, Rapid Manufacturing-an Industrial Revolution for the Digital Age, Wiley, Chichester, 2006.
[14] J. DeGrange, Steps to improve direct manufacturing readiness levels, in: Proceedings Euromold 2006, Frankfurt, 29 November−2 December 2006, 2006.
[15] C. Emmelmann, P. Scheinemann, M. Munsch, V. Seyda, Laser additive manufacturing of modified implant surfaces with osseointegrative characteristics, in: Proceedings of the International WLT-Conference on Lasers in Manufacturing, Munich, Germany, May 23−26, 2011, 2011.
[16] P. Reeves, C. Tuck, R. Hague, Additive manufacturing for mass customization, in: F.S. Fogliatto, G.J.C. da Silveira (Eds.), Mass Customization, Springer, London, 2011, p. 275.
[17] NN, Additive Manufacturing in the Medical Field, EOS GmbH. https://www.eos.info/medical/applications/download/medicalbrochure.pdf.
[18] M. Munsch, Reduzierung von Eigenspannungen und Verzug in der Laseradditiven Fertigung (Ph.D. thesis), Hamburg University of Technology, Cuvilier, Goettingen, 2013.
[19] P. Bendsøe, O. Sigmund, Topology Optimization − Theory, Methods and Applications, Springer, Berlin, 2003.
[20] C. Emmelmann, P. Sander, J. Kranz, E. Wycisk, Laser additive manufacturing and bionics: redefining lightweight design, in: Proceedings of the International WLT-Conference on Lasers in Manufacturing, Munich, Germany, May 23−26, 2011, 2011.
[21] E. Wycisk, J. Kranz, C. Emmelmann, Leichtbaupotenzial durch das lasergenerieren bionischer strukturen, in: Proceedings of the RapidTech 2010, Erfurt, May 18−19, 2010, 2010.
[22] J. Kranz, D. Herzog, C. Emmelmann, Methodik für die fertigungsgerechte konstruktion von laseradditiv gefertigten bionischen leichtbaustrukturen aus $TiAl_6V_4$, in: Proceedings of the RapidTech 2014, Erfurt, May 14−15, 2014, 2014.
[23] C. Klahn, F. Bechmann, S. Hofmann, M. Dinkel, C. Emmelmann, Laser additive manufacturing of gas permeable structures, in: Proceedings of the International WLT-Conference on Lasers in Manufacturing, Munich, Germany, May 12−15, 2013, 2013.
[24] C. Klahn, Laseradditiv Gefertigte, Luftdurchlässige Mesostrukturen − Herstellung und Eigenschaften für die Anwendung. Light Engineering für die Praxis, Springer, Berlin, 2015.
[25] SAE International, Aerospace Engineering and Manufacturing, vol. 2 (No. 29), 2010.

Modelling of laser additive manufactured product lifecycle costs

11

C.F.W. Lindemann, U. Jahnke
Paderborn University, Paderborn, Germany

11.1 Introduction into profitability and part selection for additive manufacturing

Before thinking about part costs, one needs to address the strategic question of whether the use of additive manufacturing (AM) is beneficial for the field of application. This question itself is very complex, and not many approaches have be successfully pursued. One of the additive models which is to be named is the model by Siegwart and Singer [39]. Furthermore, the project 'Development of an Additive Manufacturing Potential Check System (DynAMICS)' is giving a lot attention to the strategic questions. The project keeps in mind that AM is more than only the production of parts. It can be a gamechanger in product design, value chains and business models [40]. Keeping that in mind, the uncertainty of whether and especially when to invest is crucial and needs to be well thought out. While standard accounting methods such as return on investment calculations may be performed, there are several other aspects to consider. One can assume that one can get a good feeling of the suitability of AM if most of the questions in Fig. 11.1 can be answered with yes. As a matter of course, the measurements of the considered products cannot exceed the current build chamber sizes. This clearly depends on the different technologies and their further technological development.

If one has come to the decision that AM is an interesting addition to current manufacturing processes, one has mastered the first step towards direct manufacturing. Coming back to the question of when AM shall be introduced, it needs to be considered that AM can nowadays be considered as a learning process more than a 'plug and play' solution. 'Just like CNC machining, additive manufacturing is a powerful, sophisticated manufacturing resource that has to be understood on its own terms'. [26,41]. When deciding to use AM, one should consider these aspects as training, and gathering experience is necessary before starting production.

Now, one of the crucial points for the successful use of AM is the selection of promising part candidates. Therefore one needs to decide on promising product groups or parts which seem to benefit from additive production. In a next step the application potentials for certain parts can be discussed. Similar to all other manufacturing technologies, AM is not the optimal production method for every

Laser Additive Manufacturing. http://dx.doi.org/10.1016/B978-0-08-100433-3.00011-7
Copyright © 2017 Elsevier Ltd. All rights reserved.

Figure 11.1 Indications of whether additive manufacturing is beneficial.

part. Thus a methodological approach is needed to identify specific parts or applications feasible for this technology. Appropriate part selection aims to solve three major tasks [44]:

1. Finding a part which can be produced by AM (technically)
2. Finding a part which offers an (economic) benefit
3. Finding a part which may be used as an end product (cost-benefit/quality control)

The literature and applications have proven that producing parts additively which were not designed for AM is not suitable. This is true for the means of manufacturability as well as for the economic success of a certain part [12].

Despite the design freedom AM has to offer, the development of 'direct manufacturing design rules' has shown that not every geometry can be produced with AM. This is especially true if stable and repeatable production processes are desired [31]. Therefore, the economic success of the technology is strongly related to the part selection and the part design. For example, one would not try to manufacture a milling-optimized part with casting technologies and vice versa. The costs of AM technology are difficult to assess and are hardly to be approached by inexperienced users. The advantages of the technology often make it necessary to consider more than just the production costs [13,34,35].

Finding a part which may be used as an end product seems easy when one has successfully mastered producibility and economic considerations. But for use as an end product, aspects such as the availability of material data and the possibility of conducting postprocessing steps or process stability tests play a crucial role, depending on the part requirements.

To check these aspects, a methodological repeatable approach has been developed that can be applied before starting the product design. This general approach can be split in three phases and is usable for experienced and inexperienced AM users [27]. Inexperienced AM users are guided based on a workshop concept.

The central tool in this methodology is called the 'trade-off methodology matrix' (TOM) and can be seen in Fig. 11.2. In general, it is a multi-criteria decision-support methodology adapted to AM. It can be adapted based on a company's requirements and the current state of the art. It consists of three parts, which split in a part definition, a preliminary section, and a final trade-off section. The part definition contains basic

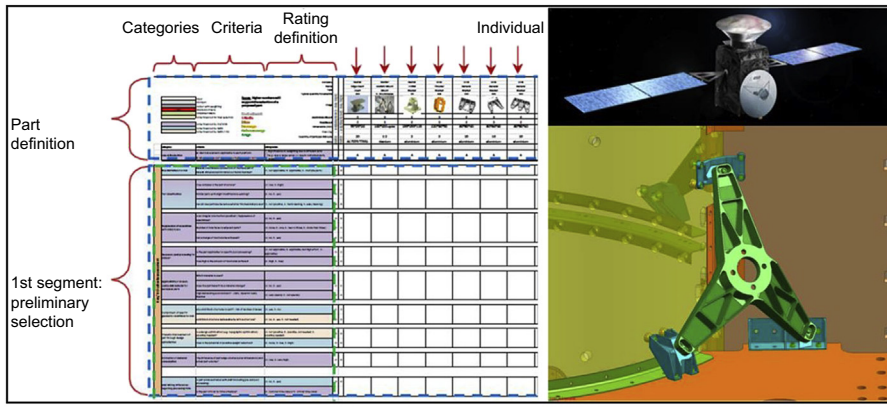

Figure 11.2 Excerpt from the trade-off methodology matrix (left). Exomars satellite (top right). *(Source: ESA.)* Reaction wheel bracket (bottom right).

information such as a brief description of the function, typical production quantities, traditional or target production costs, dimensions and mass of the part, as well as the currently used material. This data are already sufficient to get a first quote of rough production costs with the later presented technology. For an easy-to-use tool in this early phase, the production costs are calculated based on certain assumptions such as appreciation times and a specific demand. Detailed costs can be assessed later in the methodology (compare Fig. 11.5).

The tool is proposed to be divided into two segments. The first segment may be filled by any engineer, whereas the second segment aims more at experienced AM users. The first segment of the TOM aims at inexperienced users and marks some k.o. criteria such as size limitations [32]. A first ranking is now available and can rule out parts that will make it to the second segment. To achieve an efficient process and to easily assess the part, the second segment aims at more experienced users. The assessment is based on different criteria, definitions and ratings which are defined according to different branches and industries or companies' different strategies and requirements [27]. For example, in the aerospace industry weight-saving potential and the availability of reliable material data are crucial, and the existence of a flame-retardant material might come into play, especially for the polymers.

Every section is structured into different main categories that include several sub-criteria (eg, 'Compliment of specific geometric conditions for AM') An example for these categories is given in the following figure. These sub-criteria can be rated similar to a value benefit analysis. By changing ratings or adapting sub-categories, the matrix can be adapted to several different applications. Taking 'possible weight savings' as one example criterion, one can see that this aspect is more important for the aerospace industry or race car applications than for medical components. The third segment is the final trade-off, which requires detailed information on the part and includes a much more detailed cost analysis to finally decide whether a part should be manufactured additively or not.

Category	Criteria	A
Conformity of specific geometric conditions for AM	Any solid block structures in part? - risk of residual stresses	1
	Solid block structure replaceable by lattice structure?	2

	Block structures	Block structures replaceable by lattice structures
	Solid block structures induce arisk of residual stresses (e.g. horizontal faces bigger than 40×40 mm² hardly possible for some steels, aluminium more possible)	Wall-thickness > 3 mm
1	-	-
2	Large portion of block structures / >30%	No lattice structure possible
3	Mainly block structures / 10-30%	-
4	Hardly block structures / <10%	Replacement with lattice structure possible
5	No block structures strength/stiffness/lower CTE mismatch/...	No replacement needed

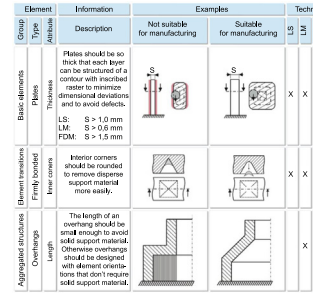

Example catergory and criteria from the TOM [32].

One example of a part selected using the TOM matrix is shown in Fig. 11.2. The considered part is a reaction wheel bracket, used to mount a reaction wheel in a telecommunication satellite. This assembly is used four times per satellite to control the orientation of the satellite in space. This part was selected mainly because of a good feasibility rating for AM with criteria such as weight reduction possibility, potential for a monolithic design and consequent interface reductions, a small amount of solid block structures hampering AM, and a high buy-to-fly ratio, requiring a high milling effort and thereby waste production. The main bracket is shown in Fig. 11.2, and there are three additional smaller brackets. Two of the smaller brackets can be integrated to save milling effort and weight.

When redesigning existing parts, one must keep in mind that building the same geometry is not economic in most cases. It is necessary to go one step back and question the 'true function' of the part. Thus it may be seen as a 'black box'. Furthermore, one must investigate the part surroundings for possibilities of functional integration (and then again question the intended function) and check for interfaces to other parts and components (compare Fig. 11.3). This approach will save money later in the lifecycle process because it helps to achieve part integration and reduce the post-processing effort [44].

By now, one can infer that the product designer has a significant influence on later part costs. During the product design phase, many aspects need to be considered to achieve a cost-efficient design. According to Eppinger [42], the advantage is that the product development for AM is now a more flexible process. Part characteristics such as build direction and support strategies can be permanently adapted without incurring high costs. For traditional manufacturing processes, costs are mainly locked once the first design has been approved for production. The additive process allows more freedom in later costs, as part characteristics may be permanently optimized as long

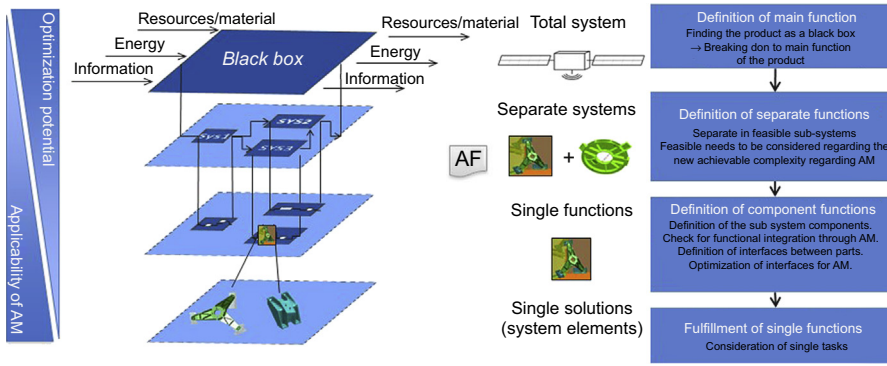

Figure 11.3 Principle of black box systems for redesigning additive manufactured parts, for example, satellite structures. *AM*, additive manufacturing. (Based on [23]).

as these changes do not interfere to much with the interfaces with other components of the product. This section has helped to explain which parts to choose for the application of AM. As a result readers shall be able to screen for promising AM part candidates.

The following section deals with methodologies to calculate AM production part candidates.

11.2 Introduction to lifecycle costing in additive manufacturing

To understand the costs of AM, one needs to understand the process chain. Each of the different AM technologies, from stereolithography to selective laser melting, have their own peculiarities which affect the process and its overall costs. If one compares, for example, build speed details from machine manufacturers, one finds that they are not always stated or sometimes provided in different units. Despite that, manufacturing speeds, energy consumption and the need for post-processing vary strongly between the different AM technologies and the respective part requirements. The following steps describe a methodology to build a costing framework for all laser based AM technologies, keeping in mind that the total value chain of a company may be affected.

Deciding to use this technology therefore often means a trade-off between production costs and added value. The approach of lifecycle costs thus delivers an appropriate framework. Lifecycle costs consider more than just the production or self-costs (producers' view) or the purchase price (customers' view). Costs occur during the whole lifecycle of a product. In many cases customers do not necessarily consider this aspect. The cost structure can be compared with an iceberg (Fig. 11.4). A customer sees the purchase price as the main criteria, but there are many other aspects where costs occur, for example, during the usage of the product [18].

Additive manufactured parts can provide benefits that can affect the lifecycle costs of a product; they are usually lighter and can provide increased value for the customer.

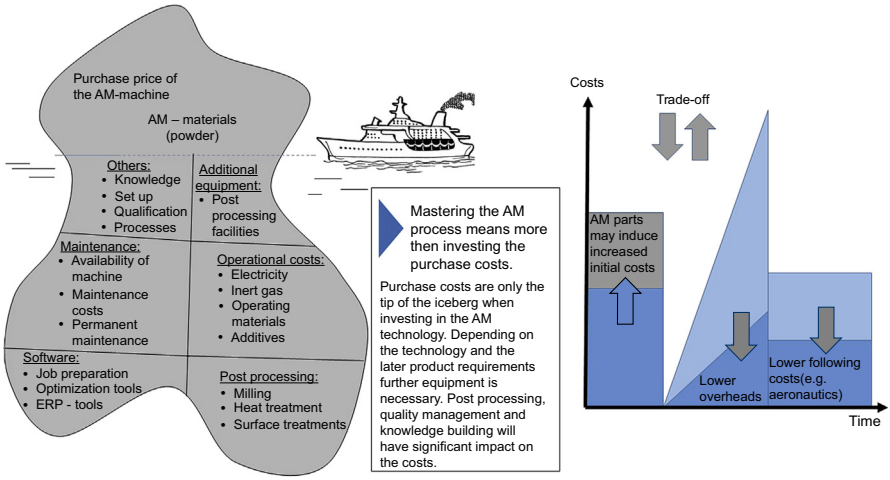

Figure 11.4 Aspects regarding the product lifecycle [Based on 18,23].

During the whole lifecycle, products generate costs that users are often not aware of. Usually only the acquisition price is what customers take into account when they are about to buy a product. But this is usually only the 'tip of the iceberg', as Fig. 11.4 illustrates, using the example of buying an additive manufacturing production machine. Several other costs arise during usage and removal. The production and acquisition costs are usually only a small amount of the costs that are generated during a product's life. The lifecycle costs cover all expenditures during the different phases of the lifecycle, from the perspective of the manufacturer and user ([18], p. 124).

An advantage of a lifecycle cost analysis is that potential for optimizing the product can be discovered. This is advantageous for both parties, the manufacturer and the user/customer. The user has lower operating costs, whereas the manufacturer can merchandise the product's benefits. It is even possible to charge a higher price for the product because of lower operating expenses. Usually this is necessary because more effort during development is required to be able to reduce the operating expenses [16,19].

The lifecycle costs are far more than the costs the customer pays to purchase a product. The technology might have increased initial costs (compare Fig.11.4), which might be balanced by lower overhead and subsequent costs. The aspects of every AM part candidate should be balanced thoroughly.

One methodology for lifecycle costing that can be easily adapted to the needs of AM is the 'DIN EN 60300-3-3 Dependability management – Application guide – Life cycle costing'. In general it splits the costs into six different phases that need to be considered (compare Fig. 11.5). While the model in general has a sequential approach, it has been split into three different phases in Fig. 11.5. It distinguishes between production costs, which in the early phase of product development are the main point of discussion; continues with self-costs, which include the design process; and finally ends with the lifecycle costs in phase three.

AM is still considered an expensive process and therefore needs to justify its use against traditional manufacturing methods. AM production with concurrent redesign

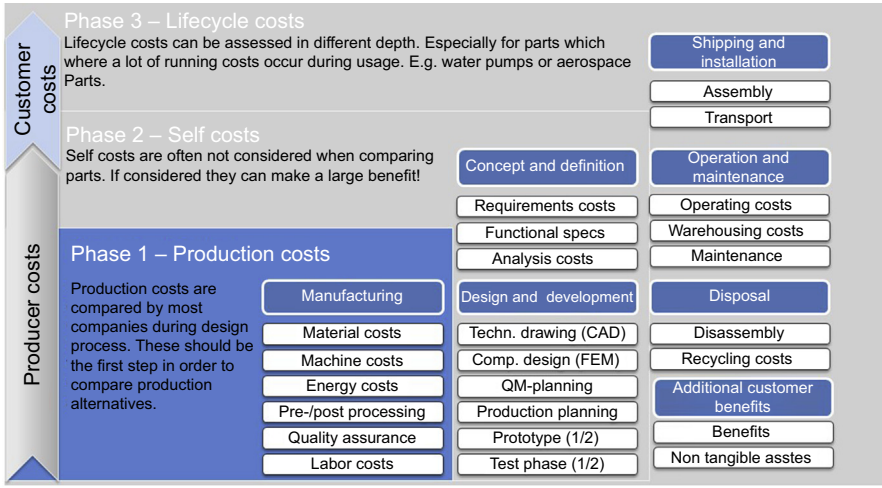

Figure 11.5 Three phases of costs in product lifecycle [17,23].

and post-processing is considered reasonable only when the costs can compete with traditional manufacturing technologies or if AM offers some major functional benefits that cannot be achieved any other way.

Therefore, one has to keep in mind that the comparison of production alternatives should not be limited to production costs. A more holistic view is needed, as AM generates benefits in different areas which also have to be assessed and compared. Here lists for the different phases listing possible cost drivers and cost saving potential are beneficial for the development process. Many aspects cannot be generalized (especially comparing different technologies) and need to be evaluated based on the current part and its requirements [9]. The designer has to be aware of the different factors influencing the total costs his decisions affect [10].

Fig. 11.5 can be understood as a model for comparing theses alternatives. It describes a general approach to justify AM part costs compared with traditional methods. The first step is always to start by estimating the production costs in an early phase of product development. This phase is in general very particularly dependent on the peculiarities of the used AM process, as each process has slight differences important to the cost estimation. Much AM-dependent knowledge is necessary to accurately calculate part costs. These calculations need to be adapted as the product design process evolves and more part details become fixed. For a dedicated cost estimation, vast knowledge about the process is necessary. If after this phase AM is still a production alternative, the self-costs need to be considered next.

These include all costs occurring on the producer's side. The model highlights the costs for 'concept and definition' as well as for 'design and development'. The self-costs and the production costs need to be updated during the product development process as the final part evolves. In this phase, AM may play out its advantages according to prototyping and testing; much time can be saved through the use of 'final' prototypes. While during this phase most of the other costs are influenced and fixed, the

impact of this phase is often underestimated. Shorter development cycles may be a major benefit if product designers are used to AM and its design rules. Since the later product characteristics are set in this phase, the lifecycle costs are set as well. Intelligent product design with the use of design catalogues helps to reduce lifecycle costs.

Considering all lifecycle-based costs can be time-consuming. And again, if AM is still a production alternative after consideration of the self-costs, the later lifecycle costs need to be considered. These play a special role as AM enables the production of parts with special benefits (increased efficiency, less assembly, etc.) and can be a game changer for supply chains and business models. The development of special costing tools can be one solution to handle the effort in this phase [13,34,35]. As one needs to think about customer benefits as well; it is strongly recommended to discuss the costs and benefits during this phase with different roles in an interdisciplinary team (eg, engineering, marketing, sales). The next sections discuss the three phases in particular.

11.3 Production costs

All laser based additive manufacturing technologies have in common several process steps that all have a significant impact on the overall cost of the technology. Parameter values for the different steps may change between technologies, especially in AM, since it is a quickly evolving technology. In general, the four major process steps, which can be seen in Fig. 11.6, comprise the total overall costs. As stated by Thomas and Gilbert [37], the major costing models in the history of AM have been developed by Hopkins and Dickens [20] and Ruffo et al. [24], amongst others. Furthermore, Gibson, Rosen, and Stucker, as well as Augsburg [46], have been influential authors. A comparison of the models shows that all authors chose a similar approach to calculate costs in their models. Each of them set a specific emphasized a certain topic, for example, Gibson and Rosen [21] were strong in estimating building times, whereas Augsburg considered the post-processing costs. The model presented here is strongly influenced and based on these authors.

Time-driven, activity-based costing has been chosen as a general method for calculations. It represents a good means for allocating cause-based costs and thus

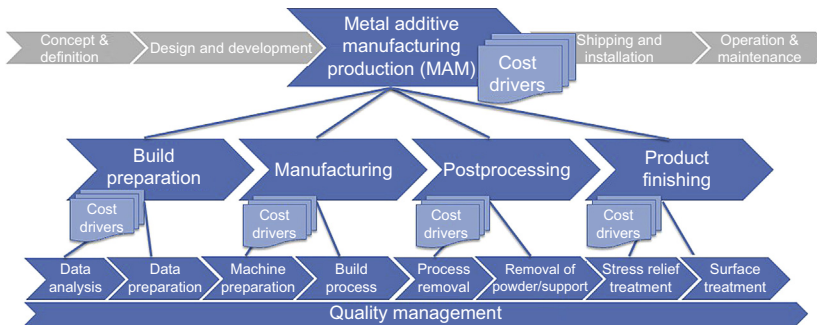

Figure 11.6 Phases during additive manufacturing production.

allows for a comparison of additive and traditional manufacturing methods. This is a further development of activity-based costing, representing a combination of activity-based costing and the hourly machining rate. Here, process factors are replaced by time consumption. Time-driven, activity-based costing uses the duration of a process as a general cost driver. Every process with defined starting and ending points can be represented and calculated by this method. The process time is multiplied by a predetermined time cost rate. The sum of the individual sub-processes yields the cost for the overall process [48]. Based on these aspects, each company can build their own model regarding costs for AM. The manufacturing costs are discussed in more detail here; the other steps can be modelled accordingly to Fig. 11.6.

11.3.1 Build preparation and manufacturing strategy

Build preparation includes all steps from the initial computer-aided design (CAD) data, placement of the parts in the building chamber and creation of the support structures, where necessary. Interviews with engineers have shown that the costs in this step greatly depend on the complexity of the different parts and the complexity of the build job itself. Therefore, the duration of this task greatly depends on the kind of job being prepared. This is especially important because this process requires an experienced engineer, whose labour costs represent one of the main costing factors in this step. The build preparation in general has a strong impact on the later manufacturing costs. Fig. 11.7 shows the significance of this process step; all important build parameters are determined here.

Therefore, one can also say that this phase defines the manufacturing strategy. Layer thickness, part orientation and support structures are set in this step. The influence of the utilization of the building chambers is especially high for powder-based additive manufacturing processes. Fig. 11.7 shows the significant difference in build speed depending on the utilization rate of the building chamber. This is mainly due to the recoating times per layer which need to be considered. Fig. 11.7 shows e.g. the build rate for two different parts manufactured with the same material parameters and the same material on the same machine.

It is not unusual that preparation for a building job can take up to 2 h, depending on the technology and the composition of the job. Almost all aspects that affect the build rate are set here. Based on the activity-based costing approach, one possibility for estimating the preparation time is to determine an hourly rate that includes manufacturing.

11.3.2 Manufacturing

Factors influencing manufacturing costs can be seen in detail in Fig. 11.8 and are modelled regarding the work of Ruffo et. al. [24]. This production model is completely time driven and gets an additional fixed cost rate for initial process steps such as gas flooding or the pre-heating of the machine. A fixed labour cost is also estimated, as the preparation processes to start a build job are considered constant for each building process. The hourly machine rate consists of an indirect and a direct cost rate and is

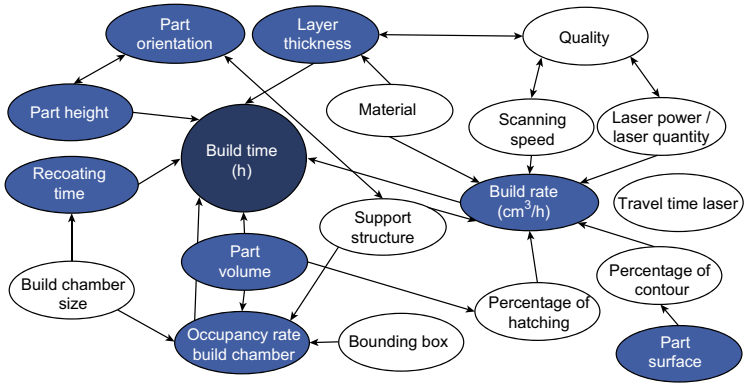

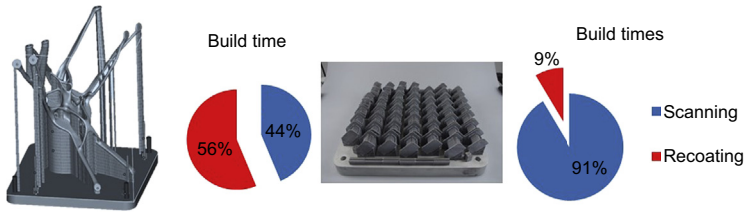

Parts (build with same parameters in AlSi10Mg)	Part 1 (left)	Part 2 (right)
Build speed	10,3 cm^3	21,2cm^3
Scanning time	16:21	18:59 h
Recoating time	21:05	1:37 h

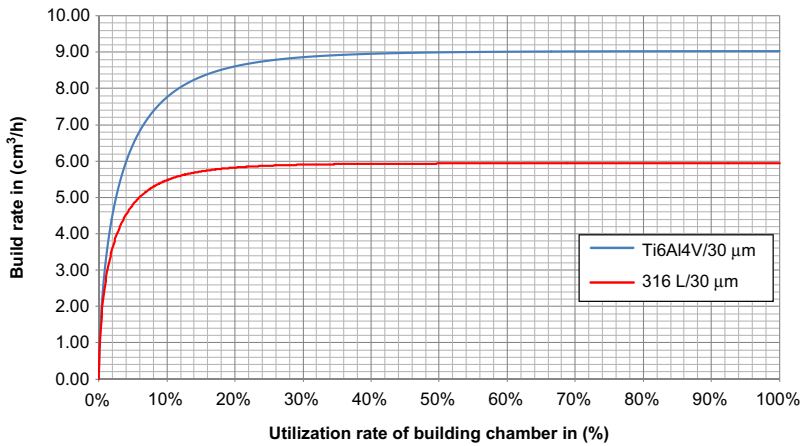

$$\text{Utilization rate} = \frac{\textit{Max part height * max usable build plattform area}}{(\Sigma\ \textit{support volume} + \Sigma\ \textit{part volume})\ \textit{the build}}$$

$$\text{Build rate} = \frac{(cm^3)}{h} = \frac{\textit{Molten parts volume } (cm^3)}{\textit{Time of manufacture } (h)}$$

Figure 11.7 Influences on build speed. Build rate according to utilization rate of the build chamber [44].

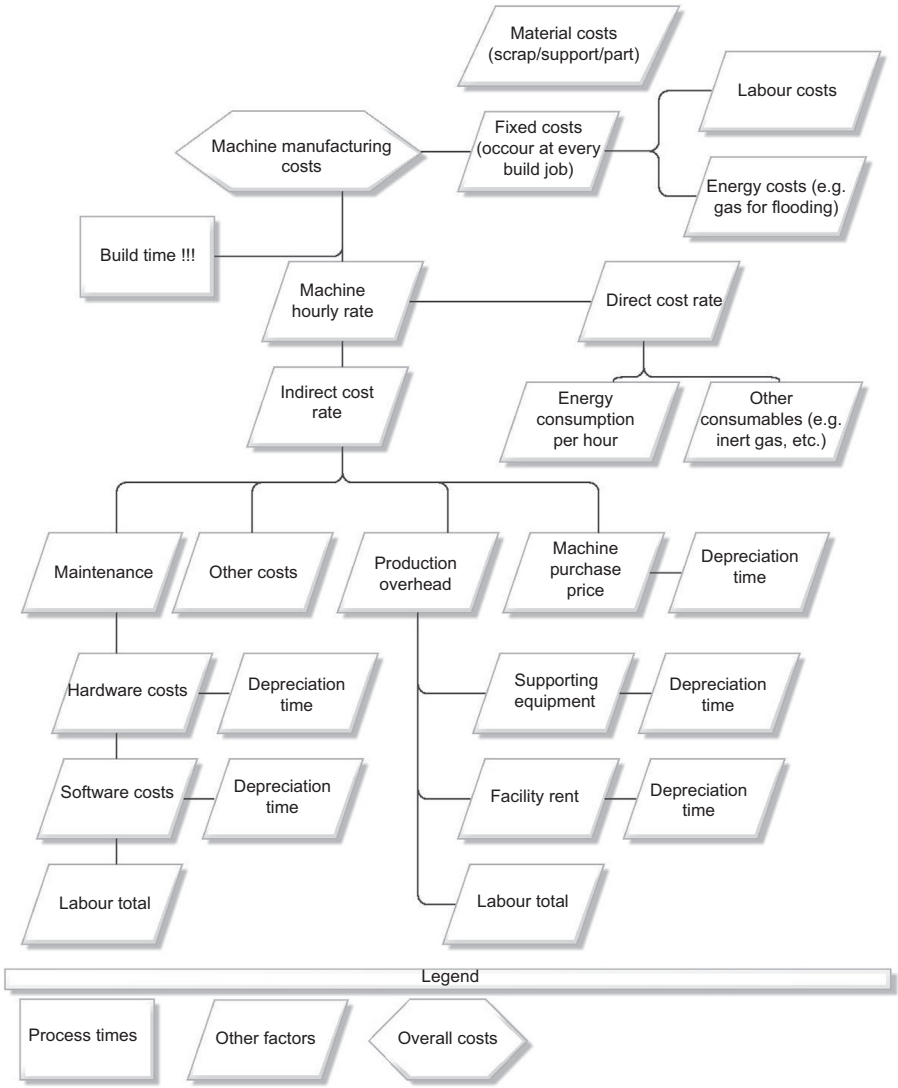

Figure 11.8 Costing structures for additive manufacturing.

multiplied by the build time afterwards. Many factors are already available as the energy consumption of different machines (compare [15]).

$$\text{Costs}_{\text{Build}} = \text{Costs}_{\text{Fixed}} + \text{Machine hourly rate} \times \text{Build time} + \text{Material costs}$$

Estimating the build time is certainly one of the most important factors in costing models because it significantly influences the costs of the build job. Many authors have put some effort into calculating the building time (compare [22] and Gibson

and Rosen [21]). Therefore, different approaches can be taken. As stated earlier, the model of Gibson, Rosen, and Stucker is the most detailed concerning the estimation of the build time. Hence, the equations from Gibsonet. al. can be adopted for a general model.

Other options for estimating build time include a calculation with the build speed values displayed by the manufacturers. These in general are much slower in reality then the optimum noted in the product documentation. Another option is experimental or empirically generated data. As seen in Fig. 11.7, it is important to include the usage factor of the building chamber. Data to be considered when choosing such an option can be seen in Fig. 11.9. Once one has collected this data, it is easy to predict part build time according to only a few part-specific parameters. A sample build platform to achieve curves similar to those in Fig. 11.7 is shown in Fig. 11.9. It is designed to result in minimum effort and minimum costs in order to achieve accurate results. With the resulting log-files, a build speed curve for a certain machine material combination can be achieved. It is designed to result in minimum effort and minimum costs in order to achieve accurate results. With the resulting log-files, a build speed curve for a certain machine material combination can be achieved (compare Fig. 11.7).

The sample part on the platform is in its biggest area 15 mm x 15 mm and split into 14 different steps, which will help to determine the overall build speed. Each step has a height of 0.045 mm. This size has been chosen as all currently used layer thickness (0.25 µm /0.3 µm /0.5 µm) can achieve this height. Through the evaluation of the build rates of the different steps on can generate a build peed curve in relation the build chamber utilization. Steps 1-10 will determine build speed without support while steps 11-14 are used to revise the data according to the influence of the support structures. The volume of steps is equivalent in the steps 6-9 and the steps 14-11.

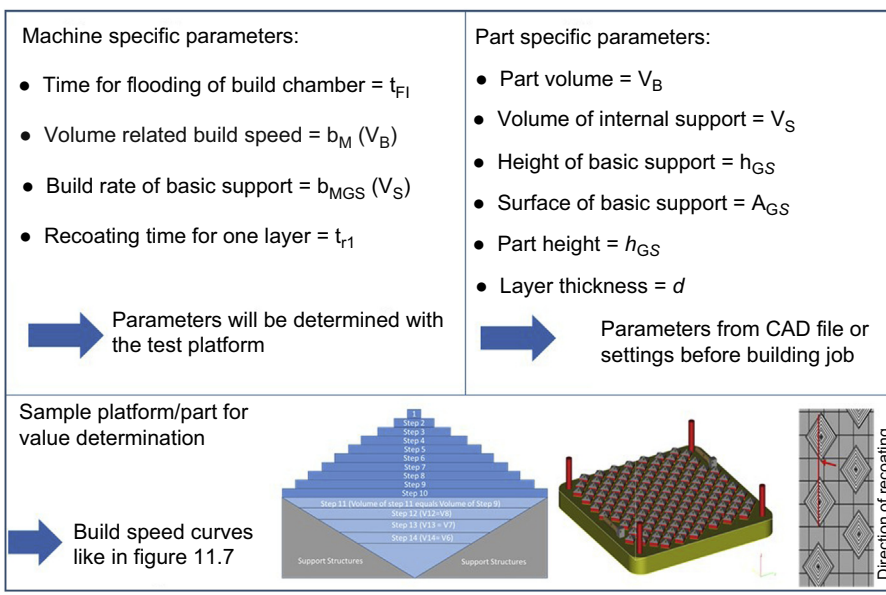

Figure 11.9 Data necessary for predicting empirically generated build speed.

The further setup of the build platform was designed to suit multiple machine and has been evolving over time with regards to manufacturability. Therefor the parts are placed in a 45% degree angle to the recoating direction and are not placed directly in one straight line. Experiments showed that the build speed does not increase significantly after 45% of total usage of the build chamber. Therefore the number of parts per build platform will be estimated the following:

$$Number\ of\ parts = \frac{0.45 * (length * width\ of\ build\ chamber)}{15\,mm * 15\,mm\ (maximum\ area\ of\ test\ part)}$$

Once the curves for the support and for the build rate have been elaborated, these curves can serve as a quick calculation method for the engineers in combination with the machine hourly rate. The according method of the build time estimation can be seen in the following:

Method for build time estimation: $T = t_{Fl} + t_B + t_{GS} + t_r$

Expected build time $= T$; additional processing times (e.g. pre-heating)$= t_{Fl}$; scanning time part$= t_B$; Scanning time basic support$= t_{GS}$; recoating time $= t_r$

Scanning time of the part: $t_B = \frac{V_B}{b_M(V_B) * K_S(V_S)}$

Volume of the part$= V_B$;

Volume related production speed$= b_M(V_B)$(*compare Fig* 11.7);

support based correctional factor$= K_S(V_S)$

Recoating time: $t_r = t_{r1} * (\frac{h_B + h_{GS}}{d}) * K_r(A_{GS})$

Recoating time for one layer $= t_{r1}$; max part height$= h_B$; height of basic support$=h_{GS}$; layer thickness $= d$

Correctional factor for basic support$= K_r(A_{GS})$

The advantage of this methodology is that is applicable for almost all additive manufacturing processes and may incorporate technical developments as well (e.g. multiple lasers). Furthermore is the graphical representation easily manageable even by non-technical staff in the company. The methodology may be seen as a methodology for early build time estimation (quick calculation method).

Another methodology by Merlus et. al. allows estimating the overall build time with only a few machine-material dependent parameters, which need to be known for the build job. The authors differentiate the build jobs into the different categories build speed of the hatches, build speed of the contour, the build speed of the support and the overall recoating time of the build job. Needed machine parameters are the layer thickness $(L_1 t)$, the hatch distance $(h_1 d)$, as well as the different possible scanning speeds for the hatches (S_h), the contour (S_c), and the support (S_s) as well as the average recoating time $(t_1(r))$ [22].

$$Build\ time(t_B) = \frac{Vol_{part}}{L_t * h_d * S_h} + \frac{A_{surf}}{L_t * S_c} + \frac{Vol_{\sup}}{L_t * S_s * h_d} + n_l * t_r$$

Part specific factors, which are needed are the volume of the part (Vol_{part}), the volume of the support structure $(Vol_{\sup})$ and the surface area of the part (A_{surf}) as

well as the number of layers $(n_1(l))$ which are built during the manufacturing process. The number of layers is determined by the layer thickness used for the build as well with the total part height. This methodology needs more exact input and is mainly focused on one laser systems. It would need adaption for multi laser systems in the future, but shall work out for all laser based powder bed processes quiet accurate.

11.3.3 Post-processing

This step sums up all necessary mechanical post-processing steps, including support removal, sand blasting or milling and drilling activities. In total, these are all activities that remove the part from the production system and ensure that the surface quality meets the product requirements.

Post-processing is often underestimated while talking about AM. It can be a main part of the total part costs. Therefore a designer needs to think about post-processing aspects in the original design phase; these aspects include removing supports and adjusting surface quality. If one can foresee that a milling process will be necessary, milling jigs and clamping positions need to be considered beforehand. In cases where a high dimensional accuracy is required, an offset of the surface is needed so near net-shape geometries can be avoided in these places, as they can be a barrier for traditional tools (eg, drilling in a non-centric hole). Part design with AM is always a trade-off between functional optimization, cost-efficient design and manufacturability [44].

11.3.4 Adjustment of mechanical properties

The adjustment of mechanical properties is an optional step which mainly applies to laser-based metal processes. These steps aim to change the microstructure of the material to obtain different mechanical properties. Studies have shown that post processing with e.g. hot isostatic pressing can significantly change the mechanical properties and reduce inner stresses of AM parts. [33] For many parts especially metals it is necessary to have some post processing steps. Therefore is should be considered when talking about the overall costs. Common steps are heat treatments or hot isostatic pressing (HIP).

11.3.5 Quality control costs

One aspect which is not to be forgotten is the aspect of the quality costs. These can play an important role on the total part costs, depending on the part requirements. Sometimes it may be necessary to conduct extensive testing before one is able to use AM for "direct manufacturing" purposes of end-products. As is true for all other manufacturing technologies, the quality requirements set during the design phase need to be addressed. For direct manufacturing, mainly six main influence factors need to be considered:

- Knowledge about the overall process
- Part characteristics
- Proper data preparation of the STL and manufacturing files
- Material properties
- Manufacturing system, including maintenance and its condition
- Selected process parameters

The overall process knowledge plays a superior role in all these factors. This also includes knowledge about possible sources of error. The quality costs of AM can be differentiated into three different categories [44].

Initial set-up costs: The initial set-up costs include all activities which are necessary to qualify the process for the desired application. This can include the development of a certain set of process parameters for new materials [44].

Costs for ensuring process stability: AM needs to be performed with a well-maintained machine to ensure constant part quality. To ensure that every build job stays within certain process windows, it is recommended to include process samples in every build job (eg, tensile bars or density cubes). The process samples incur costs for materials for general testing [44].

Tests for ensuring part quality: Depending on the later part application, further tests may be required. For the aerospace industry, this might be computed tomography scans of metal parts. These costs need to be taken into account as well. Furthermore, a designer needs to think about possible test methods in an early phase, since complex part structures often make it impossible to perform current nondestructive testing methods [44].

One needs to consider that post processing and quality costs may take up to 50% of the final part costs.

11.4 Self-costs

Self-costs occur directly at the beginning of the product development process but are often forgotten when comparing different production alternatives. They include practically all costs to produce and distribute a product and are incurred directly on site at the manufacturer. Here, only AM-specific aspects are discussed; other literature on this topic can help to optimize all aspects of self-costs [18]. This phase also has a high influence on the later part costs, as can be seen in Fig. 11.10. In general, AM offers a higher degree of freedom, as the design can be adapted more easily, without changing the complete production system.

Nevertheless, designers are currently often not capable of appropriately using the technology. According to Ref. [30], the existing software tools for product development do not have the full capabilities to be efficient and to design with free-form surfaces. Though finite element modelling—optimized designs often take some time during product development, production optimization rules are not available. It is, however, often more economical to work out an easy-to-sculpture design.

AM also makes it possible to replace several traditionally manufactured parts, as monolithic structures, the number of spare parts that have to be managed, decreases as well. Fewer parts provides other advantages, too. For example, fewer parts must be sourced, labelled and evaluated. In the end this also reduces the spare parts that have to be stocked. Since there is no need for tooling to produce spare parts, it is unnecessary to hold legacy tooling in storage. The complexity of the production and management process decreases, and therefore savings in the entire business can be achieved [21]. This simple way to produce complex geometric structures offers the ability to mass-produce individual parts, as is

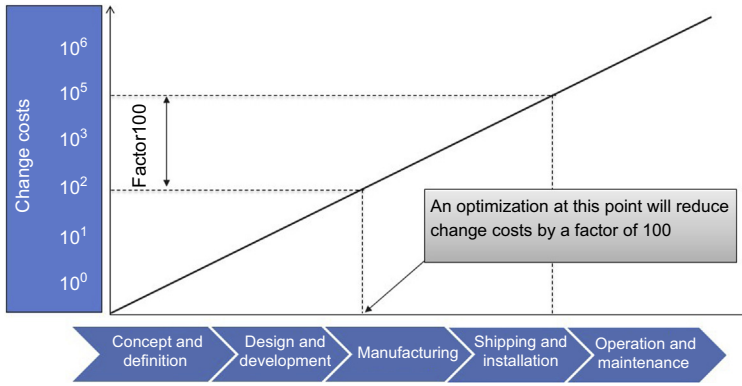

Figure 11.10 Cost incurrence and possibilities to influence during design [based on 18].

done with hearing aids, for example. There are key economic criteria in the area of AM, which cannot be directly expressed monetarily. AM helps to shorten the time-to-market, which can result in competitive advantages (e.g. new functions) [4].

The resulting advantage is not allocable by hard facts in general. Before AM machines replace entire warehouses, it is conceivable that chosen parts are subject to production on demand. Technical limitations and economic reasons, however, constrain the number of parts that could be manufactured additively.

AM has the potential to overcome some of the challenges of spare parts logistics. One can easily imagine what cost savings could be achieved if AM machines were to replace large warehouses (Fig. 11.11). It would enable spare parts providers to understand better the capabilities of AM, and thus research activities in this field could be intensified and improved. In addition, a future maintenance-organization structure where the logistic department is replaced by a production department could be developed.

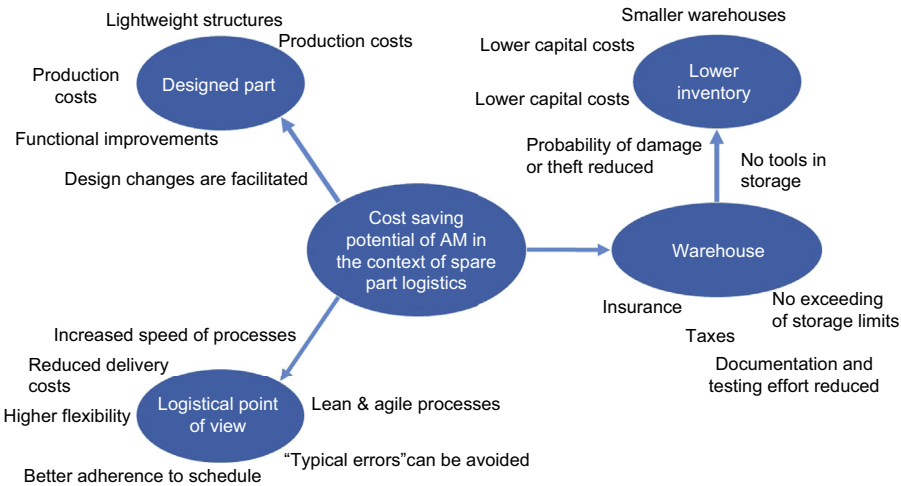

Figure 11.11 Cost-savings potential of additive manufacturing (AM) in (spare part) logistics.

11.5 Lifecycle costs

Lifecycle costs are an important aspect in AM. Here we use the definition of the intrinsic lifecycle. *Intrinsic lifecycle* means all different steps a product passes through, from the first product concept to the production processes and ending with disposal of the product [23]. These processes are modelled and investigated for lifecycle costs. 'Lifecycle costs are the costs associated with product users as the sum of all costs due to the purchase and during the period of use of a product (plant, machinery, equipment, apparatus) (product life)' [18].

In many cases the technology can make a big difference. Especially operational costs or other customer benefits can play an important role when approaching this costing sector. This can be clearly seen in Fig. 11.12. Detailed lifecycle costing remains a task for the accounting department, but product designers need to give basic consideration to the costs that will be incurred during use. Designers need to find a trade-off between optimized functions and cost-efficient design. As AM offers many additional benefits which cannot be valued directly, the communication between designers, marketers, and engineers becomes more important when discussing possible production alternatives.

AM is capable of cutting costs in a variety of areas. This starts with the reduction of parts and, therefore, a savings in the time required to design a part. Tests and tolerances can be reduced significantly [DiCu11], as can warehousing and assembly costs. Integrating an assembly into a single part also means that fewer subcontractors need to be controlled and managed. Digital tooth cap (Invisalign) production has demonstrated the ability to optimize the entire process chain. The transition from analogue global dental production to digital local production saved 85% of the logistics steps, reducing the production activity and the energy consumption during production by 80% (www.melotte.be).

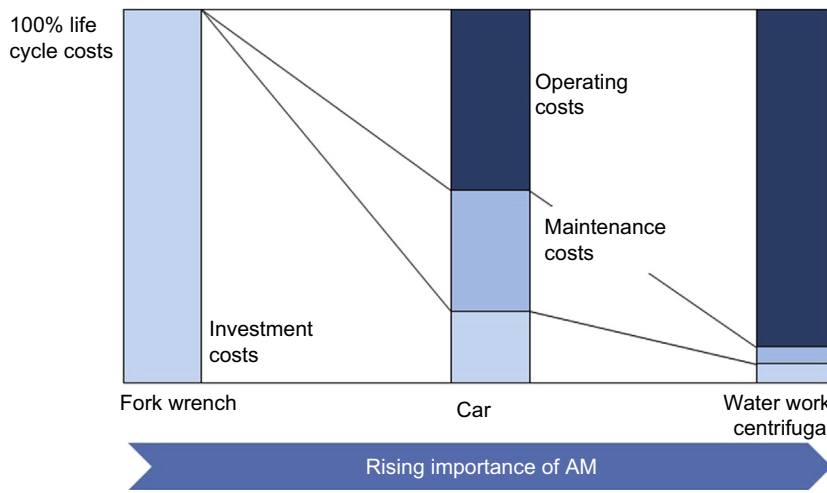

Figure 11.12 Costing structures of different product types (left) Costing types at the user/producer levels [18].

But the ability to realize cost savings and added value does not stop at the company. It also benefits the customer through increased functionality and reduced lifecycle cost for the use of a product.

Redesigns of sample aerospace parts have shown a weight-reduction potential of up to 70% of the original part weight. Reducing the weight of an aircraft by 1 kg/year saves $3000 in fuel annually [25], keeping in mind that an average aircraft has a 30-year lifespan. Especially in this sector, this means weight savings have an incredible capability to reduce lifecycle costs. But not only weight reduction can benefit the costs of a product.

As Fig. 11.13 shows, AM might have different influences in different phases compared with traditional manufacturing. The figure shows how a redesigned bracket would compare to a milled one under conditions of use in an airplane. The technology clearly shows it strengths in the usage and maintenance phase.

The total lifecycle cost combine all costs that have been incurred or that make a difference between production alternatives (compare Fig. 11.14). The final decision

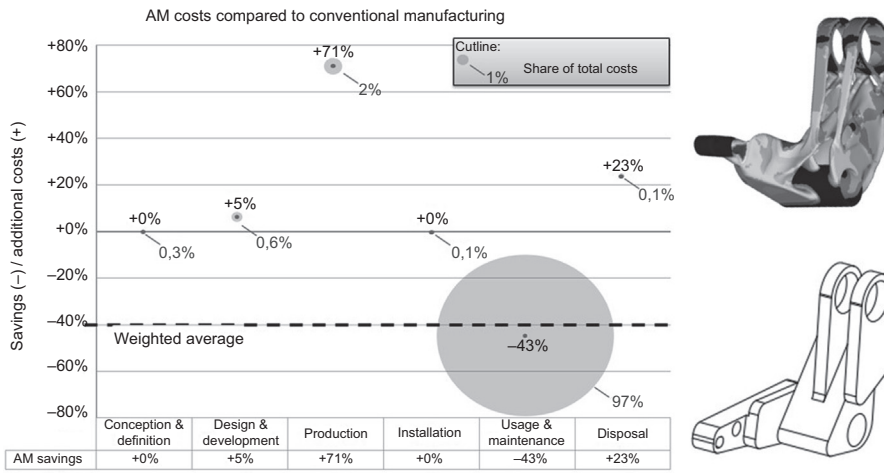

Figure 11.13 Comparison of lifecycle costs for conventional and additive manufacturing [29].

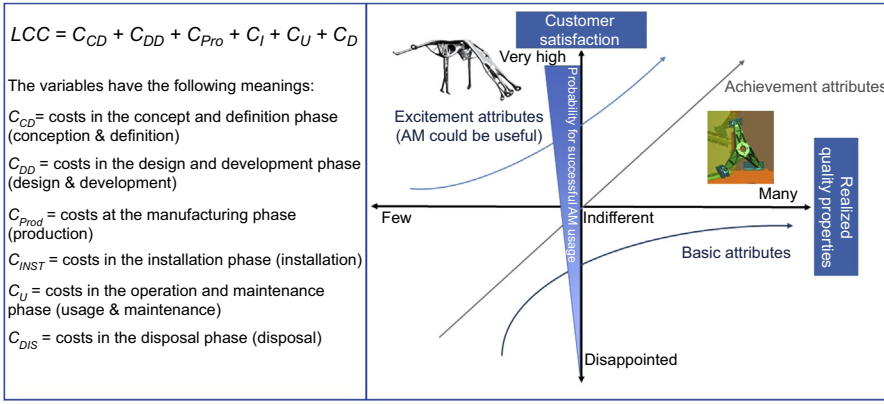

Figure 11.14 Composition of lifecycle costs (left) [17] and a Kano diagram (right) [38].

should be based on further thought regarding the pure numbers. If an AM-produced part can achieve an attractive quality (compare Fig. 11.14), it is more likely to be accepted by customers. In contrast, quality parts which can be simply achieved with other technologies may end up being produced with AM.

Factors that need to be considered for AM complete product lifecycle comparison are manifold. One aspect which can influence these is the costs of counterfeit products. These are discussed in the next section.

11.6 Aspects of product piracy for lifecycle costing

The number of counterfeit and plagiarized product on the market continues to grow, as published in various officially recognized studies. The disastrous economic impacts comprise not only the audiovisual and pharmaceutical sectors, as often mentioned in the media, but also the automotive and electronics industries [8], as well as the mechanical and plant engineering field [11]. Plagiarism of spare parts and machine components have been detected, as have imitations of complete machines, with a total loss of €7. 3 billion in the German mechanical and plant engineering industry alone. In addition, this product piracy implies a high risk to employment: the mentioned economic damage equals roughly 34,000 jobs. Damages caused by product piracy can be classified as direct impacts, such as the loss of profits caused by reduced turnover volume and costs for product liability, and indirect impacts such as a loss of market share because of a negative image or the loss of know-how [6]. Thus product piracy affects the later phases of a product lifecycle, as shown in Fig. 11.15.

On the other hand, product piracy can also influence lifecycle costs in the early phases as a result of activities aimed at preventing these damages. Fig. 11.15 shows a loss of sales after product piracy occurs; therefore companies should endeavor to postpone that point in time. The later imitators are able to join the market, the fewer

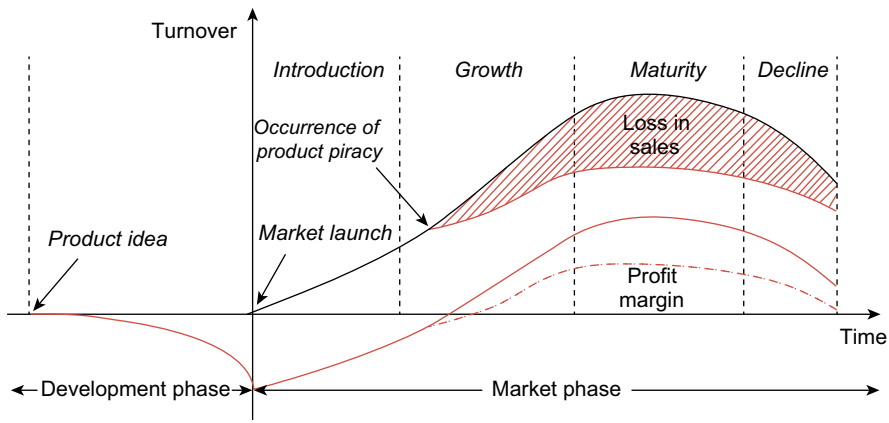

Figure 11.15 Impact of product piracy in a product lifecycle [3].

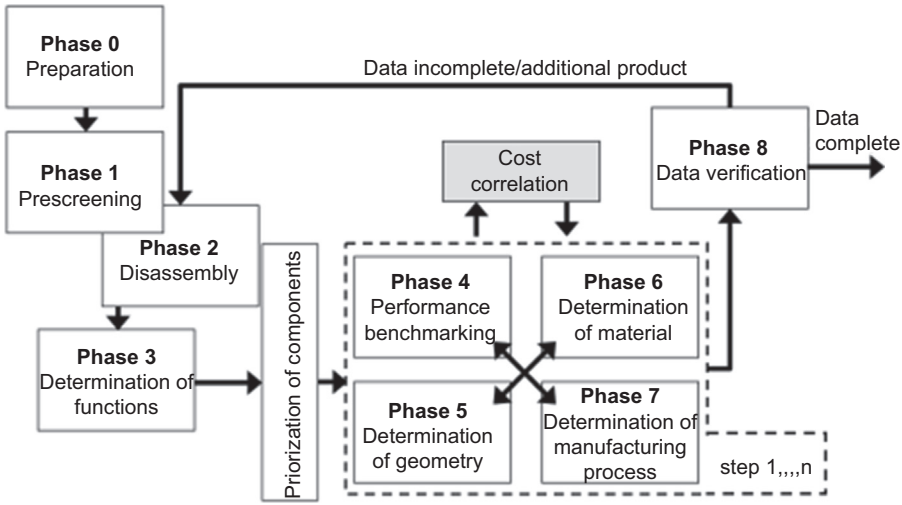

Figure 11.16 Phases and correlated activities of the reverse engineering process [2].

the losses in sales will be for the original manufacturers. The crucial question is how to achieve advantages over imitators so that it becomes more complicated for them to plagiarize. Therefore it is necessary to understand how imitators reach their goal of a counterfeit product or plagiarism.

The study by VDMA [11] mentioned above highlights reverse engineering (RE) as the most important process used by imitators to gather required information. Thus a detailed analysis of the RE process builds the basis for the development and selection of protective measures. In this process the technical feasibility is proofed during eight phases (Fig. 11.16); the simultaneous cost correlation considers an economical point of view. The next sections discuss the potential of AM to complicate one or more phases of the RE process.

11.7 Product piracy and additive manufacturing

In public media and advertisements, AM is often discussed as a driver of product piracy and is promoted to ease the RE process. But in most cases RE is used as a synonym for just one or two phases of the whole RE process, most often the extraction of geometry and sometimes reproduction. This simplification is mostly explained by the capability to copy arbitrary three-dimensional (3D) objects using related scanning technologies [9]. But many factors need to be considered to achieve suitable results. The accuracy of the scanning device used, for example, is important for the level of detail of the digital representative of a physical object. Undercuts are not scannable with usual 3D-scanning devices because a shadowing effect occurs, and 3D-scanning devices are not able to look inside. Thus specific technologies like computed

tomography or X-ray devices are required to fulfil such a task. Furthermore, the production process – no matter if fused deposition modelling, laser sintering or selective laser melting is used – is not as easy as promoted, especially when material properties and tolerances are important to fulfil the functionality. Thus many factors have an influence when copying a 3D object from physical to digital to physical, leading to enormous error propagation. This is more a hindrance for functional parts or products than for designed objects.

Knowing this complex of problems for successful RE and rebuilding of a product can be used for a good cause – the prevention of product piracy – in this case by complicating the phase of geometry extraction. Furthermore, AM can be used consciously considering major advantages to adjust the design process towards a protective design. For this reason it is crucial to understand the main advantageous differences to conventional manufacturing. First, the manufacturing costs and the part complexity do not correlate using AM. This correlation is valid only for traditional manufacturing processes that require additional costs for tooling and molding. Because of the layer-wise building processes, AM offers 'complexity for free' [4].

Although designers have to respect specific design rules for AM, they are not as restricted by limiting factors used in traditional manufacturing, such as draft angles for de-moulding processes. Thus they can spend more attention and effort in function-driven design compared with a design process limited by restricted manufacturing processes. For example, using AM allows a product to be 'pre-assembled' during the production process so that further steps to assemble several parts after production are not necessary. This is certainly an advantage, depending on the parts' functionality and properties. Many real-world examples benefit from AM because of an integral design joining several traditional parts into one part that is producible by AM. The potential for costs savings is obvious.

One major advantage compared with traditional manufacturing process is the economic production of individualized products, as the production process is based on digital CAD data and some preparation work regarding data and machine parameters. Thus is it much easier to produce multiple variants without increasing costs for moulds and tools that have separate part costs. This advantage is relevant for the development of new products as well as for changes to existing products. The innovation speed can be increased since only the design needs to be changed with the help of CAD tools [4].

Furthermore, layer-wise production offers the potential to realize highly complex 3D structures because the complexity is broken down into multiple two-dimensional layers with less complexity. It is very expensive, if not even impossible, to imitate highly complex parts using traditional manufacturing methods. This is one example of how AM can contribute to the prevention of product piracy in terms of raising the hurdle for imitators in a technical and economical way.

11.8 Measures to prevent product piracy with the help of additive manufacturing: design for protection

As decribed above three main potentials of AM can be derived and defined as elementary potentials for protection:1. Manufacturing without tooling – economic

advantages at least for small batch sizes 2. Geometrical freedom in design − layer wise process from 1D over 2D to 3D allows manufacturing of high complex geometries 3. Freedom in mechanical properties − layer wise process from 1D over 2D to 3D allows adjustment of mechanical properties very locally and heterogeneously. These elementary potentials have been considered when developing protection measures to aggravate reverse engineering regarding to the results of the VDMA study. Therefore the following measures have been developed based on the elementary potentials of AM for protection. Some of them are innovative ones and some are further developments of already existing measures also applicable with conventional machining:

The relation between the potential of AM and a protective effect that can be achieved using AM in the right way can be defined in a couple of protective measures. Exemplary measures that aim to complicate the RE process are described here.

11.8.1 Integration of functions

To achieve a protective effect of this measure, 'integration of functions' combines many functions, even if fulfilled by separate components, into one component or product. The main goal is to focus on a function-oriented design and to reach a higher level of complexity. Thus the effort to extract the geometry of the physical parts and to redraw it in a CAD system to digitalize it is greatly aggravated [5].

From the additive point of view, the technology allows the easy implementation of functional integration through the layer-wise production process. As the production of individualized parts becomes economically feasible, functionalities can be tailored to the products' and customers' needs. Standard parts are not that relevant any more. Pre-assembly is another way to integrate functions in a product. The effort for assembly is thereby decreased, but the number of individual components stays constant. The negative effect when talking about this measure to be applied using AM is on support material and its removal after the production process. Depending on the material and the specific technology process, the digital preparation of the support as well as the physical removal afterwards is a time-consuming and technologically limiting factor.

11.8.2 Black box design hiding the main functions

As the title of this measure indicates, the components that are important for the functionality of the entire product are hidden in a 'black box'. Thus the main functional parts are not visible from the outside [1,7]. Obviously, this measure is ideally combined with functional integration so that the knowledge needed to imitate the product is not accessible directly and without destroying the product.

AM can contribute much to the realization of this measure, as functional parts can be directly enclosed and integrated in a black box as a result of the layer-wise production process during manufacturing. Furthermore, concealment is achievable in cavities that can be integrated at various locations so that product pirates aiming at RE do not obviously detect the black box.

11.8.3 Self-destructive design

This measure is a useful supplement when thinking about realizing the above mentioned measures. The protection of a product can be further increased if, for example, self-destructive elements destroy all functionality when imitators try to open the black box. Thus it is recommended to integrate several functions into one component, enclose this component in a black box and add a self-destructive mechanism. Opening the black box has to result in the irrevocable destruction of essential properties of the product [1,7].

In addition to integrating functionalities inside a black box, AM can help to realize mechanical self-destructive mechanisms. For example, springs can be integrated during the production process, aiming at the destruction of functional components or its positioning when the black box is opened.

11.8.4 Avoidance of standard dimensions

Defining the complication of RE as the main goal of technical measures such as this one aims at making the measurement of the physical object more difficult. Standard dimensions are easily measurable using established tools, but when measuring crooked values, one may become uncertain of whether the values have been measured properly. The more complex the component design, the more complicated their measurement and the more uncertainty the person executing the measuring might have. Extracting geometry is a crucial phase of the RE process, so this measure helps to complicate the imitation process.

AM allows individual parts to be produced without increasing costs. Avoiding standard geometries is comparable with individualization and therefore is a measure that benefits greatly from the use of AM. Applying this measure requires little additional effort in the design process to modify the dimensions of areas of the component that do not interact with other parts. Otherwise the interfaces have to be considered and modified as well.

11.8.5 De-standardization

The effect of this measure has a similar aim as the one described before but is more applicable from a market-oriented point of view. At least some elements that are crucial for a product's functionality should not be available on the market as standard items [1,7]. Imitators thinking economically – most of them will do so since the main motivation is to make money with little effort – try to obtain most parts directly from suppliers because this is more inexpensive than RE of each component in detail. Thus this measure can put imitators off copying a product for financial reasons.

Since AM does not require costs for tools to develop and implement individual parts, there is no need to strive for de-standardized parts. Costs and efforts can be kept low since only the design needs to be touched. Preparation of production and the manufacturing process itself do not change.

11.8.6 Marking by internal structures

There is no need for a detailed description of the usefulness of marking in general because everyone knows marking from, for example, everyday goods. Further applications depend on the complexity of the marking and address industrial requirements of the traceability and authentication of parts and products. Because the measures is called 'marking' by internal structure, the name leads to AM technologies since there are not many options to mark products internally using conventional manufacturing processes.

The benefits of AM regarding individualization have been explained already. To mark products internally or externally is simply a kind of individualization. The main difference from other marking methods that are usually implemented after production is that AM allows a direct mark, which is produced during the manufacturing of the part itself. When talking about cavities that can be integrated into components, AM offers the option to implement such cavities as a marking, as well as cavities that can be purposely positioned [10]. For example, the traceability of parts manufactured additively, in particular for parts with critical functionalities, is one crucial requirement for broadening the use AM over various industries.

A demonstration product built additively in the professional laser sintering powder-bed process combining several measures is shown in Fig. 11.17. Gearwheels have been positioned by springs to give an idea of how to integrate a self-destructive mechanism. Obviously, the whole gearbox was intended to be hidden in a black box, but for demonstration purposes the housing can be opened. It can be imagined that the whole functionality could be hidden. The housing itself is marked by internal QR codes, and the ball on the right is an example of what is possible using AM. This complex shape shows its proper form when viewed from the right perspective. Otherwise all information is hidden in a confusing geometry.

Another example of how AM can contribute to part protection is shown in Fig. 11.18. The part on the left is a design for traditional injection moulding, whereas the part on the right is optimized for AM using a kind of lattice structure. The shape of the original is easy to draw using CAD; it takes roughly 5 min for a skilled designer and half an hour for a CAD novice. The complex design of the part manufactured additively requires some more effort because there is no regularity in the

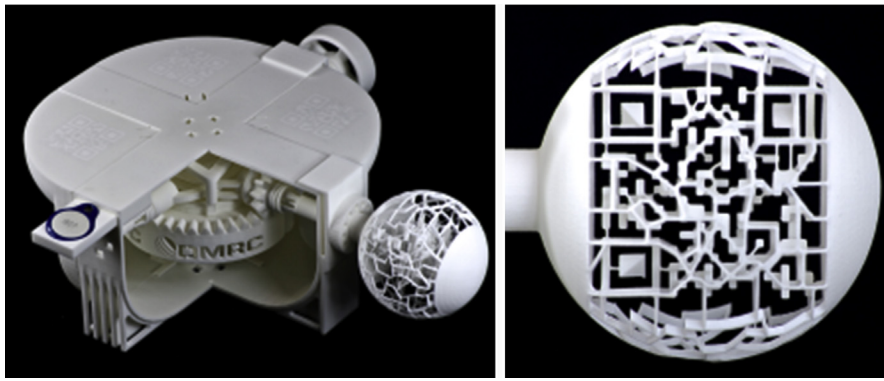

Figure 11.17 Example of product protection measures.

Figure 11.18 Product piracy prevention for an aquarium pump wheel. The original is shown on the left and the additively manufactured version is on the right. According to [1]

layers of the lattice structure. Therefore the same persons – skilled in or new to design processes – need roughly a effort of factor 50 to create the part's geometry in the CAD system.

In addition, this part is a good example of the economical use of AM as shown in Fig. 11.12. Due to its innovative design and bigger surface of the wheel the operating costs of the whole pump have been reduced as by far. As the dimensions are not that big, a usual EOS P396 allows the simultaneous production of more than 1000 pieces in one build job that takes roughly 3 days, including heating and cooling time. Thus it is a good example for economical benefits for both: customer and manufacturer.

11.9 Working with guidelines during product development

When working with new technologies, some guidance in the product development process is helpful for the product developer. According to the Association of German Engineers , catalogues that allow fast access to the information a designer needs are helpful and can result in a cost advantage (Fig. 11.19). In general, it recommends the use of design catalogues for a smooth design process [49].

This knowledge is not, however, always available – especially for AM – and the engineers may lack the necessary information and or experience. Nowadays it is difficult to get hold of a set of design rules that are available and taught at universities for all other manufacturing technologies.

A systematic approach for developing design rules, including a first set for selective laser melting, laser sintering and the fused deposition modelling processes, was published in 2015 [31]. This set of rules builds a solid basis for the product development process. Using the example in Fig. 11.20. These rules help to reduce build and especially failure costs in the product development process with AM. If followed properly they will help reduce support structures or dimensional deviations, which in turn will reduce material costs and the costs of post-processing. Sticking to these rules will help to develop a stable and repeatable process, but according to Reiher and Koch [47], this will not lead to the full utilization of the technology's possibilities. Pushing the technology to it's limits does also mean an increase of failure costs during product development and production. Documenting best practices can push the boundaries and achieve a more efficient process. This may include experiences with the build speed of the machines.

Element			Information	Examples		Techn.		
Group	Type	Attribute	Description	Not suitable for manufacturing	Suitable for manufacturing	LS	LM	FDM
Basic elements	Plates	Thickness	Plates should be so thick that each layer can be structured of a contour with inscribed raster to minimize dimensional deviations and to avoid defects. LS: S > 1,0 mm LM: S > 0,6 mm FDM: S > 1,5 mm	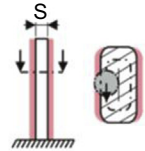	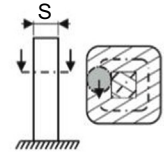	X	X	X
Element transitions	Firmly bonded	Inner coners	Interior corners should be rounded to remove disperse support material more easily.	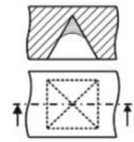	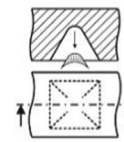	X	X	
Aggregated structures	Overhangs	Length	The length of an overhang should be small enough to avoid solid support material. Otherwise overhangs should be designed with element orientations that don't require solid support material.	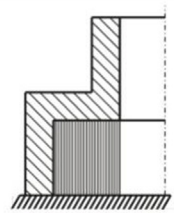	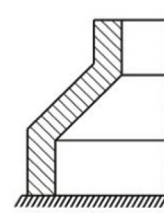		X	X

Figure 11.19 Excerpt from the Direct Manufacturing Design Rules catalogue [31].

In general, today the documentation of best practices and experiences plays a crucial role in mastering a technology and leads to its optimal use. Design catalogues may help to evolve capabilities regarding the technology. These catalogues not only help to collect necessary information for product designers but also foster the creativity process and companies' acceptance of the technology. These will be living documents that can be enhanced as the experience with the technology grows. As a starting point, they should include design rules, material properties and testing results and testing methods for given materials. An excerpt of such a design catalogue is shown in Fig. 11.20.

In addition to the categories included in Fig. 11.20, the catalogue should encompass protective design measures to support designers during the development process. Thus the risk of product piracy can be easily addressed as a preventive approach in the design phase, avoiding financial losses in the later lifecycle phases. The protective effect and the influence of AM is one application example to help designers implement measures (see Fig. 11.21).

Building chamber utilization as high as possible

Description	✗	✓
For a high productivity of a machine, it is generally advisable to choose the machine utilization very high. This situation is also true in the systems of selective laser sintering (10). The impact of the occupancy rate for the building chamber is very important for the productivity. If there is only one part in the building chamber the productivity is on a very low level (5), because after every layer there is a recoating time including the refill of the coating unit. After every layer there is an interruption of the scanning time in the machine. A high occupancy rate can strongly contribute to reduce the average recoating time per part and helps increasing the ratio of scanning time vs. coating time.	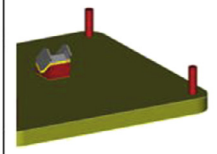	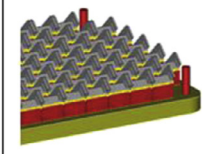
	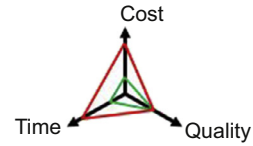	

Pro	Contra
• Higher productivity • Very low recoating time per part • Different parts can be placed on one building chamber • Possibility to cut of all parts by e.g. waterjet cutting	• Higher building time • Small distance between the parts effects the quality • Obeying of this rule is sometimes not possible due to urgent parts etc.

Calculation example:

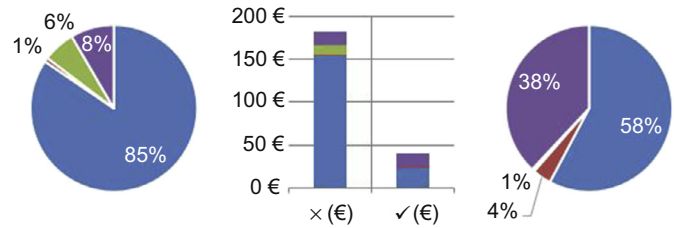

Manufacturing costs (€)	Material costs (€)	Pre-processing	Post-processing

Buildspeed / buildtime per part	✗	✓	Change of price	77,84%
	1,6	68,9		

Figure 11.20 Example rules for cost-efficient design.

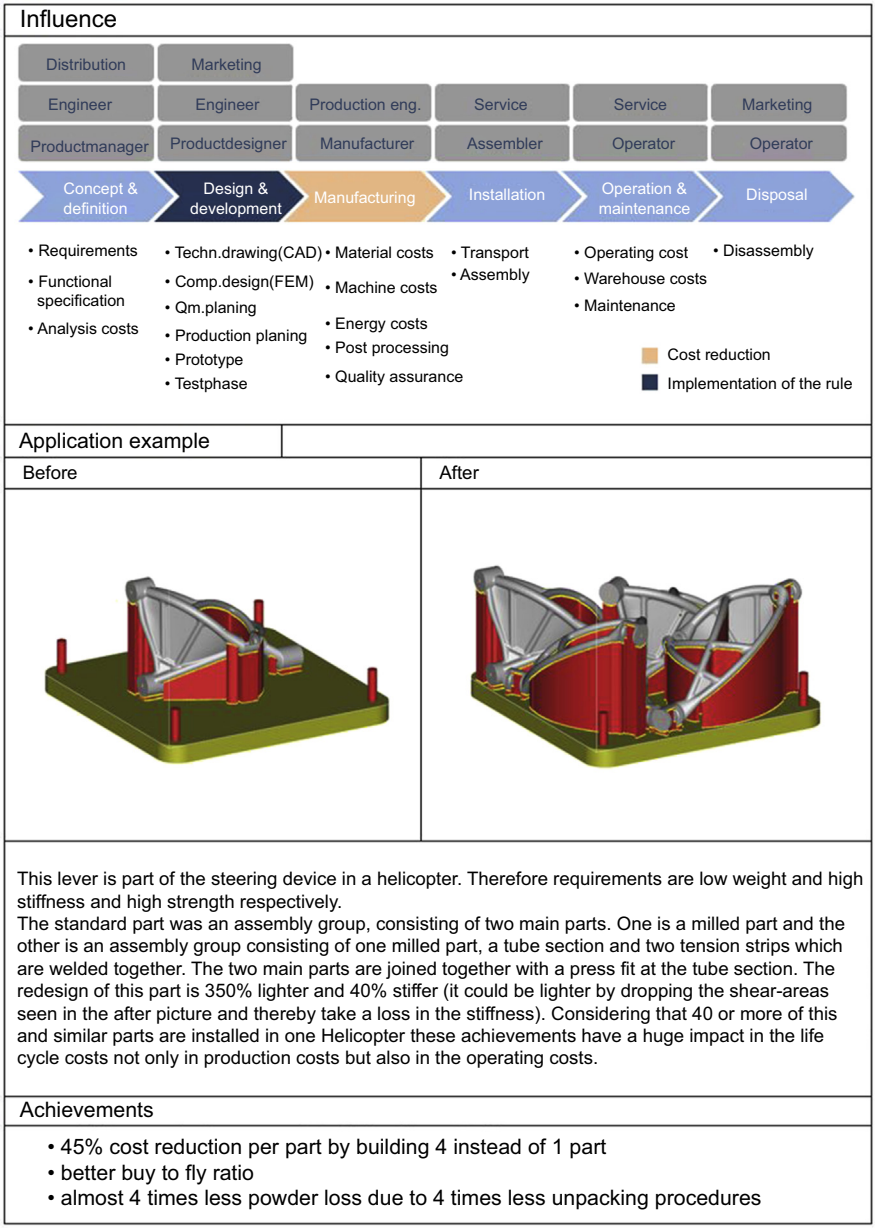

Figure 11.20 (*Continue*)

Protection measures 3P

Integration of functions

Description

The “integration of functions” describes the fulfillment of as many functions as possible by as few components as possible in one product. To implement the functional integration a manufacturer has to develop the parts of a product individually tailored to the components. Counterfeiters usually focus on standard components and have not that sophisticated skills for the imitation of complex and individual parts.

Influence by additive manufacturing

The layer wise manufacturing of additive manufacturing allows a very easy implementation of functional integration. Beside the easily attained individualization of components, products can also be manufactured pre-assembled. Hereby the number of components will not be reduced but the implied aim of avoiding assembly work can be achieved.

In the area of development and design of integrated functional components for additive manufacturing the removal of support material has to be considered.

Business units

- [x] Product planning
- [x] Development/ design
- [ ] Purchasing
- [ ] Work preparation
- [ ] Production
- [ ] Distribution
- [ ] Service

Categories of protection measures

- [x] Product-related measures
- [ ] Marking measures
- [ ] Strategic-process-related measures

Assessment of measure

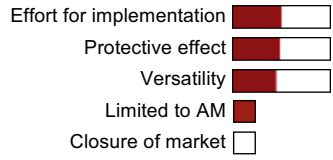

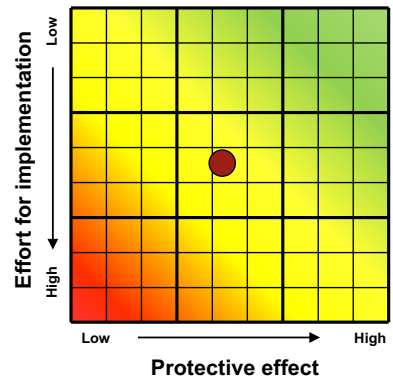

Lowering the attractiveness of Imitation | **Complication of expertise-acquisition** | **Complication of reproduction** | Complication of marketing | Offer for cooperation | Prevention of product liability

References

Figure: *author*

Figure 11.21 Example of a measure creating a design for protection.

11.10 Technology and cost development

But when is the optimal time for entering the AM market or for buying a new machine?

In the study 'Thinking Ahead the Future of Additive Manufacturing – Innovation Roadmapping of Required Advancements' (Gausemeier et al., 2013), the authors conducted a survey of 150 industry experts on the future development of several AM technologies. The aim was to get a consolidated picture of the realization time of possible technical advancements in the fields of AM. The study is divided into Metal Additive Manufacturing (MAM) and selective laser melting powder-bed processes as well as fused deposition modelling processes.

Combining technology roadmaps with costing models and a company's innovation planning allows the optimal entry point into AM to be predicted. Once promising parts have been identified, the technical realization can be double-checked and mapped on the company's innovation roadmap. Part costs can then be estimated for different time points in the future.

As indicated in the paper by [14,36], build rate, machine costs, material costs and utilization rate have been identified as most critical factors regarding AM production costs. Some potential has been seen for the optimization of pre- and post-processing of the building job as well [44].

The development of most of these factors was investigated as well in the study 'Innovation Roadmapping of Required Advancements'. As realistic measures, building rates of up to 120 cm^3/h and building chamber sizes up to 2 m^3 have been predicted to be feasible by 2020 (see Fig. 11.22). The increases in build chamber size and build speed strongly affect costs. One can clearly see that building speed and building chamber size will increase significantly in future. Quality control will be adapted more easily by in-line process-monitoring tools, which are currently being developed by different companies. Fig. 11.23 shows an AM costing model combining the possibilities of today's technology up to 2023.

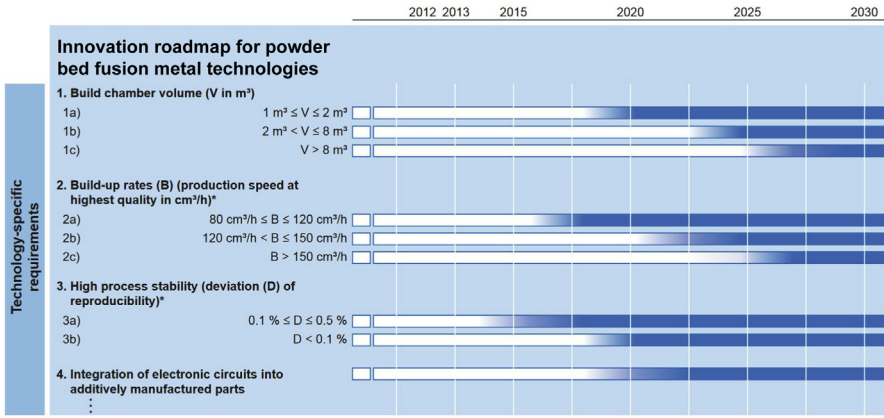

Figure 11.22 Future estimated developments powder-bed fusion metal technology [45].

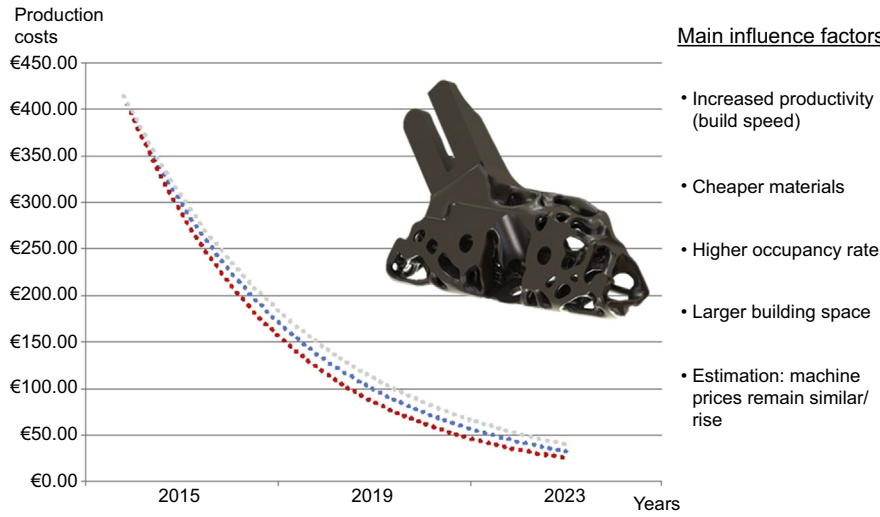

Figure 11.23 Cost estimation for powder-bed fusion metal technologies by the example of an aerospace bracket.

If experts are correct, by 2020 the total manufacturing costs for a sample part will have dropped by 90% compared with today (see Fig. 11.23). The distribution of the different costs factors will also have changed by then. The share of machine rate costs will have decreased significantly, whereas other factors such as material prices will have increased notably.

Although not part of the study by Gausemeier et al. (2015), this calculation estimates that machine costs will not drop significantly over the next few years as performance and quality control systems undergo permanent development. Assuming these possibilities and a strong regression of material prices, one can easily predict the higher productivity of AM technology in the future [44].

The increase in quality and the decrease of costs will significantly increase the number of possible part candidates. Therefore the process for justifying the use of AM technology will be much easier compared with today's possibilities. If the AM production costs equal those for traditional processes, and if quality control possibilities improve, the advantages of AM technologies will make a decision in favor of AM production easier.

11.11 Summary and Outlook

In total the additive manufacturing technologies have the potential to be disruptive technologies. The advantages as well as the areas influenced by the technology are manifold. Therefore product development and cost accounting for AM parts will require a more interdisciplinary product development approach. AM will play its part in the orchestra of manufacturing methods next to formative and the subtractive methods. Nevertheless AM is not going to let the world spin in a different direction.

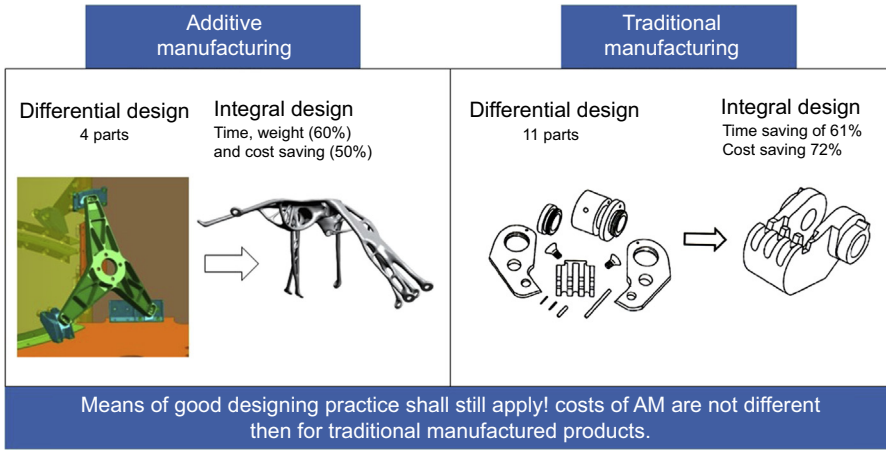

Figure 11.24 Comparison of product optimization potentials [18,44]

As one can see in Fig. 11.24 intelligent product design has led to cost advantages in the past before and it will stay the same in the future.

Companies dealing with AM and in particular with digital product data should be aware of the threat of product piracy even when they consider a "design for protection" using the measures described. Those will only protect physical products from being copied. Approaches to protect already the digital stage of products need to be developed and integrated in widespread software tools in the future as known from media files. Currently it is highly recommended at least to mark products manufactured additively to avoid product liability. As markings do not increase production costs there is no reason not to use this potential.

For a sustainable cost management, for AM as well as for other production technologies there are some important aspects [18]:

- Process Knowledge and resulting cost knowledge needs to be available
- Interdisciplinary collaboration, organization and motivation is crucial
- Systematic approaches enable cost efficient design.

The biggest problem about bringing additive manufacturing into the companies is not the cost accounting for manufacturing. But the general lack of knowledge about the processes and furthermore not many companies have incorporated the lifecycle costing approach.

Until the designers will gather experience they'll need the specific knowledge about the AM processes. This it will already lead to lower overall production costs while using the technology. Tools like trade off methodology matrix, described in this chapter can be tailored to every companies needs and will help to bridge the gap until organizational knowledge about additive manufacturing has been established. The consequent usage of knowledge management tools is mandatory.

Cost models can be set up easily with the help of activity based costing and a good build time estimation methodology. Models still need to be adapted to the

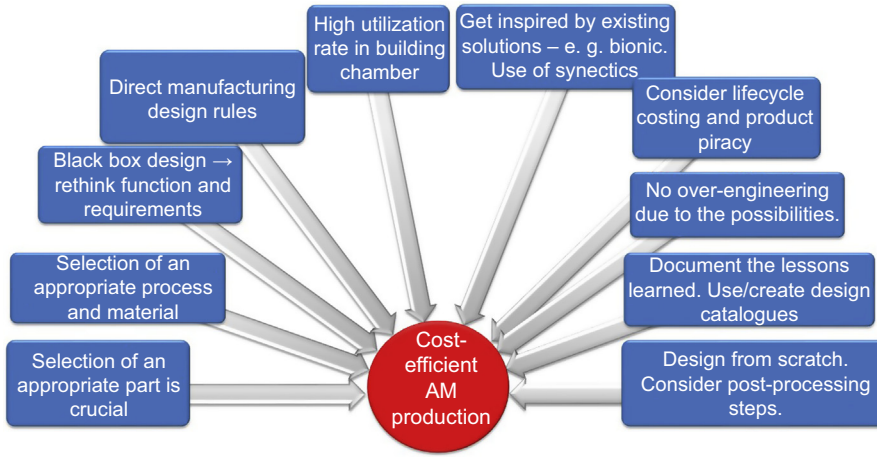

Figure 11.25 Rules for cost efficient AM production.

manufacturing process and the company dependent data. These aspects always need to be tailored to a certain case or a certain company.

Until this is achieved Fig. 11.25 has compiled a couple of hints for a cost efficient AM production. If the costing development is proceeding as predicted by the experts the decision for the use of AM might become a lot easier.

References

[1] J. Gausemeier, R. Glatz, U. Lindemann, Präventiver Produktschutz. Leitfaden und Anwendungsbeispiele (München), 2012.
[2] J.B. Guillory, Foundations of a Reverse Engineering Methodology, The University of Texas at Austin, 2011 (Master thesis).
[3] H.-O. Günther, H. Tempelmeier, LPS-Journal, Bochum (2007).
[4] N. Hopkinson, R.J.M. Hague, P.M. Dickens, Rapid Manufacturing. An Industrial Revolution for the Digital Age (Chichester), 2006.
[5] U. Jahnke, F. Wigge, Potenzial additiver Fertigungsverfahren zur Prävention gegen Produktpiraterie, in: CNC-Arena eMagazine 03/2014, 2014.
[6] O. Koester, in: Gausemeier, et al. (Eds.), Imitat, Plagiat, Fälschung – Was ist was und was ist (il)legal?, 2012.
[7] C.W. Neemann, Methodik zum Schutz gegen Produkt-imitationen (Aachen), 2007.
[8] Organisation for Economic Co-operation and Development, The Economic Impact of Counterfeiting and Piracy, 2008.
[9] D. Quitter, Artec 3D und 3D Systems stellen Reverse-Engineering-Set vor, Kontruktionspraxis, Vogel media, 2015. Online source: http://www.konstruktionspraxis.vogel.de/artec-3d-und-3d-systems-stellen-reverse-engineering-set-vor-a-509959/?cmp=nl-194.
[10] P. Reeves, D. Mendis, The Current Status and Impact of 3D Printing Within the Industrial Sector: An Analysis of Six Case Studies, Published by The Intellectual Property Office, Newport, 2015.

[11] VDMA, Verband Deutscher Maschinen- und Anlagenbau, Arbeitsgemeinschaft Produkt- und Know-How-Schutz: VDMA Studie Produktpiraterie, 2016.
[12] M. Zaeh, F. Hagemann, Wirtschaftliche Fertigung mit Rapid-Technologien. Anwender-Leitfaden zur Auswahl geeigneter Verfahren (München), 2006.
[13] C. Lindemann, U. Jahnke, M. Moi, R. Koch, Impact and influence factors of additive manufacturing on product lifecycle costs, in: Proceedings of Solid Freeform Fabrication Symposium 2012, Austin, 2012.
[14] C. Lindemann, U. Jahnke, M. Moi, R. Koch, Analyzing product lifecycle costs for a better understanding of cost drivers in additive manufacturing, in: Proceedings of Solid Freeform Fabrication Symposium 2012, Austin, 2012.
[15] M. Baumers, T. Tuck, D. Bourell, Sustainability of additive manufacturing – measuring energy consumption of the laser sintering process, Journal of Engineering Manufacture (2011).
[16] A.G. Coenenberg, T. Fischer, T. Günter, Kostenrechnung und Kostenanalyse; 6. Überarbeitete und erweiterte Auflage, 2009.
[17] European standard DIN EN Guideine Dependability management - Part 3-3: Application guide - Life cycle costing (IEC 60300-3-3:2004), 2005.
[18] K. Ehrlenspiel, A. Kiewert, U. Lindemann, Kostengünstig Entwickeln und Konstruieren Kostenmanagement bei der integrierten Produktentwicklung, Springer Verlag, Berlin Heidelberg, New York, 2007.
[19] R. Ewert, A. Wgenhofer, Interne Unternehmensrechnung (Internal Accounting), 7. Auflage, Springer Verlag, München, Berlin, Heidelberg, 2008.
[20] Hopkinson Neil, P. Dickens, Analysis of Rapid Manufacturing — using Layer Manufacturing Processes for Production. Pro ceedings of the Institution of Mechanical Engineers, Part C: Journal of Mechanical Engineering Science 217 (1) (2003) 31–39.
[21] I. Gibson, D.W. Rosen, Additive Manufacturing Technologies, Springer Science Business Media, New York, Heidelberg, Dordrecht, London, 2010.
[22] L. Le Merlus, P. Reeves, Multiplatform Algorithms for STL File Analysis – Understanding the Relationship between Surface Roughness, Support Structure Position, Building Time and Cost, Econoloyst Ltd., 2012.
[23] G. Pahl, W. Beitz, J. Feldhusen, K.-H. Grote, Engineering design – A Systematic approach, Springer Verlag, Heidelberg, 2007.
[24] M. Ruffo, C. Tuck, R. Hague, Cost Estimation for Rapid Manufacturing – Laser Sintering Production for Low to Medium Volumes, Wolfson School of Mechanical and Manufacturing Engineering. Loughborough University, Leicestershire, 2005.
[25] K. West, Melted Metal Cuts Plane's Fuel Bill, Sunday Times on Sun, 2011.
[26] P. Zelinski, The Future of Manufacturing, in: Modern Machine Shop, 2012. http://www.mmsonline.com/articles/the-future-of-manufacturing. Date of Access: 20.12.2012.
[27] C. Lindemann, U. Jahnke, T. Reiher, R. Koch, Towards a sustainable and economic selection of part candidates for additive manufacturing, Rapid Prototyping Journal (2015) 216–227.
[28] G. Adam, D. Zimmer, Design rules for additive manufacturing – basic elements, Rapid Prototyping Journal (2015).
[29] G. Deppe, T. Reiher, Exploring the cost and lifetime benefits of a topology optimized aerospace part applying additive manufacturing, in: International Conference Production Engineering and Management 2015, Trieste, 2015.
[30] A. Riemer, Einfluss von Werkstoff, Prozessführung und Wärmebehandlung auf das bruchmechanische Verhalten von Laserstrahlschmelzbauteilen, Shaker Verlag, Paderborn, 2015.

[31] G. Adam, Systematische Erarbeitung von Konstruktionsregeln für die additiven Fertigungsverfahren Lasersintern, Laserschmelzen und Fused Deposition Modeling, Shaker Verlag, Paderborn, 2015.
[32] C. Lindemann, U. Jahnke, T. Reiher, R. Koch, Towards a sustainable and economic selection of part candidates for additive manufacturing, in: 25th Annual International Solid Freeform Fabrication Symposium, Austin, 2014.
[33] S. Leuders, M. Thöne, A. Riemer, T. Niendorf, T. Tröster, H.A. Richard, H.J. Maier, On the mechanical behaviour of titanium alloy TiAl6V4 manufactured by selective laser melting: fatigue resistance and crack growth performance, International Journal of Fatigue (2013) 300−307.
[34] C. Lindemann, U. Jahnke, M. Plass, R. Koch, Opportunities and Influence of Additive Manufacturing on MRO-Processes in Aeronautics, Rapid Tech, Erfurt, 2013.
[35] C. Lindemann, U. Jahnke, M. Moi, R. Koch, Impact and influence factors of additive manufacturing on product lifecycle costs, in: 24th Annual International Solid Freeform Fabrication Symposium, Austin, 2013.
[36] C. Lindemann, U. Jahnke, M. Moi, R. Koch, Analyzing product lifecycle costs for a better understanding of cost drivers in additive manufacturing, in: 23rd Annual International Solid Freeform Fabrication Symposium, Austin, 2012.
[37] D.S. Thomas, S.W. Gilbert, Costs and Cost Effectiveness of Additive Manufacturing, National Institute of Standards and Technology, 2014.
[38] N. Kano, N. Seraku, F. Takahashi, Tsuji, Attractive Quality and Must-be Quality, Journal of the Japanese Society for Quality Control 14 (2) (1984) 147−156.
[39] A. Gebhard, Generative Fertigungsverfahren: Additive Manufacturing und 3D Drucken für Prototyping − Tooling - Produktion, Carl Hanser Verlag, München, 2013.
[40] DMRC Annual Report − 2015 http://www.uni-paderborn.de/fileadmin/dmrc/04_DMRC/04_AnnualReport/dmrc_report_2015.pdf
[41] P. Zelinski, How Additive Manufacturing is Like CNC Machining (and How It's Very Different), 2013. http://www.mmsonline.com/articles/how-additive-manufacturing-is-like-cnc-machining-and-how-its-very-different]. Date of access: 10.12.2014.
[42] J. Breuninger, R. Becker, A. Wolf, S. Rommel, A. Verl, Generative Fertigung mit Kunststoffen − Konzeption und Konstruktion für Selektives Lasersintern, Springer-Verlag, Berlin, Heidelberg, 2013, ISBN 978-3-642-24325-7.
[43] C. Lindemann, G. Deppe, R. Koch, Scenario Based Outlook of Additive Manufacturing Applications for the Aerospace Market. In: C. Haag, T. Niechoj, (Hrsg.) eds., Digital Manufacturing − Prospects and Challenges. Weimar bei Marburg: Metropolis ISBN 978-3-7316-1156-1.
[44] C. Lindemann, T. Reiher, U. Jahnke, G. Deppe, R. Koch, Holistic approach for industrializing AM technology − from part selection to test and verification, Published in Progress in Additive Manufacturing, 2016.
[45] J. Gausemeier, N. Echterhoff, M. Wall, Thinking ahead the Future of Additive Manufacturing − Innovation Roadmapping of Required Advancements, Study of the DMRC, 2013.
[46] Gibson, David W. Rosen, Brent Stucker, Additive Manufacturing Technologies, Springer Augsburg, Martin: Ein Vorgehensmodell zum Einsatz von Rapid Prototyping-Verfahren für die werkzeuglose Fertigung kleiner Bauteilserien im Automobilbau, Sirke Verlag, Göttingen, (2010) 2007.

[47] Thomas Reiher, Rainer Koch, FE-Optimization and data handling for Additive Manufacturing of structural parts; 26th Annual International Solid Freeform Fabrication Symposium Austin / Texas / USA - 8th-10th August (2015). http://3dprintingindustry.com/2014/08/20/consumer-3d-printing-5-years-away-mainstream-adoption-says-gartner/.
[48] D. Remer, Einführung in die Prozesskostenrechnung − Grundlagen, Methodik, Einführung und Anwendung der verursachungsgerechten Gemeinkostenzurechnung Schäffer-Poeschel Verlag, Stuttgart, 2005.
[49] Verein Deutscher Ingenieure: VDI-Richtlinie 2222: Methodic development of solution principles in VDI-Handbuch Konstruktion; Berlin: Beuth Verlag, 1997.

Laser additive manufacturing of embedded electronics

12

R.C.Y. Auyeung, H. Kim, S. Mathews, N. Charipar, A. Piqué
Naval Research Laboratory, Washington, DC, United States

12.1 Introduction

Doing more with less has been the driving force behind many of the advances in microelectronics for many decades. The aerospace, medical, consumer, and military markets seek electronics components with increased performance, portability, and versatility while reducing their physical footprint, power consumption, and thermal budget. This theme is nowhere more evident than in the rapidly maturing field of flexible or conformal electronics, which requires thinner and smaller components to take full advantage of a flexible substrate [1]. All of these drivers, of course, must result in a product with a cost-to-benefit ratio that is advantageous in their respective markets.

Miniaturization at the integrated circuit (IC) level has been advancing dramatically since the invention of the transistor, with a 1000-times decrease in the node dimension since 1970. By comparison, the printed circuit assembly (or board) (PCA) that integrates these chips with other heterogeneous components has decreased by only five times using the interconnect pitch as the metric [2]. A significant portion of today's PCAs contains about 80% passive components, of which most are resistors and capacitors, that occupy over 40% of the PCA surface area [3,4]. These discrete components (such as memory, passive elements, and other processing elements) could be combined into a single chip [application-specific integrated circuit (ASIC)] or assembled into a three-dimensional (3D) architecture (eg, die stacking). However, these are costly and time-consuming techniques that do not easily accommodate design changes once finalized.

Further miniaturization of the PCA can occur by utilizing surface-mount devices (SMDs) for many of the passive elements and narrowing the interconnect pitch; however, the ultimate gains in component density can be achieved by burying or embedding these components into the substrate to create a vertically integrated packaging and design architecture. Benefits of embedding electronics include shorter resistor-capacitor (RC) time delays, reduced inductance, better shielding, new functionalities/architectures on novel (eg, flexible) substrates, proprietary design protection and weight savings. The challenges of effectively embedding electronics at the highest possible density require careful handling of small and ultrathin bare dies and connecting them to the circuitry with high-quality fine-pitch interconnects.

Currently, these miniature components, such as SMDs, semiconductor bare (ie, unpackaged) dies, and microelectromechanical systems (MEMSs), are carefully handled and precisely placed on a substrate with "pick-and-place" or SMD placement machines. However as their areal size shrinks below a few hundred microns and

Laser Additive Manufacturing. http://dx.doi.org/10.1016/B978-0-08-100433-3.00012-9
Copyright © 2017 Elsevier Ltd. All rights reserved.

thickness drops below 50 μm, these dies can be easily damaged or mishandled by these machines. Various die pickup and transfer methods have been adapted for ultrathin dies, but further development is needed to increase the yield, speed, and range of die thickness and size that can be used in the process [5]. Laser-based methods that do not directly contact the receiving surface can transfer millimeter- to micron-sized components from a donor substrate (carrier) to a receiver substrate without damage; these techniques are reviewed in the next section.

Once these discrete components are placed inside the substrate, they are interconnected and encapsulated using methods such as PCA lamination (which includes flip-chip and micro-via processes for chip−substrate connections), or low-temperature cofired ceramic. [Traditional wire-bonding is not suitable because their bond pads (tens of micrometers wide) and loop heights (>75 μm) limit the packing density of embedded components [6]]. These techniques build the design layer by layer (and could be considered as a basic form of additive manufacturing), but unfortunately they have long design/build cycles or may expose components to high temperatures (<1000°C). In addition, both these methods use batch patterning processes such as screen printing and photolithography, which do not allow quick design changes, have limited feature size resolution (screen print), consume excessive material, or involve costly and complex steps (eg, photomask).

Alternatively, instead of placing preexisting devices inside a substrate, functional components can be directly fabricated and connected inside a substrate by additive manufacturing. Because this technique does not depend on fixed masks or templates, design changes are quick, and rapid prototyping can be performed [7,8]. In particular, using a laser additive manufacturing technique called laser direct write (LDW) enables the capabilities of additive manufacturing (laser transfer of dies and thin-film structures) and subtractive manufacturing (laser micromachining) to be combined into a single tool [9,10]. This is a unique capability that no other additive manufacturing tool possesses. (As used in this chapter and in the literature, "LDW" refers to all laser processes that can add, modify, or remove material in specific locations in/on a substrate and is usually performed under ambient conditions). LDW developed from the laser-induced forward transfer (LIFT) process [11], which was originally used to print copper lines in a vacuum. (LIFT, as used in this chapter, is used to describe laser processes that strictly add material or structures to a substrate). LIFT has been demonstrated for many functional materials such as metals, oxides, and organics over a wide range of viscosities without affecting their functionality. By laser-transferring functional materials in exact locations and geometries, LIFT can effectively shrink and replace SMDs with "print-on-demand" components with (ideally) similar performance. As an example of LDW's capability, the pocket in the substrate that houses the die could be created by laser micromachining, then the die can be placed into the pocket by laser device transfer and the interconnects from the circuit to the die printed by laser forward transfer.

This chapter focuses on the different additive processes that LDW can be used to embed electronics. (Subtractive LDW techniques such as laser micromachining have been firmly adopted by industry and will not be discussed in detail). First, the different techniques used to laser transfer prefabricated discrete components

(eg, SMD, die) from a donor to a receiving substrate are presented. Second, LIFT of functional materials that could replace discrete elements, such as metallic interconnects, microbatteries, and photovoltaics, are discussed. Third, circuit elements from the first two discussions (discretes and interconnects) are combined in examples of completed circuits using laser transfer. The combined capability of laser additive manufacturing to transfer discrete components and/or print their counterparts in precise locations (as well as to remove material) will enable the rapid prototyping of embedded electronics in both form and function, thus reducing time to market in manufacturing as well as advancing new nontraditional applications.

12.2 Laser-induced forward transfer of discrete components

Laser-based transfer of discrete components from a donor to a receiving substrate typically involves three steps in the following order: release, propulsion across a gap, and emplacement. A laser pulse could provide energy for all three steps or just be used for release and then be assisted by other forces (eg, gravity, magnetic forces) for transfer to the substrate. Other laser-based transfer processes such as laser release [12] or laser debonding [13], in which structures are released from a donor substrate by laser ablation or heating after first making physical contact with a receiving substrate, are not discussed in this chapter.

A history of the LIFT of microstructures along with selected metrics is shown in Table 12.1. In the first demonstration [14], prefabricated nickel and MEMS-like microstructures were first attached to a polymer sacrificial layer coated on an ultraviolet (UV)−transparent donor substrate. Upon absorption of an incident 248-nm laser pulse, they were released and propelled across a small gap by gases resulting from ablation of the polymer layer. Transfers of 100-μm^2 "pads" onto complementary "frames" and a laser-assembled "wobble" motor were demonstrated. Although it was noted that the placement accuracy may require structural features to guide the trajectory of the transfer, a placement error of $\sim$40 μm could be estimated from the images of the transferred frames onto the pads.

In another study, an infrared (IR) laser pulse ($\lambda = 1064$ nm, 45 ns) with a flat-top spatial profile was used to release silicon bare dies (tiles) from a polyvinyl chloride (PVC) tape carrier [15]. The authors suggested that since the tape was IR-transparent, the laser energy was absorbed by the silicon, which, through heat conduction, melted and vaporized part of the tape adjacent to the silicon, thereby releasing the die. In this process, the nonactive (back) side of the silicon faced the laser pulse, so it would have been difficult to establish electrical connections in this configuration since precise die alignment would have been needed. No receiving substrates were used, so the placement accuracy could not be evaluated. A thermal model was developed that predicted a releasing fluence threshold of 2.9 J/cm^2, which agreed reasonably with the observed value of 3.7 J/cm^2. The model also predicted a die-release speed of $\sim$15 m/s at 4.5 J/cm^2, which roughly agreed with the observed value of $\sim$12 m/s, but the

Table 12.1 Historical summary of laser-assisted die transfer processes

Laser process	Laser λ (nm)	Fluence (J/cm^2)	Structures transferred	Accuracy (μm)	References
Ablative: DRL (single pulse)	KrF 248	0.1	Ni (100 × 100 × 15 μm) Wobble motor demo (1 mm ø)	~40[a]	[14]
Thermal: PVC carrier (single pulse)	YAG 1064	4.5 (45 ns)	Silicon bare die (200 × 200 × 150 μm)	–	[15]
Thermal: PET carrier + gas-filled adhesive (single pulse)	YAG 532	6 (0.2 ms)	Silicon (300 × 300 × 130 μm)	35[a]	[16]
Ablative: DRL (L&P) (single pulse)	KrF 248	0.1–1.4 (15 ns)	SMD (1 × 0.5 mm), bare die IC (LM555, 2.6 mm^2), LED (0.25 mm^2), Silicon (1 mm^2 × 10 μm)	<50	[17,18]
			Bare dies (LM555, LED array), microgear, silicon beam, silver ink	–	[19]
	YAG 355	0.2–0.3 (35 ns)	Copper metal interconnects (1 mm × 100 μm × 12.5 μm)	–	[20]
Ablative/mechanical: dual-DRL/blister (multi-pulse)	YAG 355	<10[a]	RFID tag (680 μm^2 × 65 μm), silicon (510 μm^2 × 65 μm)	~50	[21,22]
		4	Silicon (670 μm^2 × 50 μm)	~25	[23]
			Silicon (350 μm^2 × 20 μm), RFID-embedded paper	–	[24]
Thermal: CTE (single pulse)	Diode 805	3.5[a] (4 ms)	Silicon (100 μm^2 × 3 μm), LED	<5[a]	[25,26]
Ablative DRL/ magnetic(single or multi-pulse)	YAG 266	–	Silicon (1 mm^2 × 50 μm), silicon (2 mm^2 × 50 μm)	40–50 10–100	[27]

DRL, dynamic release layer; *LED*, light-emitting diode; *L&P*, lase and place; *RFID*, radiofrequency identification; *PVC*, polyvinyl chloride; *PET*, polyethylene terephthalate; *CTE*, coefficient of thermal expansion; *SMD*, surface mount devices.
[a]Estimated.

predicted speeds were underestimated at higher fluences. It was reported that the laser fluence of 4.5 J/cm^2 to release the die was below the calculated fluence threshold of 17 J/cm^2 for silicon damage, but no experimental evidence was given. A fluence of 4.5 J/cm^2 in 45 ns lies very close to the ablation fluence threshold of 6−8 J/cm^2 in silicon for a single 1062-nm, 65-ns laser pulse [28]. This process could have operated just below the ablation threshold and provided gradual heating of the PVC tape, resulting in a more predictable transfer.

In a subsequent study, the same group used high-speed video imaging to study the laser release of silicon bare die from a carrier tape under separate mechanisms: ablative and thermal [16]. Using 1064-nm pulses for the ablative and thermal regimes (nanoseconds and milliseconds, respectively), the released die velocity decreased by a factor of 10 in the thermal case, but the releasing velocity and angle were unstable because of nonlinear IR absorption in silicon. Therefore, a frequency-doubled neodymium-doped yttrium aluminium garnet (Nd:YAG) (532 nm, 0.2 ms) laser pulse was used to minimize this nonlinear absorption, and a flat-top beam spatial profile was used to reduce beam inhomogeneities. By examining the die release from different camera angles, a die placement accuracy of ±35 μm within a 9 degree release angle was calculated, assuming a donor-receiver gap of 0.2 mm. This measurement was made with no receiving substrate in close proximity. Die velocities were measured ranging from 0.7 to 1 m/s.

To that point in time, only discrete demonstrator components had been laser transferred to a receiving surface, but their functionality was not verified after the transfer. At the Naval Research Laboratory (NRL), by selecting the proper type and amount of sacrificial polymer to act as a dynamic release layer (DRL), the "lase-and-place" (L&P) process was used to transfer structures and devices (LM555 timer chip, light-emitting diode (LED), SMD resistors, capacitors) with sizes ranging from 0.1 to >6 mm^2, thicknesses from 500 to 10 μm, and placement accuracies of 50 μm [17] onto receiving substrates. These devices were then verified to be fully functional after the laser transfer. In addition, the LIFT process was used to directly print a wide array of electronic materials such as metals, dielectrics, nanocomposites, polymers, and electrochemically active compounds for applications such as interconnects, resistors, microbatteries, and photovoltaics. These components were also shown to have good functional properties after the laser printing process. Note that the laser fluences used in the NRL transfer process were near the lower range of fluences used in the other techniques. These lower fluences were achieved through careful DRL engineering (to create "pedestals" underneath the component) and/or using a shorter wavelength laser pulse to minimize the absorption depth; this may help explain the high placement accuracy and lack of damage to the die when using this technique. A recent application of the L&P process was in the transfer of freestanding copper interconnects between an array of capacitors [20]. Flat and bent copper metal strips (12.5 μm thick) were laser transferred to connect four capacitors in parallel with no degradation in performance. A more detailed discussion of the laser transfer work at NRL is presented in subsequent sections.

A different approach to using LIFT to transfer dies used a mechanical rather than an ablative or thermal process [21] to propel the die toward the receiving substrate. Here, a double DRL on the donor substrate consisted of a laser-absorbing polyimide layer

and an adhesive layer, which held the die. Upon 355-nm laser illumination, a small region of the DRL was vaporized, which created a blister without any rupture of the layers. This confined ablation of the DRL allowed the blister to act as a mechanical actuator that gently propelled the die toward the receiving substrate. Laser beam parameters (power, scan speed) had to be carefully chosen to avoid rupture of the DRL, which would contaminate or damage the surface of the die. The placement accuracy on a receiving substrate was studied as a function of laser parameters, adhesive layer properties, and dicing method (laser vs. reactive ion etching) [23]. A mean displacement accuracy of $\sim 22-27$ μm was found for a 670-μm^2 × 50-μm silicon die. Limited by their available laser options, multiple laser pulses were used to create the blister, which may not have resulted in a uniform release had a single laser pulse been used. It was also noted that the properties of the adhesive layer significantly affected the transfer yield and placement accuracy.

Another variant of the LIFT process, which did not use ablation of a sacrificial layer to drive die transfer, exploited the difference in coefficients of thermal expansion (CTEs) between the donor substrate and the die itself [25]. Here, a patterned elastomeric [polydimethylsiloxane (PDMS)] transfer tool (stamp), picked up a 100-μm^2 × 3-μm silicon die and positioned it over, but not touching, the receiving substrate (<10-μm gap). A 4-ms pulse from a continuous wave (cw) IR ($\lambda = 805$ nm) laser diode was then focused through the IR-transparent tool onto the die, which in turn heated the PDMS tool by conduction. Because of a two-order-of-magnitude difference between the CTEs of the PDMS and silicon, the interface is stressed and eventually results in delamination and release of the die from the tool. Transfers of silicon die pyramid structures and a functioning LED were demonstrated, as were depositions onto structured, curved (liquid droplet), and recessed surfaces [26]. A study of the placement accuracy showed that errors were insignificant below a separation of 20 μm between the die and the receiving surface. The IR laser fluence was estimated to be 3.5 J/cm^2 (assuming 2.5 W in a 600-μm-diameter spot) but delivered over 4 ms onto the die. An advantage of this technique was the ability of the stamp to pick up structures from another substrate and then (laser) release them onto another without any damage; this reusability of the transfer tool makes it similar to a pick-and-place process. Some disadvantages of this technique are that thicker dies (>10 μm) may not transfer reliably because of interfacial temperature requirements, the size of the pattern on the stamp must be >1.5 times the die size for reliable placement accuracy, and a "solid" die with a large interfacial surface area with the stamp transfers more reliably than one that is highly structured (eg, annulus) [29]. In a production environment, this may require stamp patterns to be specialized for each die.

The previous laser-transfer techniques focused on different release mechanisms for the die: ablative, thermal, mechanical, or some combination thereof. In another approach the trajectory of the die across the gap was controlled by a magnetic field *after* release from a DRL [27]. Here, different nickel patterns were deposited on square silicon chips to guide their trajectory in an external magnetic field. Single 266-nm pulses were used to transfer 1-mm^2 × 50-μm chips onto water-filled recesses on a glass coverslip. Multiple pulses scanning three concentric rings were required to release a 2-mm^2 × 50-μm chip. The placement accuracy on the receiving substrate

depended greatly on the initial release angle of the die (hence the wide range of accuracy values shown in Table 12.1), but the placement accuracy was found to be 40 μm (1 mm^2) and 10 μm (2 mm^2) for a specific initial release angle and nickel pattern, respectively, on the chip.

In summary, a variety of laser-assisted mechanisms have been used to transfer dies onto a receiving substrate. Laser ablation, heating, or mechanical processes were used to release the die and then propel it to the receiving substrate by residual kinetic energy or gravitational or magnetic forces. For ablation, a thin sacrificial DRL between the die and the donor substrate was used to absorb the laser energy, which was then converted into the kinetic energy of the die. The lasers used in Table 12.1 operated at UV, visible, or IR wavelengths and typically exposed the dies to fluences ranging from 0.1 to many Joules per centimeter square. For the excimer (KrF) and frequency-converted YAG lasers, their pulse widths at full-width-half-maximum (FWHM) are typically in the tens of nanoseconds, and this results in incident peak intensities of many megawatts per centimeter square. This high peak intensity is required to ablate and vaporize enough of the DRL to release and propel the die, but at the same time it could run the risk of damaging the die (especially the active side, which includes the contact pads). Some of the techniques in Table 12.1 attempted to mitigate this high intensity requirement by using (1) DRL engineering to lower the ablation threshold for transfer (NRL) and (2) confined ablation within the DRL to shield the die from exposure to the laser and to create a blister for mechanical actuation [21].

The other two mechanisms for releasing the die were thermally and mechanically based, which do not require high peak intensities and can be achieved with the use of longer pulsed and cw lasers. In Table 12.1, the thermal-PET method used peak intensities of 30 kW/cm^2 (6 J/cm^2 in 0.2 ms), whereas the thermal-CTE method used 880 W/cm^2 (3.5 J/cm^2 in 4 ms). Note that the definitions of *peak intensity* and *average intensity* are identical for cw lasers. These lower peak intensities lie below the ablation threshold of many materials and would minimize any damage to the die.

The placement accuracy of the transferred dies was typically 40−50 μm for the ablative techniques and a few tens of micrometers for the thermal/mechanical processes. Some angular misalignment was present in many of the techniques as well. The higher fluences required in ablative rather than thermal processes resulted in higher transfer speeds that increased the translational and rotational motion of the die as it reached the receiving substrate. Minimizing the donor−substrate gap may decrease these displacement and rotational errors.

The viability of each of the techniques in Table 12.1 could be demonstrated by measuring the functional properties of the components after laser transfer; however, this was done in only three of them: ablative (DRL-L&P), ablative (blister), and thermal (CTE). The first and the third techniques transferred the die or chip with the active side up (facing the laser pulse), whereas the second method used a “flip chip” configuration in which the back side faced the laser. It is important to note that all three methods used relatively low fluences (intensities) or shielded the die from most of the laser energy (blister). This lower fluence or peak intensity would have minimized any possible damage to the active side. In the blister technique, interconnects were made to an radiofrequency identification (RFID) tag by stencil-printing conductive

paste into vias or patterns on a substrate after laser transfer. In the thermal (CTE) case, an electrical connection was made by physically contacting probe tips to the LED die after laser transfer. In the ablative (DRL-L&P) case, timer chips, LED arrays, SMD resistors, and capacitors were successfully laser-transferred and functionally verified. Probe tips electrically powered these SMDs and IC chips to verify their functionality; alternatively, this technique also used LIFT to print metallic interconnects to an LED array on polyimide, which remained functional after laser transfer [19]. This is the only technique where the same tool could be used to both transfer the die and build the interconnections.

In the next section, the use of this technique to transfer and embed various discrete components, called "lase-and-place," is discussed. The performance of the components after the transfer are characterized and the transfer kinetics are examined. As mentioned earlier, this technique is a subset of LDW processes, which can be used to machine the pocket, transfer the component into the pocket, and make interconnections to the supporting circuit using essentially the same apparatus.

12.2.1 Lase-and-place

This technique was developed in 2007 as part of NRL's efforts to extend LDW processes to the fabrication of embedded electronic components and devices. The experimental setup is similar to other LIFT schemes using a donor and receiving substrate, as shown in Fig. 12.1.

The discrete components were attached, with the active side facing the laser pulse, to a sacrificial DRL layer coated on a laser-transparent donor substrate. The sacrificial layer could be a spin-coatable solution such as photoresist, wafer protective coating, or polyimide precursor. After attachment to the DRL, the donor substrate could be rinsed in a solvent to remove excess DRL material, resulting in components that are supported by "pedestals" on the donor substrate [18]. This geometry reduces the amount of adhesion between the component and the donor substrate and therefore decreases the transfer threshold fluence and minimizes the potential of damage. The donor substrate was then placed in close proximity to a receiving substrate. Upon exposure to a laser pulse, the sacrificial layer was ablated and the generated vapors were released, propelling the component away from its support toward the receiving substrate.

A wide range of devices and structures was successfully laser-transferred, as seen in Fig. 12.2. They included 0.3-mm^2 InGaN LED's, 1.2-mm^2 LM555 bare die, 2.6-mm^2 ASIC bare die, 0402 SMD (1 $\times$ 0.5 mm) components, and some MEMS-scale parts. The ability of the lase-and-place technique to place heterogeneous components onto the same substrate with the same tool (merely by using ribbons with different components) is an advantage this technique has over traditional pick-and-place tools, which must be adjusted to accommodate various shapes and sizes. In the lase-and-place technique, the shape and size of the laser spot can be adjusted to match each component by simply selecting the appropriate aperture. In addition, the versatility of the LDW technique was demonstrated by the laser-printed metal pattern in the center of Fig. 12.2(b). Details of the laser printing of metal interconnects are presented in Section 12.3.1.

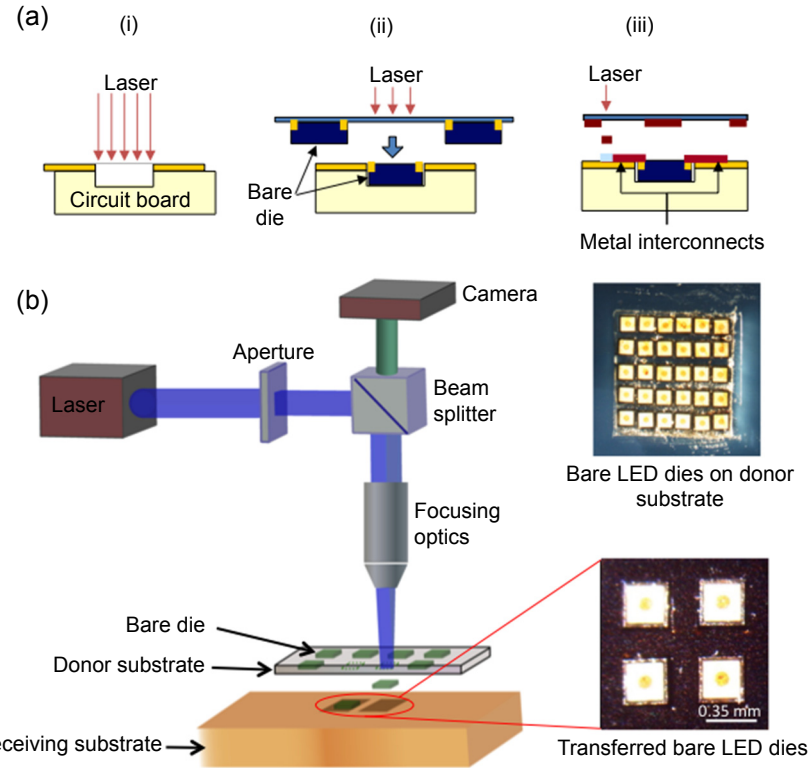

Figure 12.1 Schematic diagram (a) showing laser direct write (LDW) processes for embedding electronics: (i) micromachining, (ii) lase-and-place, and (iii) laser-induced forward transfer or laser transfer of functional materials. Some of the main components in the lase-and-place setup are shown in (b). *LED*, light-emitting diode.
Adapted and reprinted with permission from A. Piqué, N.A. Charipar, R.C.Y. Auyeung, H. Kim, S.A Mathews, Assembly and integration of thin bare die using laser direct-write, in: C.B. Arnold, et al. (Eds.), Proceedings of SPIE, San Jose, vol. 6458, 2007, pp. 645802-1−645802-10. © 2007 by SPIE.

The LM555 bare die (timer chip) and the LED were each tested for functionality after transfer. Many LM555 bare dies were tested with a probe station, and their output signals were identical to those before laser transfer. An embedded LED bare die was also electrically contacted with probe tips and displayed bright emission. A more robust demonstration of the laser transfer process is shown in Section 12.4 by a working array of embedded LED dies and interconnects, all made by L&P and laser printing.

Another advantage the L&P process has over pick-and-place machines is its ability to transfer ultrathin (10 μm) 1-mm^2 silicon substrates, as shown in Fig. 12.3. These substrates were transferred intact with a placement accuracy of better than 50 μm without any fracture. This accuracy could be improved by optimizing the DRL layer,

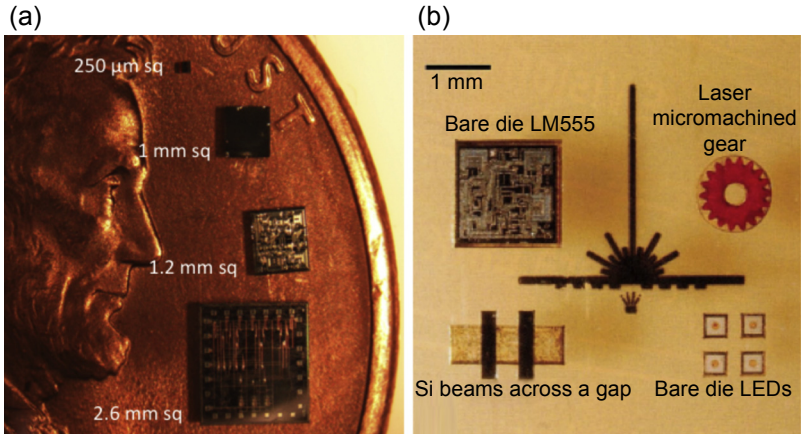

Figure 12.2 (a) Optical micrograph showing the various sizes of laser-transferred bare die and silicon substrates. The smallest device (top) is a bare die light-emitting diode measuring ~0.25 mm^2, whereas the larger device (bottom) measures 2.6 mm^2. (b) Optical image of various components transferred onto a plastic substrate by lase-and-place. The artwork in the center is a schematic illustration of the lase-and-place technique and was laser-printed using silver metallic nanoink.
Adapted and reprinted with permission from S.A. Mathews, N.A. Charipar, K. Metkus, A. Piqué, Manufacturing microelectronics using Lase-and-Place, Photonics Spectra 41(10) (2007) 70–74. © 2007 by Laurin Publishing.

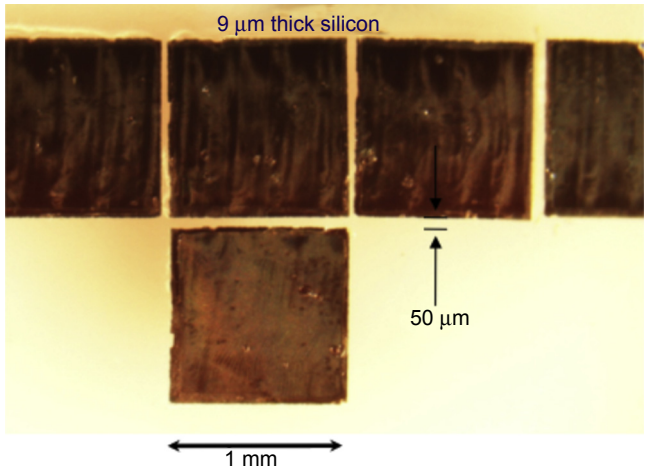

Figure 12.3 Optical micrograph showing laser transfer of adjacent 1-mm^2 ultrathin (10-μm-thick) silicon substrates demonstrating the placement accuracy and sensitive handling capability of the lase-and-place technique.
Adapted and reprinted with permission from A. Piqué, N.A. Charipar, R.C.Y. Auyeung, H. Kim, S.A Mathews, Assembly and integration of thin bare die using laser direct-write, in: C.B. Arnold, et al. (Eds.), Proceedings of SPIE, San Jose, vol. 6458, 2007, pp. 645802-1–645802-10. © 2007 by SPIE.

the donor−to−receiving substrate distance, and transfer laser parameters. The slight residue on the surface was probably polymer material from the DRL that remained after the transfer. These ultrathin substrates are beyond what is currently needed for RFID tags (50−100 μm thick), but the ability of the L&P process to transfer them without damage shows the viability of this technique in embedding and accurately placing ultrathin components.

A study of the kinetics of the laser transfer process were studied by stroboscopic imaging of the release and transfer of various discrete components from a donor substrate without a neighboring receiving substrate [17,18]. Video images of the laser release of a 1-mm^2 silicon tile, 1.4-mm^2 LM555 bare die, and a 2 × 1-mm SMD resistor are shown in Fig. 12.4. Note that the receiver substrate is typically ≪1 mm from the donor substrate, so any tilt or rotation of the transferred component would be negligible. An analysis of the component trajectories at transfer threshold showed that the velocities were approximately a few meters per second (for 1- and 2.6-mm^2 components).

An interesting application of the L&P technique was recently used to transfer thin solid metal interconnects (which could be considered as "discrete components" or "devices") to a series of millimeter-sized silicon capacitors. The laser transfer of embedded bare dies with the active side up makes the contact pads accessible for

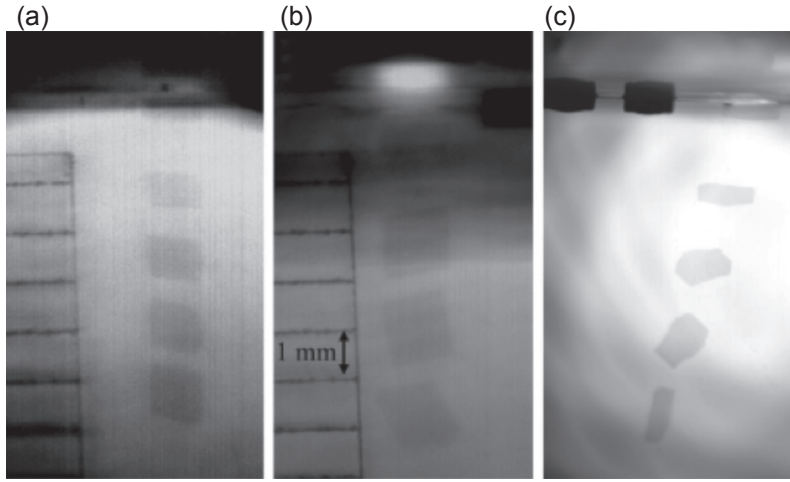

Figure 12.4 Multiple exposure optical micrograph of the laser release of (a) 1 × 1-mm silicon substrate, (b) 1.4 × 1.4-mm LM555 bare die, and (c) 2 × 1-mm surface-mount resistor device (SMT package 0402 series). The donor substrate can be observed at the top of each image. The time interval between exposures was adjusted for each image. For images (a) and (b) a glass ruler with 1-mm spacing between marks can be observed on the left.
Adapted and reprinted with permission from A. Piqué, N.A. Charipar, R.C.Y. Auyeung, H. Kim, S.A Mathews, Assembly and integration of thin bare die using laser direct-write, in: C.B. Arnold, et al. (Eds.), Proceedings of SPIE, San Jose, vol. 6458, 2007, pp. 645802-1−645802-10. © 2007 by SPIE.

interconnect assembly. These interconnects must be compact but yet able to accommodate a wide range of die sizes and shapes and display good electrical performance under varying conditions of thermal and mechanical stress (eg, temperature, vibration). A solid metal interconnect could be preferred over traditional wire bonds, which have a finite loop height above the substrate and could fail under high internal and external stress loads. Solid metal interconnects were recently bent by a laser and then laser transferred to span and connect a set of silicon capacitors, as shown in Fig. 12.5 [20]. Copper strips (1 mm × 100 μm × 12.5 μm thick) were first etched out of a copper foil attached to a donor substrate. This donor substrate was then placed over the capacitor pads and a laser pulse fired at the center of a strip resulting in a *U*-shaped bend in the copper, without releasing the strip. Next, a laser pulse was fired at the ends to transfer the entire copper strip to conductive epoxy pads (previously laser-printed) on the capacitors. The measured capacitance of the array of capacitors agreed with the expected value. This bend in the copper interconnect could accommodate mechanical or thermal stresses arising from component geometry mismatches or high electrical load. These early results indicate the potential of this technique to transfer even smaller and thinner interconnects that could be used in embedded electronics.

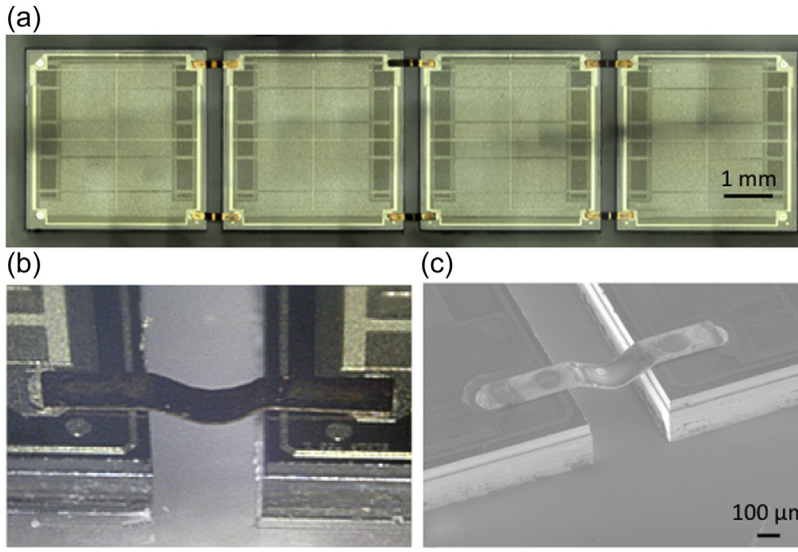

Figure 12.5 Optical micrographs of (a) an array of silicon capacitors interconnected with laser transferred, laser bent copper beams. Close-up view (b) of a single interconnect attached with conductive epoxy and (c) angled scanning electron microscopic view.
Adapted from Figs. 5 and 6 of S.A. Mathews, I. Beniam, N. Charipar, A. Piqué, Laser induced forward transfer (LIFT) for direct-write fabrication and assembly of microelectronics and reprinted with permission from 2015 ICALEO (34th International Congress on Applications of Lasers & Electro-optics) Conference Proceedings: Session LMF1, Paper M101 (October 2015), pp. 9−13. © 2015 by Laser Institute of America, Orlando, FL. All rights reserved.

L&P has been shown to be an additive manufacturing technique that surpasses the capabilities of typical pick-and-place tools by transferring and embedding miniature and ultrathin components without damage. The preserved functionality of devices during the transfer shows that the active-side-up orientation of the die is safe enough to withstand the low laser fluences used in the process. These low laser fluences can also be used to print functional materials and devices directly into a substrate to achieve an even higher level of miniaturization and embedding. The rest of this chapter discusses the use of LIFT to print complex solutions of functional materials for these embedded applications.

12.3 Laser-induced forward transfer of functional materials systems

As discussed in the introduction, LIFT can also be used to transfer functional materials directly into a substrate to form embedded devices. Traditionally, LIFT vaporizes a large portion of the donor film to transfer it to the substrate. Unfortunately, degraded functional properties, loss of feature resolution, and debris in the transfer are often the result. Instead, LIFT can be used with functional rheological fluid systems with a wide range of viscosities as the donor materials. The use of a fluid requires lower laser transfer fluence (<0.1 J/cm^2) and provides the advantages of improved functional properties, better feature resolution, and less debris. In the case of material with a very high viscosity, a novel form of LIFT called "laser decal transfer" (LDT) has even been used to fabricate freestanding interconnects and is discussed in detail next. Following that, additional examples of LIFT of functional materials (and devices), which could all be embedded in principle, are presented.

12.3.1 Laser-induced forward transfer of interconnects

LIFT was first used to transfer viscous fluids, pastes, or inks for the fabrication of metal interconnects, vias, and antenna structures [30,31]. By using a commercially available screen-printable silver ink, LIFT was used to print patterns in premachined trenches and even over a 3D surface (step). In this first demonstration, the laser spot size was adjusted to match the required line-width of the feature, and laser pulses were then used to "stitch" together a continuous line or pattern. The ink had a low enough viscosity that adjacent transferred features could merge together to ensure electrical continuity. Once completed, the transfers on the receiving substrate (usually a printed circuit board) were cured at $<150^{\circ}$C to increase its electrical resistivity. After curing, the transferred features displayed good adhesion and mechanical properties, as indicated by tape and flexing tests [30]. The ability to deposit conformal metal patterns on substrates at low temperatures also allowed for the fabrication of novel types of electronic designs such as conformal GPS antennas [32] on polymer radomes.

The next advance in LIFT came from the adoption of nanoparticle inks ("nanoink") that were undergoing extensive development for the inkjet printing industry.

By reducing the particle size (<100 nm), the printed resolution increased and the curing temperature decreased, which enabled fabrication on flexible substrates. However, these commercially available nanoinks typically have viscosities of ~15 cP (centipoise) to mitigate clogging issues with inkjet nozzles. If these nanoinks were used on the donor substrate without modification, then the transfers made by the LIFT process would suffer from the same issues as inkjet, namely, feature spreading caused by wetting interactions between the substrate and ink, satellite droplets ("splatter"), possible deleterious interactions between the solvent in the ink and the receiving substrate, and low mass of material deposited as a result of low solids content in the ink. By using heat or vacuum to increase the viscosity of the as-received inkjet silver ink before transfer, LIFT was used to print a pair of 25-μm-wide × 1-mm-long silver lines separated by only 50 μm, with high definition and without any debris [33,34]. The measured resistivity of these silver lines were ~12 times the bulk silver value after curing, and device performance was similar to those made by ebeam deposition. The resolution and length of these patterns demonstrated the capability of LIFT to print electrodes that met the critical dimension requirements in organic thin-film transistors.

Although increasing the viscosity of the as-received inkjet ink improved the quality of laser transfers, there was a limit to the amount of solvent removed from the ink and the maximum viscosity (~400 cP) achieved. A better way was to start with higher-viscosity nanoink for the donor layer. A silver nanoink with a viscosity ~10,000 cP was used to laser-print 19-μm-wide lines on polyimide [35]. A silver nanopaste, commercially produced for screen-printing, with viscosity ~100,000 cP, was used to laser-print 5-μm-wide lines on glass [36,37]. The as-transferred lines displayed excellent definition and resolution without any surrounding debris. After laser curing, these lines were measured to have a resistivity near two times that of bulk silver, demonstrating no significant loss of functional properties as specified by the manufacturer. The high viscosity of nanopaste allowed the transfer of patterns that were highly congruent in shape and size to the illuminated laser area on the donor layer. This high congruence led to naming this LIFT process LDT, and it allowed the laser transfer of patterns with feature fidelity and thickness uniformity comparable to lithographically patterned thin films. LDT is a unique form of LIFT in that ink−substrate interactions are minimal, functional properties are preserved in the transferred material (since minimal vaporization occurs), and the geometric dimensions of the transfer are identical to those of the incident laser spot with sharp edge definition.

The high fidelity of the transfer to the shape and size of the laser beam implies that the laser spot (and hence the transfer) can be arbitrarily shaped to the design element. Each transferred volume element (voxel) in the donor layer directly corresponds to a pixel in the two-dimensional design, thus enabling true digital microfabrication in the LIFT process. Not only does this minimize prototyping time, but the LDT process can process entire interconnects, transmission lines, pads, or perhaps an entire device such as a capacitor [38] with a single laser pulse. One of the early applications of LDT was for additive repair of defective metal patterns in liquid crystal displays [36]. Fabrication of arrays comprising individual split-ring elements was demonstrated for rapid prototyping of resonators for metamaterial applications [39]. The viscosity of silver

nanopaste was sufficiently high that silver microcantilevers and microbridges could be placed over a trench with a single laser pulse and remain freestanding without the use of any sacrificial layers [40,41]. Similarly, multilayer structures [38] and cavity-sealing membranes [42] have also been demonstrated via LDT. Such freestanding structures could not be generated by lithographic techniques without the use of sacrificial layers and demonstrates the unique capabilities of LDT among traditional direct-write processes.

The ability of LDT to create freestanding structures becomes extremely valuable in providing interconnects to embedded dies. These interconnects could bridge the narrow gap that typically surrounds the embedded component and/or accommodate any height differences between the die contact pads and the rest of the circuitry.

As demonstrated in Fig. 12.6, interconnects printed by LDT spanned across a gap and adapted to a ~15-μm height mismatch between an embedded LED die and a gold/polyimide substrate [43]. Light emission from the LED demonstrated the functionality of the interconnects even after 500 cycles of bending (13-mm radius). As shown in Fig. 12.7, the LDT process can be repeated over the same location to build 3D structures for crossover interconnect or via applications. In addition, by adjusting the laser transfer fluence, it is possible to fold the voxel along an edge, thus allowing interconnects alongside two orthogonal planes on the same substrate [44]. This ability has no parallel in lithography and can be used to generate top-to-side or top-to-bottom interconnects.

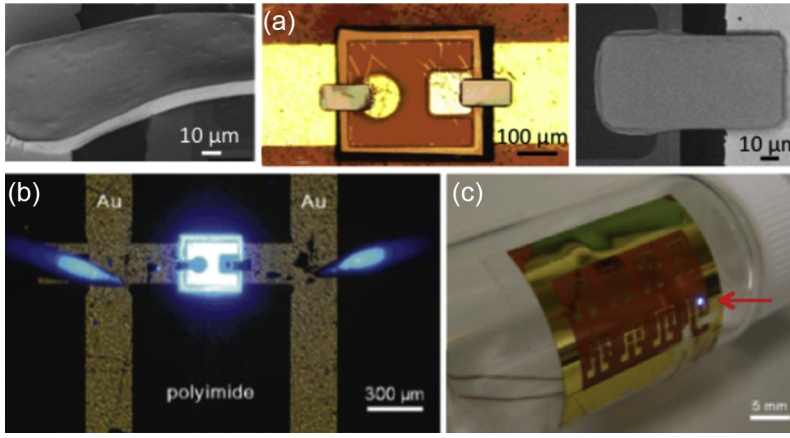

Figure 12.6 Optical micrograph showing (a) bare light-emitting diode (LED) die embedded inside a polyimide substrate connected with laser decal transferred silver interconnects. Left and right insets show scanning electron micrographs of interconnects spanning a gap; left interconnect "climbs" a height mismatch between the die and the substrate. (b) Optical micrograph showing LED emission powered through probe tips. (c) Optical micrograph of emission from the same LED device after 500 bending cycles.
Adapted and reprinted with permission from J. Wang, R.C.Y Auyeung, H. Kim, N.A. Charipar, A. Piqué, Three-dimensional printing of interconnects by laser direct-write of silver nanopastes, Advanced Materials 22 (40) (2010) 4462−4466. © 2010 by Wiley & Sons.

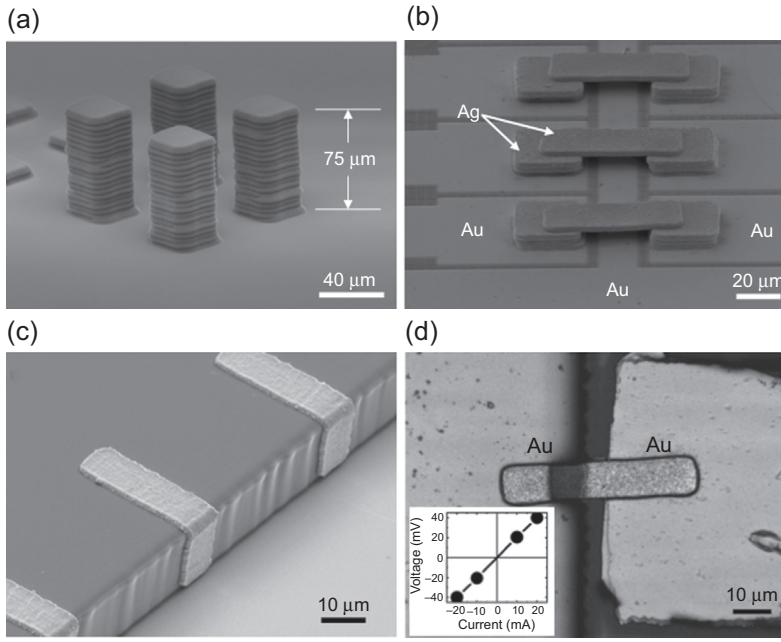

Figure 12.7 Scanning electron micrographs of silver interconnect structures made by laser decal transfer: (a) high aspect ratio micropillars on silicon, (b) crossover interconnect, (c) folded interconnect on a step edge printed with a single laser pulse by laser decal transfer. Confocal microscope image and (d) of a printed voxel connecting two gold (Au) electrodes separated by a 20-µm-high polymer (SU8) layer. Inset shows its I-V plot indicating ohmic behavior with a resistivity of ~7.3 µΩ-cm [4.6 times bulk silver (Ag)].
(a) and (b) Adapted and reprinted with permission from J. Wang, R.C.Y Auyeung, H. Kim, N.A. Charipar, A. Piqué, Three-dimensional printing of interconnects by laser direct-write of silver nanopastes, Advanced Materials 22 (40) (2010) 4462−4466. © 2010 by Wiley & Sons. (c) and (d) Adapted and reprinted with permission from H. Kim, M. Duocastella, K.M. Charipar, R.C.Y Auyeung, A. Piqué, Laser printing of conformal and multi-level 3D interconnects, Applied Physics A 113 (1) (2013) 5−8. © 2013 by Springer.

Solid metallic interconnects can also be laser transferred as was shown previously in Section 12.2.1. LIFT of conductive materials was combined with the L&P technique to transfer solid bent metal beams across a series of millimeter-sized capacitors. This hybrid technique shows promise in fabricating interconnects that can handle die-to-substrate height differences, high current loads, and thermal or mechanical strain arising from substrate movement.

12.3.2 Laser-induced forward transfer of materials for passives

LIFT could be used to directly fabricate and embed passive components into a substrate in a single step. Ideally, these printed components would retain all the functionality of discrete SMDs but with much smaller form factors.

Thick-film resistors satisfy a wide variety of electrical design requirements in hybrid microelectronics and are suitable for polymer substrates because of their low processing temperatures. LIFT was demonstrated for polymer thick-film resistors [45] and their resistance characterized for radiofrequency applications. The temperature coefficient of resistance of these printed resistors was measured to be similar to those made by screen-printing.

Dielectric materials present many challenges in their processing because of their brittleness, high processing temperatures, and microstructure-dependent properties. Nevertheless, LIFT was used to transfer a pad of 150-nm-diameter barium titanate particles in titania ink over an interdigitated capacitor structure on alumina and polyimide substrates [46]. After curing at 400°C, a dielectric constant of 50−55 with a loss tangent <2% were measured from 1 MHz to 1.5 GHz. It was shown that the dielectric properties of the ink were not affected by the transfer process.

LIFT of inductors was demonstrated by using an ink of $Y_3Fe_5O_{12}$ (YIG) powder dissolved in a poly(butyl methacrylate)/chloroform solution [47]. A four-turn flat YIG core ($1.0 \times 0.3\ mm^2 \times 20\ \mu m$ thick) was laser-printed over patterned gold electrodes on a printed circuit board substrate. The measured inductance was 9 nH at 1 MHz and displayed high losses as a result of porosity in the YIG transfer.

An alternative laser-based method to fabricate an electronic circuit comprising several passive components and interconnects was demonstrated using low-temperature cofired ceramic technology [48]. LIFT was used to transfer silver, dielectric, inductor, and resistor paste onto green tape to form a multilayer laminated radiofrequency band pass filter. The measured center frequencies of the filters were near 1 GHz.

12.3.3 Laser-induced forward transfer of microbatteries

LIFT techniques have been used to print active electrochemical materials for the fabrication of electrochemical micropower sources, such as batteries and solar cells [49,50,51]. These micropower sources comprise three main components: a negative electrode (anode), a positive electrode (cathode), and an electrolyte/separator. Each of these components was typically assembled with a large degree of structural complexity, such as mixtures of electrochemically active materials, solid-state polymers, liquids, or nanocomposites. Thus the LIFT process must preserve the electrochemical activity and structural integrity of these components during the transfer.

One of the advantages of the LIFT process is that it allows for the deposition of highly porous, multicomponent materials without modifying their properties. These porous structures are an essential requirement for electrochemical devices, since enhanced contact between the electrodes and the electrolyte leads to better charge transfer, allowing a more complete utilization of the electrode materials. Another important feature of the LIFT process in fabricating electrochemical cells is the flexibility in the design of operating geometries. The simplest system is a planar structure where the electrodes of the cells are placed adjacent to each other in the same plane. Another geometry is to construct the cells in a stacked electrode. Both geometries have particular advantages and disadvantages. In the case of a stacked geometry, one can obtain higher areal densities, but each layer must be rigid enough to support the upper

layers while preserving their electrochemical properties. For a planar geometry, the fabrication process is much easier because it can handle softer and rougher materials, but they have higher internal resistances, resulting in low cell performance particularly at high currents. In addition, by combining LIFT of battery materials with laser-micromachined substrates, it is possible to further reduce the packaged size of an entire microdevice by embedding the cell components directly within a substrate while allowing its geometry to be adjusted to fit any form factor.

Planar alkaline microbatteries have been fabricated by laser printing zinc (as an anode), AgO_2 (as a cathode), and a KOH electrolyte in the form of complex suspensions or inks on various substrates [52,53]. Laser micromachining was subsequently used to provide clear electrical isolation between the electrodes. These planar microbatteries produced 0.6 mWh/cm^2 of energy density and 160 mWh/g of specific energy density [54]. Stacked microbatteries have also been demonstrated by LIFT. One challenge in fabricating the stacked batteries was printing the electrolyte. Since the use of a liquid electrolyte is limited by leakage and safety issues, it was important to replace the liquid electrolyte with a solid-state electrolyte. Our group at NRL developed a nanocomposite solid-polymer ionic liquid (nc-SPIL) as a solid-state electrolyte for the LIFT process [55,56,57]. The laser-printed nc-SPIL membranes exhibited the acceptable electrochemical behavior for ionic liquids, with a high conductivity of 1−3 mS/cm, while maintaining the strength and flexibility of the commonly used poly(vinylidenefluoride-hexafluoropropylene) (PVDF-HFP) copolymer binder. Thus, these laser-printed solid-state membranes were able to serve as both the electrolyte and separator [56]. LIFT has been used to print sequential layers of $LiCoO_2$ cathode, nc-SPIL electrolyte, and carbon anode into a laser micromachined pocket in a thin polyimide substrate to form an embedded all-solid-state lithium-ion microbattery. Although the total thickness of this stacked structure (30−50 μm) was much larger than sputter-deposited thin-film microbattery structures (1−5 μm), the stacked microbattery was thin enough to lie entirely inside the substrate. Fig. 12.8(a) and (b) shows a cross-sectional schematic diagram and a cross-sectional scanning electron micrograph of this embedded lithium (Li)-ion microbattery on a polyimide/aluminum substrate. As seen in Fig. 12.8(c) and (d), these embedded microbatteries charged/discharged more than 100 cycles at C/3 rate ($\sim$110 μA/cm^2) with an energy density of 1.32 mWh/cm^2 (or a specific energy of 330 mWh/g) [57].

Packaged Li-ion microbatteries were fabricated and then embedded into laser micromachined pockets in printed circuit boards. In this design, the $LiCoO_2$ cathode and the carbon anode were printed by LIFT on aluminum and copper current collectors, respectively, then assembled by placing the gel polymer electrolyte-soaked membrane between two electrodes. To package the batteries, the current collectors were sealed together with a thermally curable polymer spacer (Surlyn SF-71). The sealed batteries were then excised by the laser. Fig. 12.9(a) shows a cross-sectional scanning electron micrograph, showing individual layers of the packaged microbatteries made by LIFT. Fig. 12.9(b) shows a packaged Li-ion microbattery that was then embedded into the laser-machined pocket in the circuit board (Fig. 12.9(c)). The brown side in the microbattery is the copper-foil (anode) side (negative), while the silver side is the Al-foil (cathode) side (positive). Similarly packaged microbatteries made with thicker

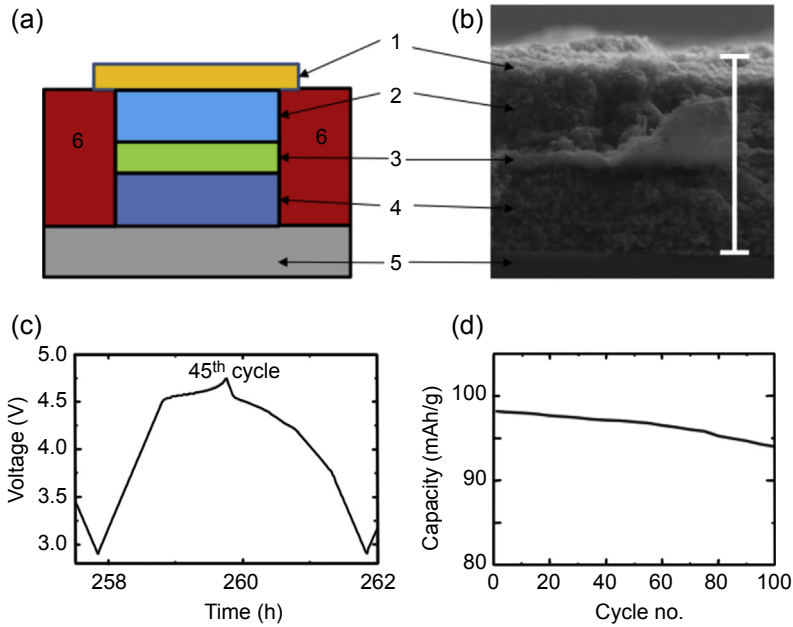

Figure 12.8 (a) Cross-sectional schematic diagram of an embedded lithium (Li)-ion microbattery (Pt/Carbon/nc-SPIL/$LiCoO_2$/Al). (b) Cross-sectional scanning electron micrograph of an embedded Li-ion microbattery. For both (a) and (b), 1 is the platinum metal deposited by sputtering, 2 is the carbon anode, 3 is the nanocomposite solid-polymer ionic liquid membrane, 4 is the $LiCoO_2$ cathode, 5 is the aluminum-current collector, 6 is the polyimide. The vertical scale bar is 30 μm. (c) and (d) Cycling performance of an embedded Li-ion microbattery. The battery was charged/discharged at C/3 rate (~110 μA/cm^2) between 4.2 and 3 V. The active electrode area was 3 × 3 mm.
(b) Adapted and reprinted with permission from T.E. Sutto, M. Ollinger, H. Kim, C.B. Arnold, A. Piqué, Laser transferable polymer-ionic liquid separator/electrolytes for solid-state rechargeable lithium-ion microbatteries, Electrochemical and Solid-State Letters 9 (2) (2006) A69−A71. © 2006 by The Electrochemical Society.

cathodes (~100 μm) showed excellent cycling performance over 100 cycles at low current density (0.1 mA/cm^2) with a discharge capacity of ~2.5 mAh/cm^2 [51], which was an order of magnitude higher than those achieved from sputter-deposited thin-film microbatteries with a 2.5-μm-thick $LiCoO_2$ cathode [58].

Using laser structuring to increase the active surface area of the laser-printed $LiCoO_2$ thick films for improved Li-ion diffusivity has been investigated [59,60]. Microbatteries fabricated with these laser-structured 3D cathodes exhibited improved capacity retention compared with those made with unstructured cathodes when cycling the batteries at C/5 rates (~100 μA/cm^2). After 100 cycles, the laser-structured electrodes showed a capacity of ~70 mAh/g, which was twice the remaining capacity of the unstructured cathode. This improvement was the result of the improved Li-ion diffusion paths and artificial porosity created by the laser structuring.

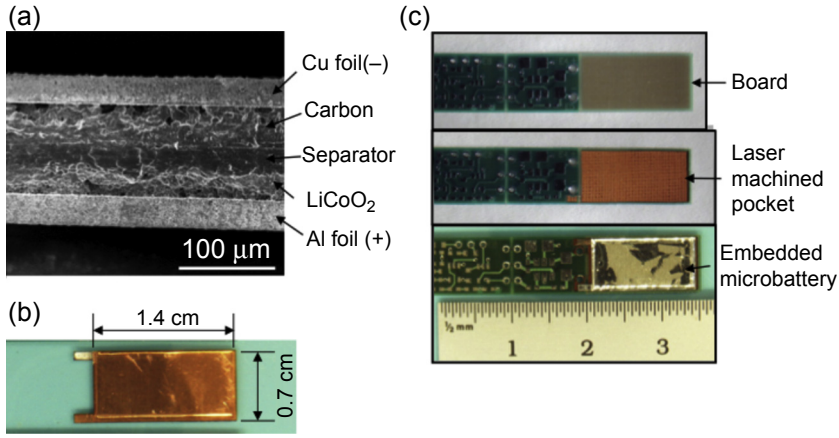

Figure 12.9 (a) Cross-sectional scanning electron micrograph of a packaged lithium (Li)-ion microbattery (Cu/Carbon/separator/$LiCoO_2$/Al). (b) Photograph of sealed Li-ion microbattery made by laser-induced forward transfer. (c) Photograph showing the starting circuit board that incudes an extra area for an embedded battery (top), laser machined pocket (middle), and the Li-ion microbattery embedded within the laser-machined pocket on the printed circuit board (bottom).

(a) Adapted and reprinted with permission from H. Kim, R.C.Y. Auyeung, A. Piqué, Laser-printed thick-film electrodes for solid-state rechargeable Li-ion microbatteries, Journal of Power Sources 165 (1) (2007) 413−419. © 2007 by Elsevier.

12.3.4 Laser-induced forward transfer of dye-sensitized solar cells

LIFT has been used to print porous nanocrystalline TiO_2 (nc-TiO_2) films to serve as active working electrodes for embedded energy-harvesting devices such as dye-sensitized solar cells [50]. These solar cells require a porous microstructure of an active TiO_2 layer with a large surface area so that a large number of dye molecules can be absorbed on the surface of the nanocomposite TiO_2 particles to achieve high efficiency. Under the right conditions, LIFT can print porous structures with large surface areas.

For LIFT of TiO_2 layers, the inks were prepared by mixing water-based colloidal suspensions of nanocomposite TiO_2 powders with organic additives. Mesoporous nanocomposite TiO_2 films were laser printed onto fluorine-doped tin oxide−coated glass substrates [50,61]. After sintering in the oven at 450°C, the TiO_2 electrodes were then soaked in the dye solution to coat the TiO_2 surface with dye molecules. The completed cells were assembled and sealed using a thermally curable polymer spacer (Surlyn) to separate the anode and cathode layers and to provide a reservoir for the I^{3-}/I^- electrolyte. Fig. 12.10(a) shows a schematic structure of a dye-sensitized solar cell. As seen in Fig. 12.10(b), the printed materials maintain a homogeneously distributed network of nanoparticles with a high degree of porosity. This 3D network of interconnected TiO_2 nanoparticles allows for good electron conduction,

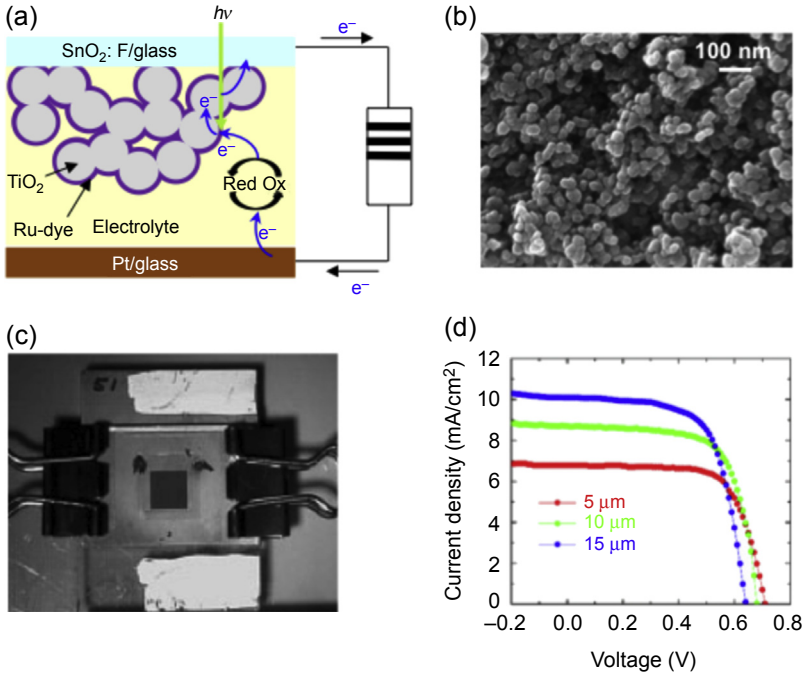

Figure 12.10 (a) Schematic cross-sectional diagram of a dye-sensitized solar cell. (b) Scanning electron micrograph of the surface of nanocomposite TiO_2 layer printed by laser-induced forward transfer on fluorine-doped tin oxide coated glass. The film was sintered at 450°C for 30 min. (c) Photograph of a packaged dye-sensitized solar cell fabricated with a laser-transferred nanocomposite TiO_2 electrode. (d) Current density versus voltage (J-V) of dye-sensitized solar cells fabricated by laser-based techniques with different thicknesses of active TiO_2 layers under a light intensity of 100 mW/cm^2 (AM 1.5 simulated solar illumination). The active cell area in all samples was 0.25 cm^2.

while the highly porous structure maximizes the amount of dye molecules adsorbed on the surface of the TiO_2 particles. Fig. 12.10(c) shows a photograph of a sealed dye-sensitized solar cell fabricated with the laser-printed nanocomposite TiO_2 electrode. Fig. 12.10(d) shows the current density (J) versus voltage (V) characteristics of dye-sensitized solar cells with three thicknesses of laser-printed nanocomposite TiO_2 layers. The short-circuit current density (J_{sc}) increases with the nanocomposite TiO_2 film thickness as a result of the increased surface area of the TiO_2 films, resulting in an increased amount of dye molecules. However, an increase of the TiO_2 thickness also increases defect/recombination sites, leading to an overall decrease in the open circuit voltage (V_{OC}). Thus the TiO_2 film thickness must be optimized to improve both J_{sc} and V_{OC} parameters jointly. The solar cells based on the optimized nanocomposite TiO_2 film ($\sim$15 µm) exhibit a light power conversion efficiency of $\sim$4.7%, which is comparable to those reported earlier for analogous cells fabricated with commercial TiO_2 powders (P25) using traditional screen-printing techniques [62,63].

The laser sintering process has also been explored to form a 3D network of TiO_2 nanoparticles for developing flexible dye-sensitized solar cells. To prepare the porous 3D network structures of TiO_2 working electrodes, printed TiO_2 electrodes must be sintered at relatively high temperatures ($\sim$450°C) to remove the organic additives to form an electrically connected nanostructure network within the mesoporous TiO_2 electrode. Laser sintering can form this connected network without causing any damage to flexible plastic substrates [61]. Typical laser sintering at IR wavelengths is not sufficient for TiO_2 because of its large band gap ($\sim$3.2 eV) and accordingly low absorption. However, the same UV source ($\lambda = 355$ nm) that was used for the LIFT of the nanocomposite TiO_2 inks can be used for the laser sintering of TiO_2 electrodes. The power conversion efficiency of the device based on the laser-sintered nanocomposite TiO_2 electrode is 1.8%, which is more than a twofold improvement from that of the device based on a non-laser-sintered TiO_2 electrode (0.7%). However, the 1.8% efficiency is still low compared with that of the standard cell (4.7%) fabricated with the high-temperature (450°C for 1 h) sintered nanocomposite TiO_2 electrode. This low efficiency indicates the insufficient necking of nanocomposite TiO_2 particles, which can be improved by further optimization of the laser sintering conditions. An advantage of this approach is that it allows both the transfer of the TiO_2 ink and in situ sintering of the mesoporous nanocomposite TiO_2 electrodes using the same UV laser, thus simplifying the steps required for fabricating dye-sensitized solar cells at low temperatures.

12.3.5 Laser-induced forward transfer of sensors

Chemical vapor sensors were the first type of sensor made by LIFT that relied on the ability of chemoselective polymers loaded with graphite particles to reversibly change its volume in the presence of vapors from a solvent [64,47]. Upon exposure, the chemoselective polymer (polyepichlorohydrin) expanded, which increased the average distance between its graphite particles and thereby increased its electrical resistance. Fig. 12.11(a) shows a photograph of a chemiresistor sensor element (black portion) laser printed across a set of silver interdigitated electrodes also fabricated by LIFT [65]. Fig. 12.11(b) displays the change in resistance as a function of time for this sensor element as it was challenged with vapors containing various concentrations of solvents (acetone in this case). Note that this sensor, which was entirely laser printed, was capable of detecting vapor traces down to the parts per million range and performed similar to one made by spray-coating.

Fig. 12.11(c) shows a fully operational chemiresistor sensor circuit with a chemiresistor sensor element, silver metal interconnects, and polymer thick-film resistors all made by LIFT [66]. The 4-Quad comparator device chip and the surface-mount LED components were soldered to the silver interconnects, and power to the circuit was provided by an external battery. In the presence of organic vapors, the resistance change across the chemiresistor sensor caused the 4-Quad comparator to sequentially light up individual LEDs, depending on the magnitude of the change in resistance across the sensor, proportional to the vapor concentration.

The NRL group has used LIFT to fabricate other small sensor devices such as temperature sensors [67], strain sensors on polyimide substrates [68], and simple

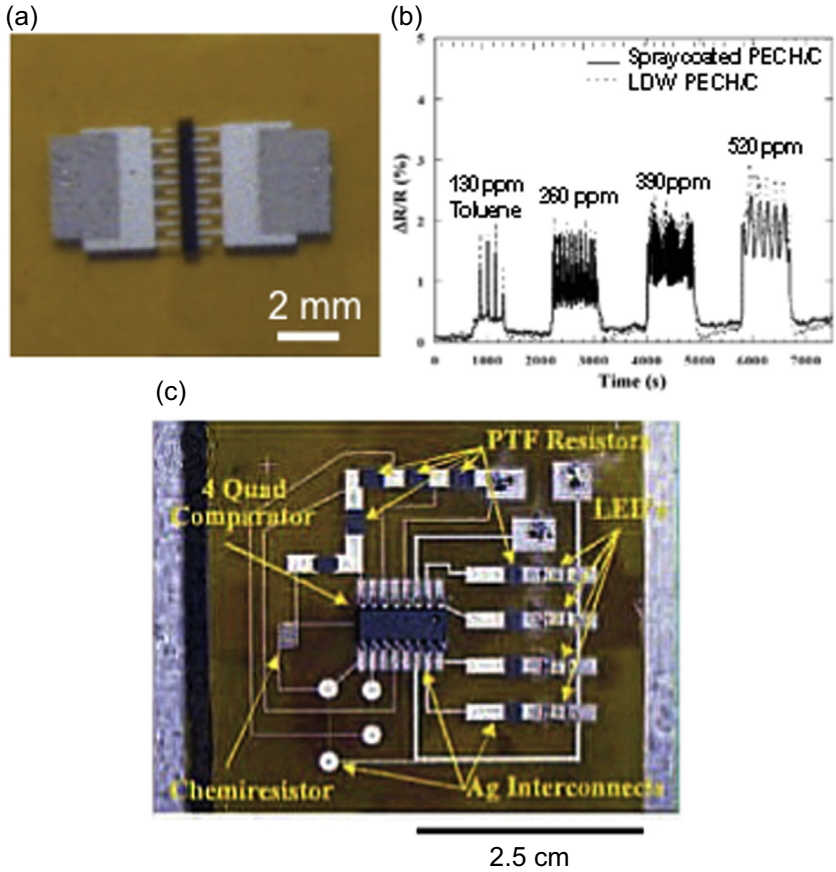

Figure 12.11 Example of an embedded chemical sensor fabricated using laser-induced forward transfer. (a) Chemiresistor gas sensor element (*black stripe*) and associated interdigitated silver metal electrodes (gray) on a polyimide substrate. (b) Change in resistivity with time for a laser-printed versus a spray-coated chemoselective sensor exposed to toluene. (c) Fully functional gas sensor circuit with a chemiresistor sensing element and light-emitting diode (LED) flashing indicators. *PECH*, polyepichlorohydrin; *PTF*, polymer thick film.
Adapted and reprinted with permission from A. Piqué, D.W. Weir, P.K. Wu, B. Pratap, C.B. Arnold, B.R. Ringeisen, R.A. McGill, R.C.Y. Auyeung, R.A. Kant, D.B. Chrisey, Direct-write of sensor devices by a laser forward transfer technique, in: Proceedings of SPIE, vol. 4637, 2002, pp. 361−368. © 2002 by SPIE.

electrochemical biosensors for the detection of small concentrations of dopamine on aqueous solutions [69]. Other groups have used laser-transfer techniques for depositing micropatterns of tin oxide layers with various oxygen ratios, which have potential application as gas sensors [70]. A capacitive chemical sensor array was recently produced using LIFT by laser transferring three different types of polymer materials sensitive to organic solvent vapors. Droplets of each polymer in solution were deposited

onto an array of thin silicon membranes to demonstrate a micromechanical capacitive vapor sensor [71,72].

12.3.6 Laser-induced forward transfer in parallel

Up to this point, the LIFT process has remained a serial direct-write process by nature, given the limited energy available from existing lasers. But the LIFT of fluids typically requires lower laser fluence (and energy) than traditional LIFT, so the laser beam could be expanded to print a larger area than just a small voxel. This would transform LIFT from a serial to a parallel printing technique and greatly increase its efficiency.

Nowhere is the parallel mode more useful than in the implementation of LDT (Section 12.3.1). Because the laser-transferred pattern in LDT is highly congruent to the dimensions of the incident laser spot, a spatial light modulator such as a commercial digital micromirror device (DMD) can impart an arbitrary shape to the laser beam, which would be exactly duplicated in the printed feature [73–75]. Thus the pixels in a DMD bitmap pattern would be "transformed" into the corresponding voxels of the laser-transferred pattern, creating a true "design-to-print" process. Combining the DMD's ability to quickly reload bitmap patterns with the synchronization of laser pulses and sample movement would result in a highly parallel, rapidly reconfigurable direct-write process.

Examples of the power of parallel direct-writing using DMD-LDT are shown in Fig. 12.12 [76]. In the laser printing of a grid (Fig. 12.12(a)), overlapping lines at the intersections would undergo bulging and loss of resolution if voxels were just stitched together serially, as in traditional LIFT, but with congruent LIFT and a DMD-shaped laser beam, the entire grid pattern can be printed with one single laser

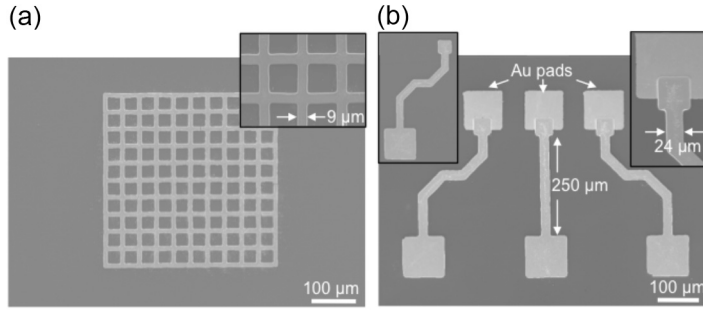

Figure 12.12 Scanning electron micrographs of the printing of a grid with (a) a single laser pulse and (b) three interconnects with three separate pulses using digital micromirror device—laser decal transfer. The left inset in (b) shows one type of interconnect; the right inset shows one end of the interconnect in contact with a pre-deposited gold (Au) pad on silicon. Adapted and reprinted with permission from A. Piqué, H. Kim, R.C.Y. Auyeung, A.T. Smith, Laser forward transfer of functional materials for digital fabrication of microelectronics, Journal of Imaging Science and Technology 57 (4) (2013) 040404. © 2013 by The Society for Imaging Science and Technology.

pulse [76]. In interconnect applications, DMD-LDT can print a pattern with a range of feature resolutions with a single pulse. Three types of interconnects in Fig. 12.12(b) were printed with three separate pulses, each pulse dynamically reconfigured for each interconnect type. These two examples demonstrate the ability of DMD to arbitrarily shape the laser pulse spatial profile and the ability of LDT to faithfully reproduce that profile in its transfer.

The combination of LDT with DMD is a potentially disruptive technology in the field of laser additive manufacturing since it transforms what was considered until now to be a serial process into a parallel printing technique. In fact, the well-established technology of DMD could "parallelize" other laser additive manufacturing techniques that require only low to moderate amounts of laser energy.

12.4 Laser-induced forward transfer of embedded circuit

At the board level, an embedded circuit could be broken down into discrete components (eg, SMDs, dies) and interconnects. In the preceding sections, successful laser-transfer and posttransfer functionality were demonstrated separately for discrete components (passives and actives), functional materials, and interconnects. Now, to demonstrate the full capability of all LDW processes together, all these components were transferred into one circuit board [77].

A simple blinker circuit comprising six passive SMD components (four resistors and two capacitors), two SMD LEDs, and one unpackaged integrated circuit (LM555 chipset in bare die form) was embedded in ULTEM, a thermoplastic polyetherimide substrate, using LDW, as shown in Fig. 12.13(a) and (b). Laser micromachining was used to excavate the pockets in the substrate that would contain each component. Once in place, the components were planarized with a layer of polyimide. The interconnects were made by laser micromachining blind vias through the polyimide to expose the contact pads on each device. The metal interconnects were then generated by laser printing a conductive silver ink. The resulting embedded circuit occupied a footprint smaller than a single packaged LM555 chip, as shown in Fig. 12.13(a). Fig. 12.13(b) shows a close-up of the LM555 chip with its laser-printed silver interconnects. It is estimated that these LDW embedded circuits can occupy footprints $\leq$1/4 and thicknesses $\leq$1/10 of those called out in a printed circuit board design, resulting in an overall circuit volume reduction of nearly two orders of magnitude. This shows that LDW processes can fabricate functional electronic circuits buried underneath the surface, with the surface or substrate serving as both circuit board and enclosure.

In Fig. 12.13(c), an array of blue LEDs was laser-transferred into laser-premachined pockets in a 125-μm-thick polyimide foil. After transfer, the LEDs were encapsulated by a polymer and then interconnected with laser-printed silver nanoink lines. In this demonstration, the entire circuit, consisting of the die and the interconnects (except for the power source), was laser transferred. The light emission from the LED array

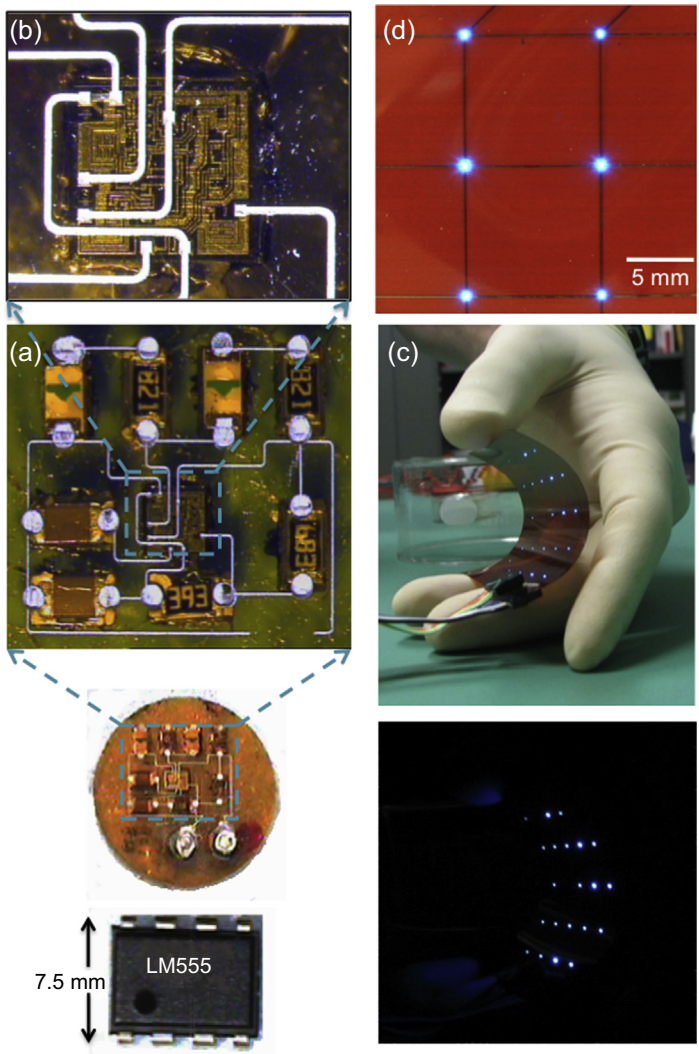

Figure 12.13 Embedded circuits made completely by laser direct write. (a) Optical micrograph of blinker circuit laser-embedded with resistor, light-emitting diode (LED), and capacitor surface-mount devices with an LM555 timing bare-die semiconductor chip in the center, shown to scale next to a packaged LM555 chip for size comparison. (b) Higher-magnification micrograph showing the laser-printed interconnects over the LM555 chip. (c) Array of embedded LEDs on a polyimide substrate. (d) Close-up view of emission of LEDs. (a) and (b) Adapted from A. Piqué, S.A. Mathews, B. Pratap, R.C.Y. Auyeung, B.J. Karns, S. Lakeou. Embedding electronic circuits by laser direct-write, Microelectronic Engineering 83 (11−12) (2006) 2527−2533. © 2006 by Elsevier. (c) and (d) Adapted and reprinted with permission from S.A. Mathews, N.A. Charipar, K. Metkus, A. Piqué, Manufacturing microelectronics using Lase-and-Place, Photonics Spectra 41(10) (2007) 70−74. © 2007 by Laurin Publishing.

embedded on a curved substrate in Fig. 12.13(c) demonstrated the viability of the laser transfer method in preserving the functionality of the LEDs and their interconnects on a flexed substrate.

12.5 Summary and outlook

Laser additive manufacturing is a promising technique for embedding electronics. Two approaches can be used: prefabricated discrete components (eg, SMDs, dies) can be laser transferred directly into a substrate or functional components (eg, interconnects, actives, passives) can be laser printed "on demand" into a substrate. LDW processes can provide all these additive processes as well as subtractive ones in a single tool. Subtractive processes such as laser micromachining are needed to remove material to create cavities for embedding and housing components inside a substrate. The advantage of using discrete components is that they are readily available components with the highest performance, and it is more reasonable to incorporate them into existing architecture rather than to "reinvent the wheel." Many laser-based techniques have been described for transferring these discrete components into a substrate, and some have more potential than others. The requirements for laser-transferring a small discrete component and especially a (thin) die are very stringent. The process or tool must impart just enough energy to release a die, propel it across a finite distance toward a receiving substrate, guide and place it without rotational/displacement error, and be useable for a wide range of die geometries. All of this must be done without degrading any of the die's functional properties, generating excess debris, or contaminating the die or surrounding substrate. Minimizing the laser transfer fluence ($\ll 1$ J/cm^2) is an important parameter that would enable many of these requirements to be satisfied.

LDW was used to successfully transfer and embed many discrete functional components into substrates at relatively low fluence. In addition, functioning interconnects, microbatteries, photovoltaics, and chemical sensors were directly printed from their constituent materials and offer an equivalent alternative to discrete components, depending on the application. These directly printed components would provide even smaller form factors than their discrete components and enable higher integration densities in embedded systems.

There is no doubt that much research is needed to develop new tools for reliably handling ultrasmall and ultrathin electronic components and integrating them into denser circuitry, especially at the packaging and systems level. Laser-based manufacturing is a unique tool that combines both additive and subtractive processes that could help fabricate and embed electronics into new geometries and structures for next-generation applications and technologies.

Acknowledgment

This work was funded by the Office of Naval Research through the Naval Research Laboratory Basic Research Program.

References

[1] J. Govaerts, W. Christiaens, E. Bosman, J. Vanfleteren, Fabrication processes for embedding thin chips in flat flexible substrates, IEEE Transactions on Advanced Packaging 32 (1) (2009) 77−83.

[2] R. Tummala, System scaling: the next frontier for a new era of electronic systems, Chip Scale Review 19 (5) (2015).

[3] R.D. Gerke, Embedded Passives Technology, NASA Report, NEPP, 2005.

[4] D.W. Lee, L. Li, S.X. Wang, J. Lu, C.P. Wong, S.K. Bhattacharya, J. Papapolymerou, Embedded passives, in: D. Lu, C.P. Wong (Eds.), Materials for Advanced Packaging, Springer, New York, 2009, pp. 459−502.

[5] R.M. Marks, Z. Hassan, K.Y. Cheong, Ultrathin wafer pre-assembly and assembly process technologies: a review, Critical Reviews in Solid State and Materials Sciences 40 (2015) 251−290.

[6] H.K. Charles, Advanced wire bonding technology: materials, methods, and testing, in: D. Lu, C.P. Wong (Eds.), Materials for Advanced Packaging, Springer, New York, 2009, pp. 113−179.

[7] J. Hoerber, J. Glasschroeder, M. Pfeffer, J. Schilp, M. Zaeh, J. Franke, Approaches for additive manufacturing of 3D electronic applications, Procedia CIRP 17 (2014) 806−811.

[8] M. Vaezi, H. Seitz, S. Yang, A review on 3D micro-additive manufacturing technologies, International Journal of Advanced Manufacturing Technology 67 (5−8) (2013) 1721−1754.

[9] C.B. Arnold, A. Piqué, Laser direct-write processing, MRS Bulletin 32 (1) (2007) 9−11.

[10] A. Piqué, D.B. Chrisey, Direct-Write Technologies for Rapid Prototyping Applications: Sensors, Electronics and Integrated Power Sources, Academic Press, San Diego, 2002.

[11] J. Bohandy, B. Kim, F.J. Adrian, Metal deposition from a supported metal film using an excimer laser, Journal of Applied Physics 60 (4) (1986) 1538−1539.

[12] F.E. Doany, C. Narayan, Laser release process to obtain freestanding multilayer metal-polyimide circuits, IBM Journal of Research and Development 41 (1−2) (1997) 151−157.

[13] R. Guerre, U. Drechsler, D. Jubin, M. Despont, Selective transfer technology for micro-device distribution, Journal of Microelectromechanical Systems 17 (1) (2008) 157−165.

[14] A.S. Holmes, S.M. Saidam, Sacrificial layer process with laser-driven release for batch assembly operations, Journal of Microelectromechanical Systems 7 (4) (1998) 416−422.

[15] N.S. Karlitskaya, D.F.D. Lange, R. Sanders, J. Meijer, Study of laser die release by Q-switched Nd:YAG laser pulses, in: Proceedings of SPIE, vol. 5448, 2004, pp. 935−943.

[16] N.S. Karlitskaya, J. Meijer, D.F.D. Lange, H. Kettelarij, Laser propulsion of microelectronic components: releasing mechanism investigation, in: Proceedings of SPIE, vol. 6261, 2006, 62612P.

[17] A. Piqué, N.A. Charipar, R.C.Y. Auyeung, H. Kim, S.A. Mathews, Assembly and integration of thin bare die using laser direct-write, in: C.B. Arnold, et al. (Eds.), Proceedings of SPIE, San Jose, vol. 6458, 2007, pp. 645802-1−645802-10.

[18] S.A. Mathews, R.C.Y. Auyeung, A. Piqué, Use of laser direct-write in microelectronics assembly, Journal of Laser Micro/Nanoengineering 2 (1) (2007) 103−107.

[19] S.A. Mathews, N.A. Charipar, K. Metkus, A. Piqué, Manufacturing microelectronics using 'Lase-and-Place, Photonics Spectra 41 (10) (2007) 70−74.

[20] S.A. Mathews, I. Beniam, N. Charipar, A. Piqué, Laser induced forward transfer (LIFT) for direct-write fabrication and assembly of microelectronics, in: 2015 ICALEO (34th

International Congress on Applications of Lasers & Electro-optics) Conference Proceedings: Session LMF1, Paper M101, 2015, pp. 9−13.
[21] V. Marinov, O. Swenson, R. Miller, F. Sarwar, Y. Atanasov, M. Semler, S. Datta, Laser-enabled advanced packaging of ultrathin bare diced in flexible substrates, IEEE Transactions on Components, Packaging and Manufacturing Technology 2 (4) (2012) 569−577.
[22] R. Miller, V. Marinov, O. Swenson, Z. Chen, M. Semler, Noncontact selective laser-assisted placement of thinned semiconductor dice, IEEE Transactions on Components, Packaging and Manufacturing Technology 2 (6) (2012) 971−978.
[23] V. Marinov, O. Swenson, Y. Atanasov, N. Schneck, Laser-assisted ultrathin die packaging: insights from a process study, Microelectronic Engineering 101 (2013) 23−30.
[24] V.R. Marinov, O. Swenson, Y. Atanasov, N. Schneck, Laser-assisted ultrathin die packaging: a route to a new class of microelectronic devices, in: Proceedings of SPIE, vol. 8608, 2013, 86080L-1 − 86080L-19.
[25] R. Saeidpourazar, R. Li, Y. Li, M.D. Sangid, C. Lu, Y. Huang, J.A. Rogers, P.M. Ferreira, Laser-driven micro transfer placement of prefabricated microstructures, Journal of Microelectromechanical Systems 21 (5) (2012) 1049−1058.
[26] R. Saeidpourazar, M.D. Sangid, J.A. Rogers, P.M. Ferreira, A prototype printer for laser driven micro-transfer printing, Journal of Manufacturing Processes 14 (2012) 416−424.
[27] E.E. Kuran, Y. Berg, M. Tichem, Z. Kotler, Integration of laser die transfer and magnetic self-assembly for ultra-thin chip placement, Journal of Micromechanics and Microengineering 25 (4) (2015), 045008.
[28] K. Li, M. Sparkes, W. O'Neill, Comparison between single shot micromachining of silicon with nanosecond pulse shaped IR fibre laser and DPSS UV laser, IEEE Journal of Selected Topics in Quantum Electronics 20 (5) (2014) 0900807 (Fig. 8).
[29] A. Al-okaily, P. Ferreira, Process performance of silicon thin-film transfer using laser micro-transfer printing, in: Proceedings of the ASME 2014 International Mechanical Engineering Congress and Exposition, vol. 2B, 2014 paper no. IMECE2014−37133, pp. V02BT02A043.
[30] A. Piqué, C.B. Arnold, B. Pratap, R.C.Y. Auyeung, H. Kim, D.W. Weir, Laser direct-write of metal patterns for interconnects and antennas, in: Proceedings of SPIE, vol. 4977, 2003, pp. 602−608.
[31] A. Piqué, B. Pratap, S.A. Mathews, B.J. Karns, R.C.Y. Auyeung, M. Kasser, M. Ollinger, H. Kim, S. Lakeou, C.B. Arnold, Laser direct-write of embedded electronic components and circuits, in: Proceedings of SPIE, vol. 5713, 2005, pp. 223−230.
[32] R.C.Y. Auyeung, M.W. Nurnberger, D.J. Wendland, A. Piqué, C.B. Arnold, A.R. Abbott, L.C. Schuette, Laser fabrication of GPS conformal antennas, in: Proceedings of SPIE, 5339, 2004, pp. 292−297.
[33] H. Kim, R.C.Y. Auyeung, S.H. Lee, A.L. Huston, A. Piqué, Laser forward transfer of silver electrodes for organic thin-film transistors, Applied Physics A: Materials Science and Processing 96 (2) (2009) 441−445.
[34] H. Kim, R.C.Y. Auyeung, S.H. Lee, A.L. Huston, A. Piqué, Laser-printed interdigitated Ag electrodes for organic thin film transistors, Journal of Physics D: Applied Physics 43 (8) (2010), 085101.
[35] R.C.Y. Auyeung, H. Kim, S.A. Mathews, A. Piqué, Laser direct-write of metallic nanoparticle inks, Journal of Laser Micro/Nanoengineering 2 (1) (2007) 21−25.
[36] A. Piqué, R.C.Y. Auyeung, K.M. Metkus, H. Kim, S.A. Mathews, T. Bailey, X. Chen, L.J. Young, Laser decal transfer of electronic materials with thin film characteristics, in: Proceedings of SPIE, vol. 6879, 2008, 687911.

[37] A. Piqué, R.C.Y. Auyeung, H. Kim, K.M. Metkus, S.A. Mathews, Digital microfabrication by laser decal transfer, Journal of Laser Micro/Nanoengineering 3 (3) (2008) 163−169.
[38] A.J. Birnbaum, H. Kim, N.A. Charipar, A. Piqué, Laser printing of multi-layered polymer/metal heterostructures for electronic and MEMS devices, Applied Physics A: Materials Science and Processing 99 (4) (2010) 711−716.
[39] H. Kim, J.S. Melinger, A. Khachatrian, N.A. Charipar, R.C.Y. Auyeung, A. Piqué, Fabrication of terahertz metamaterials by laser printing, Optics Letters 35 (23) (2010) 4039−4041.
[40] R.C.Y. Auyeung, H. Kim, A.J. Birnbaum, M. Zalalutdinov, S.A. Mathews, A. Piqué, Laser decal transfer of freestanding microcantilevers and microbridges, Applied Physics A: Materials Science and Processing 97 (3) (2009) 513−519.
[41] A.J. Birnbaum, R.C.Y. Auyeung, K.J. Wahl, M. Zalalutidnov, A.R. Laracuente, A. Piqué, Laser printed micron-scale free standing laminate composites: process and properties, Journal of Applied Physics 108 (8) (2010), 083526.
[42] A.J. Birnbaum, M. Zalalutdinov, K.J. Wahl, A. Piqué, Fabrication and response of laser-printed cavity-sealing membranes, Journal of Microelectromechanical Systems 20 (2) (2011) 436−440.
[43] J. Wang, R.C.Y. Auyeung, H. Kim, N.A. Charipar, A. Piqué, Three-dimensional printing of interconnects by laser direct-write of silver nanopastes, Advanced Materials 22 (40) (2010) 4462−4466.
[44] H. Kim, M. Duocastella, K.M. Charipar, R.C.Y. Auyeung, A. Piqué, Laser printing of conformal and multi-level 3D interconnects, Applied Physics A 113 (1) (2013) 5−8.
[45] R. Modi, H.D. Wu, R.C.Y. Auyeung, C.M. Gilmore, D.B. Chrisey, Direct writing of polymer thick film resistors using a novel laser transfer technique, Journal of Materials Research 16 (11) (2001) 3214−3222.
[46] D. Young, H.D. Wu, R.C.Y. Auyeung, R. Modi, J. Fitz-Gerald, A. Piqué, D.B. Chrisey, P. Atanassova, T. Kodas, Dielectric properties of oxide structures by a laser-based direct-writing method, Journal of Materials Research 16 (6) (2001) 1720−1725.
[47] A. Piqué, D.B. Chrisey, R.C.Y. Auyeung, J. Fitz-Gerald, H.D. Wu, R.A. McGill, S. Lakeou, P.K. Wu, V. Nguyen, M. Duignan, A novel laser transfer process for direct writing of electronic and sensor materials, Applied Physics A − Materials Science & Processing 69S (1999) S279−S284.
[48] C. Zhang, D. Liu, S. Mathews, J. Graves, T.M. Schaefer, B. Gilbert, R. Modi, H.D. Wu, D.B. Chrisey, Laser direct-write and its application in low temperature co-fired ceramic (LTCC) technology, Microelectronic Engineering 70 (1) (2003) 41−49.
[49] C.B. Arnold, R.C. Wartena, K.E. Swider-Lyons, A. Piqué, Direct-write planar micro-ultracapacitors by laser engineering, Journal of the Electrochemical Society 150 (5) (2003) A571−A575.
[50] H. Kim, G.P. Kushto, C.B. Arnold, Z.H. Kafafi, A. Piqué, Laser processing of nano-crystalline TiO_2 films for dye-sensitized solar cells, Applied Physics Letters 85 (3) (2004) 464−466.
[51] H. Kim, R.C.Y. Auyeung, A. Piqué, Laser-printed thick-film electrodes for solid-state rechargeable Li-ion microbatteries, Journal of Power Sources 165 (1) (2007) 413−419.
[52] A. Piqué, S.A. Mathews, R.C.Y. Auyeung, M. Ollinger, H. Kim, B. Pratap, C.B. Arnold, T.E. Sutto, Application of laser direct-write techniques for embedding electronic and micropower components, in: SPIE Proceedings, vol. 5662, 2004, pp. 564−569.
[53] A. Piqué, C.B. Arnold, H. Kim, M. Ollinger, T.E. Sutto, Rapid prototyping of micropower sources by laser direct-write, Applied Physics A: Materials Science and Processing 79 (4−6) (2004) 783−786.

[54] C.B. Arnold, H. Kim, A. Piqué, Laser direct write of planar alkaline microbatteries, Applied Physics A: Materials Science and Processing 79 (3) (2004) 417−420.
[55] M. Ollinger, H. Kim, T.E. Sutto, T.E. Martin, A. Piqué, Laser direct-write of polymer nanocomposites, Journal of Laser Micro/Nanoengineering 1 (2) (2006) 102−105.
[56] M. Ollinger, H. Kim, T.E. Sutto, A. Piqué, Laser printing of nanocomposite solid-state electrolyte membranes for Li micro-batteries, Applied Surface Science 252 (23) (2006) 8212−8216.
[57] T.E. Sutto, M. Ollinger, H. Kim, C.B. Arnold, A. Piqué, Laser transferable polymer-ionic liquid separator/electrolytes for solid-state rechargeable lithium-ion microbatteries, Electrochemical and Solid-State Letters 9 (2) (2006) A69−A71.
[58] J.B. Bates, N.J. Dudney, B. Neudecker, A. Ueda, C.D. Evans, Thin-film lithium and lithium-ion batteries, Solid State Ionics 135 (1−4) (2000) 33−45.
[59] H. Kim, J. Proell, R. Kohler, W. Pfleging, A. Piqué, Laser-printed and processed $LiCoO_2$ cathode thick films for Li-ion microbatteries, JLMN-Journal of Miro/Nanoengineering 7 (2012) 320−325.
[60] J. Pröll, H. Kim, A. Piqué, H.J. Seifert, W. Pfleging, Laser-printing and fs-laser structuring of $LiMn_2O_4$ composite cathodes for Li-ion microbatteries, Journal of Power Sources 255 (2014) 116−124.
[61] H. Kim, R.C.Y. Auyeung, M. Ollinger, G.P. Kushto, Z.H. Kafafi, A. Piqué, Laser-sintered mesoporous TiO_2 electrodes for dye-sensitized solar cells, Applied Physics A: Materials Science and Processing 83 (1) (2006) 73−76.
[62] S. Nakada, M. Matsuda, S. Kambe, Y. Saito, T. Kitamura, T. Sakata, Y. Wada, H. Mori, S. Yanagida, Dependence of TiO_2 nanoparticle preparation methods and annealing temperature on the efficiency of dye-sensitized solar cells, Journal of Physical Chemistry B 106 (2002) 10004−10010.
[63] M. Okuya, K. Nakade, S. Kaneko, Porous TiO_2 thin films systhesized by a spray pyrolysis deposition (SPD) technique and their application to dye-sensitized solar cells, Solar Energy Materials and Solar Cells 70 (2002) 425−435.
[64] A. Piqué, D.B. Chrisey, R.C.Y. Auyeung, S. Lakeou, R. Chung, R.A. McGill, P.K. Wu, M. Duignan, J. Fitz-Gerald, H.D. Wu, Laser direct writing of circuit elements and sensors, in: Proceedings of SPIE, 3618, 1999, pp. 330−339.
[65] A. Piqué, R.C.Y. Auyeung, J.L. Stepnowski, D.W. Weir, C.B. Arnold, R.A. McGill, D.B. Chrisey, Laser processing of polymer thin films for chemical sensor applications, Surface and Coatings Technology 163−164 (2003) 293−299.
[66] A. Piqué, D.W. Weir, P.K. Wu, B. Pratap, C.B. Arnold, B.R. Ringeisen, R.A. McGill, R.C.Y. Auyeung, R.A. Kant, D.B. Chrisey, Direct-write of sensor devices by a laser forward transfer technique, in: Proceedings of SPIE, vol. 4637, 2002, pp. 361−368.
[67] A. Piqué, C.B. Arnold, R.C. Wartena, D.W. Weir, B. Pratap, K.E. Swider-Lyons, R.A. Kant, D.B. Chrisey, Laser-induced forward transfer direct-write of miniature sensor and microbattery systems, in: SPIE Proceedings, vol. 4830, 2003, pp. 182−188.
[68] A. Piqué, C.B. Arnold, R.C. Wartena, B. Pratap, B. Shashishekar, K.E. Swider-Lyons, D.W. Weir, R.A. Kant, Laser direct-write of miniature sensor and microbattery systems, in: RIKEN Reviews, vol. 50, 2003, pp. 57−62.
[69] P.K. Wu, B.R. Ringeisen, D.B. Krizman, C.G. Frondoza, M. Brooks, D.M. Bubb, R.C.Y. Auyeung, A. Piqué, B. Spargo, R.A. McGill, D.B. Chrisey, Laser transfer of biomaterials: matrix-assisted pulsed laser evaporation (maple) and maple direct write, Review of Scientific Instruments 74 (4) (2003) 2546−2557.
[70] K. Komorita, T. Sano, H. Yamada, I. Miyamoto, Oxidation state control of micro metal oxide patterns produced by using laser-induced forward transfer technique, in: Proceedings of SPIE, vol. 4830, 2003, pp. 20−24.

[71] C. Boutopoulos, V. Tsouti, D. Goustouridis, S. Chatzandroulis, I. Zergioti, Liquid phase direct laser printing of polymers for chemical sensing applications, Applied Physics Letters 93 (19) (2008), 191109.
[72] V. Tsouti, C. Boutopoulos, D. Goustouridis, I. Zergioti, P. Normand, D. Tsoukalas, S. Chatzandroulis, A chemical sensor microarray realized by laser printing of polymers, Sensors and Actuators B: Chemical 150 (1) (2010) 148−153.
[73] R.C.Y. Auyeung, H. Kim, N.A. Charipar, A.J. Birnbaum, S.A. Mathews, A. Piqué, Laser forward transfer based on a spatial light modulator, Applied Physics A: Materials Science & Processing 102 (1) (2011) 21−26.
[74] R.C.Y. Auyeung, H. Kim, S.A. Mathews, A. Piqué, Laser forward transfer using structured light, Optics Express 23 (1) (2015) 422−430.
[75] R.C.Y. Auyeung, H. Kim, S.A. Mathews, A. Piqué, Spatially modulated laser pulses for printing electronics, Applied Optics 54 (31) (2015) F70−F77.
[76] A. Piqué, H. Kim, R.C.Y. Auyeung, A.T. Smith, Laser forward transfer of functional materials for digital fabrication of microelectronics, Journal of Imaging Science and Technology 57 (4) (2013), 040404.
[77] A. Piqué, S.A. Mathews, B. Pratap, R.C.Y. Auyeung, B.J. Karns, S. Lakeou, Embedding electronic circuits by laser direct-write, Microelectronic Engineering 83 (11−12) (2006) 2527−2533.

Aerospace applications of laser additive manufacturing

13

R. Liu, Z. Wang, T. Sparks, F. Liou, J. Newkirk
Missouri University of Science and Technology, Rolla, Missouri, United States

13.1 Introduction

Additive manufacturing (AM) has been used in aerospace applications from the beginning. In the late 1980s the first commercial rapid prototyping machine was developed at 3D Systems. The American aerospace manufacturer Pratt & Whitney was one of the first five customers [1]. Boeing, for example, has approximately 300 different part numbers on 10 different aircraft production programs, which amounts to more than 20,000 nonmetallic additive manufactured parts that are on vehicles delivered to their customers. Approximately 150 parts in the forward fuselage area of the F/A-18 Super Hornet are produced through selective laser sintering [2]. AM, which is a completely new manufacturing process compared with the conventional subtractive manufacturing process, has profoundly influenced product design, manufacturing, and assembly in the aerospace industry. It not only plays a role as a rapid prototyping technology for saving capital and time during the product development period, it can also be adopted for rapid tooling, direct part manufacturing, and repair in the aerospace industry. Because of recent developments, AM has rapidly become a strategic technology that will generate revenue throughout the aerospace supply chain [3]. This chapter discusses new opportunities and benefits brought by AM technologies for aerospace applications.

This chapter is organized with the following structure. Section 13.1 gives a brief introduction of aerospace applications of AM and discusses the characteristics of aerospace components favoring AM. Section 13.2 describes metallic and nonmetallic aerospace components fabricated by different AM processes. Section 13.3 discusses repair applications for aerospace components, illustrating the advantages, general processes using AM for repair. Application examples both from commercial and academia areas are analyzed in Section 13.1 and 13.2. Finally, this chapter discusses the challenges of applying AM to the aerospace industry and potential future aerospace applications.

13.1.1 Characteristics of aerospace components favoring additive manufacturing

Aerospace components usually have the following characteristics, which make them highly suitable for fabrication by AM:

- *Components have a complex geometry or a large volume envelope—to—volume ratio*: Aerospace components often have complex geometries because aerospace applications

Laser Additive Manufacturing. http://dx.doi.org/10.1016/B978-0-08-100433-3.00013-0
Copyright © 2017 Elsevier Ltd. All rights reserved.

usually require components with integrated functions. For instance, structural components may also act as conduits, such as an airfoil with an embedded cooling channel or an engine turbine blade that may also have an internal structure for coolant. Furthermore, geometric specifications of parts may be defined by complex mathematical formulae based on, for example, fluid flow. On the other hand, many aerospace components have a large volume envelope—to—volume ratio, as in thin-walled structures for example, combustion chambers or a turbine blade. Those features make the tool path planning algorithm very complicated, time-consuming, and material-consuming by conventional computer numerical control (CNC) machining. The capability for freeform fabrication makes AM very suitable for these kinds of aerospace components.

- *Difficult-to-machine parts and high buy-to-fly ratio*: Aerospace components are usually made from advanced materials, such as titanium alloys, nickel-based superalloys, special steels, or ultrahigh-temperature ceramics, which are difficult, costly, and time-consuming to manufacture. In addition, current buy-to-fly ratios result in a massive waste of materials.
- *Small production runs*: AM processes tend to be more expensive for large production runs than conventional machining processes. Compared with the conventional machining processes, however, AM does not need design and fabricate fixtures, molds, or dies. Therefore AM is most competitive for customized parts and applications with small production runs, which are common in the aerospace industry.
- *Parts that need quick turnaround time*: Many aircraft have a long working life; some airplanes have an average service life of more than 30 years. Maintaining and replacing old tooling is a notable inventory cost for manufacturers. AM enables these parts to be quickly shipped and installed in a broken plane to help get it back in the air and making money for the airline [3]. According to Airbus, the turnaround for test or replacement parts can now be as short as 2 weeks.
- *High-performance parts*: Aerospace components require that materials be lightweight with a high strength-to-weight ratio to improve fuel efficiency and reduce emissions. Furthermore, some aerospace components work in extreme conditions, such as ultrahigh or low temperatures or extreme chemical environments. Engine components are subject to very high temperatures in which innovative cooling solutions are used and internal components are required to be made from flame-retardant materials. AM brings new opportunities to fabricate tailored parts in aerospace applications [1].

13.2 Aerospace component fabrication with additive manufacturing

13.2.1 Overview of additive manufacturing methods for aerospace applications

In the manufacturing industry, the main applications of additive manufacturing include rapid prototyping, rapid tooling, direct part production, and part repair of metal, plastic, ceramic, and composite materials [4]. Both metallic and nonmetallic parts fabricated by AM technology have potential applications in the aerospace industry. A number of different technologies developed for metal AM processes can be classified by the energy source (laser beam, electron beam, and arc), feedstock state (metal powder, wire, and sheet), or the method of feed material (blown powder and powder

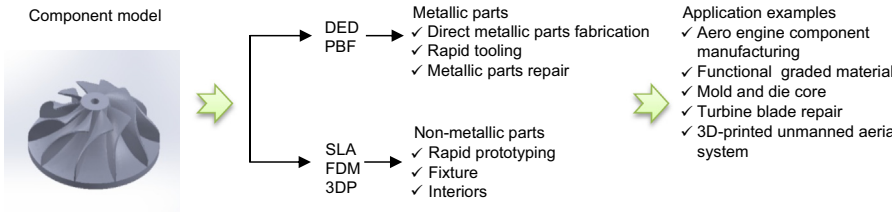

Figure 13.1 Overview of additive manufacturing methods for aerospace applications. *3D*, three-dimensional; *3DP*, three-dimensional printing; *DED*, directed energy deposition; *FDM*, fused deposition modeling; *PBF*, powder bed fusion; *SLA*, stereolithography.

bed). The two primary metal AM categories are (1) directed energy deposition (DED) [5–7], which covers laser metal deposition (LMD)—also known as laser engineering net-shape (LENS) or direct metal deposition—and electron beam free-form fabrication [8]; and (2) powder bed fusion (PBF), which includes selective laser sintering [9], selective laser melting (SLM) [10], and electron beam melting [11]. As shown in Fig. 13.1, metallic AM processes for aerospace applications include direct metallic parts fabrication, rapid tooling, and metallic parts repair. Application examples include aero engine component manufacturing, functional graded materials, mold and die cores for casting, turbine blade repair, and so on. As for nonmetallic parts such as plastics, ceramics, sand, and composite materials, the typical available AM technologies are stereolithography [12], multijet modeling [13], fused deposition modeling (FDM) [14], freeze-form extrusion fabrication [15], and three-dimensional printing (3DP) [16]. The application areas of nonmetallic parts include rapid prototyping, fixtures, and interiors, among others.

13.2.2 Directed energy deposition in aerospace applications

DED processes [1] enable the creation of parts by melting material as it is being deposited. Although this basic approach can work for polymers, ceramics, and metal matrix composites, it is predominantly used for metal powders or wires. A wide range of metals and alloys, such as titanium, inconel, stainless steel, aluminum, and their alloys, is broadly applied in the aerospace industry and can be fabricated by DED processes. DED processes use a focused energy source (a laser beam, electron beam, or arc) to locally melt feedstock material (powder or wire) and build up three-dimensional (3D) components. Compared with PBF processes, multiple-axis deposition (such as additional rotary axis for substrate) and multiple material delivery (such as multipowder hoppers) can be used in DED processes. In addition, DED processes can also be easily integrated with conventional subtractive manufacturing for finishing machining. The multiaxis deposition capability of DED processes enable the fabrication of complex geometry parts without support structures, such as thin-walled structures, overhauling, and inner channel feature parts for aerospace components. DED processes can also produce functionally graded material (FGM) parts with multiple powder hoppers with different materials. Compared with the welding process, the low heat input along with the DED process's clamping flexibility can be adopted for repairing high-

value aerospace components such as turbine blades, blisks, and engine combustion chambers.

DMG Mori [17] developed the LASERTEC 65 3D hybrid manufacturing system (AM and subtractive manufacturing) using the LMD process. The hybrid manufacturing system has automated switching between laser deposition and milling with shuttle handling via the HSK interface. The large work area can support pieces with dimensions up to 500 mm in diameter and 350 mm high, a maximum weight of 600 kg, and a layer thickness varying from 0.1 to 5 mm. It is 10 times faster than the current powder bed process, and machining can be completed without a process chamber (works with most materials). Fig. 13.2 shows an example of a turbine housing made from stainless steel using the hybrid manufacturing process. The dimensions of the turbine housing are 180 × 150 mm, and build-up time is 230 min for deposition and 76 min for milling. This hybrid manufacturing process produces quality finished parts by combining the precise accuracy of CNC machining and the freeform fabrication capability of the AM process.

TWI [18] adopted a five-axis LMD process for overhanging geometries without support mechanisms. A helicopter engine combustion chamber, which is a thin-walled structure, was successfully built using this process (as shown in Fig. 13.3), with an accuracy of 0.8 ± 0.9 mm. Mechanical testing showed that wall density was more than 99.5% throughout the whole part. A total of 700 g of powder were fused in the part and 1.2 kg passed through nozzle, which means there was about 70% powder efficiency and the deposition rate was around 0.9 kg/h. The buy-to-fly ratio was obviously less compared with subtractive machining. This combustion chamber was 300 mm in diameter and 90 mm high, with a build time reduced from months to 7.5 h.

Optomec [19] developed a five-axis hybrid manufacturing system using the LENS process. The LENS 850-R system has a large work envelope (900 × 1500 × 900 mm) to build or repair large-volume components such as blisks, impellers, and shafts. The deposition rates are up to 0.5 kg/h for standard steels, titanium, and nickel alloys.

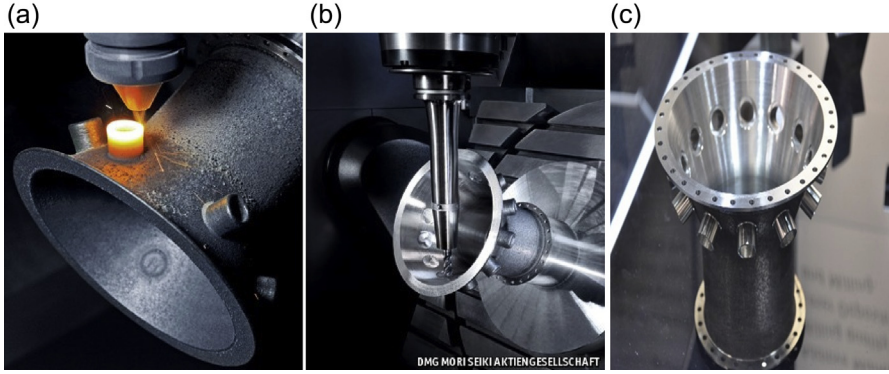

Figure 13.2 Turbine housing fabricated by the LASERTEC 65 3D System using (a) multiaxis deposition and (b) multiaxis machining. (c) Finished part.
Courtesy DMG Mori and Siemens.

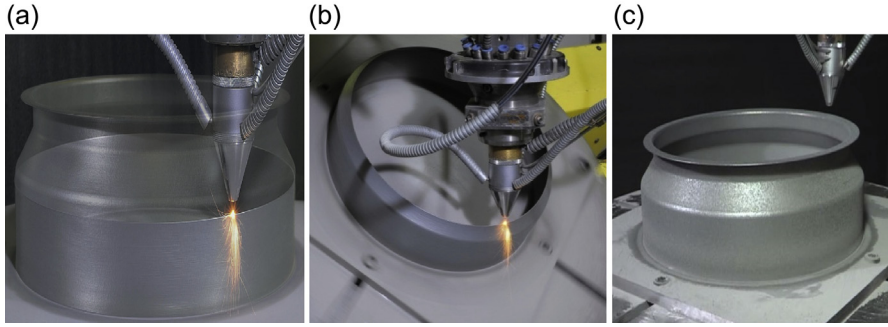

Figure 13.3 IN718 helicopter engine combustion chamber fabricated by a five-axis LMD process: (a) deposition showing the 2.5-dimensional tool path; (b) multiaxis deposition; and (c) the finished part.
Courtesy TWI.

Graded materials can be deposited by multiple powder feeders (two feeders hold up to 14 kg of powder each in the LENS 850-R system). As shown in Fig. 13.4, a one-sixth-scale mixing nozzle for a gas turbine exhaust was fabricated for Bell Helicopter using the LENS process.

In addition to commercial applications in the aerospace industry, there are also examples from academia. Liou et al. [20] developed a hybrid process combining multiaxis laser deposition and CNC machining. The hybrid process provides greater build capabilities in accuracy and surface quality for freeform fabrication, which was successfully applied to build and repair functional metallic parts. Xue and Islam [21], from the Integrated Manufacturing Technologies Institute of the National Research Council in Canada adopted the LMD process to directly fabricate metallic components.

Figure 13.4 Exhaust duct fabricated using the laser engineering net-shape process.
Courtesy Optomec.

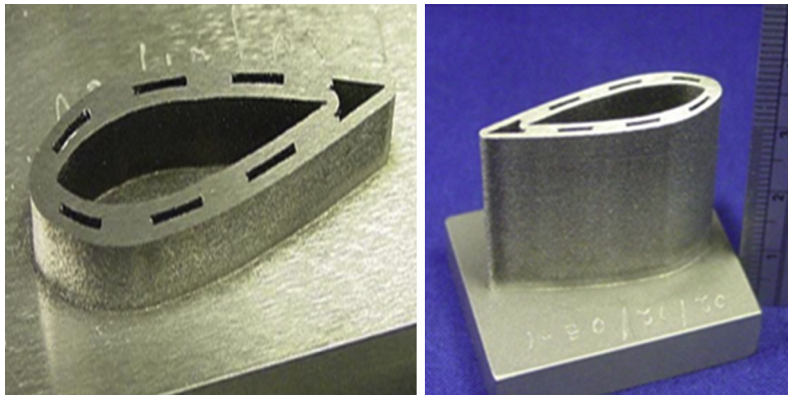

Figure 13.5 Ti-6Al-4V airfoils with embedded cooling channels built using the laser metal deposition process.
Courtesy Integrated Manufacturing Technologies Institute of the National Research Council, Canada.

Materials including nickel-based IN-625 and IN-738 superalloys, titanium-based Ti-6Al-4V alloy, cobalt-based Stellite 6 alloy, and iron-based CPM-9V tool steel were investigated. Mechanical property testing showed that the LMD-processed materials are comparable to, and sometimes better than, conventionally cast and wrought materials. As Fig. 13.5 shows, the LMD process has been used successfully to build net-shape Ti-6Al-4V airfoils with embedded cooling channels, which accurately represent the geometric features described in the computer-assisted design (CAD) model.

13.2.3 Powder bed fusion in aerospace applications

Different from the DED process, PBF-based AM processes spread a powder layer onto a substrate plate and selectively melt the powder with a focused energy source (a laser beam or electron beam) to build 3D parts. A wide range of materials—typically stainless and tool steels, titanium and its alloys, nickel-based alloys, and some aluminum alloys—are available for aerospace applications using PBF-based AM processes. A key advantage of the PBF process is that it can serve as an in-process support structure for overhangs and undercuts, and therefore complex shapes with a high geometric accuracy ($\pm$0.05 mm) can be manufactured; this separates this AM technology from the DED process [22]. It provides a great capability for optimizing the topology of component design and functional integration for aerospace applications. Available commercial systems include LaserCUSING from Concept Laser, 3DP from ExOne, direct metal laser sintering from EOS, SLM from Renishaw and SLM Solutions, and electron beam melting from Arcam.

GE Aviation [23] uses EOS's metal PBF machine to produce their next-generation jet engine components using the direct metal laser sintering process. The AM-fabricated part that gets the most attention is the new fuel nozzle shown in Fig. 13.6. Each LEAP engine has inside it 19 fuel nozzles created via 3DP. The new design features

Figure 13.6 GE Leap Engine fuel nozzle created using direct metal laser melting via the EOS metal powder bed fusion machine.
Courtesy GE Aviation and EOS.

have more intricate cooling pathways and support ligaments, which result in five times the service life compared with the predecessor part made by conventional manufacturing. The AM process allows engineers to use a simpler design that reduces the number of brazes and welds from 25 to only 5; the number of parts used to make the nozzle was reduced from 18 to 1. In addition, the weight of these nozzles is 25% lighter than that of the predecessor part.

Concept Laser [24] adopted the SLM process to fabricate aircraft components with a "bionic" design using their LaserCUSING system. An example of the bracket connector used in the Airbus A350 XWB is shown in Fig. 13.7. The bone-like porous structure significantly reduces the weight. The component was previously a milled part made of aluminum. Now it is made of titanium using AM and is significantly lighter. The new structure design is more than 30% lighter than conventional designs realized using casting or milling processes. The considerable weight reduction results in lower fuel consumption and the potential to increase the load capacity of the aircraft. On the other hand, toolless fabrication with the Concept Laser SLM process saves money and shortens the development time by up to 75%: Component development time was previously 6 months but is now down to 1 month.

ExOne [25] developed another powder bed−based AM process called "digital part materialization," otherwise known as 3DP. Since the process uses a selective-spraying liquid binder to solidify a layer, the material could be sand, metal, or glass. For the aerospace industry, 3DP in sand offers the largest build size available, capably of printing parts as large as 1800 × 1000 × 700 mm (70 × 39 × 27 in.). Standard foundry

Figure 13.7 The first titanium bracket connector produced using additive manufacturing on board the Airbus A350 XWB.
Reproduced from Airbus. Cabin bracket produced on Concept Laser's LaserCUSING machine.

industry materials are used, enabling the process to be easily integrated into existing manufacturing and foundry procedures. The large build volume and high build rate combine to make patternless production a reality for metal-based prototype castings and low-volume production using aluminum and copper alloys, gray and ductile iron, and magnesium. Applications include complex gear cases and covers, fuel tanks, transmission housings, and components requiring draft-free walls, lightweight engine parts, and structural hinges. The Airbus A320 door hinge cores and casting are large-component casting examples fabricated by 3DP [26].

13.2.4 Nonmetallic parts fabricated with additive manufacturing in aerospace applications

In addition to the fabrication of direct metallic components by AM processes for use in aerospace applications, the aerospace industry also has a great demand for the AM of non-metallic materials such as plastics, wax, sand, ceramics, and composites. The application areas cover rapid prototyping, tooling, and molding and direct part manufacturing. Available commercial systems for fabricating non-metallic parts include stereolithography, multijet printing from 3D Systems, FDM from Stratasys, and 3DP from ExOne, among others.

Stratasys [27] used its FDM system to discover a wide range of applications covering rapid prototyping, manufacturing tooling, and parts production with aerospace companies such as Piper Aricraft, Bell Helicopter, Aerialtronics, and NASA. The free-form fabrication capability provided by AM makes prototyping much easier, shortens the product development cycle, and reduces costs. For example, the Gas Turbine Research Establishment [28] used the FDM machine from Stratasys to prototype a jet engine. There are about 2500 engine components included in the assembly. In the past, the Gas Turbine Research Establishment would have taken a minimum of 1 year and paid an estimated $60,000 to build the physical prototype assembly

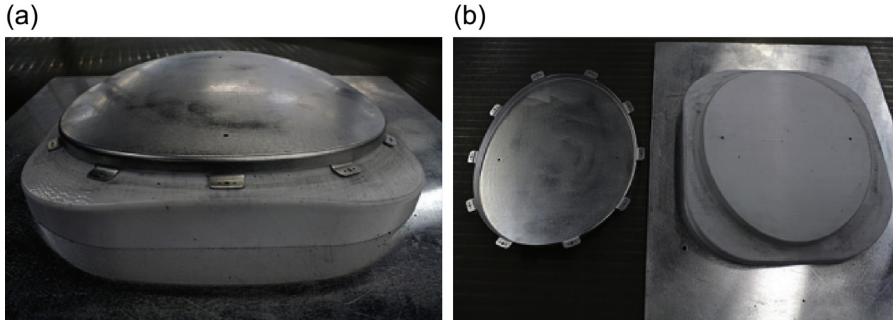

Figure 13.8 Piper Aircraft used fused deposition modeling (FDM) to make tools for hydroforming aluminum structural components. (a) An aluminum window pan on top of the FDM tool. (b) An aluminum window pan (left) and the FDM tool.
Courtesy Stratasys and Piper Aircraft.

by CNC machining. However, the AM process for prototyping cuts that time from 1 year to 6 weeks and reduces the cost from $60,000 to $20,000. Fit-for-purpose manufacturing tools made by AM have improved quality and production efficiency. For example, Piper Aircraft [29] uses the FDM process to make tooling for hydroforming aluminum structural components. Fig. 13.8 shows an aluminum window pan built using the tool made by the FDM machine. Piper Aircraft uses hydroforming to produce hundreds of aluminum structural components of aircraft, such as the inner frame, gussets, brackets, and skins. In the past, tools were produced by CNC machining for use in hydroforming machines. The amount of time required for programming and machining time, the necessary skilled labor, and the considerable material waste involved in machining resulted in machining complex form tools being very expensive. By contrast, FDM tooling reduces machining time by about 68%: from 14 to 4.5 days. High-performance thermoplastic can be adopted for hydroforming applications. For instance, ULTEM 9085, a flame-retardant resin, can withstand pressures up to 10,000 psi and can be produced by Stratasys's Fortus machine.

The FDM process can also be used to directly manufacture aircraft parts. Bell Helicopter [30] builds tough polycarbonate wiring conduits for their heavy-lift "tilt-rotor" Osprey; these conduits are shown in Fig. 13.9. Technicians installed the branching conduits in six mating sections inside the Osprey's twin vertical stabilizers for on-the-ground testing of its wiring. After some minor variations, the team requested five more complete sets for a total of 42 conduit models. It took only 2.5 days to make them all. In the past it would have taken take 6 weeks if the prototypes were made of cast aluminum. NASA [31] also adopted Stratasys's 3D printer for the Mars rover; about 70 of the parts that make up the rover were built digitally, directly from computer designs, in a production-grade heated chamber.

Another interesting example is a fully nonmetallic gas turbine engine fabricated by AM. The program, entitled "A Fully Non-Metallic Gas Turbine Engine Enabled by Additive Manufacturing," was sponsored by the NASA Aeronautics Research Institute [32]. The objective of this program was to use lightweight, high-temperature-resistant

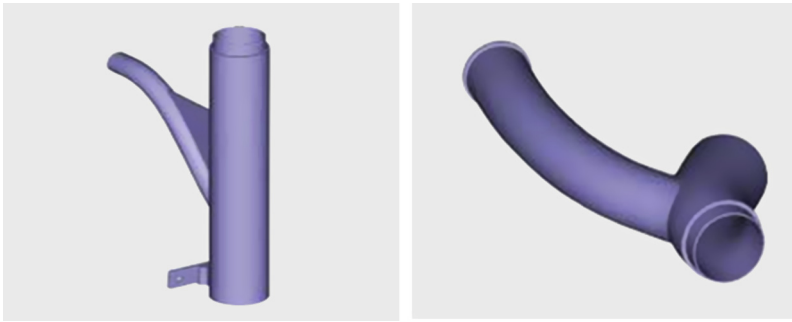

Figure 13.9 Polycarbonate wiring conduits made by fused deposition modeling. Courtesy Stratasys and Bell helicopter.

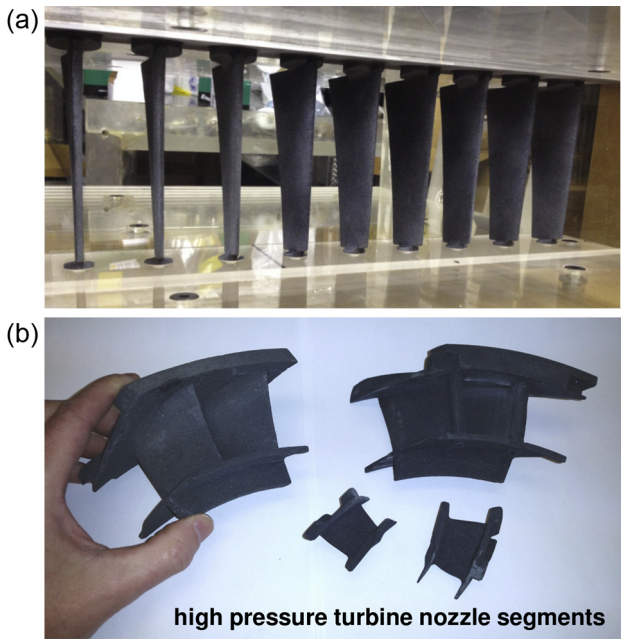

Figure 13.10 Nonmetallic gas turbine engine fabricated using additive manufacturing processes. (a) Compressor inlet guide vanes made from a polyetherimide composite using the fused deposition modeling process. (b) Turbine nozzle segments made from ceramic matrix composite using 3DP.
This excerpt is taken from 20150020812/GRC-E-DAA-TN25404, "A Fully Non-Metallic Gas Turbine Engine Enabled by Additive Manufacturing," and used with permission of NASA.

composite materials to improve engine efficiency. The first comprehensive evaluation of emerging materials and manufacturing technologies that enable fully nonmetallic gas turbine engines for reduced aircraft emissions, fuel burn, and noise was conducted. FDM was used to deposit polymer matrix composites, and the first polyetherimide composite was adopted to produce the compressor inlet guide vanes and acoustic liner (shown in Fig. 13.10(a)). The binder jet process was adapted for fabricating ceramic matrix composites (CMCs) using the M-Flex machine from ExOne. The first high-pressure CMC turbine nozzle segments were produced (Fig. 13.10(b)).

The aerospace industry also has a great demands on ceramic components, especially those made from ultra-high-temperature ceramics (UHTCs), such as ZrB_2, ZrC, TiC, and others, which have an excellent capability to withstand extreme high temperatures and tough chemical environments. Such parts can be applied in hypersonic flight systems and rocket propulsion systems. Since UHTC components are extremely brittle, it is difficult to fabricate them using a conventional subtractive manufacturing process. The AM process provides a great potential to make complex geometric UHTC components for the aerospace industry. Leu et al. [33] used ZrB_2 by selective laser sintering to fabricate a fuel injector strut with crossing channels inside that could potentially be used to provide resistance to extremely high temperatures in a hypersonic aircraft engine. Leu et al. also developed free-form extrusion fabrication for ceramic components.

13.3 Aerospace component repair with additive manufacturing

13.3.1 Background

13.3.1.1 Why repair aerospace components?

High-performance aerospace parts such as compressors, blisks, turbines, blades, and airfoils are expensive because they are typically made from high-value materials (ie, Ti-6Al-4V and Inconel 718) and involve complex processing during manufacturing [34]. Aerospace components may be subject to corrosion, impacts, variable thermal cycles and stresses, and other conditions that could cause defects or cracking during the service life. Fatigue and stress cracks are common initiators of failures that cause high-performance and high-value components to be scrapped. Defects such as milling ball indentation and cutter pull out may also occur during the manufacturing process. Because of the extreme cost of materials and labor for fabricating high-value components, it is necessary to repair those components instead of replacing them.

13.3.1.2 Why use additive manufacturing for repair?

Conventionally, the welding process has been used for repair. One of the first methods was tungsten inert gas welding [35]. This method is easy to perform, but it produces a lot of heat that can cause high residual stresses, resulting in distortion and heat-related effects in the base metal [36]. Plasma transferred arc welding [37] and electron beam

welding [38] are alternative processes that satisfy a lower heat input but need a more complex and expensive apparatus. The high-velocity oxyfuel thermal spraying technique [39] is used in many industries. There is less component distortion than with tungsten inert gas welding, and it has many advantages over plasma spraying, including deposition of a thicker and lower porosity coating. However, control of the depth and spread of the deposited material is not possible. In conclusion, conventional welding processes and thermal spraying techniques do not allow control of the deposit of exact materials with low input heat to melt and bond materials to the base metal.

AM technologies, through adding materials layer by layer to make parts, provide new opportunities to repair high-value metal components. The basic principle of the AM process used for repair is a laser beam that creates a metallurgical bond between the damaged surface area of a part, known as the substrate, and the added repair material, which is a metal powder [40]. For example, the LMD process could deposit local powder to the defect area according to the defect geometry. Compared with conventional repair techniques, the low input heat of AM leads to a small heat-affected zone in the surrounding substrate materials, causing minimal distortion, which allows AM to be used to create thin-walled structures such as wing spars or bulk heads for aircraft [41]. Distortion-sensitive components or components made by "nonweldable" materials that previously had to be scrapped because of the lack of a suitable repair technique can now be repaired with AM [7].

13.3.2 How does additive manufacturing work for repair?

13.3.2.1 Hybrid manufacturing process for repair

As illustrated in Fig. 13.11, a typical layout of the hybrid manufacturing process for component repair includes two major systems: an LMD system and a CNC milling machine system. The LMD process provides the ability to spread metal powder locally in the defect area. Combining AM and CNC results in a hybrid process that can provide greater build capability, better accuracy, and better surface finishing because the benefits of both processes are included [42,43]. In addition, the multiaxis CNC machine is able to do multiaxis deposition and machining for complex aerospace components such as blisks and turbine blades.

13.3.2.2 General repair process

In general there are three stages for the repair process: the repair preparation stage, the manufacturing stage, and the evaluation stage, as shown in Fig. 13.12. During the first stage, repair preparation, the worn component is evaluated in terms of whether it is cost-effective to repair it using the AM process, whether there was a collision with the deposition nozzle, whether the defect area needs machining, and whether the defect surface is accessible by the powder. After evaluation, the worn component is measured and compared with its nominal CAD model to extract the worn area. Common measurement methods, such as a touch trigger probe, charge-coupled device camera, and laser sensor,

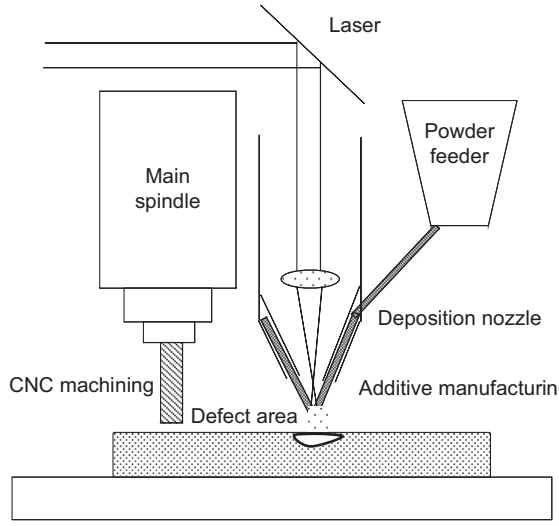

Figure 13.11 Hybrid manufacturing process for component repair.

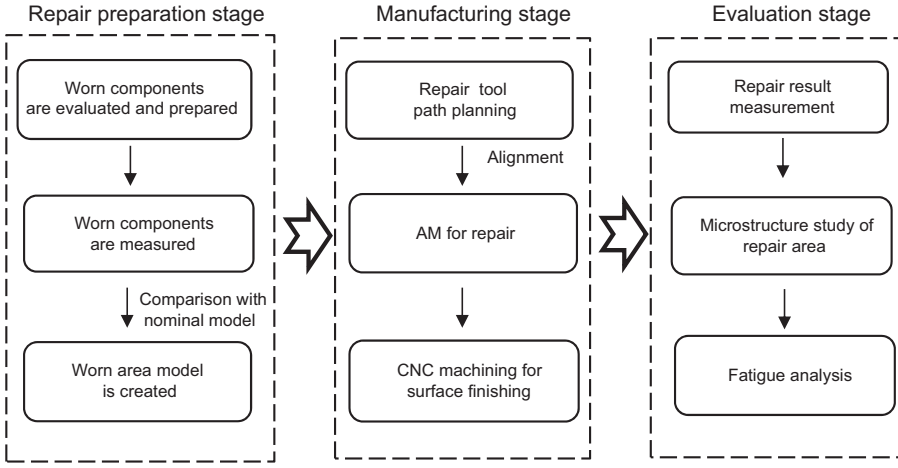

Figure 13.12 Overview of the general repair process. *AM*, additive manufacturing; *CNC*, computer numerical control.

can be divided into two categories: contact and noncontact [44]. The second stage of repair is the manufacturing process, during which the deposition tool path is generated according to the model of the worn area, and the hybrid process is adopted to repair the worn area and surface finishing. The final stage is evaluation of repair, when the resulting repair is measured and evaluated in terms of component tolerance. Mechanical properties such as ultimate tensile strength, yield strength, and hardness can be tested and microstructures can be studied. Fatigue analysis is also necessary to represent the repair

quality. Because components have different working environments and fatigue types, fatigue analysis should correspond to the practical situation.

13.3.3 Repair examples for aerospace applications

Optomec [45] enables aircraft engine components to be repaired using the LENS process. LENS-based repair solutions can precisely add material to worn components to restore their geometry. Integrally bladed rotors, also known as blisks, are high-value components that may cost tens or hundreds of thousands of dollars to fabricate. Without repair, any single airfoil that is worn out causes entire blisks to be scrapped. For example, a T700 blisk that was made from AM355 steel and suffered from erosion on the airfoil's leading edges during service was repaired with the LENS process. Fig. 13.13 illustrates the repair of the leading edge of a Ti64 airfoil, the blisk after deposition, and the blisk after finishing. Optomec used a cobalt-based wear-resistant material to repair the leading edge. The unique capabilities of the LENS repair system include [45]:

- *Low heat input*: The airfoil does not distort beyond dimensional limits.
- *Small heat-affected zone*: This minimizes degradation of the mechanical properties of the airfoil.
- *Superior mechanical properties*: LENS Ti-6Al-4V fatigue properties are equivalent to those of the wrought material.
- *Excellent quality*: Full environmental control ensures extremely low microporosity levels.
- *Complex shapes*: Virtually any cutout can be filled.
- *Greater repair access*: Even areas not in the line of sight can be repaired.
- *Near net shape*: The shape minimizes finishing time.

RPM Innovations [41,46] demonstrated a low-wattage (<500 W) repair using the LENS process. A Ti-6Al-4V bearing housing from a gas turbine engine was repaired to demonstrate the repair process. The bearing seating area was worn to an out-of-tolerance condition, and the housing was considered scrap. The process was used to build up the worn area, which was followed by final machining to print tolerances.

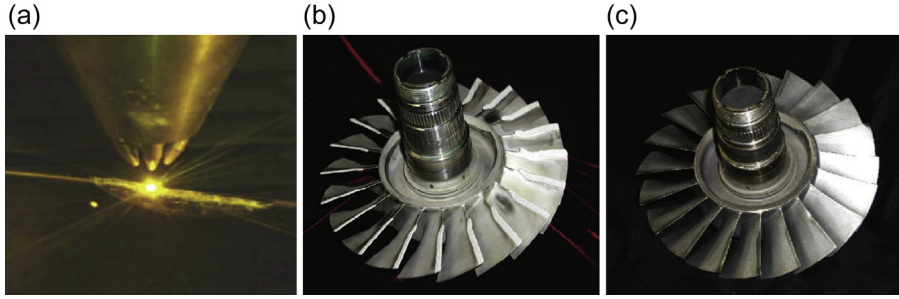

Figure 13.13 T700 blisk repair using the laser engineering net-shape process: (a) in-process repair of the leading edge of a Ti64 airfoil, (b) the blisk after deposition, and (c) the blisk after finishing.
Courtesy Optomec.

This housing was successfully repaired with no measurable distortion, and it completed an evaluation run in a test engine. The repair costs were about 50% of new pricing, plus it saved all of the materials that would be required to manufacture a new housing. Delivery for the repaired housing was a few days compared to several weeks for a new housing.

The European Commission [7] launched project FANTASIA (flexible and near-net-shape generative manufacturing chains and repair techniques for complex-shaped aero engine parts) in June 2006. The Fraunhofer Institute for Laser Technology (ILT) (Germany) joined the project with three major aero engine and component manufacturers, three repair excellence centers as end users, and five industrial partners. The objective was to reduce repair costs by at least 40% and reduce part repair turn-around time by 40% using AM. Some components that previously had to be discarded because of a lack of a suitable repair technique can now be repaired with the help of LMD. Fraunhofer ILT has been successfully certified by Rolls-Royce Deutschland for 15 different repair applications, two of which are for the repair of BR715 high-pressure turbine and BR715 high-pressure compressor front drum [7,47]. Geometric features on the surface of a BR715 high-pressure turbine case, such as bosses, brackets, and flanges, are repaired locally with just one layer deposited. Because of the minimized heat input of the LMD process, distortion of the component can be avoided almost completely. The contamination (oxidation)—free LMD result is guaranteed by a proper local gas shielding using a newly developed powder nozzle.

In addition to examples from commercial systems, universities and research institutes have also investigated using AM for repair applications in the aerospace industry. Gao et al. [48,49] proposed and developed an integrated repair solution adapted to worn component geometry for aerospace industries. Based on the scanned repair model with different defects, a reverse engineering—based geometry reconstruction method was developed to create a normal model of a worn component. Xue and Islam [21] demonstrated repair of the tips and seal of a damaged IN738 blade using the LMD process, as shown in Fig. 13.14. Richter et al. [50] applied LMD to repair a Ti6242

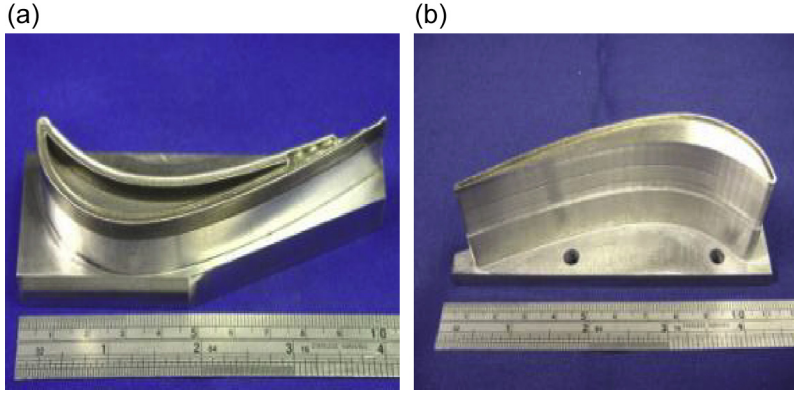

Figure 13.14 Repair to the tip of a cast IN738 blade (a) and the rebuild of the damaged seal (b). Courtesy Integrated Manufacturing Technologies Institute of the National Research Council, Canada.

blade and studied the microstructure, hardness, residual stress, mechanical properties, and fatigue of the repaired parts. Jones [51] combined laser cladding, machining, and in-process scanning in a single machine to realize automated component alignment, defect characterization, defect removal, and defect repair.

13.4 Challenges and potential future applications

13.4.1 Challenges of additive manufacturing for aerospace applications

AM technologies have been merged and developed for more than 25 years, transforming significantly from rapid prototyping to rapid tooling, direct part manufacturing, and repair. AM technologies have revealed great capabilities and the potential to reduce component weight, improve fuel efficiency, and reduce cost and turnaround time for aerospace applications. However, technical challenges of AM remain for aerospace applications, related to design, material characteristics, process control, process understanding, and modeling. The following summarizes the main challenges from publications and workshops [52].

- *Aerospace component design based on AM*: New designs based on the AM process, such as the new GE Aviation LEAP engine fuel nozzle and the "bionic" design of the bracket connector used in the Airbus A350 XWB, appeared in the aerospace industry and demonstrated the unique capabilities of AM processes, including their ability to fabricate complex geometry, handle functional complexities, and greatly enhance the freedom of designers. Progress is still required for conceptual design methods to aid designers in defining and exploring design spaces enabled by AM, methods for simultaneous product-process design and multifunctional design, and methods by which to assess lifecycle costs and the effects of parts and products fabricated by AM. A new foundation for CAD systems that overcome the limitations of parametric, boundary representation solid modeling in representing very complex geometries and multiple materials is needed [53].
- *Material characteristics for aerospace components fabricated by AM processes*: AM processes offer the unique advantage of fabricating difficult-to-machine materials, such as titanium alloys, nickel alloys, special steels, and ceramics, for the aerospace industry. However, there is no standard material characteristics database within the AM industry to provide mechanical properties fabricated by different AM processes, such as specifications of the mechanical properties of available materials and more detail on how parts made from these materials perform [54]. Engineers and designers cannot design without fully understanding the properties of the materials used to manufacture the parts being designed. If the properties for AM materials are not available, designers will not consider AM as a manufacturing method [52].
- *Process control*: For the AM process to be widely accepted by the industry, the ability for predictable, repeatable, consistent, and uniform fabrication is critical. In-process monitoring, closed-loop feedback, and building process-structure-property relationships modeled and integrated with CAD/E/M tools for each material and process are needed [55]. In situ sensors are an area that should be examined to provide nondestructive evaluation and enable early defect detection, particularly relating to thermal control. Better process controls could also lead to decreased downtime, which is currently a major issue for many machines and processes [55].

- *Process understanding and modeling*: New physics-based models of AM processes are needed to understand and predict material properties such as surface roughness and fatigue [56], especially for aerospace components working in extreme environments. A better understanding of the basic physics could then potentially lead to predictive modeling, allowing designers, engineers, scientists, and users to estimate the functional properties of the part during design and tweak the design to achieve the desired outcomes [52].

13.4.2 Potential future applications

In the past, the aerospace industry demonstrated many application areas and examples of topological optimization, functional integration, and direct fabrication for parts with complex geometry and new materials. AM applications in the aerospace industry especially focus on the design, fabrication, and repair of aero engine components. The following potential applications of AM are expected in the aerospace industry in the near future:

- *AM for the design of aircraft components*: AM provides a promising opportunity to design multifunctional or integral aircraft components that could reduce assembly or connection, simplify the design and manufacturing process, eliminate fixture and tools, and save materials and fuel costs. As a structure component with an internal channel, similar to airfoils, upgraded functional components could be realized by integrating acoustic and thermal insulation into aircraft parts or by embedding entire sensor/actuator systems, including electronic wiring and connectors. This can contribute to the realization of self-optimizing parts [57]. Integral aircraft components without joints enhance the design of parts for improved connectivity. The main purpose is to replace connectors, such as bolts and screws, which weaken the structural integrity and also represent a considerable cost factor [58].
- *Fabrication of large-scale aerospace components using AM*: While smaller aircraft parts are already being developed using AM techniques, the aerospace industry also envisions printing large-scale components, such as an entire airplane wing, in the future. The current AM techniques have limitations for fabricating large-scale objects because with the increase in dimensions, the internal stresses cause distortion. A recent technique developed by BAE Systems allows the new possibility to relieve stress by using an ultrasonic tool to strike metal parts repeatedly as each layer is built [59].
- *Manufacturing on demand*: Manufacturing on demand refers to the flexibility of AM technologies to produce parts "just in time". Storage costs can be reduced significantly. Furthermore, on-demand production fosters the intactness of parts because no damage can occur during storage [55]. In addition, printing parts on demand directly in space would significantly reduce the cost and planning cycles required to send a rocket into space with the necessary replacement and repair tools. On-demand 3DP of parts in space is currently being investigated by groups like Made in Space and Lunar Buildings. In collaboration with NASA, Made in Space is conducting zero gravity tests to experiment with 3DP on the International Space Station, which would allow astronauts to print tools and parts when required [56].
- *FGMs in aerospace*: FGMs can provide designers with a tailored material response and exceptional performance to thermal environments or mechanical loading. In the AM process, for instance, LMD can deliver different materials (usually through multiple feeding systems) to build tailored materials and properties for components with FGM. The potential FGM components could be used in severe thermal environments, such as aerospace and space vehicles. For example, space vehicles use ceramic tiles as thermal protection

from the heat generated during reentry into the Earth's atmosphere. However, these tiles are laminated to the vehicle's superstructure and are prone to cracking and debonding at the superstructure−tile interface as a result of the abrupt transition between thermal expansion coefficients. An FGM comprising ceramic on the outside surface and metal on the inside surface can eliminate the abrupt transition between coefficients of thermal expansion [60].

- *Automated repair process for aerospace components*: The aerospace industry and academia both have some cases for adopting the AM process to repair high-value components such as turbine blades, blisks, and bearing housings. This is cost-effective and reduces turnaround time for fabricating and replacing a new component. Currently, most of the time and cost are spent at the repair preparation stage. Future automated repair processes based on AM are expected to repair components effectively.

References

[1] I. Gibson, D.W. Rosen, B. Stucker, Additive Manufacturing Technologies: 3D Printing, in: Rapid Prototyping, and Direct Digital Manufacturing, Second ed., Springer, 2015.
[2] Boeing Files Patent for 3D-printed Aircraft Parts, 2015. Available from: http://3dprinting.com/news/boeing-wants-to-patent-3d-printing-of-aircraft-parts/.
[3] Smar Tech Additive Manufacturing in Aerospace: Strategic Implications, 2014. Available from: http://smartechpublishing.com/images/uploads/general/AerospaceWP.pdf.
[4] T. Wohlers, Additive Manufacturing State of the Industry, Wohlers report, Wohlers Associates, Inc, 2010.
[5] J. Mazumder, A. Schifferer, J. Choi, Direct materials deposition: designed macro and microstructure, Material Research Innovations 3 (3) (1999) 118−131.
[6] W. Hofmeister, M. Griffith, Solidification in direct metal deposition by LENS processing, JOM 53 (9) (2001) 30−34.
[7] A. Gasser, et al., Laser metal deposition (LMD) and selective laser melting (SLM) in turbo-engine applications, Laser Technik Journal 7 (2) (2010) 58−63.
[8] K.M. Taminger, R.A. Hafley, Electron Beam Freeform Fabrication (EBF3) for Cost Effective Near-net Shape Manufacturing, National Aeronautics and Space Administration, Langley Research Center, 2006.
[9] J.J. Beaman, et al., Solid Freeform Fabrication: A New Direction in Manufacturing, Kluwer Academic Publishers, Norwell, MA, 1997, pp. 25−49, 2061.
[10] J.-P. Kruth, et al., Selective laser melting of iron-based powder, Journal of Materials Processing Technology 149 (1) (2004) 616−622.
[11] D. Cormier, O. Harrysson, H. West, Characterization of H13 steel produced via electron beam melting, Rapid Prototyping Journal 10 (1) (2004) 35−41.
[12] P.F. Jacobs, Fundamentals of stereolithography, in: Proceedings of the Solid Freeform Fabrication Symposium, 1992.
[13] C.K. Chua, K.F. Leong, S. L.C, Rapid Prototyping, Principles and Applications, in: 3rd ed.Assembly Automation, Vol. 30, World Scientific Publishing Company, 2010.
[14] S.S. Crump, Fused deposition modeling (FDM): putting rapid back into prototyping, in: The 2nd International Conference on Rapid Prototyping, 1991, pp. 354−357. Dayton, Ohio.
[15] T. Huang, et al., Aqueous-based freeze-form extrusion fabrication of alumina components, Rapid Prototyping Journal 15 (2) (2009) 88−95.
[16] H.J.S. Sachs M E, M.J. Cima, P.A. Williams, Three Dimensional Printing Techniques, 1993. US Patent.

[17] D. Mori, Additive Manufacturing for Quality Finished Parts, 2014. Available from: http://us.dmgmori.com/blob/354972/7009c74e7ad96fad7ad34555d81bc316/pl0us14-lasertec-65-3d-pdf-data.pdf.
[18] Case Study: Laser Powder Metal Deposition Manufacturing of Complex Real Parts, T. Ltd, 2014. Available from: http://www.lortek.es/files/merlin/05-C_Hauser-TWI-Case-Study.pdf.
[19] LENS™ 850-R: Proven Industrial Additive Manufacturing System for Repair, Rework, Modifi cation and Manufacturing, Optomec, 2014. Available from: http://www.optomec.com/wp-content/uploads/2014/04/LENS_850-R_datasheet.pdf.
[20] F.W. Liou, et al., Research and Development of a hybrid rapid manufacturing process, in: Proceedings of the Solid Freeform Fabrication Symposium, Citeseer, 2001.
[21] L. Xue, M.U. Islam, Laser consolidation-a novel one-step manufacturing process for making net-shape functional components, in: Cost Effective Manufacture via Net-Shape Processing, 2006. Neuilly-sur-Seine, France.
[22] D. Ding, et al., Wire-feed additive manufacturing of metal components: technologies, developments and future interests, The International Journal of Advanced Manufacturing Technology (2015) 1−17.
[23] T. Kellner, Fit To Print: New Plant Will Assemble World's First Passenger Jet Engine With 3D Printed Fuel Nozzles, Next-Gen Materials, 2014. Available from: http://www.gereports.com/post/80701924024/fit-to-print/.
[24] ConceptLaser. Laser melting with metals in aircraft manufacturing: 3D printing enables "bionic" aircraft designs. Available from: http://www.conceptlaserinc.com/portfolio-items/laser-melting-metals-aircraft-manufacturing-2/#prettyPhoto.
[25] Exone. Available from: http://www.exone.com/.
[26] Exone. Aerospace: Large, Complex Parts and Fully Dense Components with Reduced Lead Time. Available from: http://www.exone.com/Industries-Applications/Industries/Aerospace.
[27] Stratasys. Aerospace 3D Printing Means Innovating Fast and Flying with Confidence. Available from: http://www.stratasys.com/industries/aerospace.
[28] Stratasys. Gas Turbine Research Establishment (GTRE) FDM Cuts Time to Prototype Jet Engine from 1 Year to 6 Weeks. Available from: http://www.stratasys.com/resources/case-studies/aerospace/gas-turbine-research-establishment.
[29] Stratasys. Piper Reduces the Cost and Leadtime of Hydroforming Tooling to Build a Personal Jet. Available from: http://usglobalimages.stratasys.com/Case%20Studies/Aerospace/SSYS-ACS-PiperAircraft-MetalForming-09-11.pdf?v=635168261622081483.
[30] Stratasys. Bell Helicopter FDM Helps Bell Helicopter Build Quality Prototypes Available from: http://www.stratasys.com/resources/case-studies/aerospace/bell-helicopter.
[31] Stratasys. NASA's Human-Supporting Rover has FDM Parts. Available from: http://www.stratasys.com/resources/case-studies/aerospace/nasa-mars-rover?.
[32] J.E. Grady, M.C. Halbig, M. Singh, A Fully Non-Metallic Gas Turbine Engine Enabled by Additive Manufacturing, 2015.
[33] M.C. Leu, S. Pattnaik, G.E. Hilmas, Optimization of selective laser sintering process for fabrication of zirconium diboride Parts, in: Proceeding of International Solid Freeform Fabrication Symposium. Austin, TX, 2010.
[34] N.K. Dey, Additive Manufacturing Laser Deposition of Ti-6Al-4V for Aerospace Repair Application, 2014.
[35] K. Nakata, et al., Re-weldability of neutron-irradiated stainless steels studied by multi-pass TIG welding, Journal of Nuclear materials 307 (2002) 1578−1583.
[36] J. Tušek, R. Ivančič, Computer-aided analysis of repair welding of stamping tools, Zeitschrift für Metallkunde 95 (1) (2004) 8−13.

[37] C. Su, et al., Plasma transferred arc repair welding of the nickel-base superalloy IN-738LC, Journal of Materials Engineering and Performance 6 (5) (1997) 619−627.
[38] M. Henderson, et al., Nickel based superalloy welding practices for industrial gas turbine applications, Science and Technology of Welding & Joining 9 (1) (2004) 13−21.
[39] J. Tan, L. Looney, M. Hashmi, Component repair using HVOF thermal spraying, Journal of Materials Processing Technology 92 (1999) 203−208.
[40] B. Graf, A. Gumenyuk, M. Rethmeier, Laser metal deposition as repair technology for stainless steel and titanium alloys, Physics Procedia 39 (2012) 376−381.
[41] R.P. Mudge, N.R. Wald, Laser engineered net shaping advances additive manufacturing and repair, Welding Journal-New York- 86 (1) (2007) 44.
[42] F. Liou, J. Ruan, A hybrid metal deposition and removal system for rapid manufacturing, in: International Conference on Metal Powder Deposition for Rapid Manufacturing, San Antonio, 2002.
[43] J. Ruan, et al., Automatic process planning of a multi-axis hybrid manufacturing system, in: ASME 2002 International Design Engineering Technical Conferences and Computers and Information in Engineering Conference, American Society of Mechanical Engineers, 2002.
[44] J. Zheng, Z. Li, X. Chen, Worn area modeling for automating the repair of turbine blades, The International Journal of Advanced Manufacturing Technology 29 (9-10) (2006) 1062−1067.
[45] Optomec. LENS Blisk Repair Solution. Available from: http://www.optomec.com/wp-content/uploads/2014/04/Optomec_LENS_Blisk_Repair_Datasheet.pdf.
[46] I. RPM Innovations. Laser Repair Technology (LRT). Available from: http://www.rpm-innovations.com/laser_repair_technology.
[47] I. Kelbassa, et al., Manufacture and repair of aero engine components using laser technology, in: Proceedings of the 3rd Pacific International Conference on Application of Lasers and Optics, 2008.
[48] J. Gao, et al., Investigation of a 3D non-contact measurement based blade repair integration system, Aircraft Engineering and Aerospace Technology 77 (1) (2005) 34−41.
[49] J. Gao, et al., An integrated adaptive repair solution for complex aerospace components through geometry reconstruction, The International Journal of Advanced Manufacturing Technology 36 (11-12) (2008) 1170−1179.
[50] K.-H. Richter, S. Orban, S. Nowotny, Laser cladding of the titanium alloy Ti6242 to restore damaged blades, in: Proceedings of the 23rd International Congress on Applications of Lasers and Electro-optics, 2004.
[51] J.B. Jones, et al., Remanufacture of turbine blades by laser cladding, Machining and In-process Scanning in a Single Machine, 2012.
[52] N. Gupta, C. Weber, S. Newsome, Additive manufacturing: Status and Opportunities, 2012.
[53] N. Guo, M.C. Leu, Additive manufacturing: technology, applications and research needs, Frontiers of Mechanical Engineering 8 (3) (2013) 215−243.
[54] T. Campbell, et al., Could 3D Printing Change the World. Technologies, Potential, and Implications of Additive Manufacturing, Atlantic Council, Washington, DC, 2011.
[55] D.L. Bourell, Ming C. Leu, Roadmap for Additive Manufacturing: Identifying the Future of Freeform Processing, 2009. Austin, TX.
[56] W.E. Frazier, Direct digital manufacturing of metallic components: vision and roadmap. direct digital manufacturing of metallic components: Affordable, Durable, and Structurally Efficient Airframes, at Solomons Island, MD, 2010.

[57] B. Baron, Multifunctional Airframe Concepts with Structurally Integrated Electronics – Direct Part Manufacturing Workshop, Wright State University, 2011.
[58] I.J. Gausemeier, Thinking ahead the Future of Additive Manufacturing - Innovation Roadmapping of Required Advancements, 2011. Paderborn.
[59] G. Trivedi, 5 Potential Future Applications of 3D Printing Within the Aerospace Industry, 2014. Available from: http://3dprint.com/26081/3d-printing-aerospace-5-uses/.
[60] W.G. Cooley, Application of functionally graded materials in aircraft structures, in: Department of the Air Force, Air Force Institute of Technology, 2005, p. 2.

Laser sintering of ceramic materials for aeronautical and astronautical applications

14

A. Goulas, R.J. Friel
Loughborough University, Loughborough, United Kingdom

14.1 Introduction

Modern advanced structures and components intended for use in aerospace and astronautics are often complex geometries that require the use of materials capable of serving in an extreme range of environmental conditions for a variety of applications. Current metal alloys can no longer meet these increasing requirements for new applications, and thus the focus of materials development has often moved to the use of ceramics that exhibit superior performance (resistance to high temperatures, corrosion, wear, and so on) and can increase the overall reliability and lifetime over those of metal alloy materials.

Although these ceramic materials offer the benefit of superior performance, they often suffer in manufacturability when compared with metal alloy materials. The use of more traditional machining methods such as milling and turning are not suited to most ceramic materials, and therefore the normal methods of pressing or extruding green-state ceramic components is the typical manufacturing method used. These pressing and extruding methods put significant constraints on the geometry of the final ceramic product and as such restrict design freedoms.

The advent of laser additive manufacturing (LAM) is a key enabler in creating ceramic components with considerably greater design freedoms. The technology is allowing the creation of ceramic components that not only meet the increasing material requirements of aero/astro applications but also provide new opportunities in terms of the complex structures that can now be produced. This chapter reviews the state of the art in LAM of ceramic materials for aerospace and astronautic applications. This chapter focuses on ceramic materials, and it is therefore prudent to explain what ceramics are and their key properties.

14.1.1 Ceramic materials

For the purposes of this chapter, the term ‘ceramic’ is being used to describe an inorganic, non-metallic material [1]. The material bonding types in ceramics are often a mix of ionic, covalent and, less commonly, metallic; the material exists as a large formation of interdependent atoms, so there are no distinct molecules of the material [2].

Laser Additive Manufacturing. http://dx.doi.org/10.1016/B978-0-08-100433-3.00014-2
Copyright © 2017 Elsevier Ltd. All rights reserved.

In addition, the ceramics have a large range of crystallinities, from fully amorphous (glasses) to highly oriented structures (eg, ZrO_2).

Ceramics are a large group of materials; the majority are in the form of oxides [eg, alumina (Al_2O_3)]. However, other common groups of ceramics exist: nitrides [eg, boron nitride (BN)], silicides [eg, tungsten disilicide (WSi_2)], carbides [eg, silicon carbide (SiC)], and borides [eg, titanium diboride (TiB_2)] [3]. These examples are classed as technical, industrial or engineering ceramics and are used because of their favourable characteristics such as resistance to wear, corrosion and temperature. These differ from other ceramics such as those used for structural (eg, bricks) and refractory applications (eg, furnace insulation), whiteware (eg, sanitary ware) and clay/pottery (eg, porcelain). The typical properties of engineering ceramics that make them favourable for aero and astro engineering materials are [1,4–6]:

- High/low temperature resistance
- High wear resistance
- High corrosion resistance
- Low weight

The main unfavourable properties of engineering ceramic materials is that most exhibit poor tensile strength with low toughness and brittle failure mechanisms; this results in the ceramic components typically failing catastrophically as opposed to gradually [2]. This manner of failure and the specific properties of the engineering ceramics also makes them unsuitable for many of the manufacturing techniques that are suitable for metals and polymers, such as machining and forging. To avoid many of these issues, many engineering ceramic manufacturing techniques use powdered materials that are formed via dies and moulds to near net-shape. Fig. 14.1 shows a selection of typical engineering ceramic components.

Post-processing of engineering ceramic components usually involves a densification step that heats the components, typically in a furnace, to sinter or 'densify' the ceramic material. This is usually necessary because the components are formed via powders or slurries that result in high porosity. Densifying reduces the porosity, which improves the mechanical performance of the component; however, this densifying reduces the volume of the component. Because of the high sintering temperature of many ceramics, the post-processing step is energy intensive and time-consuming.

There are many applications of technical ceramics ranging through many sectors, from consumer electronics to rocket engines. A few examples are:

- Silicon dioxide used for high-performance heat shielding on spacecraft (Fig. 14.2)
- Zirconium dioxide used as a membrane for high-temperature fuel cells
- Tungsten carbide used for cutting tool inserts (Fig. 14.3)

14.2 Conventional manufacturing methods for ceramic components

As mentioned in Section 14.1.1, there is a range of established conventional manufacturing techniques available for manufacturing high-value technical ceramic products. From the oldest technique of firing clay ceramics to some of the more

Figure 14.1 Typical engineering ceramic components [7].

Figure 14.2 Silica heat tile from a space shuttle thermal protection system. National Science Museum of London. Licenced under Creative Commons.

Figure 14.3 Tungsten Carbide (WC) cutting tool inserts [7].

modern production methods, such as microwave sintering [1], ceramics have often been one of the more challenging materials to manufacture with because of their complex properties and often high energy input requirements. In this section a few selected methods, representing conventional manufacturing methods, are explained, together with their typical characteristics [2]. The area of hydraulic ceramics is not discussed in this chapter because the majority of these materials are for composite ceramics, typically used for construction (eg, concrete).

14.2.1 Extrusion and pressing methods

Extrusion is the process of forcing a material through a nozzle or die to produce parts with a constant desired cross section. It is a manufacturing technique that was used extensively for many years to produce common ceramic products such as bricks and tiles [8]. Extrusion's application to technical ceramics is less common because of the need to combine the material in a paste- or clay-like form to be able to extrude the material and for the extrusion to be able to hold its newly formed shape [9]. This combination with other materials results in less pure material than for other powder-based techniques. The main benefit of using an extrusion system is that it can be a continuous process, with the constant cross-section being produced in many metre lengths. A few application examples of the extrusion method are for the manufacturing of furnace tubes, heat exchangers, catalyst supports and heavy graphite electrodes (Fig. 14.4).

Ceramic extrusion systems are typically divided into two subcategories based on their extrusion mechanism: (1) a piston type and (2) a screw (auger) type. The first subcategory (piston) has the advantage of being able to apply higher pressure during extrusion for materials with higher ceramic content (more viscous, shrinks less upon densification) (Fig. 14.5); however, it comes with the drawback that it can only carry and deposit a specific amount of material because of the limitation introduced by the piston chamber size [1]. The second subcategory (screw) can operate with continuous and unceasing extrusion, but its drawback is the high wear of the mechanism's movable parts [2].

The extrusion process can be broken down to four basic steps: blending, packing, extrusion and, finally, cutting/drying [11]. These steps involve mixing the constituents of the raw materials into a uniform liquid medium, pressing them into a cylindrical chamber to remove trapped air, feeding to the expansion chamber and to the nozzle for extrusion and, finally, after extrusion, cutting the parts into the desired size (via a

Figure 14.4 Example of ceramic extrusion components [10].

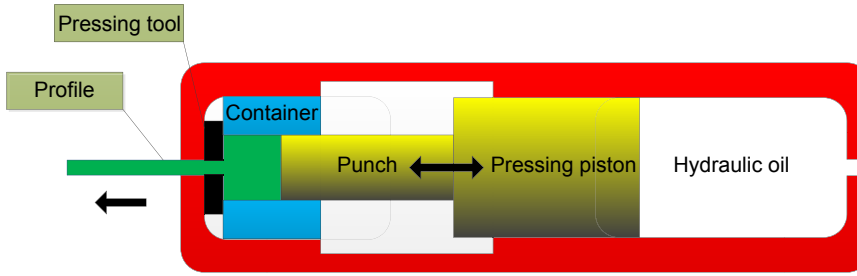

Figure 14.5 Piston-based extrusion process schematic.

wire cutter or other tool). The extruded materials must be fired/densified/sintered after they have been extruded and have dried. This process removes the majority of the additives in the material and creates a hard, solid, stable final ceramic component.

Pressing is one of the most essential processing techniques for manufacturing ceramics with a simple geometrical shape, such as tiles, cutting tools and various structural products. This technique is mainly divided into uniaxial and isostatic pressing (Fig. 14.6).

In uniaxial pressing, the raw, granulated materials are loaded and pressed into a mould from one or both sides. Pressing is typically performed in the range of 10−100 MPa, and consolidation of the granulated material is achieved via particle sliding, fragmentation and pore elimination (Fig. 14.7). The addition of binders and lubricants (eg, starch, cellulose) are often used to improve the particle movement and resultant packing; mechanical oscillation can also be used [12]. After the pressure is removed, macroscopic defects such as delamination and cracking can occur as the pressed ceramic particle construct undergoes a certain level of recovery. This drawback can be reduced by optimising the pressing process parameters and the ceramic material powder characteristics and by adding a binder material.

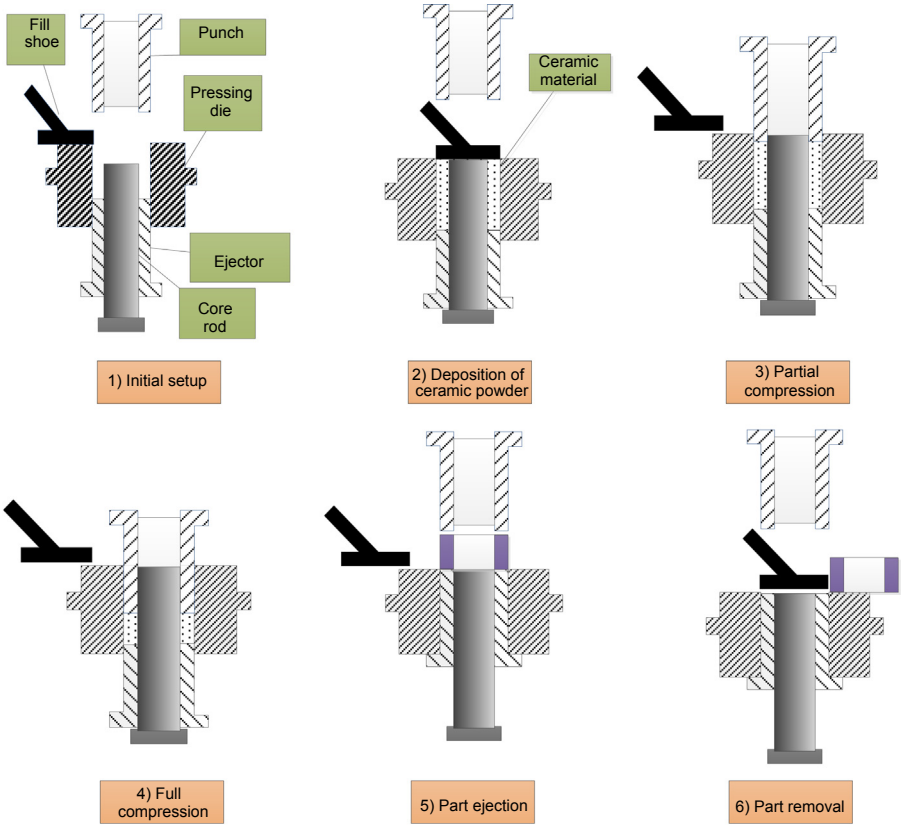

Figure 14.6 Schematic of uniaxial ceramic pressing.

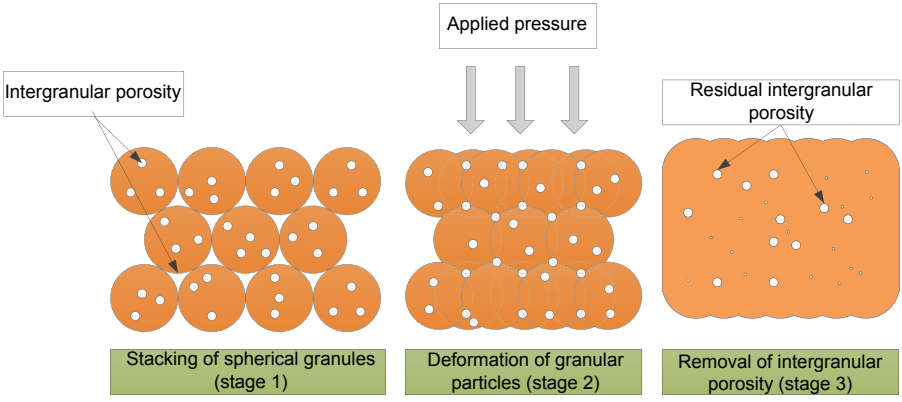

Figure 14.7 Inter- and intra-granulation changes during ceramic powder pressing.

By using isostatic pressing, common issues such as delamination, cracking or very limited die shapes are removed. Isostatic pressing techniques use fluid pressure to form ceramic parts within a flexible plastic die [13]. The enclosed ceramic material is pressurised, often up to several hundred megapascals, by a fluid such as water or oil (cold isostatic pressing) or argon gas (hot isostatic pressing). It should be noted that hot isostatic pressing techniques form the ceramic shape and sinter the material in a single operation (Fig. 14.8). Isostatic pressing techniques are able to produce components with relatively large dimensions and good final part properties; however, the process is pre-form (mould)—driven and is batch based. Common components manufactured by ceramic isostatic pressing are crucibles, capacitors and heating elements.

14.2.2 Slurry methods

The manufacturing methods of slip and electrophoretic casting are the most common examples of slurry-type systems for ceramic components. The slurry is made from fine ceramic powders, and suitable binder agents and a range of additives are added to improve the properties (ie, plasticity and solubility) of the power particles [14].

In slip casting, the slurry is filled into a porous die; the liquid additions to the material are drained via capillary action, leaving a fully dried green component within the mould (Fig. 14.9). Slip casting is more suited to manufacturing geometrically complex shapes, such as turbine blades, vases and tableware, than are pressing and extrusion. However, because it is a time-consuming approach, it is more suitable for the production of limited batches.

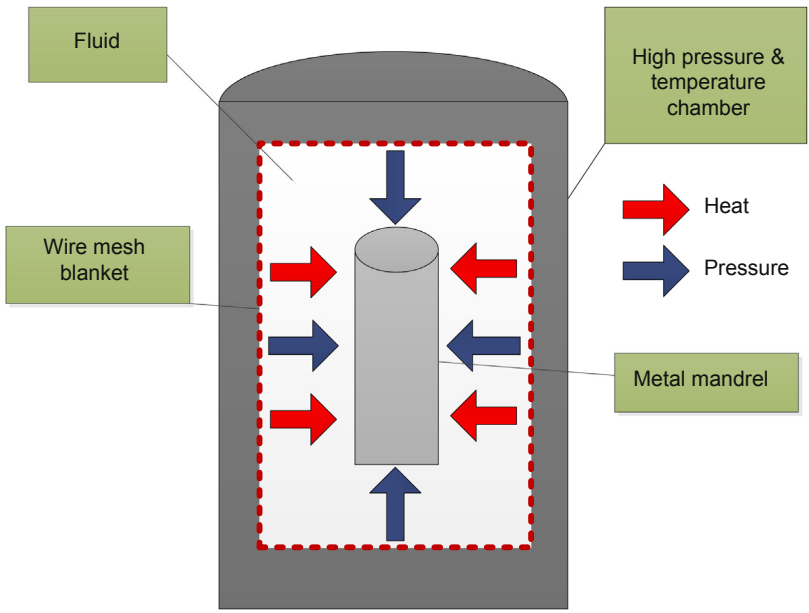

Figure 14.8 Schematic of hot isostatic pressing process.

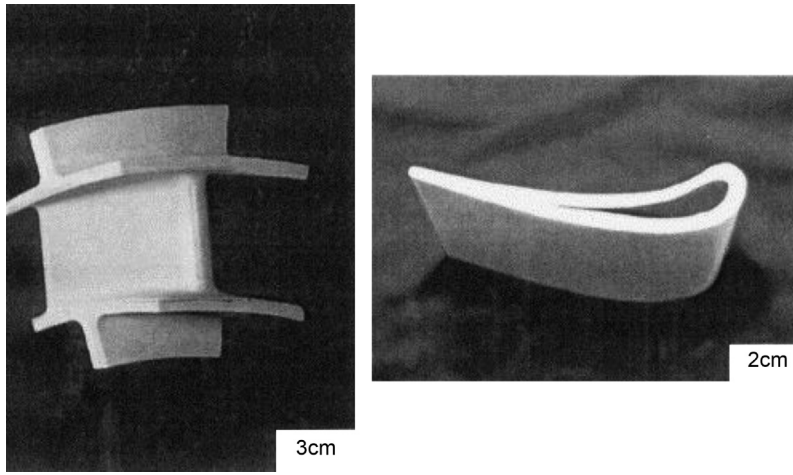

Figure 14.9 Example of slip casting [15].

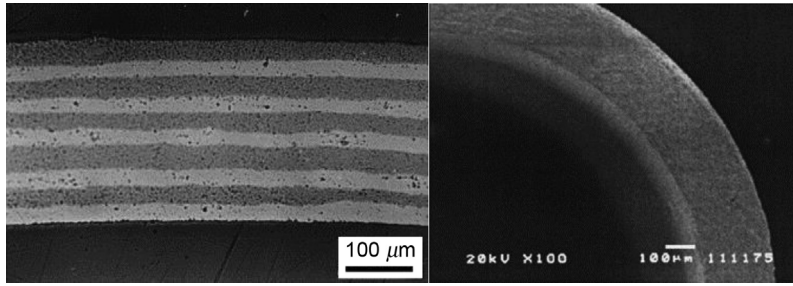

Figure 14.10 Examples of electrophoretically coated ceramic products [17].

Electrophoretic casting is a newer manufacturing method that also utilises ceramic slurry materials (Fig. 14.10). Electrophoresis describes the motion of dispersed particles within an electrically charged fluid via the application of a uniform electric field; with respect to ceramics, the process is used to deposit ceramic particles onto a pre-existing surface or manufacture ceramic components with minimal thicknesses [16]. The most common application of this technique is the fabrication of wear-resistant and heat-resistant ceramic coatings. The main drawback of the process is the limitation on the thickness that can be deposited; however, the deposited layers can be formed quickly and to a highly accurate thickness.

14.2.3 Sintering of ceramics

Sintering of ceramics is the process of forming a ceramic bulk structure from a ceramic particulate material through the input of thermal energy [18]. Sintering is performed at temperatures below the melting point of the material (typically at 0.6−0.8 T_m) and can also be performed under pressure to assist the sintering mechanisms. Sintering is used

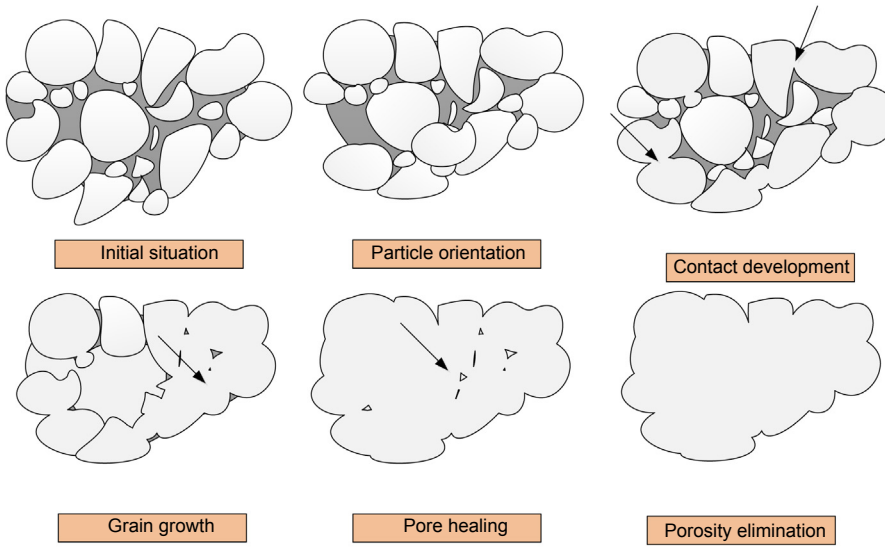

Figure 14.11 Schematic of the solid-state sintering mechanism.

as a final step for many of the ceramic-forming processes already discussed in this section (pressing, extrusion, slip casting). The sintering process re-forms grain interfaces in the material and reduces the porosity to create a denser and more robust ceramic bulk component or coating. Sintering for a sufficiently long period of time at the correct temperature and pressure can result in densities close to 100%. The driving mechanism of sintering is the tendency to minimise the total surface energy of a particulate material [18]. This reduction in total surface energy is led by two interactive and rival mechanisms: (1) grain coarsening and (2) pore shrinkage [19].

Densification mechanisms are thermodynamically favoured, and the main parameters affecting the process include temperature, pressure, processing atmosphere (eg, nitrogen, argon), particulate material impurities and particle and pore size distribution. The ceramics sintering process is subdivided into two distinct types: solid-state sintering (SSS) [20] and liquid-phase sintering (LPS) [21].

In SSS (Fig. 14.11), the intended pre-shaped body is heated to a temperature below the melting point, where atom migration and rearrangement mechanisms take place, resulting in solid-state neck formation and growth until inter-particle porosity is reduced and separated from the grain boundaries. These mechanisms are viscous flow, evaporation, volume, surface and grain boundary diffusion and plastic flow. These mechanisms can function individually, but more often they function in combination [22].

In LPS (Fig. 14.12), a small amount of liquid phase exists near the sintering temperature, and a neck forms via particle rearrangement as a result of capillary forces [23]. The mechanisms involved in this case are melting, wetting, spreading and liquid re-distribution. At the final stage of LPS, the liquid phase stops, resulting in the formation of solid-to-solid bonds between consolidated particles, known as

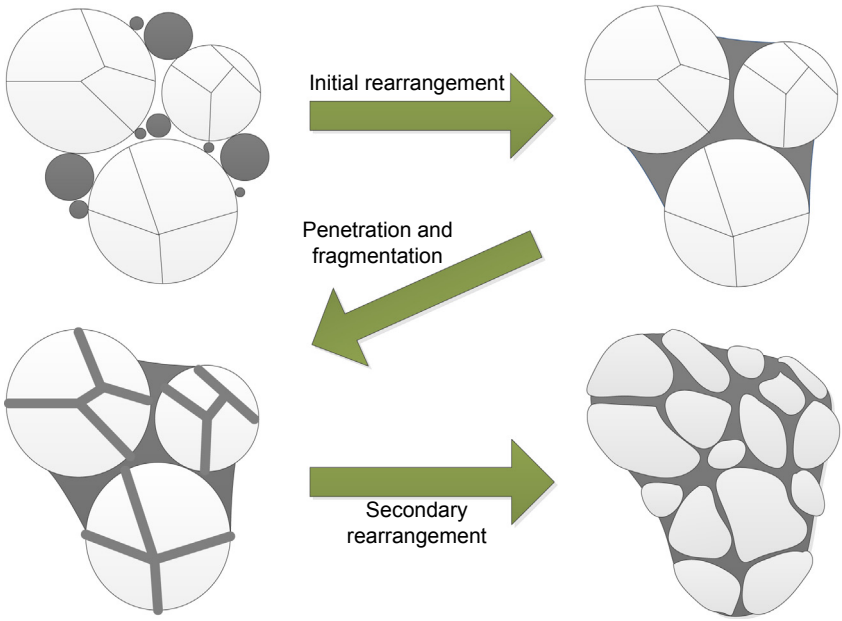

Figure 14.12 Schematic of liquid-phase sintering.

coalescence. LPS is a desirable from of sintering because the presence of a liquid phase can result in an improved densification of the bulk ceramic material at lower temperatures.

14.2.4 Review of conventional methods

The conventional manufacturing methods for ceramics are well established and can create high numbers of ceramic components at a relatively low cost with almost fully dense structures and maximal material properties. However, although ceramics manufacturing has been established for many years and rigorously researched and developed towards optimisation, there are still some inherent drawbacks in the typical processes. As the demands of technology, environmental impact and cost reduction are constantly increasing, so too are the requirements of the ceramic materials, components and manufacturing methods. The mechanisms underpinning the traditional manufacturing methods are restricting the potential for further development in the field of ceramics manufacturing.

For many areas of the ceramic industry, the main objective is to achieve economically feasible mass production of ceramic goods. However, this push for mass production is a limiting factor for one-off or limited production runs as a result of the high costs of tooling and setup for most of the conventional processes. In addition, using conventional fabrication methods limits/restricts the ability to build physical assets with complex external and internal geometric features. These complex geometries are often desired as a response to the increasing demands of the components and applications.

In addition to a restriction on the viability of smaller production runs and component complexity is the limitation of traditional methods to build functionally graded ceramic products, that is, components with controlled mechanical, microstructural or morphological characteristics and properties. These components would require a method of manufacture that could alter the physical and/or chemical makeup of the component in situ during manufacturing.

14.3 Applications of ceramics in aeronautics and astronautics

14.3.1 Ceramics

Aeronautics and astronautics are two of the most challenging engineering areas for the development and application of all material types (polymers, metals, ceramics and composites). The harsh operating environment (eg, high/low temperatures, corrosion, ionising radiation), in combination with the need for ever greater performance at lighter weights that can operate under the harsh conditions, requires the development of new enhanced materials that are able to perform well and promote more efficient engine and structure designs [24]. At present, most common aerospace super-alloys and composites are unable to fulfil the most demanding criteria and do not perform as well as ceramics under the above mentioned conditions. Technical ceramics offer superior performance that is highly desirable for certain aero/astro applications:

- *Thermal protection*: Ceramics have been used for many years for rocketry, civil and military aviation and space applications. Ceramics provide protection against the very high temperatures that exist during high-speed flight. An example of these high temperatures is rockets or re-entry vehicles, where the flight surface and atmosphere interaction can achieve temperatures up to 2200°C. An example of where the ceiling temperature for material performance is being elevated is through the use of ultra-high-temperature ceramics [25] such as ZrB_2 and HfB_2 (Fig. 14.13). As the name implies, these materials have extremely high melting temperatures (close to 3000°C) [26]. The promise of ultra-high-temperature ceramics materials has still not been fully realised, in part because of issues of oxidation that change the ceramic composition and reduce its ultra-high-temperature properties [27].
- *Propulsion:* Current internal combustion engines and in particular aero-engines, despite their continuous development, are responsible for the production of a large amount of carbon dioxide (CO_2) emissions and thus have an impact on the total atmospheric carbon dioxide level. The option of developing 'ceramic engines' that are equipped with a higher proportion of ceramic components, taking advantage of the thermal properties of ceramic materials, could enable higher operating temperatures. Increased operating temperatures can increase an engine's combustion efficiency, which can reduce fuel consumption and various harmful emissions. The opportunity presented by ceramic materials has resulted in a shift in focus for the aero/astro industries into researching and pursuing the greater use of ceramics (Fig. 14.14). Current candidate materials for manufacturing engine ceramics parts are silicon nitride, silicon carbide and high-strength alumina and zirconia oxides. It should be noted that despite their superior thermal and oxidation/corrosion performance, these materials are still more susceptible to damage from foreign objects/debris than current metallic alloy alternatives [29].

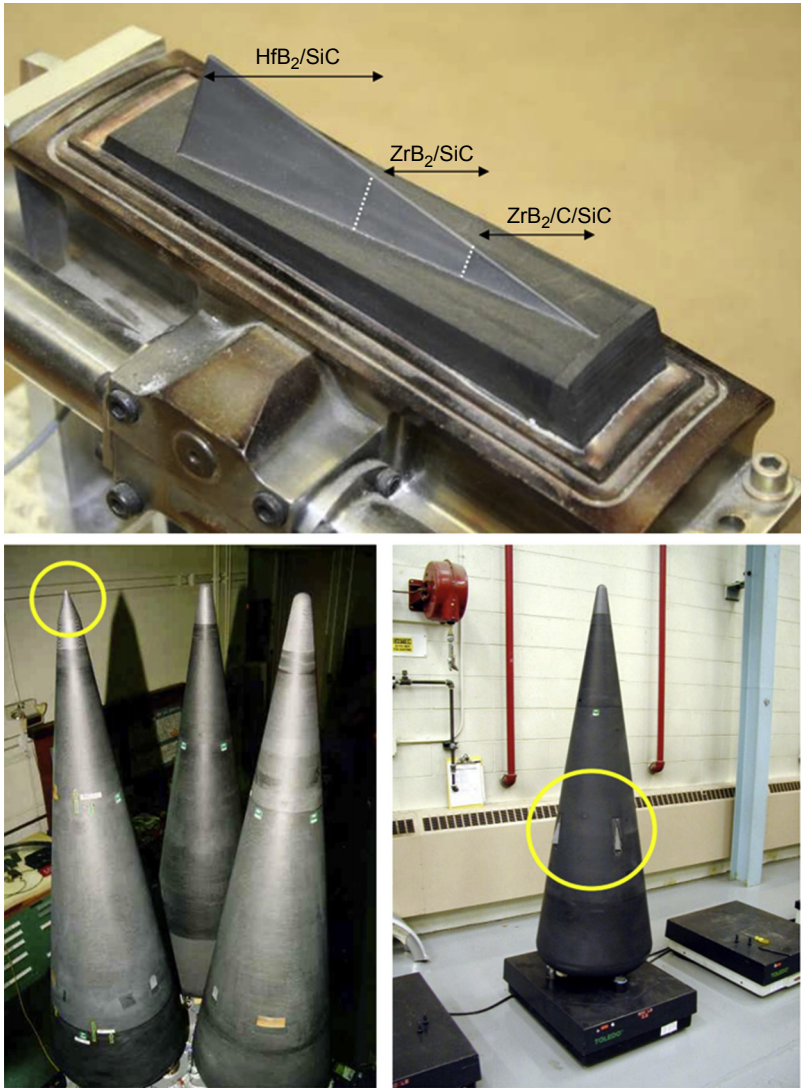

Figure 14.13 Examples of thermal protection [28].
NASA.

- *Instrumentation and control*: A specific category of ceramic materials known as 'electroceramics' are combining specific characteristics such as piezoelectric and dielectric properties with corrosion and thermal resistance and can serve as sensors under harsh conditions, providing accurate and reliable readings. The use of ceramics can significantly increase the robustness and service envelope of avionic systems. Modern commercial and civil aviation aircraft use such types of sensors on, for example, their fuel tanks and fuselages to acquire readings related to fuel quantities and in more advanced scenarios to conduct measurements regarding to an aircraft's stress situation [31] (Fig. 14.15).

Figure 14.14 Examples of propulsion applications [30].

- *Shielding*: Another application of technical ceramics is in their use as means of shielding. Technical ceramics have been specifically tailored and designed to act as a ballistic shielding against foreign objects coming from both internal and external locations – for example, around an engine or on the outside of a space vehicle – to reduce the consequences of impact with various space debris and micrometeoroid particles. An example of such a ceramic material is the application of porous ceramic tiles fabricated from fibre-reinforced alumina that act as ballistic protection [33] (Fig. 14.16).

14.3.2 Multicomponent ceramics

The term 'multi-component ceramics' (MCs) covers a wide range of dissimilar ceramic materials. The first category of MCs includes ceramic composites (CCs), which are specifically designed and tailored to possess a combination of mechanical, physical and thermal properties superior to the properties of their individual constituents in order to be applied for a specific application. Characteristic examples of such materials are ceramic matrix composites (CMCs) in which a combination of a ceramic slurry, serving as a matrix, and ceramic fibres, whiskers or particulates, which act as reinforcement (Fig. 14.17). The result is a synthesised material exhibiting improved properties at elevated temperatures where metals and polymers (and composites thereof) would have reached their service temperature and/or melting temperature, which could result in a catastrophic failure. The presence of the fibres/particulates can enhance the toughness characteristics of the CMCs with basic mechanisms: (1) deflecting/hindering crack formation and propagation, (2) absorbing energy by the fibre pull out and (3) bridging cracks [35].

A large range of ceramics can and are used for CMCs. However, fewer ceramics have been developed for advanced applications, but they include zirconium diborides, which are commonly used for ultra-high-temperature environments [35]; lead zirconate titanate ceramics that are suitable for applications that require piezoelectric and dielectric properties [37]; and alumina-yttria [38] and yttria-stabilised zirconia, which represents the state of the art in high-performance ceramics [39].

The other category of MCs includes dissimilar ceramic materials that co-exist together as a result of a natural high-temperature processes such as the ones found in igneous and volcanic rocks. These forms of ceramics are the most abundant and include indigenous materials that are found off-world (ie, on the surface of

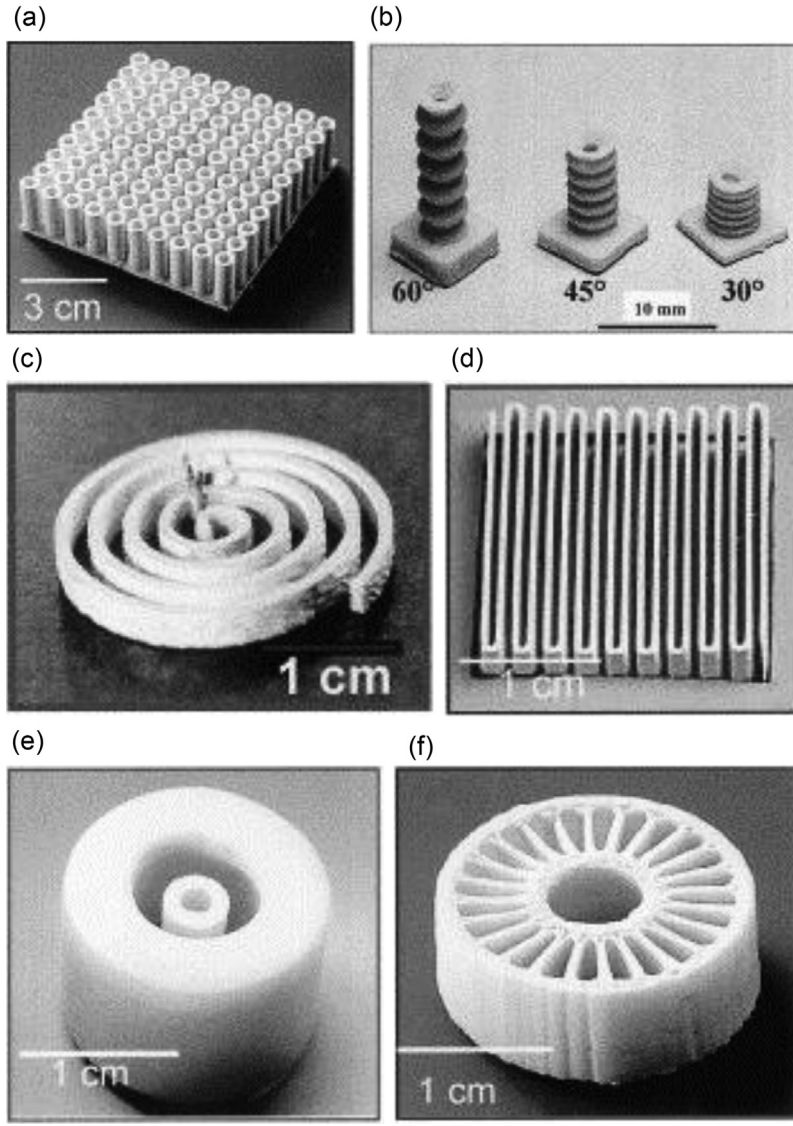

Figure 14.15 Examples of instrumentation and control applications. A variety of transducers made from piezoelectric ceramics and ceramic/polymer composites via fused deposition of ceramics: (a) a 10 × 10 tube array; (b) bellows; (c) a spiral transducer; (d) a curved transducer; (e) telescoping; (f) radial actuators [32].

atmosphere-abundant planetary bodies). These materials are often in powdered form as a result of the exposure to space conditions and the weathering effects of long-term exposure to space caused by continuous interaction with intense ionising cosmic radiation, micro-meteoroid bombardment and steep thermal gradients [40]. The most common example in this category is regolith materials such as those found on the surface of the Moon and Mars [41,42] (Fig. 14.18).

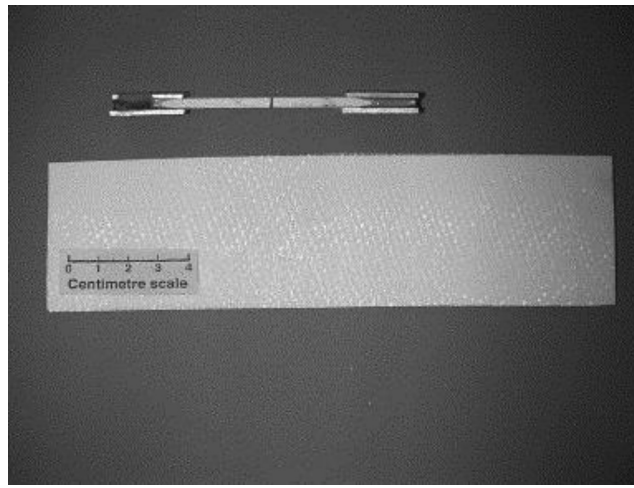

Figure 14.16 Examples of shielding [34].

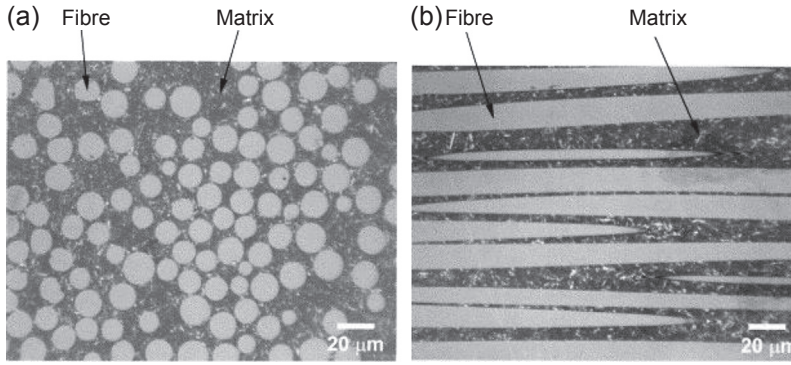

Figure 14.17 Ceramic matrix composite examples [36].

14.4 Laser additive manufacturing methods for ceramic components

LAM describes a group of manufacturing technologies that have proven to be capable of producing three-dimensional net-shape assets out of ceramic materials. They have also been shown to be a promising approach to developing ceramics that are a significant challenge for conventional ceramic processing methods [43].

All seven additive manufacturing (AM) categories, as established by the ISO/PRF 17296-1 standard, have been applied to the manufacturing of ceramic components [44] (Fig. 14.19). However, the various processes that have been used to manufacture these components can also be separated into either single-step or multi-step methods, according to the number of processing steps required to build the geometry and to acquire its final material properties [45].

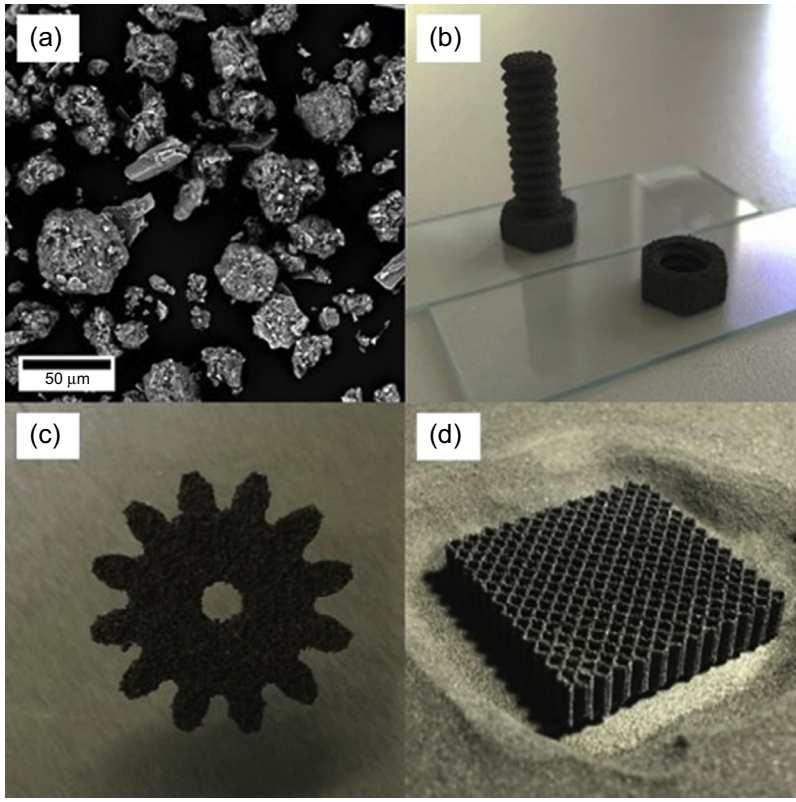

Figure 14.18 Examples of regolith materials and laser additive manufacturing build examples: (a) raw material, (b, c) typical engineering components and (d) fine lattice structure. Copyright: Athanasios Goulas.

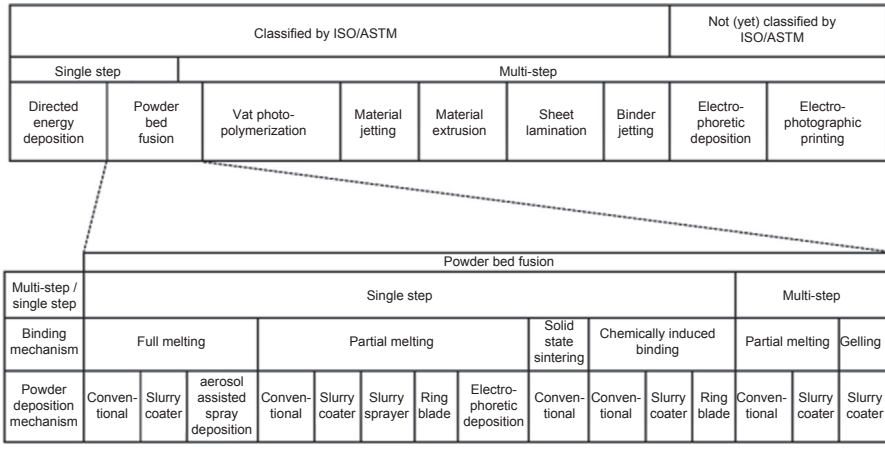

Figure 14.19 Range of additive manufacturing techniques for ceramics [43].

Most of the AM processes that have been used for ceramics are multi-step (eg, binder jetting, where the use of a sacrificial binder agent is used and removed during the post-processing stage) [46,47]. However, the potentially more exciting method is the single-step process. This is because AM single-step systems generate final ceramic components from raw materials in a layer-by-layer fashion (ideally) without the need for post-process densification. Two of the single-step AM systems that have been successfully utilised to directly fabricate ceramic components are direct energy deposition [44,48] and powder bed fusion [45,49]. The focus of this section is on the LAM techniques applicable for ceramics materials.

14.4.1 Laser interaction with ceramic materials

During the laser-scanning process, a focused beam is scanned over the powder bed containing the ceramic powder, causing the irradiated particles of the pre-layered material to melt and fuse together via melt-solidification mechanisms. The laser−material interaction is highly complex, and identification of suitable process parameters is of great importance in achieving desirable results during processing. For this reason, the most important parameter that must be controlled is the input thermal energy per material volume. When the laser is irradiating the ceramic material, the beam's electromagnetic energy is absorbed by the material's particles and is transformed into thermal energy, creating localised melt pools, where the instantaneously created liquid phase wets the nearby particles, thus facilitating further consolidation. The size and characteristics of the formed melt pool are evidently governed by the exposure to the laser input. Optimisation of the exposure time ideally leads to a fully controlled melt pool that aids in achieving the highest possible processing speeds, improving the overall process efficiency.

Because of abnormalities existing within the powder bed (eg, poor packing density, inter-granular gaps), it is difficult to predict the beam's scatter pattern because of the multiple scatterings and reflections that take place between the ceramic particles (Fig. 14.20). As a result, the temperature distribution across the powder bed is heterogeneous, thus leading to uncontrolled heating and cooling phases.

In comparison to other common engineering materials such as polymers and metals, which laser sintering was initially used for, ceramic materials have different physical properties, such as higher melting points and differing absorption mechanisms; thus they require greater energy input to ensure adequate processing. The most common laser systems used for sintering of ceramics are continuous-wave CO_2 and ytterbium fibre lasers; however, both categories have specific drawbacks that are related to (1) laser beam wavelength and (2) the beam-focussing capabilities.

Absorbance is dependent on wavelength and is related to the optical response of the material to be processed. For oxides and polymers, absorbance ability increases with increasing wavelength, whereas the inverse effect is obtained for metals and carbides [50]. Because of this, a CO_2 laser operating at $\lambda = 10.6$ μm is more suitable than a ytterbium fibre laser that is producing $\lambda = 1.06$ μm. Despite the better absorption, CO_2 lasers lack the ability to achieve smaller focussing diameters, whereas fibre lasers

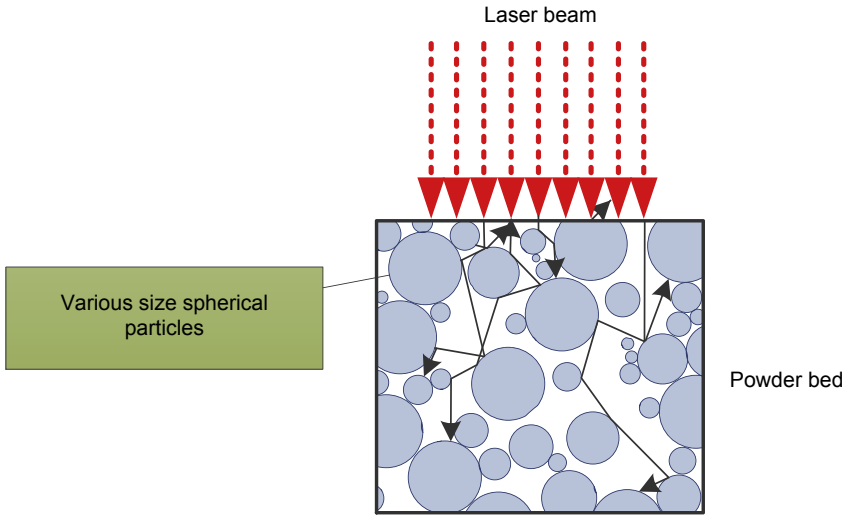

Figure 14.20 Schematic demonstrating scattering issues.

have a significant advantage and can achieve better beam quality and focussing diameters – as low as a few microns. The importance of this key difference is the ability of a fibre laser to achieve a greater energy input per material volume {as a result of greater energy density [Energy (J)/Area (mm^2)]}, minimising the overall processing time (Fig. 14.21).

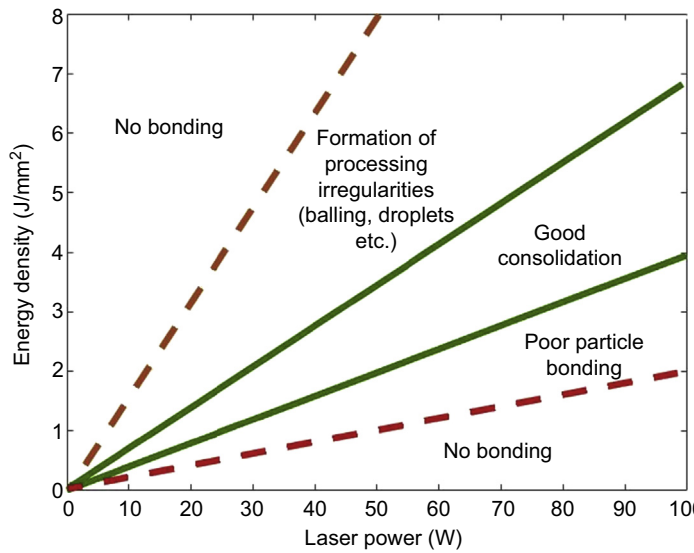

Figure 14.21 Diagram showing energy density.

However, because of a heterogeneous thermal gradient on the powder bed, as explained earlier, the material, when irradiated with excessive energy input, does not sinter and goes through complete melting, which, because of the surface tension of the formulated melt pool (trying to minimise its surface energy), leads to the formation of irregularities such as balling and droplets. In these situations the use of a Q-switched pulsed laser, operating in a nanosecond or femtosecond pulsed mode, could address this unwanted effect.

The surrounding atmosphere where processing is taking place is also of key importance during laser scanning. Processing within a vacuum environment minimises oxidation and removes air trapped between the material granules. This eventually enhances the absorption characteristics of the powder bed. The use of a processing atmosphere using an inert gas such as argon or nitrogen is also often adopted for ceramics processing. Laser processing under a controlled gaseous environment of oxygen or nitrogen can promote further sintering mechanisms, known as 'reaction sintering' [45].

Finally, one important set of parameters affecting the laser−material interaction of ceramics are the characteristics of the powder bed. The first factor related to the powder bed is the packing performance of the ceramic material, which is controlled by a combination of the particle shape and particle size of the granulated material. Spherical particles together with an appropriate ratio of sizes are known to achieve the best packing behaviour (Fig. 14.22), in comparison to angular particles or particles of the same size, because of the minimisation of inter-granular gaps within the power bed [18].

In addition, it is suggested that an optimum range of particle sizes is preferred to achieve a formation of well-distributed liquid phase among the particles and to assist capillary forces. This eases infiltration through the gaps, aiding in reducing the porosity of the built components [51]. The second key factor related to powder bed performance is the material's homogeneity. The overall composition and volume ratio of the constituents composing the ceramic material affect the overall melting temperature. High variation between melting temperature characteristics results in partial melting and consolidation of the ceramic material.

14.4.2 Laser sintering/melting of ceramic materials

The laser sintering (LS) process uses a laser source to provide thermal energy and selectively fuse together particles of a powder material into complex three-

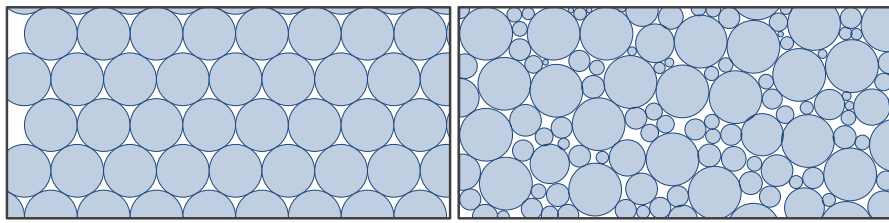

Figure 14.22 Schematic of the packing behaviour of particle types in powder bed fusion systems.

dimensional shapes in a layer-by-layer strategy [52]. The manufacturing process is fully automated and computer controlled, following the computer-aided design (CAD) data of the processed geometry.

A typical LS system consists of a laser source, a laser scanner (X and Y galvanometers) and a powder deposition system enclosed in a controlled environment build chamber, which typically operates under a vacuum or an inert-gas atmosphere. A focused laser beam selectively scans the powder bed containing the ceramic material, according to the computed sections of the previously sliced CAD geometry, and causes either full melting, partial melting, SSS or gelation between the particles.

According to the results of the laser irradiation, the process is classified as laser melting when the power is fully melted and LS for the rest of the resulting cases. It should be mentioned that in reality, because of the very fast and dynamic nature of the process, it is difficult to identify which of the abovementioned consolidation mechanisms is occurring. It is suggested that the process begins with SSS and rapidly advances to the liquid phase, resulting in complete melting of the particles for a brief period of time [45].

14.4.3 Laser additive manufacturing methods for aeronautical and astronautical ceramic components

There are multiple advantages of using the AM approach to produce physical assets and components out of ceramic materials. From both a manufacturing and a materials point of view, the laser processing systems have established a good basis for achieving end products with properties comparable to those of ceramics fabricated via traditional methods (Fig. 14.23).

The AM approach also offers the following advantages over traditional manufacturing techniques:

- An ability to build defect-free ceramic materials with mechanical properties comparable to those of materials fabricated via traditional methods.
- Development of functionally graded ceramics via complete control of the manufacturing process.
- With multi-step AM methods, different types of ceramics are more easily processed; single-step AM can drastically reduce build times.
- Fabrication of net-shaped ceramic physical assets with no need for further forming via machining or other subtractive methods, which could potentially damage the material because of its brittle nature.
- Manufacturing of parts with complex external and internal geometric characteristics that are impossible to achieve with conventional methods.
- Cost-efficient manufacturing of large ceramic components.
- The enabling of limited production runs or one-off designs without the excessive costs of expensive tooling (moulds, dies, etc.) or skilled craftsmanship.
- Production of advanced ceramics with non-equilibrium-phase assemblages and hierarchically structured heterogeneities that are impossible to achieve via traditional sintering means.
- The possibility of processing any type of monolithic and dissimilar ceramic materials that can exist in powder form.

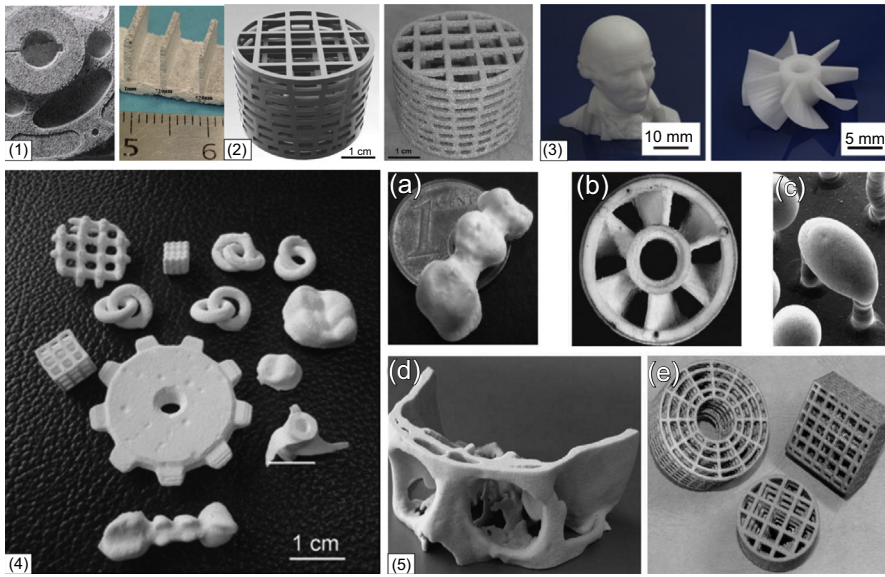

Figure 14.23 Example of additive manufactured ceramic components to show current capabilities.

1. Accurate geometry performed by selective laser sintering (SLS)/melting technology using pure zirconia powder (part of a turbine blade (a) and walls (b)) [38].
2. Demonstration of near-net-shape capability of three-dimensional (3D) printing SiSiC ceramics [53].
3. Parts made of Al_2O_3 fabricated using digital light processing−based 3D printing technology [54].
4. Alumina parts fabricated by the SLS/debinding/sintering process [55].
5. Exemplary ceramic structures fabricated with direct and indirect printing techniques: (a) dental restoration, (b) impeller, (c) micro-pillar array, (d) bone implant, (e) microcellular structures with variable ligament lengths [56].

- Using the high-energy-density laser systems permits irradiation levels that can achieve temperatures up to 3000°C within the reacting powder bed and ensure melting of ceramic materials with even the highest melting/sintering points.
- Enables the building of physical assets by utilising readily available, onsite resources in powder or granulated form and potentially serves as a feasible fabrication method for building physical assets in remote sites and even off-world.

14.5 Future developments

Although the technology governing LAM of ceramics is being researched by multiple teams around the world, the systems have not currently been fully designed and optimised to process ceramic materials. There is still room for further advancement with

regard to process control and material development. Future trends towards improving LAM of ceramics is likely to involve:

- further process development and optimisation for achieving reliable ceramic products by adopting greater levels of process monitoring for a better understanding of the laser−material interaction
- development of suitable adaptive optics that will allow the efficient delivery of thermal input and will prevent the steep thermal gradient that leads to thermal shock
- greater process control, minimising the residual stresses that are a result of thermal processing
- improvement of the single-step LAM processes toward more speedy and/or cost-efficient production of ceramic components
- development of new ceramic materials that are only possible through LAM and that have enhanced properties to address a wider range of applications
- research into more accurate simulation techniques of the material behaviour under laser processing

14.6 Conclusions

This chapter has given an overview of LAM for ceramic materials and a discussion of the application areas and the benefits of using LAM for ceramics.

Ceramic products have been manufactured for many decades via conventional techniques such as extrusion, oven sintering and casting. However, these methods have several inherent disadvantages with regard to capabilities. With the continuous progress and development of laser technology and the newer AM methods, capabilities have emerged that allow cost and time reductions of bespoke/low-volume, high-value ceramic components. In addition, the ability to fully control the manufacturing processing via precise laser−material interaction time direct from CAD data in a layer-by-layer method has enabled the creation of ceramic components with superior properties, design complexities and material combinations that are not possible or feasible via conventional manufacturing techniques.

The use of LAM for metals and polymers has been more rigorously studied and has progressed significantly compared with LAM for ceramic materials. Ceramics represents a new frontier for these AM systems, with many challenges and research needs; however, the material properties that ceramics offer over polymers and metals make the AM of ceramic components an enticing engineering opportunity for aerospace, astronautical and potentially many other technology areas.

References

[1] P. Boch, J.-C. Niepce, Ceramic Materials: Processes, Properties and Applications, ISTE, London, 2007, ISBN 1905209231.

[2] C.B. Carter, M.G. Norton, Ceramic Materials: Science and Engineering, Springer Science & Business Media, New York, 2007, ISBN 0387462716.

[3] W.D. Kingery, H.K. Bowen, D.R. Uhlmann, Introduction to Ceramics, Wiley-Interscience, New York, 1976, ISBN 0471478601.
[4] D.R. Lide, CRC Handbook of Chemistry and Physics, CRC Press, Boca Raton, 2009, ISBN 1420090844.
[5] J.K. Wessel, The Handbook of Advanced Materials: Enabling New Designs, Wiley, Hoboken, 2004, ISBN 9780471454755.
[6] Corrosion performance of ceramic materials in high temperature sulphuric acid environments, in: E.N. Wright, A.W. Merrill, A.L. Charles (Eds.), AIChE Annual Meeting, American Institute of Chemical Engineers, San Francisco, 2006, pp. 31−35.
[7] V.N. Gaitonde, et al., Machinability investigations in hard turning of AISI D2 cold work tool steel with conventional and wiper ceramic inserts, International Journal of Refractory Metals and Hard Materials 27 (4) (2009) 754−763. Elsevier, ISSN:0263-4368.
[8] T. Latka, J. Latka, Ceramic Extruding: Inspiration & Technique, Iola: Krause Publications, 2001, ISBN 0873419030.
[9] J.J. Benbow, S.H. Jazayeri, J. Bridgwater, The flow of pastes through dies of complicated geometry, Powder Technology 65 (1−3) (1991) 393−401. Elsevier B.V., Amsterdam, ISSN:0032-5910.
[10] R. Bayer, M. Knarr, Thermal precipitation or gelling behaviour of dissolved methylcellulose (MC) derivatives—behaviour in water and influence on the extrusion of ceramic pastes. Part 1: fundamentals of MC-derivatives, Journal of the European Ceramic Society 32 (5) (2012) 1007−1018. Elsevier.
[11] M.N. Rahaman, Ceramic Processing, CRC Press, Boca Raton, 2006, ISBN 0849372852.
[12] M. Bengisu, Engineering Ceramics, Springer-Verlag, Berlin, 2001, ISBN 9783642087196.
[13] R.W. Rice, Ceramic Fabrication Technology, Marcel Dekker Inc., New York, 2002, ISBN 0203911024.
[14] D.W. Richerson, Modern Ceramic Engineering: Properties, Processing, and Use in Design, CRC Press, Boca Raton, 2005, ISBN 1574446932.
[15] H. Ohnabe, et al., Potential application of ceramic matrix composites to aero-engine components, Composites Part A: Applied Science and Manufacturing 30 (4) (1999) 489−496. Elsevier, ISSN:1359-835X.
[16] E.I. Suzdal'tsev, D.V. Kharitonov, Methods for the electrophoretic shaping of ceramic products from aqueous slips of inorganic materials (a review), Refractories and Industrial Ceramics 45 (1) (2004). Kluwer Academic Publishers, Dordrecht, ISSN:1573−9139.
[17] I. Corni, M.P. Ryan, A.R. Boccaccini, Electrophoretic deposition: from traditional ceramics to nanotechnology, Journal of the European Ceramic Society 28 (7) (2008) 1353−1367. Elsevier, ISSN:0955-2219.
[18] S.-J.L. Kang, I - Sintering Processes, in: Sintering, Butterworth-Heinemann, Oxford, 2005.
[19] S. Somiya (Ed.), Handbook of Advanced Ceramics: Materials, Applications, Processing and Properties, Elsevier Science Publishing Co. Inc., Oxford, 2012, ISBN 9780123854698.
[20] D.L. Johnson, Solid-State Sintering, J.J. Burke, N.L. Reed, V. Weiss, Ultrafine-grain Ceramics, Springer, New York, US, 1970, pp. 173−183.
[21] R.M. German, P. Suri, S.J. Park, Review: liquid phase sintering, Journal of Materials Science 44 (1) (2009) 1−39. Springer US, New York, ISSN:0022-2461.
[22] S.-J.L. Kang, 4-Initial Stage Sintering, in: Sintering, Butterworth-Heinemann, Oxford, 2005, pp. 39−55.

[23] O.-H. Kwon, Liquid-phase Sintering, John Wiley and Sons, 2006. Materials Science and Technology. Wiley-VCH Verlag GmbH & Co. KGaA, Weinheim.
[24] R. M'Saoubi, et al., High performance cutting of advanced aerospace alloys and composite materials, CIRP Annals - Manufacturing Technology 64 (2) (2015) 557−580, http://dx.doi.org/10.1016/j.cirp.2015.05.002, ISSN:0007-8506.
[25] W.G. Fahrenholtz, et al., Ultra-high Temperature Ceramics: Materials for Extreme Environment Applications, John Wiley & Sons Inc., Hoboken, 2014, ISBN 9781118924419.
[26] F. Monteverde, A. Bellosi, L. Scatteia, Processing and properties of ultra-high temperature ceramics for space applications, Materials Science and Engineering: A 485 (1−2) (2008). Elsevier B.V., Amsterdam, ISSN:0921-5093.
[27] E. Opila, S. Levine, J. Lorincz, Oxidation of ZrB2- and HfB2-based ultra-high temperature ceramics: effect of Ta additions, Journal of Materials Science 39 (19) (2004). Kluwer Academic Publishers, Amsterdam, ISSN:0022-2461.
[28] S.M. Johnson, et al., Recent development in ultra high temperature ceramics at NASA AMES, in: 6th AIAA/DLR/DGLR International Space Planes and Hypersonic Systems and Technologies Conference, vol. 6, American Institute of Aeronautics and Astronautics, 2009, p. 7219. http://arc.aiaa.org/doi/abs/10.2514/6.2009-7219.
[29] A.S. Gohardani, O. Gohardani, Ceramic engine considerations for future aerospace propulsion, Aircraft Engineering and Aerospace Technology 84 (2) (2012). Emerald Group Publishing Ltd., Bingley, ISSN:0002-2667.
[30] S. Schmidt, et al., Advanced ceramic matrix composite materials for current and future propulsion technology applications, Acta Astronautica 55 (3−9) (2004). Elsevier.
[31] K. Parker, Advanced ceramics soar to new heights: advantageous physical properties help these inorganic, nonmetallic materials expand their usage into the manufacture of critical aerospace components, Metal Finishing 104 (3) (2006). Elsevier B.V., Amsterdam, ISSN: 0026-0576.
[32] M. Allahverdi, et al., Processing of advanced electroceramic components by fused deposition technique, Journal of the European Ceramic Society 21 (10−11) (2011) 1485−1490. Elsevier, ISSN:0955-2219.
[33] J.E. Miller, et al., Ballistic performance of porous-ceramic, thermal protection systems, International Journal of Impact Engineering 56 (1) (2013). Elsevier B.V., Ansterdam, ISSN:0734-743X.
[34] F. Kaya, Damage assessment of oxide fibre reinforced oxide ceramic matrix composites using acoustic emission, Ceramics International (2007) 279−284. Elsevier, ISSN:0272-8842.
[35] J. Lin, et al., Effects of sintering velocity on the microstructure and mechanical properties of hot-pressed ZrB_2−SiC−ZrO_2f ceramics, Materials & Design 49 (1) (2013). Elsevier B.V., Amsterdam, ISSN:0261-3069.
[36] N. Chawla, et al., Thermal-shock behavior of a Nicalon-fiber-reinforced hybrid glass-ceramic composite, Composites Science and Technology 61 (13) (2001) 1923−1930. Elsevier.
[37] S.A. Bernard, et al., Direct laser processing of bulk lead zirconate titanate ceramics, Materials Science and Engineering: B 172 (1) (2010). Elsevier B.V., Amsterdam, ISSN:0921-5107.
[38] Ph. Bertrand, et al., Ceramic components manufacturing by selective laser sintering, Applied Surface Science 254 (4) (2007). Elsevier B.V., Amsterdam, ISSN:0169-4332.

[39] Q. Liu, B. Song, H. Liao, Microstructure study on selective laser melting yttria stabilized zirconia ceramic with near IR fiber laser, Rapid Prototyping Journal 20 (5) (2014). Emerald Group Publishing Limited, Bingley, ISSN:1355-2546.
[40] L.A. Taylor, et al., The effects of space weathering on Apollo 17 mare soils: petrography and chemical characterization, Meteoritics & Planetary Science 36 (2) (2001). Blackwell Publishing Ltd, New York, ISSN:1945-5100.
[41] J.A. Happel, Indigenous materials for lunar construction, Applied Mechanics Reviews 46 (6) (1993). ASME, New York, ISSN:0003-6900.
[42] B. Bonin, Extra-terrestrial igneous granites and related rocks: a review of their occurrence and petrogenesis, Lithos 153 (1) (2012). Elsevier B.V., Amsterdam, ISSN:0024-4937.
[43] J. Deckers, J. Vleugels, J.-P. Kruth, Additive manufacturing of ceramics: a review, Journal of Ceramic Science and Technology 5 (4) (2014). Göller Verlag GmbH, Baden Baden, ISSN:2190-9385.
[44] A. Zocca, et al., Additive manufacturing of ceramics: issues, potentialities, and opportunities, Journal of the American Ceramic Society 98 (7) (2015). John Wiley & Sons Ltd, New York, ISSN:1551-2916.
[45] B. Qian, Z. Shen, Laser sintering of ceramics, Journal of Asian Ceramic Societies 1 (4) (2014). Elsevier B.V., Amsterdam, ISSN:2187-0764.
[46] S.M. Gaytan, et al., Fabrication of barium titanate by binder jetting additive manufacturing technology, Ceramics International 41 (5) (2015). Elsevier B.V., Amsterdam, ISSN:0272-8842.
[47] K. Shahzad, et al., Additive manufacturing of zirconia parts by indirect selective laser sintering, Journal of the European Ceramic Society 34 (1) (2014). Elsevier Ltd., Oxford, ISSN:0955-2219.
[48] V.K. Balla, S. Bose, A. Bandyopadhyay, Processing of bulk alumina ceramics using laser engineered net shaping, International Journal of Applied Ceramic Technology 5 (3) (2008). Blackwell Publishing Inc., Hoboken, ISSN:1744-7402.
[49] H.C. Yen, H.H. Tang, Study on direct fabrication of ceramic shell mold with slurry-based ceramic laser fusion and ceramic laser sintering, International Journal of Advanced Manufacturing Technology 60 (9−12) (2012). Springer-Verlag, Berlin, ISSN:0268-3768.
[50] N.K. Tolochko, et al., Absorptance of powder materials suitable for laser sintering, Rapid Prototyping Journal 6 (3) (2000). Emerald Group Publishing Limited, Bingley, ISSN: 1355-2546.
[51] E.O. Olakanmi, K.W. Dalgarno, R.F. Cochrane, Laser sintering of blended Al-Si powders, Rapid Prototyping Journal 18 (2) (2012). Emerald Group Publishing Limited, Bingley, ISSN:1355-2546.
[52] J.-P. Kruth, et al., Binding mechanisms in selective laser sintering and selective laser melting, Rapid Prototpying Journal 11 (1) (2005). Emerald Group Publishing Limited, Bingley, ISSN:1355-2546.
[53] Z. Fu, et al., Three-dimensional printing of SiSiC lattice truss structures, Materials Science and Engineering: A 560 (2013) 851−856. Elsevier.
[54] G. Mitteramskogler, et al., Light curing strategies for lithography-based additive manufacturing of customized ceramics, Additive Manufacturing 1 (2014) 110−118. Elsevier, ISSN:2214-8604.
[55] K. Shahzad, et al., Preparation and indirect selective laser sintering of alumina/PA microspheres, Ceramics International 38 (2) (2012) 1241−1247. Elsevier, ISSN:0272-8842.
[56] N. Travitzky, et al., Additive manufacturing of ceramic-based materials, Advanced Engineering Materials 16 (6) (2014) 729−754. Wiley, ISSN:1527-2648.

Further reading

[1] A. Goulas, R.A. Harris, R.J. Friel, Additive manufacturing of physical assets by using ceramic multicomponent extra-terrestrial materials, Additive Manufacturing 10 (2016) 36−42.
[2] A. Goulas, R.J. Friel, 3d printing with moondust, Rapid Prototyping Journal 22 (5) (2016).
[3] J. Deckers, J. Vleugels, J. Kruth, Additive manufacturing of ceramics : a review, Journal of Ceramic Science and Technology 260 (2014) 245−260.
[4] S. Bose, S. Vahabzadeh, D. Ke, A. Bandyopadhyay, in: Additive Manufacturing, CRC Press, 2015, pp. 143−184, http://dx.doi.org/10.1201/b18893-6.

Laser additive manufacturing of customized prosthetics and implants for biomedical applications

15

M. Munsch
Implantcast GmbH, Buxtehude, Germany

15.1 Introduction

Personalization by tailoring a product to serve a specific need has become an area of great interest in the medical industry. Instead of using standard products that are designed to accommodate many, an individual approach offers much potential for the optimal treatment of a disease.

Today, many biomedical applications are based on personalized products, such as prosthetics and implants that replace lost limbs or bone, or that rebuild a joint function specific to a patient's situation. Other examples are bone augments or partial bone replacements, limb diaphysis components, or full anatomic replicas.

While advancements in the digitization and processing of patient data have greatly facilitated this development over the past decade, one key enabler was progress in the production technology of additive manufacturing (AM), such as laser AM (LAM). It allows for the layer-by-layer production of prosthetics and implants with complex anatomic surface shapes made of a variety of biocompatible or load-bearing materials. Because of the digital process chain, it is feasible to apply patient-specific and custom-made designs to optimally treat the medical condition.

This chapter gives an overview of the potential of LAM for use in customized medical applications, which materials are available, and how the process chain works.

15.2 Biocompatible materials and properties

Biocompatibility is generally viewed as the lack of interaction of a material with living tissue. The biocompatibility of a material is evaluated according to a set of standards defined in ISO 10993 [1]. Today, a broad range of materials that are processed by LAM fulfill this property and can be used to fabricate medical devices. Which material is best suited for each specific application is determined during the product development process, based on a list of requirements. Many variables come into play, such as purpose of use, mechanical and chemical properties, geometric boundaries, and cost.

Laser Additive Manufacturing. http://dx.doi.org/10.1016/B978-0-08-100433-3.00015-4
Copyright © 2017 Elsevier Ltd. All rights reserved.

The following gives a general overview of LAM materials that are in production today or are in development and that offer great future potential for use in medical applications.

15.2.1 Polymeric materials

15.2.1.1 Polyamide

Polyamide (PA) is today the most widely used synthetic LAM material for medical devices. A variety of medical applications have been developed using PA12. Processed by selective laser sintering, PA12 is biocompatible according to EN ISO 10993-1 and U.S. Pharmacopeia classification VI. It is suitable for heat sterilization at 121°C [2].

15.2.1.2 Polyaryletherketones

Polyaryletherketones are thermoplastic polymers with high temperature stability, high mechanical strength, and high chemical resistance. They have been used in biomedical applications of trauma, orthopedic, and spinal implants since the 1980s [3]. LAM technology to process polyetheretherketone is commercially available from EOS [4]. Polyetherketoneketone, another polyaryletherketone material, has received US Food and Drug Administration approval [5]. The technology to process this material is offered by Oxford Performance Materials.

15.2.1.3 Polylactide

Polylactides are a polymeric material with promising potential because they are bioresorbable. A composite of a polylactide and ceramic β-tricalcium phosphate (β-TCP) can be processed with selective laser melting to achieve up to 99.5% density [6]. Further studies of β-tricalcium phosphate $\beta$and poly(D,L)-lactide showed the feasibility of the production of interconnected porous structures with the selective laser melting process [7].

15.2.1.4 Polycaprolactone

Polycaprolactone is another biodegradable polymer that can be processed by selective laser sintering. Scaffolds for repairing skeletal defects were produced successfully [8].

15.2.2 Metallic materials

15.2.2.1 Cobalt–chromium

Cobalt–chromium (CoCr) alloys have a long history of use in dental applications. In orthopedics they come into play for joint replacement and fixation of bone fractures. LAM of CoCr alloys has been well studied and creates manufactured parts with a density more than 99.9% [9]. The in vitro corrosion resistance of additively manufactured CoCr parts is reported to be superior to CoCr cast material [9,10].

15.2.2.2 Commercially pure titanium

Commercially pure titanium (cpTi) and its alloys Ti-6Al-4V and Ti-6Al-7Nb are biocompatible materials and are widely used to treat osseous defects. While cpTi offers good ductility, a higher stiffness and fatigue resistance can be achieved by alloying titanium. The general downside of using metallic materials to treat osseous defects is the difference in the stiffness of the metal compared with that of bone and the resulting stress shielding effect. The mechanical shielding of the bone can cause bone degradation and consequently implant failure. Compared with stainless steel or CoCr, titanium has about half the elastic modulus (around 110 GPa) and thus causes a lower stress shielding effect.

Conditioned by the stable TiO_2 layer that forms on the surface, titanium implants are osseoconductive and can be used for cement-free implant devices. Bone growth onto the implant surface creates secondary stability after the press-fit primary stability decreases. Titanium and its alloys are not used directly as articulation surfaces in joints unless they are coated to reduce wear.

Additive manufacturing of titanium alloys has been well studied because of its numerous applications in the medical industry. Because of the challenge it poses in conventional processes such as cutting or casting, the additive manufacturing of titanium offers great potential.

Compared with casted cpTi, the material showed similar wear characteristics when processed by LAM and offered better wear resistance, finer grain size, and superior microhardness [11]. Processing of porous cpTi structures is feasible and offers a variety of applications in the medical industry [12].

15.2.2.3 Titanium alloy Ti_6Al_4V

The titanium alloy Ti-6Al-4V is widely used in joint replacement because of its good mechanical properties. This versatile material offers high fatigue resistance, good biocompatibility, and osseoconductivity.

LAM-processed Ti-6Al-4V forms a predominant martensitic-like microstructure. As a result of the high temperature gradient and fast cooling, the as-built material has very high strength (yield strength and ultimate tensile strength typically are $>$1.000 MPa); however, at the same time it is brittle with a relatively low ductility of elongation (5%) [13]. Furthermore, considerably high residual stresses remain in the part and can cause part deformation [14,15]. A heat treatment after processing is used to relax stresses and can raise elongation to above 10%, which is required for medical applications, according to current standards for the material.

Several studies have looked at the bone regeneration performance of LAM Ti-6Al-4V. Surface treatment with acids, alkalis, and an anodizing heat treatment was demonstrated to be feasible for the biofunctionalization of LAM Ti-6Al-4V and improved its bone regeneration performance [16]. A method for functionalizing the surface of LAM Ti-6Al-4V with bioactive compounds for drug delivery after implantation was successfully developed [17].

15.2.2.4 Nickel titanium

Nickel titanium, also known as nitinol, is a pseudo-elastic material. Because of a phase transformation during deformation, this alloy displays a high recovery strain. After a would-be plastic deformation of the material, heating causes the part to reset to its previous geometry; hence a shape memory exists. This feature can be used as a controlled function of medical products that is initiated by body heat, as in self-expanding stents.

LAM-processed nitinol shows good biocompatibility [18]. The process parameters not only influence the surface structure and topography but also ion release. Shape recovery of up to 3% was demonstrated for LAM-processed nitinol. Further, the process parameters can locally influence the behavior and tailor the pseudo-elastic effect [19]. Porous structures of nitinol with a porosity up to 88% and lattice material with a density up to 99.8% were fabricated [20].

15.2.2.5 Other titanium alloys

A preliminary study of LAM of the titanium alloy Ti-6Al-7Nb displayed the general feasibility of the process and established the importance of a heat treatment after processing [21]. Depending on the heat treatment parameters, the microstructure could be specifically altered and influenced. Several coatings on LAM Ti-6Al-7Nb samples were tested in an in vivo rat model [22]. The animal study showed no inflammatory reaction for plain, hydroxyapatite, and SiO_2—TiO_2 coatings and suggests that the LAM-processed alloy is well tolerated biologically. LAM processing of the titanium alloy Ti-24Nb-4Zr-8Sn was used to fabricate scaffolds. The solid struts yielded a density up to 99.3% [23].

15.2.2.6 Tantalum

Because of the development of a conventional process to create tantalum sponges, the material came into focus around the year 2000 and found its way into many applications for repairing bone defects. With characteristics similar to titanium, tantalum can be used for cement-free applications at the bone—implant interface. The feasibility of its use in LAM has been successfully demonstrated [24]. Porous tantalum structures were produced and mechanical test results were in the range of cancellous bone. Another study in a rat segmental bone defect model in vivo demonstrated good osseoconductivity and biomechanical performance.

15.2.2.7 Precious metals

Precious metals such as gold and platinum can be processed well via LAM [25,26]. Because of the high investment cost and difficult management of powder waste, typically only small to medium-sized machines are used for processing.

15.2.2.8 Stainless steel

Stainless steel was among the first metals to be used in laser melting processes using only a single component material. Today, LAM of several biocompatible stainless steel alloys, such as 304 or 316L, are readily available on the market.

15.2.2.9 Magnesium and its alloys

Magnesium is a biodegradable material and because of its load-bearing property has a large range of potential medical applications. Initial attempts to process this highly reactive material using LAM were done by melting single tracks of pure magnesium [27,28]. To overcome the difficulty in meeting the narrow window between melting and boiling during the process, the concept of an overpressure LAM machine and the use of magnesium alloys was proposed [29]. The alloy AZ91 was processed to a density of up to 99% [30]. Pure magnesium was later processed to a lattice with a 600-μm pore size [31]. Today, the outgassing of alloying elements and the resulting high residual stresses are challenges for fabricating solid parts and make the material and its alloys the subject of ongoing research and development efforts [32].

15.2.3 Ceramics

Ceramics are bioinert materials with high application potential. Because of their hardness and resistance to wear, ceramics show excellent behavior in tribological systems such as joint bearings. Wear debris is regarded as less critical compared with plastic or metal abrasion, which can lead to infection and consequently implant failure. In general, biodegrable ceramics can also be used as a bone substitute.

The challenge in LAM of ceramics is to fabricate dense and crack-free parts. High melting points cause steep temperature gradients, which lead to residual stresses and crack formation. Technology and process developments are ongoing, such as preheating the material to reduce temperature gradients [33].

15.2.4 Cellular structures

Cellular structures are omnipresent as a building block in nature. Adapting their principles into product design can optimize resulting properties, such as the weight-to-strength ratio, energy absorption, and heat transfer [34].

In medical devices, cellular structures can be used to copy biomimetic features. In tissue engineering, additively manufactured scaffolds are used as a substrate matrix for cells. The mechanical properties or appearance of prosthetics and orthotics can be influenced to a desired state. Today, cellular structures made by LAM of metallic materials are widely used in the field of endoprostheses. A foam-like porous structure similar to trabecular bone is manufactured directly on an implant. The application of such open porous structures at the bone−implant interface can facilitate permanent bone on- and ingrowth and provide secondary stability for cement-free cases.

No secondary coating process is needed to provide the required rough surface properties on implants. Resulting pore sizes of around 0.5 mm can be completely bridged by osteoblast cells [35].

Common approaches for the design of cellular structures are unit cell–based periodic designs that are arranged in two- or three-dimensional (3D) arrays [36], as stochastic or randomized structures [37], or as complex surfaces [38]. The characteristics of cellular structures are influenced by several parameters such as geometry, material, and postprocessing and are typically described in their respective relative or specific values [39]. The resulting properties of such cellular structures can be specifically designed to meet desired requirements. For example, by reducing the apparent density, the Young's modulus can be reduced to that of cancellous bone, which offers potential for reducing the stress shield effect of implants.

Highly filigreed cellular structures are manufactured by pointwise exposition of a powder instead of the conventional scanning strategy of contour and core. Here, the minimal lattice diameter or wall thickness correlates with the resolution of the weld bead. To avoid issues with large data sets that result from the surface representation of such cellular structures, data processing in point clouds or layer format is sometimes applied.

Many studies focused on process development and the characterization of resulting cellular structures for a variety of materials [40–42]. The effect of applying cellular structures at the bone–implant interface also showed great potential [43,44].

Further treatment of the cellular structure with a biomaterial can tap a significant potential for medical applications. In an in vivo study, high-molecular-weight bone morphogenetic proteins were applied into the titanium cellular structure to enhance bone regeneration. After 4 weeks, full regeneration of the segmental bone defect, including the medullary canal and cortex, was observed [45] (Fig. 15.1).

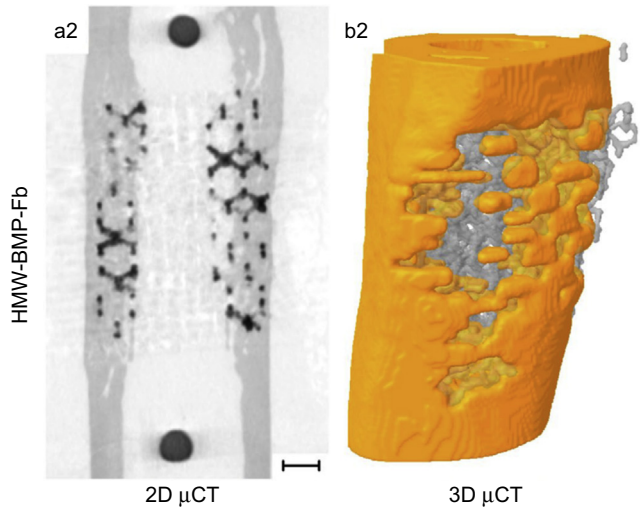

Figure 15.1 Full bone regeneration with the addition of a biomaterial to the porous scaffold [45]. *HMW-BMP-Fb*, high molecular weight fibrinogen with bone morphogenetic proteins.

15.3 Process chain for customized prosthetics and implants

15.3.1 Product requirements

The main goal of the process chain for customized prosthetics and implants is to satisfy the customers' – that is, the patients' – needs by transferring the requirements into a product (see Fig. 15.2). Such requirements are constrained by each individual clinical case and the patient's situation. Decisions on a multitude of options such as function, geometry, material, and interfaces have to be made throughout the development of the product.

15.3.2 Design process

The conventional design process for series prosthetics and implants relies on a computer-aided design (CAD) approach. Based on an average body geometry, a product is developed to serve a function and is subdivided into different sizes to cover a large quantity of the population.

The design process for customized medical devices, however, is based on a reverse-engineering principle. The initial position for the process is the individual patient's clinical situation, which has to be recorded and transferred into a virtual model. Based on this unique data set, a unique product is designed to meet the patient's need.

Advancements in imaging technology enable such applications. Imaging technology used today includes 3D surface scanning or volume scanning techniques such as computed tomography (CT) and magnetic resonance imaging (MRI). For prosthetics or orthodontics, a 3D surface scan of the region of interest can be sufficient. This scan is either performed directly on the patient or indirectly using an impression.

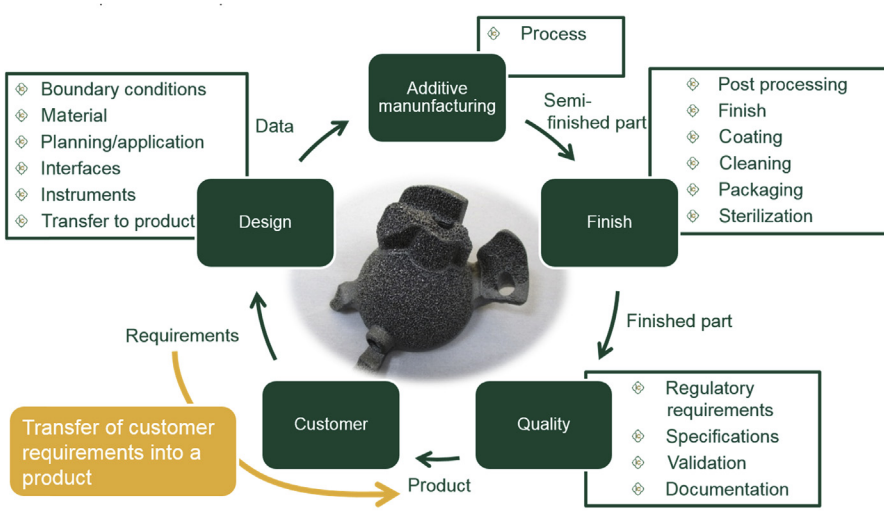

Figure 15.2 Challenges of individualization in the additive manufacturing of medical products.

Volume scanning techniques such as CT or MRI capture a stack of two-dimensional slices of the patient's body. The imaging data are gathered from different angles and then processed by a software algorithm. This allows a virtual 3D model to be reconstructed that accurately reflects the patient's situation. For CT and MRI, the process of segmentation yields a model in which tissue type can be distinguished and classified.

For customized endoprostheses, the subsequent design process is highly interdisciplinary. Clinicians and design engineers, in close collaboration, make use of the resulting model as well as the underlying clinical situation to plan the implant and decide on its features, such as type, positioning, bone resection lines, and type of fixation. Based on this information, a design is derived and, if necessary, iterated and optimized.

Processing the virtual model poses a significant challenge for design engineers because of its complex anatomic shape, represented by free-form surfaces. Conventional CAD software can be used only conditionally to derive a solution. A set of software tools has yet to be procured that allows for complex surface modeling or the design of osseointegrative cellular structures. Moreover, the design of customized endoprostheses not only includes the implant but also incorporates surgery planning, consisting of resection lines, patient-specific instruments, and screw positioning.

The design space and medical boundary conditions have to be considered during the design process, but the AM process itself and subsequent finishing operations also have to be taken into account. Best results are achieved by training designers in AM and establishing a continuous process of knowledge transfer between design and production departments. By implementing such manufacturing knowledge into the design process, customized implants can be fabricated correctly the first time, without the need for prototyping or testing. During the design phase, building directions can be defined, surfaces for support structures described, and additional material stock for postprocessing included.

In general, the nature of the product calls for reducing risk as much as possible. One approach to achieve this is to combine the customized implant with standard components. Using predefined implant connection interfaces, larger defects can be repaired by a combination of standard and modular implant systems. Such interfaces can be incorporated well into the design of the custom components. Instead of conventional postprocesses such as milling or turning, interfaces can be additively manufactured, reducing the overall production effort. Templates for interfaces of sockets, screw threads, or bayonet joints can be established and validated for use.

15.3.3 Production process

The production of medical devices is an extremely regulated process, with requirements defined by higher-level regulatory agencies. Technologically, the actual additive production process does not differ from that used for nonmedical products. Nonetheless, for conformity, the additive production and subsequent processes require the application of good manufacturing practices to ensure product quality. The implementation of such guidelines for LAM has not yet ultimately been established in industry and is up to interpretation by each manufacturer. However, the first industry standards,

such as the ASTM specification for powder bed fusion of the titanium alloy Ti-6Al-4V [46], have been approved and are ready for adoption by the industry. In general, the process chain for customized AM of medical devices should aim for specified and validated production, allowing for complete traceability and assurance of the quality of all its products.

15.3.4 Postprocessing

The postprocessing of customized products has to be applied in such a way that previously determined product requirements are met. The selection of postprocesses depends on the design, material, and LAM process. Metallic materials usually require a heat treatment to reduce residual stress and meet the material specifications.

Customized products for the purpose of implantation need to be sterile at the end of production. Endoprostheses with cellular structures especially have to be thoroughly cleaned to remove any adhering powder particles or residues, such as contamination from the grinding paste or the cooling liquid from computer numerical control processes. Typical methods are shot peening, ultrasonic cleaning, and applicable sterilization processes.

15.4 Applications

15.4.1 Endoprostheses

Endoprostheses are implants that remain in the body and restore the natural function of defective bones or joints. Bone and joint replacements have many requirements because of their load-bearing nature.

The majority of metallic LAM implants today are produced from the titanium alloy Ti-6Al-4V and used for cement-free applications. Here, the implant fixture is not achieved using polymethylmethacrylate (so-called bone cement). Instead, a porous structure at the bone−implant interface facilitates osseointegration and, after losing primary stability through press-fit insertion, secondary stability is achieved.

The need for custom-made implants typically only arises for larger or highly complex defects that cannot be treated with standard products. Such severe cases include trauma, revision of implants, or tumors. Compared with series implants, the share of such customized endoprostheses is negligible.

Today, LAM technology is used to fabricate a variety of products, both custom-made and series products, for application during surgery. Several remarkable applications are presented in the following subsections.

15.4.1.1 Patient-specific surgical guides

The implantation of series or individual implants can be facilitated through custom-made instruments. Such patient-specific instruments (PSIs) are used to objectively identify anatomic landmarks for surgical guidance. Based on preoperative patient

imaging data (CT, MRI), PSIs are custom designed to fit to a unique position and thus orient a drilling or cutting guide to its desired position (see Fig. 15.4). Though a controversial issue among surgeons, claimed benefits are improved implant alignment, reduction of tissue loss, less instrument inventory, and shorter operating time [47].

Since there is low mechanical stress on PSIs during application, a biocompatible polymeric material can be used, such as PA, by selective laser sintering. To avoid plastic debris during application, PSIs can include a metallic cover at the drilling or sawing guide interface.

15.4.1.2 Hip implants

A LAM-fabricated revision hip cup for series application was developed using the titanium alloy Ti-6Al-4V (see Fig. 15.3). The osseointegrative structure at the bone–implant interface facilitates bone ingrowth and secondary stability [48].

Depending on the resection lines of the hip, there is a variety of clinical cases for custom-made partial hip replacements [49]. The LAM-produced part typically replaces the defective bone. The actual joint function is restored using a standard hip cup-and-stem system that is fixated into the custom-made part. Examples of a PSI drilling guide and a custom-made partial hip replacement implant with osseointegrative surface modification are displayed in Figs. 15.4 and 15.5, respectively.

Figure 15.3 MUTARS revision hip cup.
Courtesy of Implantcast GmbH.

Figure 15.4 Patient-specific instrument drilling guide for a partial hip replacement. Courtesy of Implantcast GmbH.

Figure 15.5 Laser additively manufactured custom-made partial hip replacement. Courtesy of Implantcast GmbH.

While much effort is made to design and fabricate to match the implant exactly to the patient's bone model, the in situ situation can be different. Larger defects especially can involve the revision of implants or bone grafts that alter the bone surface. This can ultimately cause misalignment of the custom implant. However, the clinical relevance of the positional accuracy of such custom-made implants is still unclear [50].

A methodology for simulating and designing patient-specific hip stems has been presented [51]. The custom design allows for an optimal load transfer and biomechanical situation. The production of customized hip stems was studied using the additive manufacturing process of electron beam melting with the material Ti-6Al-4V [52]. While commercially viable, the study pointed out that an appropriate postprocessing surface finish is indispensable to achieve a high fatigue limit.

15.4.1.3 Knee implants

Today, customized knee endoprostheses for primary implantation are offered as mass customized service. Not LAM but an indirect manufacturing technology is reportedly used [53]. A wax pattern of the customized knee implant is additively manufactured and then used for investment casting. Clinically, custom-made partial knee replacements show good promise [54].

The process chains for custom-made knee replacements using LAM as a direct manufacturing technology are still being developed and have not been publically announced. Because of the complexity of the geometry of the articulating surface of the knee, LAM has much potential as a viable production technology in the future. An initial study showed the successful application of a partial knee arthroplasty for a large bone and joint defect [55] (Figs. 15.6 and 15.7, respectively).

15.4.1.4 Spinal implants

Interbody fusion cages are used for spinal arthrodesis. Their relatively small size, complex form, and need for surface modification for osseointegration make LAM a viable method for series production today. An evaluation of the structural and mechanical

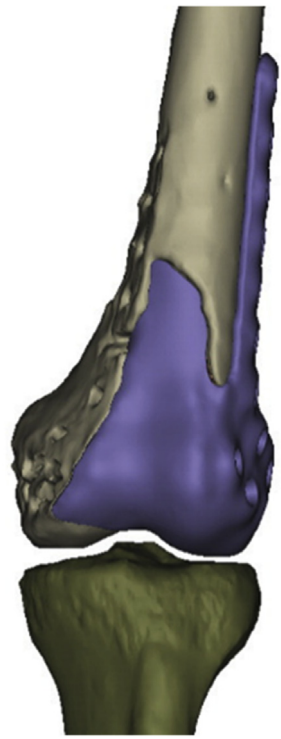

Figure 15.6 Three-dimensional design of a knee implant [55].

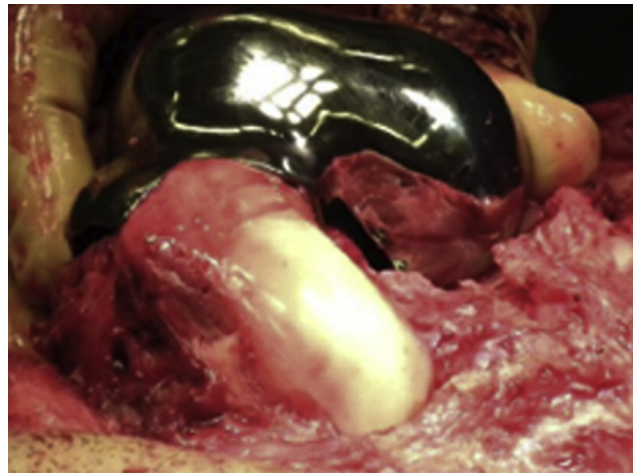

Figure 15.7 Custom-made lateral femoral hemiarthroplasty (Stuyts et al. [55]).

properties of such a spinal implant produced by LAM showed good results [12]. Introducing a porous structure to reduce the specific Young's modulus allows for lower stress shielding and promises a better clinical outcome.

The idea for a process chain to produce patient-specific intervertebral disc implants was proposed [56]. Based on imaging data, bone landmarks were identified and used to design the disc surface. An artificial ball-and-socket joint was designed and positioned with regard to the biomechanical analysis of the patient (see Fig. 15.8).

Figure 15.8 Intervertebral disc implant made of Ti-6Al-4V [56].

15.4.1.5 Upper extremities

Customized joint and partial bone replacements of the humerus, radius, and ulna are facilitated by the LAM process chain and are in production today. But LAM also offers great potential for the treatment of other parts of the upper extremities, such as the complex carpal bones. A method for scaphoid reconstruction using titanium templates was developed [57]. Based on patient imagery, templates are fabricated to fit to surfaces of the proximal and distal scaphoid poles in order to achieve a defined relative position after resection. An in vitro study showed that better preoperative planning can largely improve the outcome.

The symmetry of the bone structure of the human body can benefit and facilitate the problem-solving process. This came into play for the treatment of a shoulder blade affected by a tumor. The imaging data from the area of interest was not fit for reconstruction. Hence, a virtual model of the healthy left side was created, mirrored, and used as the basis for the implant design. The resulting full anatomic scapula replacement for the right side was made by LAM of Ti-6Al-4V (Fig. 15.9).

15.4.1.6 Chest wall

Several procedures for rigid reconstruction of the chest wall are in use today, such as plates, meshes, and polymer composites. However, they may not restore the full function of the chest wall and can limit stability [58].

Large anterior chest wall defects have recently been treated successfully using customized LAM implants. The customized sternal implant shown in Fig. 15.10 was used to reconstruct the chest wall, which was resected because of a tumor [59]. The artificial sternum was made from Ti-6Al-4V. The reported benefits are time savings and rigid reconstruction of the whole sternum without any complications.

Figure 15.9 Full anatomic scapula replacement.
Courtesy of Implantcast GmbH.

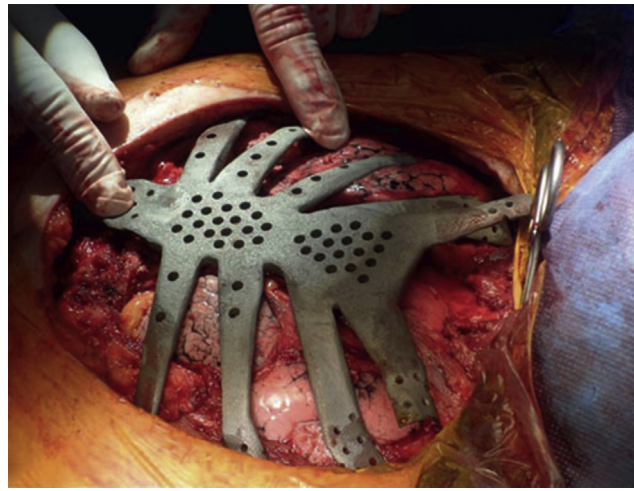

Figure 15.10 Customized sternal implant [59].

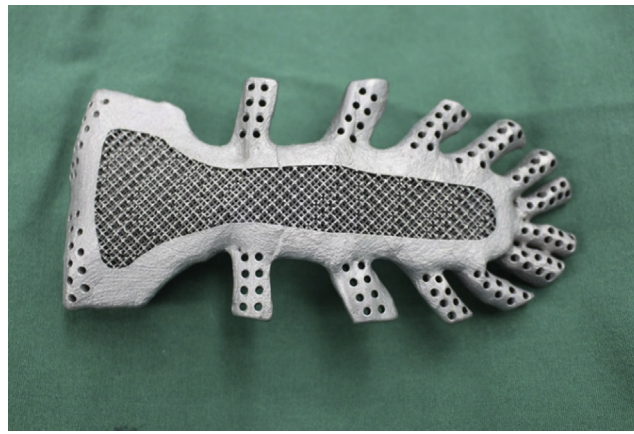

Figure 15.11 Custom-made titanium sternal replacement (Tang Du Hospital, Xi'an, China) [58].

Another custom-made sternal replacement fabricated from a titanium alloy replaced a resected chest bone after cancer [58] (see Figs. 15.11 and 15.12). The implant protects the patient's heart and other organs.

15.4.1.7 Other customized endoprostheses

Looking beyond LAM, other AM technologies are in use today to satisfy patients' needs. A patient-specific foot joint implant was developed based on the simulation of motion. The implant was produced by investment casting based on a printed fused deposition model [60].

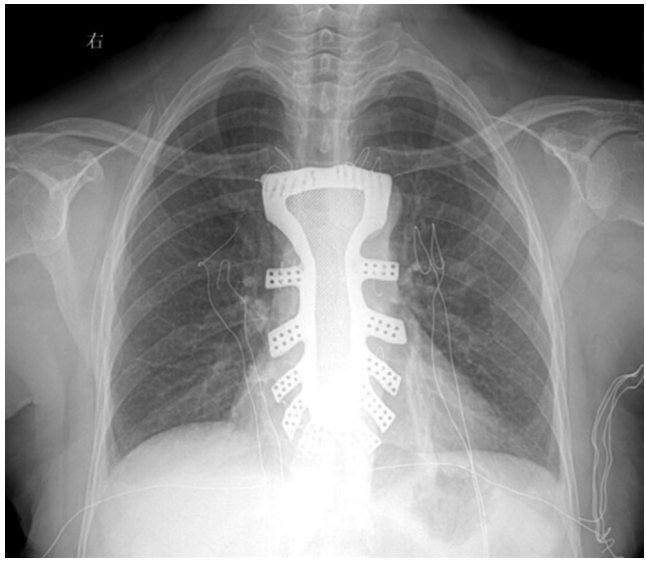

Figure 15.12 Radiograph of the inserted sternal replacement (Tang Du Hospital, Xi'an, China) [58].

A custom-made heel bone made from titanium was used to treat a cancer patient (see Figs. 15.13 and 15.14). It was produced with an electron beam melting process and implanted in Australia in 2014.

15.4.2 Prosthetics and orthotics

Prosthetics and orthotics are externally applied to replace, modify, or support limbs or other bodily functions. AM has played an important role in this field for many years

Figure 15.13 Custom-made heel implant (St. Vincent's Hospital, Melbourne, Australia).

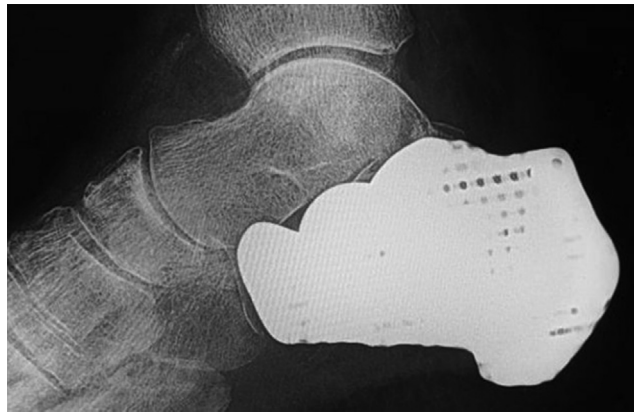

Figure 15.14 Radiograph of a custom-made heel implant (St. Vincent's Hospital, Melbourne, Australia).

Figure 15.15 Artificial limb cladding with a cellular surface structure. Courtesy of 3D Systems, Inc.

and has become one of the standard processes for fabrication of, for example, customized hearing aids and artificial limbs (see Fig. 15.15).

Advancements in 3D imaging create further potential in this field. Typically, imprints and molds are used to re-create a patient's situation. These steps may become obsolete. Camera technology and software allow the outer surface shape of body parts to be scanned directly. The image information is reconstructed into a virtual 3D model used to design the product. AM technology is then used to transfer the designed solutions into an application. This process chain allows for the optimal fit of medical devices and subsequent fulfillment of their desired function.

In a pilot study, a methodology and workflow were developed to build a customized wrist orthosis [61]. Orbital prosthesis are created by stereolithography to restore a natural look [62]. AM also is available for the mass customization of products such as shoe insoles to correct malposition [63]. Traditionally, such customized products require intensive manual work. The shift to a digital process chain with AM as the production technology opens great potential for savings in costs and time.

15.5 Summary

LAM of customized prosthetics and implants has become an essential part of the treatment of certain medical conditions. Such tailored products can meet a patient's needs without compromise.

A broad range of biocompatible materials for LAM processes is available today. This allows the requirements of a multitude of applications to be fulfilled. With future developments along the whole process chain, including in manufacturing technologies and data preparation, further improvement can be expected for customized solutions that enhance even more a patient's situation.

References

[1] ISO 10993−1:2010, Biological Evaluation of Medical Devices Part 1: Evaluation and Testing in the Risk Management Process, 2010.
[2] EOS GmbH, Material Properties Polyamide, 12, 2010, p. 2.
[3] S.M. Kurtz, J.N. Devine, PEEK biomaterials in trauma, orthopedic, and spinal implants, Biomaterials 28 (2007) 4845−4869, http://dx.doi.org/10.1016/j.biomaterials.2007.07.013.
[4] EOS GmbH, EOS PEEK HP3, 2015.
[5] FDA, FDA 510k Clearance Oxford Medical PEKK, 2013. http://www.accessdata.fda.gov/cdrh_docs/pdf12/K121818.pdf.
[6] S. Hoeges, M. Lindner, H. Fischer, W. Meiners, K. Wissenbach, Manufacturing of bone substitute implants using selective laser melting, Analysis (2009) 2230−2234.
[7] M. Lindner, S. Hoeges, W. Meiners, K. Wissenbach, R. Smeets, R. Telle, et al., Manufacturing of individual biodegradable bone substitute implants using selective laser melting technique, Journal of Biomedical Materials Research − Part A 97 A (2011) 466−471, http://dx.doi.org/10.1002/jbm.a.33058.

[8] A. Mazzoli, C. Ferretti, A. Gigante, E. Salvolini, M. Mattioli-Belmonte, Selective laser sintering manufacturing of polycaprolactone bone scaffolds for applications in bone tissue engineering, Rapid Prototyping Journal 21 (2015) 386–392, http://dx.doi.org/10.1108/RPJ-04-2013-0040.
[9] B. Vandenbroucke, J.-P. Kruth, Selective laser melting of biocompatible metals for rapid manufacturing of medical parts, Rapid Prototyping Journal 13 (2007) 196–203, http://dx.doi.org/10.1108/13552540710776142.
[10] F. Alifui-Segbaya, P. Foley, R.J. Williams, The corrosive effects of artificial saliva on cast and rapid manufacture-produced cobalt chromium alloys, Rapid Prototyping Journal 19 (2013) 95–99, http://dx.doi.org/10.1108/13552541311302941.
[11] H. Attar, K.G. Prashanth, A.K. Chaubey, M. Calin, L.C. Zhang, S. Scudino, et al., Comparison of wear properties of commercially pure titanium prepared by selective laser melting and casting processes, Materials Letters 142 (2015) 38–41.
[12] C.Y. Lin, T. Wirtz, F. LaMarca, S.J. Hollister, Structural and mechanical evaluations of a topology optimized titanium interbody fusion cage fabricated by selective laser melting process, Journal of Biomedical Materials Research – Part A 83 (2007) 272–279, http://dx.doi.org/10.1002/jbm.a.31231.
[13] L.E. Murr, S.A. Quinones, S.M. Gaytan, M.I. Lopez, A. Rodela, E.Y. Martinez, et al., Microstructure and mechanical behavior of Ti-6Al-4V produced by rapid-layer manufacturing, for biomedical applications, Journal of the Mechanical Behavior of Biomedical Materials 2 (2009) 20–32, http://dx.doi.org/10.1016/j.jmbbm.2008.05.004.
[14] C. Over, Generative Fertigung von Bauteilen aus Werkzeugstahl X38CrMoV5-1 und Titan TiAl6V4 mit “Selective Laser Melting.”, Shaker, Aachen, 2003.
[15] M. Munsch, Reduzierung von Eigenspannungen und Verzug in der laseradditiven Fertigung, Cuvillier, Göttingen, 2013.
[16] S. Amin Yavari, J. van der Stok, Y.C. Chai, R. Wauthle, Z. Tahmasebi Birgani, P. Habibovic, et al., Bone regeneration performance of surface-treated porous titanium, Biomaterials 35 (2014) 6172–6181, http://dx.doi.org/10.1016/j.biomaterials.2014.04.054.
[17] J. Vaithilingam, S. Kilsby, R.D. Goodridge, S.D.R. Christie, S. Edmondson, R.J.M. Hague, Functionalisation of Ti6Al4V components fabricated using selective laser melting with a bioactive compound, Materials Science and Engineering: C 46 (2015) 52–61, http://dx.doi.org/10.1016/j.msec.2014.10.015.
[18] T. Habijan, C. Haberland, H. Meier, J. Frenzel, J. Wittsiepe, C. Wuwer, et al., The biocompatibility of dense and porous Nickel-Titanium produced by selective laser melting, Materials Science and Engineering: C 33 (2013) 419–426, http://dx.doi.org/10.1016/j.msec.2012.09.008.
[19] T. Bormann, R. Schumacher, B. Müller, M. Mertmann, M. Wild, Tailoring selective laser melting process parameters for NiTi implants, Journal of Materials Engineering and Performance 21 (2012) 2519–2524, http://dx.doi.org/10.1007/s11665-012-0318-9.
[20] M. de Wild, T. Schollbach, R. Schumacher, E. Schkommodau, T. Bormann, Effects of laser parameters and scanning strategy on structural and mechanical properties of 3D NiTi implants fabricated with selective laser melting, Biomedical Engineering/Biomedizinische Technik 58 (2013) 9–10, http://dx.doi.org/10.1515/bmt-2013-4088.
[21] T. Sercombe, N. Jones, R. Day, A. Kop, Heat treatment of Ti-6Al-7Nb components produced by selective laser melting, Rapid Prototyping Journal 14 (2008) 300–304, http://dx.doi.org/10.1108/13552540810907974.

[22] H. Rotaru, G. Armencea, D.I. Spîrchez, C. Berce, T.E. Marcu, In vivo behavior of surface modified Ti 6 Al 7 Nb alloys used in selective laser melting for custom-made implants. A preliminary study, Romanian Journal of Morphology and Embryology 54 (2013) 791−796.
[23] Y.J. Liu, X.P. Li, L.C. Zhang, T.B. Sercombe, Processing and properties of topologically optimised biomedical Ti − 24Nb − 4Zr − 8Sn scaffolds manufactured by selective laser melting, Materials Science and Engineering: A 642 (2015) 268−278.
[24] R. Wauthle, J. van der Stok, S. Amin Yavari, J. Van Humbeeck, J.-P. Kruth, A.A. Zadpoor, et al., Additively manufactured porous tantalum implants, Acta Biomaterialia 14 (2014) 217−225, http://dx.doi.org/10.1016/j.actbio.2014.12.003.
[25] M. Khan, P. Dickens, Selective laser melting (SLM) of gold (Au), Rapid Prototyping Journal 18 (2012) 81−94, http://dx.doi.org/10.1108/13552541211193520.
[26] D. Zito, A. Carlotto, A. Loggi, P. Sbornicchia, D. Bruttomesso, S.A. Progold, Definition and Solidity Idity of Gold and Platinum Jewels Produced Using Selective Laser Melting SLM^{TM} Technology, 2015.
[27] C.C. Ng, Selective laser sintering of magnesium powder for fabrication of porous structures, in: 17th International Conference on Advanced Laser Technologies, Antalya, 2009.
[28] C.C. Ng, M.M. Savalani, H.C. Man, I. Gibson, Layer manufacturing of magnesium and its alloy structures for future applications, Virtual and Physical Prototyping 5 (2010) 13−19, http://dx.doi.org/10.1080/17452751003718629.
[29] M. Gieseke, C. Noelke, S. Kaierle, V. Wesling, H. Haferkamp, Selective laser melting of magnesium and magnesium alloys, in: Magnesium Technology, 2013, John Wiley & Sons, Inc., Hoboken, NJ, USA, 2013, pp. 65−68, http://dx.doi.org/10.1002/9781118663004.ch11.
[30] L. Jauer, W. Meiners, R. Poprawe, Selective laser melting of biodegradable metals, European Cells and Materials 26 (2013) 21.
[31] J. Matena, S. Petersen, M. Gieseke, M. Teske, M. Beyerbach, A. Kampmann, et al., Comparison of selective laser melted titanium and magnesium implants coated with PCL, International Journal of Molecular Sciences 16 (2015) 13287−13301, http://dx.doi.org/10.3390/ijms160613287.
[32] M. Gieseke, T. Kiesow, C. Nölke, S. Kaierle, H.J. Maier, H. Haferkamp, Selektives Laserstrahl-schmelzen von Magnesium und Magnesiumlegierungen, Rapid Technologies, Erfurt, 2015.
[33] Q. Liu, Y. Danlos, B. Song, B. Zhang, S. Yin, H. Liao, Effect of high-temperature pre-heating on the selective laser melting of yttria-stabilized zirconia ceramic, Journal of Materials Processing Technology 222 (2015) 61−74.
[34] L.J. Gibson, M.F. Ashby, Cellular Solids: Structure and Properties, second ed., Cambridge University Press, Cambridge, U.K, 1999.
[35] P.H. Warnke, T. Douglas, P. Wollny, E. Sherry, M. Steiner, S. Galonska, et al., Rapid prototyping: porous titanium alloy scaffolds produced by selective laser melting for bone tissue engineering, Tissue Engineering Part C, Methods 15 (2009) 115−124, http://dx.doi.org/10.1089/ten.tec.2008.0288.
[36] L. Mullen, R.C. Stamp, W.K. Brooks, E. Jones, C.J. Sutcliffe, Selective Laser Melting: a regular unit cell approach for the manufacture of porous, titanium, bone in-growth constructs, suitable for orthopedic applications, Journal of Biomedical Materials Research Part B Applied Biomaterials 89B (2009) 325−334, http://dx.doi.org/10.1002/jbm.b.31219.

[37] L. Mullen, R.C. Stamp, P. Fox, E. Jones, C. Ngo, C.J. Sutcliffe, Selective laser melting: a unit cell approach for the manufacture of porous, titanium, bone in-growth constructs, suitable for orthopedic applications. II. Randomized structures, Journal of Biomedical Materials Research − Part B, Applied Biomaterials 92 (2010) 178−188, http://dx.doi.org/10.1002/jbm.b.31504.

[38] C. Yan, L. Hao, A. Hussein, P. Young, Ti-6Al-4V triply periodic minimal surface structures for bone implants fabricated via selective laser melting, Journal of the Mechical Behavior of Biomedical Materials 51 (2015) 61−73, http://dx.doi.org/10.1016/j.jmbbm.2015.06.024.

[39] O. Rehme, Cellular Design for Laser Freeform Fabrication, Cuvillier, Göttingen, 2010.

[40] S.M. Ahmadi, G. Campoli, S. Amin Yavari, B. Sajadi, R. Wauthle, J. Schrooten, et al., Mechanical behavior of regular open-cell porous biomaterials made of diamond lattice unit cells, Journal of the Mechical Behavior of Biomedical Materials 34 (2014) 106−115, http://dx.doi.org/10.1016/j.jmbbm.2014.02.003.

[41] H. Attar, M. Calin, L.C. Zhang, S. Scudino, J. Eckert, Manufacture by selective laser melting and mechanical behavior of commercially pure titanium, Materials Science and Engineering A 593 (2014) 170−177, http://dx.doi.org/10.1016/j.msea.2013.11.038.

[42] Y. Wang, Y. Shen, Z. Wang, J. Yang, N. Liu, W. Huang, Development of highly porous titanium scaffolds by selective laser melting, Materials Letters 64 (2010) 674−676, http://dx.doi.org/10.1016/j.matlet.2009.12.035.

[43] J.E. Biemond, G. Hannink, N. Verdonschot, P. Buma, Bone ingrowth potential of electron beam and selective laser melting produced trabecular-like implant surfaces with and without a biomimetic coating, Journal of Materials Science Materials in Medicine 24 (2013) 745−753, http://dx.doi.org/10.1007/s10856-012-4836-7.

[44] J. Matena, M. Gieseke, A. Kampmann, S. Petersen, H. Murua Escobar, K. Sternberg, et al., Characterisation of cell growth on titanium scaffolds made by selective laser melting for tissue engineering, Biomedical Engineering/Biomedizinische Technik 58 (2013) 9−10, http://dx.doi.org/10.1515/bmt-2013-4047.

[45] J. van der Stok, M.K.E. Koolen, M.P.M. de Maat, S.A. Yavari, J. Alblas, P. Patka, et al., Full regeneration of segmental bone defects using porous titanium implants loaded with BMP-2 containing fibrin gels, European Cells and Materials 29 (2015) 141−153 (discussion 153−4).

[46] ASTM F3001-14, Standard Specification for Additive Manufacturing Titanium-6 Aluminum-4 Vanadium with Powder Bed Fusion, 2014, http://dx.doi.org/10.1520/F3001.

[47] L. Renson, P. Poilvache, H. Van den Wyngaert, Improved alignment and operating room efficiency with patient-specific instrumentation for TKA, Knee 21 (2014) 1216−1220, http://dx.doi.org/10.1016/j.knee.2014.09.008.

[48] V. Seyda, M. Munsch, P. Scheinemann, C. Emmelmann, Laser additive manufacturing of modified implant surfaces with osseointegrative characteristics, Physics Procedia 12 (2011) 375−384, http://dx.doi.org/10.1016/j.phpro.2011.03.048.

[49] M. Rudert, B.M. Holzapfel, H. Pilge, H. Rechl, R. Gradinger, Partial pelvic resection (internal hemipelvectomy) and endoprosthetic replacement in periacetabular tumors, Operative Orthopädie und Traumatologie 24 (2012) 196−214, http://dx.doi.org/10.1007/s00064-012-0161-z.

[50] M. Baauw, G.G. van Hellemondt, M.L. van Hooff, M. Spruit, The accuracy of positioning of a custom-made implant within a large acetabular defect at revision arthroplasty of the hip, The Bone and Joint Journal 97-B (2015) 780−785, http://dx.doi.org/10.1302/0301-620X.97B6.35129.

[51] S. Rahmati, F. Abbaszadeh, F. Farahmand, An improved methodology for design of custom-made hip prostheses to be fabricated using additive manufacturing technologies, Rapid Prototyping Journal 18 (2012) 389–400, http://dx.doi.org/10.1108/13552541211250382.
[52] M. Cronskär, M. Bäckström, L.-E. Rännar, Production of customized hip stem prostheses – a comparison between conventional machining and electron beam melting (EBM), Rapid Prototyping Journal 19 (2013) 365–372, http://dx.doi.org/10.1108/RPJ-07-2011-0067.
[53] A. Gregg, Perfect Knee Implants, Courtesy of a 3-D Printer, 2015. Washington Post, http://www.washingtonpost.com/business/capitalbusiness/surgeons-turn-to-printed-implants/2014/12/23/0d5c353e-8486-11e4-9534-f79a23c40e6c_story.html.
[54] M.K. Demange, A. Von Keudell, C. Probst, H. Yoshioka, A.H. Gomoll, Patient-specific implants for lateral unicompartmental knee arthroplasty, International Orthopaedics (2015) 4–7, http://dx.doi.org/10.1007/s00264-015-2678-x.
[55] B. Stuyts, G. Peersman, E. Thienpont, E. Van den Eeden, H. Van der Bracht, Custom-made lateral femoral hemiarthroplasty for traumatic bone loss: a case report, Knee (2015) 6–10, http://dx.doi.org/10.1016/j.knee.2015.06.008.
[56] N. De Beer, A. Van Der Merwe, Patient-specific intervertebral disc implants using rapid manufacturing technology, Rapid Prototyping Journal 19 (2013) 126–139, http://dx.doi.org/10.1108/13552541311302987.
[57] M. Haefeli, D.J. Schaefer, R. Schumacher, M. Müller-Gerbl, P. Honigmann, Titanium template for scaphoid reconstruction, The Journal of Hand Surgery, European Volume 40 (2015) 526–533, http://dx.doi.org/10.1177/1753193414549008.
[58] W. Hipolite, Woman with the Metal Chest : Surgeons Implant World's First 3D Printed Titanium Sternum, 2015. 3DPrint.com. http://3dprint.com/79908/3d-printed-sternum-implant/.
[59] A. Turna, K. Kavakli, E. Sapmaz, H. Arslan, H. Caylak, H.S. Gokce, et al., Reconstruction with a patient-specific titanium implant after a wide anterior chest wall resection, Interactive Cardiovascular and Thoracic Surgery 18 (2014) 234–236, http://dx.doi.org/10.1093/icvts/ivt408.
[60] S.C. Raghatate, A.M. Kuthe, T.R. Deshmukh, S.W. Dahake, Rapid prototyping-assisted fabrication of the customized metatarsophalangeal joint implant (SamKu): a case report, Rapid Prototyping Journal 20 (2014) 270–279, http://dx.doi.org/10.1108/RPJ-08-2012-0077.
[61] D. Palousek, J. Rosicky, D. Koutny, P. Stoklásek, T. Navrat, Pilot study of the wrist orthosis design process, Rapid Prototyping Journal 20 (2013) 27–32, http://dx.doi.org/10.1108/RPJ-03-2012-0027.
[62] J. Sun, Y. Xiong, X. Chen, J. Xi, Imperfect symmetry transform for orbital prosthesis modelling, Rapid Prototyping Journal 19 (2013) 180–188, http://dx.doi.org/10.1108/13552541311312175.
[63] SOLS Systems. http://www.sols.com/, 2015.

Laser additive printing of cells

16

L. Koch, A. Deiwick, B. Chichkov
Laser Zentrum Hannover e.V., Hannover, Germany

16.1 Introduction

Three-dimensional (3D) printing or additive manufacturing was used for industrial rapid prototyping for decades, and now these techniques are becoming increasingly attractive for biomedical applications, including the printing of implants, which are usually made of biocompatible (but not biodegradable) materials, and the printing of so-called scaffolds, made of biodegradable materials that are, after implantation, decomposed by cells and replaced with autologous (the body's own) material. Proteins, DNA, and living cells have also been printed, and tissue printing has been demonstrated. However, printing fully functional organs as the ultimate goal of cell printing is still far from being realized.

The following three techniques are mainly applied to print cells [23,40]: inkjet printing, extrusion printing (also called bioplotting, syringe-based printing, and robotic dispensing), and laser-assisted bioprinting (LaBP; also called laser-induced forward transfer, biological laser-printing, laser bioprinting, and matrix-assisted pulsed laser evaporation direct-write).

With inkjet printing [2,12,45], droplets with very small volumes can be generated at high repetition rates. Because of shear forces in the nozzle, however, only materials with low cell densities (typically 10^6/mL, compared with 10^8/mL for LaBP) and low viscosity [typically <10 mPa s, compared with 1 Pa s for LaBP [28]] are printable.

Extrusion printing also uses nozzles [8,35,46]; the biomaterial is pressed (extruded) through them as a strand. Nozzles with inner diameters between 50 and 1000 μm are applied. Since high shear forces occur in small nozzles, similar to inkjet printing, this implies that only materials with low viscosity and low cell density can be printed; therefore bigger nozzles with diameters between 500 and 1000 μm are usually used. Because of this, the printing resolution is relatively low. Since in some native tissues the distance between neighboring blood vessels is only 200 μm, the printing resolution of 500 μm is not suitable for printing such complex tissues. As a nozzle-free technique, LaBP has the advantage of printing materials with high cell densities and high viscosity at high resolutions.

In addition to these three bioprinting techniques (each of which is used by several groups), there are others; however, some of them have been tested only for a short time by one or two groups, so estimating their potential for tissue printing is not yet possible. One example is a technique referred to as "acoustic droplet ejection," which

Laser Additive Manufacturing. http://dx.doi.org/10.1016/B978-0-08-100433-3.00016-6
Copyright © 2017 Elsevier Ltd. All rights reserved.

is nozzle-free but seems to be limited to low viscosity (eg, 1−18 mPa s [11]) and low cell density.

Some techniques are being investigated for two-dimensional (2D) arrangements of cells, which are likely not suitable for 3D printing of cells. For example, the imprint technique or procedure whereby cells are seeded randomly on a surface, which is partially patterned with proteins so that the cells adhere only on the protein patterns falls into that category.

Another laser-based technique is called "laser-guided direct-write" [36]. With this method, based on the optical tweezer effect, cells swimming in a culture medium are trapped by a laser beam. The laser beam is directed onto a surface in the cell culture medium, causing the cells to adhere to the surface position predetermined by the laser beam or to the cells already present at this position (analogous to 3D printing). However, this technique is extremely slow and therefore is rarely used.

With laser-assisted bioprinting, more than 100,000 cells per second can be printed, with a high cell survival rate. Printing tissue with tens of millions of cells has already been demonstrated.

16.2 Laser-assisted bioprinting

In principle, the setup for LaBP consists of two horizontal co-planar glass slides [or quartz slides, if ultraviolet (UV) lasers are applied]. The upper glass slide (called donor) is coated with a thin layer of a laser-absorbing material and a thicker layer of the biomaterial to be printed (Fig. 16.1). Typically, the biomaterial is a sol, the

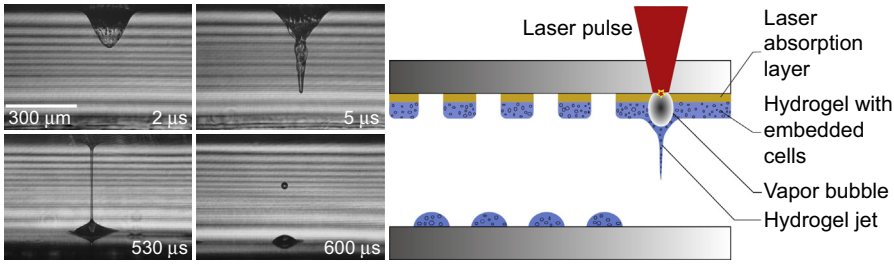

Figure 16.1 (Left) Stroboscopic images of the printing process between glass slides. The images were taken at different time delays with respect to the laser pulse. The distance between the glass slides is about 500 µm. Because of interference at the glass slides, *dark horizontal lines* appear. Shortly after the laser pulse impact, a bubble develops and grows, driven by the expanding vaporized absorption layer. This bubble collapses after a few microseconds without reaching the lower glass slide, forming a liquid jet. This jet lasts for a few hundred microseconds, reaches the lower glass slide, and remains there as a droplet. (Right) Sketch of laser-assisted bioprinting. The upper glass slide is coated underneath with a laser-absorbing layer and a layer of biomaterial to be transferred—a hydrogel or sol with embedded cells. Laser pulses are focused through the upper glass slide into the absorbing layer. Evaporating this layer generates an expanding vapor bubble that propels the biomaterial toward the lower glass slide.

nongelled precursor of a hydrogel, with cells embedded within it. Then, the donor slide is mounted upside down above the second, lower glass slide (called the acceptor) in the setup so that the sol faces the acceptor slide. The laser pulses are focused through the glass slide into the absorption layer. The laser photons are absorbed by the electrons in this layer, generating plasma within tens of picoseconds. This plasma is further heated by laser irradiation. The absorption layer is thereby evaporated in the focal spot, generating a vapor bubble. This bubble expands into a half-space, since it was generated at the surface of the glass slide (Fig. 16.1). However, resistance against expansion is lowest perpendicular to the surface because in this direction the amount of hydrogel is small compared to the amount in the lateral direction. Therefore the expanding vapor bubble possesses an elongated shape. Because the sol layer stretches, a flow is initiated inside of this layer. By expansion, the inner pressure decreases below the atmospheric pressure, causing the vapor bubble to collapse within a few microseconds after the laser pulse impact. Because of inertia, surface tension, and the bubble collapse, the sol forefront of the bubble moves on, forming a sol jet that is fed further by the sol flow [43].

Thus the sol flows as a jet toward the lower acceptor glass slide. Because of a limited "reservoir" of sol, springing from an area on the donor slide with about 200 μm in diameter, the sol jet disrupts after a few hundred microseconds. The sol remains as a droplet on the acceptor slide. By moving the laser and the glass slides independently, any desired 2D pattern can be generated on the acceptor, and 3D patterns have also been printed layer by layer.

A 10- to 100-nm-thick layer of metal (gold [13], titanium [15], silver [24]) is usually used as the laser-absorbing material. Alternatively, polymer layers (90−150 nm triazene [37], 7 μm polyimide [6], 1.35 μm polyethylene naphthalate foil [44]), gelatin layers [42], a two-layer system (10 μm cyanoacrylate + 25 μm brass foil [29]), and a system without an absorption layer [4] have been used. In the latter case, the biomaterial to be printed also serves as the absorption material. However, the biomaterial does not necessarily have good optical properties for absorbing laser radiation, and laser radiation, especially if in the UV range, can potentially harm the cells.

These diverse absorption materials have been applied for different reasons. Ablating and vaporizing the absorption material generates debris and, in the case of polymer materials, altered chemical substances. These substances may be gaseous and volatile. However, some debris is deposited in the printed pattern. This is not necessarily problematic, since gold and titanium oxide, for example, are inert. Nevertheless, if thicker 3D structures are printed, the debris may be clearly visible. If one day complete organs can be printed for implantation, this debris presumably will not be tolerated. Therefore the two-layer system of an adhesive cyanoacrylate layer on the glass slide and a brass foil on top [29] was investigated. The laser pulse evaporates the cyanoacrylate only and the vapor bubble bulges the brass foil without disrupting it. Using a 7-μm layer of polyimide [6], this so-called blister effect can be integrated into one layer. A part of the polyimide directly at the glass slide is evaporated, bulging the remaining part. This bulging/blister effect is powerful enough to induce biomaterial transfer.

In addition to the diverse laser absorption materials, different lasers have also been applied. Two groups used near-infrared lasers with a 1064-nm wavelength [7,26]; other groups applied UV laser systems with wavelengths between 193 [29] and 355 nm [15]. UV lasers are advantageous for polymeric absorption materials, since single UV photons have enough energy to induce chemical reactions. Thus they break up solid polymers and convert them (in an ideal situation, converting them completely) into gaseous substances. On the other hand, UV radiation may be harmful to cells.

So far, near-infrared lasers have been combined with metal (gold, titanium) absorption layers only, causing debris to be deposited in the printed structure. However, metal absorption layers are advantageous for spreading biomaterials most evenly on the absorption layer surface.

16.2.1 Printing material compositions

On one hand, in the creation of a 3D printed pattern, a certain stiffness of the printed material is required. On the other hand, for the printing process, a viscous sol, not a stiff gel, has to be used; the gelling should occur after printing.

Cell printing usually applies multicomponent biomaterials that have four major properties: (1) a cell-friendly environment, (2) an appropriate viscosity for the printing process, (3) stiffness by gelling after printing, and (4) no unwanted stimuli are induced in the cells. These properties are ensured by the different components. As an example, alginate (1−6% w/v) provides a suitable viscosity for printing and can be gelled by adding calcium ions. For a cell-friendly environment, blood plasma can be added. Thus alginate would be printed mixed with plasma and cells. After printing, a calcium chloride solution is sprayed on the printed pattern.

Another example is fibrin gel, which is found in the human body. Gelation starts when fibrinogen is mixed with thrombin. Both provide a cell-friendly environment, but their viscosity is too low. Therefore fibrinogen (or thrombin) is printed mixed with cells and hyaluronic acid, which is also found in the human body and has a high viscosity. Thrombin (or fibrinogen) is used for the next printed layer. Thus the fibrinogen and the thrombin from the succeeding layers gel and stiffen the printed structure. Fibrin is also an example for stimulating the migration of keratinocyte cells. If printed with fibrin, these cells might reorganize in the printed structure and later be found in a completely different pattern than the printed one.

Another gel of interest is collagen, the most abundant protein in the human body. A collagen sol is acidic, however, and cells inside would quickly die. Therefore it needs to be mixed with a base to yield a physiological pH of 7.4 before cells are embedded. Collagen then starts to gel. The gelation process takes some minutes, depending on temperature and concentration, whereas the viscosity changes with the locally different advanced gelation. If the neutralized collagen with cells is printed during the gelation process, only printing with a reduced resolution is possible because of the inhomogeneous viscosity.

16.2.2 Controlling the droplet volume

The volume of the printed droplets depends on several parameters. Obviously, it depends on the laser pulse energy and focus area, but also on the biomaterial's viscosity and surface tension and on the thickness of the laser absorption layer and the biomaterial layer.

In this case it is the dynamic viscosity that is important; this can differ significantly from the static viscosity. The dependence of viscosity on the shear velocity is specific to the material. Since shear forces can destroy cells, shear-thinning sols, such as alginate and hyaluronic acid, are advantageous. Their viscosity decreases when propelled forward by the vapor bubble and in the sol jet, inducing lower shear forces on the cells. Shear-thickening sols would be problematic.

In general, there are three laser pulse energy domains. Below a certain threshold (the lower limit), there is no material transfer; though a vapor bubble is generated and a jet might form as well, the biomaterial remains at the donor slide because of the surface tension. Above an upper limit, the vapor bubble will not collapse but burst, causing strong splashing and depositing several droplets in an irregular pattern on the acceptor. In the energy domain of interest between these limits, a jet dynamic occurs, leading to the deposition of a single droplet at a predefined position. In this energy domain the droplet volume increases with the laser pulse energy in a nearly linear correlation. Of course, in addition to the laser pulse energy, the laser focus area is also of importance for the printed droplet volume.

The dependence of the printed droplet volume on viscosity and thickness of the biomaterial layer is more complex. A thicker layer usually results in a larger droplet volume. By contrast, there is no systematic dependence on viscosity at different laser pulse energies. The droplet volume increases with increasing viscosity until a maximum value is reached, then it decreases with further increases in the hydrogel's viscosity [18]. This effect is even more pronounced with an increased sol layer thickness. The specific viscosity, at which the printed droplet volume reaches its maximum, increases with increasing sol layer thickness. Depending on the printed material, the volume of a printed droplet can be in the range of sub-picoliter to several nanoliters and more.

Examples of laser-printed cell patterns with different droplet volumes are shown in Fig. 16.2.

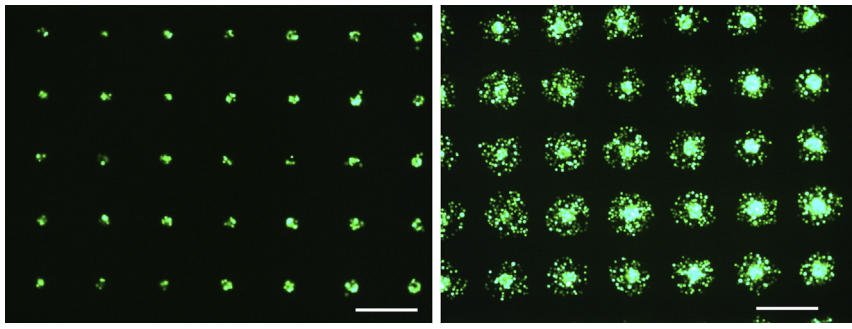

Figure 16.2 Dependence of the droplet volume on laser pulse energy: 20 μJ (left) and 30 μJ (right). NIH/3T3 cells embedded in a 1:1 mixture of fibrinogen and hyaluronic acid and printed onto a layer of fibrin. Scale bars are 300 μm.

16.2.3 Impact on cells

Several groups have reported successful printing of diverse cell types using different laser printing setups. Cells cannot be affected by the printing process: This is a key requirement for applying these bioprinting techniques. This means that the printed cells must maintain their vitality and behavior, as well as their phenotype and genotype, and that stem cells must retain their differentiation potential. To ensure this, the effect of the printing process on cells was studied comprehensively.

The cell vitality was determined directly after printing. A nearly 100% survival rate was reported by several groups with different lasers, absorption layers, and cell types [3,24,26]. Apoptosis was investigated with cell lines and human mesenchymal stem cells (MSCs) up to 48 h after printing; no increase in apoptosis was detected [26]. Proliferation of the printed cells was also studied with cell lines and stem cells [3,26]. Compared with nonprinted control cells, no difference in the proliferation behavior was observed. Furthermore, single-cell electrophoresis demonstrated that the printing process does not induce DNA strand breaks [26,39]; the genotype of printed cells is not affected. Since high temperatures were generated in the absorption layer by the laser pulses, heat shock protein expression was investigated via immunocytochemical studies [3,3,19]; no increase of the expression was detected.

For the printing of stem cells, it is important that the printing does not affect their differentiation potential and behavior. In a flow cytometric analysis of the immunophenotype of human MSCs 4 days after printing, Koch et al. [26] detected no significant difference in the ratio of expression of typical MSC marker proteins on the printed cells versus control cells; the immunophenotype was not influenced. Gruene et al. [19,20] studied the influence of laser printing on the differentiation behavior of MSCs. No difference in the differentiation behavior of the printed and nonprinted stem cells toward different lineages was observed.

Summing up, so far all studies consistently showed that printed cells are not affected by the laser printing procedure; they are vital and fully functional.

16.3 Applications

For the generation of replacement tissue and organs, as well as cell-based therapies, an extensive understanding of interactions between different cells and their environment is essential. However, conventional cell studies ex vivo conducted on 2D plastic cell culture surfaces are significantly limited and are not appropriate to simulate complex interactions in cell microenvironments in vivo and in 3D tissue; cell behavior differs dramatically in three dimensions [10,16].

Printed 3D cell models could enable a better understanding of tissue-specific cell behavior, tissue regeneration, and the effects of pharmaceuticals or chemical agents ex vivo. Complex tissue, especially with an integrated vascular network, has not yet been printed. Nevertheless, first steps in this direction have already been taken. Different laser-printed 3D cell constructs are presented below, including defined 3D spot arrays for microscopic observation of cell−cell interactions, a monocellular 3D

stem cell graft, a multicellular 3D skin equivalent, stackable biopapers with printed cells, and in situ printing of cells into mice.

16.3.1 Printed multicellular patterns for cell–cell interaction studies

Cellular microarrays have been developed to study cell responses in multiple experiments in parallel [17]. They enable reproducible studies of the effects of drugs, proteins, growth factors, and biomaterials. Recent studies indicate that local cell density, cellular spacing, cell–cell communication, and binding of cells to their 3D environment affect or even control cell behavior and tissue functionality [14].

Gruene et al. [21] printed droplet arrays of human adipose-derived stem cells (ASCs) and endothelial colony-forming cells (ECFCs). These cell droplets were arranged layer by layer in 3D arrays. It was demonstrated that any cell-to-cell ratio, cell quantity, cell-type combination, and spot spacing can be realized within this array. The height of the 3D array is freely scalable. Therefore layers of fibrin hydrogel and a 2D pattern of printed droplets containing different cell types, fibrinogen, and hyaluronic acid were applied alternately. Cell–cell interactions in a vascular endothelial growth factor (VEGF)-free medium were observed for 10 days, as were monoculture 3D cell arrays consisting of ASCs or ECFCs as the control.

It was predicted that the secretion of VEGF by the ASCs, which is well known to promote endothelial cell proliferation, would lead to the outgrowth of ECFCs toward the ASCs along the VEGF gradient, as had been reported by other groups [1,33].

However, as depicted in Fig. 16.3(d), the ASCs (+) migrated toward the ECFC (○) spots, whereas the ECFCs showed negligible activity. After the ASCs came into direct contact with the ECFCs between days 3 and 5 [21], the ECFCs began to form vascular-like networks with big branches together with the ASCs (see Fig. 16.3(e)). These networks were not observed in either the ASC or the ECFC controls.

The migration of ASCs toward ECFCs may be the result of a gradient of platelet-derived growth factor. The subtype platelet-derived growth factor-BB is expressed in large amounts by ECFCs and is well known to stimulate ASC proliferation and migration [22].

Printed cell arrays are a suitable tool for investigating complex interactions between different cell types, such as vascular network formation in engineered tissue constructs.

16.3.2 Printed stem cell grafts

In regenerative medicine, stem cells are of great interest because of their capability for self-renewal and differentiation regulated by their 3D microenvironment. Within this microenvironment, also called the stem cell niche, cell–matrix adhesion, cell–cell contacts, cell density, and the exchange of growth factors and oxygen are pivotal [14]. Cell printing could be applied to fabricate niche-like environments as in vitro models in stem cell biology and regenerative medicine.

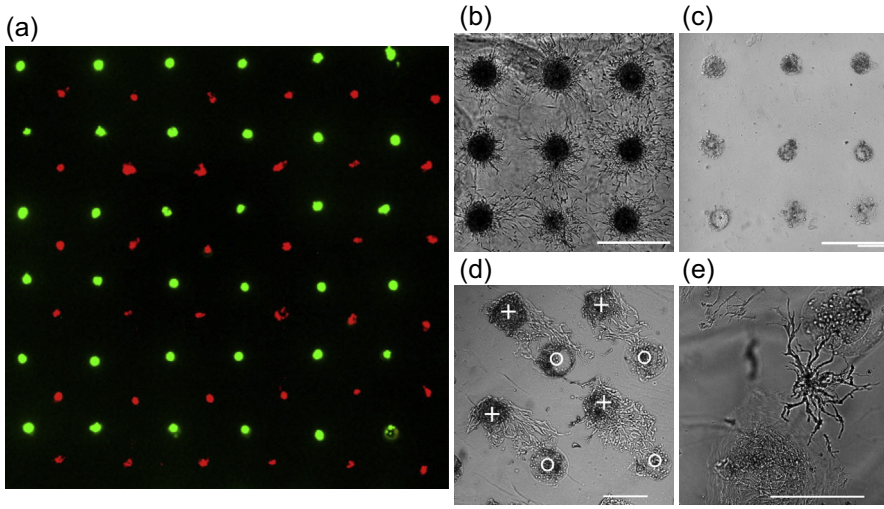

Figure 16.3 (a) Array of droplets of hyaluronic acid and fibrinogen sol, containing two different cell types, printed on a fibrin layer. The distance between two neighboring droplets with cells of the same color is 600 μm. (b–e) Visualization of cell-cell interactions by cell arrays in mono- and cocultures of adipose-derived stem cells (ASCs) and endothelial colony-forming cells (ECFCs) cultivated for 5 days under vascular endothelial growth factor–free conditions. (d) The *circles* indicate the printed ECFC spots and the *crosses* indicate the printed ASC spots. Interactions of ASCs and ECFCs (d and e) can be compared with separated arrays of ASCs (b) and ECFCs (c). A vascular-like network forms after 9 days in the coculture (e). Distance between spots with the same cell type is 800 μm.

3D structures of MSCs were printed by Gruene et al. [19,20] to investigate the ability of LaBP to generate such 3D environments. They studied whether the potential of the stem cells [porcine bone-marrow derived and human adipose-derived MSCs (ASCs)] to differentiate toward different lineages was affected by the printing process and whether these stem cell grafts can be differentiated within the printed pattern. Since MSCs are promising for the regeneration of different tissues such as bone and cartilage, these cells are attractive for tissue-engineering applications.

Since alginate with ethylenediaminetetraacetic blood plasma (autologous for the cells) is compatible with cells and enables the exchange of nutrients and soluble factors, it was applied as the sol for printing as the extracellular matrix including the embedded MSCs. Material elasticity and forces, which are known to influence stem cell differentiation [22], have to be taken into account. Furthermore, differentiation is dependent on the initial cell density; chondrogenesis especially requires a high cell density.

Stem cells may undergo forces during the printing procedure that would not affect their proliferation ability but might induce uncontrolled differentiation [9]. To rule out such negative effects of the laser printing procedure on stem cell behavior, diverse quantitative and qualitative investigations were conducted, showing that the differentiation potential of MSCs into osteogenic, adipogenic, and chondrogenic lineages is

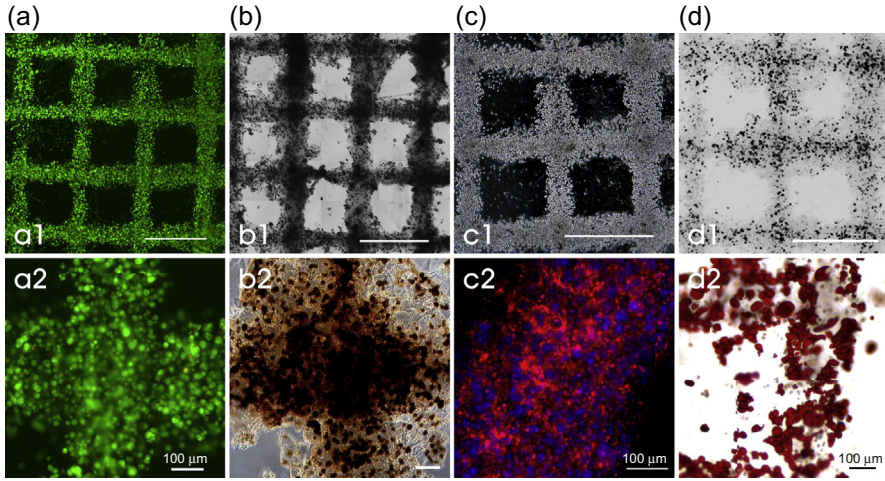

Figure 16.4 Osteogenic, adipogenic, and chondrogenic differentiation potential of printed mesenchymal stem cells (MSCs) in a three-dimensional printed grid pattern directly after printing (a), after 25 days under osteogenic culture conditions (b), and after 21 days under chondrogenic (c) or adipogenic (d) culture conditions. Microscopic images with phase contrast (b1, b2, c1, d1), vitality staining (a1, a2; Calcein AM), collagen type II immunofluorescence (c2), and Oil-Red-O staining (d2). The accumulation of calcium phosphate for osteogenic differentiation (b); collagen type II, specific for chondrogenesis (c); and lipid vacuoles indicating adipogenic differentiation (d) can be seen. Scale bars are 1 mm (a1, b1, c1, d1) and 100 µm (a2, b2, c2, d2).

not affected by the printing procedure; the laser-printed MSC grafts can be differentiated toward bone, cartilage, and adipose tissue (Fig. 16.4). Furthermore, LaBP allows the printing of cell densities high enough to promote chondrogenesis. 3D, scaffold-free, autologous tissue grafts can be fabricated with LaBP, keeping their predefined shape even after several weeks in culture and also after removal of the matrix material after 2 weeks in culture [19,20].

16.3.3 Printing skin tissue

The ultimate goal of cell printing—the printing of fully functional organs—requires integrated, perfusable vascular networks. Although we are still far from reaching this goal, simple tissue constructs have already been printed.

Reproducibly printed 3D tissue models can serve as test systems for chemical agents, cosmetics, and pharmaceuticals. They could be integrated in so-called body-on-a-chip systems—more complex systems consisting of different tissue types combined in a microfluidic system. Such printed systems could improve our understanding of cell behavior, tissue function, and regeneration.

To explore the tissue generation potential of LaBP, Koch et al. [27] printed skin tissue equivalents as ex vivo tissue models from 20 layers of fibroblasts and 20 layers of keratinocytes, both embedded in collagen type I on a collagen–elastin matrix

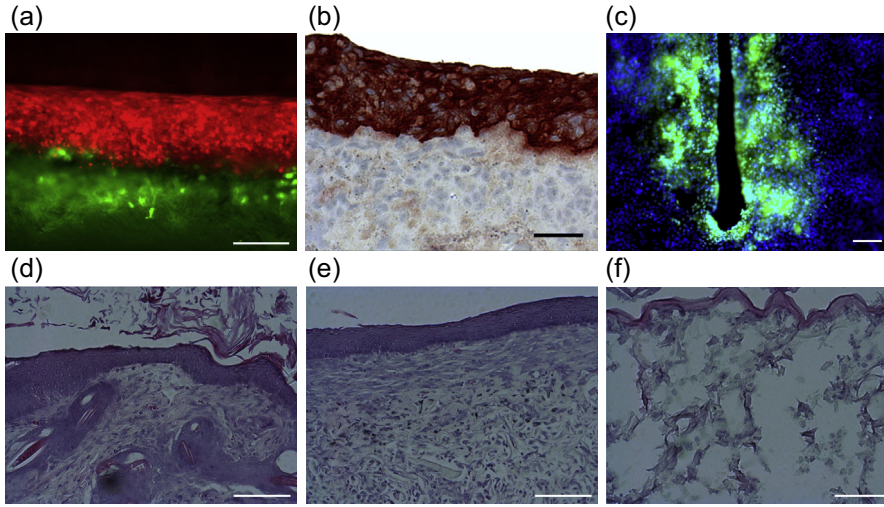

Figure 16.5 Microscopic images of three-dimensional (3D) printed fibroblasts and keratinocytes in collagen type I; cryostat sections were prepared 10 days after printing, except (a) and (c). Scale bars are 50 μm (b), 100 μm (c−f) and 200 μm (a). (a) Section through the laser-printed structure directly after printing with transduced fibroblasts (green) and keratinocytes (red). (b) Immunoperoxidase staining of cytokeratin 14 (top brown layer) depicts keratinocytes in the bilayer structure, whereas fibroblasts can be seen in the light layer underneath. (c) Visualization of gap junction coupling with Lucifer yellow dye (green), the nuclei of the HaCaT keratinocytes are stained blue (Hoechst 33342); a 3D printed skin cell pattern was scratched with a razor blade; the dye moved into the destroyed cells and through the cell−cell channels into neighboring cells. The dye covered a distance of about 10 cells in 5 min, which is a sign of good gap junction coupling. (d−f) Hematoxylin-eosin staining of histologic paraffin sections prepared after implantation for 10 days in the dorsal skin of nude mice; native dorsal skin (d), printed skin (e) -skin cells embedded in collagen type 1 on a collagen-elastin matrix, and the collagen-elastin matrix (Matriderm), implanted without cells.

(Matriderm; Dr. Suwelack Skin & Health Care, Billerbeck, Germany), to mimic the layered structure of natural skin with a dermis and epidermis (Fig. 16.5).

The applied murine fibroblast (NIH3T3) and human keratinocyte (HaCaT from adult human skin) cell lines were also combined in other studies [5]. 3T3 fibroblast cells are widely used to cultivate keratinocytes because they secrete growth factors favorable for keratinocytes [30]. Collagen is the main component of the extracellular matrix in skin; it was used to approximate native skin as much as possible.

Tissue formation after laser printing of cells was verified by the existence of intercellular junctions that can be found as cell−cell and cell−matrix connections in all kinds of tissue and are abundant in epithelium like the epidermis. Koch et al. [27] investigated intercellular adherens junctions [34], which are fundamental for tissue morphogenesis and cohesion, and gap junctions [31], cell−cell channels that allow intercellular communication by passing chemical signals. Koch et al. observed the extensive formation of intercellular adherens junctions between printed keratinocytes

and minor formation between fibroblasts. This is expected because there is typically a higher level of junctions in the dermal epithelium (epidermis) [34] that is formed by the keratinocytes.

Furthermore, they observed gap junctions, localized within the cell membrane, between all neighboring cells 10 days after printing. The functionality of cell−cell communication via gap junction coupling was verified with a dye-transfer method in vital 3D cell constructs. Thus it was demonstrated that the printed skin grafts mimic tissue-specific functions with respect to adherens and gap junctions [27]. The formation of a basement membrane between keratinocytes and fibroblasts was also observed, as it exists between the epidermis and dermis in natural skin.

The skin constructs were also implanted into full-thickness skin wounds in nude mice, applying a dorsal skin fold chamber. After 11 days, they were fully connected to the surrounding tissue. A multilayer epidermis with beginning differentiation and stratum corneum was formed by the printed keratinocytes. Blood vessels have been observed to grow from the wound bed and the wound edges into the printed cells [32].

However, natural mouse skin (Fig. 16.5(d)) is much more complex than the printed skin (Fig. 16.5(e)). Fig. 16.5(f) depicts Matriderm without printed cells 11 days after implantation.

16.3.4 Biopapers

As an alternative to directly printing layer by layer, the application of so-called biopapers was proposed to generate 3D cell constructs that are thicker than the diffusion limit of a few 100 µm. Biopapers are flat scaffolds, also called "sheets." Cells are printed onto each sheet in a 2D pattern, then the biopapers are stacked to generate a 3D structure.

Pirlo et al. [38] and Catros et al. [7] generated porous 300-µm-thick scaffolds of poly(lactic-co-glycolic acid) coated with Matrigel (BD Biosciences, Bedford, MA) and 100-µm-thick electrospun polycaprolacton scaffolds, respectively. They printed human umbilical vein endothelial cells onto the Matrigel-coated poly(lactic-co-glycolic acid) sheets and MG63 osteoblastic cells onto the polycaprolacton scaffolds in a 2D pattern. These sheets with printed cells were later stacked to achieve a 3D cell construct.

This is a promising approach if it could be possible to generate functional vascular networks on the biopapers. The sheets can be stacked several days after printing, so that there is enough time for the vessels to form while the sheets are in cell culture medium and the supply of the cells is ensured. If biopapers with functional vascular networks are stacked later, the cell supply is provided, even in very thick 3D cell constructs. Furthermore, there are fewer requirements for the cell-embedding sol since it does not need to provide stiffness for three-dimensionality.

However, to generate a predefined 3D pattern with high fidelity, precise stacking without any shift or rotation is necessary. Furthermore, a connection between the cells and the vascular networks of the individual biopapers is necessary to achieve 3D tissue. Otherwise, each cell is involved only in a 2D cell pattern.

16.3.5 In situ printing

Instead of printing tissue and later implanting the printed construct, direct printing of cells into wounds was investigated. Keriquel et al. [25] printed nano-hydroxyapatite (n-HA) in a mouse calvaria defect model in vivo. With a trephine, two 4-mm-diameter defects were drilled into the skull. Laser printing was applied at one defect, while the other one was used as control.

Thirty layers of a mixture containing n-HA and glycerol, each about 20 μm in thickness and 3 mm in diameter, were printed layer by layer in one defect. After printing, the defects were re-covered with soft tissue. Mature bone tissue was observed 3 months later in many defects with printed n-HA, whereas bone repair was incomplete in the control defect of many mice. However, the bone regeneration was inhomogeneous from one sample (mouse) to another, and no statistical significance in bone repair enhancement by n-HA printing was observed. Nevertheless, in vivo bioprinting was successful, even though it occurred without printed cells.

16.4 Discussion

LaBP is a promising microfabrication technique for arranging vital cells in predefined 2D and 3D patterns and for generating tissues and organs ex vivo.

Reproducibly fabricated tissue structures can be applied as 3D environments for studying cell behavior. By integrating other cell types into the printed skin tissue, such as endothelial cells for vascularization and dendritic cells for immune reactions, these tissue equivalents can be developed further to their natural archetype and can be used to test pharmaceutical or cosmetic agents, reducing animal testing. Compared with animal testing, reproducibility of the printed skin tissue could become a significant advantage.

The ultimate goal of tissue printing is definitely the generation of complete and fully functional organs, such as a heart or kidney ready for implantation. Printed from autologous cells, such organs may someday even outclass donor organs, since it is expected that no rejection reaction will occur and the lifelong intake of immunosuppressants can be avoided.

Currently, research is far from printing such organs. However, first steps in this direction have been made. Diverse cell types including cell lines, primary cells, and stem cells have been successfully printed, and it has been demonstrated that they are not harmed by this technique and that the differentiation potential of the printed stem cells is not affected.

LaBP offers the capability to print cells in amounts ranging from a single cell to hundreds of cells per droplet, embedded in hydrogel precursors (sols) with a wide range of rheological properties, with micrometer resolution in a high-throughput manner. In addition to cells, growth factors and biological agents can also be printed.

To explore the potential of LaBP, different cell-printing applications were investigated. Printed 3D patterns of MSCs differentiated toward osteogenic, chondrogenic,

and adipogenic linages kept their predefined structure. Thus fabrication of 3D, scaffold-free, autologous stem cell grafts was demonstrated with LaBP. Large clinical potential for autologous tissue reconstruction therapies is offered by human ASCs because of the ease of their withdrawal from adipose tissue and their ability to differentiate down the mesenchymal and nonmesenchymal pathways [41].

For cell−cell and cell−environment interaction studies, LaBP was used for precise arrangement of different cells in 3D spot arrays. Interactions between endothelial cells and stem cells toward generating new blood vessels were investigated.

In addition, 3D laser printing of multicellular skin tissue constructs was conducted to study whether the printed cells establish tissue. It was demonstrated that the printed skin cells evolve intercellular adhesion and communication via adherens and gap junctions, which proves tissue formation.

As an alternative to scaffold-free printing of 3D cell constructs and tissue, 3D stacking of biopapers was conducted, each with a printed 2D pattern on the biopaper surface. If precise stacking is provided, this technique can enable the generation of well-defined 3D patterns within a 3D scaffold structure. In addition to some special scaffold geometries, this is not possible with a usual scaffold that is fabricated in one piece and later seeded with cells.

Furthermore, direct printing into wounds of test animals was successfully tested. In the future, such in situ printing might be applied in surgery to repair, for example, cartilage or bone.

Some obstacles need to be surmounted before fully functional organs can be printed. Most important, a complex perfusable vascular network system has to be generated and integrated in the printed tissue. This vascular network needs to be functional after a relatively short time period to supply the printed cells with nutrition. Alternatively, the strategy with stackable biopapers may be applied if the formation of a vascular network on the 2D surface of the biopaper can be induced.

Furthermore, for many organs not all cell types are available yet. Isolated from tissue and brought to conventional cell culture, cells may change their phenotype and lose their functionality. Some cell types still cannot be cultivated outside their 3D microenvironment.

If for example heart muscle tissue printing is intended, simply printing cells is not sufficient. The printed cell structure needs to be stimulated by mechanical forces to induce a parallel orientation of the cells. A fabrication technique of very small cardiac tissue pieces has been already developed; it needs to be modified to fabricate larger tissues, including the integration of a vascular network.

The development of reproducible well-defined 3D cell models is a key challenge for future progress in tissue engineering. Since the structural dimensions of natural tissue are significantly lower than 100 μm, the ability to precisely position different cells in complex 3D patterns is of essential importance.

Other printing techniques are also under investigation, such as techniques based on ink-jet printing, acoustic droplet ejection, or extrusion systems. LaBP enables the printing of droplets of biomaterials (with or without cells) combining very low volumes with high viscosities (much higher than can be done with an ink-jet printer or acoustic droplet ejection) and high cell densities. Each of these techniques possesses

its advantages and disadvantages, and it is not yet clear which technique will come out on top; there probably will be applications for all of them.

16.5 Summary

Printed 3D cell systems offer new approaches for investigating cellular behavior and tissue genesis and for engineering tissue and organs. Currently, LaBP (among other techniques) can print such 3D cell constructs with the required cell density and spatial resolution, with added extracellular matrix material and bioagents.

Although printed replacement organs are far from being realized, substantial progress has been achieved toward printed 3D tissue. The integration of a printed perfusable vascular network poses the major challenge toward broad application of printed tissue—first in test systems and later in clinics. 3D laser additive manufacturing of cells and biomaterials promises to close the gap between conventional cell culture and test animal models and to substitute the latter, with printed cell-based test systems being more ethical and more meaningful.

Acknowledgments

The studies described here were supported by Deutsche Forschungsgemeinschaft, SFB TransRegio 37, REBIRTH Cluster of Excellence (Exc62/1), and by Land Niedersachsen and Volkswagenstiftung in the Biofabrication for NIFE project.

References

[1] A. Akeson, A. Herman, D. Wiginton, J. Greenberg, Endothelial cell activation in a VEGF-a gradient: relevance to cell fate decisions, Microvascular Research 80 (2010) 65.
[2] K. Arai, S. Iwanaga, H. Toda, C. Genci, Y. Nishiyama, M. Nakamura, Three-dimensional inkjet biofabrication based on designed images, Biofabrication 3 (2011) 034113.
[3] J.A. Barron, D.B. Krizman, B.R. Ringeisen, Laser printing of single cells: statistical analysis, cell viability, and stress, Annals of Biomedical Engineering 33 (2) (2005) 121−130.
[4] J.A. Barron, B.R. Ringeisen, H. Kim, B.J. Spargo, D.B. Chrisey, Application of laser printing to mammalian cells, Thin Solid Films 453−454 (2004) 383−387.
[5] R.L.H. Bigelow, E.Y. Jen, M. Delehedde, N.S. Chari, T.J. McDonnell, Sonic hedgehog induces epidermal growth factor dependent matrix infiltration in HaCaT keratinocytes, Journal of Investigative Dermatology 124 (2005) 457.
[6] M.S. Brown, C.F. Brasz, Y. Ventikos, C.B. Arnold, Impulsively actuated jets from thin liquid films for high resolution printing applications, Journal of Fluid Mechanics 709 (2012) 341−370.

[7] S. Catros, F. Guillemot, A. Nandakumar, S. Ziane, L. Moroni, P. Habibovic, C. van Blitterswijk, B. Rousseau, O. Chassande, J. Amédée, J.-C. Fricain, Layer-by-layer tissue microfabrication supports cell proliferation in vitro and in vivo, Tissue Engineering, Part C Methods 18 (1) (2012) 62−70.
[8] R. Chang, J. Nam, W. Sun, Effects of dispensing pressure and nozzle diameter on cell survival from solid freeform fabrication-based direct cell writing, Tissue Engineering: Part A 14 (1) (2008) 41−48.
[9] K.C. Clause, L.J. Liu, K. Tobita, Directed stem cell differentiation: the role of physical forces, Cell Communication and Adhesion 17 (2) (2010) 48−54.
[10] E. Cukierman, R. Pankov, D.R. Stevens, K.M. Yamada, Taking cell-matrix adhesions to the third dimension, Science 294 (2001) 1708−1712.
[11] U. Demirci, G. Montesano, Single cell epitaxy by acoustic picolitre droplets, Lab Chip 7 (2007) 1139−1145.
[12] B. Derby, Bioprinting: inkjet printing proteins and hybrid cell-containing materials and structures, Journal of Materials Chemistry 18 (2008) 5717−5721.
[13] V. Dinca, A. Ranella, A. Popescu, M. Dinescu, M. Farsari, C. Fotakis, Parameters optimization for biological molecules patterning using 248-nm ultrafast lasers, Applied Surface Science 254 (2007) 1164−1168.
[14] D.E. Discher, D.J. Mooney, P.W. Zandstra, Growth factors, matrices, and forces combine and control stem cells, Science 324 (2009) 1673.
[15] M. Duocastella, J.M. Fernández-Pradas, J.L. Morenza, P. Serra, Sessile droplet formation in the laser-induced forward transfer of liquids: a time-resolved imaging study, Thin Solid Films 518 (2010) 5321−5325.
[16] D.B. Edelman, E.W. Keefer, A cultural renaissance: in vitro cell biology embraces three-dimensional context, Experimental Neurology 192 (2005) 1−6.
[17] T.G. Fernandes, M.M. Diogo, D.S. Clark, J.S. Dordick, J.M.S. Cabral, High-throughput cellular microarray platforms: applications in drug discovery, toxicology and stem cell research, Trends in Biotechnology 27 (6) (2009) 342.
[18] M. Gruene, C. Unger, L. Koch, A. Deiwick, B. Chichkov, Dispensing pico to nanolitre of a natural hydrogel by laser-assisted bioprinting, Biomedical Engineering Online 10 (2011) 19.
[19] M. Gruene, A. Deiwick, L. Koch, S. Schlie, C. Unger, N. Hofmann, I. Bernemann, B. Glasmacher, B. Chichkov, Laser printing of stem cells for biofabrication of scaffold-free autologous grafts, Tissue Engineering, Part C Methods 17 (2011) 79−87.
[20] M. Gruene, M. Pflaum, A. Deiwick, L. Koch, S. Schlie, C. Unger, M. Wilhelmi, A. Haverich, B. Chichkov, Adipogenic differentiation of laser-printed 3D tissue grafts consisting of human adipose-derived stem cells, Biofabrication 3 (2011) 015005.
[21] M. Gruene, M. Pflaum, C. Hess, S. Diamantouros, S. Schlie, A. Deiwick, L. Koch, M. Wilhelmi, S. Jockenhoevel, A. Haverich, B. Chichkov, Laser printing of three-dimensional multicellular arrays for studies of cell−cell and cell−environment interactions, Tissue Engineering, Part C Methods 17 (10) (2011) 973−982.
[22] M. Hellström, M. Kalén, P. Lindahl, A. Abramsson, C. Betsholtz, Role of PDGF-B and PDGFR-β in recruitment of vascular smooth muscle cells and pericytes during embryonic blood vessel formation in the mouse, Development 126 (1999) 3047.
[23] K.K.B. Hon, L. Li, I.M. Hutchings, Direct writing technology—advances and developments, CIRP Annals 57 (2008) 601.
[24] B. Hopp, T. Smausz, N. Kresz, N. Barna, Z. Bor, L. Kolozsvari, D.B. Chrisey, A. Szabo, A. Nogradi, Survival and proliferative ability of various living cell types after laser-induced forward transfer, Tissue Engineering 11 (11−12) (2005) 1817−1823.

[25] V. Keriquel, F. Guillemot, I. Arnault, B. Guillotin, S. Miraux, J. Amédée, J.-C. Fricain, S. Catros, In vivo bioprinting for computer- and robotic-assisted medical intervention: preliminary study in mice, Biofabrication 2 (2010) 014101.
[26] L. Koch, S. Kuhn, H. Sorg, M. Gruene, S. Schlie, R. Gaebel, B. Polchow, K. Reimers, S. Stoelting, N. Ma, P.M. Vogt, G. Steinhoff, B. Chichkov, Laser printing of skin cells and human stem cells, Tissue Engineering, Part C Methods 16 (2010) 847−854.
[27] L. Koch, A. Deiwick, S. Schlie, S. Michael, M. Gruene, V. Coger, D. Zychlinski, A. Schambach, K. Reimers, P.M. Vogt, B. Chichkov, Skin tissue generation by laser cell printing, Biotechnology and Bioengineering 109 (2012) 1855−1863.
[28] Y. Lin, Y. Huang, D.B. Chrisey, Droplet formation in matrix-assisted pulsed-laser evaporation direct writing of glycerol-water solution, Journal of Applied Physics 105 (9) (2009) 093111.
[29] Y. Lin, Y. Huang, D.B. Chrisey, Metallic foil-assisted laser cell printing, Journal of Biomechanical Engineering 133 (2011) 025001.
[30] C. Linge, Establishment and maintenance of normal human keratinocyte cultures, in: J. Picot (Ed.), Methods in Molecular Medicine, second ed.Human Cell Culture Protocols, vol. 107, Humana Press Inc., Totowa, NJ, 2004, p. 1.
[31] G. Mese, G. Richard, T.W. White, Gap junctions: basic structure and function, Journal of Investigative Dermatology 127 (2007) 2516−2524.
[32] S. Michael, H. Sorg, C.-T. Peck, L. Koch, A. Deiwick, B. Chichkov, P.M. Vogt, K. Reimers, Tissue engineered skin substitutes created by laser-assisted bioprinting form skin-like structures in the dorsal skin fold chamber in mice, PLoS One 8 (3) (2013) e57741.
[33] N. Mirsky, Y. Cohen, VEGF and ECGF induce directed migration of endothelial cells: qualitative and quantitative assay, Endothelium 255 (1995) 5444.
[34] C.M. Niessen, Tight junctions/adherens junctions: basic structure and function, Journal of Investigative Dermatology 127 (2007) 2525−2532.
[35] C. Norotte, F.S. Marga, L.E. Niklason, G. Forgacs, Scaffold-free vascular tissue engineering using bioprinting, Biomaterials 30 (2009) 5910e7.
[36] D.J. Odde, M.J. Renn, Laser-guided direct writing of living cells, Biotechnology and Bioengineering 67 (3) (2000) 312−318.
[37] A. Palla-Papavlu, I. Paraico, J. Shaw-Stewart, V. Dinca, T. Savopol, E. Kovacs, T. Lippert, A. Wokaun, M. Dinescu, Liposome micropatterning based on laser-induced forward transfer, Applied Physics A 102 (3) (2011) 651−659.
[38] R.K. Pirlo, P. Wu, J. Liu, B. Ringeisen, PLGA/hydrogel biopapers as a stackable substrate for printing HUVEC networks via BioLP™, Biotechnology and Bioengineering 109 (1) (2011) 262−273.
[39] B.R. Ringeisen, H. Kim, J.A. Barron, D.B. Krizman, D.B. Chrisey, S. Jackman, R.Y.C. Auyeung, B.J. Spargo, Laser printing of pluripotent embryonal carcinoma cells, Tissue Engineering 10 (3−4) (2004) 483−491.
[40] B.R. Ringeisen, C.M. Othon, J.A. Barron, D. Young, B.J. Spargo, Jet-based methods to print living cells, Biotechnology Journal 1 (2006) 930.
[41] A. Schaeffler, C. Buechler, Concise review: adipose tissue-derived stromal cells − basic and clinical implications for novel cell-based therapies, Stem Cells 25 (2007) 818−827.
[42] N.R. Schiele, D.B. Chrisey, D.T. Corr, Gelatin-based laser direct-write technique for the precise spatial patterning of cells, Tissue Engineering Part C 17 (3) (2011) 289−298.

[43] C. Unger, M. Gruene, L. Koch, J. Koch, B. Chichkov, Time-resolved imaging of hydrogel printing via laser-induced forward transfer, Applied Physics A 103 (2011) 271−277.
[44] A. Vogel, K. Lorenz, V. Horneffer, G. Hüttmann, D. von Smolinski, A. Gebert, Mechanisms of laser-induced dissection and transport of histologic specimens, Biophysical Journal 93 (2007) 4481−4500.
[45] T. Xu, J. Jin, C. Gregory, J.J. Hickman, T. Boland, Inkjet printing of viable mammalian cells, Biomaterials 26 (2005) 93−99.
[46] Y. Zhang, Y. Yu, H. Chen, I.T. Ozbolat, Characterization of printable cellular micro-fluidic channels for tissue engineering, Biofabrication 5 (2013) 025004.

Additive manufacture of tools and dies for metal forming

17

R. Hölker-Jäger, A.E. Tekkaya
Technische Universität Dortmund, Dortmund, Germany

17.1 Introduction

In metal forming processes, additive manufacturing technologies are mostly used to manufacture dies for traditional forming processes, and not for the direct mass production of parts, since additive manufacturing processes to date are often not as fast and thereby time- and cost-efficient compared with conventional manufacturing processes (machining, casting, forming). Furthermore, additive manufacturing processes are not yet as accurate as desired regarding surface quality, which means that producing a net-shape is often not possible. For that reason, in metal forming processes, additive manufacturing technologies are mostly used to manufacture dies with high geometric complexity with, for example, inner channels for a functional integration, which leads to an additional benefit for the whole process, or dies that cannot be manufactured by conventional subtractive methods because of production-related restrictions. Nevertheless, minor surface finishing often has to be applied locally using subtractive methods. According to the condition or shape of the base material and the manner of its deposition, additively manufactured dies for metal forming applications are presented in this chapter, grouped into layer-laminated tools (Section 17.1), the powder bed (Section 17.2), and the powder nozzle–based tools (Section 17.3).

17.2 Layer-laminated manufacturing

In layer-laminated manufacturing, single layers made of paper, wood, polymer, ceramics, or metal are cut from sheets by a knife, a laser beam, or in general by a separating die are stacked and joined together mechanically by bonding or welding. Strictly speaking it is a combination of a subtractive and an additive manufacturing process.

Compared with powder-based methods, the layer-laminated manufacturing methods are characterized by the possibility to fabricate a large volume and massive dies in a short time. For metal forming processes, layered dies have been made of metal sheets. Kunieda and Nakagawa [19] proved the suitability of horizontally layered deep drawing (Fig. 17.1(a)) and trimming tools (Fig. 17.1(b)).

The tool for deep drawing consists of the die itself, a punch, an ejector, and a blank holder. All parts are cut out of 2-mm-thick laminated sheets stacked and joined by bolts. To have a positive effect on clamping during the drawing operation, the

Laser Additive Manufacturing. http://dx.doi.org/10.1016/B978-0-08-100433-3.00017-8
Copyright © 2017 Elsevier Ltd. All rights reserved.

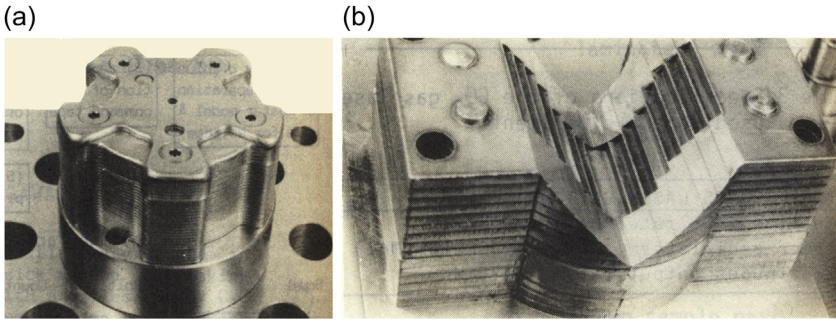

Figure 17.1 (a) A horizontally layered deep drawing die. (b) A layered trimming die [19].

laminated sheets are kept on the plane of the sheet that is the same as the direction of the drawing load. Since the single added layers have a step effect, die and punch radii were formed by manual grinding and polishing. A layered trimming die (the upper and lower parts) was manufactured and used to get the end contours of a V-bent component (Fig. 17.1(b)). Both edges normal to the bend line of the component were predeformed to get the required contour of the V-bent component with a reduced step effect. Each part of the die was manufactured from fifteen 3.2-mm-thick tool steel sheets, and the layers were fastened together by bolts and dowels. The experimental results showed chipping of the cutting edge at the interface of the laminated sheets, and large burrs were observed in the sheared zones according to the chipped cutting edges. To avoid this, Kunieda and Nakagawa [19] proposed reinforcing and strengthening the mechanical fastening of trimming dies by diffusion bonding. In experimental tests they proved that the shearing strength of the joint material is very close to the strength of the base material.

Walczyk and Hardt [27,29] improved the layer-laminated manufacturing method with "profiled edge lamination" tooling (Fig. 17.2), developed at the Massachusetts Institute of Technology. Here the lamellas are aligned vertically in a clamping device and get a profiled and beveled top edge adopted based on the geometry that will be manufactured. In this way, stair-stepping between the single layers can be eliminated. The beveling is accomplished by using a line-of-sight cutting process such as abrasive

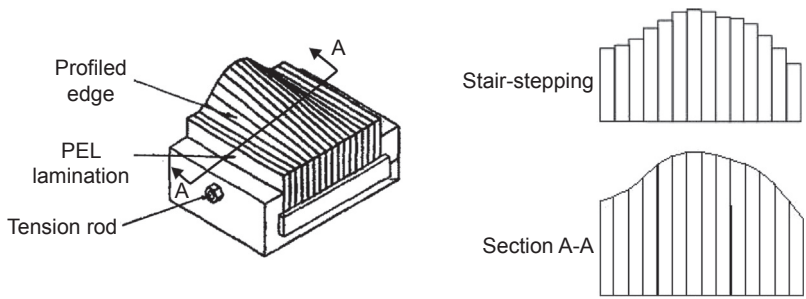

Figure 17.2 Schematic of the profiled edge laminae (PEL) tool [27,30].

water-jet cutting, laser cutting, or wire electro-discharge machining. A plant concept for cutting and assembling the lamellas was developed on the basis of a Nd:YAG laser cutting machine with a maximum die size of 600 mm in the diagonal and 250 mm in height [27].

An overview of possible contour adjustments during horizontal layering is shown in Fig. 17.3. To reach a constant radius, lamellas with different thicknesses and a bevel cut can be used. Despite this, the target contour often cannot be reached because a critical angle for three-dimensional (3D) laser cutting must be considered depending, for example, on the material and the thickness of the layer.

Geiger et al. [8] investigated two different strategies for manufacturing dies using deep-drawing processes. In manufacturing strategy 1, layers with different thicknesses were used, the edges got a bevel cut with a 3D laser-cutting machine at angle β, and the layers were joined by welding. In manufacturing strategy 2, the lamellas were cut with an allowance and joined by sticking using a high-strength two-component adhesive. Then the layered die was finished by machining. Sheets of the soft deep-drawing steel 1.0338 and simple mild steel 1.0037 were used as die material. These dies were used to process 1-mm-thick sheets of steel 1.0338. The drawing clearance was set to 1.5 mm and the depth of draw to 93 mm. Applying strategy 1 to manufacture the die, the surface quality of the workpieces directly depends on the quality of the laser cut. Here, the angle for the bevel cut of the lamella edges via laser cutting is limited ($\beta < 25°$) and depends on the sheet material and sheet thickness. The raw die edges result in marks on the workpieces. The surface roughness R_z of the deep-drawn workpiece matches between 24 and 45 µm (Fig. 17.4). Hence, strategy 1 cannot be used to manufacture parts with high demands on the surface quality as it is required. However, this strategy is applicable for prototypes. Manufacturing strategy 2 can also be used for small-batch

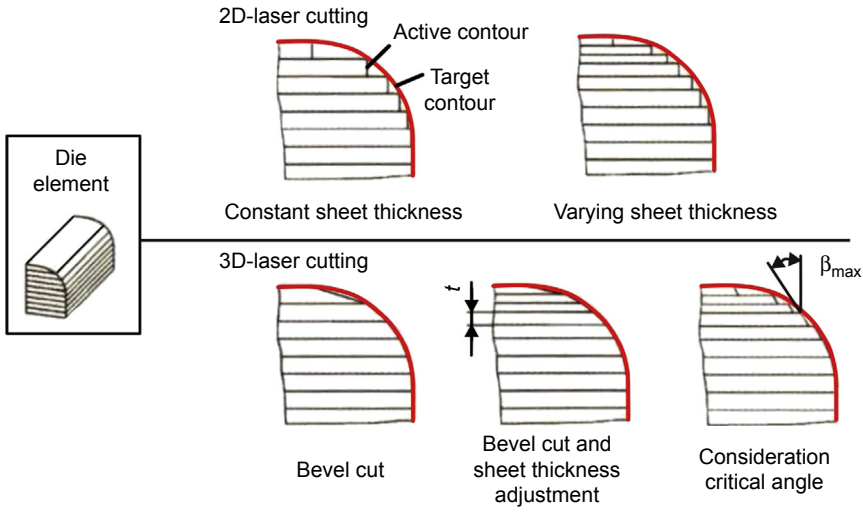

Figure 17.3 Possibilities for adjusting the contour of a horizontal layer [8]. *2D*, two-dimensional; *3D*, three-dimensional.

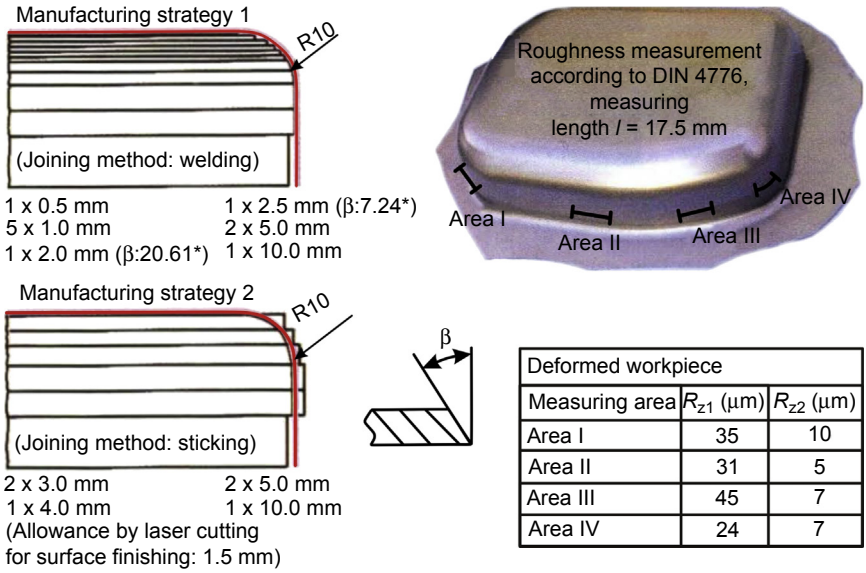

Deformed workpiece		
Measuring area	R_{z1} (µm)	R_{z2} (µm)
Area I	35	10
Area II	31	5
Area III	45	7
Area IV	24	7

Figure 17.4 Effect of the manufacturing strategies on the surface quality of the deep-drawn workpiece [8].

production [8]. Here, the surface roughness R_z is between 5 and 10 µm (Fig. 17.4). The manufacturing time for strategy 1 was 23 h and for the strategy 2, approximately 20 h. The additional time necessary for machining in strategy 2 is overcompensated by fewer lamellas and minor requirements in the laser cutting quality [8].

Kleiner and Krux [18] developed and tested experimentally vertically layered dies for deep drawing and stretch drawing in sheet metal formation (Fig. 17.5).

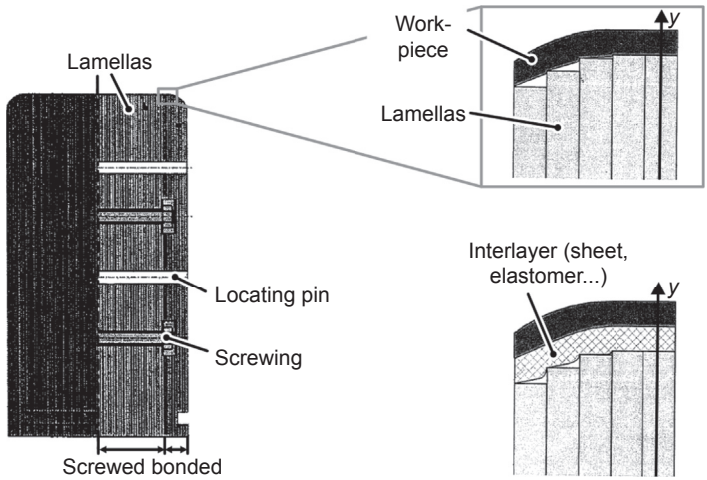

Figure 17.5 Vertically layered deep-drawing die [18].

The cylindrical drawing punch consists of 147-sheet lamellas of the material DC04, with a thickness of 1 mm. After the lamellas were cut in a laser-cutting machine, they were positioned by locating pins (10 mm in diameter). The lamellas are clamped by two screw joints. To countersink the screw nuts and screw heads, the 20 outer lamellas are provided with pockets and bonded with adhesive (Fig. 17.5).

Deep-drawing experiments were carried out using a conventionally manufactured die with a diameter of 152 mm and a conventionally manufactured blank holder. Blanks with different diameters, sheet thicknesses, and materials were deep drawn to cups with a maximum deep-drawing depth of 110 mm. The results of the trials using the layered punch were compared with the results of trials using a conventionally manufactured punch.

In the experiments using the layered cylindrical drawing punch, no significant differences in force could be observed in comparison to the conventionally manufactured punch. The limiting drawing ratio is the same using both the additively manufactured or the conventionally manufactured punch. To improve the surface quality, intermediate layers made of a metal sheet (DC04; layer thicknesses, 0.5, 0.8, and 1 mm) and elastomer (rubber foils; layer thicknesses, 0.5, 1, and 2 mm) were successfully applied [18].

Kleiner and Krux [18] also investigated the use of layered dies in high-pressure forming (Fig. 17.6). This forming process offers the advantage of saving one tool half, which is replaced by a fluid. Instead of a conventional punch, here the forming process occurs by applying a direct active medium on the sheet blank.

The layer thickness of the die lamellas was set to 1 mm, and the material used was a steel DC04. The layers were manufactured by laser cutting. Two bore holes (diameter = 10 mm) were inserted to integrate locating pins, which improve the handling of the stacked layers. The stack of layers is inserted into a circular die

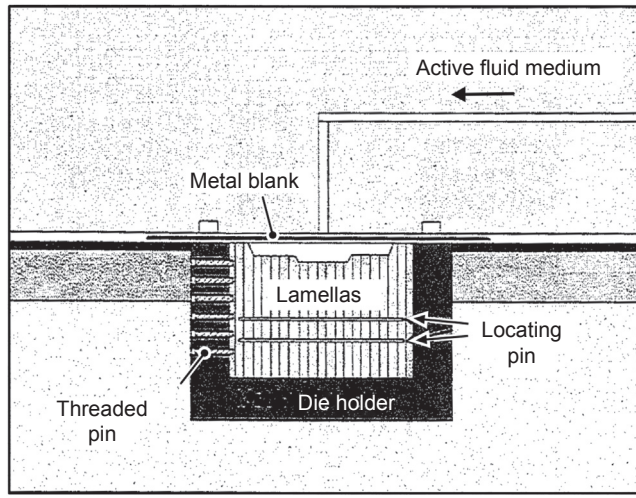

Figure 17.6 Layered die for high-pressure forming [18].

holder (inner diameter $d_i = 200$ mm) and clamped by threaded pins (Fig. 17.6). Metalforming experiments were carried out using intermediate layers made of rubber or a steel sheet (DC04), and fluid pressures between 5 and 30 MPa were used. The qualities of the produced parts are satisfactory for prototypes. Even small-batch series are possible. The intermediate layers made of rubber are not destroyed and can be reused.

Techel [25] developed a process chain for metal laminated tooling for the rapid manufacturing of dies for prototype or small-batch series, called "MELATO." Geometrically complex dies can be manufactured quickly and flexibly by an automated system for cutting, assembling, and joining the blank sheet lamellas. The process chain (Fig. 17.7) includes the manufacturing of the die contour from steel sheets and a suitable surface treatment process for adapted time and wear behavior. A better surface quality and accuracy can be obtained by machining the laminated dies.

To increase the stability of the layered dies, different postprocessing procedures of the surfaces can be used, such as a thermomechanical treatment or a thermal or galvanic coating. Local changes can be realized by laser-beam hardening or laser cladding [25]. In addition to stability, the effect of the surface improvement is often essential. To manufacture accurate and high-quality parts, a smooth tool surface is essential. Fig. 17.8 shows a test specimen of a lamella die before and after galvanic coating.

Challenges in galvanic coating are undercuts and hard-to-reach areas. Because of the small exchange of electrolyte, only a thin coating can be realized, whereas in areas that are highly flushed, such as the edges, thick coverage by the coating results. Accordingly, Techel [25] does not recommend galvanic coating for parts containing sharp-edged corners or contours with deep cavities.

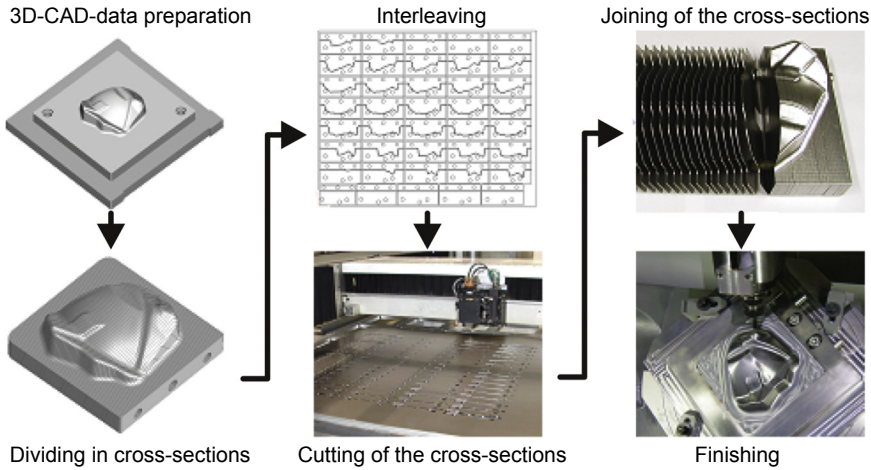

Figure 17.7 The MELATO process chain [25]. *3D*, three-dimensional; *CAD*, computer-assisted design.

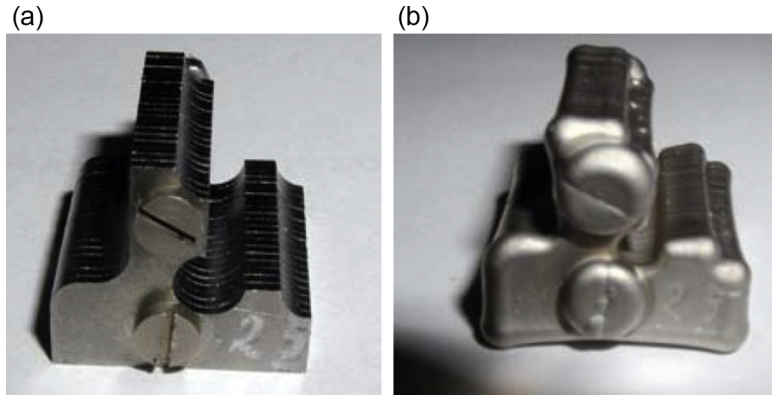

Figure 17.8 Test specimen before (a) and after (b) galvanic coating [25].

Geiger and Franke [7] introduced the manufacturing of bending dies from sheet lamellas (Fig. 17.9(a)), segments (Fig. 17.9(b)), or a combination of both (Fig. 17.9(c)) using laser cutting.

To fulfill the requirements for bending dies, such as the plane parallelism between the die holder area and the tip of the die, high qualities in the cutting process must be reached. Therefore a smooth, flat, and vertical laser-cutting contour, as well as a high geometric accuracy of each lamella, is required. In the optimum case, lamellas with a geometric tolerance of 0.02 mm can be manufactured [7]. Furthermore, the cutting result is essentially influenced by the processed sheet material. For small series and prototyping dies, Geiger and Franke [7] recommend using low-carbon steels with low strength values (e.g., St 1403), which do not tend toward uncontrolled exothermic reaction with oxygen as the processing gas in laser cutting.

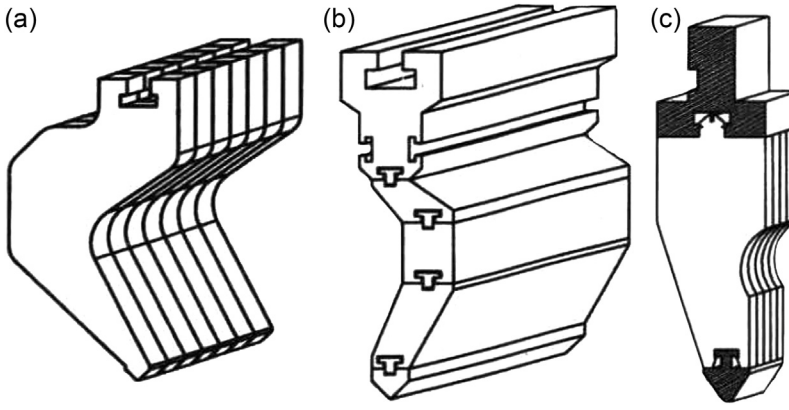

Figure 17.9 Forms of bending dies from lamellas (a), a segmented die (b), and a combination from lamellas and segments (c) [7].

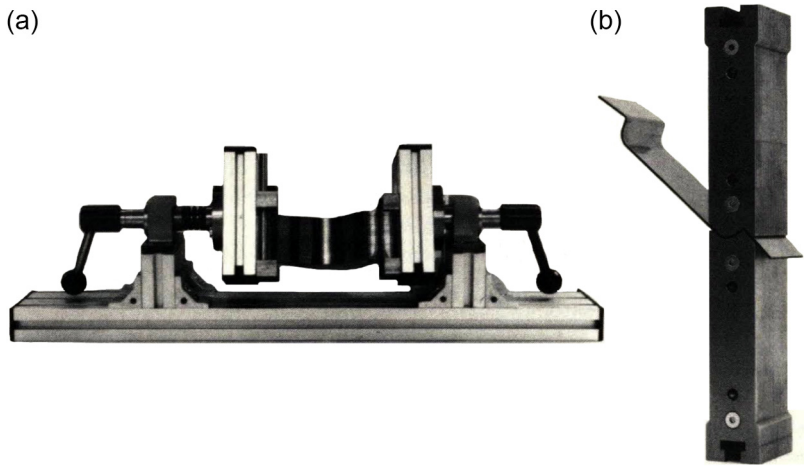

Figure 17.10 (a) Mounting device with a laser beam−welded bending tool. (b) Example of a realized tool [7].

Bonding of the single layers can be realized by, for example, screwing, laser beam welding, and adhesive bonding [7]. All joining techniques need the lamellas to be aligned. Using a mounting device (Fig. 17.10(a)), precise alignment of the lamellas can be achieved, but this means additional equipment and effort. The lamellas are clamped together in the stacking direction by screws. For welding, the mounting device can be rotated on the horizontal axis.

The manufacturing time of a bending tool, shown in Fig. 17.10(b), is 2.5 h, including the time for design and process planning as well as for cutting and assembling the layers. The die has a width of 60 mm and was manufactured from deep-drawing steel St 1403 with a layer thickness of 2 mm. Especially in bending softer materials, the workpiece surface can be damaged by an indentation of single lamellas. This phenomenon can be suppressed by mechanically finishing the tool stack or by using intermediate layers, for example, foils of spring steel [7].

A huge benefit of the layer laminate technology is that even large tools can be manufactured in a timely and cost-efficient way. The Warwick Manufacturing Group investigated the production of "large scale tooling for rapid manufacture," predominantly for applications in the aerospace industry [2]. Tooling in the aerospace industry is very costly since the size of the tools can be large ($>2 \times 2 \times 2$ m), whereas the number of parts is small (<100 pieces) [2]. Rapid tooling technologies for the production of large-scale tools for processes such as super plastic forming ($>900°C$), hot creep forming ($>900°C$), resin transfer molding, and autoclave and injection molding tooling, all operating at a maximum temperature $<250°C$, were investigated. For the lower-temperature applications, mild steel sheets were selected as the material for the lamellas; for the higher-temperature applications an austenitic stainless steel alloy (RA310s), in this case a heat-resistant chromium nickel steel, was applied [2]. There are two options to stack the layers: horizontally or vertically. Bryden et al. [2] proposed

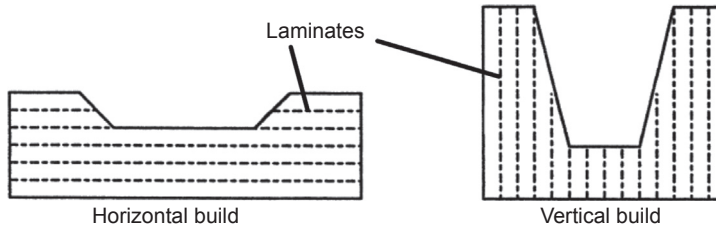

Figure 17.11 Horizontal and vertical strategies to build up lamellas [2].

horizontal stacking for shallow components and a vertical build for parts where deep cavities are required (Fig. 17.11).

One advantage of the horizontal build is that the waste from the cavity can be used to make the core. However, problems occur when islands are required. These islands can be manufactured by massive tooling inserts (Fig. 17.12(a)), by lamellas that are located and fixed by dowels (Fig. 17.12(b)), or by laser-cut tabs that support the tooling islands (Fig. 17.12(c)) [2]. The vertical build direction automatically supports islands in the die.

Bryden et al. [2] tested experimentally the high-temperature application of super plastic forming to manufacture a titanium nose-cone fairing (Fig. 17.13). A horizontally layered die was selected because a high compressive force was required to maintain a gas-tight seal. A small machining allowance allowed a later machining operation.

Sheets of the high-temperature- and corrosion-resistant Ni-Cr steel RA310s with a thickness of 2 mm were used for the lamellas, which were joined by high-temperature brazing. The major advantage of this layered tool was the reduced manufacturing time: The layered die was delivered within 7 days, compared with 40 days for a casting-based tool.

Walczyk and Dolar [28] discussed the suitability of different bonding methods for laminated tools depending on the acting stresses, temperatures, and forces in different manufacturing processes (Fig. 17.14). In sheet metal forming, including drawing and hydroforming, where high normal and shear forces act, the die surface tends to peel and shear the bonds between single laminations. Hot metal extrusion dies operate under high shearing and normal forces, meaning that the lamination bonds must absorb tensile and shear loads.

Walczyk and Dolar [28] discussed the applicability of diffusion bonding, brazing, welding, and soldering to join single lamellas. In general, plane laminar bonding

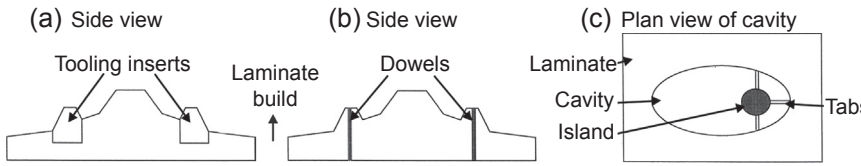

Figure 17.12 The use of tooling inserts to avoid tooling islands (a), dowels to locate tooling islands (b), and laser-cut tabs to support tooling islands (c) [2].

Figure 17.13 Scaled nose-cone fairing tool [2].

methods such as brazing or adhesive bonding, resulting in the joining of an entire interface, are more suitable than linear methods such as welding, which only act locally at the lamellas' edges and require additional mechanical finishing.

Misiolek et al. [22] proposed the use of layered tools for extrusion dies. For extrusion dies, a stepped die surface is only a minor disadvantage because a so-called dead zone is formed in the edges of the lamellar layers, which level the die's surface. Experimental investigations were carried out only with modeling materials such as plasticine (Fig. 17.15).

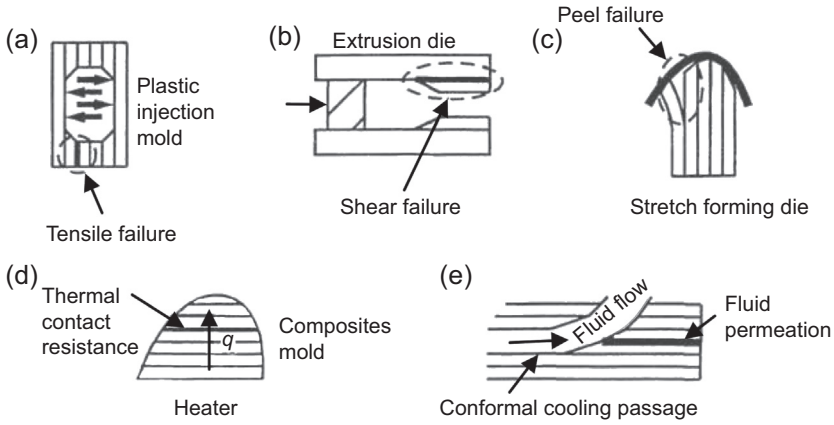

Figure 17.14 Example of tensile (pull) failure (a), shear failure (b), peel failure (c), thermal contact resistance (d), and fluid permeation (e) of various laminated dies and molds [28].

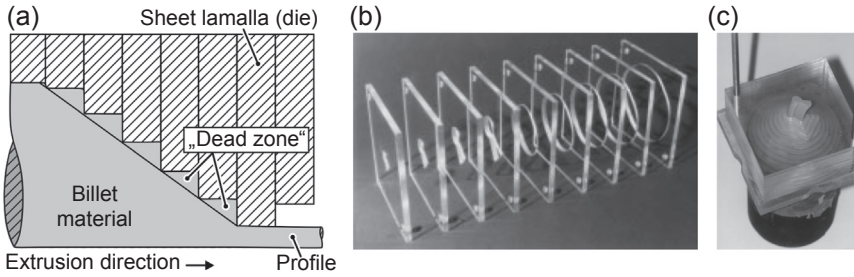

Figure 17.15 (a) The setup of an extrusion die. (b) A layered die. (c) A layered die stack, billet, and dummy block with an extruded profile [22].

This concept from Misiolek et al. [22] was used by Hölker et al. [12] for the real manufacturing of hot metal extrusion dies by layer-laminated manufacturing methods. By layering transverse to the extrusion direction, additional clamping devices are not necessary, since the layers are pressed together by the pressure of the press. The lamellas were positioned and fixed using alignment pins and screws. Even though the die bearings were manufactured by only laser cutting, without any mechanical finishing, the surface of the fabricated profiles was satisfactory ($R_a = 2.3$ µm; surface roughness $R_z = 13.4$ µm).

In the first experimental trials, bending of the layers in the extrusion direction was observed. To avoid this, better support of the die-bearing lamella was provided. This can be realized by a higher-strength material or an increase in the die's stiffness. The latter was achieved by using a thicker dimensioning of the single layers respectively the supporting plate. As lamella material, hot working steels (e.g., 1.2343/H11 or 1.2344/H13, hardened to 54−56 Rockwell value (HRC)) with a tensile strength >1000 MPa at the operating temperature (around 500°C) could be qualified. For the dimensioning of the lamellas, Hölker [9] developed an analytical model for the lamella deflection. Using this model, extrusion dies were successfully developed that could withstand the high thermal and mechanical loads they were exposed to.

Another possibility to increase further the potential of layered extrusion dies is the integration of cooling channels close to the forming zone, where heat is mainly generated. According to the die opening, cooling channels can be cut in single lamellas by laser cutting. To manufacture a square hollow profile (22 × 22 × 3 mm), the cooling channels were aligned around the circumference of the die opening (Fig. 17.16).

To keep each lamella as one single unit, the cooling channels were split into two lamellas that are alternately equipped with slots and bridges. These lamellas including the cooling channels were positioned directly behind the die-bearing lamella. They do not have any contact with the exiting profile and no radial forces must be sustained that could damage the cooling lamellas. Fig. 17.17(a) shows the assembled layered die cap with the geometry (negative; Fig. 17.17(b)) of the inner cooling channel. The coolant inlet and outlet are realized by two brass tubes.

During extrusion of the hard-to-extrude aluminum alloy EN AW-7075, using water as coolant in a layered die, overheating of the processed material could be

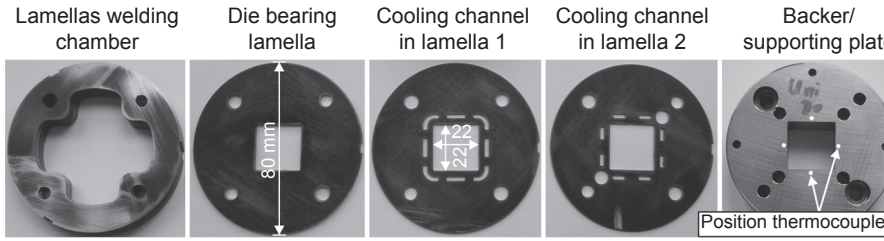

Figure 17.16 Lamellas for a die cap of an extrusion die with integrated cooling channels made of 1.2343/H11, hardened to 56 HRC, according to [12].

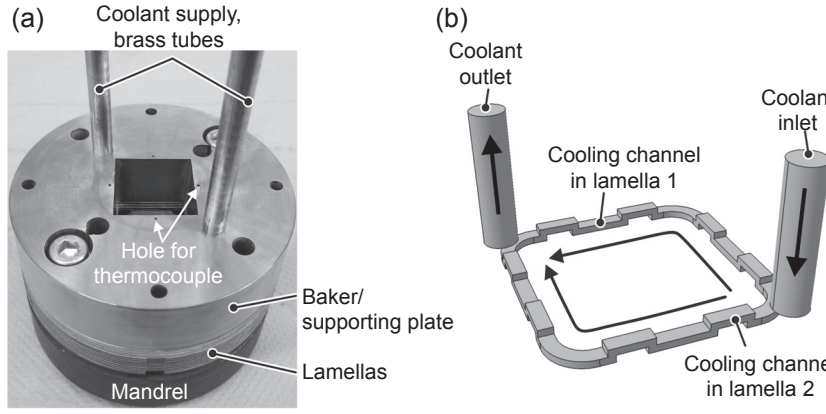

Figure 17.17 (a) Layered extrusion die cap. (b) Geometry (negative) of the cooling channel [13].

suppressed, and an increase of the productivity up to 300% was achieved [9]. Furthermore, the investigations showed that the inner die cooling improved the surface quality of the profiles [9,11]. Hot cracks that generally occur during overheating of the billet material could be avoided by the inner die cooling as well as the formation of coarse grains, which leads to better mechanical properties of the fabricated profiles.

17.3 Powder bed–based additive manufacturing

In powder-based additive manufacturing, parts are generated successively layer by layer. The geometry information of the part that is to be manufactured is provided by a volume model (a 3D computer-assisted design model). The geometric information of the model is virtually sliced into several layers, with a defined layer thickness in the magnitude of 10–80 µm, by a slicing software program [6].

The major advantage of powder-based additive manufacturing processes compared with conventional subtractive methods (such as turning, milling, drilling, or eroding) is the nearly unlimited geometric freedom of the components to be produced, such as shapes with undercuts or 3D conformal cooling channels. Another benefit is that no specific dies are necessary to manufacture individual products.

In the field of metal forming, additive manufacturing is mostly used to fabricate dies (so-called rapid tooling). The dies are used for mass production, but the dies themselves are unique products.

Levy et al. [20] investigated dies for a scaled deep-drawing process where the die, punch, and blank holder were manufactured by selective laser sintering (Fig. 17.18). The material was ST-100 powder, a mixture of gas-atomized stainless steel metal particles (average particle size, 17 μm), the stainless steel alloy 420 (Cr-Ni-Fe), mixed with approximately 4% organic binder [20]. The selective laser sintering process is a two-stage sintering operation that produces by selective laser sintering in the first step a so-called green part with a layer thickness of 0.08 mm and a part bed temperature of 93°C. Afterward, this green part is infiltrated in an oven with an 80% Cu, 20% Sn bronze alloy, resulting in fully dense parts (up to 99.9%; Fig. 17.18(b)). The peak temperature was set to 1070°C and the holding time was 3 h. Without mechanical finishing, the measured surface roughness after the oven process was $R_a = 5.8$ μm.

The tool set was tested experimentally in stamping a medium-strength carbon steel. The wear evolution on the punch surface was monitored using a 3D scanner. The results of the experiments using the laser-sintered die were compared with the results using a conventionally manufactured tool made of the cold work steel D2.

While in the reference trials with a conventionally manufactured die no significant wear effect occurred, in the experimental trials using the laser-sintered die during the first 100 stamped parts, the punch area (Fig. 17.19(a)) was reduced and the punch

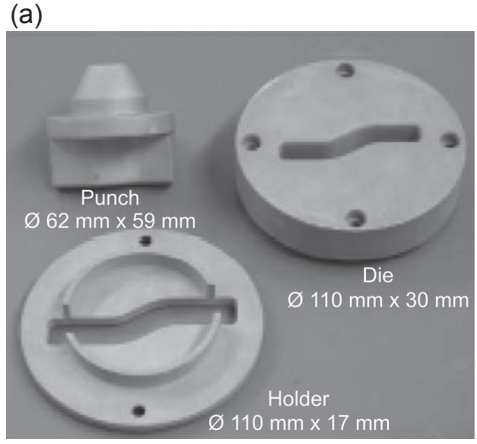

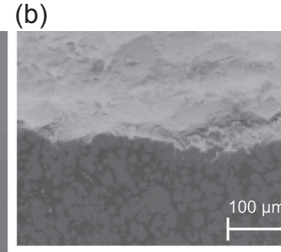

DTM sinter station 2500		
Build parameter	Layer thickness	0.08 mm
	Part bed temperature	93°C
	Building up rate	177 mm/min
Part parameter	Laser power	35 W
	Outline power	5 W
	Scan spacing	0.08 mm

Figure 17.18 (a) Die, punch, and blank holder for a deep-drawing process manufactured by selective laser sintering. (b) The microstructure and surface [20]. Ø, diameter.

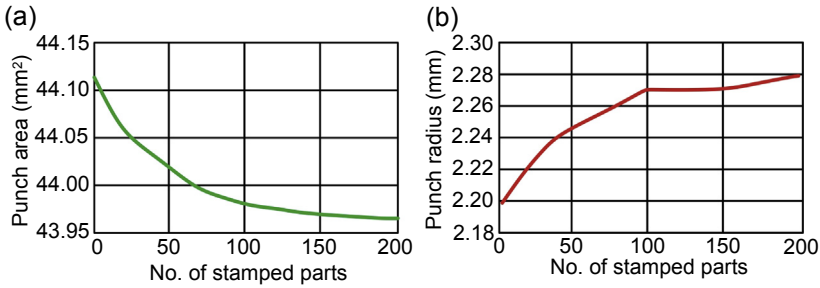

Figure 17.19 The punch area (a) and punch radius (b) at the critical section as a function of stamped parts [20].

radius (Fig. 17.19(b)) increased remarkably. However, stagnation of the wear could be observed at between 100 and 200 stamped parts.

Huskic et al. [16] investigated deep-drawing dies manufactured by selective laser melting. An inner channel for lubrication distributes the lubricant in the inside of the die and exits at the surface through small lubrication channels (Fig. 17.20). The diameter of the channel was set to 0.6 mm. Experimental investigations of steel sheet blanks made of 1.4301 with a thickness of 0.8 mm revealed that the lubricant exits the ring through the channels and is distributed homogenously in the area of the flange and the draw ring. As a result, the deep-drawn parts do not show imprints on the surface by the lubrication channels.

Cheah et al. [3] used a punch and a die, fabricated by selective laser sintering, for a hollow stamping process (Fig. 17.21). Because of intricate geometric features, this pattern is challenging and proves the potential of rapid tooling in producing highly detailed surface features.

The dimensions of the sides of the punch and the die inserts were provided with a 4-mm allowance to compensate the shrinking and the surface finishing by machining.

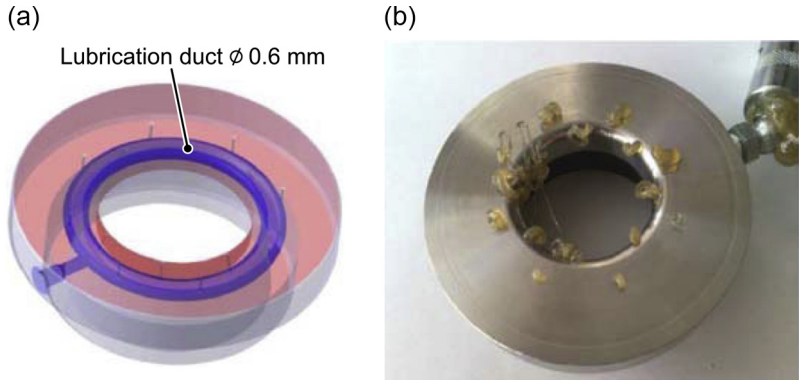

Figure 17.20 Deep-drawing die with an inner lubrication duct manufactured by selective laser melting: a schematic [16] (a) and a real die with lubrication [14] (b). Ø, diameter.

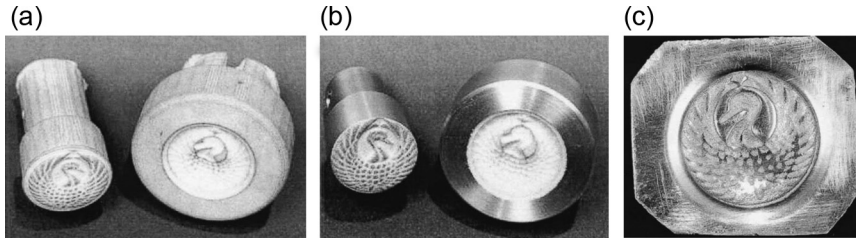

Figure 17.21 Laser-sintered punch and die insert before (a) and after (b) surface finishing. (c) An embossed sample on a 2-mm-thick aluminum sheet [3].

The tools are manufactured from a stainless steel—based powder and coated with a polymer binder in a Sinterstation 2500 (DTM Corp.). During manufacturing, the polymeric binder is melted by a carbon dioxide laser. In this way the steel powder is bounded. Then the parts are subjected to a sintering cycle in a furnace (1120°C at a rate of 120°C/h for 3 h), where the polymer binder is burned out. In the subsequent infiltration cycle in the furnace, the parts are infiltrated with molten bronze to achieve fully dense materials (the temperature of the furnace is raised to 1050°C at a rate of 120°C h^{-1} for 3 h). The maximum deviation in the dimensions in the additively manufactured part was 0.31 mm. The surface roughness after the printing was 7.84 μm. Only surfaces on the punch and the die inserts, which are critical for fitting the tools in the holders, were finished. The forming surfaces were kept in their original conditions. After machining the parts to their actual dimensions, the dies were tested experimentally in a 20-ton turret punch press machine. During the embossing of 1.5- and 2-mm-thick aluminum sheet stocks, no tearing of the aluminum sheet blanks was observed, and the embossed samples were of good quality. After 15 stamping operations, no significant tool wear was observed. A cost and lead time comparison of the laser-sintered dies versus the conventional hardened reference tools show significant savings. The additively manufactured dies cost only one-third of the conventionally manufactured dies. The lead time for die manufacturing could be reduced from 2.5 weeks for conventional hard tooling to approximately 1 week using selective laser sintering.

In the field of bulk metal forming, Müller and Neugebauer [24] proved the applicability of laser-melted die inserts for die forging. The die inserts have dimensions of $170 \times 54 \times 47$ mm^3 and were manufactured from the hot working steel 1.2709 (X3NiCoMoTi 18 9 5). This martensite hardening die steel combines high strength with good ductility at elevated temperatures. The accuracy of the laser melted part is ±0.1 mm.

The die insert was mechanically refinished by only simple manual polishing and sand blasting, except from the mandrel area, which was polished on a high-speed cutting machine with a polishing tool because of limited accessibility (Fig. 17.22(a)). Experimental trials were performed on a 20-MN press, and parts could be forged successfully (Fig. 17.22(b)). Since die inserts were not tested until failure occurred or visible wear appeared, no information can be provided about the lifetime of the dies.

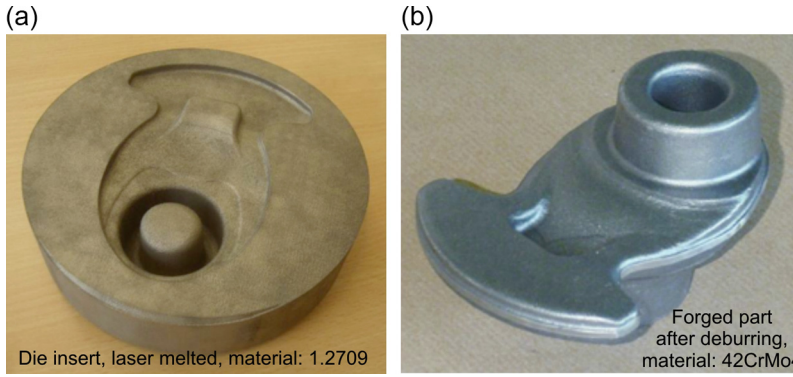

Figure 17.22 (a) Die insert of a forging die manufactured by selective laser melting. (b) The forged part [24].

Comparing the new process chain for the fabrication of forging dies with conventional die manufacturing, Müller and Neugebauer [24] concluded the following changes for the new process chain of additive manufacturing:

- Until today, the tool size is limited to 200−300 mm by the laser melting machine. This size is not sufficient for manufacturing industrial dies.
- Current build volumes in laser melting of 4−5 cm^3/h are low. The manufacturing of a size-optimized tool with a volume of 1000 cm^3 would take 200 h.
- The current prices for metal powder (€245/kg for the hot working steel 1.2709) plus the machine hour rate (€80) result in significantly higher manufacturing costs compared with conventional production, even for medium-sized die inserts [24].

Additively manufactured forging dies were also developed by Huskic et al. [15] (Fig. 17.23(a)). The forging dies were manufactured by selective laser melting using the hot working steel 1.2709, with a yield strength of 1800 MPa and a hardness of 54 HRC in the tempered condition. Since forging dies are exposed to high mechanical,

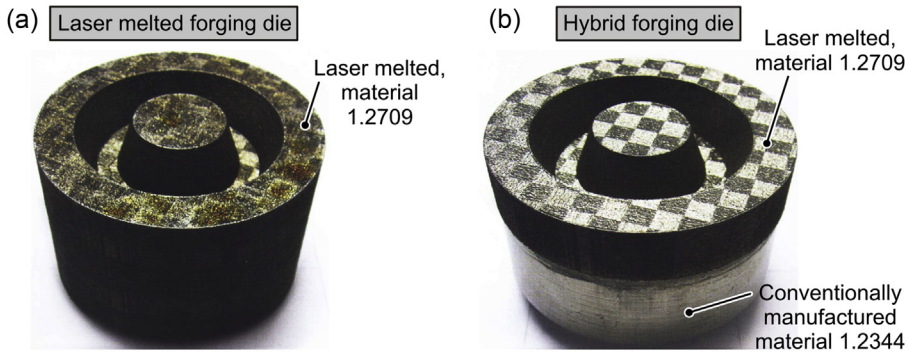

Figure 17.23 Forging dies manufactured by selective laser melting: a fully additively manufactured die (a) and a hybrid die (b) [15].

thermal, and tribological loads during forming, Huskic et al. [15] attempted to optimize and increase the tool life. Selective laser melting allowed them to integrate into the dies conformal cooling channels and channels to measure temperature. In this way the current die temperature can be measured and observed and, when required, cooling can be initiated to avoid exceeding the tempering temperature of the material used. Exceeding the tempering temperature in areas near the surface of the dies leads to a loss of hardness, which results in limited lifetimes of the dies. Huskic et al. [15] proved in industry-related trials on a 3.1-MN eccentric press that the forging tools manufactured additively could withstand more than 500 trials. The workpieces were cylindrical parts made of C45 (diameter, 30 mm; $h = 40$ mm) which were forged at a temperature of 1150°C. After use, the surface of the additively manufactured die was compared with that of a conventionally manufactured die made of 1.2344/H13 (X40CrMo V 5 1). The additively manufactured mandrel showed no significant breakouts, cracks, or deformations, whereas the conventionally manufactured die showed adhesive wear.

To reduce the powder costs and the building time (the machine hour rate), hybrid forging dies were developed and tested [15]. The basic part is conventionally manufactured of hot working steel 1.2344 and the upper part, made of 1.2709 metal powder, is additively built on it (Fig. 17.23(b)). Additionally, cooling channels were integrated (Fig. 17.24(a)). However, a coolant was not yet applied. The experimental results show that the hybrid die can withstand the high mechanical loads during forging. No damage by, for example, cracking was observed macroscopically.

Microscopic analysis of the tools reveals changes in the microstructure of the tool surface caused by thermal load. Also, micro cracks appear in the tool surface, originating from thermal cycling. However, the surface of the conventionally manufactured reference tool is damaged even more [15] (Fig. 17.25).

During press hardening, workpieces are heated above the austenitizing temperature (>950°C) and they must be cooled rapidly to below 200°C. In this way, a high-strength martensitic microstructure is obtained. To achieve the rapid cooling, conformal cooling channels with complex geometries are necessary. These channels can be manufactured only additively. Huskic et al. [16] investigated the use of

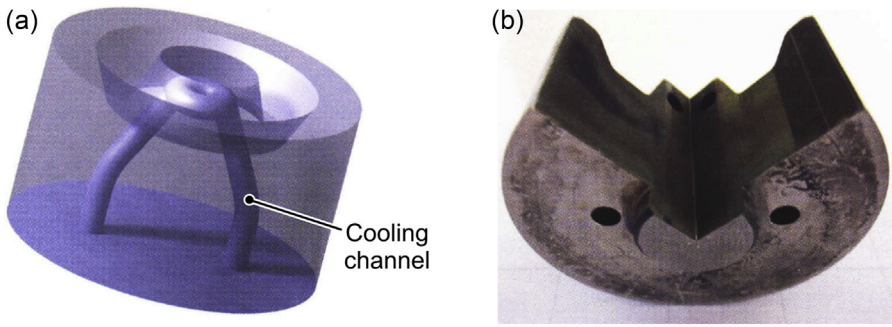

Figure 17.24 (a) Schematic of a forging die with inner cooling channels. (b) A real manufactured die with an inner cooling channel [15].

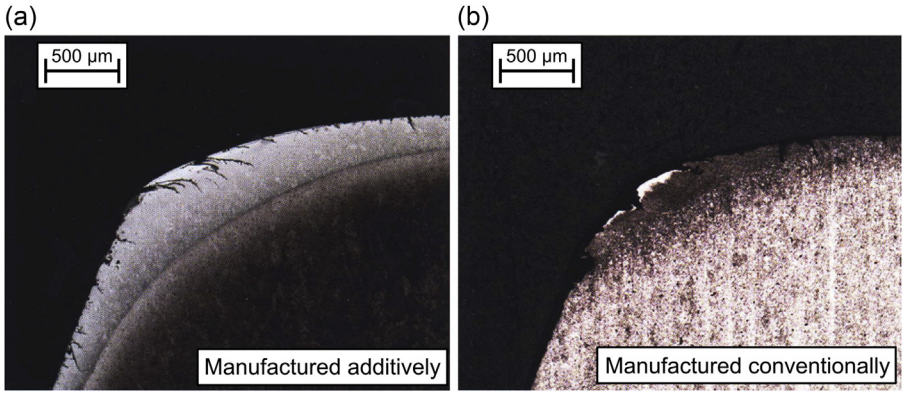

Figure 17.25 Micrograph of a forging punch manufactured additively (metal powder 1.2709) (a) and manufactured conventionally (hot working steel 1.2344) (b) [15].

press-hardening tools with conformal cooling channels manufactured by selective laser melting (Fig. 17.26(a)).

The material CL50WS (by Concept Laser GmbH) was used as powder; with regard to mechanical properties, this is similar to the hot working steel 1.2709. The cooling channels have a diameter of 7 mm. In preinvestigations the die shown in Fig. 17.26(a) was used. Steel sheet blanks made of 22MnB5, with a diameter of 80 mm and a sheet thickness of 1.5 mm, were successfully deep drawn to a depth of 12 mm [14]. Water was used as the coolant, and the experimental trials were carried out on a hydraulic forming press. Current investigations deal with the use of cooling channels in the die, punch, and blank holder (Fig. 17.26(b)) to quantify the cooling effect of the complex cooling channels and to investigate the lifespan of additively manufactured dies.

Müller [23] explored the use of hybrid press-hardening dies with conformal cooling channels (Fig. 17.27). The basic body is manufactured conventionally by machining and a functional geometry with inner cooling channels is additively built up on it. Numerical simulations revealed the best position and geometry of the cooling channels for rapid cooling in the die. The net of cooling channels, with a diameter of 4 mm, was

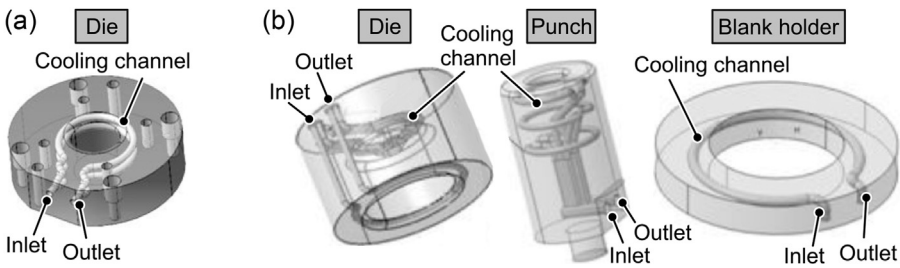

Figure 17.26 (a) Press-hardening tool used in preinvestigations with conformal cooling channels made by selective laser melting. (b) Press-hardening tools with conformal cooling channels in the die, punch, and blank holder [16].

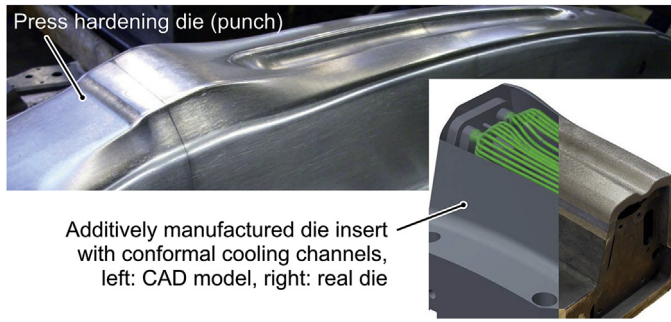

Figure 17.27 Tool for sheet metal forming (punch) with an additively manufactured insert [23]. *CAD*, computer-assisted design.

positioned close to the die' surface. The experiments showed that the additively manufactured die insert cooled six times faster than the conventional die insert with drilled cooling channels [23]. Using the additively manufactured die, the holding time can be reduced by 50% (from 10 s to 5 s), which results in a total cycle time reduction of 20%. In serial production this would lead to energy savings of 248 MW h per year [23].

Hölker et al. [11] introduced dies for hot aluminum extrusion applications manufactured by selective laser melting. Manufacturing by laser melting provides the possibility to integrate multidirectional channels to supply a coolant and to integrate thermocouples into hot extrusion dies to measure temperature. By applying the cooling close to the main forming zone and the die bearings, a significant reduction of the temperature of the die as well as of the extruded profile is possible, and thermally induced surface defects on the profile can be avoided.

Fig. 17.28(a) shows the geometry of the cooling channel and the channel for inserting the thermocouples to measure die temperature. Because of the design of the applied extrusion press and the die holder, a supply of the cooling medium and the measuring setup are only possible from the exit end face of the die. Holes for the inlet and the

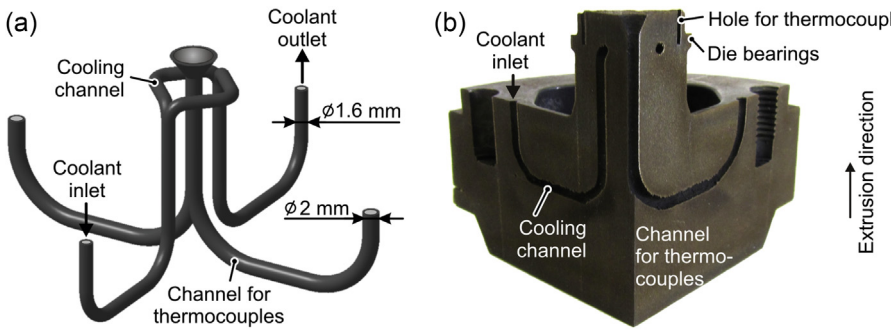

Figure 17.28 (a) Geometry of the cooling channel and the channel for feeding the thermocouple. (b) Quarter piece of a mandrel with cooling channels through the die bridges [11]. Ø, diameter.

outlet of the cooling medium were inserted into the die. To supply the coolant, a multi-directional cooling channel through the mandrel part of the die was designed to supply the cooling medium into the mandrel close to the main forming zone. The cooling channel has a diameter of 1.6 mm. In the upper part of the mandrel the channel is split into two parts, with an included angle of 90 degree on the level of the die bearing (Fig. 17.28(a)). The inner cooling channel follows in a square shape the geometry of the die bearings and merges together in the opposite direction, where the coolant is dissipated. This special multidirectional design of the cooling channels could only be manufactured by a powder-based additive manufacturing process. To measure the cooling effect, channels with a diameter of 2 mm for introducing thermocouples are inserted in the bridges that merge into one single central channel through the square mandrel. On top of the mandrel, up to eight thermocouples with a diameter of 0.5 mm can be guided into eight holes (0.6 × 4 mm) near the die bearings to measure the temperature on the level of and along the die bearings (Fig. 17.28(b)).

To manufacture a square, hollow aluminum profile (18 × 18 × 1 mm), a mandrel with external dimensions of 84 × 42 mm was manufactured in a powder bed of CL50WS (similar to hot working steel 1.2709) in a nitrogen atmosphere using a laser cusing machine m3 linear (Fig. 17.28(b)), by Conept Laser GmbH. The fabrication of the die, with a volume of 116 cm^3 and a deposition rate of 3.8 cm^3/h, took around 30 h. A total of 1580 layers, each with a thickness of 30 μm were manufactured additively [11]. The mandrel was manufactured with an allowance of 0.3 mm for mechanical finishing, which took around 1 h of milling for the external contact and sealing areas, the holes, and the die bearings. Finally, the mandrel was heat treated (aging 500°C for 8 h) to a final hardness of around 55 HRC.

The mandrel was tested in combination with a conventionally manufactured die cap on a 2.5-MN direct extrusion press with a container diameter of 66 mm using aluminum billets of EN AW-6060 alloy. Compressed air and water were used as coolants. In extrusion trials a significant reduction of the profile's exit temperature was achieved, while the extrusion force increased only moderately as a consequence of the temperature-affected increase of the workpiece flow stress. Regarding the surface quality of the profile, it was detected that, because of the cooling, surface defects can be reduced or even avoided [11]. Since to date additive manufacturing processes are often accompanied by longer manufacturing time and higher costs in comparison to conventional subtractive methods, Hölker [9] developed a new concept for a hybrid extrusion die (Fig. 17.29). Here the large-volume but geometrically simple die part, the die bridge, is manufactured conventionally by subtractive methods, and the smaller part with geometrical complexity, the tip of the mandrel, is built up on it additively by laser melting.

A further novelty of the developed die is the isolated feeding of the coolant to the target area, close to the die bearings, where the cooling is localized (Fig. 17.30). The experimental results showed that the hybrid tools withstand the high mechanical and thermal loads that occur during hot aluminum extrusion. The profile's exit temperature can be reduced locally and controlled, which leads to only a moderate increase of the extrusion force. A big advantage of the isolated coolant supply through the bridges can

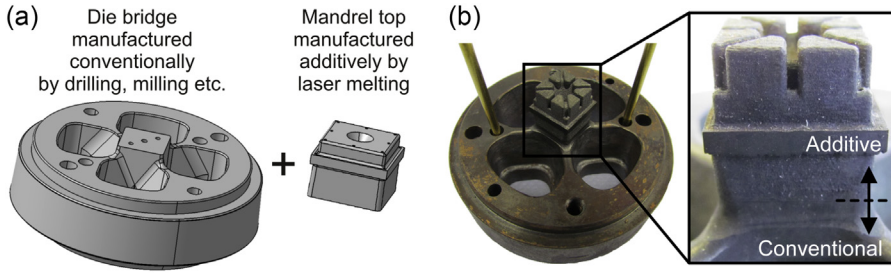

Figure 17.29 (a) Concept for a hybrid mandrel of an extrusion die. (b) The real mandrel (left), showing in detail the top of the mandrel built up additively (right) [9].

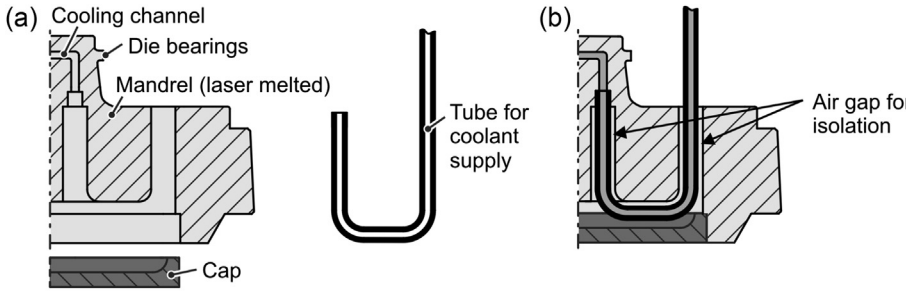

Figure 17.30 Concept for an isolated coolant feeding up to the die bearings in the mandrel before (a) and after (b) assembly [9].

be seen in cooling by using an intensive cooling medium such as water. The isolated coolant supply enables the intensive cooling of the mandrel by water, without cooling the material already in the prechamber. Without an isolated cooling media fed in through the bridges, the aluminum might freeze in the prechamber.

In the field of electromagnetic forming, additive manufacturing is used to manufacture tool coils [17] (Fig. 17.31). By making use of additive manufacturing, the geometry of the tool coil and therefore the magnetic field can be individually and freely designed and adapted to the metal forming operation.

The course and the orientation of the isolation gap between the single windings as well as the external geometry of the coil body can be manufactured three-dimensionally. The conductive winding is produced in the powder bed by selective laser melting. Materials with good electrical conductivity, such as aluminum or copper, can be used for the coils. Furthermore, additive manufacturing allows the integration of cooling channels to dissipate the heat (Joules) that is generated during the process. To increase the die life, reinforcement elements can be integrated into the coils, or hybrid coils can be used. The hybrid winding consists of an good electrically conductive layer, such as copper, in combination with a base body made of a high-strength material (eg, steel), which withstands the high electromagnetic pressure that occurs during electromagnetic forming [17].

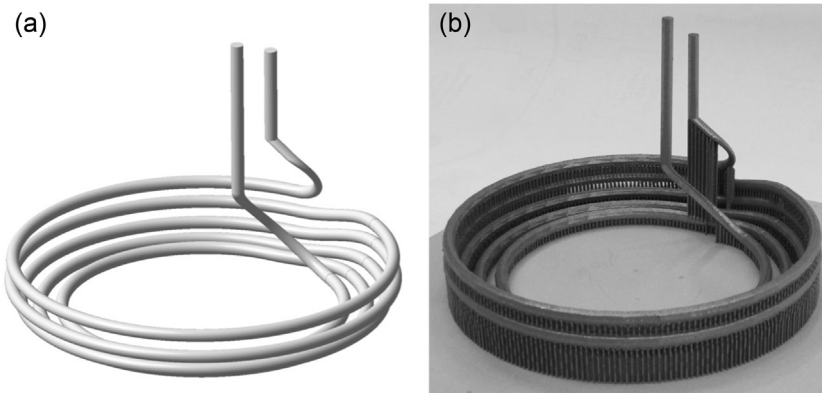

Figure 17.31 Winding of a tool coil: the computer-assisted design model (a) and the part manufactured by selective laser melting based on a building platform with a support structure (b) [17].

17.3.1 Powder nozzle–based additive manufacturing

In the examples previously described, the dies were manufactured by additive manufacturing processes that are worked in a powder bed. In addition to this, systems exist where the material is delivered directly through a nozzle. In melting by a powder nozzle, the powder is fed via nozzles to the workpiece and melted locally by a laser beam. Advantages are a material gradient by supplying/feeding different materials via several nozzles and the possibility to build up on the top of an existing structure with a curved surface (fully 3D capable) [6]. Because the geometric accuracy of the nozzle-based processes is not as good as that of the powder bed methods, it is often combined with a machining operation. One example of such a system is "controlled metal buildup," which connects the laser deposition welding with high-speed cutting [5]. It combines the advantages of the additive manufacturing processes with the accuracy and surface qualities of a machining process. By alternating between layer deposition and cutting, deep cavities can be manufactured precisely because short milling tools can be used [4]. However, the manufacturing of channels or undercuts is only possible to a limited extent.

The combination of laser deposition welding and machining is used for manufacturing new parts and dies, but mainly for modifying and repairing dies or die inserts, for example, in forging processes [1]. Forging dies are exposed during their use to high loads because of the high forming temperature (eg, 1250°C for steel), as well as friction and (abrasive) wear. Because of the high manufacturing costs, the dies have to be reworked. For this, the missing geometry is additively built on the part to be repaired by laser-deposited welding. To reach the final geometry, a machining process such as milling or eroding can be carried out.

Hölker et al. [10] developed a concept for the combined manufacturing of workpieces by incremental sheet metal forming and laser powder deposition in one setup. Workpieces are formed incrementally in one step and in one machine (simultaneously,

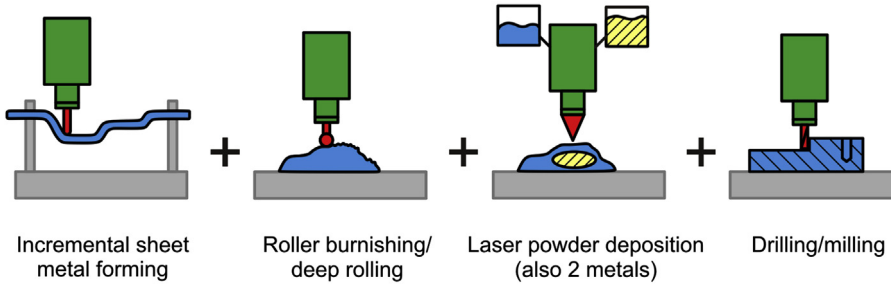

Figure 17.32 Four manufacturing processes integrated in one machine [10].

afterward, or in between) without reclamping. Geometrically complex elements can also be additively added by laser powder deposition on curved surfaces.

Furthermore, surface finishing by roller burnishing and deep rolling or drilling/milling can be carried out. Thus the rough surfaces resulting from the additive manufacturing process can be burnished. The process and the machine are based on a five-axis machining center, which can automatically pick up different tools (Fig. 17.32):

- a forming tool for incremental sheet metal forming
- a rolling tool
- a nozzle for laser powder deposition
- a die for drilling/milling

Vollmer et al. [26] investigated the process of powder laser deposit welding and in particular the integration and manufacturing of cooling channels in an additive manufacturing process working with a powder nozzle for the manufacturing of press-hardening tools. At first, slots are milled into the surface of a conventionally manufactured die. Afterward, the open surface of the channels is closed by powder laser deposit welding. To bridge the gap, weld lines are deposited at the edges of the slot (Fig. 17.33(a)). Then, a third weld line along the center closes the cooling channel. Finally, the die surface is finished by machining.

The laser deposit welding was carried out using a Trumpf DMD 505 with a 3.2-kW carbon dioxide laser. The die body is made of 1.0503, and a stainless steel powder

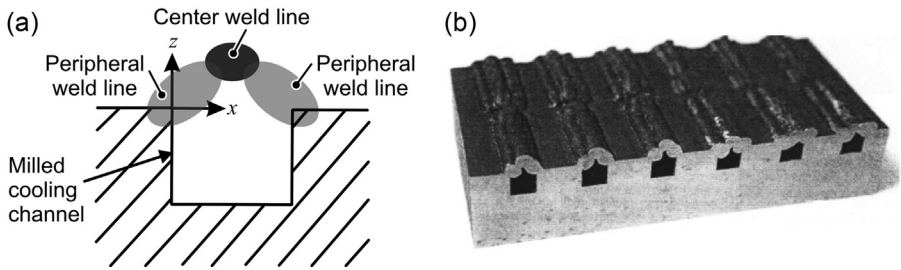

Figure 17.33 (a) Schematic of the manufacturing strategy for closing a cooling channel by powder laser deposition. (b) A die body with cooling channels (width, 6 mm) [26].

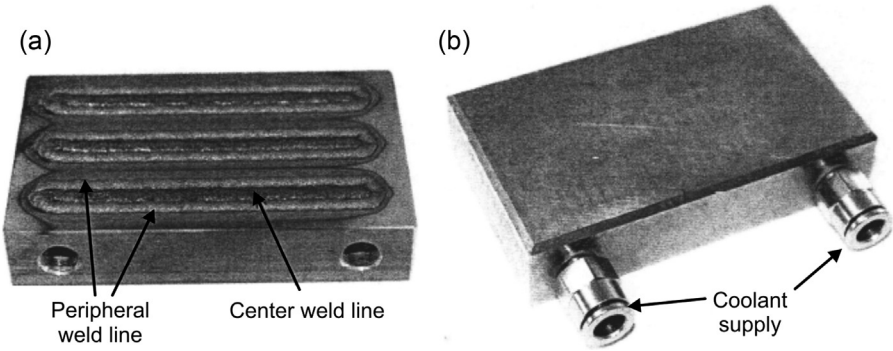

Figure 17.34 (a) Die with cooling channels closed by powder laser deposit welding. (b) A top-coated and mechanically finished part [26].

NT-316L was added as a welding substrate. Different laser powers, powder feeding rates, nozzle angles, and feeding rates were investigated (Fig. 17.33(b)). Channels up to 6 mm can be manufactured with a single-pass welding strategy. For cooling channels with larger cross sections (>6 mm), two weld lines are necessary at each channel side. In this way it is possible to achieve a width of 12 mm. To allow better bonding of the melted powder, the edge of the cooling channels can be preshaped by machining in a beveled or chamfered contour [26].

Fig. 17.34 shows a die with cooling channels closed by powder laser deposition welding. The base material is a C45. After closing the cooling channels, they were milled and sand blasted to get a flat and homogenous surface. Finally, two different metallics were deposited and machined to the final geometry (Fig. 17.34). The experiments using water as a coolant showed that the cooling channels, with a distance of 2 mm to the surface, allow a significant reduction of the die temperature, and cold as well as hot spots could be avoided [26].

17.4 Conclusion

Because of the low production speed compared with established metal forming processes, additive manufacturing of parts is currently applied to single-part or small-batch production. The additive manufacturing of dies and tools, which are applied in conventional metal forming operations, makes sense if a unique die feature that can only be manufactured additively, such as multidirectional cooling channels, can be integrated. Such features enable the traditional metal forming process to be more efficient or to produce a higher-quality product. In comparison to polymer injection molding [21], where additively manufactured die inserts with conformal cooling channels are already widely used in industrial mass production, the application of layer-laminated or powder-based tools in metal forming is being fundamentally researched and is not yet implemented in production. Current improvements in the primary

material, especially the metal powder, and the additive manufacturing processes and machines themselves, provide excellent material and product properties that will allow the application of rapidly manufactured dies in the near future, even in the case of highly mechanical and thermally loaded metal forming.

References

[1] E. Ambaum, B. Weiler, S. Jungfleisch, D. Wüstenberg, Verfahren und Anlage zur Herstellung und Aufarbeitung von metallischen Hohlformen, deutsche Patentschrift, DE 196 23 148 A1, 1998.
[2] B.G. Bryden, I.R. Pashby, D.I. Wimpenny, C. Adams, Laminated steel tooling in the aerospace industry, Materials and Design 21 (2000) 403−408.
[3] C.M. Cheah, C.K. Chua, C.W. Lee, S.T. Lim, K.H. Eu, L.T. Lin, Rapid sheet metal manufacturing. Part 2: direct rapid tooling, The International Journal of Advanced Manufacturing Technology 19 (7) (2002) 510−515.
[4] W. Eversheim, T. Pfeifer, M. Weck, 100 Jahre Produktionstechnik - Werkzeugmaschinenlabor WZL der RWTH Aachen von 1906 bis 2006, Springer-Verlag, Berlin Heidelberg, 2006, 567−568.
[5] D. Freyer, Controlled Metal Build Up (CMB): Schneller Aufbau und automatische Reparatur von Werkzeugen, in: FoKus − Newsletter, Fraunhofer Demonstrationszentrum Formen für die Kunststoffverarbeitung, Ausgabe 4/2001, 2001, pp. 16−18.
[6] A. Gebhardt, Generative Fertigungsverfahren: Additive Manufacturing und 3D Drucken für Prototyping - Tooling - Produktion, Carl Hanser Verlag, München, 2013.
[7] M. Geiger, V. Franke, Biegewerkzeuge aus laserstrahlgeschnittenen Lamellen, Blech Rohre Profile 41 (1994) 9, pp. 509−513.
[8] M. Geiger, M. Euringer, R. Neugebauer, F. Garreis, Lamellierte Aktiv-Werkzeugelemente in flexiblen Blechumformwerkzeugen, Blech Rohre Profile 1/2, 1999, pp. 34−37.
[9] R. Hölker, Additiv hergestellte Werkzeuge mit lokaler Innenkühlung zur Produktivitätssteigerung beim Aluminium-Strangpressen, Dr.-Ing. Dissertation, Technische Universität Dortmund, Shaker Verlag, Aachen, 2014.
[10] R. Hölker, N. Ben Khalifa, A.E. Tekkaya, Process and Appartus for the Combined Manufacturing of Workpieces by Incremental Sheet Metal Forming and Manufacturing Methods in One Set-up, German Patent Application, DE 10 2014 014 202.7, 2014.
[11] R. Hölker, A. Jäger, N. Ben Khalifa, A.E. Tekkaya, Controlling heat balance in hot aluminum extrusion by additive manufactured extrusion dies with conformal cooling channels, International Journal of Precision Engineering and Manufacturing 14 (8) (2013) 1487−1493.
[12] R. Hölker, A. Jäger, N. Ben Khalifa, A.E. Tekkaya, New concepts for cooling of extrusion dies manufactured by rapid tooling, in: International Conference on Extrusion and Benchmark, ICEB 2012, Bologna/Italy, Key Engineering Materials, Vol. 491, 2012, pp. 223−232.
[13] R. Hölker, A. Jäger, A.E. Tekkaya, Rapid laminated hot extrusion dies with integrated cooling channels, in: Steel Research International, Special Issue Metal Forming 2012, Krakow/Poland, 2012, pp. 503−506.
[14] A. Huskic, Forschung und Entwicklung im Bereich der generativen Fertigung an der FH Oberösterreich, 1, in: Anwendersymposium 3D Druck Metall, Generative Fertigung im Werkzeug- und Formenbau, 02.10.2014, 2014. http://www.fh-ooe.at/fileadmin/fileSystem/Konferenzen/Anwender_3D-Druck-Metall/D_Huskic_FHOOE.pdf.

[15] A. Huskic, B.-A. Behrens, J. Giedenbacher, A. Huskic, Standzeituntersuchungen generativ hergestellter Schmiedewerkzeuge, Schmiede Journal (September 2013) 66−70.
[16] A. Huskic, J. Giedenbacher, U. Pschebezin, N. Wild, Rapid Tooling für Umformwerkzeuge, RTejournal - Forum für Rapid Technologie 2012 (9) (2012) 1.
[17] A. Jäger, R. Hölker, J. Lueg-Althoff, L. Kwiatkowski, O.K. Demir, A.E. Tekkaya, Verfahren zur Herstellung von Werkzeugspulen und/oder Werkzeugen für die Magnetumformung, insbesondere dünnwandiger Werkstücke aus elektrisch leitfähigen Werkstoffen sowie entsprechend hergestellter Werkzeugspulen, August 2013. Anmeldenummer: DE 10 2013 013 335.1, Anmeldedatum: 06.
[18] M. Kleiner, R. Krux, Entwicklung eines Verfahrens zur schnellen Herstellung von Tiefund Streckziehwerkzeugen aus Blechlamellen für die Prototypen- und Kleinserienfertigung (Rapid Tooling), Forschungsbericht P 384, Stahl-Zentrum, Düsseldorf, Studiengesellschaft Stahlanwendung e.V, 2001.
[19] M. Kunieda, T. Nakagawa, Manufacturing of laminated deep drawing dies by laser beam cutting, Advanced Technology of Plasticity 1 (1984) 520−525.
[20] G.N. Levy, R. Schindel, P. Schleiss, F. Micari, L. Fratini, On the use of SLS tools in sheet metal stamping, CIRP Annals − Manufacturing Technology 52 (1) (2003) 249−252.
[21] G. Menges, W. Michaeli, P. Mohren, Spritzgießwerkzeuge -Auslegung, Bau, Anwendung, Hanser Fachbuchverlag, 2007.
[22] W.Z. Misiolek, K.T. Winther, A.E. Prats, S.J. Rock, Rapid prototyping of extrusion dies using layer-based techniques, Journal of Materials Engi-neering and Performance 8 (1) (1999) 23−30.
[23] B. Müller, Konturnahe Temperierung Beim Presshärten, Fraunhofer Institut für Werkzeugmaschinen und Umformtechnik (IWU), 2013. http://www.iwu.fraunhofer.de/content/dam/iwu/de/documents/Messen/220_2013_HZ_Konturnahe_Temperierung_Presshaerten.pdf.
[24] B. Müller, R. Neugebauer, Direkte generative Fertigung von Schmiedegesenken eröffnet neue Möglichkeiten, RTejournal − Forum für Rapid Technologie 7 (2010).
[25] A. Techel, MELATO® − metal Laminated Tooling Werkzeugfertigung durch Blechpaketierung, in: BMBF-Rahmenkonzept Forschung für die Produktion von morgen, Fraunhofer Institut für Werkstoff- und Strahltechnik, Dresden, 2005.
[26] R. Vollmer, R. Kolleck, P. Schwemberger, Herstellung oberflächennaher Kühlkanalstrukturen für das Presshärten mittels Laserauftragsschweißen, in: M. Merklein (Ed.), Tagungsband Zum 9. Erlanger Workshop Warmblechumformung 2014, Meisenbach, Bamberg, 2014, pp. 61−73, 2014.
[27] D.F. Walczyk, D.E. Hardt, Rapid tooling for sheet metal forming using profiled edge laminations: design principles and demonstration, ASME Journal of Mfg. Science and Engg 120 (4) (1998) 746−754.
[28] D.F. Walczyk, N.Y. Dolar, Bonding methods for laminated tooling, in: Solid Freeform Fabrication Symposium Proceedings, Austin, TX, 1997, p. 211.
[29] D.F. Walczyk, D.E. Hardt, A new rapid tooling method for sheet metal forming dies, in: Proc. of 5th Int'l Conf. on Rapid Prototyping, June 12−15, 1994, Dayton, OH, 1994, pp. 275−289.
[30] S. Yoo, D.F. Walczyk, Advanced design and development of profiles edge Laminae tools, Journal of Manufacturing Process 7 (2) (2005) 162−173.

Index

'*Note*: Page numbers followed by "f" indicate figures, "t" indicate tables.'

A
Acceptor, 422−423, 425
Acoustic droplet ejection, 421−422, 433−434
Activity-based costing, 288−289
Additive manufacturing (AM), 79, 99−103, 181, 281, 300−301, 351, 353f, 387, 388f, 393f, 399, 421, 459. *See also* Laser additive manufacturing (LAM)
  for aerospace applications, 352−353
  aerospace component fabrication, 352−361
  challenges
    for aerospace applications, 366−367
    of individualization, 405f
  characteristics of aerospace components, 351−352
  design for protection, 301−305
    avoidance of standard dimensions, 303
    black box design, 302
    de-standardization, 303
    integration of functions, 302
    marking by internal structures, 304−305, 304f−305f
    self-destructive design, 303
  direct laser-based AM techniques for ceramics, 171−172
  future applications, 366−368
  geometric error sources, 102−103
  indirect laser-based AM techniques for ceramics, 166−171
  lifecycle costing in, 285−288, 297−299
  nonmetallic parts fabrication, 358−361
  processes for ceramics, 165−172
  product piracy, 300−301
    for lifecycle costing, 299−300
  production costs, 288−295
  profitability and part selection for, 281−285
  for repair, 361−362
  routes, 165f
  self-costs, 295−296
  SLM, 102
  techniques, 119−120, 163, 439
    and cost development, 310−311
  working with guidelines during product development, 305−306
Additive nanofabrication
  3D micro-/nanostructures, 243−246
  TPP characterization, 240−243
    Raman spectroscopy, 241−243
    voxel dimension characterization, 240
Adipose-derived stem cells (ASCs), 427−428, 428f, 432−433
Aeronautics
  applications of ceramics
    ceramics, 383−385
    MCs, 385−386
  LAM for ceramic components, 392−393
Aerospace
  applications, 351
    AM for, 352−353
    challenges of AM for, 366−367
    DED in, 353−356
    nonmetallic fabrication with AM, 358−361
    powder bed fusion in, 356−358
    repair examples, 364−366
  automated repair process, 368
  characteristics of AM, 351
  components, 351
  fabrication with AM, 352−361
    AM for aerospace applications, 352−353
    DED in aerospace applications, 353−356
    nonmetallic parts fabricated with AM, 358−361
    powder bed fusion in aerospace applications, 356−358
  industry, 351−353, 357−358, 361, 368

Aerospace (*Continued*)
repair examples for applications, 362−364
repair with AM, 361−366
AM for repair, 361−364
hybrid manufacturing process for repair, 362, 363f
repair aerospace components, 361
repair process, 362−364, 363f
Airbus A350 XWB, 357, 358f
AISI1045 substrate material, 89, 95
Alloys, 403
aluminium, 119−120, 123, 132
Cocr, 400
magnesium and, 403
titanium, 119−120, 402
AlSi12Mg alloy, 119−120
compressive testing results, 146−151
deformation behaviour and failure modes, 151−156
experimental results, 150−151
numerical analysis, 148
lattice structures, 120−124
SLM-manufactured lattice structures, 123−124
lattice test specimen details, 131t
SLM manufacturability, 125−136
geometric fidelity of as-manufactured lattice geometry, 132−136
identification of parameters, 125
lattice specimen manufacture and testing objectives, 131
lattice strut manufacturability, 125−128
processing parameters for, 125, 126t
Alumina-yttria, 385
Aluminium alloys, 119−120, 123, 132
Aluminum oxide (Al_2O_3), 163−164, 169−170
AM. *See* Additive manufacturing (AM)
Andrew number, 193
Application-specific integrated circuit (ASIC), 319
Area-related energy density. *See* Andrew number
As-manufactured lattice geometry, 132−136
AlSi12Mg
lattice specimens, 133−134
lattice strut surface roughness evaluation, 134−136, 135t
Ti6Al4V lattice specimens, 132−133
Ascending method, 240
ASCs. *See* Adipose-derived stem cells (ASCs)
ASIC. *See* Application-specific integrated circuit (ASIC)
Aspect ratio, 123, 131
Astronautics, 373
applications of ceramics
ceramics, 383−385
MCs, 385−386
LAM for ceramic components, 392−393
Automated repair process for aerospace components, 368
Auto−oxidation process, 198−199

B
Balling, 60−61, 61f
Bare die, 326
BCC. *See* Body-centred cubic (BCC)
Beam
beam sources, reducing stress by, 82
beam-focussing capabilities, 389
electromagnetic energy, 389
Biocompatible/biocompatibility, 399
materials, 399−404
cellular structures, 403−404
ceramics, 403
metallic, 400−403
polymeric, 400
properties, 399−404
cellular structures, 403−404
ceramics, 403
metallic, 400−403
polymeric, 400
Biodegradable polymer, 400
Biomaterials, 238, 401, 421−423, 425
Biomedical applications, 399−400
Biopapers, 431
Bioplotting. *See* Extrusion printing
Bioprinting techniques, 421−422
Black box
design, 302
systems, 285f
Blister, 323−324
effect, 423
technique, 325−326
Body-centred cubic (BCC), 122, 122f, 153
Bores, 263, 263f−264f

Boundary conditions, 120
cell, 148
influence of FBCCZ, 144
sliding, 124, 130−131
Brittle fracture, 87
Bulging effect, 423

C
CAD. *See* Computer-aided design (CAD)
Carbides, 164
CCs. *See* Ceramic composites (CCs)
Cell printing, 424
Cell−cell interaction studies, printed multicellular patterns for, 427, 428f
Cells, printing impact on, 426
Cellular materials, 119
Cellular microarrays, 427
Ceramic components, 361, 373, 375f. *See also* Polymer nanocomposites for LAM
conventional manufacturing methods for, 374−383
extrusion and pressing methods, 376−379
sintering of ceramics, 380−382
slurry methods, 379−380
LAM for, 387−393
Ceramic composites (CCs), 385
Ceramic material(s), 163−165, 373−374
conventional manufacturing routes, 164f
laser interaction with, 389−391
laser melting, 391−392
LS, 391−392
microstructure, 165f
powder, 377, 378f
technical ceramics, 164f
Ceramic matrix composites (CMCs), 359−361, 385, 387f
Ceramics, 163, 373−376, 383−385, 403
AM processes for, 165−172
applications
in aeronautics and astronautics, 383−386
of AM, 172−174
direct laser-based AM techniques for, 171−172
indirect laser-based AM techniques for, 166−171
sintering, 380−382
β-tricalcium phosphate/polylactid biodegradable bone implant, 173f
Chest wall, 412−413
sternal replacement
custom-made titanium, 413f
radiograph of inserted, 414f
Chromium, 23−24
Closed-loop DMD, 21−23
CMCs. *See* Ceramic matrix composites (CMCs)
CNC. *See* Computer numerical control (CNC)
Coalescence, 381−382
Cobalt−chromium alloys (CoCr alloys), 400
Coefficient of thermal expansion (CTE), 36, 81, 324
Collagen, 424, 430
Commercially pure titanium (cpTi), 401
Composition sensor, 45−46
Compressive testing results, 136−156
AlSi12Mg lattice specimens, 146−151
deformation behaviour and failure modes, 151−156
Ti6Al4 lattice specimen, 137−146
Computed tomography (CT), 405
Computer numerical control (CNC), 21−22, 351−352
Computer-aided design (CAD), 21, 32f, 100, 101f, 129−130, 259, 289, 391−392
approach, 405
layered approximation, 102f
model, 205, 355−356
Conductive winding, 459
Constrained boundary condition, 148
Continuous wave (cw), 324
Conventional fabrication, 163−165
conventional manufacturing routes, 164f
microstructure of, 165f
technical ceramics, 164f
Conventional machining processes, 352
Conventional manufacturing methods, 382−383
for ceramic components, 374−383
extrusion and pressing methods, 376−379
sintering of ceramics, 380−382
slurry methods, 379−380
Cooling rate control, 45
Copper strips, 330
Cost structure, 285
cpTi. *See* Commercially pure titanium (cpTi)

Crack density, 64
Crack formation and delamination in LMD, 87–88
Cracking of SLM-processed parts, 63–65
Cryogenic grinding, 187–188
Crystallization, 188
CT. *See* Computed tomography (CT)
CTE. *See* Coefficient of thermal expansion (CTE)
Curling, 189, 193, 196–197, 206, 207f
Custom-made heel bone, 414, 414f–415f
Customized endoprostheses, 406–407, 413–414
Customized prosthetics and implants, process chain for
  design process, 405–406
  postprocessing, 407
  product requirements, 405
  production process, 406–407
Customized sternal implant, 412, 413f
cw. *See* Continuous wave (cw)

D
DC. *See* Degree of conversion (DC)
De-standardization, 303
Decomposition temperature, 209
DED. *See* Directed energy deposition (DED)
Deep-drawing
  die, 452f
  experiments, 443
Deformation behaviour, 151–156
Degree of conversion (DC), 242–243
Densification, 166, 171, 174, 374, 381
Design of experiments analysis (DOE analysis), 126
Design process, 405–406
Development of Additive Manufacturing Potential Check System (DynAMICS), 281
Dielectric
  materials, 335
  properties, 385
Differential scanning calorimetry (DSC), 188, 189f
  curve of PA, 190f
  curves for injection-moulding PA, 191f
  tests, 210
Digital CAD data, 301
Digital micromirror device (DMD), 342
Digital part materialization, 357–358
Direct laser-based AM techniques for ceramics, 171–172. *See also* Indirect laser-based AM techniques for ceramics
  direct SLS, 171–172
  laser-engineered net shaping technology, 172
  SLM, 172
Direct manufacturing, 165–166, 172, 282
  Design Rules catalogue, 306f
  influence factors, 172, 410
Direct metal deposition (DMD), 21–23, 32f–33f, 352–353
  with active height controller, 22f
  results and discussion, 37–48
    closed-loop DMD, 41
    creep results, 42f
    DMD laser systems, 39
    IMS-T1 sample process parameters, 39f
    injection-molding die, 40f
    integrated design and manufacturing, 43
    mold flow calculation for cycle time, 41t
    process control, 43–48
    QAMS, 43–48
    remote manufacturing, 43
    wall roughness, 38
Direct selective laser sintering, 168, 171–172
Directed energy deposition (DED), 351–353
  in aerospace applications, 353–356
Discrete component laser-induced forward transfer, 321–331, 322t, 327f
Distortion
  distortion-sensitive components, 362
  reduction by mechanical forces, 94
  SLM-processed parts, 63–65
Diverse absorption materials, 423–424
DMD. *See* Digital micromirror device (DMD); Direct metal deposition (DMD)
DOE analysis. *See* Design of experiments analysis (DOE analysis)
Donor, 422–423
Double scanning, 196
DRL. *See* Dynamic release layer (DRL)
Droplet volume controlling, 425, 425f

DSC. *See* Differential scanning calorimetry (DSC)
Duplex phase, 23–24
Duraform PA, 191
Dye-sensitized solar cells LIFT, 338–340, 339f
Dynamic release layer (DRL), 323
Dynamic viscosity, 425
DynAMICS. *See* Development of Additive Manufacturing Potential Check System (DynAMICS)

E
ECFCs. *See* Endothelial colony-forming cells (ECFCs)
Electrical conductive SLS polymer nanocomposites, 211–228
  density evaluation, 217–223
  electrical conductivity, 226
  HDT testing, 226
  mechanical properties, 223–224
  microstructural analysis, 226–227
  notch impact testing, 226
  product technical data sheet, 227–228
  thermal properties, 211–216
Electrical conductivity, 226
Electroceramics, 384
Electromagnetic forming, 459
Electrophoretic casting, 380, 380f
Electrostatic dissipation (ESD), 210
Elongated pore, 65
Embedded circuit LIFT, 343–345
Embedded electronics LAM
  LIFT, 320
    of discrete components, 321–331, 322t, 327f
    of embedded circuit, 343–345
    of functional materials systems, 331–343
EML. *See* Energy to melt layer (EML)
EMR. *See* Energy melt ratio (EMR)
Endoprostheses, 403–404, 406–414
  chest wall, 412–413
  customized, 413–414
  hip implants, 408–409
  knee implants, 410
  patient-specific surgical guides, 407–408
  spinal implants, 410–411
  upper extremities, 412
Endothelial colony-forming cells (ECFCs), 427
Energy density, 205, 389–390, 390f
Energy melt ratio (EMR), 195–196
Energy to melt layer (EML), 195–196
Engineering ceramics, 173–174
ESD. *See* Electrostatic dissipation (ESD)
Extruding methods, 373, 377f
Extrusion, 207, 376–379, 421
  dies, 448, 459f
  hard-to-extrude aluminum alloy EN AW-7075, 427
  PA11 PCG LV, 208
  printing, 421

F
Face-centred cubic (FCC), 23–24, 122
Failure modes, 151–156
  AlSi12Mg lattice specimens, 154f–155f
  Ti6Al4 lattice specimens, 152f–153f
FBCCZ/FBCCZO specimens, 137
FCC. *See* Face-centred cubic (FCC)
FDM. *See* Fused deposition modeling (FDM)
Femtosecond laser direct writing (FsLDW), 238, 240, 246–248. *See also* 3D micro-/nanofabrication
FGM. *See* Functionally graded material (FGM)
Fibrin gel, 424
Flame-retardant (FR), 208
  SLS polymer nanocomposite, 228–232
    flammability, 230–232
    mechanical properties, 232
    thermal stability, 228–230
Fluid flow
  models, 25–26
  strain, 86
Forging dies, 454f–455f
FR. *See* Flame-retardant (FR)
FsLDW. *See* Femtosecond laser direct writing (FsLDW)
Fully Non-Metallic Gas Turbine Engine, 359–361
Functional hydraulic housing for engineering application, 113–115, 113f
Functional materials system, LIFT, 331–343

Functionally graded material (FGM), 353–354
Fused deposition modeling (FDM), 352–353, 358–359, 359f
  nonmetallic gas turbine engine fabrication, 360f
  polycarbonate wiring conduits, 360f

G
Gas pores, 65
Gas Turbine Research Establishment, 358–359
GE Aviation, 356–357
Geometric error sources, 102–103
  error in STL
    manufacturing, 103
    representation of CAD data, 102–103
Geometric features of LAM, 262–264
  bores, 263, 263f–264f
  holes, 263, 264f
  minimum wall thickness, 263–264
Geometric fidelity
  AlSi12Mg
    lattice specimens, 133–134
    lattice strut surface roughness evaluation, 134–136, 135t
  of as-manufactured lattice geometry, 132–136
  SLM manufacturing fidelity of Ti6Al4V lattice specimens, 132–133
Geometry control, 44–45
Grilamid PA12, 191

H
H13 tool steel, 24, 39, 45–46
HA. *See* Hydroxyapatite (HA)
n-HA. *See* Nano-hydroxyapatite (n-HA)
Hairpin-shaped inductors, 92–93
Hatch distance, 193–195
Hausner ratio (HR), 199
HDM. *See* Homogenization design method (HDM)
HDT. *See* Heat deflection temperature (HDT)
Heat deflection temperature (HDT), 223–224
  testing, 226
Heat transfer models, 25–26
Helicopter engine combustion chamber, 354, 355f
Heterogeneous thermal gradient, 391
High buy-to-fly ratio, 352
High-strain test, 137
High-volume customised components, 99
Hip implants, 408–409
  custom-made partial hip replacement, 409f
  MUTARS revision hip cup, 408f
Holes, 263, 264f
Homogenization design method (HDM), 31–33
Hot-stage microscopy, 191–192
HP thermal inkjet array, 201–202
HR. *See* Hausner ratio (HR)
HSK interface, 354
Hybrid laser manufacturing, 79
  advantages and disadvantages, 80t
  coaxial laser metal deposition, 85f
  energy sources for, 81f
  hybrid approaches using mechanical impacts, 94
  laser-based processes, 79
  using local pre-and postheating, 83–85
  nickel-base superalloy test specimen, 91f
  procedures, 80–81
  process performance by thermal heat sources, 81–93
    crack formation and delamination in LMD, 87–88
    geometry and position of integrated inductor, 92–93
    pre-and postheating on residual stress, 88–91
    preheating in furnace, 82–83
    reducing stress by adding beam sources, 82
    substrate preheating and comparison of thermal effects, 85–87
Hybrid manufacturing
  process for repair, 362
  system, 354
Hydrogen, 88
Hydroxyapatite (HA), 167

I
ILT. *See* Institute for Laser Technology (ILT)
In situ printing, 432

In-process cooling, 189–190
IN738 blade, 365–366, 365f
Indirect laser-based AM techniques for ceramics, 166–171. *See also* Direct laser-based AM techniques for ceramics
  conventional AM techniques for mold fabrication, 171
  LOM, 169–170
  LSD, 169
  SLS, 167–168
  STL, 166–167
Indirect manufacturing, 165, 410
Indirect SLS, 168
Induction
  hybrid laser manufacturing using local pre-and postheating by, 83–85
  preheating in, 82–83
Infrared (IR), 321–323
  laser pulse, 321–323
Initial set-up costs, 295
Inkjet printing, 421
Inorganic powder additives, 186
Institute for Laser Technology (ILT), 365
Instrumentation and control applications, 384, 386f
Integration of functions, 302
Interconnects, LIFT of, 320, 331–334, 333f–334f
Internal structures, marking by, 304–305, 304f–305f
Intervertebral disc implants, 410–411, 411f
Intra-layer porosity, 65
Intrinsic lifecycle, 297
IR. *See* Infrared (IR)
Isostatic pressing techniques, 379, 379f

J
Just-stiff lattice structure, 121

K
Keyhole pores, 65
Kinetics of laser transfer process, 325–326
Knee implants, 410, 410f–411f

L
L&P process. *See* Lase-and-place process (L&P process)
LaBP. *See* Laser-assisted bioprinting (LaBP)
Lack-of-fusion, 65
LAM. *See* Laser additive manufacturing (LAM)
Lambda sensors, 163–164
Laminated object manufacturing (LOM), 166, 169–170
Lase-and-place process (L&P process), 323, 326–331, 328f–329f
Laser
  input energy density, 57
  melting of ceramic materials, 391–392
  micromachining, 343
  microsintering, 171–172
  processing, 391
Laser additive manufacturing (LAM), 259, 320, 343, 373, 399. *See also* Additive manufacturing (AM)
  for aeronautical and astronautical ceramic components, 392–393
  for ceramic components, 387–393
  customized prosthetics
    applications, 407–416
    biocompatible materials and properties, 399–404
    process chain for, 405–407
  demonstrating scattering issues, 390f
  design restrictions, 259–265
    final machining, 265
    geometric features, 262–264
    geometric resolution, 260, 260f
    guideline catalogue, 265, 266t–270t
    part alignment, 265f
    support structures, 260–261, 261f–262f
    urface quality, 260–261, 261f
  LAM-processed nitinol, 402
  laser interaction with ceramic materials, 389–391
  laser melting of ceramic materials, 391–392
  LS of ceramic materials, 391–392
  product design approaches, 265–277
    air ejector system, 277f
    bracket design, 275f
    cooling structures, 277f
    design alternatives for aircraft brackets, 275f
    hip implant with lattice structures, 271f
    LAM design, 277
    LAM's application, 265–271

Laser additive manufacturing (LAM) (*Continued*)
lattice-based osseointegrative, 271
medical sector, 271
methods for optimizing structure, 272
rapid tooling, 276
structural optimization problems, 272f
topology optimization, 273f–274f
Laser additive printing of cells
applications, 426–432
biopapers, 431
printed multicellular patterns, 427, 428f
printed stem cell grafts, 427–429, 429f
printing skin tissue, 429–431, 430f
in situ printing, 432
cellecell and celleenvironment interaction, 433
LaBP, 422–426, 422f, 432
printing techniques, 433–434
tissue printing, 432
Laser beam wavelength, 389
Laser decal transfer (LDT), 331
Laser direct write (LDW), 320. *See also* 3D micro-/nanofabrication
linear and nonlinear optical absorption in, 238–239
for micro/nanofabrication, 237–238
Laser engineering net-shape (LENS), 352–353
LENS 850-R system, 354–355
process, 354–355, 355f
Laser metal deposition (LMD), 79, 352–354
crack formation and delamination in, 87–88
Laser sintering (LS), 181–185, 183f, 340
ceramic materials, 391–392
materials for, 185
process parameters, 184t
Laser-aided direct metal deposition of metals and alloys. *See also* Direct metal deposition (DMD)
experimental procedure, 33–37
material selection, 36–37
multiple-sensor layout, 35f
negative coefficient of thermal expansion experiments, 36, 36f
primary dimensions of unit cell tool paths, 38f
laser-cladding process, 23–30
material microstructure design and realization, 30–33
Laser-assisted bioprinting (LaBP), 421–426, 422f
controlling droplet volume, 425
impact on cells, 426
printing material compositions, 424
Laser-based powder bed fusion process, 55, 55f
Laser-based processes, 79, 319–320
Laser-cladding process
laser-cladding technology, 23
materials and applications, 23–25
modeling, 25–29
fluid flow models, 25–26
heat transfer models, 25–26
laser–powder interaction, 25
mass transfer models, 26–27
self-consistent 3D transient model, 27–29
solid free-form fabrication, 29–30
Laser-engineered net shaping technology, 172
"Laser-guided direct-write", 422
Laser-induced forward transfer (LIFT), 320, 421
discrete components, 321–331, 322t, 327f
IR laser pulse, 321–323
lase-and-place technique, 326–331, 328f–329f
laser-assisted mechanisms, 325
release mechanisms for die, 324–325
of dye-sensitized solar cells, 338–340, 339f
embedded circuit, 343–345, 344f
functional materials system, 331–343
of interconnects, 331–334, 333f–334f
of materials, 334–335
of microbatteries, 335–337, 337f–338f
of microstructures, 321
in parallel, 342–343
of sensors, 340–342, 341f
Laser-scanning process, 389
Laser–powder interaction, 25
LASERTEC 65 3D hybrid manufacturing system, 354, 354f
Lattice structures, 119–124
SLM-manufactured lattice structures, 123–124
unit cells, 122f

Lattice-based osseointegrative interfaces, 271
Layer thickness (LT), 260
Layer-laminated manufacturing, 439–450
  forms of bending dies, 445f
  lamellas for die cap of extrusion die, 450f
  layered die for high-pressure forming, 443f
  manufacturing strategies, 442f
  PEL tool, 440f
  scaled nose-cone fairing tool, 448f
  tensile failure, 448f
  tooling inserts, 447f
  vertically layered deep-drawing die, 442f
Layer-wise production process, 260
Layer-wise slurry deposition (LSD), 166, 169
Layered die, 449f
Layered trimming die, 439
LDT. *See* Laser decal transfer (LDT)
LDW. *See* Laser direct write (LDW)
Lead zirconate titanate ceramics, 385
LEAP engine, 356–357, 357f
LED. *See* Light emitting diode (LED); Liner energy density (LED)
LENS. *See* Laser engineering net-shape (LENS)
Li-ion microbattery. *See* Lithium-ion microbattery (Li-ion microbattery)
Lifecycle costs, 297–299, 297f–298f
  in additive manufacturing, 285–288
    development of costing tools, 288
    methodology for lifecycle costing, 286
    phases of costs, 287f
    process chain, 285
    product lifecycle, 286f
    self costs and production costs, 287–288
  product piracy aspects, 299–300, 299f
LIFT. *See* Laser-induced forward transfer (LIFT)
Light emitting diode (LED), 323
Line-shaped inductors, 92–93
Linear optical absorption in laser direct writing, 238–239
Liner energy density (LED), 57
Liquid-phase sintering (LPS), 381–382, 382f
Lithium-ion microbattery (Li-ion microbattery), 336–337
LM555 bare die, 327
LMD. *See* Laser metal deposition (LMD)
LOM. *See* Laminated object manufacturing (LOM)
Low-strain test, 137
Low-volume
  production components, 99
  prototype cover, 110–112
LPS. *See* Liquid-phase sintering (LPS)
LS. *See* Laser sintering (LS)
LSD. *See* Layer-wise slurry deposition (LSD)
LT. *See* Layer thickness (LT)

M

Magnesium, 403
Magnetic resonance imaging (MRI), 405
Manufacturing strategy, 289, 290f–292f
Marangoni effect, 60
Mars rover curiosity, 167
Mass transfer models, 26–27
Material microstructure design and realization, 30–33
  HDM, 31–33
  system architecture, 32f
Material selection, 36–37
Maxwell criteria, 121–122
Maxwell number (*M*), 120–122
  for unit cell candidate lattice structures, 122t
MCC. *See* Microscale combustion calorimetry (MCC)
MCs. *See* Multicomponent ceramics (MCs)
Mechanical forces, distortion and stress reduction by, 94
Mechanical properties
  adjustment in laser-based metal processes, 294
  SLM-processed metallic parts, 67–69
"MELATO" process chain, 444, 444f
Melt pool, characteristics of, 58–61
Melt volume rate (MVR), 199
MEMS. *See* Microelectromechanical systems (MEMS)
Mesenchymal stem cells (MSCs), 426
Metal-forming processes, 439
  layer-laminated manufacturing, 439–450
  powder bed–based additive manufacturing, 450–462

Metallic components, 351
Metallic materials, 400–403
  CoCr alloys, 400
  cpTi, 401
  magnesium and alloys, 403
  nickel titanium, 402
  precious metals, 402
  stainless steel, 403
  tantalum, 402
  titanium alloys, 402
    Ti6Al4V, 401
Micro/nanofabrication, laser direct writing for, 237–238
Microbatteries LIFT, 335–337, 337f–338f
Microelectromechanical systems (MEMS), 237, 319–320
Microscale combustion calorimetry (MCC), 210
Microstructural analysis, 226–227
Microstructural features of PBF, 61–67
  non-equilibrium microstructure, 62–63
  SLM-processed parts
    defects and density, 65–67
    residual stresses, cracking and distortion, 63–65
  texture, 61–62
Microstructure sensor, 46–48
Miniaturization, 319
Mold flow analysis, 22–23
MPA. *See* Multiphoton ablation (MPA)
MRI. *See* Magnetic resonance imaging (MRI)
MSCs. *See* Mesenchymal stem cells (MSCs)
Multicomponent ceramics (MCs), 385–386
Multi–jet fusion technology, 201–202
Multiphoton ablation (MPA), 238
  subtractive micro-/nanofabrication using, 246–250
Multiwalled carbon nanotubes (MWNTs), 207
MVR. *See* Melt volume rate (MVR)
MWNTs. *See* Multiwalled carbon nanotubes (MWNTs)

N

Nano-hydroxyapatite (n-HA), 432
Nanocomposite formulation, 208–209
Nanocomposite solid-polymer ionic liquid (nc-SPIL), 336
Nanoelectromechanical systems (NEMS), 237
Nanographene platelets (NGPs), 208
Naval Research Laboratory (NRL), 323
nc-SPIL. *See* Nanocomposite solid-polymer ionic liquid (nc-SPIL)
NCTE. *See* Negative coefficient of thermal expansion (NCTE)
Near-infrared lasers, 424
Negative coefficient of thermal expansion (NCTE), 42f
  contraction mechanism, 37f
  experiments, 36, 36f
NEMS. *See* Nanoelectromechanical systems (NEMS)
NGPs. *See* Nanographene platelets (NGPs)
Nickel titanium, 402
Nitrides, 164
Non-equilibrium microstructure, 62–63
Nonlinear optical absorption in laser direct writing, 238–239
Nonmetallic components, 351
  fabricated with AM in aerospace applications, 358–361
Notch impact testing, 226
NRL. *See* Naval Research Laboratory (NRL)
Numerical analysis
  AlSi12Mg specimens, 148
  candidate lattice structures, 149t–150t
Nylon 11, 208t

O

One-step laser-cladding process, 25
Optimal hatching space, 57
'Orange peel', 199
Orthodontics, 405
Orthotics, 403–404, 414–416, 415f
Over-stiff lattice structure, 121
Oxides, 163–164

P

PA. *See* Polyamide (PA)
Parallel printing technique, LIFT in, 342–343, 342f
Passive components, LIFT of materials for, 334–335
Patient-specific instruments (PSIs), 407–408, 409f

Patient-specific surgical guides, 407–408
PBF. *See* Powder bed fusion (PBF)
PCA. *See* Printed circuit assembly (PCA)
PDMS. *See* Polydimethylsiloxane (PDMS)
Peak roughness avoidance, 107–108
PEL tool. *See* Profiled edge lamination tool (PEL tool)
N-Photon-absorption process, 239
Piston type, 376, 377f
Plagiarism, 299
Planar alkaline microbatteries, 336
Plasma transfer arc (PTA), 79
Plastic deformation, 85
Polyamide (PA), 185, 206–207, 400
Polyaryletherketones, 400
Polycaprolactone, 400
Polydimethylsiloxane (PDMS), 324
Polylactide, 400
Polymer nanocomposites for LAM. *See also* Ceramic components
  experimental approach, 208–211
    DSC tests, 210
    electrical conductivity, 210
    fabrication of SLS test specimens, 209
    flammability, 210–211
    materials, 208–209
    mechanical properties, 211
    TGA, 209–210
  results and discussion, 211–232
    electrical conductive SLS polymer nanocomposites, 211–228
    flame retardant SLS polymer nanocomposite, 228–232
  SLS, 205, 206f
Polymer powder bed fusion systems, 200–202
  high-speed sintering, 201
  multi-jet fusion technology, 201–202
  selective heat sintering, 201
  selective inhibition sintering, 201
  selective mask sintering, 201
Polymeric/polymer, 208
  materials, 400
    PA, 400
    polyaryletherketones, 400
    polycaprolactone, 400
    polylactide, 400
Polymethylmethacrylate, 407
Polypropylene, 191
Post-processing, 294
  densification, 389
Postheating
  hybrid laser manufacturing using, 83–85
  on residual stress, 88–91
Powder bed fusion (PBF), 181, 182f, 200–202, 352–353, 389, 391f
  in aerospace applications, 356–358
  laser-based powder bed fusion process, 55, 55f
  LS, 181–185
    build set-up consisting of multiple individual parts, 183f
    materials for, 185
  materials behaviour during processing, 196–200
    delay time, 196–197
    parts orientation and placement, 197–198
    powder reuse, 198–200
  mechanical properties of SLM-processed metallic parts, 67–69
  melt pool, characteristics of, 58–61
  microstructural features, 61–67
  physical properties, 186–188
  process characteristics, 55–56
  processing parameters, 56–58, 56f
    combined processing parameters, 57
    morphology and size of particles, 57–58
  processing parameters, 192–196
    build temperatures, 192–193
    laser and scan parameters, 193–196
    layer thickness, 192
    scan count strategy, 196
    scan strategy, 196
  thermal properties, 188–192
Powder bed–based additive manufacturing, 450–462
  deep-drawing die, 452f
  forging dies, 454f–455f
  laser-sintered punch and die, 453f
  powder nozzle–based additive manufacturing, 460–462
  press-hardening tool, 456f
  tool for sheet metal forming, 457f
Powder nozzle–based additive manufacturing, 460–462
Precious metals, 402

Preheating
in furnace, 82–83
hybrid laser manufacturing using, 83–85
on residual stress, 88–91
Pressing methods, 373, 376–379
Printed circuit assembly (PCA), 319
lamination, 320
Printed multicellular patterns for cell–cell interaction studies, 427, 428f
Printed stem cell grafts, 427–429, 429f
Printing material compositions, 424
Process control, 43–48
composition sensor, 45–46
cooling rate control, 45
geometry control, 44–45
microstructure sensor, 46–48
temperature control, 45
Product development, working with guidelines during, 305–306, 306f–307f
Product piracy
and additive manufacturing, 300–301
for lifecycle costing, 299–300
Production costs, 288–295
adjustment of mechanical properties, 294
build preparation, 289, 290f–292f
manufacturing strategy, 289, 290f–292f
phases during AM production, 288f
post-processing, 294
quality control costs, 294–295
Profiled edge lamination tool (PEL tool), 440–441, 440f
Profitability and part selection for additive manufacturing, 281–285
black box systems, 285f
costs of AM technology, 282
indications, 282f
methodology, 282–283, 283f
multi-criteria decision-support methodology, 282–283
reaction wheel bracket, 284
Propulsion applications, 383, 385f
Prosthetics, 399, 405, 414–416, 415f
Prototype
components, 99
housing, 110–111
Pseudo-elastic material, 402
PSIs. *See* Patient-specific instruments (PSIs)
PTA. *See* Plasma transfer arc (PTA)

Q
QAMS. *See* Quality-assured manufacturing system (QAMS)
4-Quad comparator device chip, 340
Quality control, 310
costs, 294–295
Quality-assured manufacturing system (QAMS), 43–48
composition sensor, 45–46
cooling rate control, 45
geometry control, 44–45
microstructure sensor, 46–48
temperature control, 45
Quasicrystal, 24–25

R
Radiation-absorbing material (RAM), 201
Raman spectroscopy of TPP, 241–243
Randomized structures, 404
Rapid tooling, 451
RE. *See* Reverse engineering (RE)
Regolith materials, 385–386, 388f
Relative standard deviation (RSD), 140
Repair process, 362–364
Residual stresses of SLM-processed parts, 63–65
Reverse engineering (RE), 300. *See also* Clinical engineering (CE)
Ring-shaped inductors, 93
Robotic dispensing. *See* Extrusion printing
Roughness, 103–109
experimental results, 103–106
objectives, 106–109
average roughness, 107
peak roughness avoidance, 107–108
roughness of relevant surfaces, 108
weighted roughness, 108–109
process parameters, 104t
Ti64 powder distribution, 104f
RSD. *See* Relative standard deviation (RSD)

S
Scaffolds, 403–404, 404f, 421
Scaled nose-cone fairing tool, 448f
Scan/scanning
count strategy, 196
space, 205
speed, 205
strategy, 196

Scanning electron microscopy (SEM), 123–124, 240
Scanning emission microscopy. *See* Scanning electron microscopy (SEM)
Screw type, 376
Selective heating, 86
Selective laser melting (SLM), 55, 99–100, 119–120, 172, 352–353
  binary STL file standard, 101t
  geometric fidelity of as-manufactured lattice geometry, 132–136
  identification of parameters, 125
  lattice specimen manufacture and testing objectives, 128–131
  lattice strut manufacturability, 125–128
  manufacturability, 125–136
  processing parameters for Ti6Al4V and AlSi12Mg, 125
  SLM-processed parts
    mechanical properties, 67–69
    residual stresses, cracking and distortion, 63–65
  surface roughness optimisation for
    binary STL file standard, 101t
    CAD, 101f
    case studies, 109
    functional hydraulic housing, 113–115, 113f
    low-volume prototype cover, 110–112
    roughness, 103–109
    surgical implant design, 109–110
Selective laser sintering (SLS), 55, 166–168, 205, 392
  build parameters, 205–206
  materials used in, 206–207
  process, 451
  SLS polymer nanocomposite
    electrical conductive, 211–228
    flame retardant, 228–232
  SLS-processed parts, defects and density, 65–67
Self-consistent 3D transient model, 27–29
Self-costs, 295–296, 296f
Self-destructive design, 303
SEM. *See* Scanning electron microscopy (SEM)
Semiempirical method, 25
Sensors LIFT, 340–342, 341f
SFF technique. *See* Solid free-form fabrication technique (SFF technique)
Shielding applications, 385, 387f
Silicon (Si), 168
  bare dies, 321–323
Silicon dioxide, 374, 375f
Silicon monoxide (SiO), 171–172
Sintering of ceramics, 380–382. *See also* Selective laser sintering (SLS)
Skin tissue, printing, 429–431, 430f
Slip casting, 379, 380f
SLM. *See* Selective laser melting (SLM)
SLS. *See* Selective laser sintering (SLS)
Slurry methods, 379–380
Small production runs, 352
SMDs. *See* Surface-mount devices (SMDs)
Solid free-form fabrication technique (SFF technique), 21–22, 29–30
Solid metallic interconnects, 334
"Solid-isotropic-material-with-penalization" method, 272–273
Solid-state sintering (SSS), 381, 381f
Spinal arthrodesis, 410–411
Spinal implants, 410–411
Sputtering, 60
SSS. *See* Solid-state sintering (SSS)
Stainless steel, 403
Standard dimension avoidance, 303
Stem cells, 428–429
Stereolithography (STL), 166–167
  format, 100
  geometric error
    in STL manufacturing, 103
    in STL representation of CAD data, 102–103
STL. *See* Stereolithography (STL)
Stochastic open-cell materials, 119
Stochastic structures, 404
Stratasys, 358–359
Stress reduction by mechanical forces, 94
Substrate preheating and comparison of thermal effects, 85–87
Subtractive micro-/nanofabrication using multiphoton ablation, 246–250
Surface energy density, 57
Surface roughness, 99
  optimisation for SLM
    binary STL file standard, 101t

Surface roughness (*Continued*)
CAD, 101f
case studies, 109
functional hydraulic housing for engineering application, 113−115, 113f
low-volume prototype cover, 110−112
roughness, 103−109
surgical implant design, 109−110
Surface-mount devices (SMDs), 319−320
Surgical implant design, 109−110
Syringe-based printing. *See* Extrusion printing

T
Tantalum, 402
β-TCP. *See* β-Tricalcium phosphate (β-TCP)
Temperature control, 45
Texture, 61−62
TGA. *See* Thermogravimetric analysis (TGA)
TGA-50, 209
Thermal protection, 383, 384f
Thermal stability, 209
Thermal-CTE method, 325
Thermal-PET method, 325
Thermogravimetric analysis (TGA), 209−210
Thermoplastic polymers, 400
Thick-film resistors, 335
Three-dimensional printing (3DP), 352−353, 357−358, 360f, 392, 421
3D cell model, 426−427, 433
3D Computer−assisted design (3D CAD), 166
3D lithography system, 243−244, 245t
3D micro-/nanofabrication, 237
additive nanofabrication
3D micro-/nanostructures, 243−246
TPP, 240−246
challenges and opportunities, 239
comprehensive 3D micro-/nanofabrication, 250−254, 251f
on FsLDW, 238
subtractive micro-/nanofabrication using MPA, 246−250
3D quasi-steady laser-cladding process, 26
3D-scanning technologies, 300−301
Ti64 airfoil, 364, 364f
Ti64 powder distribution, 104f
Ti6Al4V alloy, 119−120, 355−356, 356f, 401
compressive testing results, 137−146
convergence of mechanical properties for, 144−146
deformation behaviour and failure modes, 151−156
lattice structures, 120−124
SLM-manufactured lattice structures, 123−124
lattice test specimen details, 130t
relative modulus, 141f
SLM manufacturability, 125−136
geometric fidelity of as-manufactured lattice geometry, 132−136
identification of parameters, 125
lattice specimen manufacture and testing objectives, 129−131
lattice strut manufacturability, 125−128
processing parameters for, 125, 126t
stress−strain response of Ti6Al4 FBCZ-S2N7 specimen, 140f
Time-driven costing, 288−289
Tissue formation, 430−431
Tissue printing, 432
Titanium alloys, 119−120, 402
TOM. *See* Trade-off methodology matrix (TOM)
Topology optimization method, 31, 272
TPP. *See* Two-photon polymerization (TPP)
Trade-off methodology matrix (TOM), 282−283
β-Tricalcium phosphate (β-TCP), 400
Tungsten carbide, 374, 376f
Two-photon polymerization (TPP), 238−239
additive nanofabrication using, 240−246
characterization, 240−243
Raman spectroscopy, 241−243
voxel dimensions characterization, 240
2D fabrication techniques, 237

U
UHTCs. *See* Ultra-high-temperature ceramics (UHTCs)
UL 94 test, 210−211
Ultra-high-temperature ceramics (UHTCs), 361

Ultraviolet (UV), 321
  UV lasers, 422–423
Unconstrained boundary condition, 148
Under-stiff lattice structure, 121
Uniaxial pressing, 377, 378f
Unstable melt pool, 65
Upper extremities, 412
UV. *See* Ultraviolet (UV)

V
Vascular endothelial growth factor (VEGF), 427
Vestosint materials, 187–188
Volume scanning techniques, 405–406
Volumetric energy density, 57
Voxel dimensions characterization, 240

W
Warwick Manufacturing Group, 446–447
Weighted roughness, 108–109

Y
Young's modulus, 140–144
Yttria (Y_2O_3), 171
Yttria-stabilised zirconia, 385